Improving Reliability and Durability of Efficient and Clean Energy Systems

Prabhakar Singh (Primary Contact)
Center for Clean Energy Engineering
University of Connecticut
44 Weaver Road, Unit 5233
Storrs, CT 06268-5233
Phone: (860) 486-8379
E-mail: singh@engr.uconn.edu

DOE Managers: HQ: Dr. Dimitrios Papageorgopoulos
Phone: (202) 586-5463
E-mail: dimitrios.papageorgopoulos@ee.doe.gov

GO: Reginald Tyler
Phone: (303) 275-4929
E-mail: reginald.tyler@go.doe.gov

Technical Advisor: Thomas Benjamin
Phone: (630) 252-1632
E-mail: benjamin@anl.gov

Contract Number: DE-EE0003226

Project Start Date: August 1, 2010

Project End Date: October 31, 2013

Overall Objectives:

Overall objective of the research program was to develop an in-depth understanding of the degradation processes in advanced electrochemical energy conversion systems. It was also the objective of the research program to transfer the technology to participating industries for implementation in manufacturing of cost effective and reliable integrated systems. Research scope included:

- Advanced fuel cell based power generation systems architecture, including renewable hybridized energy conversion and storage,
- Development of novel cell and stack structural and functional materials and validation of their performance under the nominal and transient operational conditions for the evaluation of long-term bulk, interfacial and surface stability, and
- Gain fundamental understanding of chemical, mechanical, electrochemical and electrical processes related to:
  - The utilization of fuels ranging from bio-derived fuels to liquid petroleum to hydrogen,
  - The role of fuel impurities on degradation and processes for removal from feedstock
  - Surface and interface phenomena related to surface adsorption, interfacial compound formation, and electron/ion generation and transport, electrodics and electrochemistry

Novel membranes, heterogeneous catalyst materials and structures were developed and validated through experimentation. Collaborative research programs with industries were developed to improve the performance stability and long term reliability of advanced fuel cells and other power generation systems.

Technical Barriers

This project addressed the following technical barriers from the cross-section of the Hydrogen, Fuel Cells and Infrastructure Technologies Program Multi-Year Research, Development and Demonstration Plan:
(A) Durability
(B) Cost
(C) Performance

Technical Targets

The projects associated with this program addressed technical aspects of stationary fuel cells and stationary fuel processors. Targets were as follows:
Stationary PEM Fuel Cell Stack Systems (5-250 kW) Operating on Reformate

- Cost: $530/kWe
- Durability: 40,000 hours

Stationary Fuel Processors (Equivalent to 5-250 kW) to Generate Hydrogen-Containing Fuel Gas

- Cost: $220 /kWe
- Durability: 40,000 hours
- H_2S content in product stream: <4 ppbv (dry)

Accomplishments

- The Center for Clean Energy Engineering has successfully developed in total 18 industrially sponsored Research, Development and Engineering programs in the field of clean and sustainable energy.
- These collaborative programs have leveraged DOE funds with industrial financial support to accelerate the development of advanced materials, cell and stack components, catalysts and fuel cleanup, and balance of plant sub systems.
- The industrial programs supported the mission of EERE through the development of reliable and cost effective advanced clean and efficient fuel cell power generation systems.

Introduction

The scope of this energy systems and technology research and development initiative focused on the development and validation of the mechanistic understanding and subsequent creation of novel cost effective materials to mitigate degradation processes. Through a unique collaborative program with industry we evaluated and solved technology gaps through joint industry/university programs. These relationships accelerated the development and deployment of clean and efficient multi-fuel power generation systems.

The scope of the research programs included the identification and prioritization of the technology gaps and research needs along with the development of enabling technologies that met the overall stack and balance of plant improvements from a Durability, Cost and Performance perspective. Specifically the performance stability and reliability of the power generation systems were improved through the implementation of advanced materials and fabrication processes. Technical areas of interest, that were addressed by the industry/university collaborations included: a) performance stability and reliability of fuel cell systems, b) fuels, fuel processing and catalysis, c) advanced functional and structural materials,

processes and systems, d) hydrogen storage and power management and e) renewable energy and resources.

Approach

The approach used for this program consisted of developing collaborative industry / university research programs aimed specifically at accelerating the development and deployment of clean and efficient multi-fuel power generation systems. Through a competitive process faculty developed relationships with industry that provided additional amounts of cash and in kind support thus leveraging funding available through this program. By requiring a financial commitment from industry this methodology ensured that technology problems of commercialization relevance would be addressed. Industry collaborative programs have been developed with UTC Power, FuelCell Energy, UTC Research Center, nzymSys, NanoCell Systems, APSI, Oasys Water, Nissan, Corning, Proton OnSite, BC Hydro, Sci-Tech and WR Grace & Company. The program topics have addressed issues ranging from performance stability and reliability of fuel cell systems to fuels, fuel processing and catalysis and finally including advanced functional and structural materials, processes and systems.

Project Title: Role of Multi-Scale Water Transport in Dynamic Performance of Polymer Electrolyte Fuel Cells
Industrial Partner: NISSAN Motor Co.
PI: Ugur Pasaogullari

Project Objective and Goals:
The project objective was to develop a computational modeling framework of transient multi-phase water transport in polymer electrolyte fuel cells in multiple length scales. Project combined characterization and visualization experiments with modeling studies, the models aimed to aid in describing the dynamics of the PEFC operation and detailed validations aimed to be performed against the transient performance and species distribution data collected from instrumented cells operated at NISSAN, as well as transient liquid water distribution obtained from imaging studies. The imaging studies utilized national user facilities such as Neutron Imaging Facility (NIF) of NIST Center for Neutron Research (NCNR) and synchrotron X-ray facilities at Advanced Photon Source (APS) at Argonne National Laboratories to obtain high-resolution images of micro-structure and liquid water distribution in porous layers of PEFC. The ultimate goal of the project was to provide, for the first time, a fundamental understanding of the complex interactions between the transient two- phase heat and mass transport in multiple scales on the performance and degradation of PEFCs.

Background: Among the primary goals of EERE are to reduce the cost and increase the life of the automotive fuel cells to accelerate commercialization and market penetration. This project targets both aspects by developing the required understanding for operating fuel cells at very high power densities (> 2 W/cm^2) that decreases the size of the fuel cell stack and auxiliary balance of plant components. At these high power densities, fuel cell performance is limited by mass transport, which is further complicated by presence of liquid water and much higher heat generation rate. This project intends to enhance the current understanding to enable very high power density operation.

Project Tasks:
Project tasks have been broadly split into two groups: 1) Experimental characterization and 2) modeling. Experimental characterization includes 1) Micro and nano X-ray micro-tomography of porous layers, 2)

In-situ Neutron Radiography. The modeling task includes the development of a two-phase, transient multi-dimensional CFD code. Both experimental and modeling tasks have been performed in parallel.

Status:
The experiments with APS and NCNR were conducted in August and September 2012, respectively. The modeling tasks have been implemented by Star-CD software. In the following paragraphs, a summary of our experimental and numerical accomplishments is presented.

Micro X-Ray tomography Characterization of Gas Diffusion Layer (GDL) of a PEM fuel cell

Micro X-ray Computed Tomography (CT) of Xradia (Micro XCT400) have been used at the Center for Clean Energy Engineering, University of Connecticut for micro structural analysis of PEM fuel cell GDLs. First, optimum imaging parameters have been determined by conducting several experiments and tuning the parameters. PEM fuel cell components are under high compression pressure of assembly while operating. A stage was designed to study the changes in micro structure of GDL under compression. The sample holder can be loaded with various springs that can adjust the compression load on the substrate. In addition, the load discs mimic a PEFC flow plate structure with open channels and current collector lands, and a number of load discs are made to investigate different land/channel widths. The sample holder is shown in Fig. 1 and can be used to compress GDLs at different pressures. Using the sample holder, several images were taken to determine the optimum imaging parameters. To get a better resolution and favorable transmission, it was found that the x-ray power should be set to a minimum and we need to work with a higher magnification.

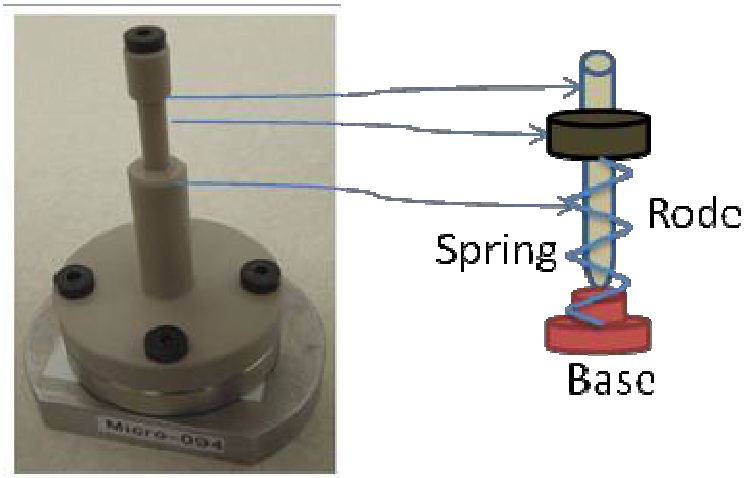

Figure 1 Compression stage for XCT experiments

2D and 3D micro structure of GDLs are visualized. Figure 2 show the 2D and 3D micro structure of TGP GDL. Carbon fibers and open pores can be distinguished. It can be clearly seen that there is non-homogeneity of the GDL micro-structure in every direction. Pores are in different sizes which affect liquid water accumulation spots. This can be more specifically investigated by an in-situ characterization.

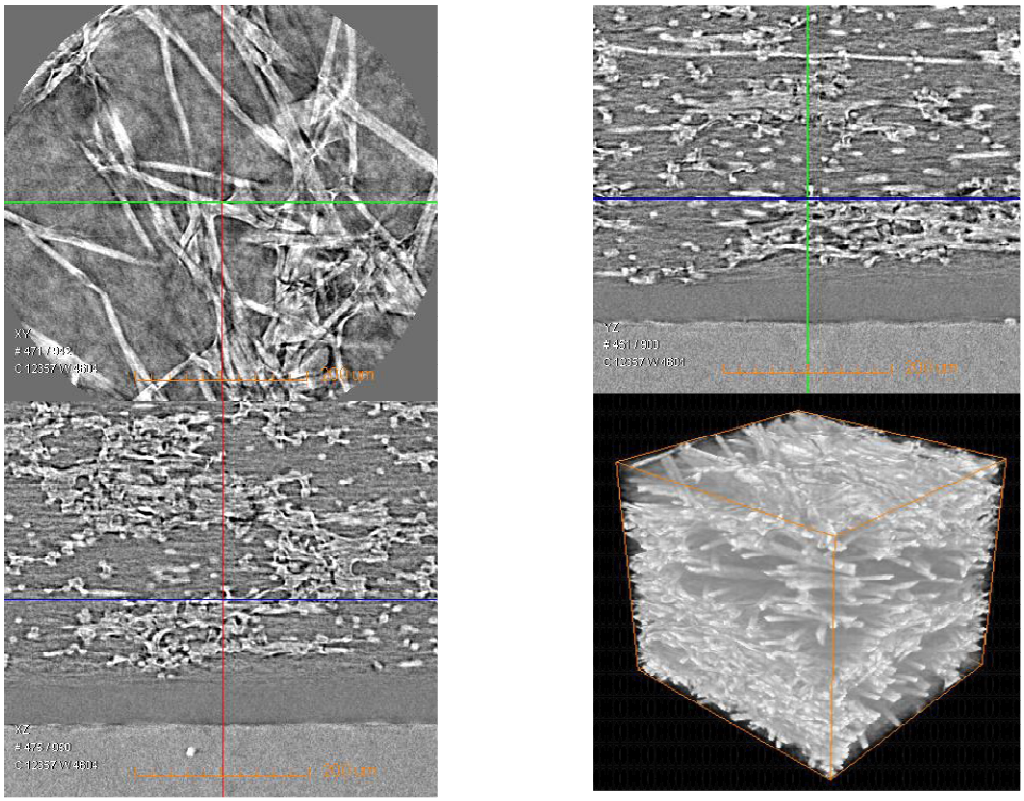

Figure 2: GDL micro structure illustration

With the designed sample holder, GDL micro structure under compression pressure was visualized. The results were obtained at the compression pressure of 0, 1, 2, and 3 MPa. The effect of compression pressure on porosity distribution through the thickness of GDL is shown in Fig. 3 for TGP-H-120 PTFE untreated. Lower porosity can be seen for the higher compression.

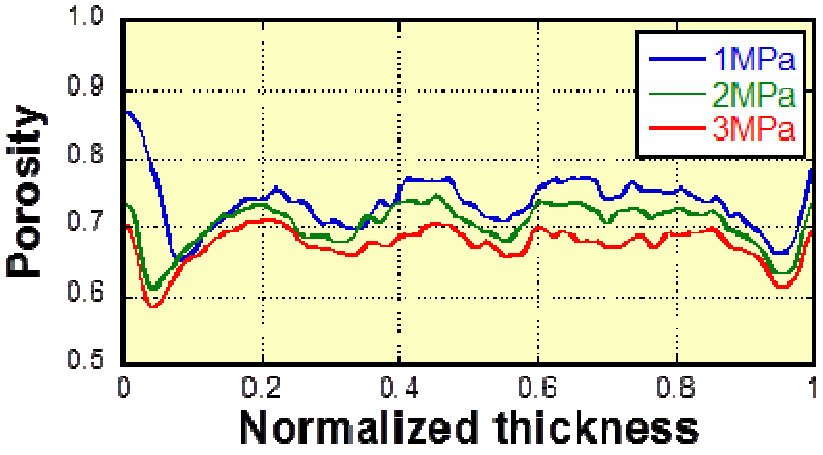

Figure 3 Porosity Distribution

Nano X-Ray Computed Tomography Characterization of Micro Porous Layer (MPL) of a PEM fuel cell

For Micro X-ray analysis, the spatial resolution was about 1 micrometer which is enough to resolve the micro structure of the GDL fibers and pores. With the Nano x-ray CT scan experiment at the APS, we were able to increase the resolution down to 20 nanometer; therefore, visualization and investigation of MPL nano structure were possible. Figure 4 displays 2D projections and 3D stack of an MPL.

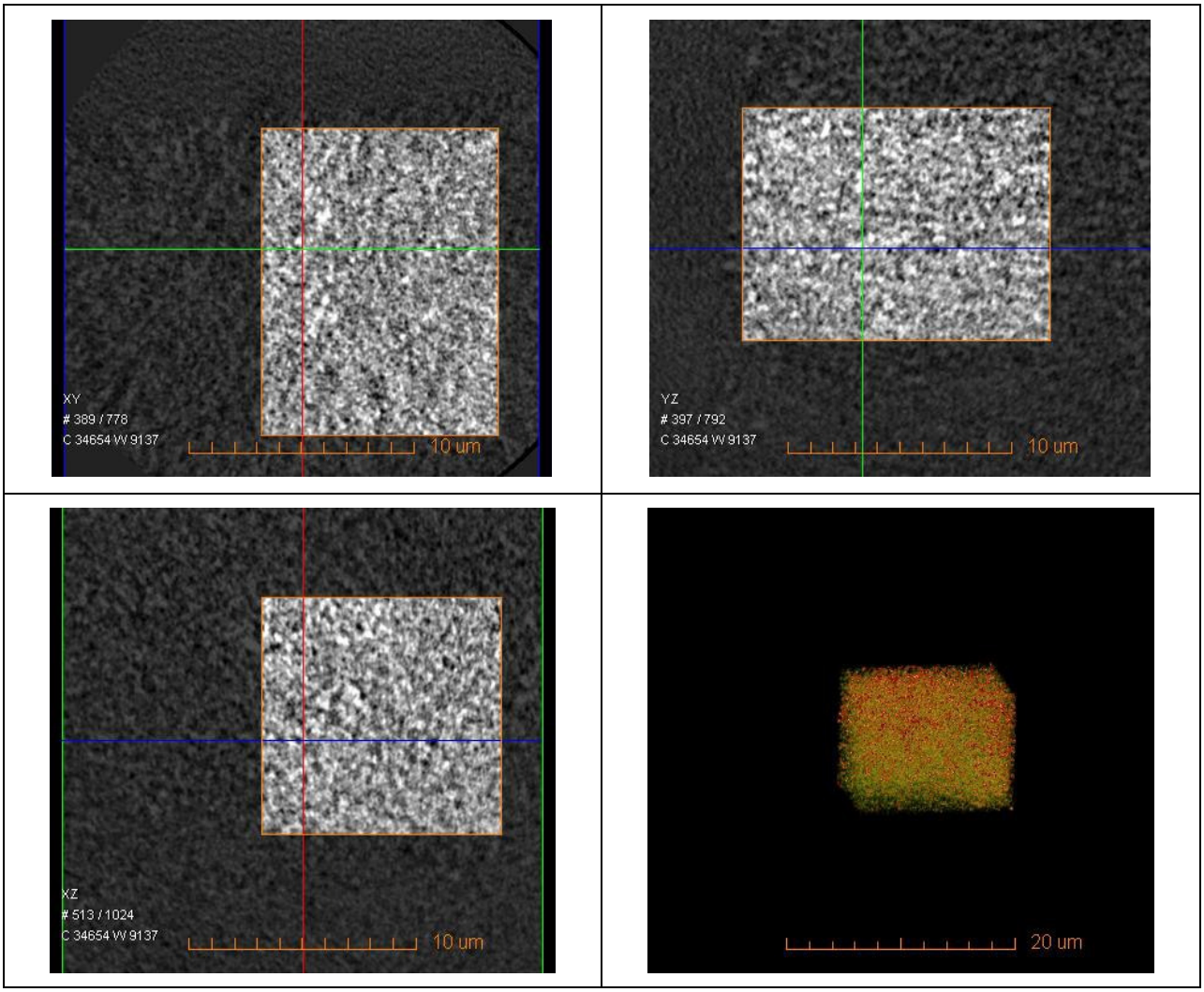

Figure 4. Nano X-ray tomography of a MPL

Using the APS synchrotron nano X-ray, not only the pixel size was reduced but also the acquisition time was reduced to less than 1 hour, compared to micro X-ray of XRadia with the order of few hours. Since the spatial resolution was fine it was possible to distinguish between solid and pores and the smaller pore sizes were observed. Further data analysis showed the potential of APS X-ray source for the study of transport phenomena in MPLs.

In situ Neutron Radiography for water visualization

With our neutron radiography experiment at NIST, the role of surface wettability on liquid water behavior in a PEM FC at very high cell current density operation has been investigated. In addition, the effect of ionomer equivalent weight (EW) in catalyst layer is explored. The experiments performed for 1) cathode flow field PTFE coated, 2) anode flow field PTFE coated, 3) a low equivalent weight, and 4) a normal equivalent weight. Putting PTFE coat in the anode side does not affect the cell performance. However, it can be used as a base case for performance enhancement measurement for the other three cases. Figure 5 shows a sample result of water thickness distribution in a cell. All data series were analyzed to greatly help understanding the role of PTFE coating on bio polar plates (BPP).

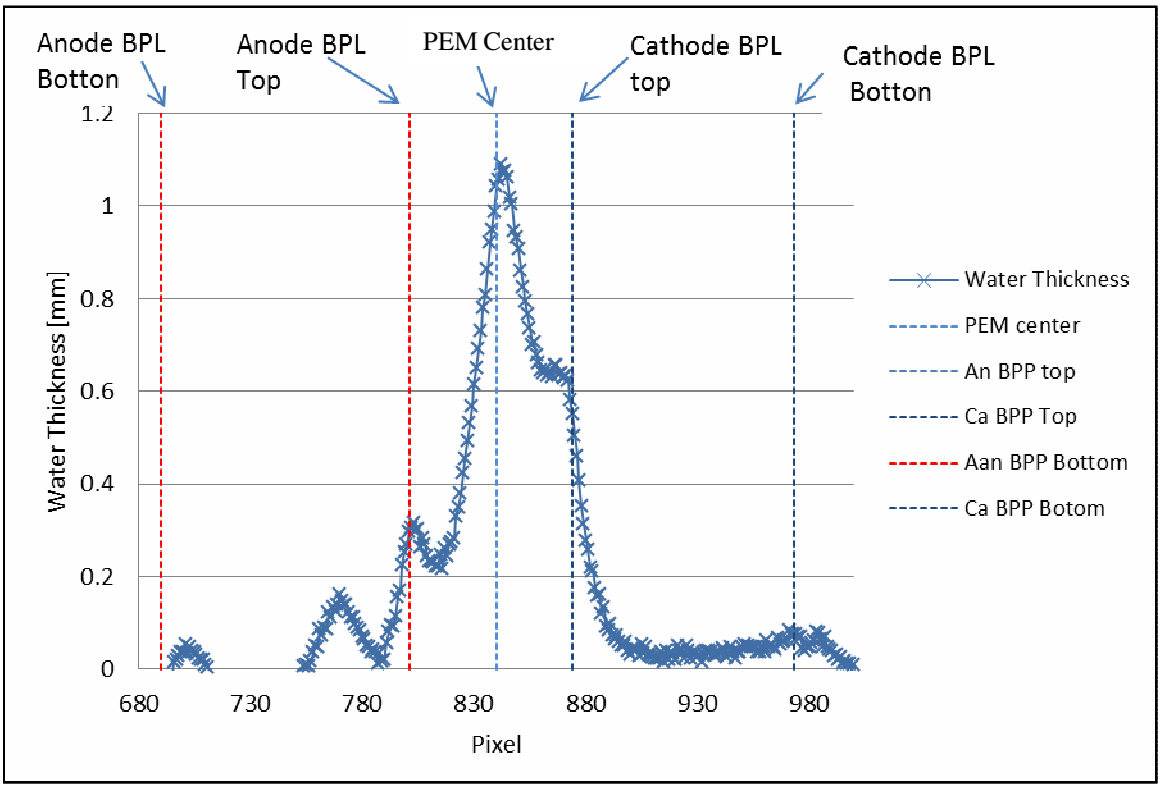

Figure 5. Water thickness distribution in an operating PEM fuel cell

Transient modeling of transport phenomena in PEM fuel cells:

For the modeling, first, a steady-state non-isothermal multi-phase model based on multi-phase mixture (M2) model employing a Kirchhoff Transformation (KT) was developed. As the next step, the model extended to transient. In the transient analysis, since the KT could not be used anymore, we first considered a single phase case. For the simulation purpose, a commercial CFD solver named star cd is used. To be able to go ahead with the transient analysis all modules written in the post file were moved to source terms.

Figure 6 show shows the dynamic response of a cell for a step change in cathode channel inlet relative humidity (RH_C). The RH_C is reduced from 26% to 50%. An undershoot is seen at the beginning followed by a sharp increase. At the time 0.45 sec, a steady state condition is reached. At the beginning there are factors affecting the cell current density: 1) oxygen gas activity decreases, and 2) membrane hydration

improves. These two factors compete each other resulting an undershoot. As time increases the effects of membrane hydration dominates and the cell current density profile goes flat ultimately.

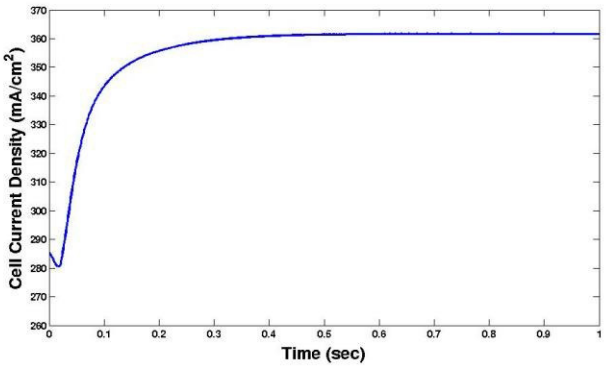

Figure 6. Cell transient response for a step change in cathode channel relative humidity

Figure 7 displays the dynamic response of a cell for a step change in cell voltage. The cell voltage is reduced from 0.6 to 0.5 V. In the beginning, an overshoot is captured which is caused by initial richer oxygen concentration at the high cell voltage.

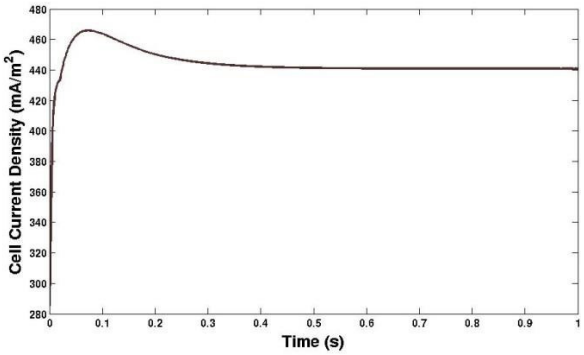

Figure 7. Cell transient response for a step change in cell voltage

Patents: None

Publications / Presentations: None

1. Fu, R.S., Khajeh-Hosseini-Dalasm, N., and Pasaogullari, U., "Numerical Validation of Water Transport in Polymer Electrolyte Membranes," ECS Transactions, 50 (2012).

Project Title: Modeling Resin Flow in PAFCs GDLs
Industrial Partner: UTC Power (UTCP)
PI: Rajeswari Kasi, Prabhakar Singh

Since this is proprietary work in collaboration with UTCP, I am unable to provide detailed results and discussions in the open forum.

Objectives:
UTC Power (UTCP) is interested in attaining stable graphitized gas diffusion layers (GDLs) that are used in phosphoric acid fuel cells. GDLs coated with catalyst are used to facilitate electrochemical reactions in PAFCs manufactured by UTCP. Resin flow into carbon fiber substrates blocks the open pore structure of the fibers impacting mass flow of various components to the catalyst layer. Furthermore, attaining stable GDLs is important to (1) increase the life time of GDLs, (2) efficiency of the power plant and (3) in lowering the cost of stationary and backup power. Thus in keeping with energy efficiency and renewable energy (EERE) effort of DOE, the stability of GDLs is important for fuel cells to provide a clean, reliable, low-maintenance option for critical energy needs. So, UTCP is interested in generally understanding the morphology of these GDLs and overall resin distribution.

Approach and Significant Technical Achievements:
To address this issue, we have used optical imaging tools to investigate the morphology of the carbon scaffold at every step of production of the GDLs. This allows us to establish where the carbonized resin is present in the final substrate. UTCP has supplied us with proprietary materials made via proprietary processing conditions and using imaging as a tool we have been able to identify 2 samples that show optimal carbonized resin distribution and overall morphology in the GDLs. Our imaging studies have proven to be a complementary tool to UTCPs subscale testing protocol to identify the best scaffolds that show optimal properties for use in PAFCs. In closing, this collaboration between UCONN and UTCP has resulted in identifying materials with optimal morphology and properties for use as GDLs in PAFCs, in keeping with the EERE efforts of DOE. Furthermore, the knowledge gained from this study will be useful to implement in other examples of supported catalysts where optimal distribution of catalytic sites is essential for best catalytic performance. Some of this knowledge has been utilized in development of scaffolds for batteries and other electrochemical devices.

Presentations and Publications:
Because of the proprietary nature of this research, this work has not been published or communicated in any conference except for presentations to the DOE program managers and collaborators/sponsors.

Side-by-Side Project with the main DOE/UTCP Project

Project Title: Design of polymer-ionic liquid gel composites with optimal conductivity and mechanical features for electrochemical device applications
PI: Rajeswari Kasi, Prabhakar Singh

Objectives
After discussions with the program manager during the summer visit, I decided to also focus on a side-project that was completely conceived in my lab and has no input from UTCP. This project was performed side-by-side along with the main DOE/UTCP project titled: Modeling of resin flow in PAFC GDLs. This current side-project builds up on some of other projects that are on-going in my group. Additionally, since the intellectual property belongs entirely to us, we would be able to leverage these results to apply for grants through other funding agencies.

We are interested in developing polymer-ionic liquid gels composites that will serve as materials for (1) solid-state electrochemical devices and (2) porous scaffolds for catalysis (akin to GDLs). The ionic liquid has many interesting properties including good conductivity and use as solvents for green reactions but has no physical integrity. The use of polymer as a mechanical enhancer not only overcomes the problems of liquid electrolytes, but also offers other features such as shape versatility and flexibility in design (thickness, area, and shape). Specifically, we want to develop ion-gels consisting of a swollen polymeric

network in an ionic liquid that constitute a promising class of solid state electrolytes owing to their combined advantages of good mechanical properties and high ionic conductivity which can be used in Li-ion batteries, electrochemical devices, sensors, electromechanical actuators, gas separation membranes, and dye-sensitized solar cells. Additionally, depending on the polymer choice, long-range alignment is feasible using thermal or magnetic fields and this may impact long-range conductivity.

1-butyl-3-methylimidazolium tetrafluoroborate, [BMIM][BF_4], has one of the highest conductivities observed in the general class of ILs and based on task-specific properties, it stands out as a good electrolyte solvent for lithium ion batteries due to its high ionic conductivity, Li-salt solubility at room temperature and broad electrochemical window with high anodic stability (5 V) compared to other ionic liquids. The only pertinent paper on [BMIM][BF_4] ion-gels using polymers is by in situ copolymerization of acrylonitrile (AN), methyl methacrylate (MMA), poly (ethylene glycol) methyl ether methacrylate (PEGMEMA) in [BMIM][BF_4]. Ion-gels from these random copolymers are obtained at high concentrations (≥ 30 wt%) with conductivities significantly lower than the bulk [BMIM][BF_4]. Nevertheless, there have been neither reports on the gelation of [BMIM][BF_4] by macromolecular self-assembly nor mechanical, thermal and conductivity investigations of the corresponding ion-gels. Thus the current study focuses on designing highly conductive polymeric ion-gels in [BMIM][BF_4] at lower concentrations through the self-assembly of block copolymer which are promising candidates for solid-state electrolyte applications.

Approach and Technical Achievements:
We have designed a new set of ion-gels prepared via self-assembly of poly(N-tert-butylacrylamide-b-ethyleneoxide-b-N-tert-butylacrylamide) triblock copolymer in [BMIM][BF_4] of PEO molecular weight 20,000 Da and varying composition of the acrylamide block. Transparent, strong ion-gels with significant mechanical strength can be formed at low concentration of the triblock copolymer (~5 wt %) with acrylamide block length of 13,000 Da (33 wt% polyacrylamide). These gels are thermoreversible and thermally stable showing 1-4 % weight loss up to 200 °C in air atmosphere. Comprehensive mechanical and conductivity studies have been performed. Gelation behavior, mechanical properties and ionic conductivity of these ion-gels can be easily tuned by varying the concentration or N-tert-butylacrylamide block length in the triblock copolymer. These new non-volatile, reprocessable, mechanically robust, [BMIM][BF4] based physical ion-gels obtained from a simple and convenient preparation method are promising materials for solid- state electrolyte applications.

Publications / Presentations:
1. Sharma, N.; Rubinder, R.K.; Zhou, Y.; Kasi, R.M.,* Physical gels of [BMIM][BF4] by N-tertbutylacrylamide/ethylene oxide based triblock copolymer self-assembly: Synthesis, thermomechanical and conducting properties. Journal of Applied Polymer Science, 2013, 128, 3982-3992.

Grants applied for:
1. ACS PRF – funded- we are currently pursuing development of electrochemical devices using ion gels from new polymer scaffolds and ionic liquids.

Project Title: Fuel Cell Electrode Microstructure: Nanoscale Stability and Efficiency
Industrial Partner: UTC Power (UTCP)
PI: Bryan Huey (with PhD student Yasemin Kutes)

Status:
Main results focus on two key aspects of fuel cell electrode microstructures.

First, atomic force microscopy ('AFM') reveals profound differences in the catalytic nanoparticles in their raw state and as a floc (upon Teflon coating). The particle size is larger, Teflon is occasionally drawn into fibers by the manufacturing process, and the <50nm particles common in the raw material increases to >100nm following Teflon coating.

Second, upon phosphoric acid ('PA') loading of the electrode, the Teflon is occasionally found to separate from the underlying catalyst particles. This is clearly observed by AFM, both in topographic images where the Teflon appears to have delaminated from the catalyst, as well as in simultaneous AFM phase contrast which reveals the local mechanical compliance. Notably, Teflon/catalyst separation was only observed following PA loading, but never before PA exposure. It is unclear whether the PA loading procedure, or the simple act of Teflon swelling upon PA exposure, causes such rupture.

Patents: None

Publications / Presentations: None

Project Title: High Performance Phosphoric Acid Fuel Cell Electrodes from Soluble Polymers
Industrial Partner: ClearEdge Power, South Windsor, CT
PI: Ned E. Cipollini

Project Objective:
NG-fueled PAFCs meet or surpass most 2012 DOE requirements for distributed power including efficiency and lifetime, but factory costs are 5-10X Target. This project addresses factory costs at a fundamental level by lowering manufacturing process costs and improving power densities.

Executive Summary:
Prior to this program, we showed that the use of a soluble TAF binder in place of PTFE allowed simplification of fabrication with surprising performance benefits. We linked these performance benefits to the higher uniformity of the polymer coating on the catalyst and the coating's ability to conform to the catalyst surface. Both of these properties lead to thinner and more uniform phosphoric acid films on the catalyst surfaces and concomitant lower mass-transport losses. Unfortunately TAF is orders of magnitude too expensive for commercial use and cheaper alternatives were sought; none were found.

Alternatively, several papers and patents indicate that the inexpensive, commercially available fluoropolymers PTFE, FEP and PFA were soluble in fluorocarbon solvents above the melting point of the fluoropolymer. We did not observe any evidence of this for PTFE. Samples made with FEP dispersion indicated that this material was too soft at operating conditions to be useful. Experiments indicated that PFA dissolved to some extent at 330°C, but did not remain in solution at or near room temperature.

The present CDP Program is an extension of the above information. Therefore, we mixed PFA and catalyst and heated both in the solvent to 330°C to coat the catalyst. SEM pictures indicated that this occurred. However, because the PFA was not soluble at room temperature, the PFA-coated catalyst particles would not stick to each other making processing almost impossible and resulting in poor adhesion to substrates and poor performance. HRSEM micrographs showed that the PFA coating was uniform on the catalyst, so we attributed the poor performance to the meso-structure ~1 to 10 μ) formed. The performance was improved with sintering, but never achieved a level on-par with that of SOA PAFC electrodes.

At this point, the use of soluble polymers for PAFC electrodes was at a dead end. The CPD Program directors allowed us the freedom to re-direct our efforts from the use of soluble polymers for PAFC electrodes to that of alternate (cheaper) fabrication of PAFC electrodes with performances equal to or better than SOA electrodes.

Performance benefits of the fluoropolymer were linked to its ability to flow over the catalyst surface, with very low viscosity in solution. We addressed the fluoropolymer flow over the catalyst in the following way. Higher melt viscosity of PTFE ($\sim 10^{12}$ P) is not processable by conventional extrusion and molding techniques. HRSEM micrographs show that PTFE does not flow over the catalyst surface during heat treatment of the PAFC electrodes. PFA was developed to afford standard extrusion and molding techniques of normal thermoplastics while providing the chemical stability of PTFE. The melt viscosity of PFA is $\sim 10^{6}$ P and may allow significant flow over the catalyst surface during heat treatment and, in fact, provided benefits similar to that of TAF, though not to that extent.

Prior art, indicated significant migration of PFA during sintering causing deleterious de-wetting of adjacent porous layers, carbon papers used for electrolyte storage and in-plane and through-plane electrolyte transport. We circumvented this problem by forming a free-standing electrode and sintering the PFA before it ever contacts the carbon paper.

Free-standing electrodes were formed by adding ~ 10 w % PTFE to the catalyst-PFA flocs. The PFA was fibrillated by rolling the floc to thickness controlled by shims. Lubrication was provided by a light-weight oil. Once rolled, the sheet has sufficient strength to be handled and sintered into an electrode. The sintering temperature used for PFA, 330°C, is well above its melt point, 305°C, and below that of PTFE, 348°C (1st melt point of dispersion), so that structural integrity is maintained during sintering.

Therefore, re-direction of the program concluded with the formation of free-standing PAFC electrodes of well-controlled thickness' which could be stacked with other cell components for testing. We are confident that free-standing, wettable layers of matrix could be made by similar methods to be stacked with the electrodes.

Novel Prior Findings as Background to the CDP Program:
Stability concerns limit the list of useful materials in phosphoric acid fuel cells (PAFC's). Therefore, PAFC-electrodes are compositionally simple; they contain only a Pt-alloy catalyst dispersed as small particles on a carbon support, PTFE, porosity and phosphoric acid in the active area. The fabrication determines the distribution of porosity and of PTFE, which in-turn controls the distribution of gas reactant, and phosphoric acid electrolyte.

Introduction, State of the Art PAFC Electrodes:
State of the art PAFC electrodes are made by a process lacking sufficient control to assure manufacturability and quality control. Significant effort is required in powerplant production, e.g., acid addition and stack electrolyte fill cycle, to compensate for for manufacturing variability.

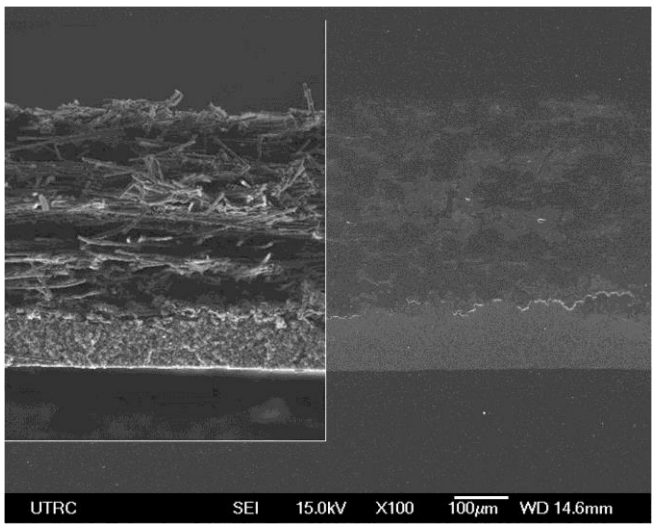

Figure 1: SEM of aUTC-Production cathode. Left fractured in LN2, right polished cross section. Top layer carbon substrate, bottom layer catalyst layer.

Figure 1 shows a cross section of a typical UTC-production cathode, liquid N_2 fracture on the left and polished cross section on the right. The subject of this report is the catalyst layer, the bottom layer in the figure, though the word "electrode" refers to the assembly. The liquid N_2 fracture brings out the graininess of the electrode while the polished cross shows the penetration of the catalyst layer into the substrate. On close inspection, both micrographs show a bimodal pore size distribution of the catalyst layer.

Details of the fabrication process are proprietary to UTC, but a general description lies within the public domain.

The processing steps are outlined below.

1. Carbon supported alloy catalyst is mixed with aqueous PTFE dispersion, surfactants, water, and phosphoric acid in specified ratio and the pH is adjusted.
2. Shear mixing makes a slurry of the components.
3. High energy mixing assures good mixing.
4. The suspension is dewatered to concentrate the slurry.
5. The suspension is slowly dried into pellets over several days.
6. Pellets are ground mechanically and then fluid milled.
7. The resulting "cloud" of PTFE-catalyst mixture is vacuum deposited onto a carbon-fiber paper.
8. Density of the deposited layer is adjusted by rolling.
9. The PTFE is sintered near its melting point for several minutes.
10. Several acceptance tests are performed and if the electrodes are acceptable, they are built into PAFC stacks.
11. Electrolyte is introduced into the electrode by proprietary high-potential cycles.

Mechanical grinding and fluid milling cause the graininess of the production electrode in Figure 1 and the vacuum deposition causes penetration of the of the catalyst layer into the carbon substrate. The slight skinning effect – bright film on the bottom of the electrode in Figure 1 left, is due to the rolling process.

The microstructure of the electrode and the diffusion and ionic resistance of the electrode is set by the initial wet processing steps. These steps determine the intimacy of interaction. Our data suggest the more intimate the mixing, the better the performance. The intimacy of the mixing is a major variable in the processing of the SOA electrodes.

Cell performance is determined by the coating characteristics of the PTFE binder on carbon catalyst support. The nature of the PTFE coating determines the properties of the phosphoric acid films on the carbon surface which are directly related to the (diffusion) limiting current and iR of the electrode. In turn, the coating characteristics are influenced by the intimacy of mixing, surface chemistry of the carbon, cohesion of the PTFE, and the amount of energy in the mixing.

We have observed two types of PTFE coatings on the carbon support. The extreme cases are shown in Figure 2. Inset (c), shows the catalyst by itself at an equivalent magnification as micrographs (a) and (b). The white arrows point to the primary carbon particles of the catalyst support which are roughly 50 nm in diameter. Catalyst particles are aggregates of these primary carbon particles with Pt deposits too small to be seen in the micrographs.

Figure 2: High Resolution SEM micrographs of freeze fractures of unsintered PAFC anodes (a) and (b), HRSEM of catalyst, inset (c) with schematics of the differing microstructures (d) and (e). Colors in (d) and (e) are black=carbon, red=Pt, blue=phosphoric acid, turquoise=PTFE. See text for further description.

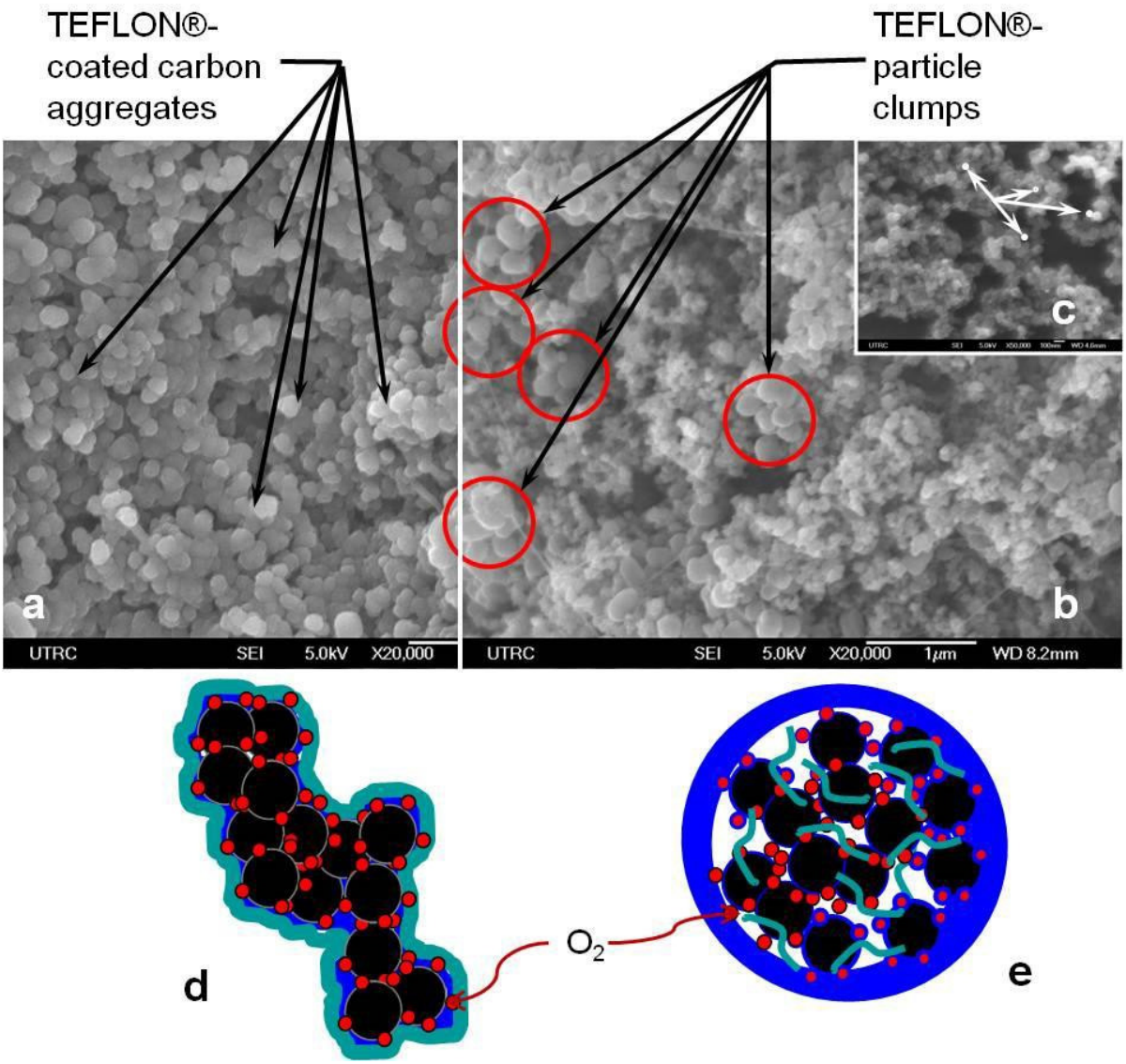

PTFE is supplied as an aqueous dispersion of ~200 nm diameter particles. Cluster of 3 to 8 PTFE particles are shown in the red circles of Figure 2b. Micrograph (a) shows a uniform coating of PTFE on the carbon surface. Clusters of 2, 3, or 4-primary carbon particles are encapsulated by a coating of PTFE. In Figure 2a, we see only PTFE, and no carbon particles – compare to Figure 2c – and no PTFE particles. A schematic of this type of PTFE coating is represented by the aqua color in Figure 2d. The phosphoric acid phase is introduced by the electrolyte fill cycle. The uniform, thin layer between the PTFE and carbon phase is represented by the deep blue color in Figure 2d.

In contrast, Figure 2b shows much less intimacy of the mixing between catalyst and PTFE though both flocs were made by the same nominal process. The "clumped" distribution is a mixing of PTFE and catalyst on the particle scale. Again, the red circles in Figure 2b show clumps of 3 to8 PTFE particles.

Comparison of the catalyst in 2b and 2c shows that the primary carbon particles are not coated with PTFE. In this case the interaction of PTFE and the catalyst surface is induced in the sintering step where the PTFE softens and surface energy causes PTFE to spread over the catalyst surface. The high viscosity of PTFE at its melt point prevents intimate mixing at this stage and the resulting electrode structure is inherently different for this case. A schematic diagram for an electrode with a "clumped" distribution of PTFE after sintering is shown in Figure 2e. The clumped nature forms a highly hydrophobic region in the center of the agglomerate while the absence of PTFE at the outside of the agglomerate causes a flooded layer of phosphoric acid.

Since the reactant-gas permeability of PTFE is much larger than hot phosphoric acid, and the PTFE film is thinner or equal to the thickness of the phosphoric acid film, higher diffusion currents are expected for the uniform PTFE distribution than the clumped distribution. Most production electrodes are combinations of these two extreme cases, but fall into mostly one or the other.

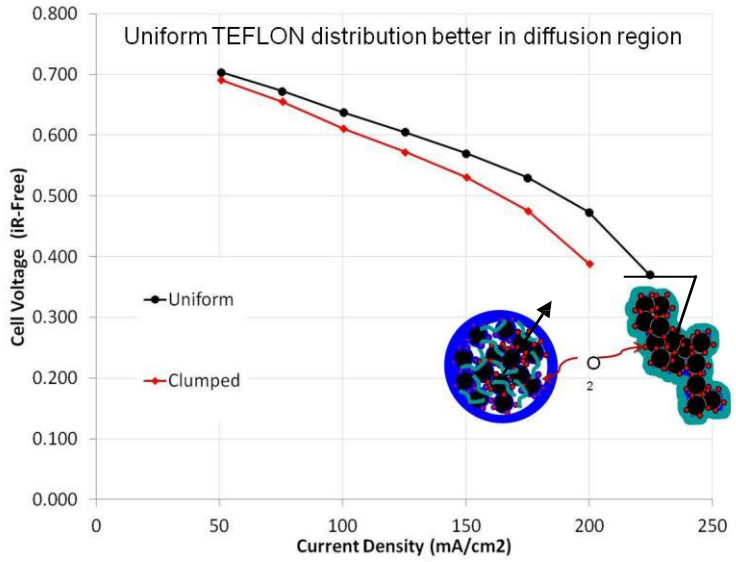

Figure 3: H_2/Air subscale data for the cases where HRSEM show uniform and clumped PTFE distributions in the cathode.

Figure 3 compares the H_2/Air performance of two subscale cells with cathodes that HRSEM have shown to have a uniform and a clumped PTFE distribution. Both diffusion and internal ionic resistance are superior in the cathode with the uniform PTFE distribution. Note that the benefit of the uniform PTFE distribution becomes larger as the oxygen concentration becomes lower.

Therefore, we have shown that for SOA PAFC electrodes, a uniform PTFE distribution shows better performance due to lower electrode internal resistance and lower mass transport losses. The catalyst activity is not affected by the PTFE distribution implying that the area of contact between catalyst and electrolyte is the same in both cases.

Inspection of a large number of PAFC-electrode flocs has shown that the SOA electrode processing does not often lead to uniform PTFE distributions. Very roughly 5% of the flocs made under the same conditions lead to uniform PTFE conditions.

Preliminary Experimental Results and Discussion for Soluble Teflon:

The micrograph in Figure 2a is essentially identical to that of a high-performance PEM electrode. In that case, the NAFION® ionomer is soluble in a solvent which is used to disperse the catalyst. The ionomer self-assembles onto the catalyst surface producing a uniform coverage. This concept was borrowed for PAFC electrodes and a soluble form of TEFLON® was used in place of NAFION®. We also borrowed the inking process of making electrodes which lead to a PEM-like structure of the new electrodes. Though PAFC cathodes are ~10X thicker than PEM electrodes the performance is improved over the SOA electrodes.

A suitable replacement for PTFE, denoted by TAF, is soluble in FLUORINERT, a perfluorinated solvent from 3M. FLUORINERTs are actually a series of solvents with perfluorinated aliphatic hydrocarbon branches tied together by either nitrogen or oxygen atoms. FC770 proved convenient.

Cathode catalyst was dispersed in of FC770 using a high-shear mixer. The soluble TEFLON solution was added to this slurry while mixing. Then the mixture is subsequently dispersed with ultrasonics. The slurry was then sprayed onto a heated piece of carbon paper and hot pressed at a temperature far below the melting point of the polymer while still wet with solvent.

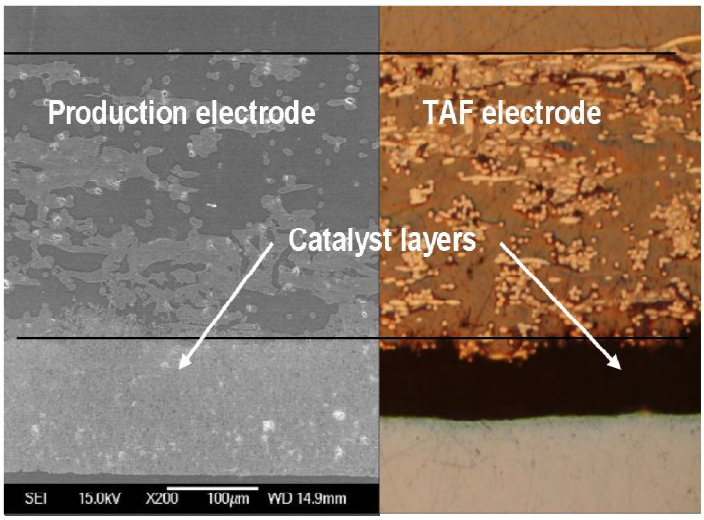

Figure 4: Polished cross sections of production and experimental (TAF) cathodes showing the electrode substrate, top layer, and the catalyst layer.

The catalyst-layer fabrication, though cumbersome, shows viability for simplifying the SOA method for making catalyst layers. For example, hot rolling could replace hot pressing; rod coating could replace spraying and obviate the need for hot pressing.

Figure 4 shows a polished cross section of one of the initial TAF electrodes. The catalyst layer loadings are the same for both electrodes with the TAF layer approximately 50% of the production layer so the porosity of the TAF catalyst layer is only about ½ that of the production catalyst layer. Therefore, higher diffusion losses were expected for this electrode, but see below.

The fabricated cathodes were coated with ~ 25 µ of SiC matrix and mated with a matrix coated production anode. Electrolyte was introduced into the electrodes by a standard proprietary subscale fill cycle.

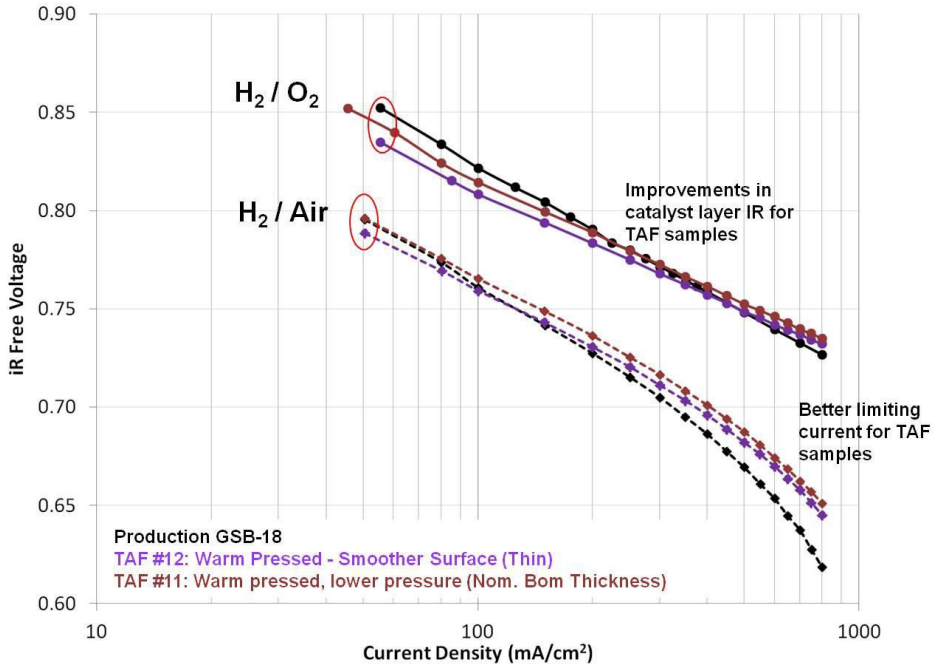

Figure 5: Subscale performance of thin cathode TAF#12 and nominal thickness cathodes TAF#11 and typicalUTC-production cathode. Conditions are 175 °C and nominally 99w% phosphoric acid low hydrogen and oxygen utilizations.

Figure 5 compares the subscale performance of production, and TAF samples # 11 and 12 in both H_2/O_2 and H_2/air. TAF binder has little improvement in oxygen and in the kinetically controlled region of the air curve over PTFE in the production cathode. However, the TAF binder shows diffusional and (internal) resistive benefits above ≈ 250 mA/cm^2.

Both TAF and PTFE are non-interacting with platinum surfaces, as evidenced by the electrochemical areas of all three cathodes being equal, so no mechanistic benefit was expected. However, a kinetic effect, due to higher oxygen solubility in the fluorocarbon phase than in hot phosphoric acid was postulated to explain the improvement by PFSA (NAFION®) [1] and PFSI [2] binders in PAFC. No such benefit is seen here, most likely because the PTFE electrodes already have benefit of increased oxygen solubility.

The diffusional benefit of TAF is accentuated as the oxygen pressure is decreased. For example, limiting cathode current in 4% oxygen increased from 250 to 350 mA/cm^2 when TAF substituted for PTFE. Therefore, the small benefit from TAF shown in Figure 5 with low utilizations will be much larger in a real PAFC which operates with oxygen concentrations ranging from ≈ 21 % to 8%. Figure 6 shows the benefit of TAF under real PAFC operating conditions.

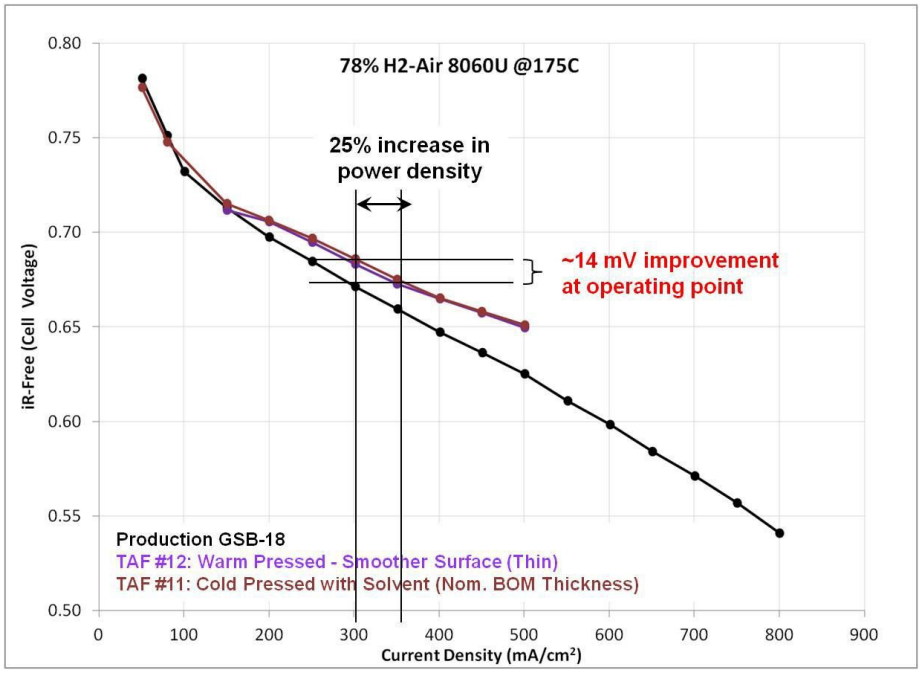

Figure 6: Subscale samples operating under simulated PAFC conditions with reasonable utilizations show large impact in power density and possibly, cost.

Both TAF samples in Figures 5 and 6 show little difference in performance even though the cathode thicknesses are different, about 0.5 and 1X of nominal. Further, both are better than the PTFE baseline which, of course, has the nominal cathode thickness. The electrode structure is also different. The TAF electrodes are PEM-like having a narrow distribution of small pores. The production cathode pore size distribution is bimodal; large gas pores are formed from the fluid milling process, several microns in diameter whereas the smaller pores formed from the flocing process are more PEM-like.

Performance independent of cathode thickness suggests that oxygen transport through the electrode is not limiting. Also, we infer that the large- gas-diffusion pores are unnecessary, due to the better performance of cathodes without them. Further, the data suggests that permeation through the polymer film and/ or a phosphoric film over the catalyst is limiting.

Pure cathode catalyst (inset) and a TAF electrode are compared in Figure 7. The figure shows that TAF occupies some of the ~100 nm pores seen in the pure catalyst, but the coating is not nearly as visible as it is for PTFE in Figure 2A – note the micrographs in Figures 2A and 7 are different magnifications. The TAF coating is much thinner and more conformal to the catalyst surface.

The major benefit of a thin, conformal, TAF coating permeable to oxygen would be to form a thin, conformal film of phosphoric acid between the catalyst support and the TAF. Based on the measured electrolyte content of typical cathodes, the phosphoric acid film would be about 17 nm. A limiting current calculation based on oxygen solubility and diffusion in hot phosphoric acid using this film thickness is in reasonable agreement with that observed in 4% oxygen/ nitrogen. This agreement also implies that the phosphoric acid, not the PTFE film, limits the diffusion.

Simple calculations based on the external surface area of VULCITE, the cathode-catalyst support, and densities of PTFE and carbon indicate that the PTFE thickness is ~2 nm. Given the higher gas permeability of PTFE than that for hot phosphoric acid, this thickness would be consistent with the phosphoric acid film limiting the diffusion current rather than PTFE. Since the TAF content is ½ of the PTFE, the thickness would be ~ 1 nm.

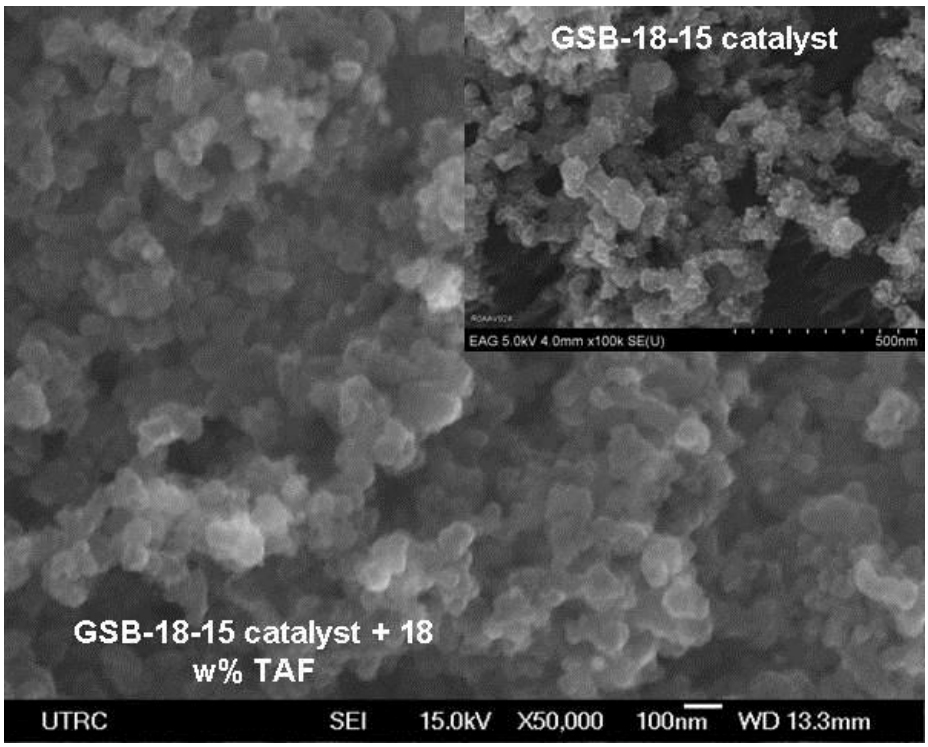

Figure 7: High resolution scanning electron microscope images of cathode catalyst and cathode catalyst + 18 w% Teflon® AF.

We therefore make a case that the TAF film is more conformal to the surface of catalyst support and the modulus of TAF is larger than that for PTFE resulting in thinner phosphoric acid films. The ratio of the limiting currents described previously would suggest a film thickness reduced from 17 nm to about 12 nm. We must corroborate this calculation by comparing electrolyte take up of PTFE and TAF.

Therefore the microstructure implied by the above analysis is that of a 17 nm coating of phosphoric acid on the catalyst surface. This structure is "wrapped" in a 2 nm thick bag of Teflon® over the catalyst surface as shown schematically in Figure 2d above. Since the primary carbon crystallite size is of the order of 50 nm, the 17 nm phosphoric acid increase this diameter to 84 nm and a significant expansion of the Teflon® coating. However, the 17 nm film must be regarded as an upper limit. Once wetted, the carbon may store acid in its internal porosity and within the interstices between the primary particles. The cubic close packed structure for spheres is still 46% porosity. Therefore the layers may be more like 5 nm thick.

We have presented the case that the use of soluble or nearly soluble polymers will lead to simplified PAFC electrode processing while at the same time improving performance. We have supported this case by subscale performance data and cathode micrographs.

Use of a soluble TEFLON® binder affords simplification of electrode fabrication and performance improvements. Soluble binders enable electrode fabrication by an inking process similar to that used for PEM MEA's, a much simpler and controllable process than the present SOA process.

However, the new binder is much too expensive to be commercially viable. Though alternatives to the soluble polymer designated as TAF were found, they were as expensive dooming the soluble binder approach

Alternatively, several papers and patents indicate that the inexpensive, commercially available fluoropolymers PTFE, FEP and PFA were soluble in fluorocarbon solvents above the melting point of the fluoropolymer. We did not observe any evidence of this for PTFE. Samples made with FEP dispersion indicated that this material was too soft at operating conditions to be useful. Experiments indicated that PFA dissolved to some extent at 330°C, but did not remain in solution at or near room temperature.

The present CDP Program is an extension of the above information. Therefore, we mixed PFA and catalyst and heated both in the solvent to 330°C to coat the catalyst.

Heating Mixtures of PFA, Catalyst and Solvent:

Previously, we have determined that the best solvent for the dissolution of PFA, following the work of Tuminello and Dee[3] is Perfluorotetradecahydrophenanthrene ($C_{14}F_{24}$). The procedure described below was developed for this program. Figure 8 shows that the coating is uniform on a nano-scale when compared with previous micrographs. Review of the procedure:

1. Enough ¼-inch PFA tubing was cut into ~ 2-mm pieces, and mixed with cathode catalyst, to make a 36 w% PFA mixture.

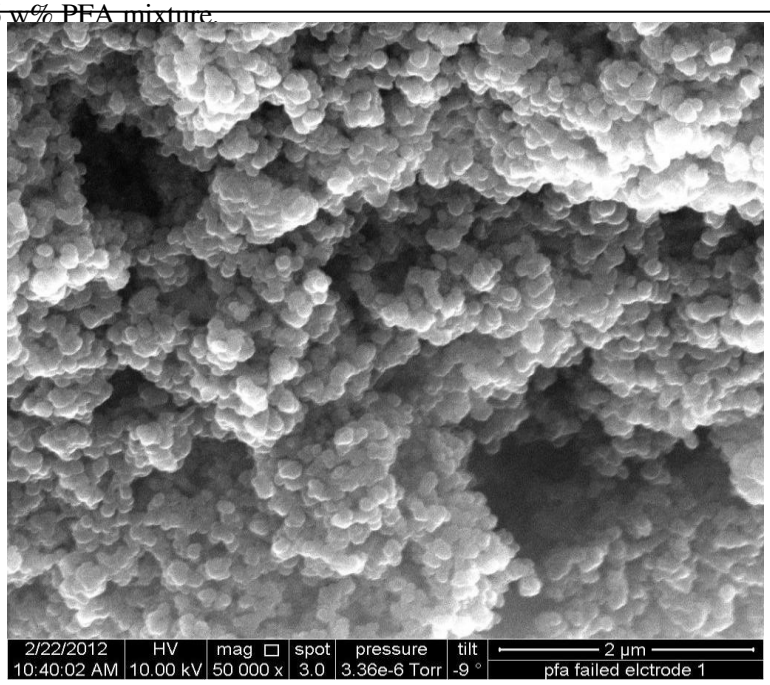

Figure 8: SEM of a fractured cathode make by the procedure in the text. Comparison to Figure 2 indicates that PFA has dissolved and coated catalyst. Note the magnification has been adjusted to be the same as that in Fig. 2.

2. This mixture and solvent were added to a PARR bomb and heated 6h at 330°C.
3. The resulting cake of solid gel and liquid solvent is mixed in a Vitamix, high shear mixer with blades.
4. The resulting slurry is filtered to recover the clear, fluorinated phenanthrene solvent.
5. The filter cake is re-mixed in FC40 FLUORINERT from 3M.
6. The resultant high-viscosity slurry is doctor bladed onto a carbon-paper substrate held on a vacuum table,
7. The electrode layer is rolled to improve adhesion to the substrate and improve electrical conductivity of the layer.

Electrodes doctor-bladed on substrates were plagued with poor cohesion, mud cracking, and poor adhesion to the substrate. We attributed these problems to the fact that the polymer was soluble above the melting point of the PFA, but not at room temperature and the postulation that PFA was not substantially swollen or softened by the solvent at room temperature. Small sections of several samples were useable for testing.

Results and Discussion:
The many graphs in Figure 9 show subscale performance data at high stoichiometry for 36 w% PFA samples made by the method described above. Representative curves of production cathodes and the TAF cathodes are displayed for reference. Normally, curves in 100% oxygen are shown to compare sample catalyst activity and electrode internal resistance (gross mass transport limitations, if present) while curves at 8% oxygen are shown to compare (catalyst activity) and mass transport of oxygen in the cathode.

Usually, performance curves are compared by normalizing by the Pt loading. The raw data curves of Figure 1 indicate a smaller activity in the PFA samples not explainable by Pt loading alone, although Pt loading measurements were an issue. To compensate for the catalyst activity changes, the PFA curves in pure oxygen were shifted upward to align with the production and TAF curves at 40 and 80 mA/cm^2. The curves in 8% oxygen were shifted by the same amount in Figure 9. The activity difference will be discussed later in this report.

One more baseline besides the production and TAF performance curves is needed to assess the benefit of the PFA treatment. The red point and red line labeled Fib PTFE H_2-O_2 represents the **performance of bare catalyst in a PAFC**. The point at 100 mA/cm^2 is roughly 350 mV below the PFA curves and 400

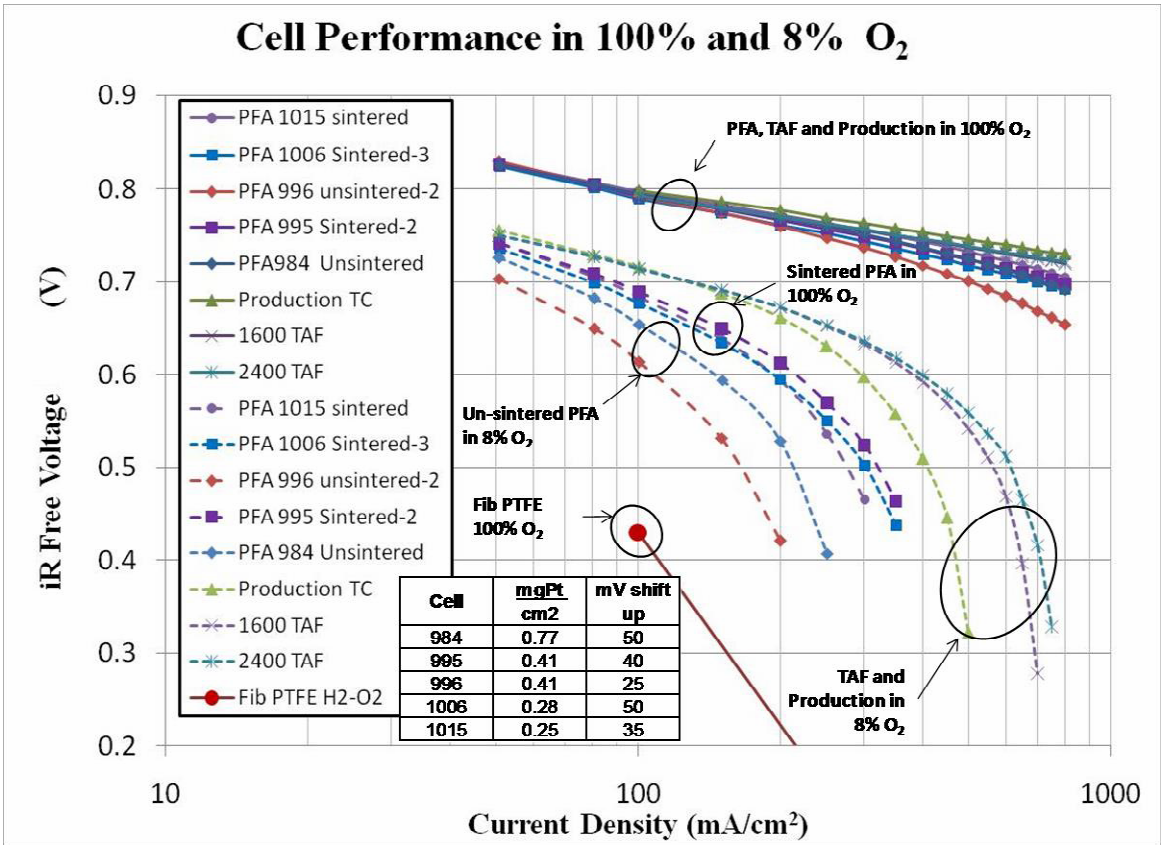

Figure 9: Subscale performance at high stoichiometry in 100% and 8% O_2/N_2 and 100% H_2. Samples are grouped into typical production cathodes, TAF Cathodes, and PFA cathodes. Inset shows PFA-sample Pt loadings in mg Pt/cm^2. Fib PTFE indicates bare catalyst in oxygen.

mV below the production and TAF curves. Discussed later, in detail, the sample is made by fibrillating a small fraction of the PTFE to make a free-standing electrode. The remainder of the PTFE remains in small deposits. The sample is not sintered.

Organized in this fashion, the data in Figure 9 supports several observations and conclusions.

1) PFA cathodes perform worse than the SOA- reference cathodes in both concentrations of oxygen, mainly because of mass transport, but not because of electrode iR. Note that with too high a concentration of TAF, e.g., 36 w%, where the catalyst was uniformly coated, the electrodes exhibited high iR and poor catalyst utilization because acid could not be made to penetrate the electrodes. **Therefore, though Figure 8 shows a uniform coating of the catalyst by PFA on a micron scale, this uniform coating occurs in some areas, but not uniformly over a large areas.** Otherwise 36w% PFA would have behaved like TAF.
2) Comparing the performance of "unsintered" PFA samples with that of bare catalyst shows that heating (catalyst + PFA + solvent) at elevated temperature provides great benefits, but not as much as the baseline PTFE.
3) The "sintered" PFA had better performance than the "unsintered," or "dissolved only," PFA. "Sintering," here, means heating at 330°C, some 25°C above the melting point of PFA at 305°C. The melt viscosity of PFA is ~10^5 P[4], ~10^6 times lower than PTFE at the same temperature. We observe significant movement of PFA after "sintering" adding to the uniformity of the PFA within the electrode and improved performance.

The difficulties in electrode fabrication alone were sufficient to eliminate the process described above as viable for production PAFC electrodes. The mixture of catalyst, PFA and solvent, after heating, broke into small platelets during doctor blading which would not stick together, nor stick to the substrate. We speculate that the reason for this behavior was that PFA is soluble at high temperature, but not at room temperature nor is the PFA substantially swelled by the solvent at room temperature so that insufficient polymer-polymer interactions remained at room temperature to cause adhesion.

Though fabrication issues prevented this technique from further experimentation, we wanted to eliminate the possibility that the poor performance of these electrodes was due any inhomogeneities of PFA due to its addition as cut-up pieces of ¼-inch tubing. In subsequent experiments with hybrid flocs, we showed that heating catalyst and PFA dispersion in solvent was slightly inferior to heating the mixtures in air. This indicates that the failure of the concept is not a result of the source of PFA.

Fibrillation of PTFE Flocs to Replace SOA Electrode Fabrication:

Therefore, fibrillation of PTFE and rolling have been pursued as an alternative to present production methods and doctor blading of PAFC cathodes. Our method is based on that developed by Solomon in 1982 [4]. We deviate from Solomon by using a non-swelling lubricant instead of alcohol and limit the fibrillation by rolling the sample rather than mechanically mixing in a Brabender –type mixer. The procedure produces a free-standing electrode of the desired thickness and loading with no mud cracks.

An outline of the procedure is:

1. Catalyst and PTFE are mixed with no added floccing agent nor pH adjustment.
    a. Floccing occurs naturally.
    b. ≥ 10w% PTFE needed for mechanical strength.
2. The floc is dewatered to about 10% solids by gravity filtration.
3. The floc is dried at 60°C to 80°C.
4. Fibrillation started
    a. ≈ 2 g Floc placed on glass plate

b. ≈ 4 g FC70 or Isopar H added to floc as lubricant (TAF solution added at this point if desired)
c. Floc crushed and spread with spatula until uniform mixing accomplished.

5. Rolling and continued fibrillation
   a. 3-mil shims placed on glass plate.
   b. Floc rolled to 3 to 6 mils with ~ 10 Kg stainless rolling pin
   c. Rolled sheet folded to quarters
   d. Process repeated 4 to 6 X.
   e. Floc rolled to 3-mils and dried 80 °C on glass*
   f. Peeled from glass, sandwiched between medical papers, cut, weighed, thickness, iR, cell test.

The procedure was used with standard cathode catalyst with 2½w%, 5w% and 10 w% PTFE to determine the minimum amount of PTFE for mechanical integrity during rolling. Figure 10 shows that only the 10% floc showed mechanical integrity to form a continuous film during the rolling procedure in #5, above.

Initial fabrication trials were performed on production GSB-18-15 catalyst floc from 2010. The floc contains 36 w% PTFE. Samples were fibrillated and rolled by a manner essentially that described above. Different substrates for rolling and drying were explored, glass, medical paper, and ½ - mil PTFE. A sample of this floc was rolled out to 3- mils on PTFE and dried. Some relaxation occurred during drying and the sample thickened to 4 mils. The sample was freeze-fractured, coated with carbon and examined in the SEM.

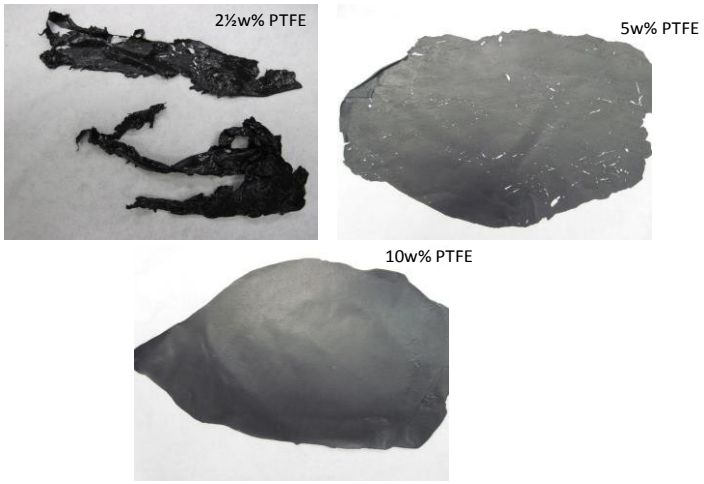

Figure 10: Optical micrographs of a sheet of floc rolled according to the procedure in the text. At least 10% PTFE is required to avoid fracturing of the sheet.

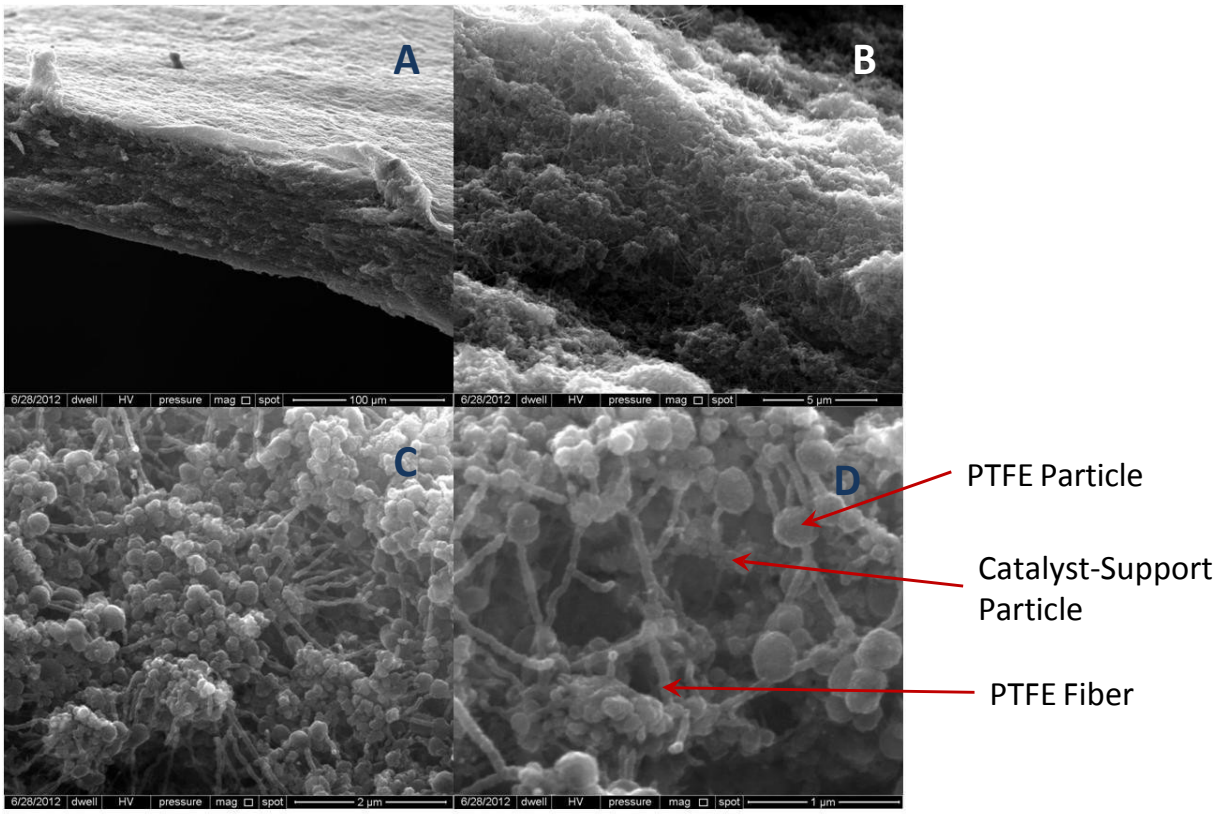

Figure 11: High Resolution SEM analysis of a rolled sample of production GSB-18-15 floc. Magnification increases from A to D. Micrograph A shows the layered nature of the sheet while D resolves the PTFE particles, fibrillated PTFE and carbon catalyst-support particles. Note that the PTFE fibers are formed by shearing the PTFE particles.

Figure 11A shows the layered nature of the sheet which results from the process of rolling and then folding the sheet ~6X. The sheet is sheared by rolling causing more particles to form into fibers. The sheet becomes harder to roll as it is "worked" by rolling and folding. 6-folds causes the sheet to be strong enough to hold its shape and be removed from the glass while still retaining the softness to be rolled into a thin sheet.

Figures 11B, 11C and 11D, show that only a small fraction of the PTFE particles are fibrillated and the rest do not coat the catalyst to impart hydrophobicity. The red point and curve in Figure 1, labeled Fib PTFE in 100% O_2 are the performance of a sample rolled out and tested in a subscale cell. The very poor performance is consistent with the statement about the PTFE particles not imparting much hydrophobicity.

While the PTFE particles do not impart hydrophobicity, they are available for sintering. The first melt of PTFE is ~ 338°C while that for PTFE fibers is ~380°C. Therefore, the PTFE particles may be sintered without destroying the mechanical integrity of the sheet, even when not mounted on a substrate.

Samples of floc were sintered 15 minutes at 349°C in air and tested in subscale cells. The results are shown in Figure 12.

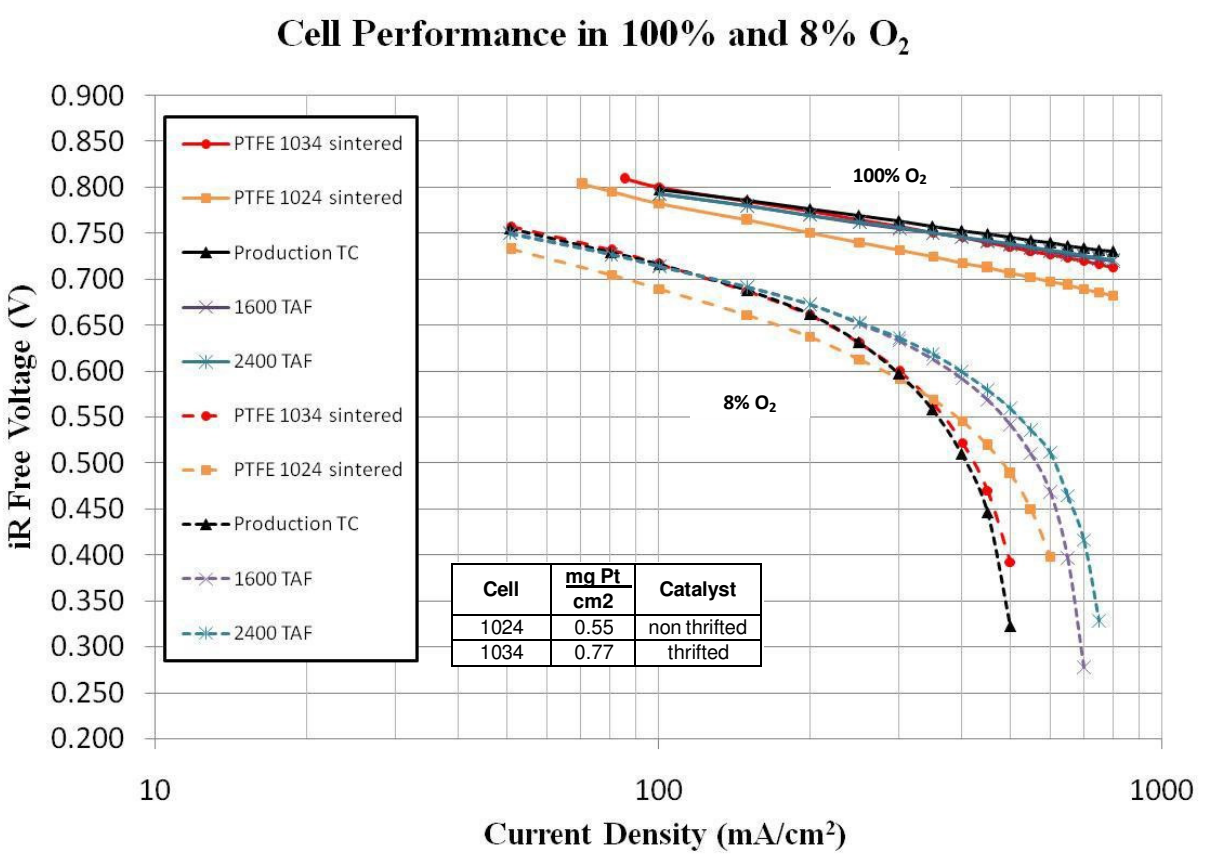

Figure 12: Performance of floc rolled into electrodes by the method described in this report and sintered at 349°C/15 minutes

Cell 1034 is a test of thrifted cathode catalyst floc made at UTC Power with 36 w% PTFE. The test shows good agreement with production samples, the loading in Cell 1024 is much higher than the baselines which were 0.53 mg Pt/cm^2. However, setting aside the catalyst activity, the internal resistance and mass transport of this sample matches that of production cathodes.

Cell 1024 is a test of standard GSB-18-15 production floc made fibrillated and rolled by the method described in this report. The loading is close to that for thrifted cathodes, 0.53 mg Pt/cm^2, the baselines in Figure 4. The oxygen curve clearly shows that the catalyst activity is lower in this sample. More intriguing is the mass transport; if the oxygen and 8% oxygen curves are displaced the same amount, about 20 mV, the performance for this sample begins to rival that of TAF.

Therefore, the rolling method not only employs the same floc already in use by production and provides a better fabrication method than the cloud tower, it also provides performance benefits.

Fibrillated Hybrid Flocs of PTFE and PFA (termed PAE):

Performance benefits of the fluoropolymer were linked to its ability to flow over the catalyst surface. At the melt viscosity of PTFE ~10^{18} P [3], PTFE is not processable by conventional extrusion and molding techniques. HRSEM micrographs show that PTFE does not flow over the catalyst surface during heat treatment of the PAFC electrodes. PFA was developed to afford standard extrusion and molding

techniques of normal thermoplastics while providing the chemical stability of PTFE. The melt viscosity of PFA is ~10^6 [3] P and may allow significant flow over the catalyst surface during heat treatment and may provide benefits similar to that of TAF.

Hybrid Sample Preparation:
DuPont PFA dispersion TE-7224 is 60 w% solids, 5.5 w% dispersant, pH10 and has a melting point of 305°C and a melt flow or 1-3 (ISO12086). Melt flow is an indication of molecular weight; the melt flow for TE-7224 is the lowest of available PFA's indicating the highest molecular weight. Klinedinst, Vogel, and Stonehart identified high molecular weight important in minimizing polymer migration and maximizing thermal stability[5]. Migration causes de-wetting of the adjacent carbon-paper substrate, used to store phosphoric acid and occurs primarily during sintering. The migration requirement is lessened in our situation because the catalyst layer is sintered as a stand-alone layer rather than adhered to the carbon-paper substrate.

Four flocs (Table 1) were made with the PFA dispersion and thrifted cathode catalyst used previously in this study. Catalyst was dispersed in water at high-shear and PFA dispersion added and blended at high shear. PTFE dispersion was blended at much lower shear, if added. The dispersion was allowed to floc naturally and the vacuum filtered and dried at 100°C. The filtrate was noticeably yellow indicating loss of Cr from the catalyst. This may account for some of the observed loss in catalytic activity of the prepared electrodes.

Table 1: Flocs made in for the CDP Program

w% PFA	w% PTFE	Testing
36	0	Fibrillation of PFA
26	10	Cell test of rolled electrodes
18	10	Cell test of rolled electrodes
18	0	Doctor blade/sinter or dissolve

Electrodes were prepared similarly described above with the following notes. ISOPAR H, a commercial hydrocarbon was used in place of the more expensive fluorocarbons. ISOPAR is not only cheaper, but lowers the adhesion of the rolled catalyst layer to the glass plate used for rolling. Therefore, samples may be rolled and dried on the glass and then removed and sintered. This process allowed better control and uniformity of thickness. Mechanical working of the fibrillated PTFE-catalyst "rubber" was limited to control its hardness – the mixture was worked with the spatula and only one rolling was performed. This treatment would affect the meso-structure of the catalyst layer.

To eliminate contamination from the steel rolling pin, we eliminated contact with the pin. Samples were rolled between the glass plate and a 10-mil PTFE sheet. Unfortunately, this procedure neither eliminated nor reduced the loss in catalyst activity, discussed in more detail, below.

Once rolled, samples were cut and sintered in air between carbon-paper substrates.

Some observations are noteworthy. The 36 w% PFA sample did not form a rubbery dough consistent with the hypothesis that the fibrillation of PTFE is the cause of the dough formation. Fibrillation is a property of high molecular weight PTFE. The hybrid samples of PFA and 10 w% PTFE (based on catalyst wt only) formed the rubbery dough and rolled very similarly to, but slightly "better" than, the 10 w% PTFE sample discussed. It may be possible to cut the PTFE content.

Use of ISOPAR solvent indicates cheaper substitutes could be used for this process. Combined with existing technologies for rolling plastics, we believe this process could be implemented on a commercial scale and compete favorably with the cloud tower.

Results and Discussion:
Figure 13 shows the subscale performance curves for three hybrid samples made and tested along with the reference curves for PAFC production and TAF samples. The PFA-PTFE curves are vertically displaced to make the oxygen curves align with those of the reference samples, the 8% curves being displaced by the same amount.

The sample run in cell 1066 contained 26w% PFA/10w% PTFE sintered 330°C/15 minutes, only the 8% oxygen curve is plotted to show the poor performance even after 60 minutes of electrolyte fill. This sample was much too hydrophobic to be effectively wet, similar to the 36 w% TAF samples. This observation supports our hypothesis that the low melt viscosity of PFA may provide uniform coating of the catalyst particles.

Therefore, the PFA content was reduced to the quantity used for TAF, 18 w%. The 10 w% PTFE content does not contribute to the catalyst coating and is used only as a fabrication aid. Cell 1083 shows the performance of sample sintered at 330°C/15 minutes. Note that this performance is better than production, but not as good as TAF.

HelOx showed a considerable amount of gas-phase polarization indicating the existence of gas-phase mass transport limitations. The mass-transport limitation reported suggest that diffusion through TEFLON and a film of phosphoric acid are dominant. We hypothesized that the gas-phase transport of cell 1083 was a result of the PTFE fibrils.

Therefore the sample for cell 1093 as sintered at 349°C/15 minutes softening of the PTFE fibrils. The curves for cells 1083 and 0193 are almost identical, except for catalyst activity (which is normalized in the figure). Therefore, interference by the PTFE fibrils seems incorrect.

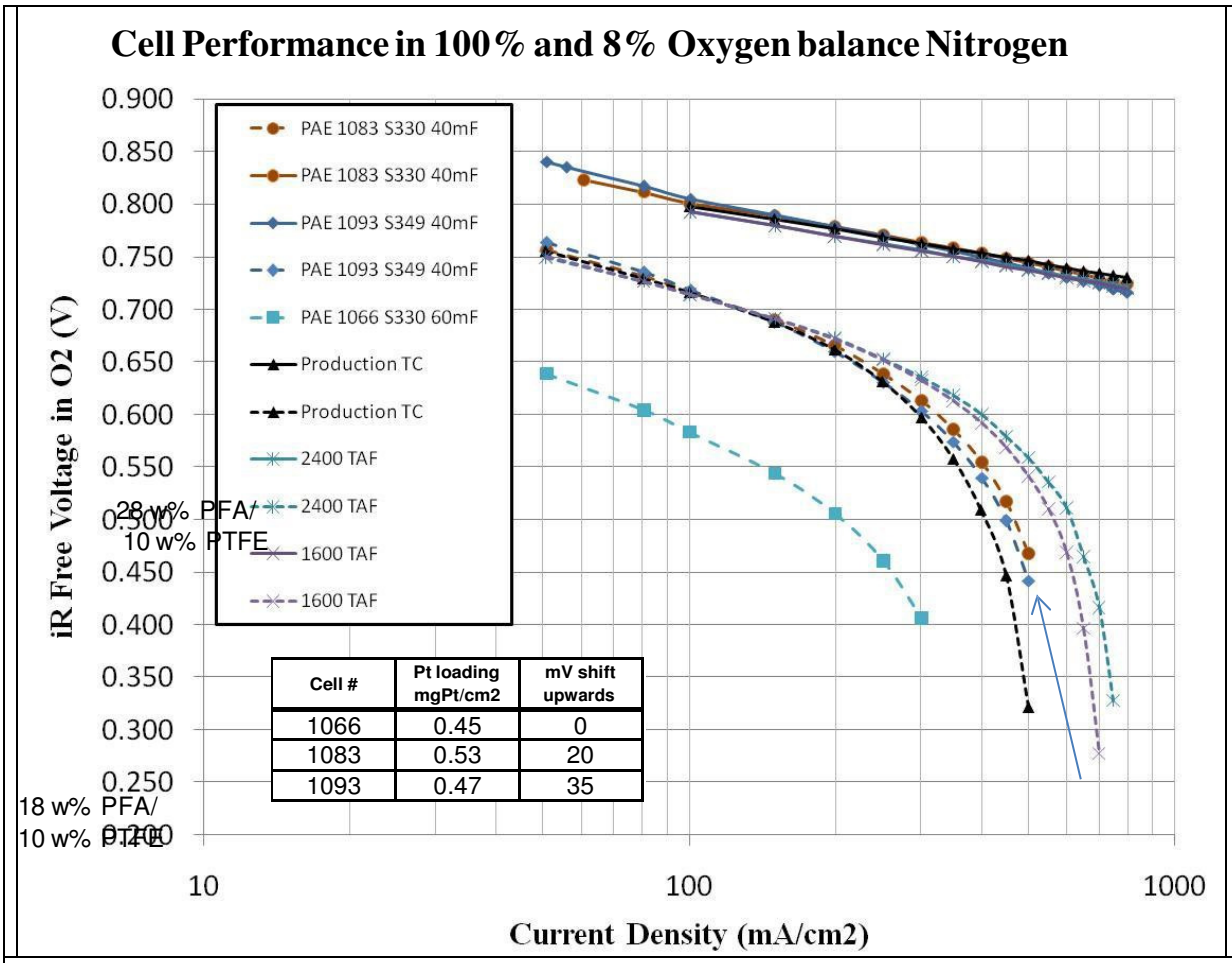

Figure 13: Subscale performance at high stoichiometry in 100% and 8% O_2/N_2 and 100% H_2. Hybrid flocs of 18w% PFA and 10 w% PTFE heat treated at 330°C for 15 minutes. 40 minute electrolyte fill cycle.

The observed gas-phase limitation may be due to a poor meso-structure. We have concentrated on the primary structure of fluorocarbon coating of the catalyst and on the macrostructure of forming the catalyst layer. These are the dominant polarizations, but may pay a 20 – 50 mV penalty for a poor meso-structure. The internal structure of the electrode as that due to jet milling of floc is the meso-structure.

Note that we have obtained better than production performance for samples produced by a simpler method than the cloud tower and for formulations that are not optimized for the PFA and PTFE content. The performance was still increasing for EFC's of 40 minutes indicating that the PFE content could be reduced further, likely increasing performance.

Loss of catalyst activity is still a concern and we are not able to determine whether it is due to chromium loss, oxidation, or some processing condition or contamination from the glass plate. Since the process involves forming fibrils of PTFE, some Pt particles may be pulled from the surface of the catalyst. ECA's should be able to determine if this effect is occurring.

Dissolved PFA-PTFE Hybrid Electrodes:
Heat treated hybrid samples show improved performance over SOA electrodes, but not as good as TAF. Though the melt viscosity of PFA is much lower than that of PTFE, it is still much higher than dissolved TAF. Heat treatment of PFA electrodes, while providing more uniform polymer coatings on the catalyst than PTFE, lack the uniformity provided by dissolved TAF. However, dissolved PFA may have better uniformity than melted PFA and so samples were made from treating a hybrid floc with solvent in the pressure vessel, the same treatment as described in the "Heating Mixtures of PFA, Catalyst, Solvent."

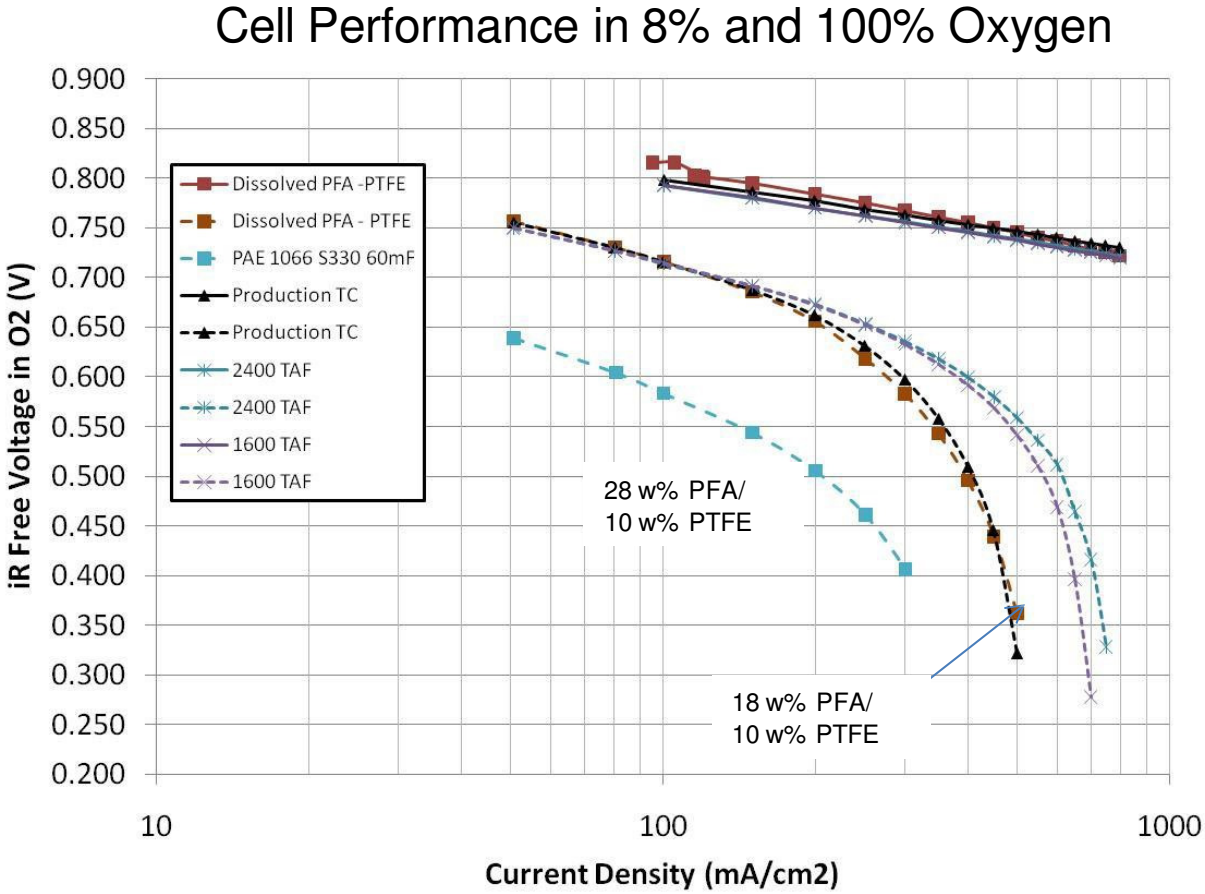

Figure 14: Subscale performance at high stoichiometry in 100% and 8% O_2/N_2 and 100% H_2. Hybrid flocs of 18w% PFA and 10 w% PTFE dissolved in solvent 4 hours at 330°C. 20 minute electrolyte fill cycle.

A hybrid floc with 18w% PFA and 11 w% PTFE, w% based on binary composition of polymer and catalyst, was heated with the "306"solvent at 330°C for 4 hours. The resultant floc was rolled similar to the method reported with the exception that the floc was rolled with the "306" solvent and ISOPAR H added as needed.

Dissolution of the PFA was evident from a different rheology of the floc as rolled than that of the undissolved floc. When rolled, the dissolved floc formed platelets ~0.5 mm discs similar to previously made "bombed" PFA-catalyst mixtures. However the fibrillated PTFE held these platelets together and

electrodes could be made. Processing was difficult because electrodes would rip easily if rolled to standard thickness.

The performance is shown in Figure 14 and is nearly identical to that of the SOA PAFC cathode. Any benefit of the more uniform coating of PFA on catalyst is likely compensated by a poor meso-structure due to the rheology of the dissolved, precipitated PFA-catalyst mixture formed by extended heat treatment with solvent.

We show benefits of using PFA dispersion rather than the cut tubing for Figure 9. Also, the hybrid-floc method was improvement over the doctor-blade method used for the previous PFA samples. Although we have improved the process, the cell performance does not warrant the difficult processing of the sample, so this method is not viable.

Microscopic Examination of Electrodes:
Figure 15 shows SEM micrographs, adjusted to the same magnification, of the starting catalyst (A)(thrifted is actually shown and non-thrifted used but are identical on this scale), the as-rolled material (C), and the sintered material used in cell 1024 (B). C is and clearly appears to be a mixture of A and D, the PTFE dispersion containing 35 to 40 w% PTFE (exact composition proprietary).

Once sintered, we no longer clearly see the PTFE particles. There appears to be a ripening of the structure which indicates that the PTFE has coated the catalyst particles. However, closer examination shows that some uncoated catalyst particles remain and the fibrils are absent. This indicates that the coating is not as uniform as with Teflon® AF.

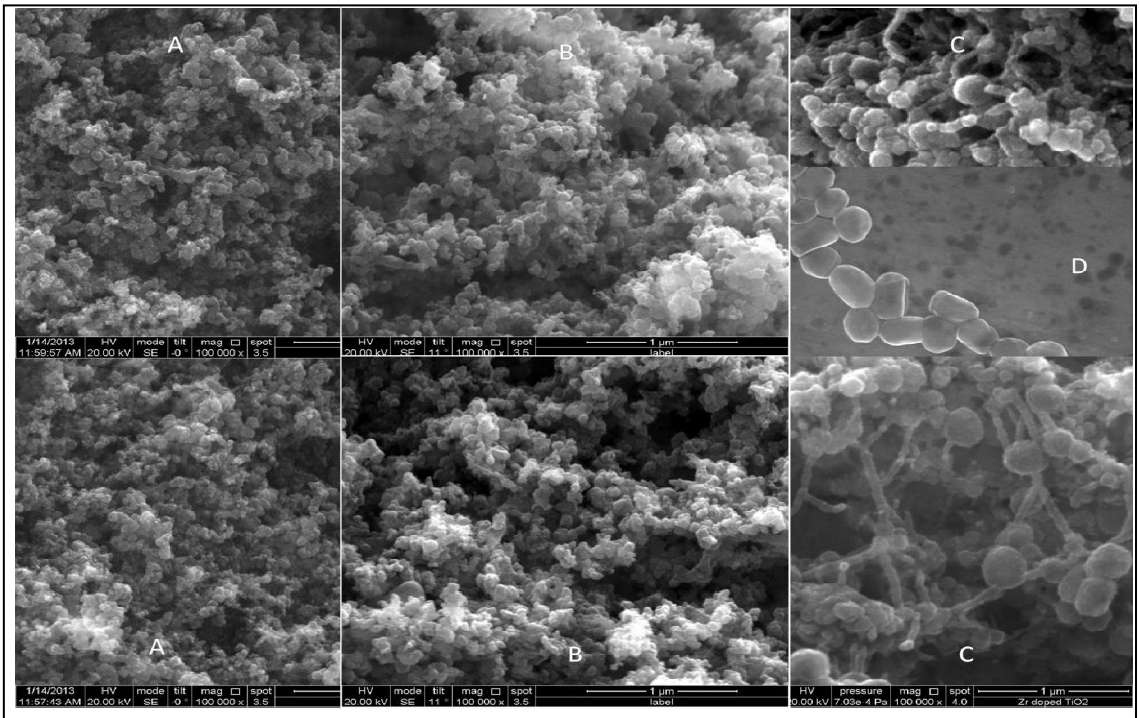

Figure 15: SEM Micrographs at ~100K, all adjusted to the same magnification. A is the starting catalyst, B is the sintered floc used in cell 1024, C is the "as-rolled" layer before sintering, and D is the starting dispersion of PTFE.

The viscosity of PTFE at the sinter temperature of 349C/15minutes is too high to allow the material to uniformly coat the catalyst and so some vestiges of the initial PTFE particles should remain.

A similar micrograph for the hybrid floc of thrifted catalyst-PTFE-PFA is shown in Figure 16. The thrifted catalyst is shown in A, C and D are repeats of the micrographs in Figure 1 because they should be the same structure. The sintered layer in B is that used in cell 1083 and was sintered at 330C for 15 minutes.

The viscosity of PFA (mp 305C) is sufficiently low to allow it to migrate and cause uniform coating of catalyst and so we no longer see any PFA particles. The micrograph supports this supposition, but does not prove it. The sinter temperature is below that of PTFE, yet we do not see well-defined PTFE particles in the micrographs, nor at lower magnification. This is not understood at this time.

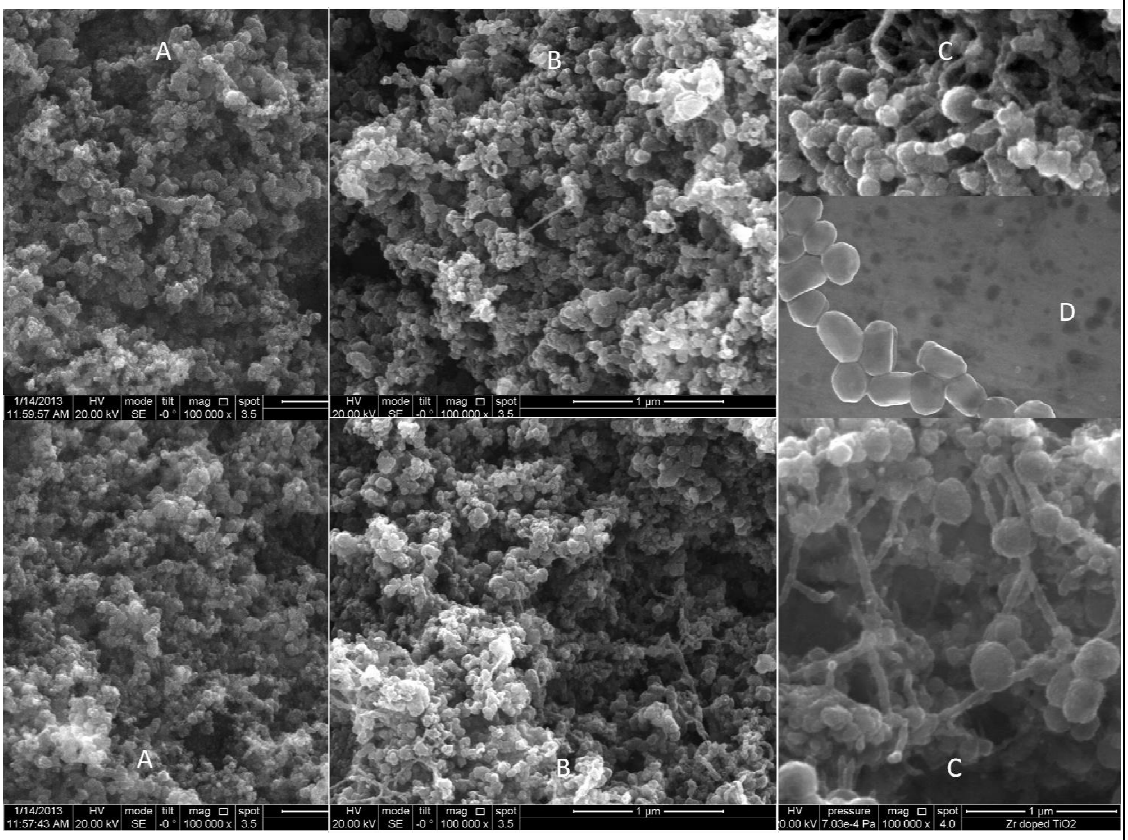

Figure 16: SEM Micrographs at ~100K, all adjusted to the same magnification. A is the starting catalyst, B is the sintered floc used in cell 1083, C is the "as-rolled" layer before sintering same as in Figure 1.D is the starting dispersion of PTFE which is identical to that of PFA.

Acronyms:

EFC	**e**lectrolyte **f**ill **c**ycle
HRSEM	**h**igh-**r**esolution **s**canning **e**lectron **m**icroscopy
FEP	**p**oly (tetrafluoro**e**thylene - perfluoro**p**ropylene) copolymer
P	poise, unit of viscosity
PAFC	**p**hosphoric **a**cid **f**uel **c**ell
PFA	poly (**p**er**f**luoro **a**lkoxy ethylene – tetrafluoroethylene) copolymer. DuPont = methoxy
PTFE	**p**oly(**t**etra**f**luoro**e**thylene)
TAF	code name for a perfluorinated polymer made soluble by the inclusion of perfluroinated oxazole moieties
UTC	**U**nited **T**echnologies **C**orporation

Patents:

Three Invention Disclosures have been filed with the University of Connecticut's Office of Economic Development and transferred to the Client, UTC Power (now ClearEdge Power) :

1) "Electrodes from Polymers Soluble at Elevated Temperatures." Case number 13-041.
2) "Phosphoric Acid Fuel-Cell (PAFC) Electrodes from Soluble or Meltable Polymers by Fibrillation of PTFE." Case number 13-042.
3) "Phosphoric Acid Fuel-Cell (PAFC) Electrodes by Fibrillation of PTFE." It has been assigned case number 13-043.

Publications / Presentations:

Project was reviewed with DOE at C2E2 on 3/28/2013.

References:

1. S. Gottesfeld, I. Raistrick, and S. Srinivasan , *J. Electrochem. Soc.* **134** 1455-1462 (1987).
2. M. Razaq, A. Razag, E. Yeager, D. DesMarteau, S. Singh, J. Electrochem. Soc. 136 385-390 (1989).
3. W.H. Tuminello and G.T. Dee, *Macromolecules* **27** 669-676 (1994).
4. PTFE has a melt viscosity of 10^{18}-10^{19} P while PFA is 10^{4}-10^{5} P both at 380°C (Polymeric Materials Encyclopedia, J. C. Salamone, ed., CRC Press, 1995 vol. 11 p 8297, Table 3) http://books.google.com/books?id=BAaD1DSTJHUC&pg=PA8297&lpg=PA8297&dq=viscosity+of+PTFE+and+PFA+at+330C&source=bl&ots=NHrq1DQSkG&sig=bI83_kIYSHesDng1rJ_YCU782uU&hl=en&sa=X&ei=woZnUJm2J4b00gHRoIGIAQ&ved=0CDIQ6AEwAw#v=onepage&q=viscosity%20of%20PTFE%20and%20PFA%20at%20330C&f=false
5. Frank Solomon, assignee - Diamond Shamrock, patents 4,337,140; 4,354,958; 4,379,772; (1982).
6. K.A. Klinedinst, W.M. Vogel, P. Stonehart, "The interaction between PTFE and porous metals and metal blacks-rheological characterization and thermal degradation of the polymer," *J. Mater. Sci.* **11** 209-214 (1976).

Project Title: Mechanistic Understanding of Matrix Stability in Molten Carbonate Fuel Cells
Industrial Partner: FuelCell Energy
PI: Prabhakar Singh

The overall objective of the proposed collaborative research effort is to develop mechanistic understanding of cell component degradation in advanced MCFC power generation system. Electrolyte matrix and cell to cell interconnection stability will be studied under simulated cell and stack operating conditions. Coarsening behavior of the electrolyte matrix in contact with the molten electrolyte and

accelerated corrosion of the interconnection under the simultaneous exposure to an oxidizing and reducing atmosphere condition have been identified as two major contributing factors leading to long term degradation.

Accomplishments:

- The factors affecting structural and thermo-chemical stability of the $LiAlO_2$ matrix have been identified.
- The solubility of the ceramic matrix in the molten carbonate has been investigated for $LiAlO_2$ matrix obtained from Fuel Cell Energy.
- Role of anode and cathode environment on Ni particle precipitation and $LiAlO_2$ particle coarsening has been analyzed.

Introduction:

Molten carbonate fuel cells (MCFC) are high temperature fuel cells that use molten carbonate salt mixture (Li, Na, K-carbonates) as an electrolyte. The electrolyte is retained in a porous, chemically inert ceramic matrix of lithium aluminate ($LiAlO_2$). The anode and the cathode electrodes are made from porous nickel alloys and lithiated nickel oxide respectively. In the MCFC, austenitic stainless steel (316L and 310S) are traditionally used for the fabrication of current collectors. Lithium aluminate ($LiAlO_2$) is widely used as the matrix material in molten carbonate fuel cell (MCFC) because it has a relatively good susceptibility for retaining the electrolyte. The electrolyte matrix is fabricated using tape casting technique and consists of $LiAlO_2$ and molten carbonate electrolyte (50-60% by volume). Long term operation of the MCFC shows significant structural and morphological changes in the bulk matrix structure predominantly due to phase transformation and coarsening (due to solubility in the electrolyte matrix), changes in the pore size distribution, and the amount of electrolyte retained in the porous structure.

Experimental:

Solubility of $LiAlO_2$ into Li-Na carbonate in simulated 'cathode' and ' anode' environment: A schematic of experimental set up for measuring $LaAlO_2$ solubility in Li-Na carbonate is shown in Figure 1. Test parameters include: $LiAlO_2$ powder from different vendors (supplied by FCE) =6 g; Li-Na carbonates (E350) =16 g; Exposure cathode atmosphere = 30 CO_2-70 air; Exposure anode atmosphere: 20 H_2 – 20 CO_2 – 60 N_2; Gas flow rate = 100cc/min; Test duration 100-1200 (cumulative) hrs. Temperature: 650°C. Dissolved Al content in carbonate melts has been quantified using Inductively Coupled Plasma-Atomic Emission Spectroscopy (ICP-AES).

Structural and microstructural stability of $LiAlO_2$: Degradation of $LiAlO_2$ due to exposure to humidity and carbon dioxide and interaction with electrodes has been studied for the post-test MCFC components obtained from FCE. SEM and 3-D tomography have been used for microstructural study. Identification of minor compounds as well as $LiAlO_2$ polymorphic transformation with temperature has been conducted using XRD.

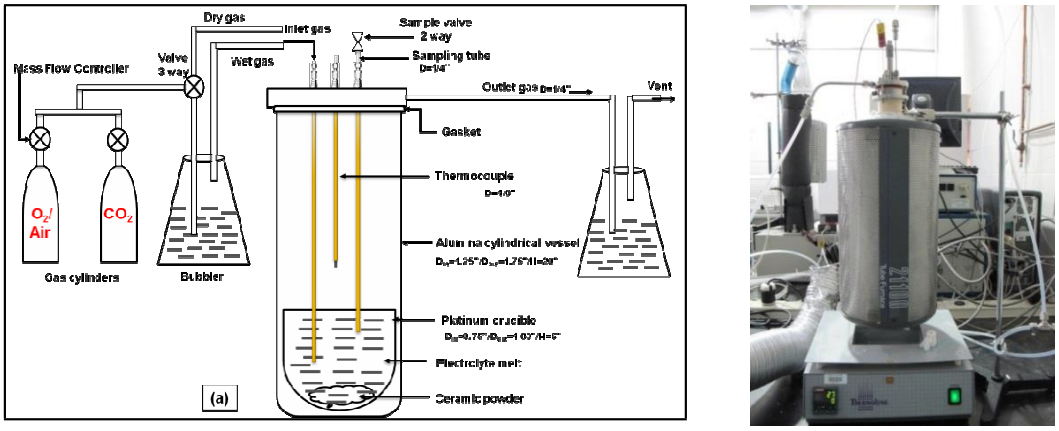

Figure 1: Schematic of experimental setup for the matrix solubility measurement. A photograph of the test-up is also shown.

Results and Discussion:

Solubility of $LiAlO_2$ in Li-Na carbonate in simulated 'cathode' and 'anode' environment:

The solubility rate of $LiAlO_2$ in Li-Na carbonate in initial 300 hrs is higher than the long term solubility rate as shown in Figure 2 and the slope of the plots. However, the $LiAlO_2$ matrix continues to be soluble in Li-Na carbonate for the studied duration. The solubility is slightly higher in anode gas atmosphere.

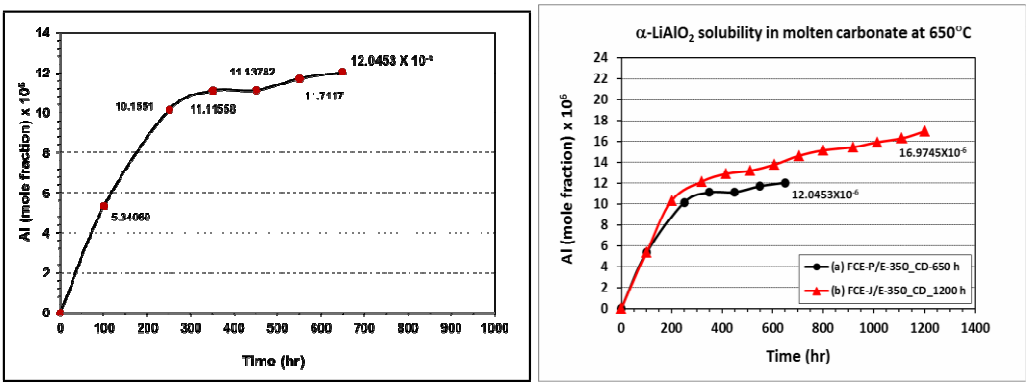

Figure 2a: Solubility of different α-$LiAlO_2$ (FCE-P, FCE-J) immersion in molten carbonate (E-350) at 650°C in cathode gas atmosphere (30CO_2 - 70 air)

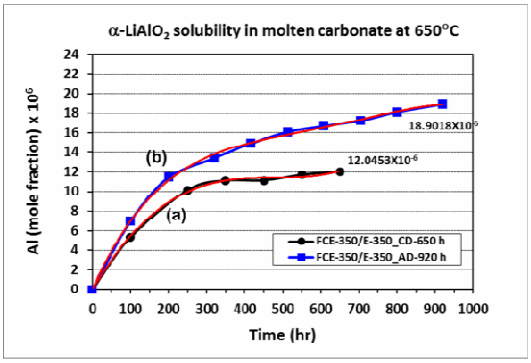

Figure 2b: Solubility of $LiAlO_2$ powder (FCE-P) in Li-Na carbonates (E350) at 650°C (a) the cathode environment (70 Air-30 CO_2) and (b) the anode environment (20 H_2-20 CO_2-60 N_2)

Structural and microstructural stability of $LiAlO_2$:

Structural stability

$LiAlO_2$ powders from different batches obtained from FCE were analyzed using XRD to detect the impurity compounds in the matrix. The predominant phase, attributed to α-$LiAlO_2$, was observed in all tested matrix samples. Presence of minor phases are in the decreasing order of γ-$LiAlO_2$<lithium aluminum hydroxide hydrates < lithium aluminum carbonate hydrate < Li_2CO_3 have been observed in the XRD patterns (Figure 3 for example). The amount of the impurity phases due to exposure to CO_2 and humidity vary from batch to batch as given below.

Li_2CO_3 : FCE-B1>FCE-C1> FCE-A1; FCE-C2> FCE-B2> FCE-A2> FCE-D; FCE-P>FCE-204T>FCE-J

$Li_2Al_4(CO_3)(OH)_{12}.3H_2O$: FCE-B1> FCE-C1> FCE-A1; FCE-C2> FCE-A2> FCE-D> FCE-B2 ; FCE-J>FCE-204T>FCE-P

$LiAl_2(OH)_7.2H_2O$: FCE-B1> FCE-C1> FCE-A1; FCE- C2> FCE-A2> FCE-D> FCE-B2; FCE-J>FCE-204T>FCE-P

γ-$LiAlO_2$: FCE-B1> FCE-C1> FCE-A1; FCE-A2> FCE-D> FCE-B2> FCE-C2; FCE-J>FCE-P>FCE-204T.

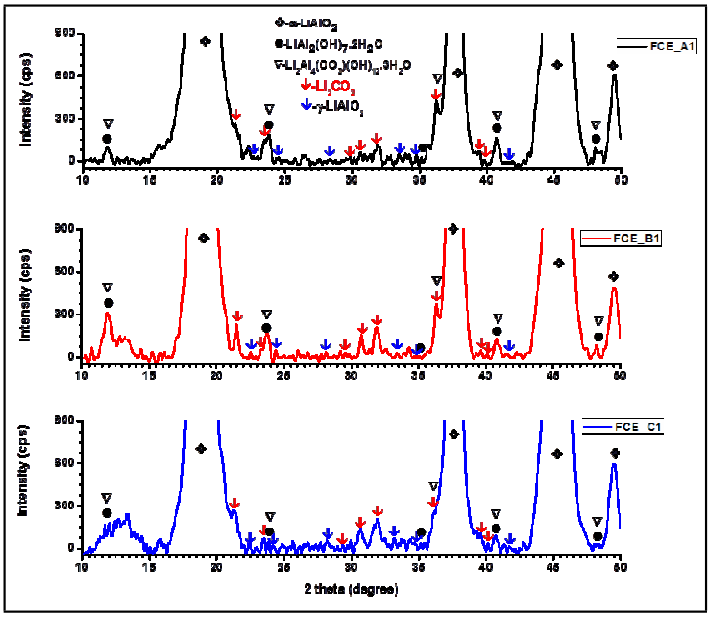

Figure 3: X-ray diffraction patterns of the $LiAlO_2$ powder samples, FCE-A1, FCE-B1, and FCE-C1.

Microstructure:

Matrix samples obtained from FCE, after electrical tests, were analyzed for matrix microstructure, compound structure, phase stability, nickel distribution, and particle coarsening. Figure 4 shows the cross-section of the anode side of the electrically tested matrix. The distinct feature of the long term (4296 and 6984 h) tested matrix include in presence of large $LiAlO_2$ particles.

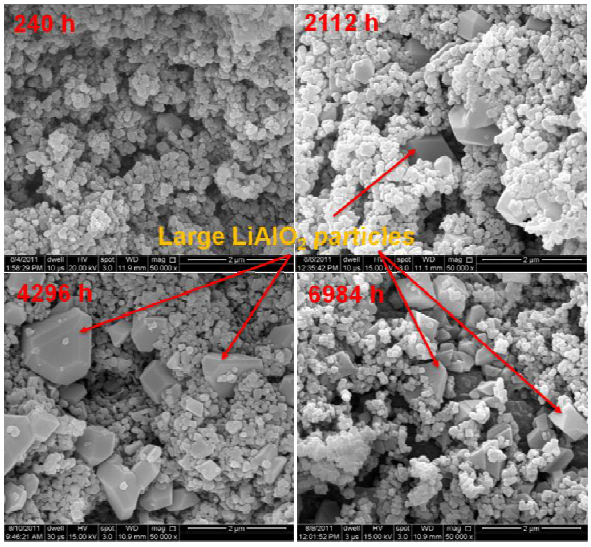

Figure 4: FESEM images of fracture cross-section of matrix samples (anode side).

Figure 5 shows the cross-section of the cathode side of the electrically tested matrix. The distinct feature of the long term (4296 and 6984 h) tested matrix include in presence of large $LiAlO_2$ particles. The $LiAlO_2$ particles growth is observed in the both cathode and anode side of the matrix.

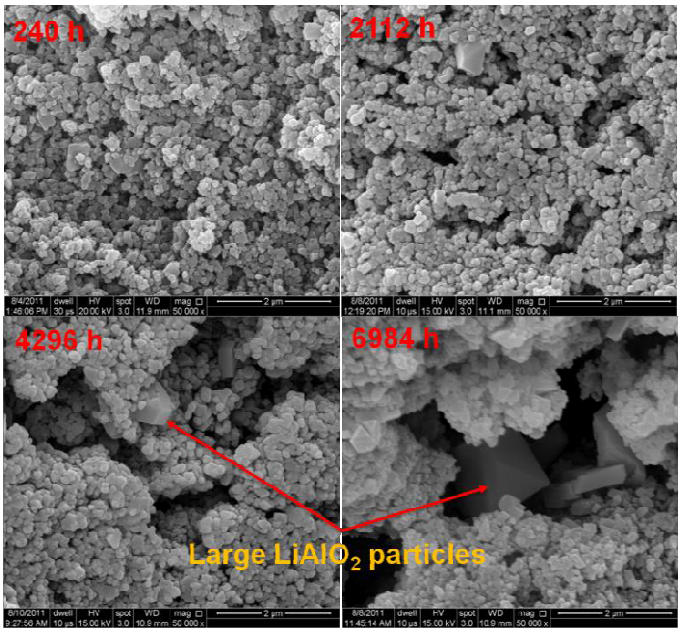

Figure 5: FESEM images of fracture cross-section of cathode side tested matrix samples (after electrolyte removal).

Core-shell morphology has been observed in the electrolyte matrix as shown in Figure 6.

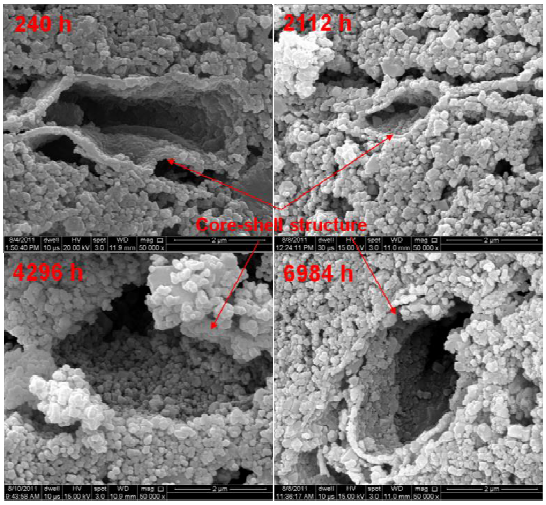

Figure 6: Core shell feature in matrix.

Figure 7 shows the elemental distribution of Ni particles near anode side for tested samples. The 2D and 3D images of nickel distribution have been shown in Figure 7. As expected, nickel precipitation is predominantly due to the reduction of dissolved nickel species at lower oxygen partial pressure (near the anode electrode).

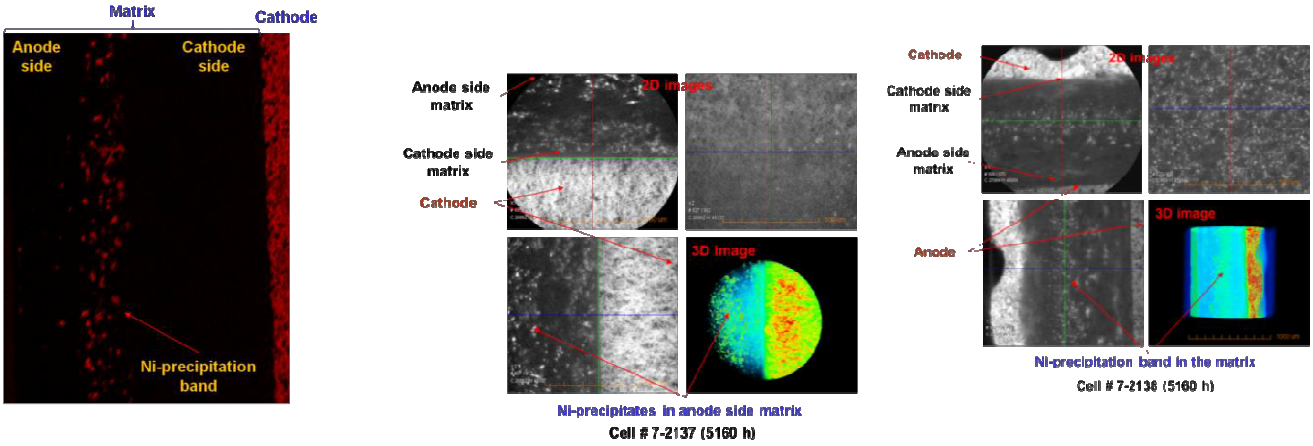

Figure 7: Images showing nickel precipitation in matrix.

Project Title: Waste to Energy: Biogas Cleanup (Desulfurization) for Energy Generation
Industrial Partner: FuelCell Energy
PI: Steven L. Suib

Status:
The overall technical objectives of the proposed work includes evaluation of biomass utilization and evaluation of sulfur cleanup process. The technical steps include:

- Synthesis of Materials
- Packed-bed Reactor assembly
- Experimental Setup
- Sulfur Capacity and Calibrations Curves
- Breakthroughs (at 5 ppm) and Sulfur Capacity
- Conclusions
- Ongoing and Future Work

Synthesized Materials:
A general procedure involved preparation of three solutions A, B and C.
Solution A has in it 19.8 g $MnSO_4$ in 67.5 mL DDW + 6.8 mL HNO_3. Solution B contains 13.3 g $KMnO_4$ in 225 mL DDW. Solution C has 10 wt.% $Fe(NO_3)_3$ in 50 mL
(or 10 wt.% $Co(Ac)_2$ or 10 wt.% $Cu(Ac)_2$). Solutions B and C were added drop-wise to Solution A while stirring vigorously. This mixture was refluxed at 100 °C for 24 h, washed, and then filtered with 4 L DDW. The resultant material was dried overnight at 80 °C. The prepared granules are shown below in **Figure 1**. Deposition of PDMS (polymimethylsiloxane) was performed on the granules for 30 min.

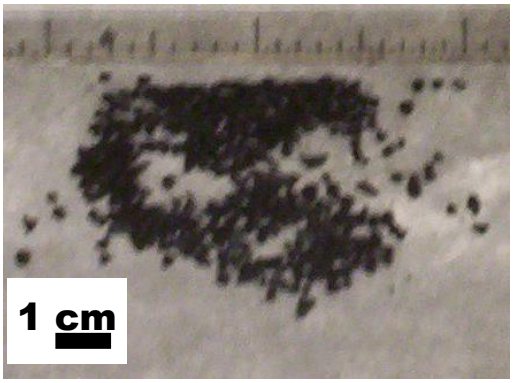

Figure 1, Granules of Manganese Oxide.

A diagram of the reactor is shown in **Figure 2**. The granules were size separated using different size sieves. Various transition metal doped manganese oxide material were studied such as those containing cobalt, copper, and iron.

In addition, amorphous manganese oxide (AMO) materials were also studied. These AMO materials have large surface areas and are porous materials. A final set of samples were prepared by coating various doped and undoped manganese oxide materials with polydimethylsiloxane (PDMS). Coating particles with PDMS leads to hydrophobic surfaces of the particles. The amount of PDMS coating is important and can control entrance of sulfur species into pores of these oxide materials. The positions of the dopant cations of cobalt, copper and iron depend on the synthesis methods. Possible locations for the dopant ions

include in the tunnel cation-exchange sites, in the framework structure of the manganese oxide materials or as separate salt phases on the surface or in the pores of the materials. The locations of these transition metals are clearly related to sorption capacities of these different systems (*vide infra*).

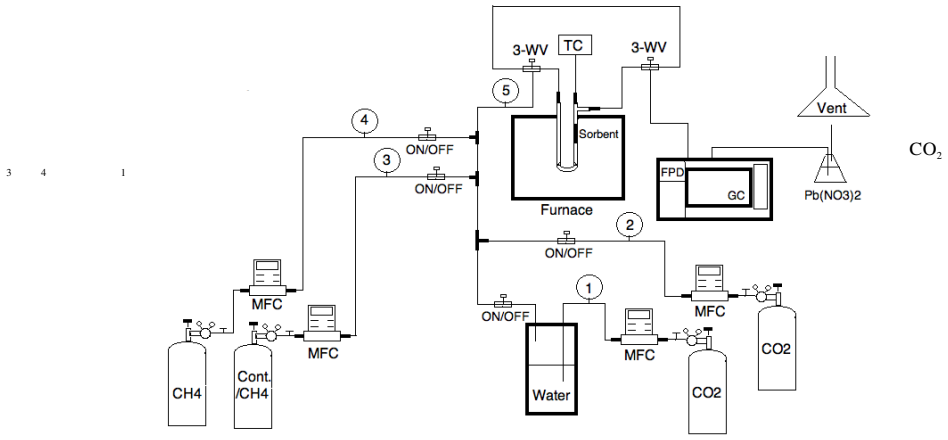

Figure 2. Diagram of Apparatus Used for Adsorption Studies.

The sulfur capacity of various transition metal doped manganese oxides was collected. These data are shown in **Figure 3**.

Sulfur Capacity (SC)

FuelCell Energy
Ultra-Clean, Efficient, Reliable Power
UCONN

Screened sorbents at **0% RH**:

#	Material	Cont.	Mass (g)	BT (h)	SC (*)	RH (%)	CO_2	Cont./CH_4	CH_4	Total (SCCM)
1	**Co-OMS2**	H_2S	0.1	**32.20**	**7.6**	**0**	30	15	30	75
2	**OMS2**	DMS	0.1	**5.28**	**1.2**	**0**	14	14	7	35
3	**Co-OMS2**	DMS	0.1	**5.67**	**1.2**	**0**	14	14	7	35
4	**Co-OMS2**	DMS	0.1	**4.97**	**1.1**	**0**	14	14	7	35
5	**Cu-OMS2**	DMS	0.1	**2.77**	**0.6**	**0**	14	14	7	35
6	**Fe-OMS2** (powder)	DMS	0.1	**11.61**	**2.5**	**0**	14	14	7	35
7	**Fe-OMS2**	DMS	0.1	**8.97**	**1.9**	**0**	14	14	7	35
8	**Fe-OMS2_PDMS**	DMS	0.1	**5.14**	**1.1**	**0**	14	14	7	35
9	**AMO**	DMS	0.1	**9.30**	**2**	**0**	14	14	7	35
10	**AMO_PDMS**	DMS	0.1	**4.02**	**0.9**	**0**	14	14	7	35

BT: Breakthrough
SC: Sulfur capacity
*: g-sulfur /100 g sorbent
H_2S: Hydrogen sulfide
DMS: Dimethyl sulfide C_2H_6S
tbd: to be determined

Figure 3, Breakthrough Curve Data for Various Adsorbents at 0% Relative Humidity.

These data clearly show that differences are observed for the various adsorbent materials. Breakthrough of various sulfur containing species were measured in this case of 0% relative humidity.

Data for various relative humidity scenarios area shown below in **Figure 4**.

#	Material	Cont.	Mass (g)	BT (h)	SC (*)	RH (%)	CO_2	Cont./CH_4	CH_4	Total (SCCM)
1	**Fe-OMS2**	DMS	0.1	**8.97**	**1.9**	**0**	14	14	7	35
2		DMS	0.1	**3.24**	**0.7**	**20**	14	14	7	35
3		DMS	0.1	**1.67**	**0.4**	**40**	14	14	7	35
4	**Fe-OMS2_PDMS**	DMS	0.1	**5.14**	**1.1**	**0**	14	14	7	35
5		DMS	0.1	**0.46**	**0.1**	**20**	14	14	7	35
6		DMS	0.1	**0.41**	**0.1**	**40**	14	14	7	35
7	**AMO**	DMS	0.1	**9.30**	**2**	**0**	14	14	7	35
8		DMS	0.1	**9.56**	**2.1**	**20**	14	14	7	35
9		DMS	0.1	tbd	tbd	**40**	14	14	7	35
10	**AMO_PDMS**	DMS	0.1	**4.02**	**0.9**	**0**	14	14	7	35
11		DMS	0.1	tbd	tbd	**20**	14	14	7	35
12		DMS	0.1	tbd	tbd	**40**	14	14	7	35

BT: Breakthrough
SC: Sulfur capacity
*: g-sulfur /100 g sorbent
H_2S: Hydrogen sulfide
DMS: Dimethyl sulfide
C_2H_6S
tbd: to be determined

Figure 4, Breakthrough Data for 0, 20, and 40% relative humidity.

Conclusions from the above studies suggest the following:

1. From screening tests at 0% RH, the best materials for DMS removal were Fe-OMS2 and AMO, giving a sulfur capacity of ~2 g-sulfur /100 g sorbent.
2. At 20 and 40% RH, Fe-OMS2 decreases its sulfur capacity to 0.7, while AMO is still active at 2.
3. Coating the sorbents with PDMS (polydimethylsiloxane) decreases the sulfur capacity of the materials, even at high moisture content.
4. XRD of the materials after sulfur removal does not show new crystal phases.

We have continued to improve upon the materials being used for sulfur adsorption. We have scaled up the material to 100 g and sent this to FCE for further testing in their reactors. Some breakthrough curves for various ZnO getters are shown in **Figure 5**.

Much of this effort has been dedicated to analyses of siloxane species. This work has involved the use of chromatography methods to analyze these species in real samples from test facilities. These samples have been provided by FCE. We have solved problems in the analyses of these materials and can provide routine analyses of these contaminants.

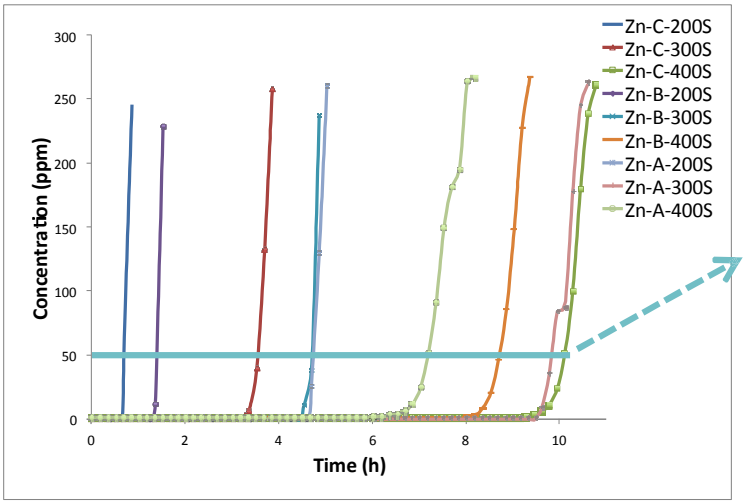

Figure 5, Various Breakthrough Curves or ZnO Materials.

Various sulfur capacities of the ZnO materials are shown in **Figure 6**. We are also focusing on coatings of these materials on stable cordierite supports such as those shown in **Figure 7.**

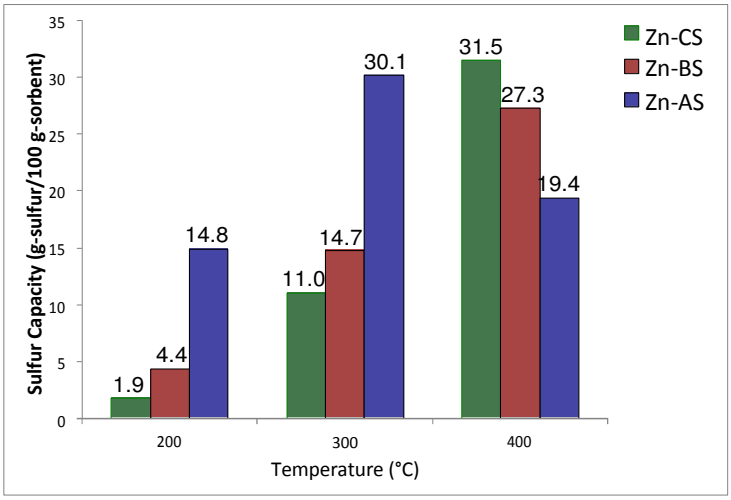

Figure 6, Sulfur Capacities for Different ZnO Getters at Various Temperatures.

We focused on optimizing the absorptive and catalytic capacities of these different systems for a variety of different contaminants including sulfur, siloxane, and mixed sulfur siloxane species. A major current and ongoing focus involves the catalytic degradation of carbon sulfur systems. These materials are proving difficult to getter. A major issue to address concerns the competitive degradation of such sulfur species. The carbon sulfur species appear to be more difficult to getter than the non-carbon containing sulfur contaminants. We do not anticipate any problems that will hinder the progress of this research. Characterization of the intermediates involved in the adsorption and catalytic processes is ongoing and involves a myriad of characterization methods such as Dynamic Analysis in Real Time (DART) mass spectrometry (MS) methods.

We have focused our studies on a variety of different materials including OMS-2, Activated carbon, and zeolites. The zeolites were chosen for comparative purposes. The activated carbon samples were also chosen primarily as standard materials. The most active materials we have studied are OMS-2 based systems. The most recent sulfur species of most interest have been carbon sulfide systems.

Figure 7, ZnO Coated On Cordierite Monolith Structure.

The primary mechanism of adsorption would appear to be physical adsorption although some chemical adsorption may also be taking place. Specific interactions appear to be related to dopant species in the OMS-2 material. A key finding has been that the surface area can be markedly affected by how the samples are prepared. This in turn clearly influences the uptake of sulfur species by these materials. The primary key task right now is the scale-up of these adsorbents with delivery to FuelCell Energy for testing in their reactors. We have been able to scale these systems to 300 g currently and are working to further scale-up.

Current Ideas and Key Issues:
Our recent work led to similar goals as previously reported as follows:

We have investigated sulfur removal mechanisms of different media (OMS-2, Activated carbon, zeolites) and the fates of different sulfur species (DMS, CS_2 and COS)

1. We have determined sulfur species captured by media, through physical adsorption and chemical means.
2. For chemical species, complex or chemical conversion to different compound(s) was observed.
3. Product(s) formed for chemical conversion were observed.
4. We have investigated impacts of other components or impurities on capacities of DMS, CS_2 and/or COS with different media (both new media and conventional) such as moisture, relative humidity, hydrocarbons, siloxanes, and oxygen.
5. We have investigated impacts of pressure, temperature, GHSV, and TSA such as impacts of pressure on sulfur capacities of different media, impact of temperature on sulfur capacities of different media, both physical & chemical means, and TSA. Capacity, regeneration & number of cycles were studied before breakthrough.
6. We have prepared large quantities of material for testing at FuelCell Energy. Considerable tests have already been done at FCE and the results are very promising. We are now making 1000 g batches of adsorbent.
7. We have determined the most important parameters of the most active adsorbent and the synthetic factors necessary in order to make these materials properly.

8. Promising adsorbents have been developed. The adsorption capacity is 35 times that of activated carbon. For this reason we are continuing to optimize these materials.
9. The mechanism of adsorption and whether or not catalytic degradation is involved is continuing to be studied.
10. These materials are now being evaluated in scaled batches for possible commercial use.

Patent:
One patent application has been submitted. This patent application concerns the high adsorption capacity of doped OMS-2 adsorbents.

Publications / Presentations:
1. Presentations have been made at FuelCell Energy on results from this project and in joint meetings at UCONN. Publications on the sulfur getters and on the novel OMS-2 materials are being prepared.
2. Garces, H. F.; Espinal, A. E.; Suib, S. L., Tunable Shape Microwave Synthesis of Zinc Oxide Nanospheres and Their Desulfurization Performance Compared with Nanorods and Platelet-Like Morphologies for the Removal of Hydrogen Sulfide, *J. Phys. Chem. C*, 2012, **116**, 8465-8474.
3. Sharma, H.; Suib, S. L.; Mhadeshwar, A., Interactions of Sulfur Oxides with Diesel Oxidation Catalysts (DOCs), in ACS Symposium Series, Novel Materials for Catalysis and Fuels Processing, 2013, **1132**, 117-155.

Project Title: Pressure retarded osmosis and membrane development
Industrial Partner: OASYS waterI
PI: Steven L. Suib

Status: Final Report

Salinity gradient energy is an area of renewable energy that has long been overlooked by North American energy companies. In the US and in neighboring countries, "renewable energy" usually meant focusing on wind, solar, biomass and geothermal sources. In Europe, though, an innovative company called Statkraft, began to develop a technology to harness the power of salinity gradients that exist at river deltas. These gradients are formed as water is evaporated from the oceans and falls as freshwater to form rivers that remix at the delta. The "energy of mixing" could theoretically be captured, essentially capturing some of the "energy of demixing" absorbed by the oceans when the sun causes water to evaporate.

This concept was not new and in fact was introduced by a famous membrane scientist known as Sidney Loeb back in the 1970s. Using a semi-permeable membrane, osmotic flow would be induced across the membrane by the salinity gradient. This flow could be "retarded" by a hydrostatic pressure in the high salinity solution. As the flow worked against this constant pressure, work could be generated ($P\Delta V$) which is called pressure retarded osmosis (PRO).

The concept was fascinating. Essentially, we could begin to capture large amounts of the suns energy that was captured by the oceans through evaporation. However, the concept was fraught with challenges. Most notably, we are limited geographically to river delta regions. Also, we are limited to the osmotic pressure of seawater (unless we consider hypersaline water sources). Most problematic is the potential of fouling of the membrane. These waters are natural and therefore contain both organics and inorganics which will lead to fouling of the membrane. Pretreatment is an option, but such an effort would cost energy and dramatically reduce the efficiency of the process.

It was these drawbacks of conventional PRO that led to the development of the osmotic heat engine (OHE). This engine works on the same principle of PRO, but replaces seawater with a thermally regenerable osmotic agent, or draw solute. Heat is captured and then used to concentrate the draw solute. The use of an engineered draw solute has multiple benefits. First, we can use pristine solutions that lack foulants. Second, we can generate far greater osmotic pressures than seawater. Both of these facts lead to much greater power generation capability than conventional PRO.

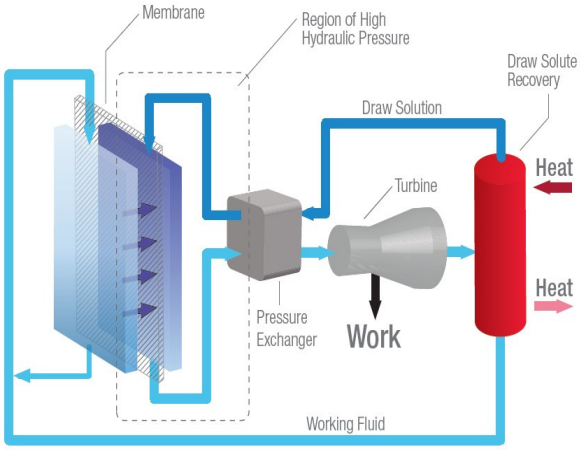

Figure 2 - Schematic diagram of the OHE system

The support from this project has touched a variety of projects throughout our lab. Overall, we have developed a better understanding of the potential of an OHE system. Our contributions can be broken down into the following areas

1. Designing and constructing a benchtop PRO testing system
2. Testing power density prospects when using high salinity draw solutions
3. Developing membranes with promise as PRO membranes

These three main thrusts led to a number of presentations and papers that have advanced the salinity gradient process field since this project began 3 years ago.

Designing a Benchtop PRO System

The first part of this project was to build a customized benchtop testing system that would test the theoretical power density of flat sheet membranes while under real PRO conditions. Our first generation system is in the figure 3.

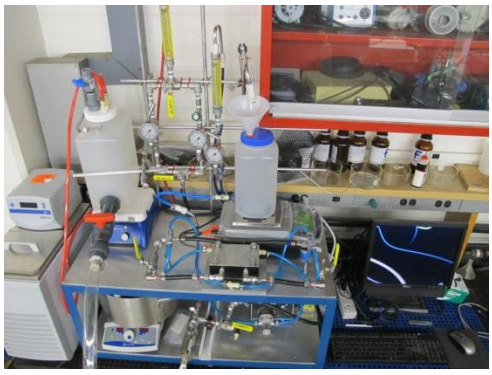

Figure 3 – a) on left, the 1st generation PRO test system. b) on right, the 2nd generation PRO system

These systems, amongst the first of their kind around the world, represent a distinctive competency added to our lab during the course of this project. These systems became the centerpiece of the data that followed.

Testing Power Density using High Salinity Brines

To test the efficacy of OHE-like conditions, we used the newly built PRO benchtop systems to evaluate membrane performance using high salinity sodium chloride brines. These brines would simulate an engineered draw solute *and its temperature* by looking at both salinity and temperature effects. Some of the data is shown in Figure 4. This data shows that higher salinity brines have the potential to generate high power density, sometimes in excess of 30 watts/m^2. For comparison, Statkraft targets for conventional PRO using natural salinity gradients is 5 watts/m^2.

In all, we found that higher salinity brines at higher temperatures exhibited higher power density. This further supported the notion that the OHE would prove to be a more versatile and valuable platform than conventional PRO.

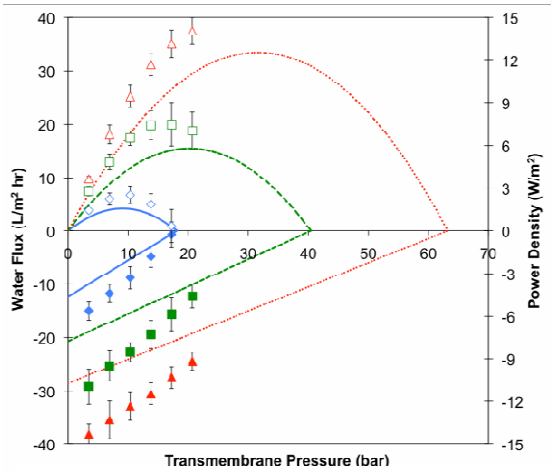

Figure 4 – Power density data for high salinity brines. Diamonds are for 0.5M NaCl draw solution (close to seawater), squares are for 1 M NaCl, and triangles are for 1.5 M draw solution.

Designing Membrane Platforms for PRO

Part of this work involved developing novel PRO membrane platforms using innovative technology developed as part of our work over the past few years in our lab. One such platform was the use of electrospun nanofibers for making highly selective thin film composite membranes for PRO. These nanofibers have excellent transport properties and lend themselves to excellent performance in osmotically driven membrane processes. Pictures of the membranes are shown in Figure 5

Figure 5 shows that a defect free film can be formed on these nanofibers using a process known as interfacial polymerization. This film is selective for water and prevents salt from passing (similar to a reverse osmosis membrane). Two membrane types were made. One was a highly selective RO membrane (mTFC). The other was a lower selectivity nanofiltration like membrane (pTFC) These membranes were shown to be pressure tolerant up to 150 psi in RO tests.

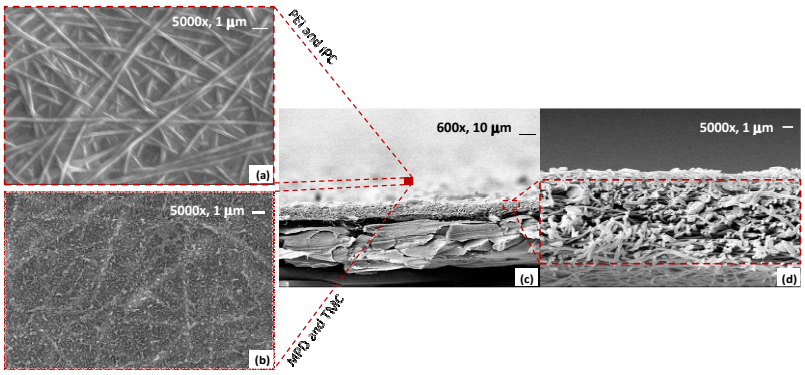

Figure 5 – SEM images of top (left) and cross sections (middle and right) of thin film composite membranes supported by electrospun nanofibers.

Both membranes performed well in PRO tests. Using a synthetic seawater solution, both membranes exceeded the Statkraft target of 5 W/m^2 power density. Results are shown in Figure 5.

These results do show some interesting behavior. The non-linear flux decline upon increasing of pressure is cause for concern and suggests that the membrane properties are changing under the condition of the test.

Development of newly designed nanocomposite membranes which showed remarkable flux performance when tested under simple osmotic flow has been reported. In this work, we have embedded silica nanoparticles into a nanofiber membrane in order to increase hydrophilicity of the membrane. This increase hydrophilicity led to dramatic increases in flux performance for the membrane under osmotic flux conditions. Figure 6a and b shows how the particles embed into the fibers either as individual particles or as clusters.

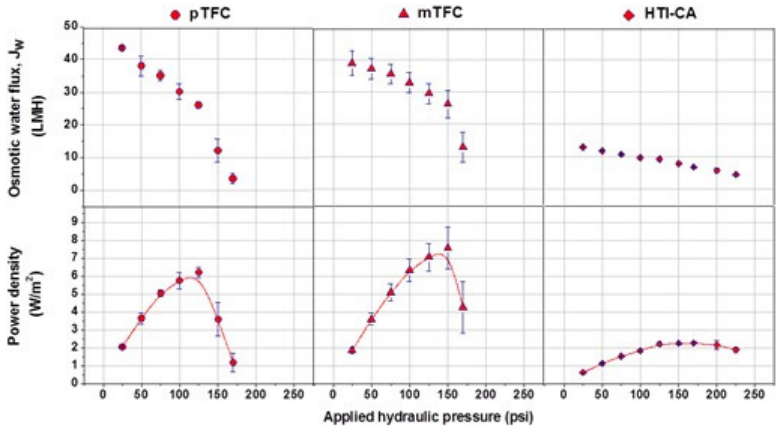

Figure 6a – Flux and power density performance of our two TFC membranes alongside a commercial FO membrane (HTI-CA).

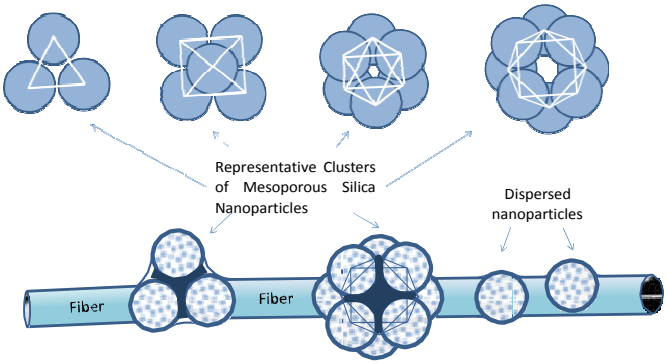

Figure 6b – illustration of nanoparticle morphologies when embedded into a polymeric nanofiber

When these nanocomposite fibers are placed into a thin film composite membrane, the water flux is enhanced by either surface transport of water along the particle surface or by transport through the mesoporous structure of the silica (Figure 7).

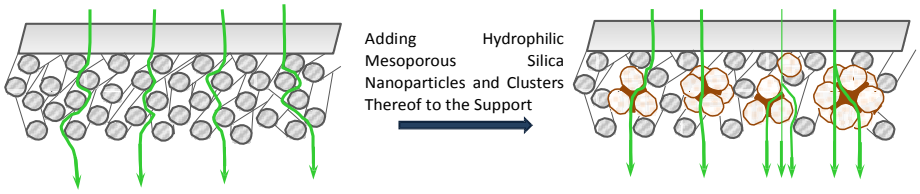

Figure 7 – Illustration of new nanocomposite nanofiber thin film composite membrane and the mechanisms of water flux enhancement.

There may be additional benefits caused by charge adsorption or surface diffusion. We continue to explore this phenomena in light of the data presented in Figure 10.

SEM (Figure 8) and TEM (Figure 9) micrographs are shown to indicate both the morphology of the nanocomposite and the mesoporosity of the nanoparticle

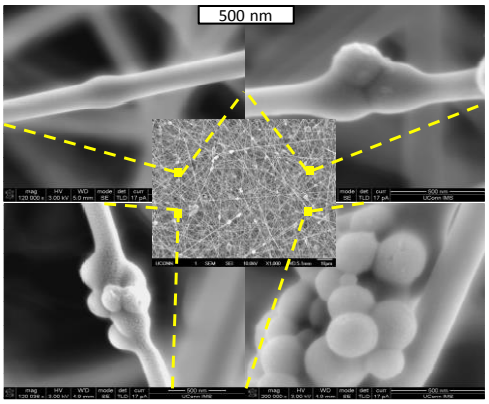

Figure 8 – SEM images of embedded silica nanopartilces in polyacrylonitrile nanofibers

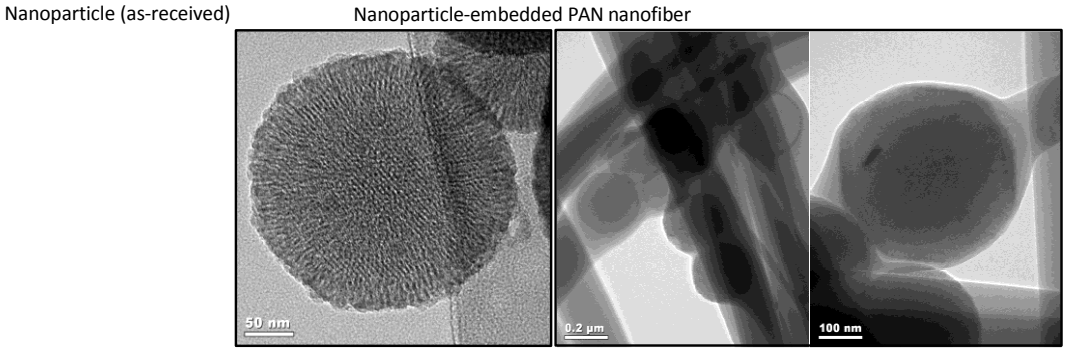

Figure 9 – TEM images of as-received nanoparticles (left) and embedded nanoparticles (middle and right)

The performance of these new nanocomposite membranes is astounding. Figure 10 shows the water, flux performance of these membranes in both the FO and PRO modes. Overall, these new membranes perform 6-fold better than the commercial HTI membrane, and about 2-fold better than our first generation nanofiber based TFC membranes.

In all, these results were astounding. These fluxes represent some of the highest osmotic fluxes ever recorded. We are currently preparing a manuscript for submission to the Journal of Advanced Materials.

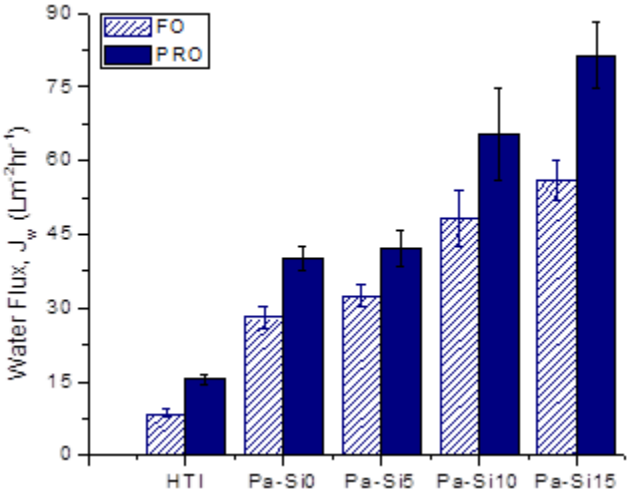

Figure 10 – Osmotic water flux data under varying loadings of silica nanoparticles in the electrospun nanofibers. Loadings of 0% (pure fiber), 5, 10, and 15% were considered

Collaboration with Oasys Water

The collaboration with Oasys Water has yielded a valuable information exchange. Oasys, which has licensed the PI's technology from Yale University, has interest in seeing this technology advanced. They have provided membranes and expertise throughout the project in addition to their cost share to match the DOE contribution. We thank them for their support and willingness to participate in this project.

Products of this Work

While every result from the work as part of this report, a number of important products were generated based on this work. Paper and presentation 9Figure 11) listings are shown below.

Publications / Presentations:

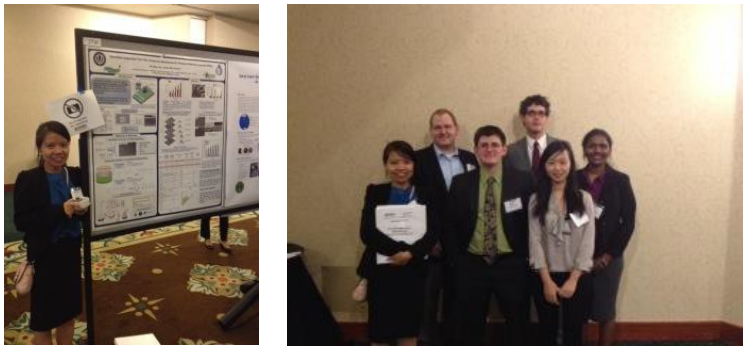

Figure 11 – Pictures of the group at the North American Membrane Society Annual Meeting in Boise, ID.

Publications and presentations since the start of the project are shown below.

Publications:
The following publications have been supported by this grant.

1. Arena, J., McCutcheon, J.R., "Surface modification of anisotropic thin film composite membrane support layers with polydopamine to facilitate water transport in pressure retarded osmosis", *Journal of Membrane Science* 375, 2011, 55-62.
2. Bui, N. Lind, M.L., Hoek, E.M.V., McCutcheon, J.R., "Electrospun supported thin film composite membranes for engineered osmosis", *Journal of Membrane Science* 385-386, 2011, 10-19.
3. Bui, N.N., McCutcheon, J.R., "Hydrophilic Nanofibers as New Supports for Thin Film Composite Membranes for Engineered Osmosis", *Environmental Science and Technology* 47, 2013, 1761-1769.

Publications in Preparation:

Publications in Preparation

1. Bui, N.N., Arena, J., McCutcheon, J.R., "Accurate Measurement of Structural Parameters for High Performance Osmotic Membranes", to be submitted to Journal of Membrane Science.
2. Anastasio, D., Arena, J.T., Cole, E., McCutcheon, J.R. "Impact of Temperature on Power Density for Closed Loop Pressure Retarded Osmosis", to be submitted to Journal of Membrane Science.
3. Huang, L., McCutcheon, J.R., "Nylon 6,6 Nanofiber Supported Membranes for Engineered Osmosis", to be submitted to Journal of Membrane Science.
4. Bui, N.N., McCutcheon, J.R., "Impacts of Nanofiber Size on Osmotic Flux Performance of Thin-film Composite Membrane for Engineered Osmosis". To be submitted to Journal of Membrane Science.
5. Bui, N.N., Manickam, S.S., McCutcheon J.R., "Improving Mechanical Integrity of Nanofibrous Membranes using Co-solvent System for Electrospinning". To be submitted to Separation and Purification Technology.
6. Bui, N.N., McCutcheon, J.R., Nanocomposite Nanofiber Supported TFC Membranes for Engineered Osmosis." to be submitted to the Journal of Advanced Materials.

Presentations:

A number of presentations have been supported by this work. Many have been invited where the PI was supported to come speak about salinity gradient power and other associated technologies.

1. Anastasio, D., Arena, J.T., Cole, E., McCutcheon, J.R., "The Promise of High Power Density Closed Loop Pressure Retarded Osmosis Via the Osmotic Heat Engine", American Institute of Chemical Engineers Annual Meeting, San Francisco, CA.
2. McCutcheon, J.R., "Engineered Osmosis for Sustainable Water and Power", Colorado School of Mines, Department of Chemical Engineering Seminar Series, September 20, 2013.
3. McCutcheon, J.R., "Engineered Osmosis for Sustainable Water and Power", Pennsylvania State University, Department of Chemical Engineering Seminar Series, September 26, 2013.
4. McCutcheon, J.R., "Engineered Osmosis for Sustainable Water and Power", Drexel University, Department of Chemical Engineering Seminar Series, September 27, 2013.
5. McCutcheon, J.R., "Electrospun Materials for Water and Power", Keynote lecture in "Materials-Based Technologies for Water and Energy Sustainability: Research Frontiers and Practical Challenges to Adoption" session at the American Chemical Society Annual Meeting, Indianapolis, IN, September 11, 2013.
6. Bui, N., McCutcheon, J.R., "High Power Density Nanofiber Supported Thin Film Composite Membrane for Pressure Retarded Osmosis", Oral presentation North American Membrane Society, Boise, ID, June 8-12, 2013.
7. McCutcheon, J.R., "Nanofiber Technology at the University of Connecticut", Hollingsworth & Vose, Groton, MA, June 18, 2013.
8. McCutcheon, J.R., "Engineering Osmosis for Water, Separations and Power Generation", Dow Water Solutions, Minneapolis, MN, June 14, 2013.
9. McCutcheon, J.R., "Nylon 6,6 Supported Membranes for Forward Osmosis", 3M Science and Engineering Faculty Day., Minneapolis, MN, June 12, 2013.
10. McCutcheon, J.R., "New Membrane Platforms for Engineered Osmosis", ACS Polymer Membrane Mediated Water Filtration Meeting, Pacific Grove, CA, February 28, 2013.
11. McCutcheon, J.R.,"New Membrane Platforms for Pressure Retarded Osmosis", Statkraft, Oslo, Norway, December 12, 2012.
12. McCutcheon, J.R., "Engineered Osmosis for Sustainable Water and Power", University of Kansas Department of Chemical and Petroleum Engineering Seminar Series, December 4, 2012.
13. Bui, N.N., McCutcheon, J.R., "Hydrophilic Nanofibers as Supports for Thin Film Composite Membranes for Engineered Osmosis." American Institute of Chemical Engineers Annual Meeting, November 2012.

14. Huang, L., Bui, N.N., McCutcheon, J.R. "Nylon 6,6 Microfiltration Membranes as Supports for Thin Film Composite Membranes for Engineered Osmosis". American Institute of Chemical Engineers Annual Meeting, November 2012.
15. McCutcheon, J.R. "Next Generation Membranes for Forward and Pressure Retarded Osmosis", International Union of Pure and Applied Chemistry. Blacksburg, VA, July 24-27, 2012.
16. Arena, J., Manickam SS, Reimund, K.K., McCoskey, B.D., Freeman, B.D., McCutcheon, J.R., "Surface Modification of Thin Film Composite Membranes with Polydopamine for Engineered Osmosis", Oral Presentation at the North American Membrane Society Annual Meeting, New Orleans, LA, June 9-13, 2012.
17. McCutcheon, J.R., "Next Generation Membranes for Forward and Pressure Retarded Osmosis", 3rd Annual Water Industry Exhibition & Conference, May 2-4, 2012.
18. "Forward Osmosis and Pressure Retarded Osmosis: Fundamentals and Applications", American Institute of Chemical Engineers Annual Meeting, Invited talk in the Membrane Tutorial Technical Sessions (sponsored by section 2d), Minneapolis, MN, October 16-21 2011.
19. McCutcheon, J.R., "New Membranes for Forward and Pressure Retarded Osmosis", 3M® Tech Forum, Minneapolis MN, October 21, 2011
20. Bui, N., Arena, J., McCutcheon, J.R., "New Approaches to Forward Osmosis Membrane Design", Oral Presentation, American Institute of Chemical Engineers Annual Meeting, Minneapolis, MN, October 16-21, 2011.
21. Bui, N., Lind, M.L., Hoek, E., McCutcheon, J.R. "Electrospun Nanofibers Support for High Flux Thin-film-composite Engineered Osmosis membrane", Poster, Raleigh, NC, August 29-31, 2011.
22. Bui, N., Lind, M.L., Hoek, E., McCutcheon, J.R. "Fabrication and characterization of novel nonwoven nano-structured thin film composite membrane for engineered osmosis applications", Oral Presentation, International Congress on Membranes and Membrane Processes, Amsterdam, The Netherlands, July 23-29, 2011.
23. McCutcheon, J.R., "Engineering Osmosis for Sustainable Water and Power", Battelle Memorial Institute, June 29, 2011
24. Bui, N., Lind, M.L., Hoek, E., McCutcheon, J.R. "Nanostructured Support for High Flux Thin-film-composite Engineered Osmosis Membrane", Oral and Poster Presentations, North American Membrane Society, Las Vegas, NV, June 4-8, 2011.
25. Arena, J., McCloskey, B., McCutcheon, J.R., Freeman, B. "Hydrophilization of Thin Film Composite Membrane Support Layers for Engineered Osmosis", Oral and Poster Presentations, North American Membrane Society, Las Vegas, NV, June 4-8, 2011.
26. Arena, J., McCloskey, B., McCutcheon, J.R., Freeman, B. "Hydrophilization of Thin Film Composite Membrane Support Layers for Engineered Osmosis Applications", Oral Presentation at the American Institute of Chemical Engineering Annual Meeting, Salt Lake City, UT, November 7-12, 2010.

Project Title: Fuel Reforming Catalysts for Efficient Energy Usage
Industrial Partner: APSI
PI: Steven L. Suib

Status Overview:
This report consists of four parts.
1. Goals of the Current Work.
2. Summary of Metal Alloy Catalysts and Rationale For Production.
3. Synthesis of Metal Alloy Thin Films.
4. Application Studies.
5. Current Research.

Goals of the Current Work:
- Reduce the amount of material per catalyst.
- Produce characteristic surfaces of the catalyst with less volume of material.
- Understand the working mechanism of the catalyst by isotope labeling.
- Scale-Up work.

Summary of Metal Alloy Catalysts and Rationale for Production:
A new family of single or multiple metal shelled and single metal cored alloys has been prepared at atmospheric conditions. In such processes, metal foils were bi-functionally used as substrates and reducing reagents with the presence of mixed organic solvents and desired metallic precursors. The metal foils were coated with thin films of multiple metallic alloys after certain controlled reaction times at different temperatures. These alloys may have many important chemical applications, such as functioning as heterogeneous catalysts in fuel reforming processes and electrode materials in Li batteries.

The construction of core-shelled alloys is a known process used to tailor the physical and chemical properties of an existing substrate. Current methods of making metallic alloys rely on high temperature or high pressure conditions, which limit large-scale producing and increase the cost of such products. In carbothermal reductive processes, carbon was ball milled with metallic precursors and heated up to 850^0C to yield such alloys. Argon was normally used as a protective gas; meanwhile carbon monoxide waste gas was generated. Such process involves using carrier gas and a sophisticated setup and initiates the treatment of harmful waste-gas problems. In gas processes, hydrogen gas was used to reduce metal oxide alloy precursors. Critical experiment conditions and expensive syngas were concerns for production of bulky materials. In wet chemistry processes, harsh reducing reagents, such as hydrazine, hydroxylamine, $NaBH_4$, or boranes, were used to reduce metal precursors. These reducing reagents require special handling due to their reactive properties. These processes are normally done in sealed pressure vessels at different temperatures. The limited reaction vessel volume eliminates the possibility of facile and large-scale preparation of such alloys.

All the aforementioned three methods not only potentially bring up safety issues in terms of chemical storage and operational management, but also unavoidably increase production cost. A green, easy-handling, and economic process is highly desirable for producing such metallic alloys.

A galvanic replacement process was used to prepare core-shelled multiple metal alloys in the presence of mixed organic solvents under atmospheric conditions. The use of thin relatively active metal foils, such as Mg, Al, Fe, Zn, as reductive reagents as well as substrates to deposit multiple metal alloys which may include single or combined multiple metal of Sn, Pb, Sb, Bi, Co, Ni, In, Cu, Hg, Ag, Pt, Pd, Au. The use

of mixed environmentally benign organic solvents at favorable temperatures mediates the galvanic reaction rate, ending up with a single metal cored, single or multiple metal shelled alloys..

Adding other carbon or silicon based materials, such as carbon black, graphite, graphene, carbon nanotubes, fullerene, silicon nanomaterials into the mixed organic solution could result in an 'ink' suspension which may lead to the formation of more advanced metallic alloy/C or metallic alloy/Si nanocomposites. Such nanocomposites are good electrode materials for Li batteries.

Synthesis of Metal Alloy Thin Films:
In such processes, metal foils were suspended in a container, which was filled with suitable single or mixed metal salt precursors and mixed organic solvents for different times at variable temperatures as illustrated in **Figure 1**. Relatively active metal foils were Mg, Al, Zn, Fe, Ni, etc. A refrigerator or ice bath was used to control the reaction temperatures at 0^0C-5^0C when necessary; otherwise the reaction was done at ambient temperature. The cationic part of metallic precursors contains one or several metals like Sn, Pb, Sb, Bi, Co, Ni, In, Cu, Hg, Ag, Pt, Pd, and Au, while the anionic part contains sulfate, nitrate, chloride, acetate, or acetylacetonate. The organic solvents used are one or several of the type ethanol, ethylene glycol, and glycerol. The reaction time was set between 2 hours and 48 hours. For example, 1.54 g $SnCl_2$, 0.39 g $SbCl_3$, 0.01 g $BiCl_3$, and 0.01 g $PbCl_2$ were dissolved in a mixed solvent which contained 5 mL ethanol and 5 mL ethylene glycol in a 25 mL vial. A piece of 1 cm × 1 cm× 0.1 mm Fe foil was suspended in such mixture at 0^0C. A piece of 1 cm × 1 cm× 0.25 mm Zn foil was also used in another same mixture. A polyvinylpyrrolidone (PVP) surfactant was utilized to control the particle sizes of formed alloy shells.

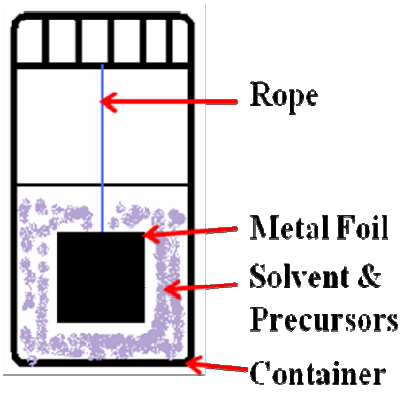

Figure 1 The scheme of a reaction setup.

The foils were gently removed from the mixture after 24 hours and dip-washed with ethanol and deionized water for several times. The products were vacuum dried at 50^0C for 48 hours and were further characterized with powder X-ray diffraction (XRD), scanning electron microscopy (SEM), and energy dispersive X-ray spectroscopy (EDX). **Figure 2** shows XRD patterns of (a) Fe/SnSb and (b) Zn/SnSb product respectively. **Figure 3** shows an SEM image and electron mapping on a Fe/SnSb product.
Catalyst testing process is shown in Figure 4.

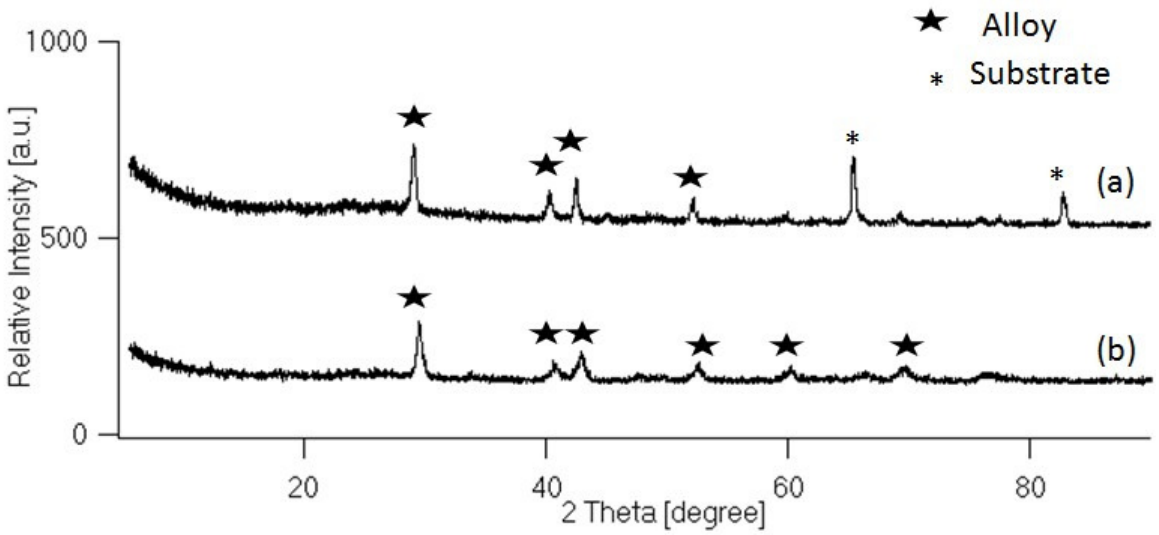

Figure 2 XRD patterns of (a) Fe/SnSb and (b) Zn/SnSb product respectively.

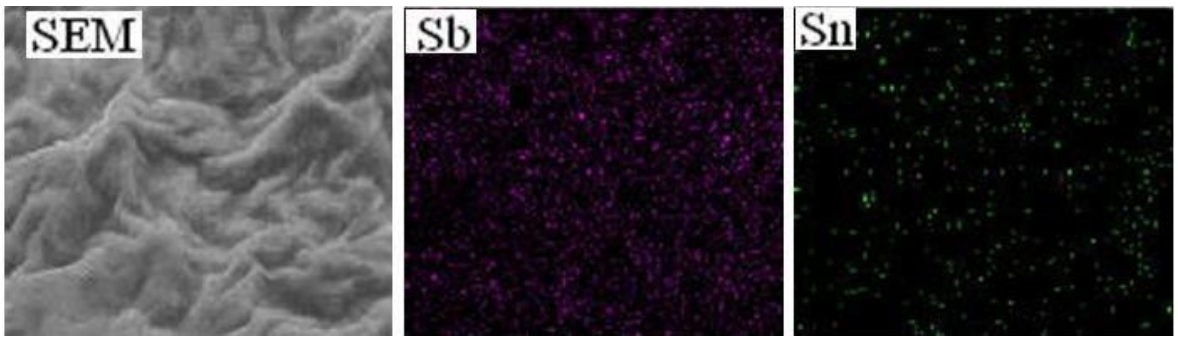

Figure 3 SEM image and EDX mapping on a Fe/SnSb product.

Application Studies:

A biodiesel synthesis experiment using FFC materials was done to identify whether FFC was catalytically active in forming biodiesel.

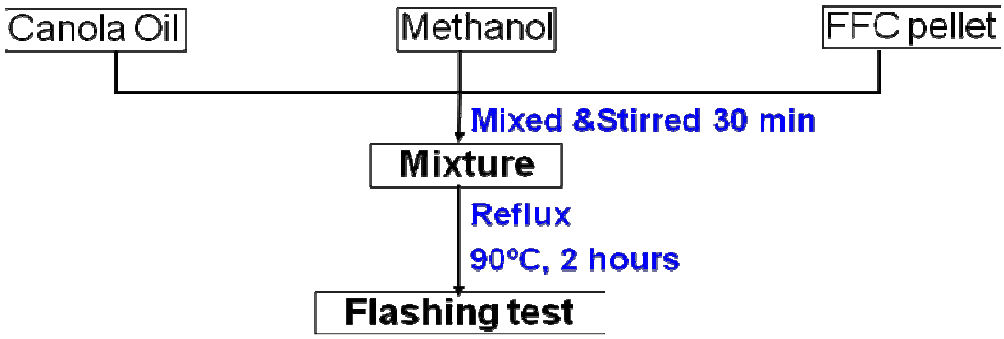

Figure 4, Catalytic Testing Process.

Results:

The following results were also obtained this past quarter:

- Continual Improvement of 2 Videos Concerning the Reforming FFC.
- The above mentioned Novel Synthetic Method for Preparation of Thin Films was Refined.
- New Synthetic Procedure concerning Dip Coating of FFC.
- Catalytic and Mechanistic Studies.

We now know that the performances of the synthetic catalysts made by the thin film route are as active or more active than the commercial product. We have a very good understanding of the mechanism of reaction of these materials by using Dynamic Analysis in Real Time (DART) mass spectrometry (MS). The DART-MS data suggest that the catalysts can selectively extract H atoms from model fuel compounds. A patent application is still in progress. We now need to thoroughly understand the mechanism of reaction of these materials and to do so need to run a variety of standard model compounds to understand the reactivity and mechanism.

Improvement of the synthesis of next generation FCC materials has been done. This method has been submitted as a patent application. The ability of this next generation catalyst to activate the reforming of hydrocarbons is continually being studied. This method involves the use of thin metal foils of various compositions (single metal precursors) that are immersed in solutions of precursors of other metals to produce metal alloy catalysts.
Characterization of these materials has involved surface composition, bulk composition, structure, electronic, and morphological properties. Various methods like atomic absorption, inductively coupled plasma, energy dispersive X-ray analysis, scanning electron microscopy, scanning Auger microscopy, X-ray powder diffraction, surface area, and pore size distribution methods are being used. The novel DAT MS studies are a major focus of our studies.

Catalytic testing of the FFC is being done with the process shown in Fig. 4 above. Characterization of reactants, products and intermediates will be done using gas chromatography, liquid chromatography, mass spectrometry, and temperature programmed desorption studies. In addition, Fourier transform infrared and Raman spectroscopy experiments are being done to study the functional groups on the surface of the FCC materials.

Current Research:
A key new set of experiments has involved use of DART-MS studies. We have used simple hydrocarbon molecules and have clearly shown that the commercial FFC and the thin film catalysts shown here act in the same way. In addition, from these model compound studies it is clear that the catalyst selectively removes only some of the C-H bonds and does not cause cracking of the model compounds. This allows formation of olefin species and the n coupling of the olefins in order to make higher hydrocarbons.

Our primary focus has been on the use of DART-MS studies to determine the mechanism of action of the Fitch Fuel Catalyst as well as the new thin film catalytic materials. We have found that there are several different mechanisms of activity of the catalyst depending on the type of substrate that is being activated. Some species are activated by hydrogen abstraction. Some others involve selective hydrogen abstraction as well as coupling reactions. Other substrates seem to form oxygenated species. A systematic study of a variety of representative species of different classes of fuels is now being investigated.

A set of single, double, and three component model compounds are currently being used to further study the mechanism of reaction of the Fitch fuel catalysts and the model new generation catalyst that have been made. Examples include straight chain hydrocarbons, aromatics, oxygenates, and mixtures of different functional groups.

Recent Ideas and Key Issues:
We have done studies on the mechanism of how such catalysts work. A key focus here was on the DART-MS studies. H abstraction is a primary process involved with most materials. Substantial cracking of C-C bonds is not occurring. This is also clear from all of our studies. In addition, it is clear that different hydrocarbons behave differently with the catalyst. Sometimes there is only isomerization. Sometimes there is minimal cracking. Our major focus was to figure out why the catalysts behave differently with different substrates. We believe that dopants in the structure of these materials may be important as well as defect sites. Concomitant product analyses with mass spectrometry, gas chromatography, and mixed GC-MS methods were done. We are planning to do studies with labeled reagents to track the transfer of hydrogen in these systems. A representative compound from a variety of classes of compounds was chosen to study the mechanism of activity by using DART MS as detection. At least two different types of mechanisms have already been identified, one involving H abstraction and the other involving O incorporation. These two mechanisms are not mutually exclusive. Our major focus was to understand mechanistic pathways of how these fuel species are reformed and to determine the best catalysts and catalytic conditions to optimize activity and stability.

Patents:
A patent application regarding synthesis of ultrathin films of next generation FCC materials has been submitted. This patent application was evaluated and UCONN is processing this application. The patent application is being negotiated with other companies now for licensing.

Publications/Presentations:
Several presentations were made to APSI on the synthesis studies that are described above. We are still writing a paper that describes the new synthesis method. We are also writing another paper concerning the mechanism of activation of the commercial catalyst and the new thin film catalyst primarily using DART-MS methods.

Project Title: Evaluation of Enzyme-Based Sulfur Removal Technology for Biogas Cleanup
Industrial Partner: nzymSys
PI: Ashish Mhadeshwar, Prabhakar Singh

Objective:
The overall goal of this project is to test and demonstrate a novel enzymatic way to reduce the sulfur content in biogas, with a primary focus on hydrogen sulfide (H_2S) removal. The application of the novel enzymatic technology for biogas desulfurization is investigated in a lab-scale semi-batch reactor. Simulated biogas containing realistic levels (~3000 ppm) of hydrogen sulfide (H_2S) is used to evaluate the effect of operating conditions, such as enzyme concentration, biogas flow rate, time-on-stream, and enzyme replenishment, on sulfur removal. From this comprehensive study, we have observed that even dilute enzyme solutions (4-5% wt.) are effective in removing up to 100% of the fed H_2S, during 8 hour tests. The enzyme is also selective to H_2S, and does not show any adverse effect on the other dominant components in biogas, such as methane and carbon dioxide. Experiments with enzyme replenishment indicate that the biogas desulfurization process could be potentially operated continuously for consistent removal of H_2S. Long term studies performed at higher enzyme concentration (20% wt.) demonstrate formation of sulfur precipitate, which could be recovered as a valuable product.

Introduction:
Widespread utilization of renewable energy sources is necessary to reduce greenhouse gas emissions and increasing dependence on fossil fuels. Renewable biofuels, such as biogas, ethanol, bio-diesel, glycerol, and bio-oil, represent a potentially alternative source of energy that could meet the ever increasing demand for more efficient heat, power, transportation, and food production.[1,2] Biogas production is a well-established technology as compared to other renewable biofuels. For example, over two million households in Asia have small scale digestion facilities that produce "gober (manure) gas". In the United States, an annual supply of over 1 billion tons of animal manure holds the potential to supply electricity to millions of homes. According to the American Biogas Council, methane (CH_4) in the renewable biogas could displace ~10-15% of current natural gas usage by 2025-2035[3]

Biogas is typically produced by microorganisms during anaerobic digestion of organic matter, such as manure, sewage sludge, household and industrial waste, as well as energy crops.[1,4-9] Biogas produced in landfills by anaerobic digestion is commonly referred to as landfill gas. The composition of biogas is determined by the raw material, the production method, and the presence of other components, such as sulfates, nitrates, ammonia, oxygen, nitrogen, and chlorinated compounds.[10-13] **Table 1** shows the typical composition of biogas, landfill gas, and natural gas.[1] CH_4 and carbon dioxide (CO_2) are the major components in biogas streams. Landfill gas contains higher concentration of nitrogen (N_2), whereas natural gas is primarily composed of CH_4 and higher hydrocarbons. Biogas offers substantial advantages over fossil fuel sources from an environmental prospective: (i) Biogas contributes to the mitigation of CH_4 – a highly potent greenhouse gas compared to CO_2 with greater potential for global warming.[2] It can be cleaned and upgraded to natural gas quality and subsequently used in the typical natural gas applications, thereby effectively utilizing the energy content of biogas rather than flaring the gas off in stacks. (ii) Biogas is considered to be carbon neutral because CO_2 is returned to the atmosphere at approximately the same rate as it is consumed during photosynthesis.[13] (iii) Biogas production reduces organic waste and yields a biodegradable and nutrient rich fertilizer.[13]

Table 1. Typical composition of biogas, landfill gas, and natural gas streams.[1]

Species	Biogas	Landfill gas	Natural gas
Methane (vol-%)	60-70	35-65	70-90
Other hydrocarbons (vol-%)	0	0	0-20
Hydrogen (vol-%)	0	0-3	0
Carbon dioxide (vol-%)	30-40	15-50	0-8
Nitrogen (vol-%)	~0.2	5-40	0-5
Oxygen (vol-%)	0	0-5	0-0.2
Hydrogen sulfide (ppm)	0-4000	0-100	0-5
Ammonia (ppm)	~100	~5	0
Aromatics (ppm)	0	0-200	0

Despite the advantages, efficient removal of sulfur components in biogas remains a formidable challenge in its widespread utilization. As shown in Table 1, H2S is the primary sulfur containing component in biogas (up to 4000 ppm) and landfill gas (up to 100 ppm). Other sulfur containing components include

mercaptans (up to 100 ppm[8]) and reduced forms such as sulfides, disulfides, and thiols. Concentration of these sulfur components is strongly dependent on the gas source. For example, H2S concentration range is determined by the sulfate content of the local water in a wastewater treatment plant.[14] The sulfur components are corrosive in nature and have potentially hazardous effects on human health and environment.[15-17] Furthermore, if biogas is used in chemical processes in the presence of catalysts, even a small concentration of sulfur species can severely affect the performance and lifetime of the catalysts involved in the reaction.[18]

Technically, biogas can be used for all applications intended for natural gas as long as it is purified and upgraded.[2] Depending on the end use of biogas, different gas quality standards are required and different desulfurization technologies can be applied. There are considerable differences among the biogas purity requirements for heating, combined heat and power (CHP), fuel cells, and vehicle fuel applications. For example, boilers do not have a high gas quality requirement; therefore, it is recommended to use stainless steel equipment and reduce the H2S concentration to less than 500 ppm.[19] CHP-engines require less H2S concentration than boilers to extend the engine operation time.[15] Use of biogas/landfill gas as a vehicle fuel requires the same fuel specifications of natural gas, which implies that the raw gas from a digester or a landfill needs to be free of sulfur and other contaminants (water, ammonia, N2, O2), in addition to the removal of CO2 in order to have a higher calorific value. Lastly, in order to use biogas in fuel cell systems, H2S concentration should be less than 1 ppm.[20] Overall, the design of a biogas purifier unit and cleaning process is influenced by several factors, such as: (i) the final gas purity required for the intended use, (ii) the composition of the gas feed (biogas or landfill gas), and (iii) the need for the purifier to be robust to handle variations in the biogas composition.

Typical H2S removal technologies from biogas and landfill gas are associated with one of the following categories: (i) precipitation, (ii) adsorption, (iii) chemical absorption, (iv) biological treatment, and (v) enzymatic treatment. Table 2 presents a summary of the main features, advantages, and disadvantages of each technology.

Table 2. Comparison of H_2S removal technologies.[1,9,21]

Precipitation			
Technique	**Features**	**Advantages**	**Disadvantages**
Air/O_2 addition [22-25]	▪ Applied during digestion process where it is used by *Thiobacillus* species ▪ O_2 addition of 2-6% ▪ Removal up to 1000 ppm ▪ Forms elemental sulfur	▪ Cheap investment ▪ Low electricity and heat needs ▪ Simple operation ▪ Removes high levels of H_2S (80-99% efficiency)	▪ Low removal rate ▪ Partial removal process ▪ O_2 overdose may cause explosions ▪ Inefficient in achieving low and stable H_2S levels
Iron ions/ iron oxide [25,26]	▪ Precipitation reaction with ions Fe^{2+}, Fe^{3+} ($FeCl_2$, $FeCl_3$, $FeSO_4$) forms FeS ▪ Endothermic	▪ Small capital investment ▪ Simple operation ▪ Ability to remove mercaptans	▪ Low removal rate ▪ Requires two beds for desulfurization and regeneration ▪ Loses 1/3rd of initial activity after regeneration cycle

Adsorption			
Technique	**Features**	**Advantages**	**Disadvantages**
$Fe_2O_3/Fe(OH)_3$bed ZnO [27-30]	▪ Forms iron sulfide, zinc sulfide ▪ Impregnated wood chips or pellets ▪ Iron sponge (rust covered steel wool)	▪ High removal efficiency >99% ▪ No air needed ▪ May capture mercaptans ▪ Inexpensive and simple operation	▪ Sensitive to water
Activated carbon [8,31-34]	▪ Dosed with KI (1-5%), K_2CO_3, ZnO, or H_2SO_4 to increase reaction rate ▪ Air addition of 4-6%	▪ High purification rate ▪ Low operation temperature ▪ Compact technique ▪ High loading capacity	▪ Expensive investment ▪ Methane losses ▪ H_2O and O_2 needed to remove H_2S ▪ Regeneration at 450 °C ▪ Spent adsorbent classified as hazardous
Absorption			
Technique	**Features**	**Advantages**	**Disadvantages**
Water scrubbing [35,36]	▪ Physical absorption	▪ High efficiency (95-100%) ▪ Inexpensive when water is available ▪ CO_2 is also removed	▪ Difficult technique ▪ Clogging possible ▪ High pressure and low temperatures
NaOH scrubbing [37]	▪ Enhances absorption capacity of water ▪ Forms Na_2S, NaHS	▪ Lower volumes are needed	▪ Non regenerative ▪ Disposal and contamination issues
Chelated iron-solutions [16,38-40]	▪ Fe(III)-EDTA is used to oxidize H_2S to elemental sulfur Thiosulfate is formed as byproduct	▪ Low O_2 residual ▪ 90-100% removal efficiency ▪ <1 ppm ▪ Can be performed at low temperature ▪ Easy regeneration	▪ Proper ratio of water and iron needs to be maintained ▪ pH of 8-10 needs to be maintained ▪ Susceptible to corrosion
Biological			
Technique	**Features**	**Advantages**	**Disadvantages**
Biofilter, Bioscrubbers Biotrickling filters [41-45]	▪ Water scrubbing combined with biological desulfurization	▪ No secondary contaminants ▪ Removal of >97% ▪ Low operational cost ▪ Environmentally friendly	▪ Only for low H_2S concentrations ▪ Extra H_2S treatment needed to reach pipeline quality

Enzymatic			
Technique	**Features**	**Advantages**	**Disadvantages**
Enzyme solutions [46-49]	▪ Enzymes enhance H_2S removal effect of Zinc salts	▪ High removal ▪ Simple operation ▪ Biodegradable ▪ Potential for elemental sulfur recovery	▪ Relatively unexplored technology

Enzymatic removal of H_2S from biogas is an emerging technology. A number of patents have been filed on the removal of sulfur components from fossil fuels, liquid hydrocarbons, sour crude oil, and sour natural gas.[46-49] However, there is a strong need for a simple and cost-effective enzymatic process to remove H_2S from biogas and landfill gases with the following desired features: (i) high sulfur removal performance with high and variable H_2S concentrations, (ii) environmentally friendly, and (iii) easily implemented at industrial scale.[1,9,21] This work focuses on evaluation of the technical performance of a natural enzyme, obtained from nzymSys, Inc., for biogas desulfurization. The enzyme contains cellulase, amylase, protease, and lipase; each harvested from specific organisms. Additional enzymes and other organic components come from a whole leaf aloe cold extraction process.

In the sections to follow, we will discuss the experimental setup, test protocols, and effect of operating conditions, followed by inferences.

Experimental:

The laboratory-scale biogas purifier setup, shown in **Figure 1**, is comprised of a 500 mL Pyrex™ gas-washing bottle packed with Raschig Ring packing material (Chemglass). Simulated biogas mixture (3009 or 3020 ppm H_2S, 40% CO_2, and 59.7% CH_4) from Airgas East is continuously fed by a fritted cylinder (sparger) connected to the bottle's stopper. The inlet gas flow rate is regulated using an Alicat mass flow controller (range = 0-100 sccm).

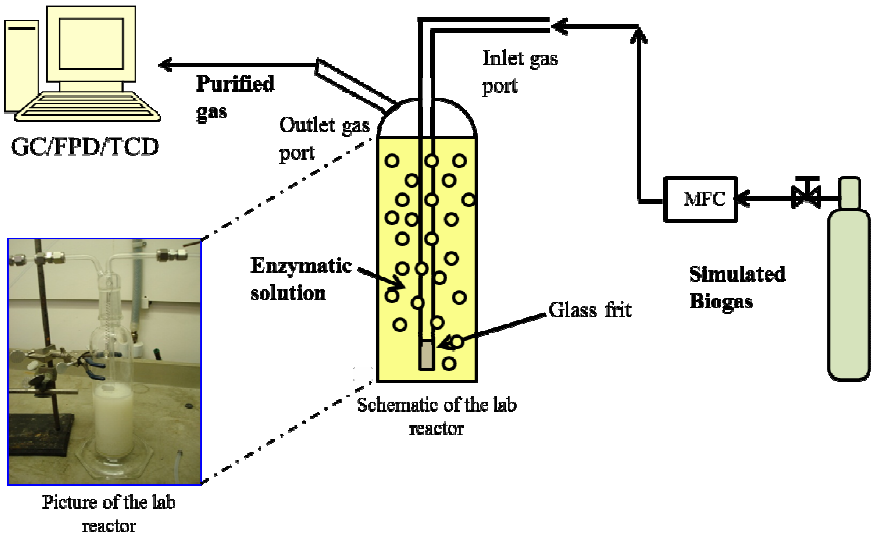

Figure 1. Schematic representation and picture of a lab-scale semi-batch reactor used for enzymatic desulfurization of simulated biogas containing ~3000 ppm of H_2S. Outlet gas mixture is analyzed using a GC equipped with a TCD and a FPD for the detection of CH_4/CO_2 and H_2S, respectively.

Accurate determination of H_2S in biogas is of utmost importance, given the significantly smaller concentration of H_2S as compared to that of CH_4 and CO_2. There are many analytical methods that could be used to quantify H_2S, along with CH_4 and CO_2.[50] Based on published literature [51-53], we selected Gas Chromatography (GC) as the preferred method to analyze these components in the simulated biogas samples. A method for the analysis of H_2S, CH_4, and CO_2 was developed (See **Table 3**) using an Agilent Model 7890A GC, which is equipped with a Flame Photometric Detector (FPD) and Thermal Conductivity Detector (TCD). The GC system has a GS-GasPro 30 m × 0.32 mm capillary column connected to the FPD and TCD for H_2S and CH_4/CO_2 analyses, respectively. Helium was used as a carrier gas. The GC/FPD/TCD operating parameters are listed in **Table 3**. All GC and reactor lines (Stainless Steel or Hastelloy) in contact with the sample (sample loop, gas sampling valve, tubing and reactor inlet and outlet) were coated with sulfur inert material (Sulfinert®/Silcosteel®). This minimizes H_2S adsorption on the active sites of the metal tubing, thus assuring a more accurate detection and measurement method.[54]

Table 3. **GC/FPD/TCD operating parameters.**

Column type Length and i.d. Carrier Gas	GS-GasPro, J&W Scientific, Folsom, California 30 m × 0.32 mm Helium, at constant pressure of 25 psi ~ 6.96 mL/min
Oven Initial temperature Ramp	 60 °C 10 °C/min to 90 °C, run time ~ 5 min
Detector Temperature H_2 Air N_2 Makeup	FPD 220 °C 50.0 mL/min 60 mL/min 50 mL/min
Detector Temperature Reference flow	TCD 250 °C 10 mL/min

All experiments were performed in the absence of any external heating or insulation, in order to demonstrate the enzyme performance under ambient conditions. Simulated biogas at different flow rates was bubbled through 250 mL of enzyme solution containing 100 g of packing material to determine the optimum enzymatic concentration, biogas residence time, and the time it takes for the enzyme to saturate or lose its activity (H2S breakthrough).

H2S gas is highly toxic and proper maintenance for corrosion of transfer piping and equipment are required to operate safely. As mentioned earlier, all the lines in contact with simulated biogas were treated with Sulfinert material to avoid possible sulfur adsorption on the metal active sites. Working with high concentration of H_2S poses a significant safety challenge, since it is lethal at concentrations greater than 40 ppmv. Appropriate safety measures (H_2S sensor, air dilution in exhaust fume hood, emergency shutdown of H_2S feed, as well as personal H_2S sensor for researchers) were implemented in the lab.

Results and Discussion:

Effect of Enzyme Concentration:

Figure 2a shows the effect of enzyme concentration (1.5-5%) on the H_2S removal from simulated biogas for a period of 8 hours. H_2S in the outlet gas was detected only for enzyme concentrations of ≤4%. H_2S concentration lines show a breakthrough that depends on the enzyme concentration. The time for H_2S breakthrough increases with the enzyme concentration. For example, for 1.5% enzyme solution, the breakthrough occurs at ~1.5 h, for 2% at ~5 h, and for 4% at ~7.5 h. The sudden step change in H_2S concentration suggests that at this time the limited quantity of enzyme is deactivated due to high H_2S concentration.

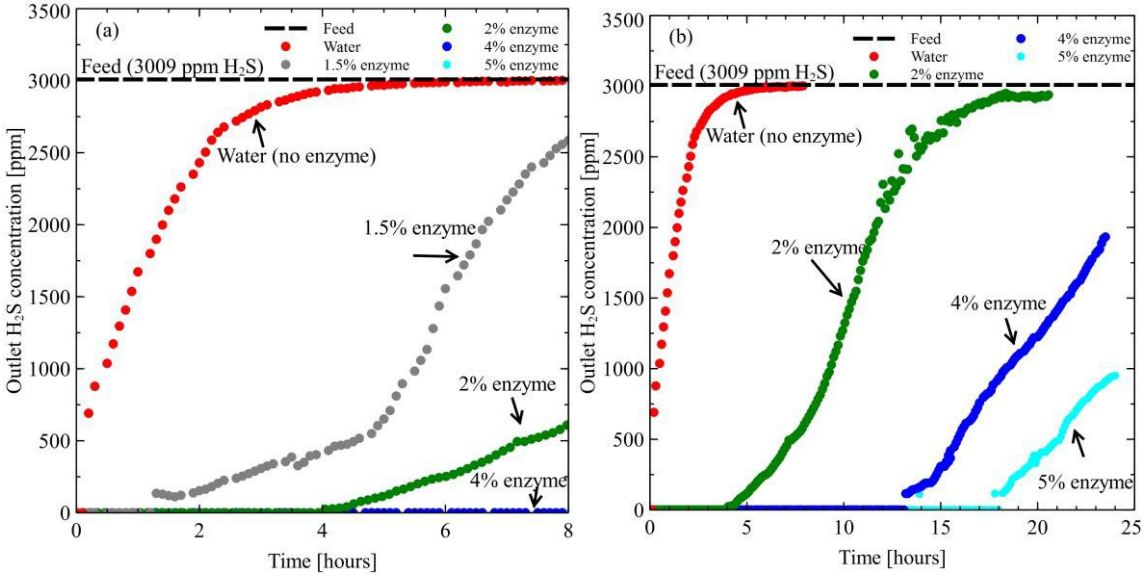

Figure 2. Transient profiles of outlet H_2S concentration for experiments conducted with simulated biogas flowing through various concentrations of enzyme solutions. The biogas flow rate is fixed at 10 sccm. Panels (a) and (b) correspond to 8 hour and 24 hour tests, respectively. Almost 100% H_2S removal is observed with enzyme concentrations ≥4% in the 8 hour tests. H_2S breakthrough is delayed and is more gradual (lower slope) with increased enzyme concentration.

Enzyme concentration of 5% was also analyzed with no H_2S response during the first 8 hours (shown in **Figure 2b**). These results demonstrate that a small quantity of enzyme is sufficient for a high removal of H_2S. Similar experiments to the ones described above were performed for 24 hours in order to investigate the enzyme's long-term ability to remove H_2S (**Figure 2b**). Results showed up to a 12-hour delay in H_2S breakthrough by increasing concentration from 2% to 5%. A comparison with water (see **Figures 2a and 2b**) shows the active effect of enzyme chemistry vs. simple absorption or solubility of H_2S in water. It can also be noted that enzyme saturation occurs more gradually at higher concentrations. For the cases where H_2S breakthrough occurred, the pH significantly reduced to ~4.5-4.7 from a starting pH of 7.8.

In addition, the enzyme did not have any adverse effect on the CH_4 and CO_2 concentrations (**Figure 3**). It takes about 2.5 hours for the system to equilibrate and evacuate the air initially contained in the reactor; during this time, CH_4 concentration in the outlet is initially greater than 59.7% due to the overlap between air (N_2, O_2) and CH_4 GC peak areas.

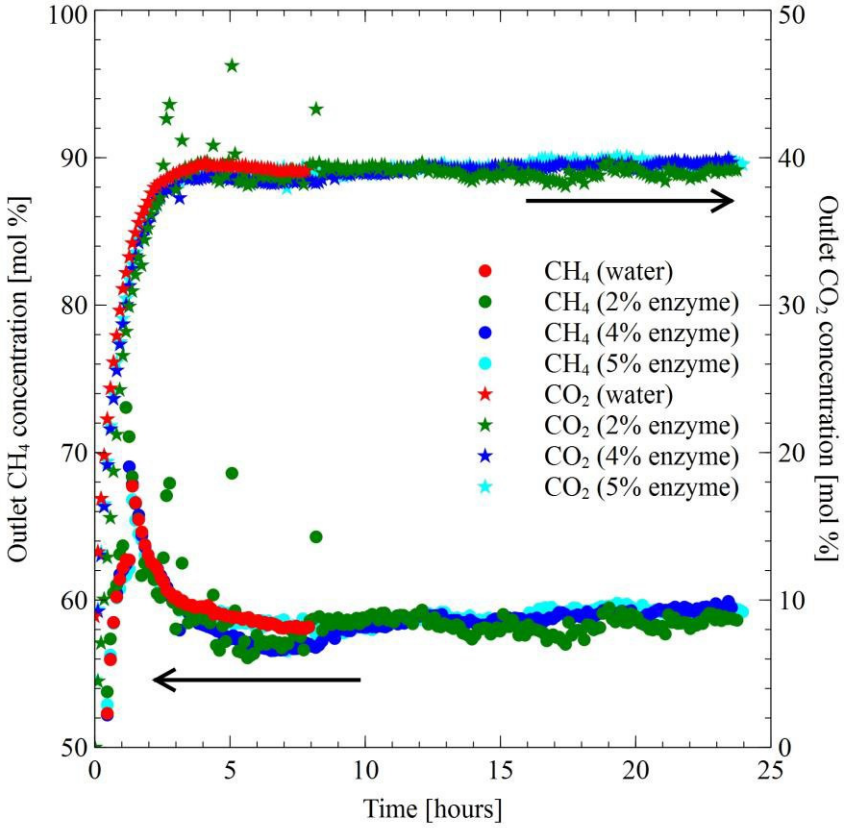

Figure 3. Transient profiles of outlet CH_4 and CO_2 concentrations for experiments conducted with simulated biogas flowing through various concentrations of enzyme solutions. The operating conditions are same as in **Figure 2b**. The enzyme has a negligible effect on the CH_4 and CO_2 concentrations in simulated biogas, indicating its selectivity to H_2S removal.

Effect of Gas Flow Rate:

Retention time plays an important role in the H_2S removal efficiency as previously demonstrated by Chaiprapat *et al.*[42] Longer reactant retention within the enzyme allows time for gas to absorb/react within/with the enzyme. Effect of biogas flow rate (residence time) on the H_2S breakthrough was studied in the range of 5-20 sccm with 250 mL of 1.5% enzyme solution. Results are reported in **Figure 4**. As expected, the enzyme performance upon H_2S removal decreases when biogas retention time in the liquid enzyme is reduced. H_2S breakthrough occurs at earlier times, less than 1 hour for 20 sccm compared to ~3 hours for 5 sccm with a very steep change in concentration for 20 sccm of simulated biogas. Furthermore, fast enzyme saturation is observed by increasing the biogas flow rate. The relationship between biogas residence time and H_2S breakthrough is critical for reactor design at larger scales.

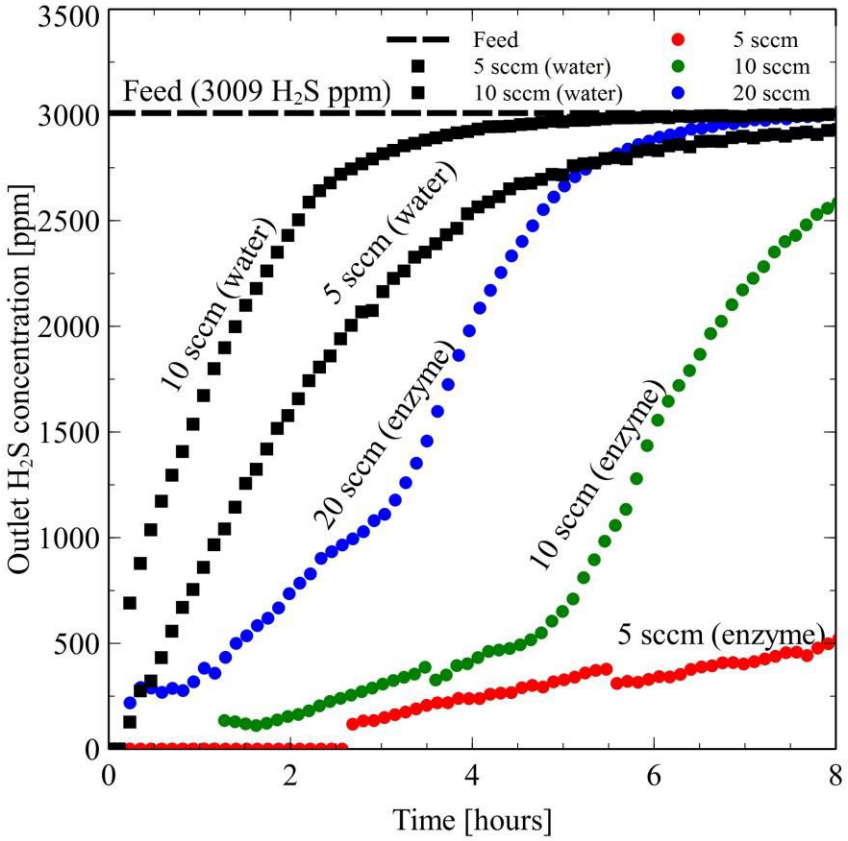

Figure 4 Effect of biogas flow rate (residence time) on the H2S removal performance. Numbers in the legend indicate biogas flow rates. Experiments are conducted with no enzyme (water) or 1.5% enzyme solution (enzyme). H2S breakthrough occurs at earlier times, with a very steep change for higher biogas flow rates, indicating faster enzyme saturation.

Effect of Enzyme Replenishment:

Replenishment at Saturation Point:

Even though faster H_2S breakthrough was observed with high gas flow rates, this challenge could be overcome with periodic addition of the fresh enzyme solution. At larger scales, we envision that this could be accomplished through a continuous addition of the enzyme and removal of the spent liquid. In our semi-batch reactor experiments, we explored the addition of fresh enzyme (hereafter, referred to as 'boost') to the saturated solution and removal of the spent liquid as a potentially promising concept. The experiments were conducted with 2% enzyme solution. Once the enzyme solution was saturated at ~3000 ppm of H_2S (indicated by the GC results), the biogas flow was stopped, 50 mL of the saturated solution was replaced with same amount of fresh 2% enzyme solution (dashed arrows in **Figure 5**), and then the biogas flow was restarted. Results show a significant decrease in the H_2S concentration after the enzyme boost, indicating that this concept could be effectively implemented in a continuous reactor system as well. The enzyme saturation is again observed in a few hours, which indicates that the effect of enzyme boost should be explored at an earlier stage, perhaps right before the H_2S breakthrough.

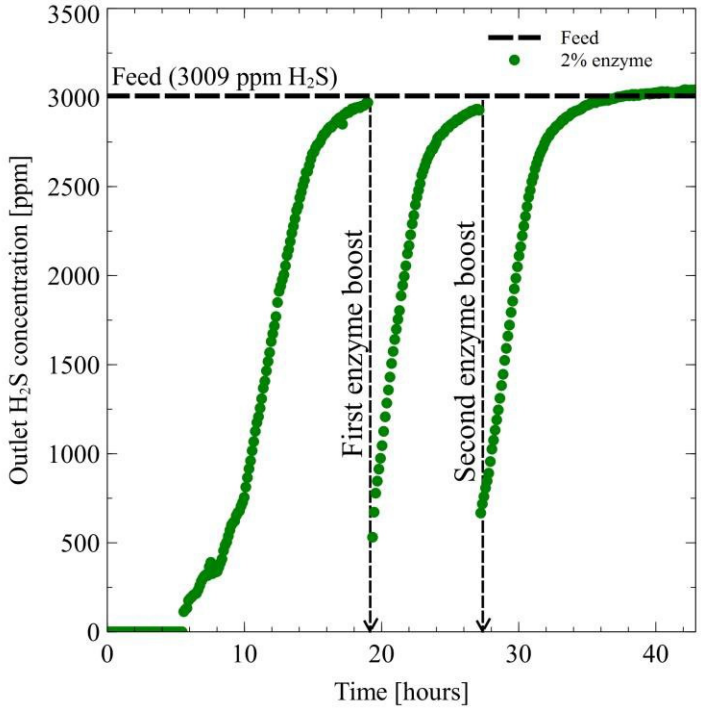

Figure 5 Demonstration of biogas desulfurization for >40 hrs using enzyme replenishment (boost) at complete saturation. Experiments were conducted with 2% enzyme solution and 10 sccm biogas flow rate. At each boost (dashed arrows), 50 mL of the saturated solution was replaced with same amount of fresh 2% enzyme solution, and then the biogas flow was restarted. The enzyme saturation following the boost indicates that the effect of enzyme boost should be explored at an earlier stage, perhaps right before the H2S breakthrough.

Replenishment at H_2S Breakthrough:

In order to study the possibility of enzyme regeneration and/or to delay enzyme saturation, the effect of enzyme boost at H_2S breakthrough was evaluated on the enzymatic desulfurization performance. The experiments were conducted with 2% enzyme solution. Once the FPD detected a quantifiable concentration of H_2S in the outlet gas (GC detection limit is 25 ppm), simulated biogas flow was stopped and 50 mL of the used (but not saturated) enzyme solution was replaced with the same amount of fresh 2% enzyme solution (dashed arrows in **Figure 6**), and then the biogas flow was restarted. **Figure 6** shows the H_2S saturation curve for 4 such boosts done at the H_2S breakthrough. Comparing results with the 2% enzyme saturation test without enzyme boost, it is observed that adding fresh 2% enzyme solution delays the breakthrough and allows the system to operate at low H_2S level (0-25 ppm), as long as fresh enzyme boost is provided periodically. Results from this test suggest that the performance of biogas desulfurization with this enzyme could be promising in a continuous reactor, where the enzyme is continuously purged and replaced with fresh enzyme solution. We plan to explore the feasibility of such a continuous process in the future.

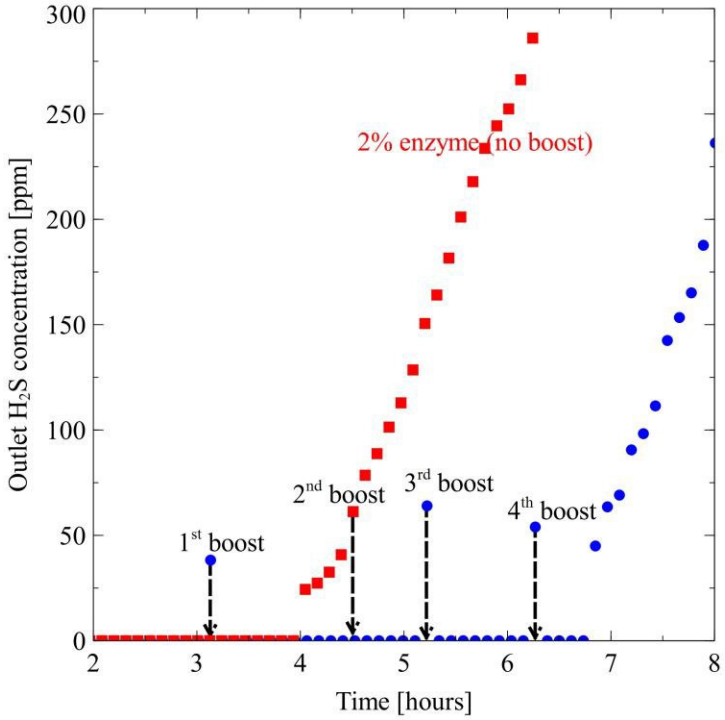

Figure 6 Demonstration of high efficiency for biogas desulfurization with enzyme boost at H_2S breakthrough. Experiments were conducted with 2% enzyme solution and 10 sccm biogas flow rate. At each boost (dashed arrows), 50 mL of the used solution was replaced with same amount of fresh 2% enzyme solution, and then the biogas flow was restarted. Performance of the 2% enzyme solution without any boost is also shown for comparison. Results indicate that adding fresh enzyme solution just after H_2S detection delays the breakthrough and allows the system to operate at low H_2S level (0-25 ppm), as long as fresh enzyme is added periodically.

Effect of Packing Material:

A set amount (100 g) of Raschig Ring packing material (8 mm x 8 mm) from Chemglass has been used in all the experiments reported here. Packing materials are commonly used in gas-liquid contact operations to increase the contact time between the two phases (e.g., enzymatic solution and biogas). Here, we explored the effect of packing material quantity on the enzymatic desulfurization performance. **Figure 7** shows the results from two additional enzymatic desulfurization experiments carried out in the absence of packing material (black filled circles) and doubling the amount of packing material (green filled circles). The significance of using packing material to increase the contact area can be noted within the first 6 hours, as the use of the packing material delays the H_2S breakthrough by around 2 hours. However, there is not a substantial difference in performance by doubling the amount of packing material.

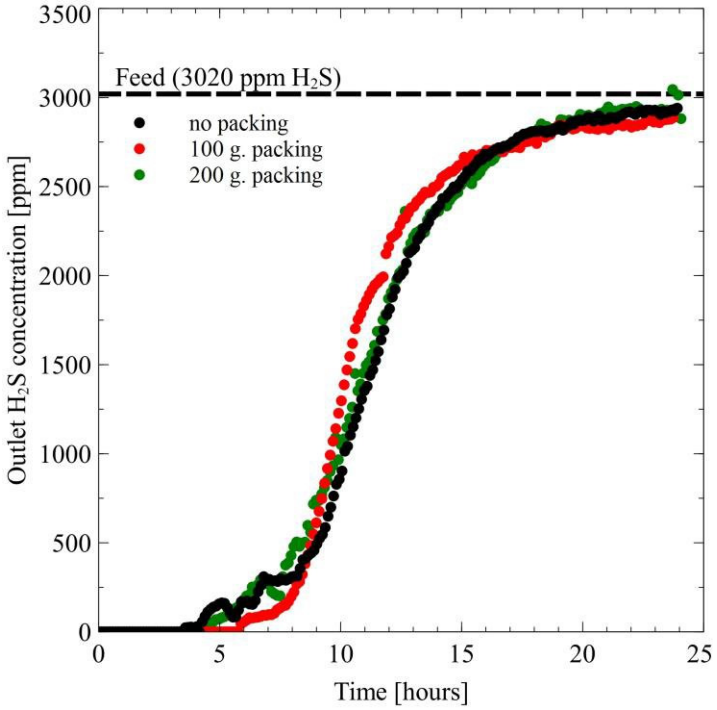

Figure 7 Effect of packing material on enzymatic desulfurization performance. Three different amounts of Raschig Ring packing material were used to evaluate the performance of 2% enzyme solution for removing H_2S from biogas. Black, red and green dots represent the tests carried with 0, 100, and 200 grams of packing material, respectively. Results for the first 6 hours confirm the importance of adding packing material to increase contact area between enzyme and biogas, as indicated by the delay in H_2S breakthrough. However, the sensitivity of desulfurization performance with the amount of packing materials is significantly lower than that for the operating conditions such as concentration and flow rate.

Sulfur Components Recovery:

In all the experiments reported so far, we did not observe any elemental sulfur formation, despite high efficiency for H_2S removal. As the tests were conducted for short times (e.g., 8-24 hrs) with dilute enzyme solutions (0-5%), the total amount of H_2S removed was low. To explore the possibility of sulfur components formation, a long-term saturation test was carried out with more concentrated enzyme solution. 10 sccm of simulated biogas was bubbled through a 20% enzyme solution and the H_2S response was monitored continuously for 100 hours, as shown in **Figure 8**. H_2S peak was not detected in the outlet gas during the first 53 hours of testing; less than 50 ppm of H_2S was detected for 6 hours after the H_2S breakthrough (53-59 hrs). Enzyme saturation was not observed even after 100 hrs of testing.

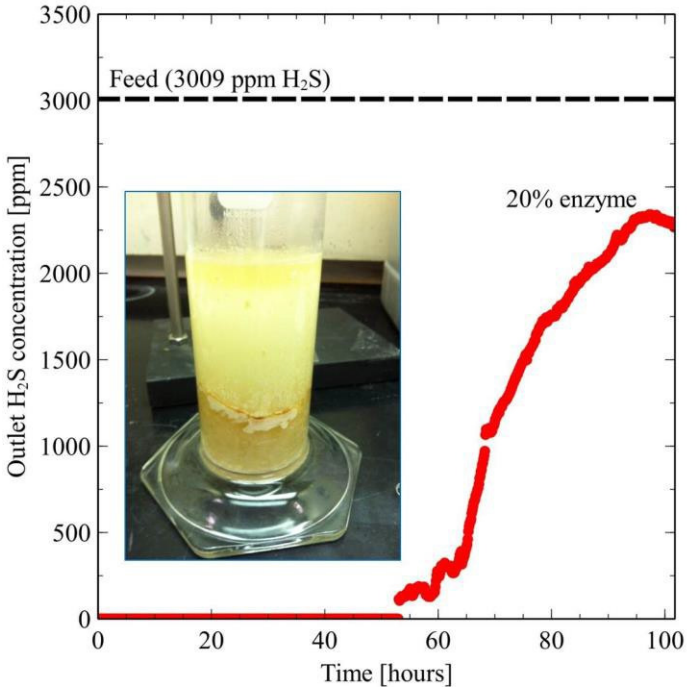

Figure 8 Demonstration of sulfur recovery from a long term saturation test performed by feeding 10 sccm of simulated biogas through a concentrated 20% enzyme solution for 100 hours. Data shows the transient profile for the outlet H_2S concentration, whereas the inset shows a picture of the yellow sulfur precipitate. These results highlight the potential of this enzymatic desulfurization technology to also recover elemental sulfur as a valuable byproduct.

A yellowish paste like compound was formed on the reactor walls as well as on the packing material, as shown in the **inset of Figure 8**. This is likely related to elemental sulfur formation from the reaction between the enzyme and H_2S. At the end of the test, solids were separated from the enzymatic solution by filtration under vacuum conditions to identify the exact form of sulfur being formed. Solids analyses done by direct thermal desorption mass spectroscopy suggest the formation of several sulfur components such as methanethiols, carbonyl sulfide, diethyl trisulfide, dimethyl trisulfur among others (**Figure 8**). Formation of sulfur components is promising, especially for a scaled-up process, where concentrated enzyme solution may be utilized continuously for biogas desulfurization, while extracting sulfur components as a valuable byproduct.

Conclusions:

Desulfurization of simulated biogas containing high levels of H_2S (3009 or 3020 ppm) is demonstrated in a semi-batch reactor using a novel enzyme. We investigated the effect of several operating parameters, such as enzyme concentration, biogas flow rate, amount of packing material, and periodic enzyme replenishment, on the enzymatic biogas desulfurization performance. Our results show H_2S removal rates up to 100% using a small amount of dilute enzyme solutions, without any adverse effects on the other primary components in biogas such as CH_4 and CO_2. The enzyme is susceptible to deactivation, as indicated by the H_2S breakthrough, which depends strongly on both the enzyme concentration and the biogas flow rate. Enzyme saturation occurs more gradually (slower) at higher concentrations; however, it occurs faster when the biogas flow rate is increased. The packing material used in this process delays the H_2S breakthrough, but its role is not significant as compared to the effect of operating conditions. Adding fresh enzyme solution (boost) delays the H_2S breakthrough and allows the system to operate at low H_2S

levels as long as fresh enzyme is added periodically and preferably as soon as H_2S is detected. Long term tests with concentrated enzyme showed formation of sulfur compounds, which were verified through direct thermal desorption mass spectroscopy analysis and could be recovered as valuable byproducts. This enzymatic technology is non-conventional, but simple and reliable. Based on the performance evaluation reported here, we believe that this technology could be potentially more effective in a continuous reactor setup with constant and periodic replenishment of enzyme and removal of the spent solution along with recovery of the sulfur compounds with high commercial value. Future work will concentrate on evaluating the effect of reactor scale-up and the implementation of a continuous process for the enzymatic desulfurization of biogas.

Patents:

1. D. Bloom, J. Fantry, A. Moreno, A. Mhadeshwar, P. Singh. Biogas desulfurization using enzyme-based technology, patent document in preparation.

Publications/Presentations:

1. Moreno, D. Bloom, P. Singh, J. Fantry, S. Gorton, and A. Mhadeshwar, "Enzyme-based sulfur removal for biogas cleanup", in preparation for submission to the Journal of Chemical Technology and Biotechnology, 2012.

References:

1. Petersson A, Wellinger A. Biogas Upgrading Technologies - Developments and Innovations. IEA Bionergy. http://www.biogasmax.com/media/iea_2biogas_upgrading_tech__025919000_1434_30032010.pdf
2. Weiland P. Biogas production: Current state and perspectives. Appl Microbiol Biotechnol 85 :849-60 (2010)
3. Anonymous Benefits of Anaerobic Digestion. http://www.americanbiogascouncil.org/biogas_benefits.asp
4. Bove R, Lunghi P. Experimental comparison of MCFC performance using three different biogas types and methane. J Power Sources 145 :588-93 (2005)
5. Trogisch S, Hoffmann J, Daza Bertrand L. Operation of molten carbonate fuel cells with different biogas sources: A challenging approach for field trials. J Power Sources 145 :632-8 (2005)
6. Abatzoglou N, Boivin S. A review of biogas purification processes. Biofuels, Bioproducts and Biorefining 3 :42-71 (2009)
7. Pöschl M, Ward S, Owende P. Evaluation of energy efficiency of various biogas production and utilization pathways. Appl Energy 87 :3305-21 (2010)
8. Mescia D, Hernández SP, Conoci A, Russo N. MSW landfill biogas desulfurization. Int J Hydrogen Energy (2011)
9. Ryckebosch E, Drouillon M, Vervaeren H. Techniques for transformation of biogas to biomethane. Biomass Bioenergy 35 :1633-45 (2011)
10. Staniforth J, Kendall K. Biogas powering a small tubular solid oxide fuel cell. J Power Sources 71 :275-7 (1998)
11. Noyola A, Morgan-Sagastume JM, López-Hernández JE. Treatment of biogas produced in anaerobic reactors for domestic wastewater: Odor control and energy/resource recovery. Reviews in Environmental Science and Biotechnology 5 :93-114 (2006)
12. van der Meijden CM, Veringa HJ, Rabou LPLM. The production of synthetic natural gas (SNG): A comparison of three wood gasification systems for energy balance and overall efficiency. Biomass Bioenergy 34 :302-11 (2010)
13. Abe J, Chaytors R, Clark C, Marshall C, Morgan E. Toward a Renewable Power Supply: The use of Bio-Based Fuels in Stationary Fuel Cells. http://www.nrbp.org/pdfs/pub31.pdf

14. Krich K, Augestein D, Batmale JP, Beneman J, Rutledge B, Salour D. Biomethane from dairy waste - A sourcebook for the production and use of renewable natural gas in california. (2005)
15. Wheeler P. Upgrading and Utilization of Biogas. Task 24: Energy from Biological Conversion of Organic Waste. http://www.iea-biogas.net/_download/publi-task37/Biogas%20upgrading.pdf
16. Frare LM, Vieira MGA, Silva MGC, Pereira NC, Gimenes ML. Hydrogen sulfide removal from biogas using Fe/EDTA solution: Gas/liquid contacting and sulfur formation. Environmental Progress and Sustainable Energy 29 :34-41 (2010)
17. Redondo R, MacHado VC, Baeza M, Lafuente J, Gabriel D. On-line monitoring of gas-phase bioreactors for biogas treatment: Hydrogen sulfide and sulfide analysis by automated flow systems. Analytical and Bioanalytical Chemistry 391 :789-98 (2008)
18. Laycock CJ, Staniforth JZ, Ormerod RM. Biogas as a fuel for solid oxide fuel cells and synthesis gas production: Effects of ceria-doping and hydrogen sulfide on the performance of nickel-based anode materials. Dalton Trans 40 :5494-504 (2011)
19. Wellinger A. Biogas production and utilization. IEA Bioenergy T37:2005:01 :1-16 (2005)
20. Shiratori Y, Oshima T, Sasaki K. Feasibility of direct-biogas SOFC. Int J Hydrogen Energy 33 :6316-21 (2008)
21. Cebula J. Biogas purification by sorption techniques. Architecture Civil Engineering Environment 2 :95-103 (2009)
22. van der Zee FP, Villaverde S, Garc a PA, Fdz.-Polanco F. Sulfide removal by moderate oxygenation of anaerobic sludge environments. Bioresour Technol 98 :518-24 (2007)
23. Díaz I, Pérez SI, Ferrero EM, Fdz-Polanco M. Effect of oxygen dosing point and mixing on the microaerobic removal of hydrogen sulphide in sludge digesters. Bioresour Technol 102 :3768-75 (2011)
24. Janssen AJH, Ruitenberg R, Buisman CJN. Industrial applications of new sulphur biotechnology. Water Science and Technology 44 :85-90 (2001)
25. ter Maat H, Hogendoorn JA, Versteeg GF. The removal of hydrogen sulfide from gas streams using an aqueous metal sulfate absorbent: Part I. the absorption of hydrogen sulfide in metal sulfate solutions. Separation and Purification Technology 43 :183-97 (2005)
26. Dhar BR, Youssef E, Nakhla G, Ray MB. Pretreatment of municipal waste activated sludge for volatile sulfur compounds control in anaerobic digestion. Bioresour Technol 102 :3776-82 (2011)
27. Sahu RC, Patel R, Ray BC. Removal of hydrogen sulfide using red mud at ambient conditions. Fuel Proc Tech 92 :1587-92 (2011)
28. Truong LV, Abatzoglou N. A H2S reactive adsorption process for the purification of biogas prior to its use as a bioenergy vector. Biomass Bioenergy 29 :142-51 (2005)
29. Cantrell KJ, Yabusaki SB, Englehard MH, Mitroshkov AV, Thornton EC. Oxidation of H2S by iron oxides in unsaturated conditions. Environ Sci Tech 37 :2192-9 (2003)
30. Wang H, Fang D, Chuang KT. A sulfur removal and disposal process through H2S adsorption and regeneration: Breakthrough behaviour investigation. Proc Safety 86 :296-302 (2008)
31. Seredych M, Bandosz TJ. Desulfurization of digester gas on catalytic carbonaceous adsorbents: Complexity of interactions between the surface and components of the gaseous mixture. Industrial and Engineering Chemistry Research 45 :3658-65 (2006)
32. Seredych M, Bandosz TJ. Desulfurization of digester gas on wood-based activated carbons modified with nitrogen: Importance of surface chemistry. Energy and Fuels 22 :850-9 (2008)
33. Pipatmanomai S, Kaewluan S, Vitidsant T. Economic assessment of biogas-to-electricity generation system with H2S removal by activated carbon in small pig farm. Appl Energy 86 :669-74 (2009)
34. Hernández SP, Scarpa F, Fino D, Conti R. Biogas purification for MCFC application. Int J Hydrogen Energy (2011)
35. Rasi S, L ntel J, Vei anen A, Rintala J. Landfill gas upgrading with countercurrent water wash. Waste Manage 28 :1528-34 (2008)

36. Tippayawong N, Thanompongchart P. Biogas quality upgrade by simultaneous removal of CO2 and H2S in a packed column reactor. Energy 35 :4531-5 (2010)
37. Dubois L, Thomas D. Comparison of various alkaline solutions for H2S/CO2-selective absorption applied to biogas purification. Chem Eng Tech 33 :1601-9 (2010)
38. Iliuta I, Larachi F. Concept of bifunctional redox iron-chelate process for H2S removal in pulp and paper atmospheric emissions. Chem Eng Sci 58 :5305-14 (2003)
39. Saelee R, Chungsiriporn J, Intamanee J, Bunyakan C. Removal of H2S in biogas from concentrated latex industry with iron(III)chelate in packed column. Songklanakarin Journal of Science and Technology 31 :195-203 (2009)
40. Horikawa MS, Rossi F, Gimenes ML, Costa CMM, da Silva MGC. Chemical absorption of H2S for biogas purification. Brazil J Chem Eng 21 :415-22 (2004)
41. Kim S, Deshusses MA. Understanding the limits of H2S degrading biotrickling filters using a differential biotrickling filter. Chem Eng J 113 :119-26 (2005)
42. Chaiprapat S, Mardthing R, Kantachote D, Karnchanawong S. Removal of hydrogen sulfide by complete aerobic oxidation in acidic biofiltration. Process Biochemistry 46 :344-52 (2011)
43. Fortuny M, Baeza JA, Gamisans X, Casas C, Lafuente J, Deshusses MA, Gabriel D. Biological sweetening of energy gases mimics in biotrickling filters. Chemosphere 71 :10-7 (2008)
44. Soreanu G, Béland M, Falletta P, Edmonson K, Seto P. Laboratory pilot scale study for H2S removal from biogas in an anoxic biotrickling filter. ; 2008 [cited 19 May 2011]
45. Ramírez-Sáenz D, Zarate-Segura PB, Guerrero-Barajas C, García-Peña EI. H2S and volatile fatty acids elimination by biofiltration: Clean-up process for biogas potential use. J Hazard Mater 163 :1272-81 (2009)
46. Collins BC, Mestetsky PA, Savaiano, NJ. Method of removing sulfur compounds from sour crude oil and sour natural gas. US Patent 5,807,476 (1998)
47. Duhalt R, Bremauntz MdP, Barzana E, Tinoco R. Enzymatic oxidation process for desulfurization of fossil fuels. US Patent 6461859 (2002)
48. Singh MP, Kumar M, Kalsi WR, Pulikottil AC, Sarin R, Tuli DK, Malhotra RK, Verma RP, Bansal B. Method for bio-oxidative desulfurization of liquid hydrocarbon fuels and product thereof. Patent 20090217571 (2009)
49. Squires CH, Ji W. Method of desulfurization of fossil fuel with flavoprotein. US Patent 09/025,527 (1999)
50. Ward AJ, Bruni E, Lykkegaard MK, Feilberg A, Adamsen APS, Jensen AP, Poulsen AK. Real time monitoring of a biogas digester with gas chromatography, near-infrared spectroscopy, and membrane-inlet mass spectrometry. Bioresour Technol 102 :4098-103 (2011)
51. Abbasian J. Novel gas cleaning/condiitoning for integrated gasification combined cycle - test plan - topical report. DE-AC26-99FT40674 :1-34 (2000)
52. Chin S, Wu Z, Morrison PD, Marriott PJ. Observations on comprehensive two dimensional gas chromatography coupled with flame photometric detection for sulfur- and phosphorous-containing compounds. Analytical Methods 2 :243-53 (2010)
53. Method 15: Determination of Hydrogen Sulfide, Carbonyl Sulfide and Carbon Disulfide Emissions from Stationary Sources. www.epa.gov/ttn/emc/promgate/m-15.pdf
54. Frito R, Quimby B. A comparison of sulfur selective detectors for low level analysis in gaseous streams - application. Agilent Technologies 5988-2426EN (2001)

Project Title: Structure-Activity Correlations in Soot Oxidation
Industrial Partner: Corning
PI: Steven L. Suib

Objective

The overall research objective of this effort is to develop structure-activity correlations for non-catalytic oxidation of soot to understand the dependence of oxidation kinetics on nature of soot. This type of work fits with the EERE objective of developing energy efficient and environmentally friendly technologies, which focus on diesel vehicles and emissions reduction. It also fits with the clean cities initiative. Successful execution will result in directions to improve particulate filter design and control strategies for efficient soot oxidation. New objectives include 1. To analyze ***structural changes upon thermal oxidation,*** Under real diesel engine exhaust gases [10% Oxygen + 500 ppm Nitrogen dioxide] and at temperatures with respect to their 10% (T10), 50% (T50), and 90%(T90) conversions.
2. To develop ***structure - activity correlations for non catalytic oxidation of soot*** at T10, T50, and T90.

Introduction

More than 13 million diesel vehicles are responsible for transportation of 94% of the goods in US and use ~4 million barrels of diesel per day.[1-3] In the European market, 53% of the passenger cars run on diesel.[4] Diesel engines are the workhorses for industrial, commercial, and personal transportation, and also play a vital role in power generation, due to the highly efficient combustion, excellent fuel economy, torque, durability, reliability, and low operating cost.[5-7] However, emissions from diesel engines contain fine particles produced during high temperature pyrolysis or combustion. Diesel Particulate Matter (PM), also known as soot, is primarily composed of carbon along with some organic compounds, inorganic compounds (ash), sulfur compounds, and traces of metals from unburnt fuel and lubricating oil. PM formation is a complex phenomenon, which depends on the engine operating conditions, fuel type, and lubricating oil, resulting in a wide range of particle sizes and chemical compositions.[8-11] PM emissions are responsible for various human health and environmental problems, such as asthma, bronchitis, lung cancer, air pollution, and global warming.[5, 12, 13] Diesel Particulate Filter (DPF) is the most popular after-treatment technology to meet the stringent PM emissions standards.[14, 15] DPFs need to be periodically regenerated through oxidation of soot; otherwise the accumulated soot can cause backpressure, resulting in decreased fuel economy and possible engine and/or filter failure.[16, 17] Given the complexity and variability in the soot structure as well as the need for periodic DPF regeneration, there is an urgent need to develop a comprehensive understanding for the kinetics of soot oxidation.

This work focuses on developing such understanding through a comprehensive investigation of fifteen carbonaceous samples (diesel engine soot provided by Corning, 13 commercial carbon black samples, and graphite). Effect of various parameters, such as oxidizer flow rate, initial sample mass, partial pressure of oxygen, crucible type, and ramp rate, were studied using Temperature Programmed Oxidation (TPO) thermogravimetric experiments.

Materials and Methods

Fifteen different samples studied included a diesel engine soot sample provided by Corning, 13 commercial carbon black samples obtained from various manufacturers, and a graphitic carbon sample. The samples were as follows: 1) diesel soot (Corning), 2) graphite (Fisher Scientific), 3) Mogul-E (Cabot), 4) Monarch 1300 (Cabot), 5) Monarch 1400 (Cabot), 6) Monarch 280 (Cabot), 7) N 120 (Continental carbon), 8) N 339 (Continental carbon), 9) N 762 (Continental carbon), 10) Printex-G (Orion), 11) Printex-U (Orion), 12) Printex-XE2B (Orion), 13) Regal 330 R (Cabot), 14) Regal 400 R (Cabot), and 15) VulcanXC72R (Cabot). Throughout the paper, the samples are referred in this order.

Two of the samples (Monarch 1300 and Monarch 1400) contained 7% moisture, as compared to negligible moisture (0-0.6%) in the other samples.

A TGA Q5000 IR Thermogravimetric Analyzer from TA Instruments was used for all the experiments. This is a thermal weight-change analysis instrument, used in conjunction with a controller computer and associated software to make up a thermal analysis system. This TGA is also equipped with an auto sampler for multiple samples loading. In this work, we developed mixed methods consisting of non-isothermal and isothermal steps. Instrumental specifications and experimental protocol details are given in **Table 1**.

In all the experiments, the oxidizer gas (UHP air or 10% O_2 in Ar from Airgas) flow rate was 60 mL/min and N_2 was used as purge gas with a flow rate of 40 mL/min. Initial mass of the carbon black samples was ~10-12 mg. However, due to the low density of diesel soot, an initial mass of only ~2.5 mg was used. For the non-isothermal experiments, the samples were heated in a Platinum (Pt) crucible (the Pt crucible was inert as discussed later) from room temperature to 800 °C at a chosen ramp rate (5-20 °C/min) followed by a 15 minute hold at 800 °C, then cooling back to room temperature. For the isothermal experiments, first the samples were heated to the desired temperature with a ramp rate of 20 °C/min and then, the samples were kept at the isothermal point for 2 hours under oxidizing environment, followed by cooling back to room temperature. Non-isothermal tests are typically preferred over isothermal tests for two reasons: i) an isothermal test always consists of a finite non-isothermal heat-up time due to which strictly isothermal tests are not possible[18]; and ii) multiple experiments are required for extraction of kinetic parameters from isothermal tests[19, 20]. On the other hand, isothermal tests provide information about the characteristic profile of the reaction, and hence provide an idea about the appropriate kinetic model.[18] In this work, we conducted isothermal tests for selected samples to extract the kinetic parameters and to validate the parameters obtained from the non-isothermal experiments.

Finally, oxidation rate is defined based on the temperature required for a certain level of fractional conversion. For example, T_{10}, T_{50}, and T_{90} represent the temperatures required to achieve 10%, 50%, and 90% mass loss, respectively. T_{10} is also referred to as the light-off temperature.

Results and Discussion

1. Factors affecting TGA experiments

1.1. Oxygen flow rate

The overall efficiency of the gas-solid reactions can be greatly affected by the gas flow rate, and hence by mass transfer limitations or limiting reactants.[19-23] For the oxidation of carbon black or soot, availability of oxygen is critical, otherwise the observed oxidation efficiency may be lower due to the lack of sufficient oxygen. This is particularly important at high temperatures, where the soot oxidation rate is high and the lack of oxygen can limit the overall soot oxidation rate. To ensure that the TGA experiments reported here were not affected by such limitations due to insufficient availability of oxygen in the oxidizer gas, we conducted a series of experiments with various oxidizer gas flow rates while maintaining other parameters the same. **Figure 1** shows the mass loss profile of Printex-U for various levels of air flow rates (20-80 mL/min). The oxidation rate at a gas flow rate of 20 mL/min was lower than that at a gas flow rate of 40 mL/min or higher; but the rate stayed constant for gas flow rates of 40 mL/min and higher. Therefore, the oxidizer gas flow rate must be at least 40 mL/min to avoid the scenario, in which oxygen becomes the limiting reactant. Based on these experiments, we used an oxidizer gas flow rate of 60 mL/min in all the TGA experiments reported in this paper.

1.2. Initial sample mass

TGA analysis is also affected, to some extent, by the initial sample mass used in the experiment.[23, 24] A large initial mass may be associated with diffusional limitations[24-27], whereas a small initial mass may result in increased uncertainty along with low reproducibility.[20] Furthermore, a large initial mass may cause self-heating (exothermic) and self-cooling (endothermic) producing a large deviation from the programmed heating rates.[28] The temperature gradient could be created due to low thermal conductivity of the samples producing regions with different temperatures.[28] As shown in **Figure 2**, we conducted multiple experiments with different initial masses and ramp rates (5-20 °C/min) for Printex-U (panel a: 2-20 mg) and Printex-XE2B (panel b: 8-14 mg, panel c: 4-14 mg, and panel d: 4-19 mg). We observed that large initial masses were affected by diffusional limitations, as evident from the delayed oxidation rate. Based on these experiments; we selected moderate initial masses of 10-12 mg for each sample, except for diesel soot (~2.5 mg) which had a much lower density.

1.3. Ramp rate

Effect of ramp rate on gas-solid reactions is well documented in the literature.[29-34] High ramp rates are typically associated with heat and mass transfer limitations.[33] On the other hand, experiments conducted with low ramp rates are not influenced by such limitations.[35] Our results in **Figure 2** for different initial masses and ramp rates showed delayed oxidation rates in case of large initial masses and high ramp rates due to their combined effect (e.g., **Figure 2d**). However, in general, the effect of initial mass was negligible in the considered initial mass range with a ramp rate of 5-15 °C/min. Based on these experiments; we have chosen a low ramp rate of 5 °C/min for most of the experiments.

1.4. Crucible

Crucible shape in the TGA experiments can significantly influence the oxidation kinetics due to mass transfer limitations.[20, 23, 26, 27, 36] Large crucible height can lead to large stagnant volume (space available in the crucible above the sample), and hence to diffusion limitations.[20, 23, 27, 36] Therefore, short and wide crucibles are typically recommended for such studies.[23, 37] In this work, we used short and wide crucibles (D = 10 mm, h = 2 mm, h/D = 0.2, actual sample h/D < 0.2) to avoid such limitations. Furthermore, to ensure that the Pt crucible is inert in the oxidation experiments, we conducted additional experiments with an alumina crucible in identical operating conditions. As shown in **Figure 3**, results with both crucibles were almost identical for two samples (panel a: Printex-XE2B and panel b: Printex-U); hence the Pt crucible could be considered as inert in the subsequent experiments.

1.5. Diffusion limitations

Diffusion limitations in soot oxidation kinetics during TGA experiments have been discussed in the literature [20, 23-25, 27, 30, 36, 38-43], and such limitations can impact kinetic parameter estimation.[24, 27, 38, 40, 43] As discussed earlier, diffusion limitations can be avoided or minimized by selecting appropriate initial sample mass, ramp rate, crucible shape, sample packing, bed height, and stagnation volume.[23, 24, 27, 36, 38, 44] Internal mass transfer limitations could also be important and could differ for each sample due to different pore sizes. Such limitations have been estimated in literature using effectiveness factor and Thiele modulus [40, 45, 46, 46]; however, they were not considered in the scope of our work presented here.

1.6. Experimental reproducibility

Prior to discussing the results and data analysis from the TGA experiments for multiple samples and various operating conditions, it was important to ensure that the experiments had a good reproducibility. **Figure 4** shows an example of the experimental reproducibility over three runs for the oxidation of diesel soot (panel a) and Printex-XE2B (panel b). As observed from the overlapping profiles, the TGA experiments were highly reproducible.

2. Data Analysis for Kinetic Parameter Extraction

Three methods were used for the TGA data analysis: a) non-isothermal single ramp rate, b) non-isothermal multiple ramp rates, and c) isothermal single ramp rate. A majority of the results presented in this work are focused around the non-isothermal single ramp rate method, whereas the other two methods are demonstrated for additional validation or comparison. Next, we discuss the details of the data analysis for the three methods.

2.1. Method A: Non-isothermal single ramp rate method:

Estimation of kinetic parameters from TGA data can be done using various approaches as recommended by the Kinetics Committee of the International Confederation for Thermal Analysis and Calorimetry (ICTAC).[18] However, the most widely used approach for kinetic parameter estimation from soot or carbon black oxidation is based on the Arrhenius equation format [20, 47, 48]

$$-\frac{dm}{dt} = k\, m^n\, p_{O_2}^r = A \exp\left(-\frac{E_a}{RT}\right) m^n p_{O_2}^r. \quad [1]$$

Here, m is the instantaneous sample mass at time t, k is the reaction rate constant, A is the pre-exponential factor, E_a is the activation energy, T is the operating temperature, p_{O_2} is the partial pressure of oxygen, and n and r are the reaction orders for carbon and oxygen, respectively. It is known that surface area of the carbonaceous samples increases during oxidation.[9] However, any change in surface area and pore size effects are not accounted for in the simplified kinetic expression. Furthermore, most literature studies for carbon black or soot oxidation show reaction orders close to unity [20, 25, 39, 40]. In that case, the above equation can be rearranged as,

$$\ln\left(-\frac{dm}{mdt}\right) = \ln\left(A\, p_{O_2}\right) - \frac{E_a}{RT}. \quad [2]$$

E_a and A can be estimated from the slope and intercept of a $\ln\left(-\frac{dm}{mdt}\right)$ against $\frac{1}{T}$ plot. In this method, TGA data at a single ramp rate is sufficient for the analysis and kinetic parameter extraction.

2.2. Method B: Non-isothermal multiple ramp rates method:

To delineate the effect of ramp rate from the kinetic parameters, they can also be estimated using a fractional conversion α (where $\alpha = 1 - {}^{m}/_{m_0}$) in the non-isothermal experiments conducted at different ramp rates β. This analysis is based on the Flynn-Wall-Ozawa method [49-52] and Doyle's approximation[53, 54]. Eq. 1 can be written in terms of fractional conversion α as,

$$\frac{d\alpha}{dt} = -\frac{1}{m_0}\frac{dm}{dt} = A \exp\left(-\frac{E_a}{RT}\right)\frac{m}{m_0} p_{O_2} = A \exp\left(-\frac{E_a}{RT}\right)(1-\alpha) p_{O_2}. \quad [3]$$

With a linear ramp rate $\beta = \frac{dT}{dt}$, Eq. 3 can be written as,

$$\frac{d\alpha}{dT} = \frac{A}{\beta}\exp\left(-\frac{E_a}{RT}\right)(1-\alpha) p_{O_2}. \quad [4]$$

Integrating this equation from very low temperature (zero conversion) to the final temperature T corresponding to a final degree of conversion α and using $x = \frac{E_a}{RT}$ gives

$$-ln(1-\alpha) = \frac{A p_{O_2} E_a}{\beta R}\int_x^{\infty} \frac{e^{-x}}{x^2} dx = \frac{A p_{O_2} E_a}{\beta R} I(x). \quad [5]$$

The integral $I(x)$ is approximated as[28, 51],

$$log\, I(x) \approx -2.315 - 0.457x. \quad [6]$$

Combining Eqs. 5 and 6 and rearranging, we get

$$\log\beta = log\left(\frac{Ap_{O_2}E_a/R}{-ln(1-\alpha)}\right) - 2.315 - 0.457\frac{E_a}{RT}. \quad [7]$$

The activation energy E_a for different conversion values α can be calculated from the slope of a $\log\beta$ versus $\frac{1}{T}$ plot.

2.3. Method C: Isothermal single ramp rate method:

Isothermal tests provide another way of studying the kinetics of gas-solid reactions occurring in carbon black or soot oxidation.[12, 23, 30, 55-57] Starting from Eq. 1, under isothermal conditions, one can write

$$ln(1-\alpha) = ln\left(\frac{m}{m_0}\right) = \int_{m_0}^{m}\frac{dm}{m} = \int_0^t -A\exp\left(-\frac{E_a}{RT}\right)p_{O_2}dt = -A\exp\left(-\frac{E_a}{RT}\right)p_{O_2}t \quad [8]$$

Rearranging Eq. 8, we get

$$-ln\, t = ln\left[\frac{Ap_{O_2}}{-ln(1-\alpha)}\right] - \frac{E_a}{RT}. \quad [9]$$

A plot of $-ln\, t$ versus $\frac{1}{T}$ at a chosen value of α gives the activation energy E_a from the slope and pre-exponential factor A from the intercept.[28]

Given the assumptions associated with Eqs. 1 and 2, the kinetic parameters (activation energies and pre-exponential factors) estimated using the aforementioned methods should be treated as *apparent* parameters only.

3. Oxidation Kinetics using Non-isothermal Experiments

3.1. Effect of oxygen partial pressure

Soot could be oxidized using the oxygen present in the diesel engine exhaust (5-15% oxygen[58, 59]) or using air. Although the oxygen content in air is higher than that in the typical diesel engine exhaust, literature studies have commonly utilized air to test the oxidation of soot samples.[20, 55, 60] Therefore, we conducted the TGA experiments with both oxidizers: i) 10% O_2 in Ar and ii) air. Experimental protocol details are provided in **Table 1**. Mass loss profiles for all 15 samples with these two oxidizers are shown in **Figures 5 and 6**, respectively, with a constant ramp rate of 5 °C/min. The diesel soot sample in this study was collected under real diesel engine exhaust conditions (engine type = light duty, engine swept volume = 2 L, rpm = 3250 min^{-1}, torque = 50 Nm, power = 17 kW, exhaust gas flow rate = 253 kg/h). It contained metal oxides and ash particles, which were not burnt off during the oxidation experiments. A very small amount of ash particles was observed in the crucible after the diesel soot experiments, which was not the case with other carbon black samples. Therefore, the diesel soot conversion was not 100% even at high temperatures, as observed in **Figures 5 and 6**. The negligible deviation from 100% conversion for other samples and the slight increase in diesel soot mass with temperature (at high temperature) could be associated with experimental uncertainty in measuring very small quantities.

Details of T_{10}, T_{50}, and T_{90} are reported in **Table 2**. The T_{50} values for the most commonly studied samples such as Printex-U and Vulcan XC72R were in close agreement with the literature data (e.g. reported T_{50} of Printex-U = 606 °C and VulcanXC72R = 683 °C by Atribak *et al.* [61], T_{50} of Printex-U = 607 °C and VulcanXC72R = 667 °C by Hinot[62]). In general, there were three major groups in the considered samples: i) Monarch 1300, Monarch 1400, and Printex-XE2B had low light-off temperatures (T_{10} < 500 °C), and hence the highest oxidation rate; ii) Printex-G, Monarch 280, Vulcan XC72R, and

Graphite showed high light-off temperatures (T_{10} > 600 °C), and hence the lowest oxidation rate; and iii) all other samples had a moderate oxidation rate with a T_{10} ranging between 500-600 °C. The trend was similar for T_{50} and T_{90} (see **Table 2**). Monarch 1300 and Monarch 1400 contained 7% moisture, as compared to negligible moisture (0-0.6%) in the other samples. Therefore, oxidation data for Monarch 1300 and Monarch 1400 are reported with and without considering the moisture content (see **Table 2**). To calculate the conversion without considering the moisture content, the conversion (~4-5%) of those two samples just before reaching 200 °C was used to compute the 'corrected' initial mass without moisture. As expected, the T_{10} values were significantly affected by the moisture content, but the T_{50} and T_{90} values were not.

Figure 7 compares the T_{10}, T_{50}, and T_{90} values for all samples with 10% O_2 and air. The T_{10}-T_{90} values of all samples were lower in case of oxidation with air than those with 10% O_2. Therefore, the oxidation of carbon black and soot samples with air was faster than with 10% O_2. As the oxidation profiles in **Figures 5 and 6** showed similar trends for both cases, the decrease in T_{10}-T_{90} values for air was due to the higher concentration of O_2 in air (21%).

Method A was utilized to extract the apparent activation energies and pre-exponential factors. **Figure 8** shows an example of data analysis for diesel soot and Printex-U. First, data in panel a confirmed that the oxidation behavior of diesel soot and Printex-U was quite similar, which explains why Printex-U is commonly used as a surrogate for diesel soot.[30, 40, 42, 59, 63-65] Second, we utilized a much wider range of conversion profile (from 10% to ~90%) for data analysis in panel b as compared to the literature studies[42, 66], which ensured the validity of the estimated kinetic parameters over almost the complete oxidation process. Third, as shown in panel b, the $ln\left(-\frac{dm}{mdt}\right)$ vs. $\frac{1}{T}$ plots for diesel soot and Printex-U are almost straight lines with R^2>0.99, which agrees with the assumption of first order kinetics. Similar analysis was conducted for all samples for both oxidizer gases (10% O_2 and air), and the kinetic parameters (along with the considered conversion ranges and R^2 values) are reported in **Table 3**. Oxidation reaction rate constants at different temperature (k_{550}, k_{600}, and k_{650}) are also given in **Table 3** for both cases (10% O_2 and air), which indicated that oxidation with air was faster than with 10% O_2.

In general, the range of activation energies reported in the literature for the oxidation of carbon black and soot samples is 100-300 kJ/mol.[9, 21, 30, 34, 40, 42, 43, 47, 60, 64, 66-69] However, the typically reported activation energies for diesel engine soot oxidation are in the range of 120-180 kJ/mol.[30, 59, 60, 68, 70-72] Neeft *et al.*[59] suggested that the activation energy increased in the following sequence: soot < activated carbon < carbon and chars < graphite, which was also observed in our experiments as graphite showed the largest activation energy and the smallest rate constant. Given the comprehensive nature of our study, literature data were not available for direct comparisons for all the samples studied; however the activation energies estimated from our TGA experiments were in close agreement with those reported in the literature. For example, the activation energy for diesel soot oxidation with oxygen was reported to be 164 kJ/mol by Higgins *et al.*[60] and Darcy *et al.*[68], and 177 kJ/mol by Lee *et al.*[70], which compare well with our estimate of 172 kJ/mol. Similarly, the activation energy for Printex-U oxidation was reported to be 168 kJ/mol by Neeft *et al.*[59] and 161 kJ/mol by Tang *et al.*[42] with 10% O_2, and 160 kJ/mol by Hinot[62] with 20% O_2, which compare well with our estimates of 165 kJ/mol with 10% O_2 and 182 kJ/mol with air. Despite the agreement with literature, it is important to note that the estimated kinetic parameters should ideally not change with O_2 partial pressure. As alluded to earlier, this fundamental limitation most likely stems from the simplified kinetic expressions (Eqs. 1 and 2), where the change in surface area during oxidation and the pore size effects were ignored, and reaction order with respect to O_2 was assumed to be unity. Therefore, we emphasize that the estimated activation energies (and pre-exponential factors) should be considered as *apparent* kinetic parameters only.

To understand the variation of oxidation rate for the different carbon black and soot samples, they were characterized using Scanning Electron Microscopy (SEM) and BET surface area.[73] SEM analysis indicated that the average particle size (over ~200 particles) varied over a wide range (20.9-74 nm). Similarly, BET surface area varied over a wide range as well (43-1005 m^2/g). The oxidation rate of carbon black and soot samples is a complex function of various structural factors and operating conditions; however the large variations in average particle size and surface area may be used to explain some of the trends in the oxidation rate.[73] Monarch 1400, Monarch 1300, and Printex-XE2B had the smallest average particle size (20.9-26.7 nm), whereas Printex-G, Monarch 280, and Mogul-E had the largest particle size (69.7-74 nm). Surface areas of Monarch 1400, Monarch 1300, and Printex-XE2B were in the higher range 342-1005 m^2/g, whereas those of Printex-G, Monarch 280, and Mogul-E were in the lower range 45-49 m^2/g. The higher rate of Monarch 1400, Monarch 1300, and Printex-XE2B ($T_{50}^{O_2}$ range of 547-616 °C) could be attributed to the smaller particle size and higher surface area. Similarly, the lower rate of Printex-G, Monarch 280, and Mogul-E ($T_{50}^{O_2}$ range of 630-674 °C) could be attributed to the larger particle size and lower surface area.

3.2. Effect of ramp rate

Ramp rate β is another operating parameter, which typically shows a large impact on the oxidation profile.[20, 30] To validate the activation energies estimated in the previous section, we conducted TGA experiments with 10% O_2 and air using four ramp rates (5, 10, 15, and 20 °C/min) for diesel soot and Printex-U samples. Experimental protocol details are provided in **Table 1**. As shown in **Figure 9**, the oxidation rate shifted to higher temperatures with an increase in the ramp rate. Higher ramp rate reduces the overall reaction time in an experiment for a given temperature range, and less mass loss occurs at the same temperature point compared to a lower ramp rate case.[31] For example, for heating from 600 °C to 800 °C, it takes only 10 minutes with 20 °C/min, whereas it takes 40 minutes with 5 °C/min. Kalogirou and Samaras suggested that the higher ramp rates could also be associated with diffusional limitations, which are more prominent in the case of low oxygen concentrations.[30] Our experimental results with different ramp rates and oxygen partial pressures were consistent with this observation. For example, comparing the 10% O_2 vs. air profiles in **Figure 9**, the delay in oxidation rate with increased ramp rate was higher for 10% O_2 as compared to that for air. This also justifies the 5 °C/min ramp rate used in Method A for kinetic parameter estimation. On the other hand, data analysis presented in this section could be affected by diffusional limitations to some extent at higher ramp rates, but provide a reasonably good validation of the kinetic parameters.

Results obtained from diesel soot and Printex-U oxidation with 10% O_2 and air for various ramp rates (5-20 °C/min) were analyzed using **Method B**. **Figure 10** shows a plot of $\log \beta$ versus $\frac{1}{T}$ for diesel soot and Printex-U for both 10% O_2 (panel a) and air (panel b) for a selected fractional conversion α of 0.5. The estimated kinetic parameters are reported in **Table 3**. With 10% O_2, the estimated activation energies for diesel soot and Printex-U oxidation were in the range of 155-198 kJ/mol and 78-142 kJ/mol, respectively (these ranges were based on applying Method B at different fractional conversions); which were comparable with the numbers estimated from Method A (154-172 kJ/mol and 87-165 kJ/mol, respectively; these ranges were based on applying method A at different ramp rates). Similarly, with air, the estimated activation energies for diesel soot and Printex-U oxidation were in the range of 121-163 kJ/mol and 136-170 kJ/mol, respectively (these ranges were based on applying method B at different fractional conversions); which were also comparable with the numbers estimated from Method A (152-169 kJ/mol and 143-182 kJ/mol, respectively; these ranges were based on applying method A at different

ramp rates). A larger deviation was observed in the case of 10% O_2 than air, which could be due to the diffusional limitations associated with larger ramp rates and low oxygen concentration. However, the rate constants calculated using Method B at any particular temperature (see k values in **Table 3** for α=0.5) showed excellent agreement with the ones with Method A.

Before moving on to the isothermal experiments in the next section, we note that the kinetic parameters estimated using Method B are dependent on the fractional conversion α. For example, parameter estimation analysis was carried out for a wider range of fractional conversion values (α=0.1-0.9), as shown in **Figure 11** for diesel soot and Printex-U. The activation energies varied with the fractional conversion (diesel soot: 155-198 kJ/mol for 10% O_2 and 121-163 kJ/mol for air; and Printex-U: 78-142 kJ/mol for 10% O_2 and 136-170 kJ/mol for air). Overall, the analysis based on Method B provided excellent validation for the kinetic parameters estimated using Method A. Nonetheless, we recommend experiments with lower ramp rates to avoid any influence of heat and mass transfer limitations.

4. Kinetics from isothermal tests

Apart from the non-isothermal experiments reported so far, we also conducted isothermal tests for selected samples (Diesel soot, Printex-U, Monarch 1300, and VulcanXC72R) to further validate the kinetic parameters. The four samples were selected to cover the range from low to high oxidation rates from the non-isothermal experiments. For each sample, we conducted isothermal experiments at multiple temperature points with the same initial mass. After reaching the set point (isothermal temperature), the sample was kept at the set point for 2 hours. Experimental protocol details are provided in **Table 1**. **Method C** was used for the analysis of the isothermal experiments.

Figure 12 shows the mass loss profiles of the four selected samples. Plots of conversion α vs. time t suggest that the reaction profiles or kinetic curves of diesel soot and commercial carbon black samples are of the decelerating type, in which the rate is maximum at the beginning and decreases continuously with the extent of conversion.[18] Reaction order models are generally used for gas-solid reactions of the decelerating type. First order reaction kinetics was used for the analysis of these data to extract the kinetic parameters, consistent with the methods A and B discussed earlier. The estimated kinetic parameters are reported in **Table 3**.

In general, the activation energies estimated using Method C (isothermal) were slightly lower than those estimated using Methods A and B (non-isothermal). Similarly, the pre-exponential factors calculated using Method C (isothermal) were lower than those estimated using Methods A and B (non-isothermal). On the other hand, the reaction rate constants computed at 550 °C, 600 °C, and 650 °C for α of 0.5 showed good agreement with the corresponding rate constants estimated from the non-isothermal experiments. This indicated that the activation energies estimated using Method C could be affected by the compensation effect between activation energies and pre-exponential factors. Compensation effect is a commonly reported phenomenon, in which change in the activation energy is compensated by change in the pre-exponential factor.[28, 74-76] Analysis conducted at different fractional conversion values for diesel soot oxidation with 10% O_2 and air is shown in **Figure 13a**. The activation energy varied with fractional conversion, consistent with literature reports on solid state reaction kinetics.[18, 76-78] For example, the estimated activation energy ranged over fractional conversion α of 0.2-0.9 for diesel soot (112-142 kJ/mol for 10% O_2, 133-155 kJ/mol for air) and Printex-U (107-136 kJ/mol for 10% O_2, 135-153 kJ/mol for air) and corresponding variation in pre-exponential factors confirmed the existence of the compensation effect. **Figure13b** shows the variation in activation energy with pre-exponential factor. Complex or multiple steps reaction kinetics of soot oxidation was ruled out due to the absence of multiple peaks and/or shoulders in

the reaction rate curve.[18] Despite this limitation, Method C (isothermal) provided a reasonably good validation of the kinetic parameters estimated using Methods A and B (non-isothermal).

To verify the assumption of first order kinetics with respect to O_2, we estimated the reaction order based on the isothermal experiments with 10% O_2 and air for the four samples studied here (Diesel soot, Printex-U, Monarch 1300, and VulcanXC72R). The estimated order was 1 for Diesel soot, whereas it was close to 1 for the other carbon black samples (0.95 for Printex-U, 0.88 for Monarch 1300, and 0.90 for VulcanXC72R). Finally, to demonstrate the validity of effective models used here, **Figure 14** shows how the apparent kinetic parameters extracted at nominal conditions (fractional conversion $\alpha = 0.5$) along with first order kinetics with respect to O_2 can adequately capture the entire range of experimental data, i.e., the compensation effect between apparent activation energy and pre-exponential factors was not critical for the effective models considered here.

5. Most Recent Research.

Our current research focuses on soot samples provided by Corning and how these materials fit the models decribed above. We are planning to use TGA methods and measure weight changes at the particular temperatures of interest with given NO_2 concentrations. TGA experiments will be done in O_2. The TGA experiments will be followed up by catalyst analyses to determine T10, T50, and others and should prove useful in seeking correlations among different data sets for different soot samples. Most of these experiments are now completed and there is preparation of another manuscript. A patent application on new catalysts that can be used to break down soot has been submitted.

Conclusions

In this work, we conducted non-isothermal and isothermal TGA experiments for more than a dozen carbon black samples and a diesel engine soot sample with 10% O_2 and air to investigate the effect of operating conditions on the oxidation rate and to extract the corresponding apparent kinetic parameters. Limitations associated with the availability of oxygen were avoided by conducting experiments in sufficient oxidizer gas flow rate conditions. Partial pressure of oxygen and ramp rates showed significant effects on the oxidation rate. Oxidation with air was faster than with 10% O_2, due to the higher concentration of oxygen in air. Activation energy for oxidation of carbon black samples ranged from 125 to 257 kJ/mol, whereas that for soot oxidation was ~155 kJ/mol. Oxidation rate trends were explained based on structural characteristics such as SEM-based average particle size and BET surface area. In general, low particle size and high surface area were associated with higher oxidation rate and vice versa. Kinetic parameters extracted using the non-isothermal experiments at a single ramp rate (Method A) were further validated using additional non-isothermal experiments with multiple ramp rates (Method B) and isothermal experiments with single ramp rate (Method C). The overall agreement for kinetic parameters estimated using the three methods (consisting of separately conducted experiments) was remarkable; however the analysis in Methods B and C indicated that the extracted parameters could be affected by a compensation effect between activation energies and pre-exponential factors as they change with the extent of conversion. Overall, the comprehensive understanding developed in this work for oxidation of carbon black and soot samples could be beneficial for improved design and optimization of diesel particulate filter operation and regeneration protocols. The new catalysts for soot decomposition are composite materials that have not before been studied. These show excellent activity for degradation of soot.

Some areas we are continuing to study include measurement of soot oxidation kinetics on a lab scale; estimation of soot properties at T10, T50, and T90 using characterization tools; and development of structure – activity correlations at T10, T50, and T90 under real diesel engine exhaust conditions.

Patents

1. Lakshitha Pahalgedara, Steven L. Suib, Catalysts for Degradation of Soot, 2013, Patent Application in Preparation.

Publications/Presentations

1. Hom N. Sharma, Lakshitha Pahalagedara, Ameya Joshi, Steven L. Suib, and Ashish B. Mhadeshwar, "Non-catalytic Oxidation Kinetics of Carbon Black and Diesel Engine Soot Samples by Thermogravimetric Analysis", Under review, Energy & Fuels, 2012.

2. Lakshitha Pahalagedera, Hom N. Sharma, Chung-Hao Kuo, Saminda Dharmarathna, Ameya V. Joshi, Steven L. Suib, and Ashish B. Mhadeshwar, "Structure and Oxidation Activity Correlations for Carbon Blacks and Diesel Soot", in preparation for submission to Chemistry of Materials, 2012.

3. Lakshitha Pahalagedera, Hom N. Sharma, Chung-Hao Kuo, Saminda Dharmarathna, Ameya V. Joshi, Steven L. Suib, and Ashish B. Mhadeshwar, "Comparative Analysis of the Structure and Chemical Nature of Carbon", in preparation for submission to Analytical Chemistry, 2013.

4. Lakshitha Pahalagedera, Chung-Hao Kuo, Saminda Dharmarathna, Hom N. Sharma, Ameya V. Joshi, Steven L. Suib, and Ashish B. Mhadeshwar, "Comparative Analysis of the Structure and Chemical Nature of Carbon Blacks and Diesel Soot", accepted, AIChE Annual Meeting, 2012.

5. Lakshitha Pahalagedera, Hom N. Sharma, Chung-Hao Kuo, Saminda Dharmarathna, Ameya V. Joshi, Steven L. Suib, and Ashish B. Mhadeshwar, "Influence of Particle Size and Microstructure on the Oxidation Behavior of Carbon Blacks and Diesel Soot", accepted, AIChE Annual Meeting, 2012.

6. Hom N. Sharma, Lakshitha Pahalagedara, Ameya Joshi, Steven L. Suib, and Ashish B. Mhadeshwar, "Non-catalytic Oxidation of Carbon Black and Diesel Engine Soot Samples - Kinetics and Structure-activity Relationships", accepted, AIChE Annual Meeting, 2012.

Table 1: Details of the TGA instrument and experimental protocols.

Technical specifications[79]		
Weighting capacity	100 mg	
Weighting precision	± 0.01%	
Sensitivity	< 0.1 µg (1 ppm)	
Signal resolution	0.002 µg	
Temperature range	Ambient to 1,200°C	
Furnace type	Infrared heating with built-in electromagnetic coil for automated temperature calibration	
Isothermal temperature accuracy	±1 °C	
Isothermal temperature precision	±0.1 °C	
Linear heating rates	0.1 – 500 °C/min in 0.01 °C/min increments	
Special heating mode	Hi-Res TGA and Modulated TGA	
Auto-sampler	16 sample carousel with automated pan punching	
Experimental protocol for non-isothermal tests		
Step	Description	Stage
1	Flow of oxidant gas with Nitrogen	Initial
2	Ramp to 800 °C with ramp rate β = 5-20 °C/min	Heating
3	Hold at 800 °C for 15 minutes	Isothermal
4	Cool to room temperature	Cooling
Experimental protocol for isothermal tests		
Step	Description	Stage
1	Flow of Nitrogen (balance and purge gasses)	Initial
2	Ramp to $T_{isothermal}$ with β = 20 °C/min	Heating
3	Hold at $T_{isothermal}$ for 120 minutes	Isothermal
4	Cool to room temperature	Cooling

Table 2: Light-off temperature data from non-isothermal experiments. * indicates data without moisture (see text for details).

SN		10% O_2, β =5 °C/min			Air, β = 5 °C/min		
	Sample name	T_{10} [°C]	T_{50} [°C]	T_{90} [°C]	T_{10} [°C]	T_{50} [°C]	T_{90} [°C]
1	Diesel soot	541	640	685	499	607	647
2	Graphite	687	764	800	671	740	784
3	Mogul-E	548	630	663	532	601	623
4	Monarch 1300	444 482*	562 563*	590	444 468*	539	550
5	Monarch 1400	478 513*	615 616*	651	452 496*	587 589*	612
6	Monarch 280	617	674	713	543	609	650
7	N 120	550	626	663	526	591	617
8	N 339	579	641	674	553	606	631
9	N 762	583	649	686	565	614	636
10	Printex-G	637	696	738	606	655	693
11	Printex-U	543	615	662	524	584	625
12	Printex-XE2B	479	547	589	459	512	545
13	Regal 330 R	587	659	696	559	626	651
14	Regal 400 R	565	641	675	548	612	635
15	VulcanXC72R	631	692	733	610	664	701

Table 3: Apparent kinetic parameters from non-isothermal and isothermal experiments. The kinetic parameters correspond to Method A with ramp rate β of 5 °C/min, unless specified otherwise (see footnotes).

SN	Samples	10% O_2							Air						
		Range [%]	R^2	E [kJ/mol]	A [1/Pa.s]	k_{550} [1/Pa.s]	k_{600} [1/Pa.s]	k_{650} [1/Pa.s]	Range [%]	R^2	E [kJ/mol]	A [1/Pa.s]	k_{550} [1/Pa.s]	k_{600} [1/Pa.s]	k_{650} [1/Pa.s]
1	Diesel soot	10-90 10-90 20-90	0.991 0.898 0.956	154-172* 155-198^{MB} 112-142^{MC}	1.0×10^{2}-9.4×10^{2}* 2.4×10^{2} - 3.4×10^{5} MB 3.3×10^{-1}- 2.6×10^{1} MC	1.1×10^{-08} 2.2×10^{-08} MB 2.3×10^{-8} MC	4.8×10^{-08} 8.6×10^{-08} MB 6.9×10^{-08} MC	1.7×10^{-07} 2.9×10^{-07} MB 1.8×10^{-07} MC	10-90 10-90 20-90	0.985 0.872 0.683	152-169* 121-163 ^{MB} 133-155 ^{MC}	1.0×10^{2}-8.5×10^{2}* 2.3×10^{0}-5.0×10^{2} MB 6.2×10^{0}-1.8×10^{2} MC	1.6×10^{-08} 2.2×10^{-08} MB 2.2×10^{-08} MC	6.6×10^{-08} 8.3×10^{-08} MB 7.9×10^{-08} MC	2.3×10^{-07} 2.7×10^{-07} MB 2.4×10^{-07} MC
2	Graphite	10-80	0.995	226	3.7×10^{4}	1.7×10^{-10}	1.1×10^{-09}	5.9×10^{-09}	10-90	0.999	229	4.8×10^{4}	1.4×10^{-10}	9.6×10^{-10}	5.3×10^{-09}
3	Mogul-E	10-75	0.980	186	9.4×10^{3}	1.5×10^{-08}	7.0×10^{-08}	2.8×10^{-07}	10-60	0.958	214	5.9×10^{5}	1.6×10^{-08}	9.4×10^{-08}	4.6×10^{-07}
4	Monarch 1300	10-80 5-80** 20-90	0.945 0.932** 0.897	164 145** 93-117 ^{MC}	2.9×10^{3} 1.9×10^{2}** 1.5×10^{-1}-1.9×10^{0} MC	1.2×10^{-07} 1.1×10^{-07}** 9.0×10^{-08} MC	4.6×10^{-07} 3.7×10^{-07}** 2.3×10^{-07} MC	1.5×10^{-06} 1.1×10^{-06}** 5.2×10^{-07} MC	10-80 5-80**	0.870 0.861**	197 156**	4.7×10^{5} 8.6×10^{2}**	1.5×10^{-07} 1.0×10^{-07}**	7.8×10^{-07} 4.0×10^{-07}**	3.4×10^{-06} 1.3×10^{-06}**
5	Monarch 1400	10-80 5-80**	0.971 0.952**	144 125**	3.6×10^{1} 2.6×10^{0}**	2.6×10^{-08} 3.1×10^{-08}**	8.9×10^{-08} 8.9×10^{-08}**	2.6×10^{-07} 2.3×10^{-07}**	10-80 5-80**	0.940 0.933**	146 133**	5.2×10^{1} 7.6×10^{0}**	2.9×10^{-08} 2.8×10^{-08}**	9.7×10^{-08} 8.5×10^{-08}**	2.9×10^{-07} 2.3×10^{-07}**
6	Monarch 280	10-90	0.989	220	2.4×10^{5}	2.6×10^{-09}	1.6×10^{-08}	8.5×10^{-08}	10-90	0.994	180	3.8×10^{3}	1.4×10^{-08}	6.5×10^{-08}	2.5×10^{-07}
7	N 120	10-90	0.980	195	3.5×10^{4}	1.5×10^{-08}	7.6×10^{-08}	3.2×10^{-07}	10-80	0.996	203	1.5×10^{5}	2.0×10^{-08}	1.0×10^{-07}	5.1×10^{-07}
8	N 339	10-80	0.993	222	9.4×10^{5}	7.7×10^{-09}	4.9×10^{-08}	2.6×10^{-07}	10-80	0.991	243	2.6×10^{7}	1.0×10^{-08}	7.7×10^{-08}	4.7×10^{-07}
9	N 762	10-80	0.994	206	8.5×10^{4}	7.2×10^{-09}	4.0×10^{-08}	1.9×10^{-07}	10-80	0.992	257	1.3×10^{8}	6.3×10^{-09}	5.4×10^{-08}	3.7×10^{-07}
10	Printex-G	10-80	0.990	187	1.9×10^{3}	2.6×10^{-09}	1.2×10^{-08}	4.9×10^{-08}	10-80	0.987	207	3.8×10^{4}	2.8×10^{-09}	1.6×10^{-08}	7.5×10^{-08}
11	Printex-U	10-90 10-90 20-90	0.999 0.959 0.987	87-165* 78-142^{MB} 107-136^{MC}	1.2×10^{-2}-8.2×10^{2}* 1.7×10^{-2}-3.8×10^{1} MB 1.2×10^{-1}-1.4×10^{1} MC	2.8×10^{-08} 7.5×10^{-08} MB 2.7×10^{-08} MC	1.1×10^{-07} 1.7×10^{-07} MB 7.6×10^{-08} MC	3.8×10^{-07} 3.6×10^{-07} MB 1.9×10^{-07} MC	10-90 10-90 20-90	0.999 0.902 0.832	143-182* 136-170^{MB} 135-153^{MC}	3.8×10^{1}-1.0×10^{4}* 1.4×10^{3}-1.2×10^{5}MB 6.2×10^{-0}-1.5×10^{2}MC	2.9×10^{-08} 4.0×10^{-08} MB 2.1×10^{-08} MC	1.3×10^{-07} 1.5×10^{-07} MB 7.3×10^{-08} MC	5.2×10^{-07} 4.8×10^{-07} MB 2.2×10^{-07} MC
12	Printex-XE2B	10-90	0.993	155	6.1×10^{2}	8.9×10^{-08}	3.2×10^{-07}	1.0×10^{-06}	10-90	0.997	196	1.1×10^{6}	4.1×10^{-07}	2.1×10^{-06}	9.2×10^{-06}
13	Regal 330 R	10-80	0.992	207	3.4×10^{4}	2.4×10^{-09}	1.4×10^{-08}	6.5×10^{-08}	10-80	0.984	171	1.6×10^{3}	2.2×10^{-08}	9.4×10^{-08}	3.4×10^{-07}
14	Regal 400 R	10-80	0.990	211	2.1×10^{5}	8.5×10^{-09}	5.0×10^{-08}	2.4×10^{-07}	10-80	0.987	249	5.8×10^{7}	9.1×10^{-09}	7.3×10^{-08}	4.7×10^{-07}
15	VulcanXC72R	10-90 20-90	0.988 0.888	210 144-156 ^{MC}	1.9×10^{4} 4.6×10^{0}-4.6×10^{1} MC	9.3×10^{-10} 4.1×10^{-09} MC	5.4×10^{-09} 1.5×10^{-08} MC	2.6×10^{-08} 4.6×10^{-08} MC	10-90 20-90	0.983 0.903	223 188-223^{MC}	2.7×10^{5} 2.8×10^{3}-1.6×10^{5}MC	1.9×10^{-09} 1.6×10^{-09}MC	1.2×10^{-08} 1.0×10^{-08}MC	6.5×10^{-08} 5.0×10^{-08}MC

* Method A was applied for different ramp rates (β=5-20 °C/min). For the given range, the first value is for 20 °C/min experiments and the second value is for 5 °C/min experiments.
** Without moisture (see text for details).
^{MB} Method B: Non-isothermal experiments with multiple ramp rates. Activation energies and pre-exponential factors are given for fractional conversion α range of 0.1-0.9, whereas the rate constants k are reported for α of 0.5.
^{MC} Method C: Isothermal experiments. Activation energies and pre-exponential factors are given for fractional conversion α range of 0.2-0.9, whereas the rate constants k are reported for α of 0.5.

Figure 1: Oxidation profile of Printex-U with different flow rates of air. Operating conditions: Non-isothermal experiment, initial mass = 10 mg, ramp rate = 5 °C/min. Data indicate that the gas flow rate must be at least 40 mL/min to avoid the limitations associated with the availability of oxygen.

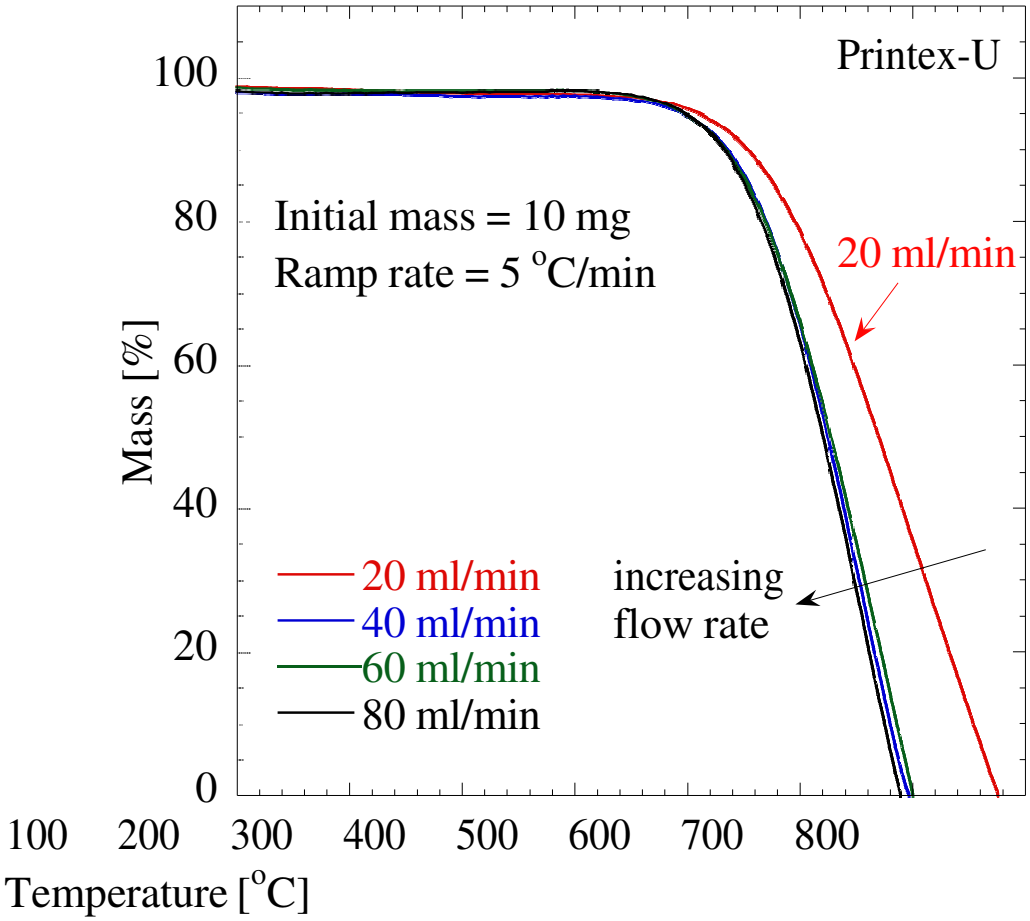

Figure 2: Effect of initial sample mass and ramp rate on the oxidation of (a) Printex-XE2B with ramp rate of 5 °C/min and initial mass of 8-14 mg, (b) Printex-U with ramp rate of 10 °C/min and initial mass of 2-20 mg, (c) Printex-XE2B with ramp rate of 15 °C/min and initial mass of 4-14 mg, and (d) Printex-XE2B with ramp rate of 20 °C/min and initial mass of 4-19 mg. Operating conditions: Non-isothermal experiment, oxidant = air, flow rate = 60 mL/min.

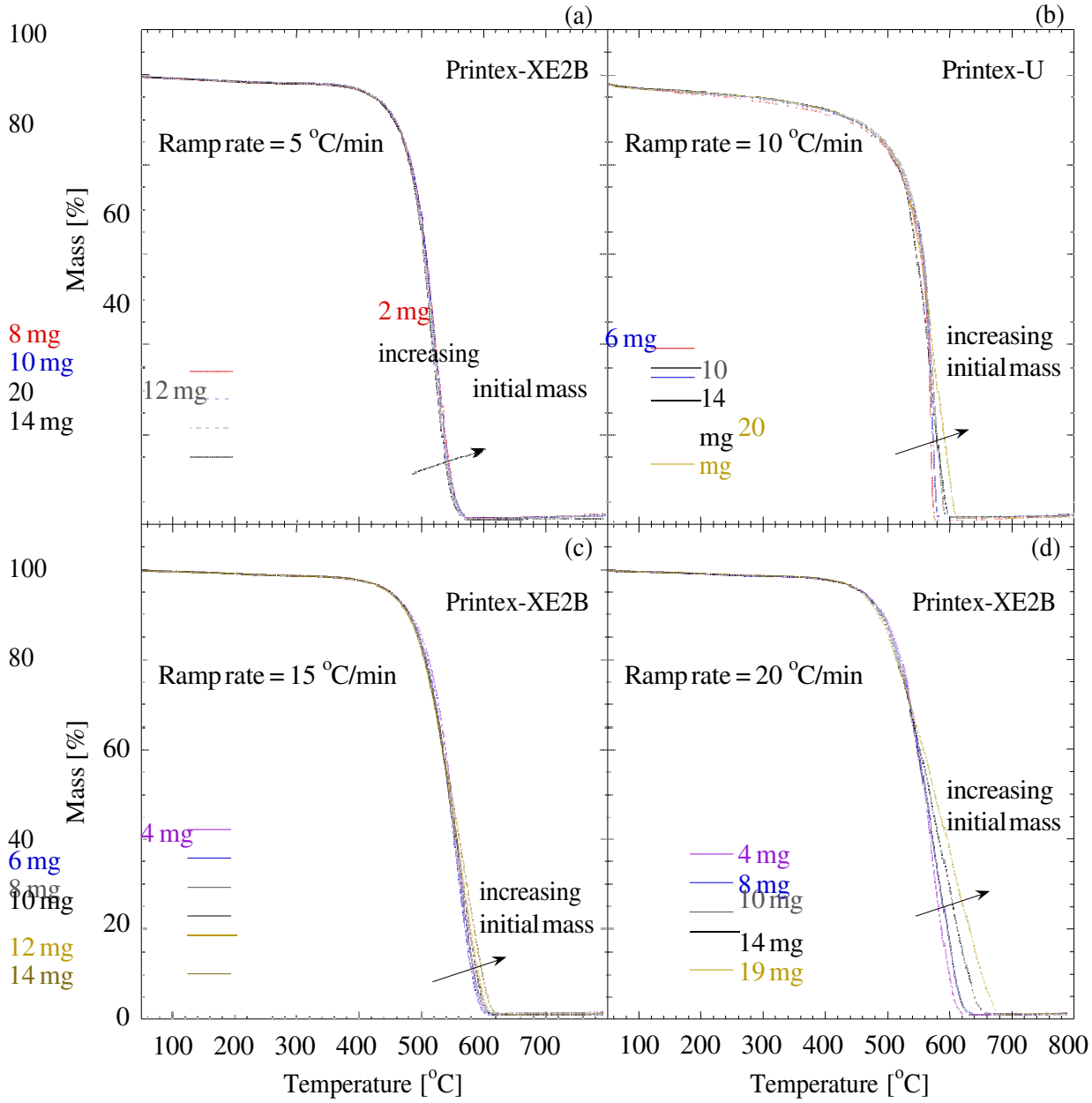

Figure 3: Effect of crucible type on the oxidation of (a) Printex-XE2B with ramp rate of 5 °C/min and initial mass of 10 mg, and (b) Printex-U with ramp rate of 5 °C/min and initial mass of 10 mg. Operating conditions: Non-isothermal experiment, oxidant = air, flow rate = 60 mL/min.

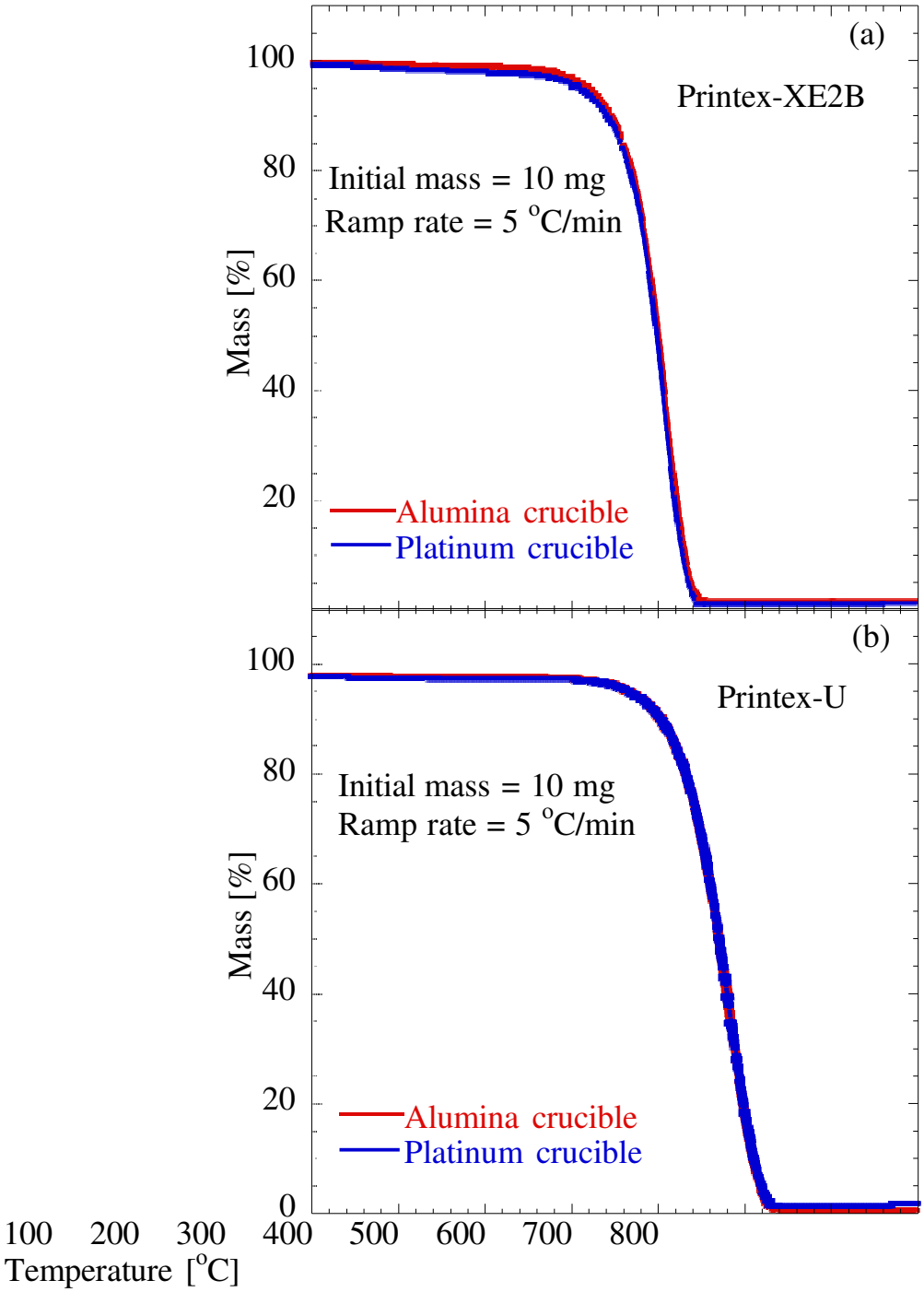

Figure 4: Reproducibility of the TGA experiments for (a) diesel soot with initial mass of 2.5 mg and (b) Printex-XE2B with initial mass of 10 mg. Operating conditions: Non-isothermal experiment, oxidant = air, flow rate = 60 ml/min, ramp rate = 5 °C/min.

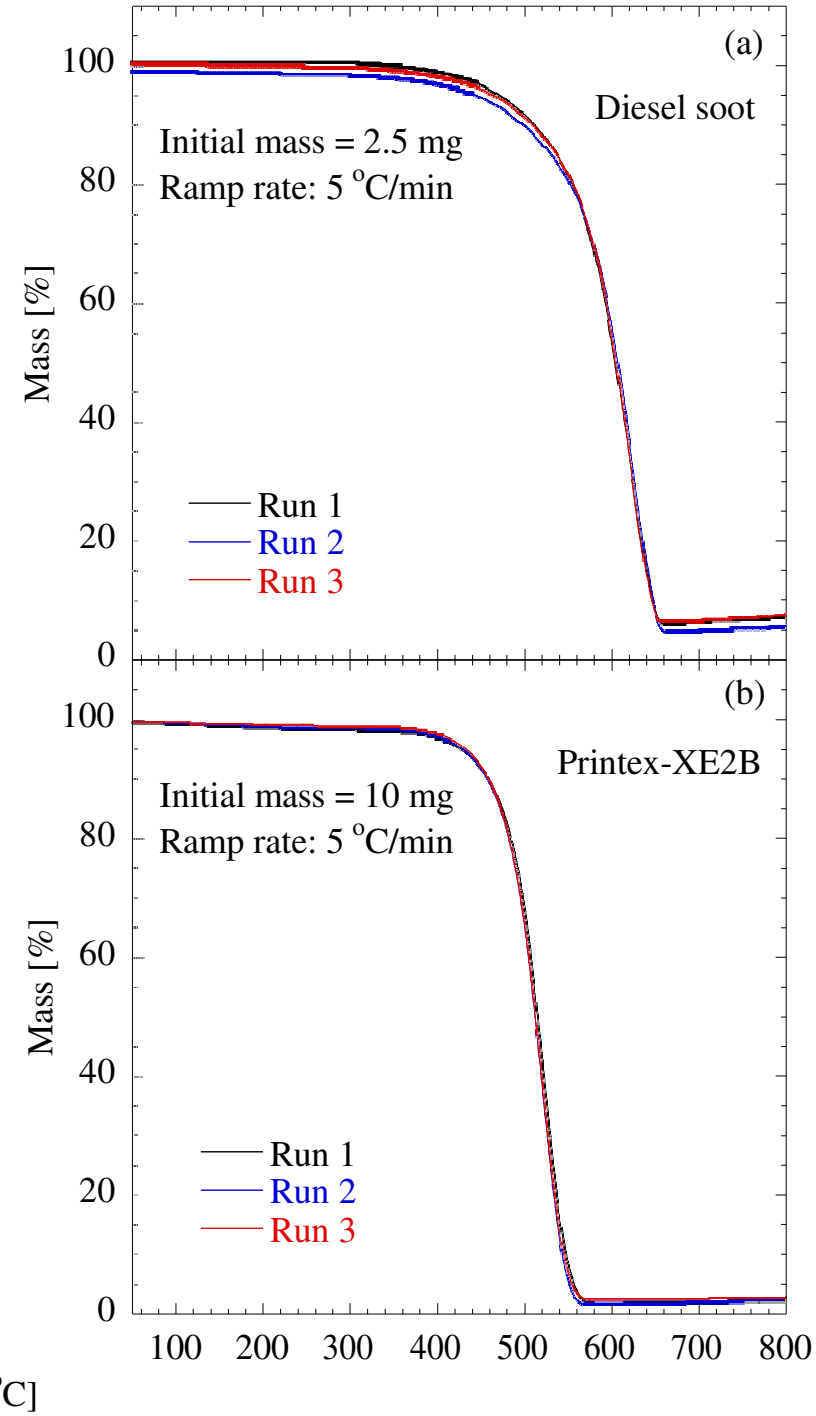

Figure 5: Mass loss profiles of all samples with 10% O_2. Operating conditions: Non-isothermal experiment, initial mass range = 2.5-12 mg, flow rate = 60 mL/min, ramp rate = 5 °C/min. Diesel soot showed incomplete conversion due to the presence of metal oxides and ash particles.

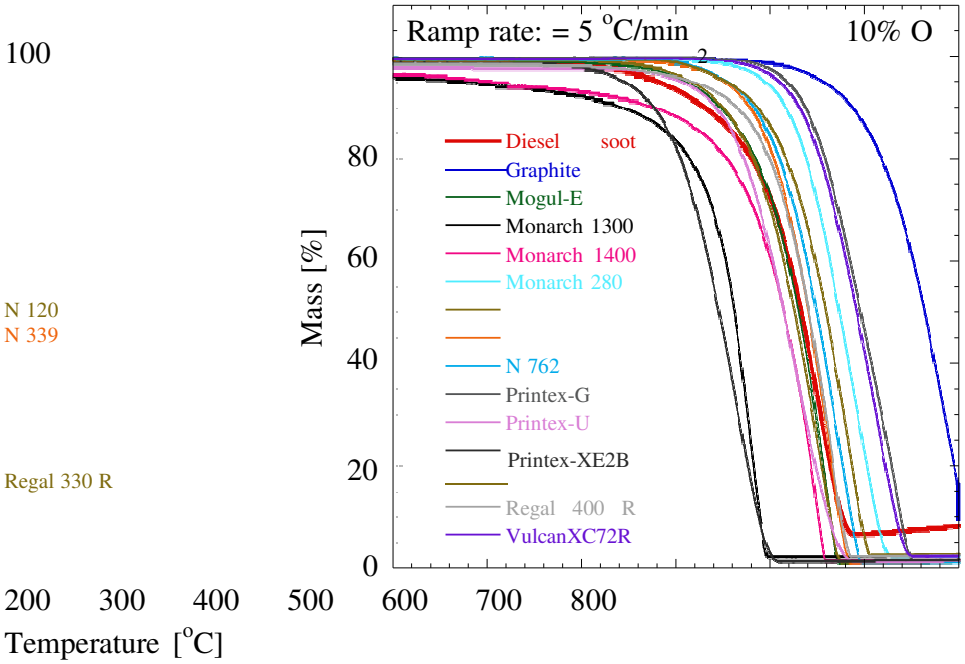

Figure 6: Mass loss profiles of all samples with air. Operating conditions: Non-isothermal experiment, initial mass range = 2.5-12 mg, flow rate = 60 mL/min, ramp rate = 5 °C/min. Diesel soot showed incomplete conversion due to the presence of metal oxides and ash particles.

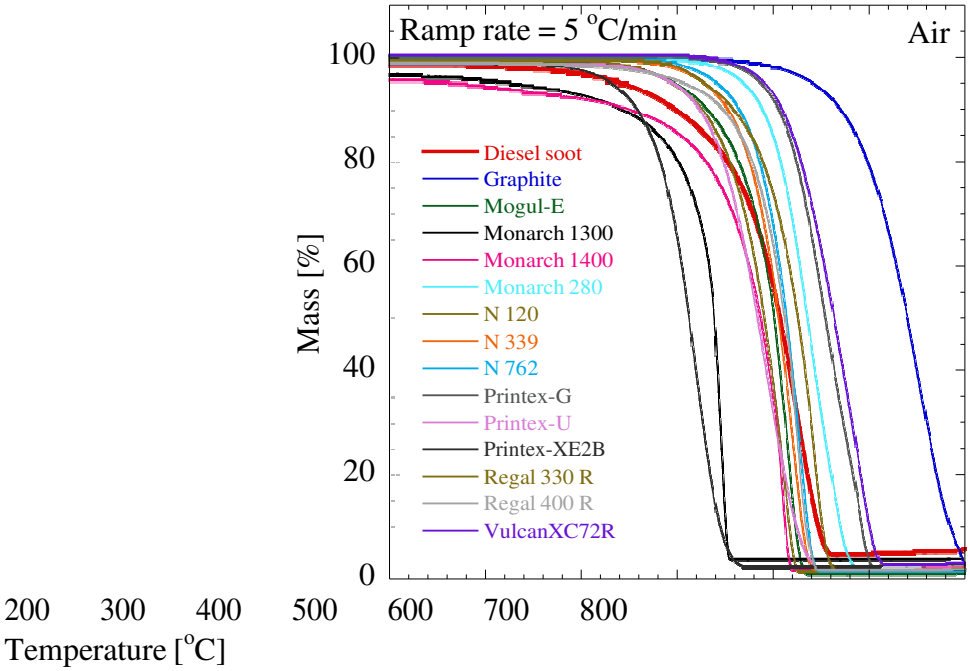

Figure 7: Comparison of T_{10}, T_{50}, and T_{90} for all samples with 10% O_2 and air. Oxidation is faster with air. The operating conditions are same as in **Figures 5 and 6**.

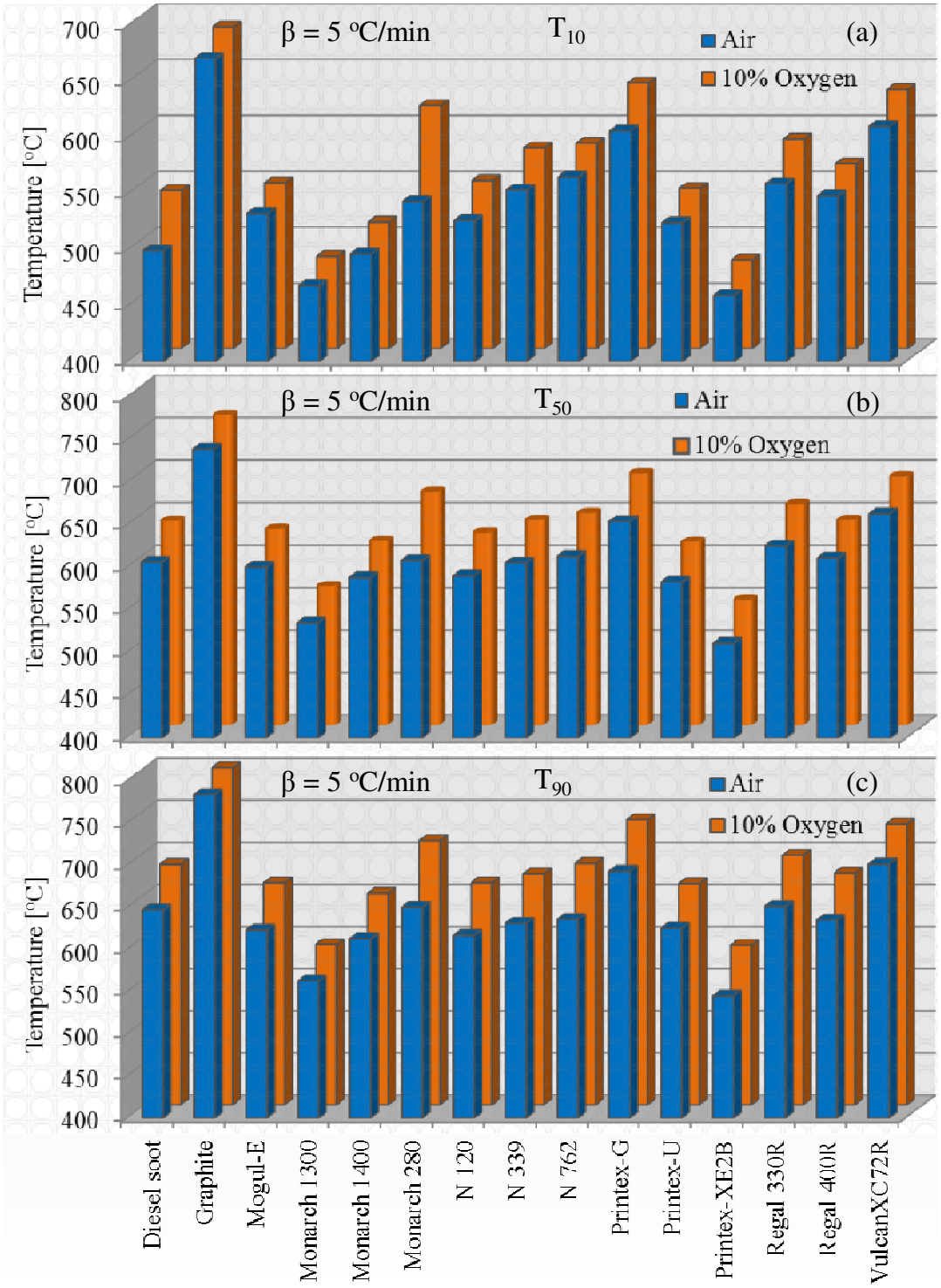

Figure 8: (a) Mass loss profiles and (b) Arrhenius plots for diesel soot and Printex-U samples using Method A. The operating conditions are same as in **Figure 5**.

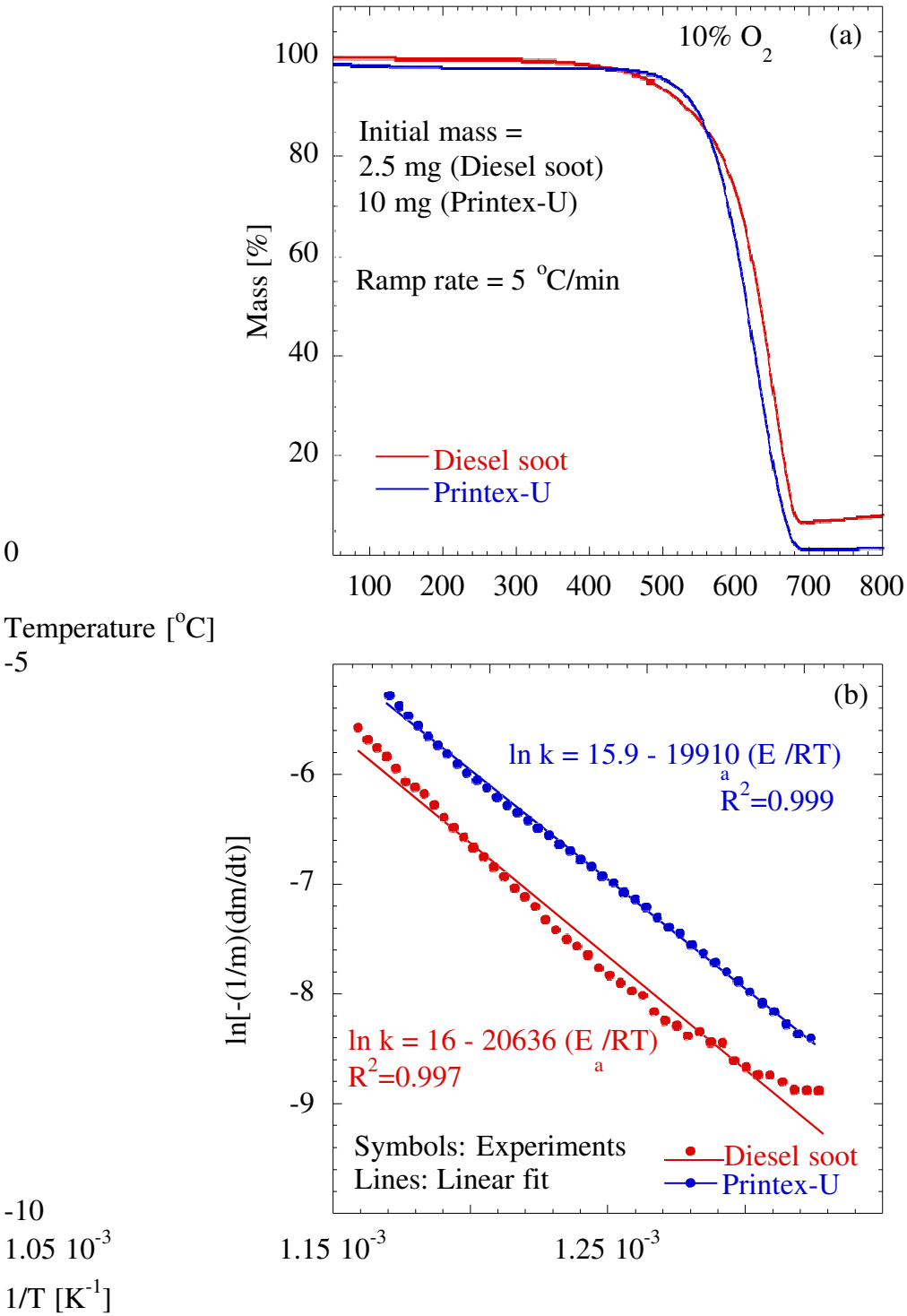

Figure 9: Effect of ramp rate and oxygen partial pressure on the oxidation of diesel soot (initial mass = 2.5 mg) and Printex-U (initial mass = 10 mg). Ramp rates of 5, 10, 15, and 20 °C/min are used. (a) diesel soot with 10% O_2, (b) diesel soot with air, (c) Printex-U with 10% O_2, and (d) Printex-U with air. Operating conditions: Non-isothermal experiment, flow rate = 60 mL/min.

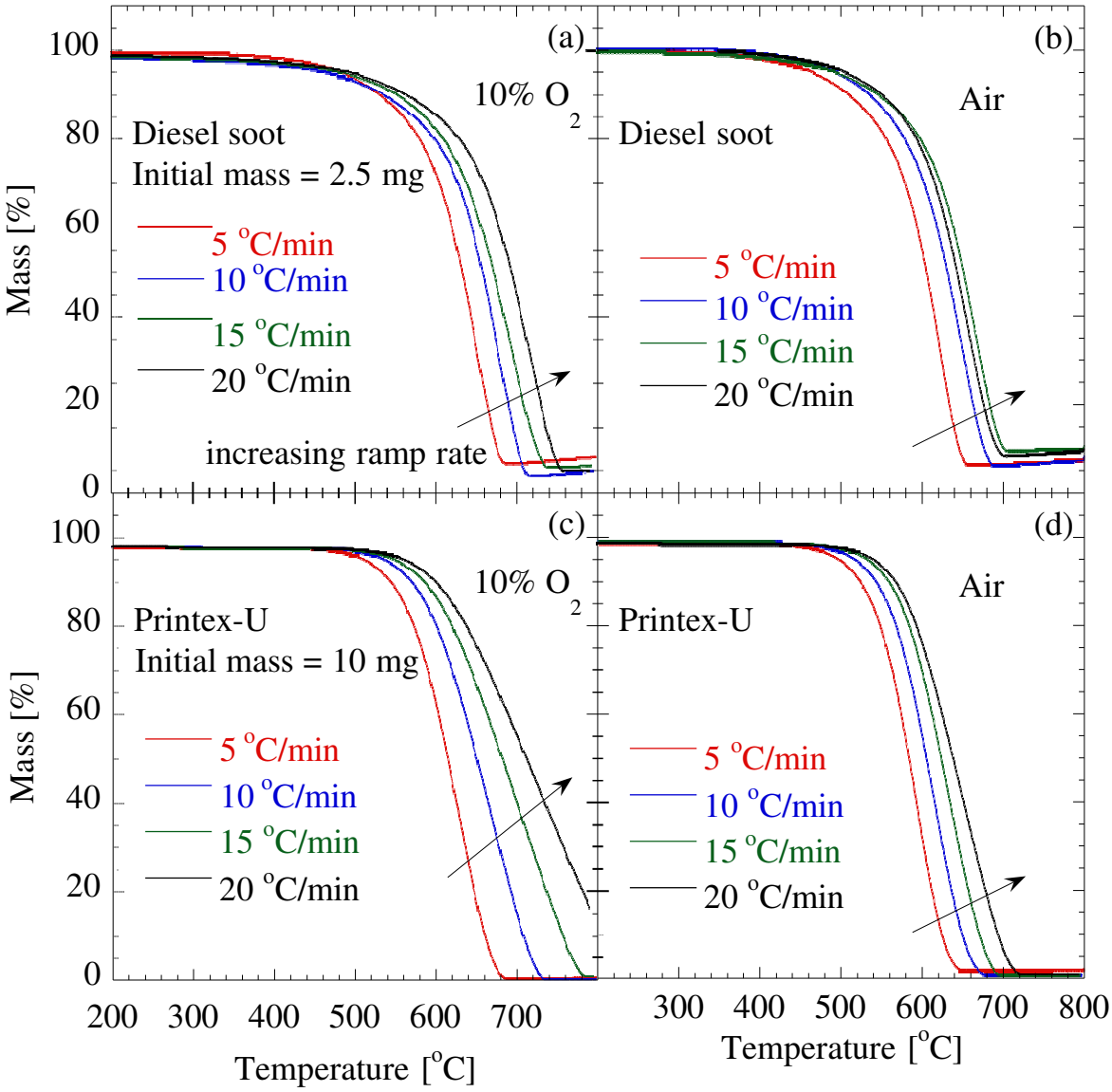

Figure 10: Kinetic parameter extraction for diesel soot (initial mass = 2.5 mg) and Printex-U (initial mass = 10 mg) oxidation with (a) 10% O_2 and (b) air using Method B for a fractional conversion α of 0.5. Operating conditions are the same as in **Figure 9**.

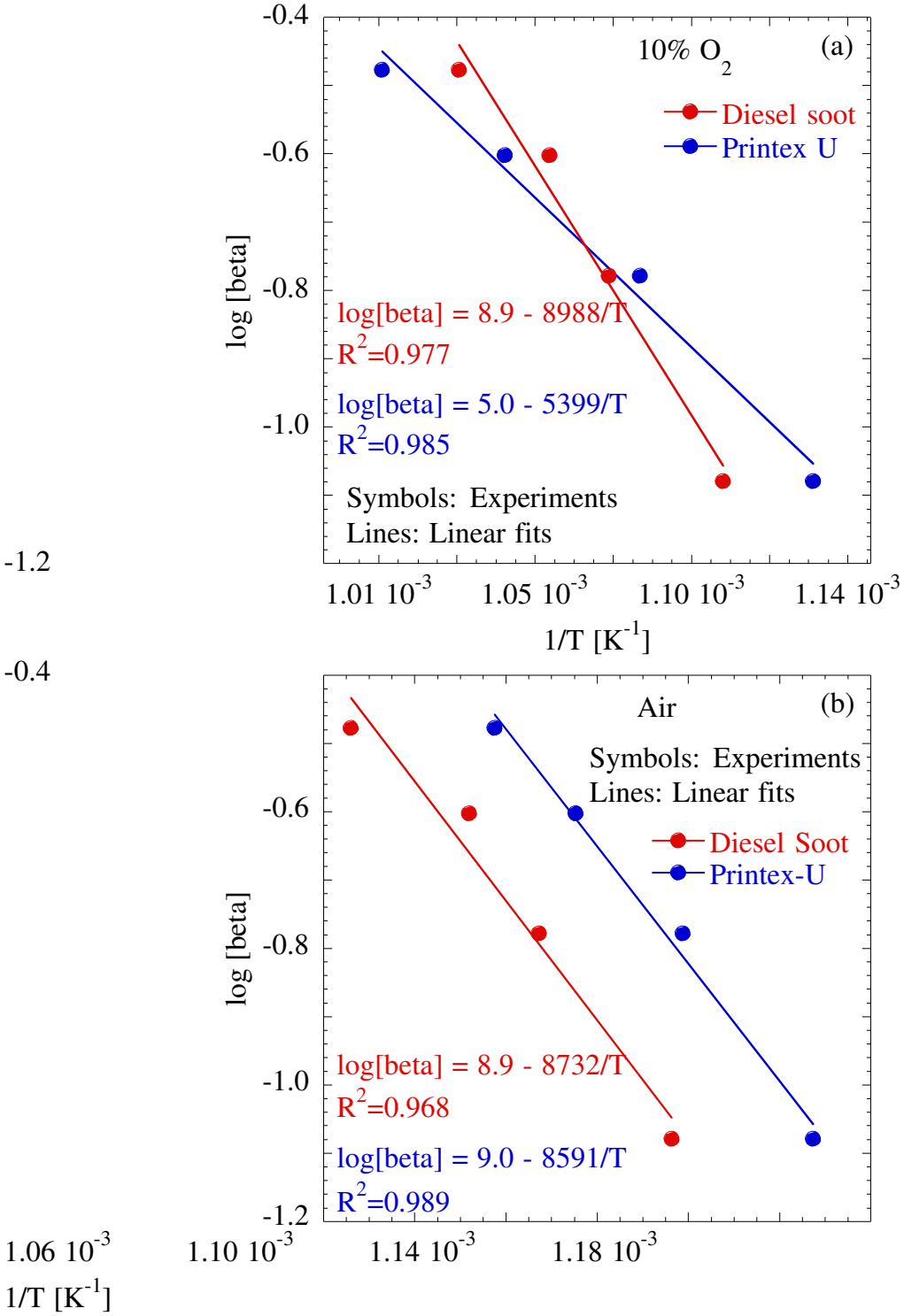

Figure 11: Flynn-Wall-Ozawa plot for diesel soot (initial mass = 2.5 mg) and Printex U (initial mass = 10 mg) oxidation. (a) Diesel soot with 10% O_2, (b) diesel soot with air, (c) Printex-U with 10% O_2, and (d) Printex-U with air, using Method B for a fractional conversion α range of 0.1-0.9. Operating conditions are the same as in **Figure 9**.

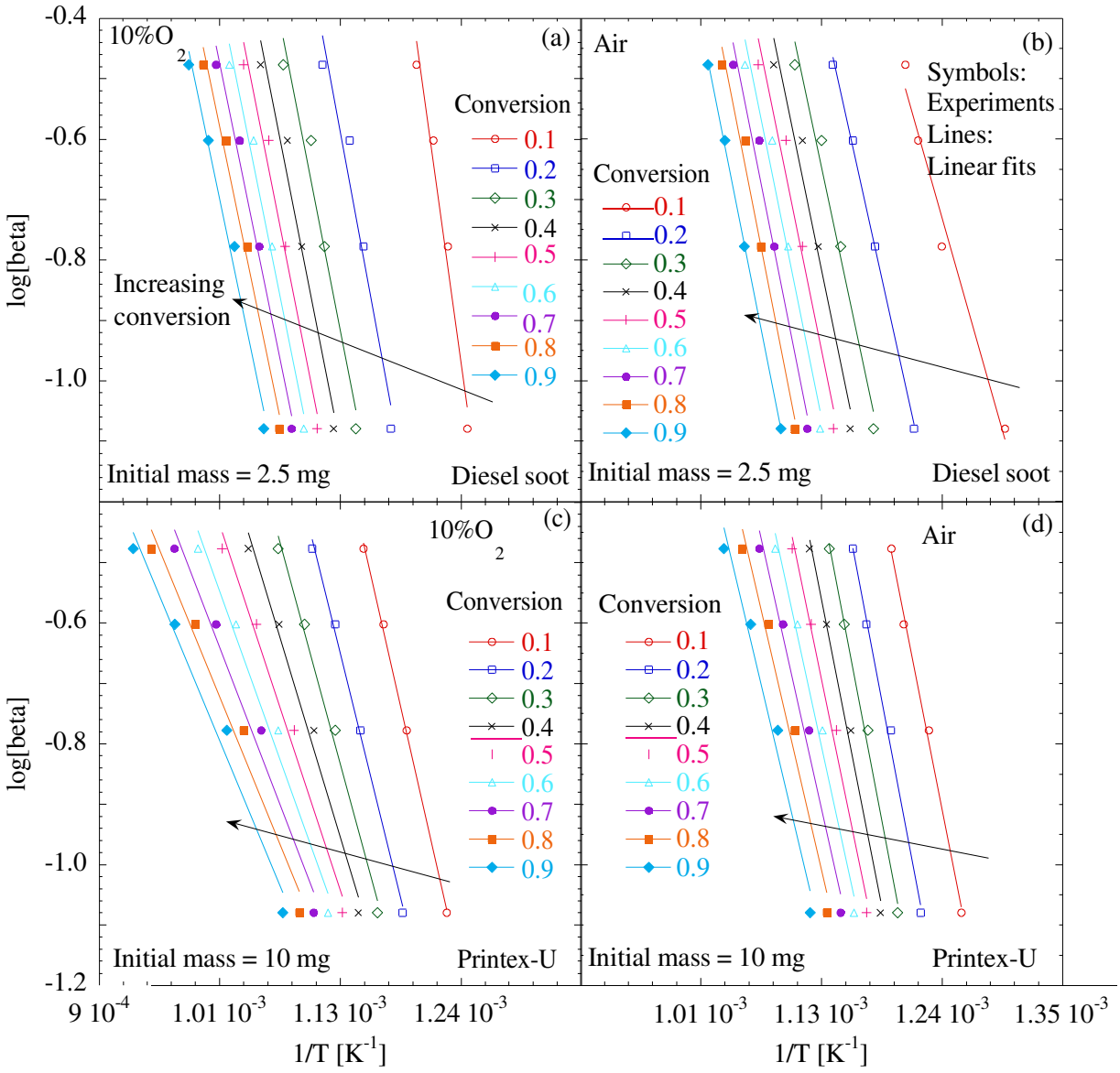

Figure 12: Isothermal conversion profiles of (a) diesel soot (initial mass = 2.5 mg), (b) Printex-U (initial mass = 10 mg), (c) Vulcan-XC72R (initial mass = 5 mg), and (d) Monarch 1300 (initial mass = 12 mg). Operating conditions: Isothermal experiment, oxidant = 10% O_2, flow rate = 60 mL/min, ramp rate to reach isothermal temperature = 20 °C/min.

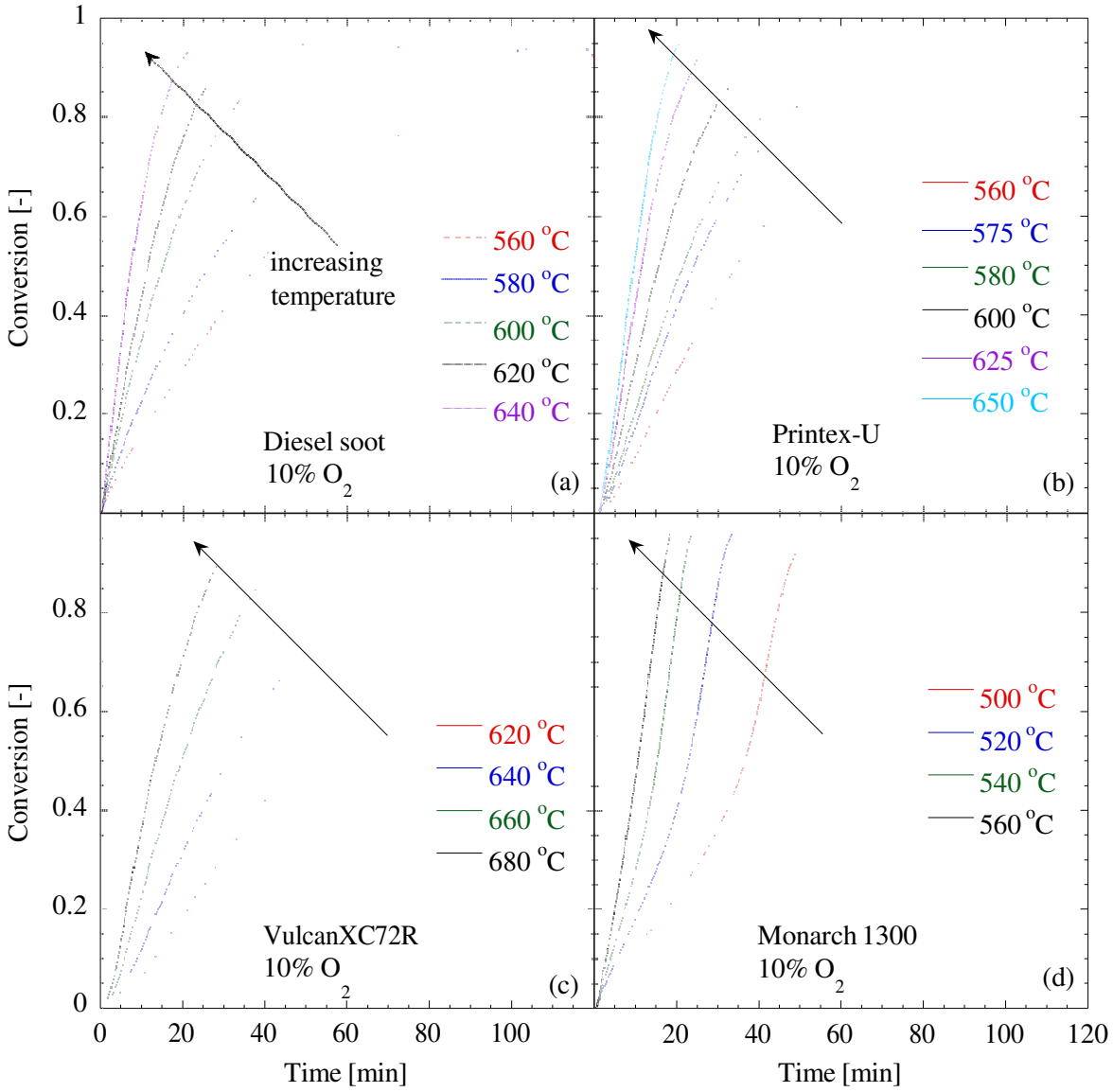

Figure 13: Isothermal kinetics of diesel soot oxidation using Method C. (a) Variation of activation energy with fractional conversion α (range of 0.2-0.9) using both 10% O_2 and air, (b) compensation effect of activation energies and pre-exponential factors. Operating conditions are the same as in **Figure 12**.

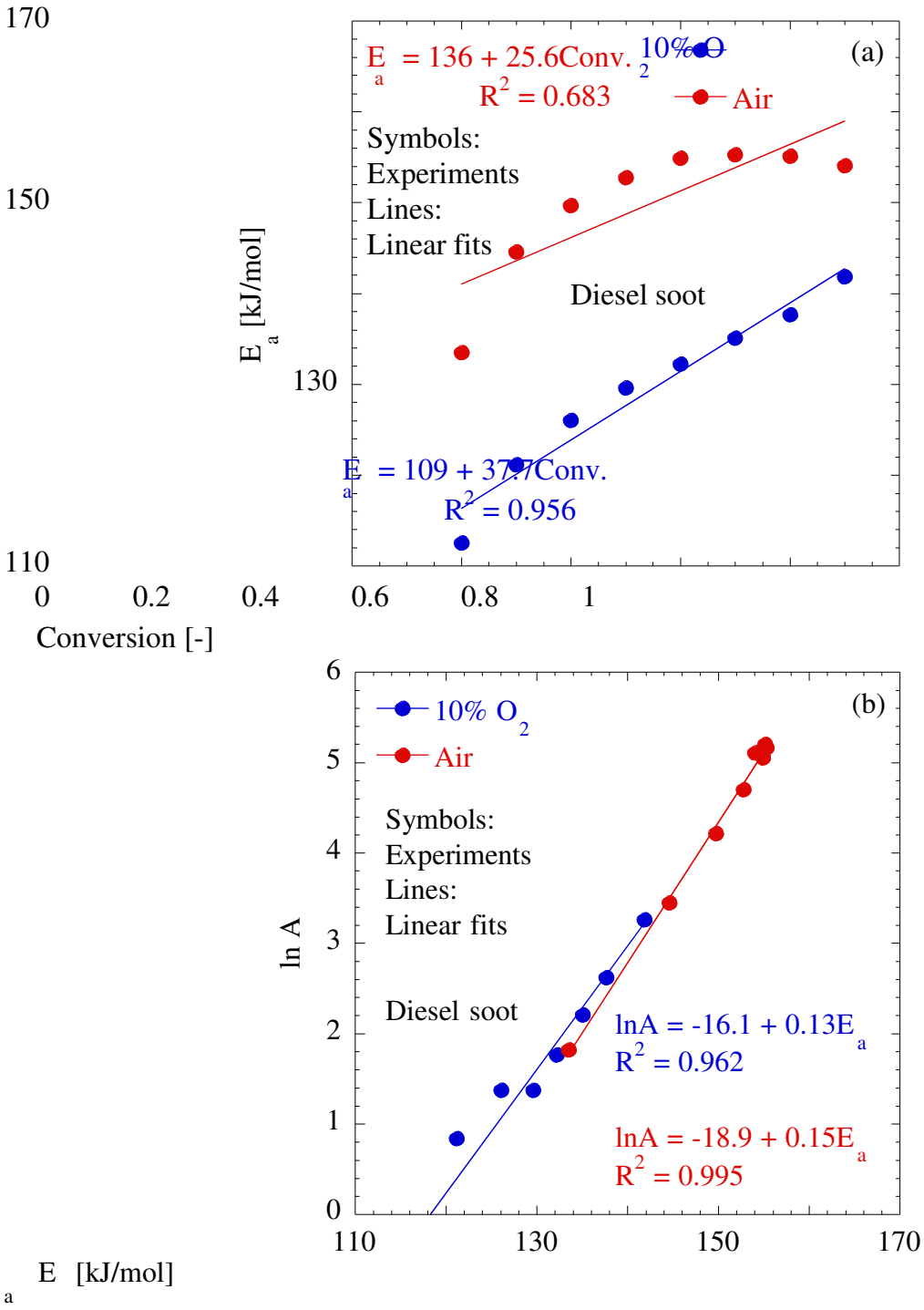

Figure 14: Validation of estimated apparent kinetic parameters and the effective model against experimental results in **Figure 12a** and also against isothermal experiments with air. Simulations were conducted using apparent activation energies and pre-exponential factors at fractional conversion α of 0.5 from the isothermal experiments for Diesel soot with (a) 10% O_2 and (b) air. Reaction order of 1 was used. Diesel soot showed incomplete conversion in the experiments due to the presence of metal oxides and ash particles.

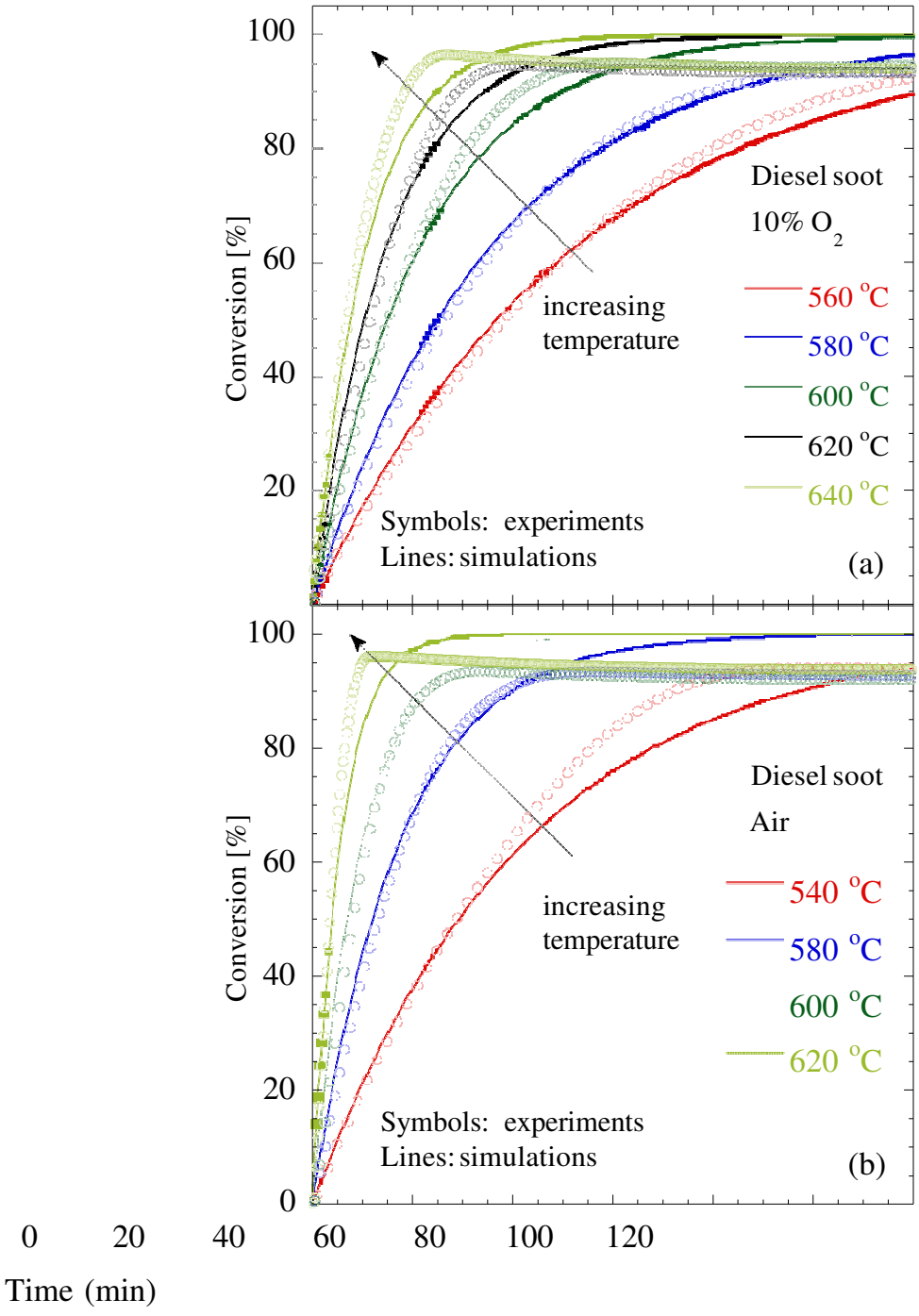

Some newer results involve TGA profiles of Diesel Soot and model Soot complexes as shown in Figure 15.

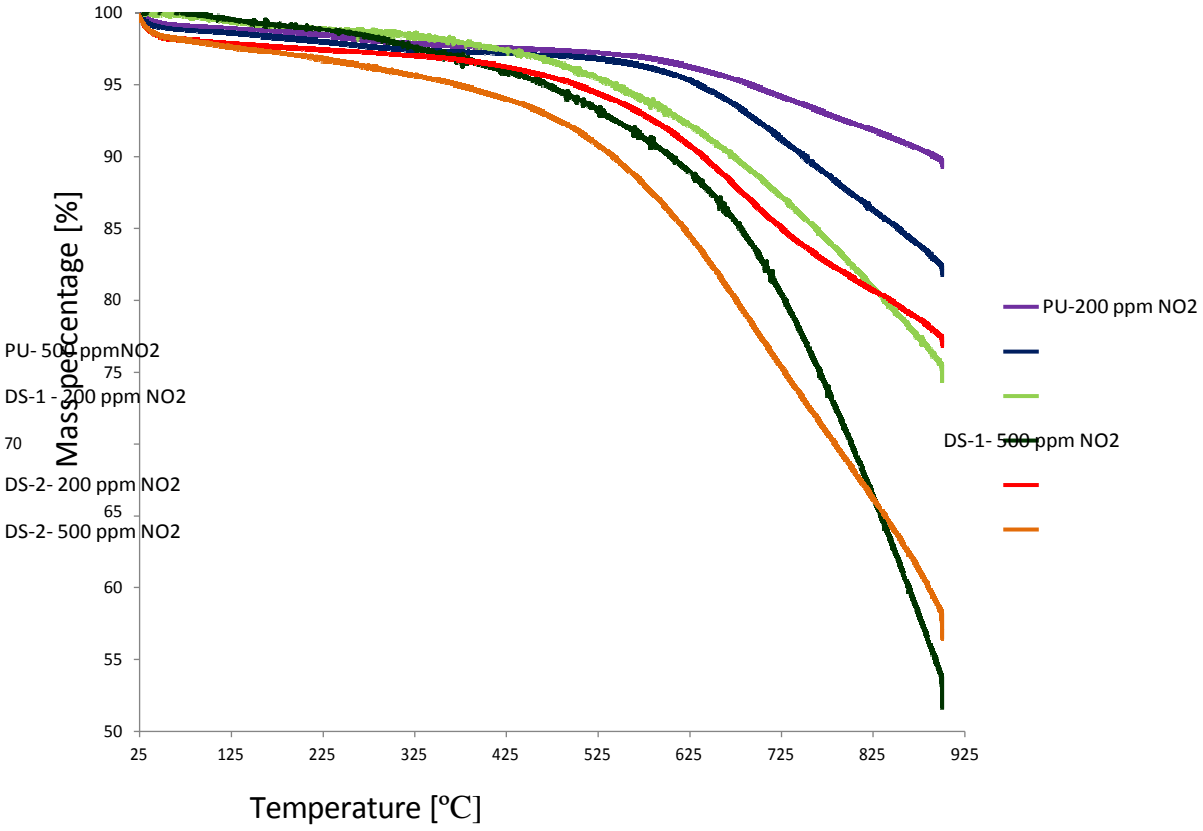

Figure 15, GA Profiles of diesel Soot and Model Soot Complexes.

References:

1. Schneider, C. G.; Hill, L. B. Diesel and health in America: the lingering threat, Clean Air Task Force, *http://www.catf.us/resources/publications/files/Diesel_Health_in_America.pdf*, **2005**.
2. Diesel fuel explained- use of diesel. *http://www.eia.gov/energyexplained/index.cfm?page=diesel_use*, **2011** (accessed 2/5, 2012).
3. Petroleum watch. *http://energyalmanac.ca.gov/petroleum/petroleum_watch/2011-09-16_Petroleum_Watch.pdf*, **2011** (accessed 2/5, 2012).
4. Bensaid, S.; Caroca, C. J.; Russo, N.; Fino, D. *Can. J. Chem. Eng.* **2011,** 89 *(2)*, 401-407.
5. Prasad, R.; Bella, V. R. *Bull. Chem. React. Eng. Catal.* **2010,** 5 *(2)*, 69-86.
6. Fino, D. *Sci. Tech. Adv. Mater.* **2007,** 8 *(1-2)*, 93-100.
7. Xi, J.; Zhong, B. J. *Chem. Eng. Technol.* **2006,** 29 *(6)*, 665-673.
8. Vander Wal, R. L.; Bryg, V. M.; Hays, M. D. *J. Aerosol Sci.* **2010,** 41 *(1)*, 108-117.
9. Yezerets, A.; Currier, N. W.; Kim, D. H.; Eadler, H. A.; Epling, W. S.; Peden, C. H. F. Appl. Catal. B-Environ. 2005, 61 (1–2), 120-129.
10. Jones, C. C.; Chughtai, A. R.; Murugaverl, B.; Smith, D. M. Carbon 2004, 42 (12–13), 2471-2484.
11. Clague, A. D. H.; Donnet, J. B.; Wang, T. K.; Peng, J. C. M. Carbon 1999, 37 (10), 1553-1565.

12. Prasad, R.; Bella, V. R. Bull. Chem. React. Eng. Catal. 2010, 5 (2), 95-101.
13. Hoyer, M.; Foureman, G.; Valcovic, L.; Grant, L.; McGrath, J.; Koppikar, A.; Pepelko, W.; Chen, C.; Ris, C. Health assessment document for diesel engine exhaust, http://www.epa.gov/ttn/atw/dieselfinal.pdf, 2002 (accessed 3/14, 2012).
14. National ambient air quality standards (NAAQS). http://epa.gov/air/criteria.html, 2011 (accessed 1/12, 2012).
15. Emissions Standards. http://www.dieselnet.com/standards/eu/hd.php, 2011 (accessed 2/15, 2012).
16. Williams, S. Surface intermediates, mechanism, and reactivity of soot oxidation, Ph.D. Thesis, University of Toronto, 2008.
17. Maricq, M. J. Aerosol Sci. 2007, 38 (11), 1079-1118.
18. Vyazovkin, S.; Burnham, A. K.; Criado, J. M.; Pérez-Maqueda, L. A.; Popescu, C.; Sbirrazzuoli, N. Thermochim. Acta 2011, 520 (1–2), 1-19.
19. Song, J.; Alam, M.; Boehman, A. L. Combust. Sci. Technol. 2007, 179 (9), 1991-2037.
20. Rodriguez-Fernandez, J.; Oliva, F.; Vazquez, R. A. Energy Fuels 2011, 25 (5), 2039-2048.
21. Kalogirou, M.; Samaras, Z. J. Therm. Anal. Calorim. 2010, 99 (3), 1005-1010.
22. López-Fonseca, R.; Elizundia, U.; Landa, I.; Gutiérrez-Ortiz, M. A.; González-Velasco, J. R. Appl. Catal. B-Environ. 2005, 61 (1–2), 150-158.
23. Zouaoui, N.; Brilhac, J.; Mechati, F.; Jeguirim, M.; Djellouli, B.; Gilot, P. J. Therm. Anal. Calorim. 2010, 102 (3), 837-849.
24. Neeft, J. P. A.; Hoornaert, F.; Makkee, M.; Moulijn, J. A. Thermochim. Acta 1996, 287 (2), 261-278.
25. Gilot, P.; Bonnefoy, F.; Marcuccilli, F.; Prado, G. Combust. Flame 1993, 95 (1–2), 87-100.
26. Stanmore, B. R.; Gilot, P. Thermochim. Acta 1995, 261 , 151-164.
27. Gilot, P.; Brillard, A.; Stanmore, B. R. Combust. Flame 1995, 102 (4), 471-480.
28. Khawam, A.; Flanagan, D. R. J. Pharm. Sci. 2006, 95 (3), 472-498.
29. Liu, C.; Yu, J.; Sun, X.; Zhang, J.; He, J. Polym. Degrad. Stab. 2003, 81 (2), 197-205.
30. Kalogirou, M.; Samaras, Z. J. Therm. Anal. Calorim. 2009, 98 (1), 215-224.
31. Castaldi, M. J.; Kwon, E. 13th North American Waste to Energy Conference 2005, (NAWTEC13-3149).
32. Costache, M. C.; Wang, D.; Heidecker, M. J.; Manias, E.; Wilkie, C. A. Polym. Adv. Technol. 2006, 17, 272-280.
33. Gašparovič, L.; Koreňová, Z.; Jelemenský, Ľ. In Kinetic study of wood chips decomposition by TGA; 36th International Conference of Slovak Society of Chemical Engineering; 2009; pp. 178.
34. López-Fonseca, R.; Landa, I.; Elizundia, U.; Gutiérrez-Ortiz, M. A.; González-Velasco, J. R. Combust. Flame 2006, 144 (1–2), 398-406.
35. Skreiberg, A.; Skreiberg, Ø.; Sandquist, J.; Sørum, L. Fuel 2011, 90 (6), 2182-2197.
36. Ollero, P.; Serrera, A.; Arjona, R.; Alcantarilla, S. Fuel 2002, 81 (15), 1989-2000.
37. López-Fonseca, R.; Landa, I.; Elizundia, U.; Gutiérrez-Ortiz, M. A.; González-Velasco, J. R. Chem. Eng. J. 2007, 129 (1–3), 41-49.
38. Gómez-Barea, A.; Ollero, P.; Arjona, R. Fuel 2005, 84 (12–13), 1695-1704.
39. Brilhac, J. F.; Bensouda, F.; Gilot, P.; Brillard, A.; Stanmore, B. Carbon 2000, 38 (7), 1011-1019.
40. Stanmore, B. R.; Brilhac, J. F.; Gilot, P. Carbon 2001, 39 (15), 2247-2268.
41. Stanmore, B.; Gilot, P.; Prado, G. Thermochim. Acta 1994, 240 , 79-89.
42. Tang, J.; Song, Q.; He, B.; Yao, Q. Sci. China. Ser. E 2009, 52 (6), 1535-1542.
43. Yezerets, A.; Currier, N. W.; Eadler, H. A.; Suresh, A.; Madden, P. F.; Branigin, M. A. Catal. Today 2003, 88 (1–2), 17-25.
44. López-Fonseca, R.; Landa, I.; Gutiérrez-Ortiz, M. A.; González-Velasco, J. R. J. Therm. Anal. Calorim. 2005, 80 (1), 65-69.
45. Leistner, K.; Nicolle, A.; Berthout, D.; Costa, P. d. Combust. Flame 2012, 159 (1), 64-76.
46. Salvador, S.; Commandré, J. M.; Stanmore, B. R. Fuel 2003, 82 (6), 715-720.
47. Hartman, J. R.; Beyler, A. P.; Riahi, S.; Beyler, C. L. Fire Mater. 2012, 36 (3), 177-184.

48. Yang, S.; Lee, K.; and Chong, H. SAE Tech. Paper Ser. 2010, 2010-01-2166.
49. Flynn, J. H.; Wall, L. A. J. Polym. Sci. Pol. Phys. 1966, 4 (5), 323-328.
50. Ozawa, T. Bull. Chem. Soc. Jpn. 1965, 38 (11), 1881-1886.
51. Li, Y.; Xu, L.; Yao, X.; Luo, T.; Li, G. J. Phys. Conf. Ser. 2012, 339 (1), 1-8.
52. Chen, X.; Yu, J.; Guo, S. J. Appl. Polym. Sci. 2007, 103 (3), 1978-1984.
53. Doyle, C. D. Nature 1965, 207 (4994), 290-291.
54. Doyle, C. D. J. Appl. Polym. Sci. 1961, 5 (15), 285-292.
55. Azambre, B.; Collura, S.; Darcy, P.; Trichard, J. M.; Da Costa, P.; García-García, A.; Bueno-López, A. *Fuel Process. Technol.* **2011,** 92 *(3)*, 363-371.
56. Tighe, C. J.; Twigg, M. V.; Hayhurst, A. N.; Dennis, J. S. *Combust. Flame* **2012,** 159 *(1)*, 77-90.
57. Kalogirou, M.; Pistikopoulos, P.; Ntziachristos, L.; Samaras, Z. *J. Therm. Anal. Calorim.* **2009,** 95 *(1)*, 141-147.
58. Neeft, J. P. A.; Makkee, M.; Moulijn, J. A. *Fuel Process. Technol.* **1996,** 47 *(1)*, 1-69.
59. Neeft, J. P. A.; Nijhuis, T. X.; Smakman, E.; Makkee, M.; Moulijn, J. A. *Fuel* **1997,** 76 *(12)*, 1129-1136.
60. Higgins, K. J.; Jung, H.; Kittelson, D. B.; Roberts, J. T.; Zachariah, M. R. *J. Phys. Chem. A* **2002,** 96 *(1)*, 96-103.
61. Atribak, I.; Bueno-López, A.; García-García, A. *Combust. Flame* **2010,** 157 *(11)*, 2086-2094.
62. Hinot, K. Catalytic soot oxidation by platinum on sintered metal filters: Influence of the platinum quantity, particle size and location, and investigation of the platinum-soot contact, Ph.D. Thesis, Universität Karlsruhe, 2006.
63. Setiabudi, A.; Makkee, M.; Moulijn, J. A. *Appl. Catal. B-Environ.* **2004,** 50 *(3)*, 185-194.
64. Wang-Hansen, C.; Kamp, C. J.; Skoglundh, M.; Andersson, B.; Carlsson, P. *J. Phys. Chem. C* **2011,** 115 *(32)*, 16098-16108.
65. Jung, H.; Kittelson, D. B.; Zachariah, M. R. *Combust. Flame* **2004,** 136 *(4)*, 445-456.
66. Stratakis, G. A.; Stamatelos, A. M. *Combust. Flame* **2003,** 132 *(1–2)*, 157-169.
67. Du, Z.; Sarofim, A. F.; Longwell, J. P.; Mims, C. A. *Energy Fuels* **1991,** 5 *(1)*, 214-221.
68. Darcy, P.; Da Costa, P.; Mellottée, H.; Trichard, J.; Djéga-Mariadassou, G. *Catal. Today* **2007,** 119 *(1–4)*, 252-256.
69. Messerer, A.; Niessner, R.; Pöschl, U. *Carbon* **2006,** 44 *(2)*, 307-324.
70. Lee, J.; Lee, H.; Song, S.; Chun, K. *SAE Tech. Paper Ser.* **2007,** 2007-01-1270.
71. Otto, K.; Sieg, M.; Zinbo, M.; Bartosiewicz, L. *SAE Tech. Paper Ser.* **1980,** 1980-02-01.
72. Fredrik Ahlström, A.; Ingemar Odenbrand, C. U. *Carbon* **1989,** 27 *(3)*, 475-483.
73. Pahalagedara, L. R.; Sharma, H. N.; Kuo, C.; Dharmarathna, S.; Joshi, A. V.; Suib, S. L.; Mhadeshwar, A. B. *Submitted to Carbon* **2012**.
74. Galwey, A. K. *Thermochim. Acta* **2003,** 399 *(1–2)*, 1-29.
75. Galwey, A. K.; Brown, M. E. *Thermochim. Acta* **1997,** 300 *(1–2)*, 107-115.
76. Vyazovkin, S.; Wight, C. A. *Annu. Rev. Phys. Chem.* **1997,** 48 *(1)*, 125-149.
77. Vyazovkin, S. *Int. Rev. Phys. Chem.* **2000,** 19 *(1)*, 45-60.
78. Vyazovkin, S.; Sbirrazzuoli, N. *Macromol. Rapid Commun.* **2006,** 27 *(18)*, 1515-1532.
79. Q500 series thermogravimetric analyzer. *http://www.tainstruments.com/product.aspx?id=20&n=1&siteid=11,* **2012** (accessed 3/ 22, 2012).

Project Title: High Reliability, Low-Cost Thermally Integrated Water Gas Shift System Design Development Support
Partner: FuelCell Energy
PI: Ashish Mhadeshwar, Prabhakar Singh

Objective:
The overall goal of this project is to support FuelCell Energy, Inc. (FCE) in the design, development and scale-up of a thermally integrated Water Gas Shift (TI-WGS) system to efficiently process reformate gas, such as from FCE's DFC® power plant anode exhaust.

Tasks and Status:
Task 1: Lab-scale TI-WGS data evaluation and design support

This task involves evaluation and analysis of the FCE lab-scale data collected using the FCE reactor facility. The objective is to conduct an overall energy balance of the reactor system to understand the heat transfer effectiveness in the High Temperature Shift (HTS) vs. the Low Temperature Shift (LTS) regions.

Status: Analysis of the FCE data has been completed. The effect of inlet temperature of the coolant, inlet flow rate of the coolant, and reactant space velocity has been analyzed. Overall energy balance has been conducted to predict the coolant temperature profile as a function of length. It is found that the heat transfer (heat loss to coolant) in the LTS section is significantly higher than that in the HTS section, resulting in decreased performance from the LTS section. The completed analysis was presented to FCE during the UConn team's visit to the FCE facility.

Revised Task 1: Lab-scale data testing in UConn reactor

This task involves evaluation and analysis of the proprietary catalyst samples provided by FCE. The BenchCAT reactor shown in Figure 1 has been utilized for the testing of catalyst samples. Catalyst performance has been evaluated for CO oxidation, CO methanation, and WGS reaction.
Status: This task has been completed. The results and conclusions are presented on next pages.

FCE P2-F1 and P2-D1 Pellets Data Summary

The objective of the following tests was to determine the activity of select catalyst for application in Water Gas Shift (WGS). The hypothesis is that the catalyst used in steam reforming can be extracted after its lifetime and used as a potential catalyst for WGS, and will not support methanation but on the other hand could be a viable candidate for WGS.

The first step in catalyst testing involved experiments for CO oxidation and CO methanation. In the second step, the catalyst was tested for WGS activity.

Experimental procedure:

- The catalyst bed was loaded with the tip of the thermocouple touching the top of the bed.
- Feed tanks valves were opened.
- The reactor was purged with argon till the gas chromatograph showed no traces of O_2 and N_2 (no leaks).
- The reactor was switched from bypass and the concentrations were monitored till traces of O_2 and N_2 were not evident (no leaks).
- The reactor was ramped up to the desired temperature along with the trace temperature (180 °C).
- The vaporizer and volumizer have very sensitive control parameters and they were ramped at small increments (10-20 °C.)
- The argon flow was switched off and the desired gas feed flow was set.
- After the intensity signal stabilized on the MS, a few GC samples were taken as a baseline.

- Water flow was started (for WGS experiments).
- GC samples were taken at regular temperature intervals after ensuring steady state. We ensured that no liquid water was reaching the mass spectrometer.
- In case of temperature spikes in the system due to water droplets condensation (if any), we waited for some time until the system stabilized and only then the GC samples were taken.
- Temperatures below 150 ^{o}C were not considered due to condensation issues within the system.

GC calibration:

The GC was calibrated for the desired concentration levels before the testing was performed. Table 1 below shows the calibrations summary for the different compounds.

Table 1: GC Calibration Data Summary

Gas species	**Retention time (min)**	**Column**	**Calibration range (%)**	**Equation**
CO	4.1	A	0.1 – 12	$Y = 1.38E\text{-}4X_A - 5.74E\text{-}2$
CO	4.1	A	1 – 12.5	$Y = 0.0001X_A - 0.2491$
CO_2	2.44	B	0.1 – 1.5	$Y = 9.07E\text{-}5X_B - 9.01E\text{-}2$
CO_2	2.44	B	30.5 – 73	$Y = 8E\text{-}05X_B + 14.378$
O_2	1.24	A	1 – 10	$Y = 8.638E\text{-}5X_A - 5.103E\text{-}1$
CH_4	2.45, 2.04	A, B	2 – 50	$Y = 4.137E\text{-}5X_A - 7.195E\text{-}01$
CH_4	2.45, 2.04	A, B	0.3 – 1.5	$Y = 4E\text{-}05X_A - 0.1348$
H_2	1.00, 1.82	A, B	0.2 – 10	Y = 8.830E-06XA - 1.621E-01
H_2	1.00, 1.82	A, B	10 – 20	Y = 8E-06XA + 1.8728

Operating conditions:

1. CO Oxidation Studies:
   - P = 1 atm
   - Flow = 50 sccm
   - Feed Composition: 5% CO, 50% O_2, 45% N_2
   - Temperature range = 30 – 425 ^{o}C at intervals of 25-50 ^{o}C (low to high)
   - Catalyst weight ≈ 0.2 g
   - Bed volume = 0.25 cm^3
   - Space velocity ≈ 12000 hr^{-1}

2. Methanation Studies:
   - P = 1 atm
   - Flow = 50 sccm

- Feed Composition = 7% CO, 20% H_2, 73% CO_2
- Temperature range = 30 – 650 ^oC at intervals of 25-50 ^oC (low to high)
- Catalyst weight ≈ 0.2 g
- Bed volume = 0.25 cm^3
- Space velocity ≈ 12000 hr^{-1}

3. Water Gas Shift Studies:
   - P = 1 atm
   - Gas flow = 19 sccm (excluding water flow)
   - Total flow = 31.6 sccm (Including water flow)
   - Feed Composition = 4% CO, 12% H_2, 44% CO_2, 40% H_2O
   - Temperature range = 150 – 550 ^oC at intervals of 25-50 ^oC (high to low)
   - Catalyst weight ≈ 0.4 g
   - Bed volume = 0.6 cm^3
   - Space velocity ≈ 3160 hr^{-1}

Experimental setup:

a) BenchCAT reactor

b) Catalyst holder

c) Gas chromatograph

d) Mass spectrometer

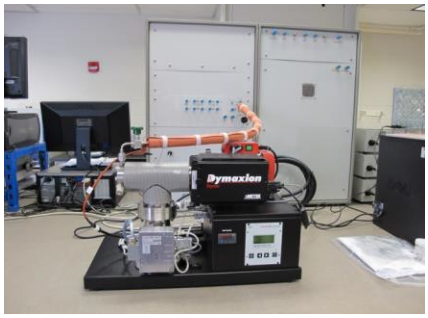

Figure 1: BenchCAT reactor and analytical equipment in Mhadeshwar lab (UConn).

Figure 2 shows the Process Flow Diagram for the BenchCAT Reactor system.

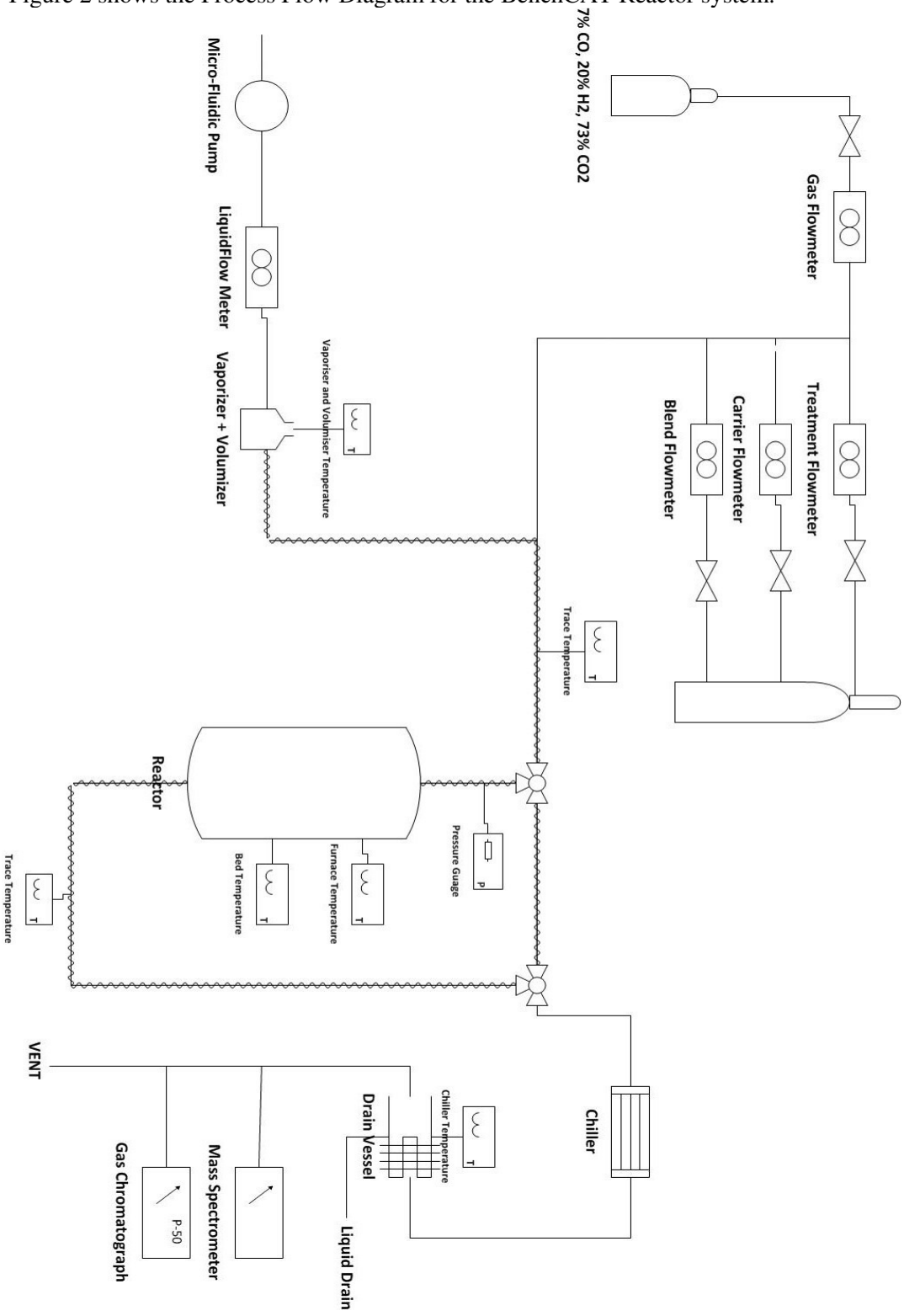

Figure 2: PFD for the BenchCAT Reactor.

Results:

1. CO oxidation:

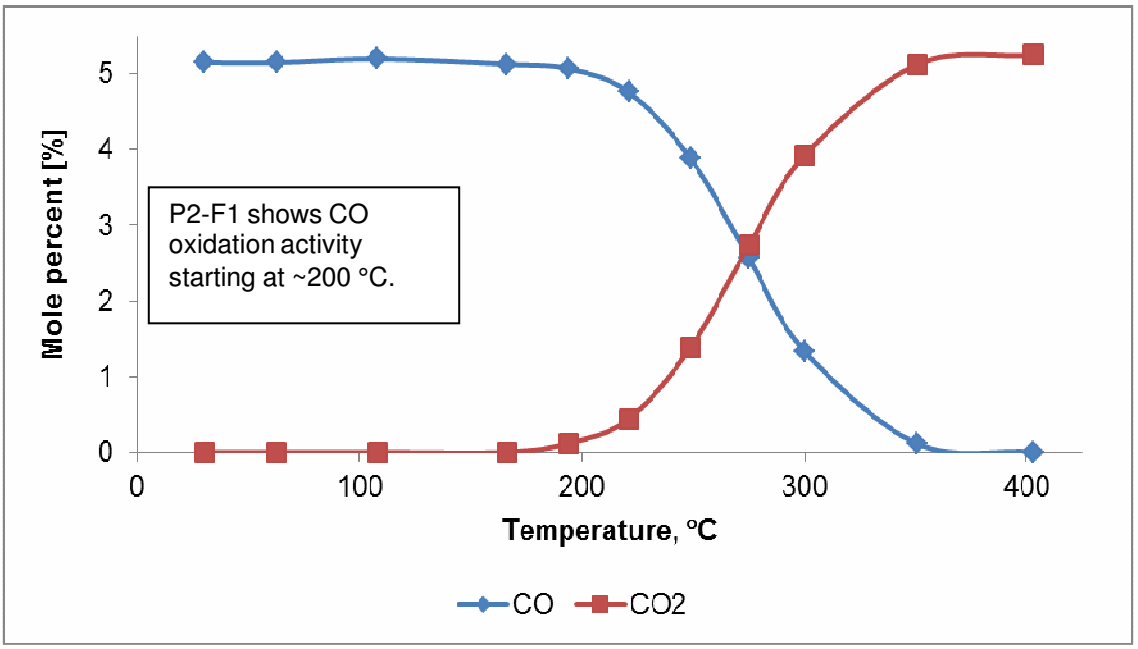

Figure 3: Molar composition of species vs. temperature for P2-F1 during CO oxidation.

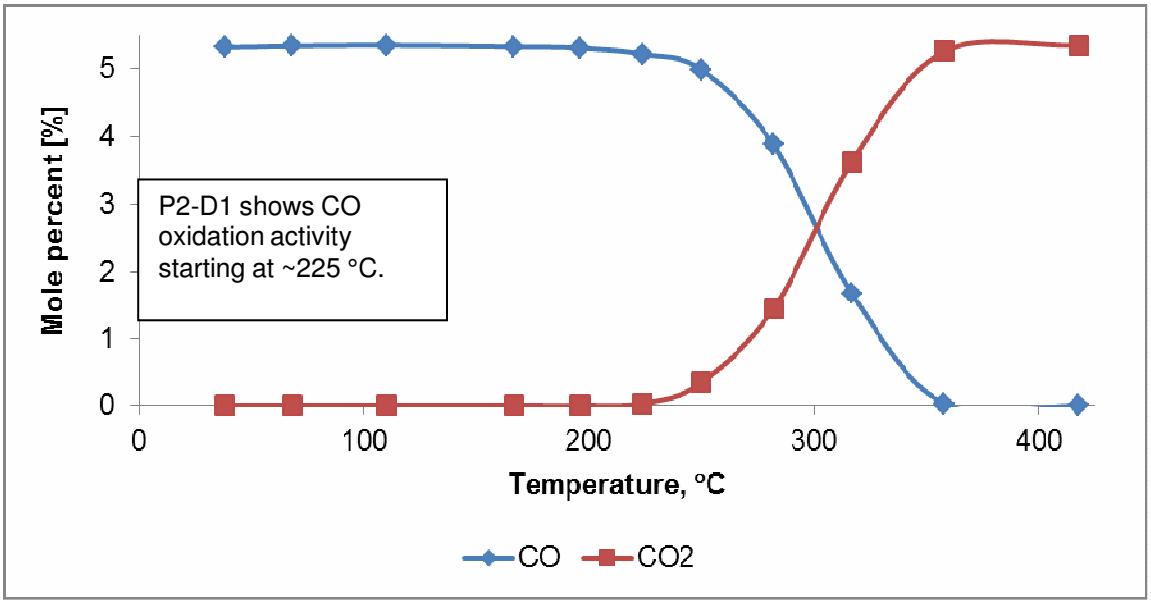

Figure 4: Molar composition of species vs. temperature for P2-D1 during CO oxidation.

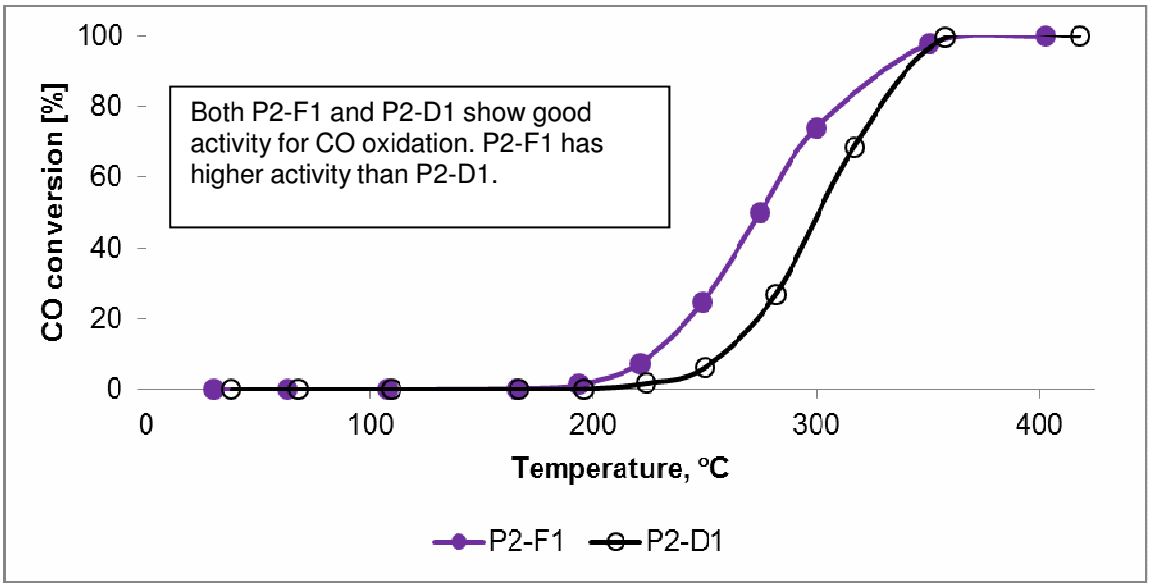

Figure 5: Comparison of P2-F1 and P2-D1 catalysts for CO oxidation.

From Figures 3-5, we can draw the following conclusions;

- CO oxidation starts at 200 °C and 225 °C for the P2-F1 and P2-D1 catalysts, respectively.
- Both catalysts eventually achieve 100% conversion of CO to CO_2; therefore both catalysts are good for CO oxidation.

2. CO and CO_2 Methanation:

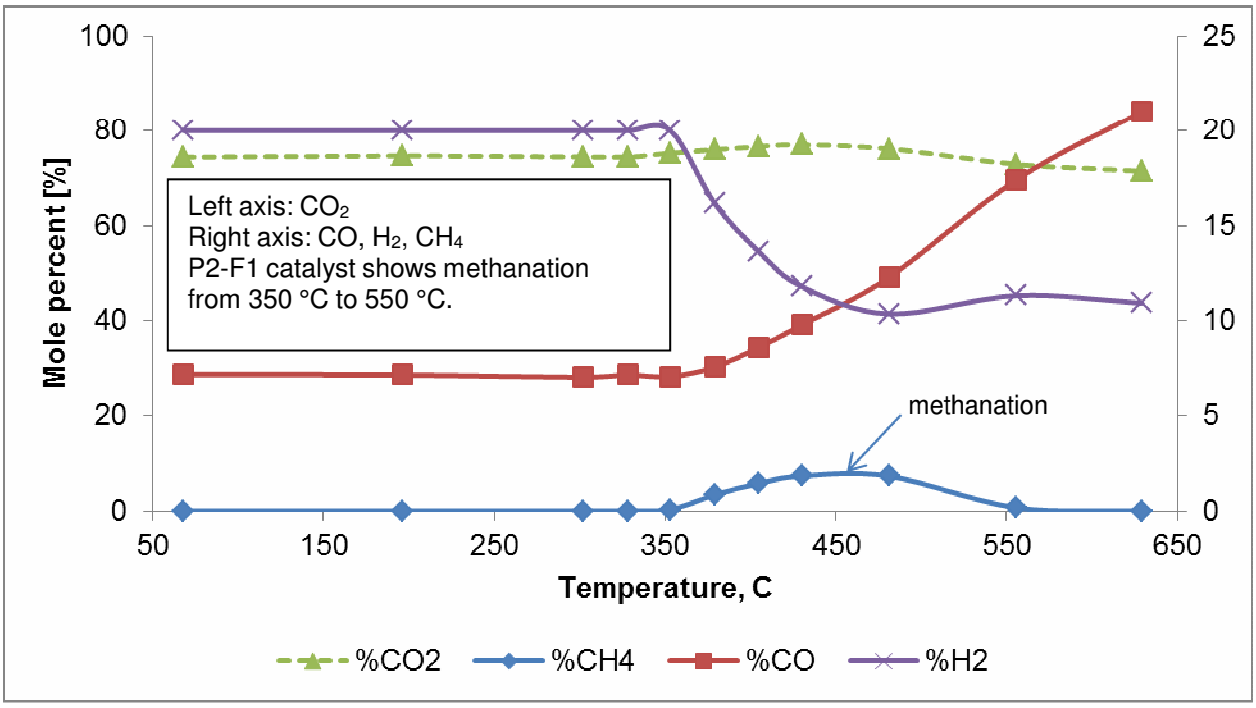

Figure 6: Molar composition of species vs. temperature for P2-F1 during methanation.

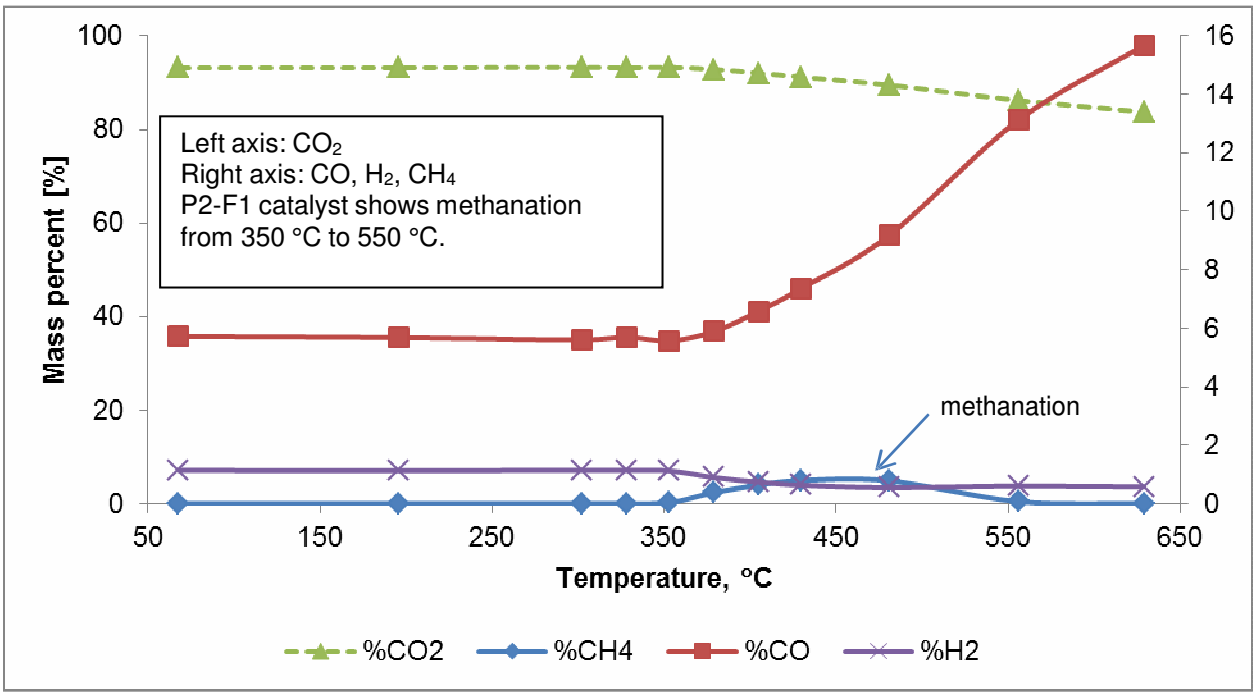

Figure 7: Mass composition of species vs. temperature for P2-F1 during methanation.

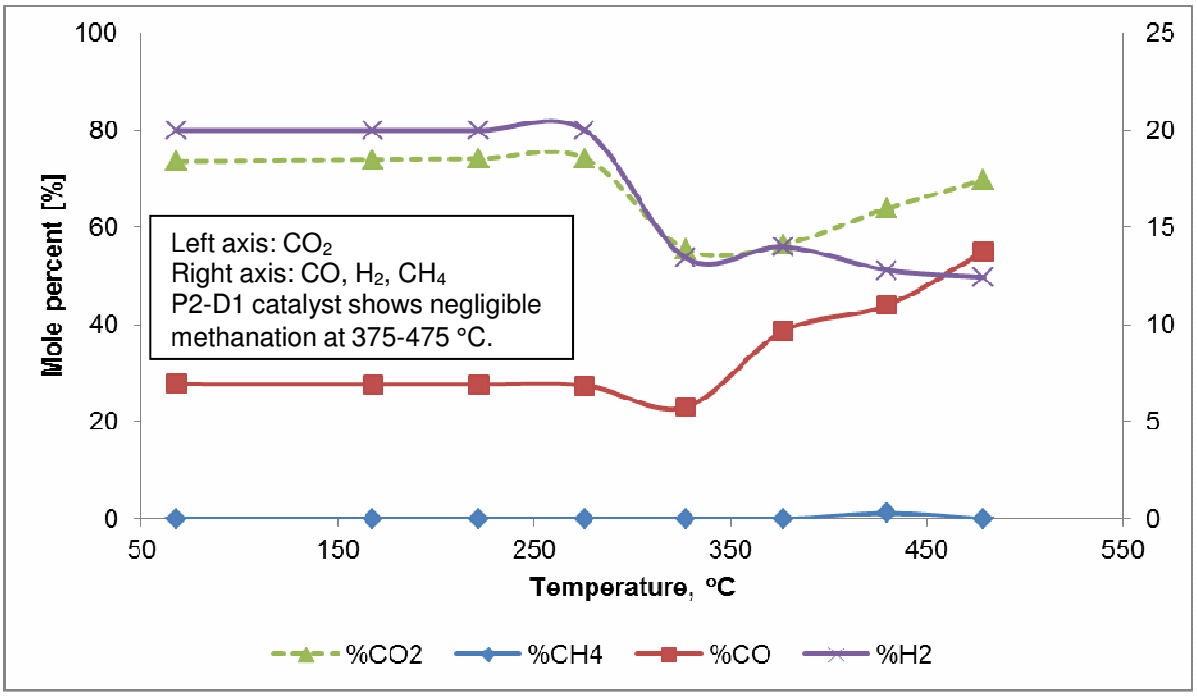

Figure 8: Molar composition of species vs. temperature for P2-D1 during methanation.

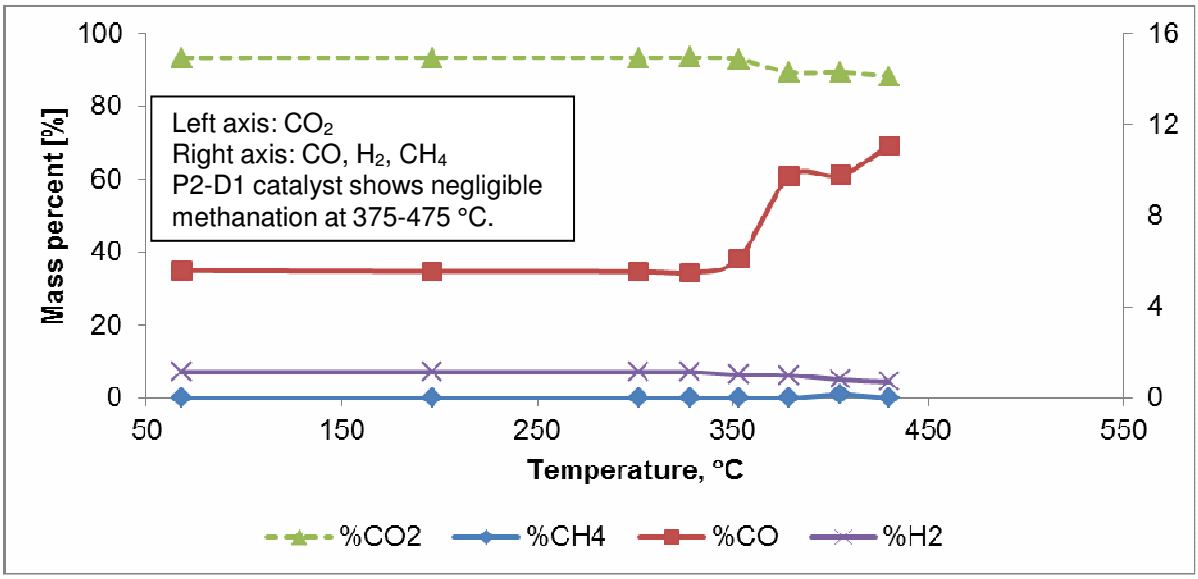

Figure 9: Mass composition of species vs. temperature for P2-D1 during methanation.

From Figures 6-9, we can draw the following conclusion:

- The P2-F1 catalyst shows significant methanation at 350-550 °C, but the P2-D1 catalyst shows negligible methanation.

3. Water-Gas Shift (WGS):

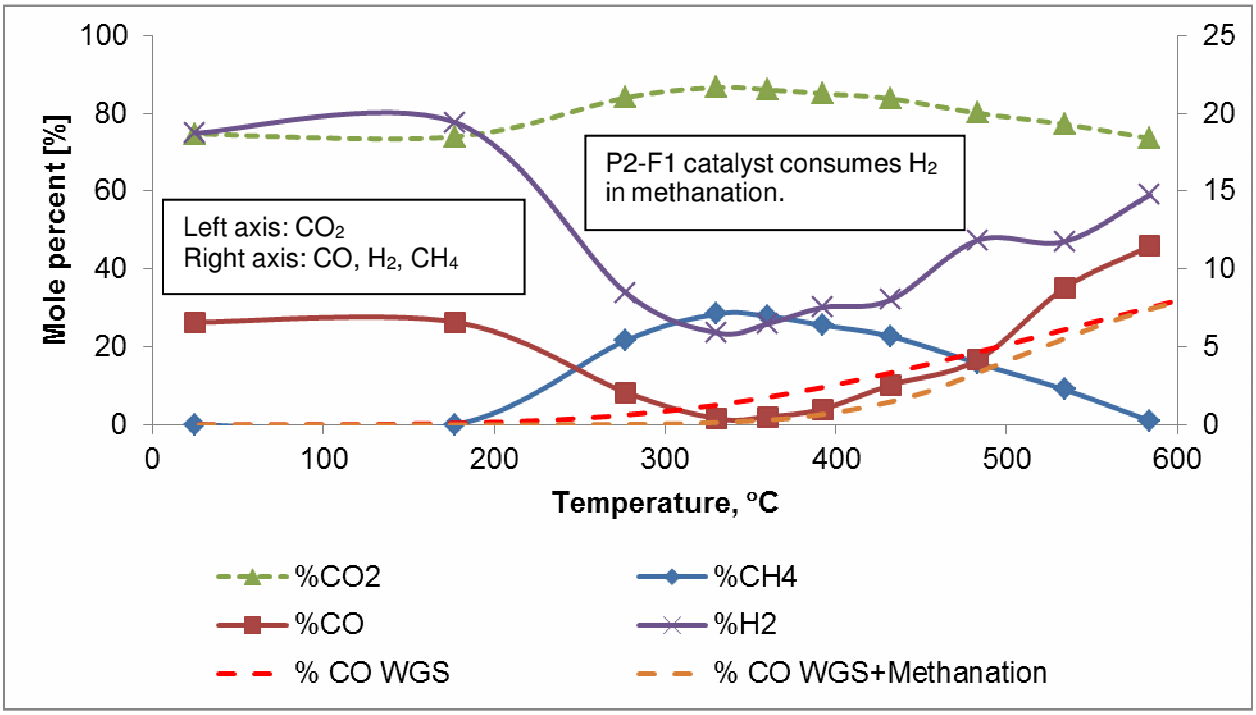

Figure 10: Molar composition of species vs. temperature for P2-F1 during WGS. Dashed lines indicate CO equilibrium predictions for WGS and WGS+methanation.

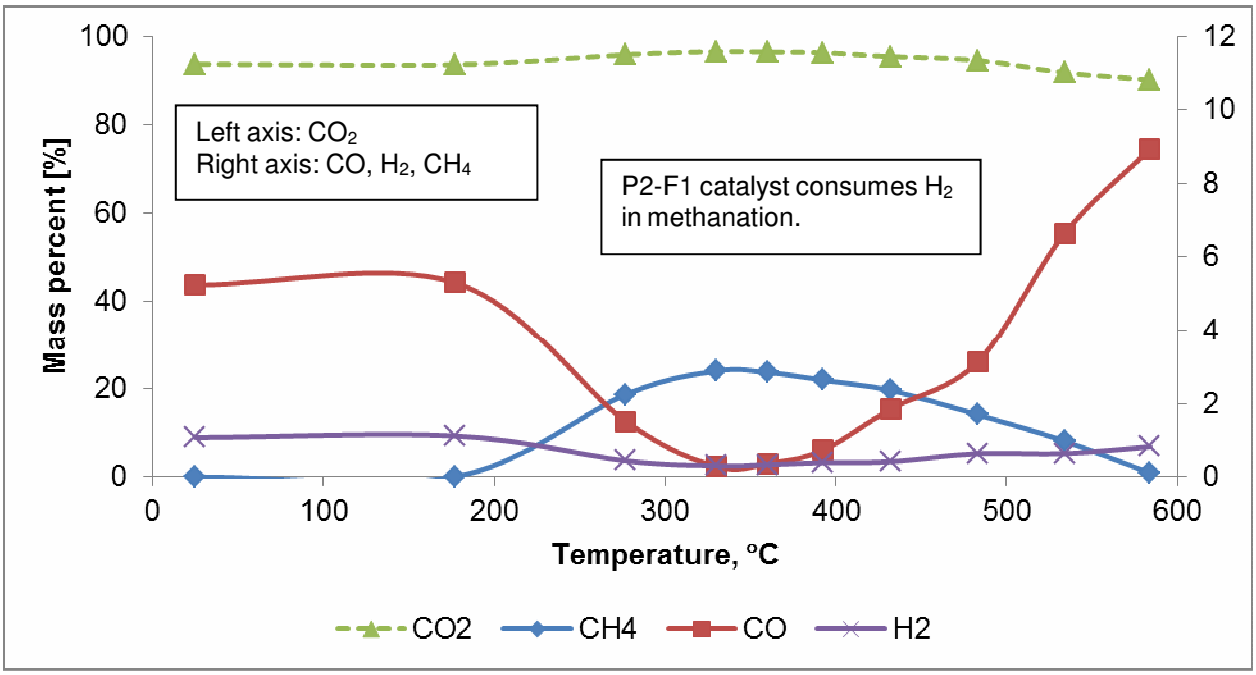

Figure 11: Mass composition of species vs. temperature for P2-F1 during WGS

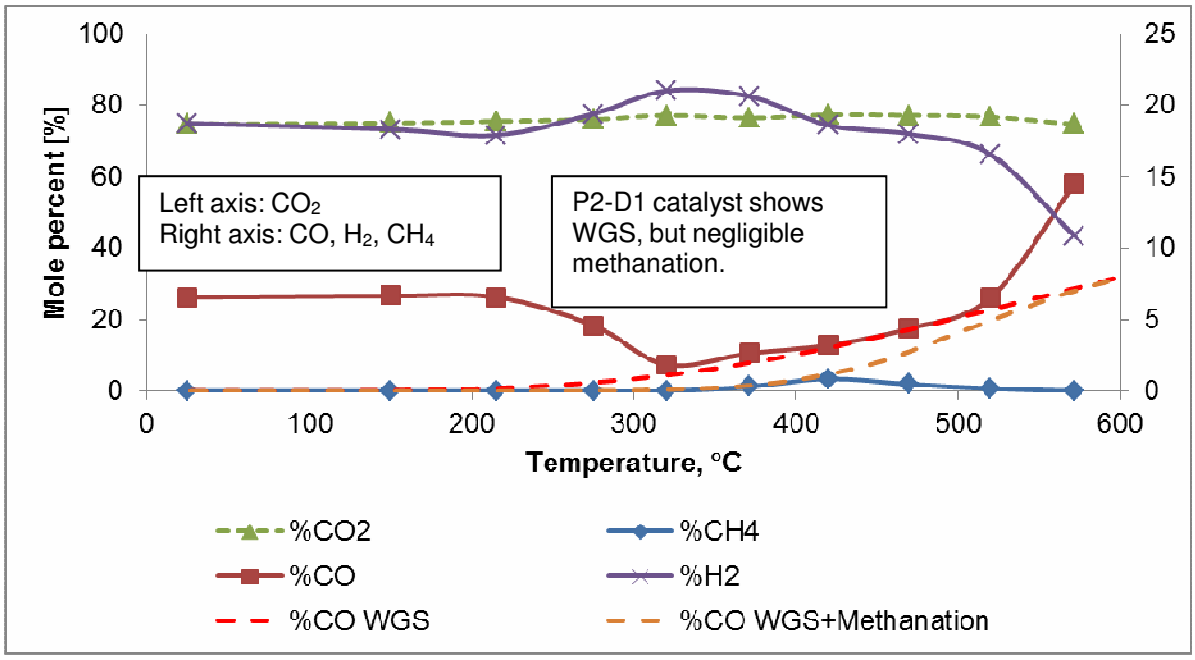

Figure 12: Molar composition of species vs. temperature for P2-D1 during WGS. Dashed lines indicate CO equilibrium predictions for WGS and WGS+methanation.

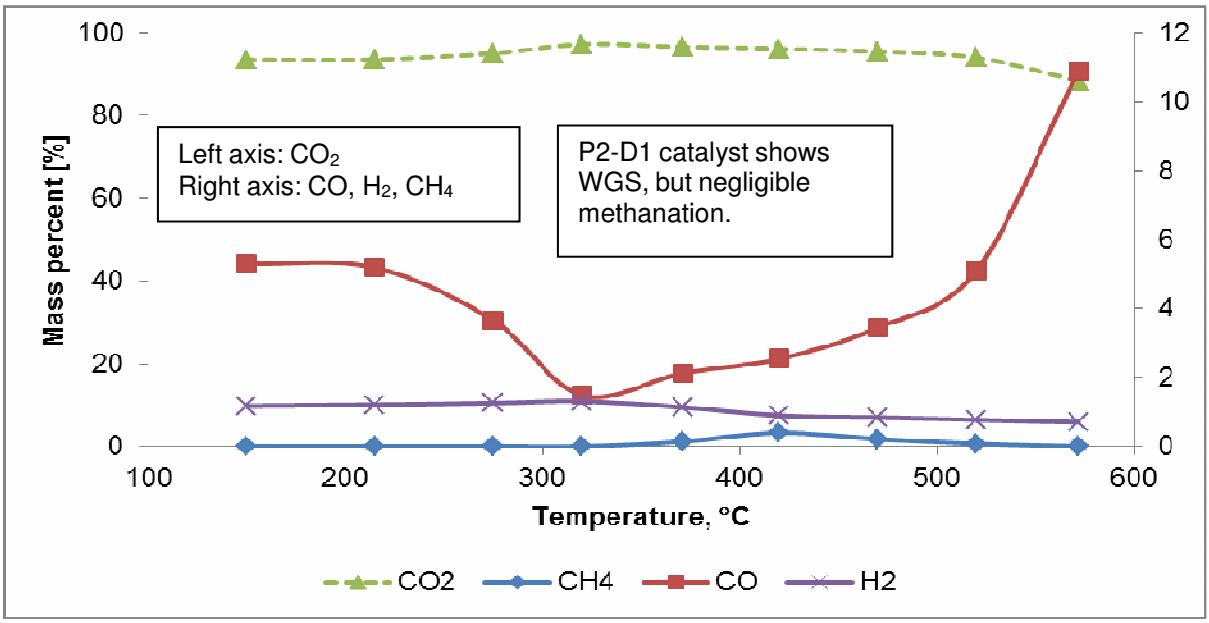

Figure 13: Mass composition of species vs. temperature for P2-D1 during WGS.

As shown in Figure 10and 11, P2-F1 catalyst shows significant methanation, where the decrease in CO and H_2 occurs in tandem with an increase in CH_4. P2-F1 catalyst shows signs of Water-Gas Shift activity, but it is masked with an overall more dominant methanation reaction, resulting in a net decrease for H_2. At higher

temperatures, however, CH_4 is consumed by reforming with H_2O. The increase in CO may be due to methane steam reforming and/or reverse WGS (r-WGS).

On the other hand, as shown in Figure 12, the P2-D1 catalyst shows no methanation at low temperatures (150-350 °C). In this temperature range, the CO concentration decreases along with an increase in CO_2 and H_2, thus indicating the occurrence of WGS reaction. At higher temperatures, the CO levels increase along with a drop in H_2 levels, which can be attributed to r-WGS. The dashed lines in Figures 10 and 12 represent the equilibrium based CO concentration for WGS and WGS+methanation. CO concentration with P2-F1 catalyst follows the equilibrium curve for WGS+methanation (see Figure 10), whereas CO concentration with P2-D1 catalyst follows the equilibrium curve for WGS only (see Figure 12).

The two catalysts (P2-F1 and P2-D1) are compared in Figures 14 and 15. The dashed lines in Figure 14 represent equilibrium CO conversion for the WGS and WGS+methanation. At high temperatures, P2-F1 catalyst follows the WGS+methnanation equilibrium, whereas P2-D1 catalyst follows the WGS equilibrium. Almost no methanation is observed with P2-D1 catalyst. Both catalysts show CO formation at high temperatures, probably due to methane steam reforming (P2-F1) and reverse WGS (P2-D1). Based on Figure 15, the P2-F1 catalyst shows net H_2 consumption (through methanation), whereas P2-D1 catalyst shows net H_2 production (through WGS).

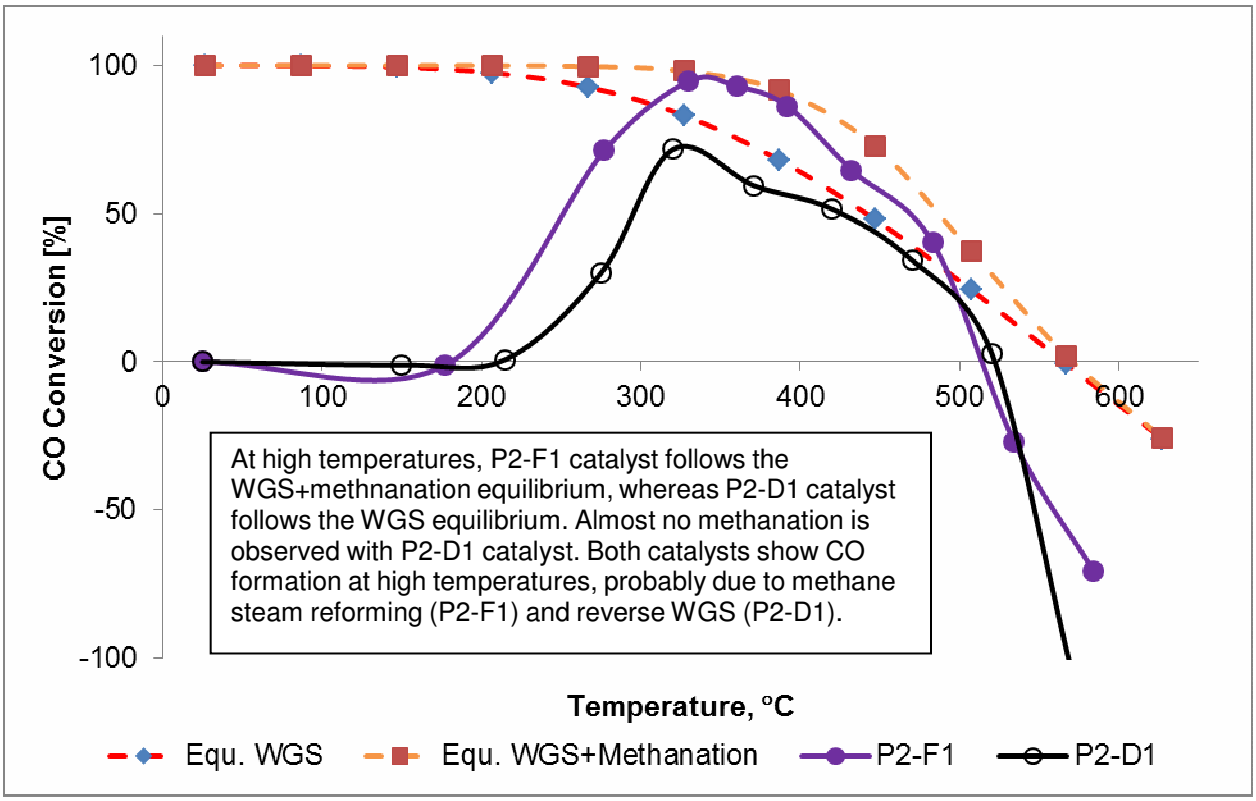

Figure 14: Comparison of P2-F1 and P2-D1 catalysts for CO conversion in WGS tests.

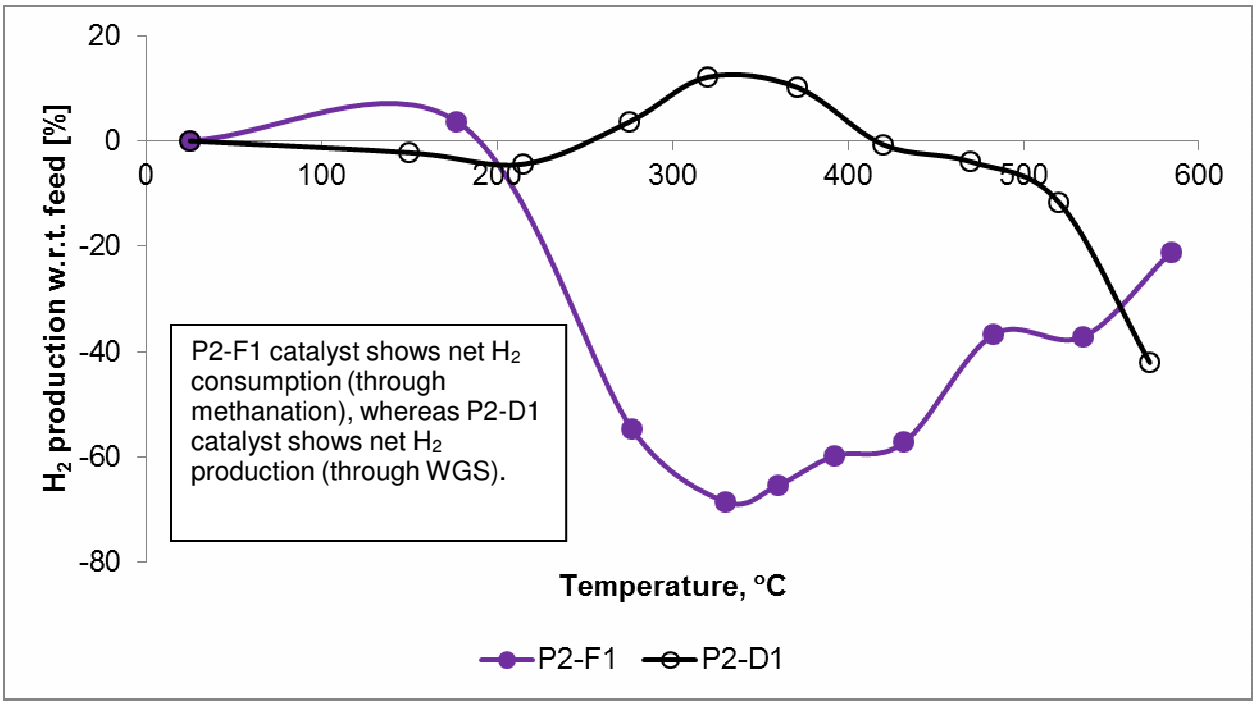

Figure 15: Comparison of P2-F1 and P2-D1 catalysts for H_2 production in WGS tests.

From Figures 10-15, we can draw the following conclusions;

- The P2-F1 catalyst shows significant H_2 consumption through methanation, but the P2-D1 catalyst shows negligible methanation.
- The P2-D1 catalyst shows net H_2 production via WGS reaction.
- Catalyst comparison suggests that the P2-D1 catalyst is indeed a promising candidate for low temperature (200-350 °C) WGS.

Patents
None.

Publications/presentations
None.

Project Title: High Reliability, Low-Cost Thermally Integrated Water Gas Shift System Design Development Support
Partner: FuelCell Energy
PI: Ashish Mhadeshwar

The overall objective of this research effort is to design, develop and test a low cost water gas shift reactor. The effort includes:
1 Zinc hydroxystannate [$ZnSn(OH)_6$] (ZHS) micro- and nanocube or nanostructures have been achieved both in solution and on transparent substrates, including ITO/quartz, SnO_2/quartz, and SnO_2/ITO/quartz substrates via hydrothermal synthetic strategy. Transmission electron microscopy (TEM), scanning electron microscopy (SEM), EDXS, and XRD spectroscopy have been utilized to investigate the micro- and/or nanostructures' composition, crystalline structure, morphology, and density.

1.1 Dense ZHS micro-/nanocube films have been obtained on transparent substrates. Some SEM images of the typical ZHS microcube (typically, 1~5 μm) films on transparent substrates are shown in Fig. 1. The insert images in Fig. 1a and 1b give their EDXS and XRD spectra, respectively. By tuning the precursor compositions, concentrations of each precursor, and treatment of the substrates, very dense and even continuous microcube films obtained on transparent and conductive quartz substrates. As shown in the inserted EDXS spectra in Fig. 1a, the quantitative analysis reveals the atom molar ratio of O: Sn: Zn is 6:1:1. And the XRD spectra also confirm the growth of crystalline ZHS cube film on these transparent and conductive substrates. It can be seen from Fig. 1, the ZHS cube film on these substrates are very dense, and even in some area a continuous monolayer of ZHS film formed. The effort towards synthesizing a continuous ZHS monolayer on whole transparent substrates is undergoing.

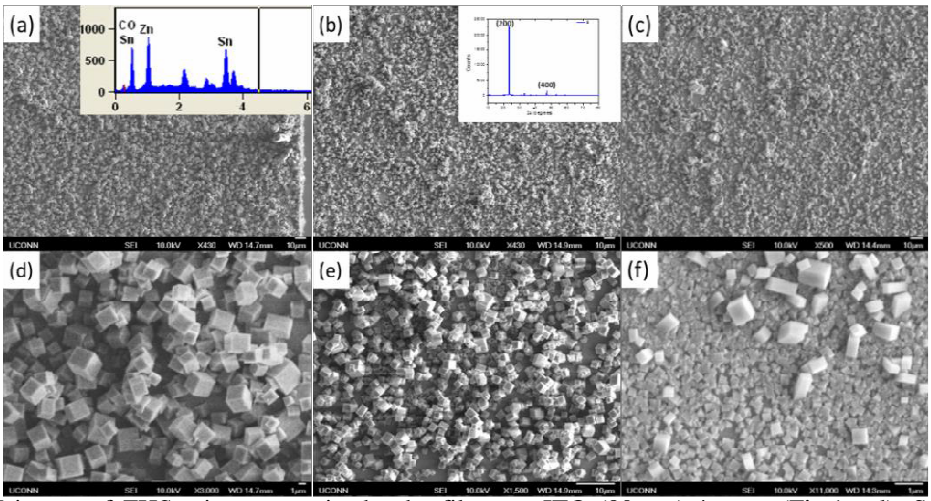

Figure 1. SEM image of ZHS micrometer-sized cube films on ITO (80 nm) /quartz (Fig.1a, d), SnO_2 (30 nm) /quartz (Fig. 1b, e), ITO (80 nm) /SnO_2 (30 nm) /quartz (Fig. 1c, f) substrates, respectively. Inserted in Fig. 1a is EDXS spectrum of a cube. And the inserted picture in Fig. 1b is a typical XRD spectrum of the ZHS film on these transparent substrates.

1.2 Via further control the grain size of the transparent conductive layer (i.e. ITO or SnO_2) on glass or quartz, continuous zinc hydroxystannate (ZHS) nanocube film have been achieved on transparent substrates using both fluidic chamber assited hydrothermal and routine hydrothermal method. From the SEM images in Fig. 2, we can see there are a continuous layer of nanocubes and an un-continuous and sparsely distributed ZHS cube layer on the top of the continuous film. The cube size is about 100 ~ 300

nm, which is much smaller than the cubes obtained previously. Their EDXS and XRD spectra confirmed that they are ZHS nanocrystals (shown in Fig. 2c and 2f). From their cross-section image, the continuous ZHS layer has an average thickness of 300~400 nm, regardless of the presence of sparsely distributed large-cube layer. In this hydrothermal method, coating layer's grain size (ITO or SnO_2 on glass and quartz), temperature, pressure, and base concentration in growth solution are key issues for cube size and film density.

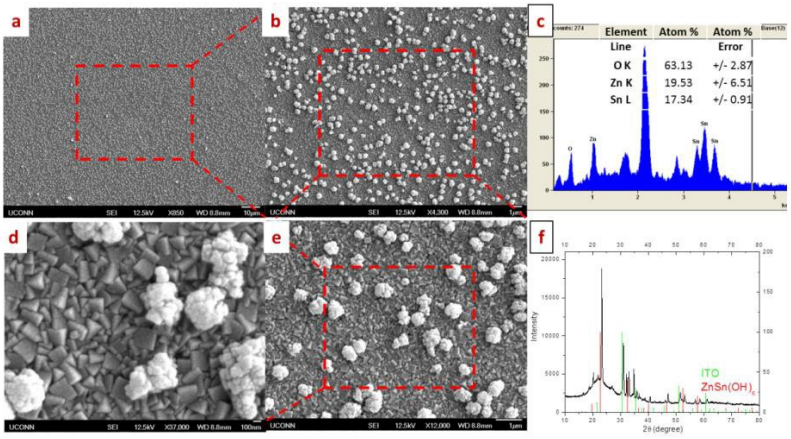

Fig. 2 SEM images for ZHS nano-cube films on SnO_2 (30 nm) / ITO (80nm) / quartz substrate (a, b, d, e) synthesized by fluidic chamber assisted hydrothermal method. Fig. 2c and 2f are the corresponding EDX spectra and XRD spectra, respectively.

1.3 The uniform and pure ZHS nanocubes either have been achieved via hydrothermal method without substrate. From SEM and TEM images shown in Fig. 3, it can be seen that large amount of uniform nanocubes have been synthesized. The statistic result from TEM images show that the average cube size is 45 nm. From Their EDX spectra and electron diffraction pattern image testify the nanocubes are ZHS crystal cubes (as shown in Fig. 3d and 3e).

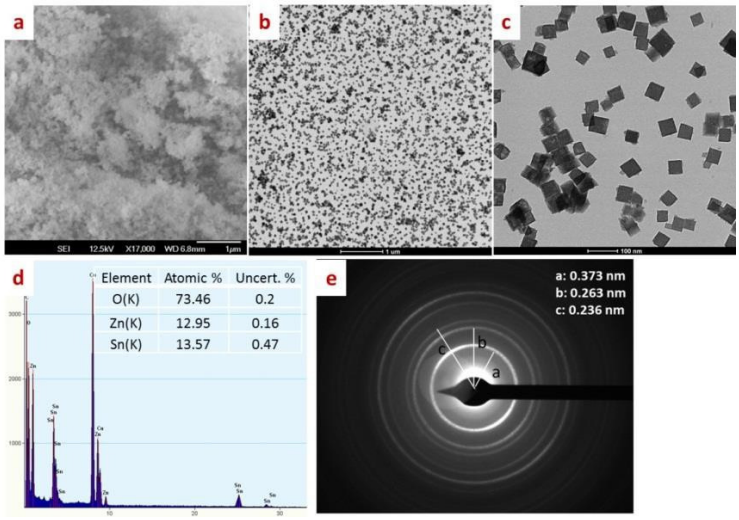

Fig. 3 SEM (a) and TEM (b and c) images, EDXs (d) and diffraction pattern image (e) of ZHS nanocubes.

2. Thermal evolution of ZHS cube films has been explored via in-situ and ex-situ characterization and measurment. Fig. 4a shows XRD mapping during ZHS heating up at 2 ℃/min. ZHS signal

decrease above 488 K and totally disappear around 523 K. Then, at 873 K, the peaks of crystal SZS and SnO_2

show up and become stronger with the temperature increase. EDX spectra (Fig. 4b) for the sample treated between 488 K and 873 K show that the atomic ratio of O:Zn:Sn is close to 3:1:1, matching the stochiometric $ZnSnO_3$. Based on the XRD experiments and SEM characterization results (as shown in Fig. 4c), the ZHS change to amorphous $ZnSnO_3$ above 488K (215 ℃), and then the amorphous ZnSnO3 mainly decomposed to Zn_2SnO_4 + SnO_2 at 873~ 1073 K (600 ~ 800 ℃).

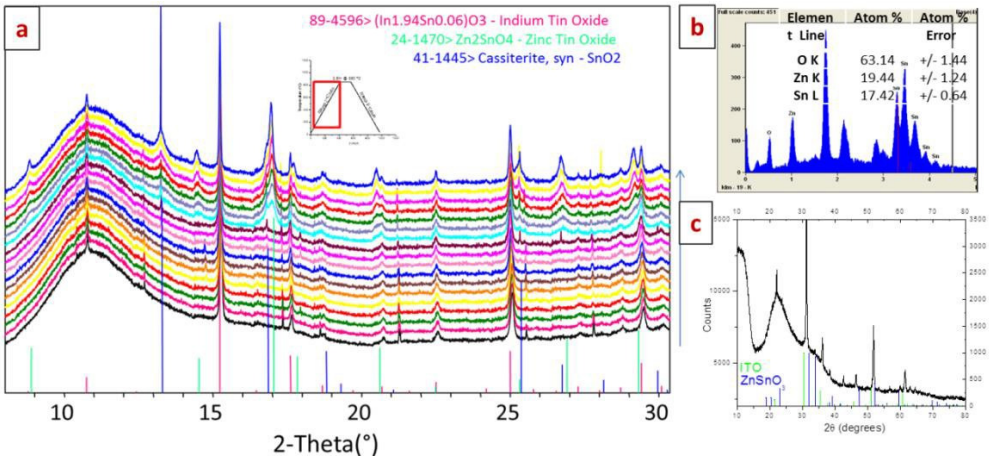

Fig. 4 In-situ synchrotron XRD mapping with the sample ramped at at 2°C/min to 850°C (a). The wavelength is 0.775192 Å and the 2-theta resolution is 0.005°. The EDX and XRD spectra of the sample after annealed at 573 K for 24 hr are shown in Fig4b and 4c. The peaks in XRD spectrum are mainly form the ITO substrate. A small shift between the XRD and standard JCPDS (ITO: JCPDS 89-4596; ZnSnO3: JCPDS 52-1381) is caused by instrumental derivation.

3. Fabrications of gradient structure by fast heating up via Joule heating have been investigated (Figure 5). Both the theoretical simulation and experiment have been conducted.

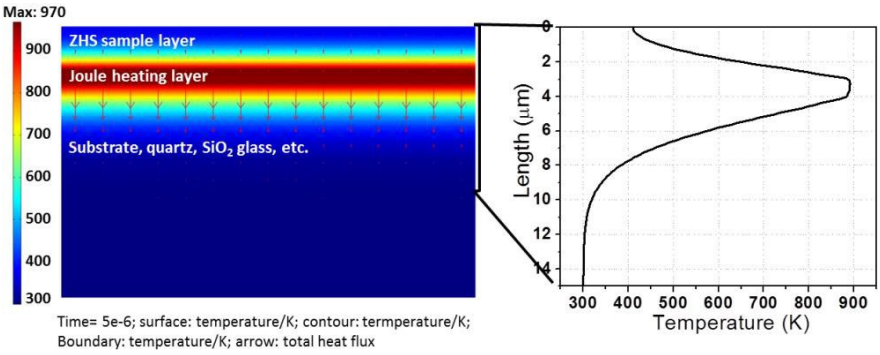

Fig. 5. Temperature distribution in the 2-D model at 5E-6 s after pulse heating, including the contour image (left) and the temperature distribution plot through ZHS layer thickness (right).

A simple model developed on COMSOL Multiphysics software that solved the heat conduction equation for thin films was employed for heat transfer simulation. A 2-D model has been set up which consisted of a thin layer of ZHS which can be 0.5 μm to several microns, a 1.0 μm Ni-Cr alloy layer as heat source, a nearly thermal insulator substrate (quartz) working as a heat sink. The aim is to find out optimal pulse energy (amount and timescale) that can generate enough temperature gradient in ZHS thin layer through the sample thickness. In this system, a certain amount of pulse energy (with micro-second scale) adds to Ni-Cr alloy layer which can be achieved via Joule heating powered by high energy capacitor discharging

in experiments. Material constants like thermal conductivity, specific heat capacity and density of these thin layers had been taken from materials data collections and/or measurements. The time-dependent temperature distribution in ZHS layer through sample thickness can be illustrated after simulation. Fig. 5 illustrates the temperature distribution in these layers at $5X10^{-6}$ s after pulse heating. The left image is the contour plot of the whole model, while the right image shows the temperature distribution through ZHS layer thickness.

Based on the simulation results, the corresponding experiments have been conducted. Generally, the samples were fabricated via sputtering coating Ni-Cr/Cu, soldering, and drop-casting (ZHS) on Si and quartz substrates. The thicknesses of Ni-Cr alloy, Cu, ZHS cube film are around 1.0 μm, 0.5 μm, 0.1-0.5 μm, respectively. According to the simulation results, ~ 1.0 J heat is required for each heating in 5~ 10 μs. Three capacitors with 50 μF capacitance are connected in series. The circuit illustrated in Fig. 6a. The current and voltage for sample in the discharging process were recorded by oscilloscope. Their typical plots are shown in Fig. 6b.

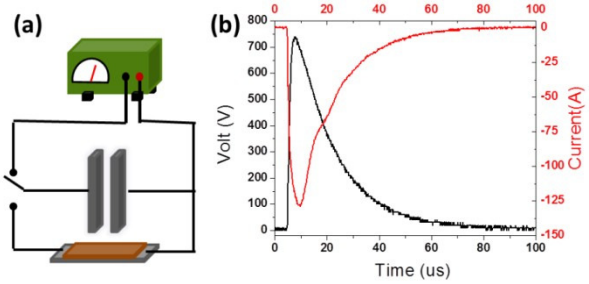

Fig. 6 (a) illustration for capacitor heating circuit, (b) typical discharging plots.

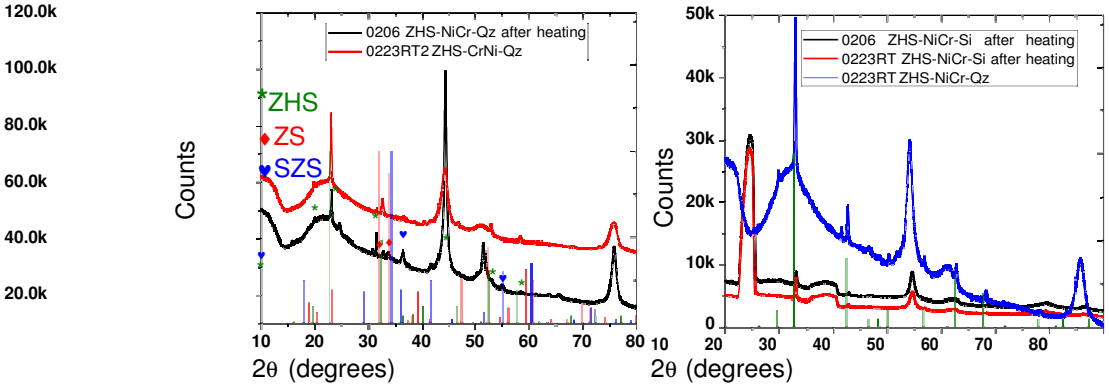

Fig. 7 XRD spectra for ZHS/Ni-Cr on quartz (left) and Si (right) substrates before (0223RT ZHS-NiCr-Qz) and after pulsed heating.

After the discharging heating, samples are characterized via XRD, SEM, TEM to explore their morphology, structure variations. From XRD spectra of the sample drop-casted on Ni-Cr/Qz substrate (as shown in Fig. 7), strong ZHS crystal diffraction peaks can be clearly observed, as well as signal from Ni-Cr and quartz substrates (0223RT ZHS-NiCr-Qz). After capacitor-discharging heating, clear ZHS peaks, SZS+SnO2 peaks, and weak ZS peaks can be found in the XRD spectra of quartz sample. It implies that the ZHS/ZS/SZS mixture structure (probably gradient structure) formed in quartz substrate sample after heating. For samples drop-casted on Si substrate such as 0206 ZHS-NiCr-Si and 0223RT ZHS- NiCr-Si, ZHS XRD peaks largely decreased after heating and no observable peaks for ZS or SZS were identified. The difference between quartz and Si substrate sample after heating can be considered as the different thermal conductivity of quartz and Si. Because Si has better thermal conductivity than quartz, more heat depletion occurs via substrate instead of ZHS layer.

There is no difference on morphology before and after capacitor heating based on the SEM and TEM observations. From the TEM diffraction pattern of the sample after heating, we can see some cubes show spot pattern and amorphous rings which are generated from amorphous zinc stannate ($ZnSnO_3$). The spots or bright rings can be attributed either to residual ZHS crystal or spinel zinc stannate (Zn_2SnO_4). This implies that after fast heating via capacitor discharging, at least two composites exist in sample. Because of the heat transfer direction, the layer-by-layer structure should be formed. However, to further confirm this structure, FIB and HRTEM will be employed.

4. Solar energy utilization – photocatalysis. We have investigated the photocatalysis property of these different zinc stannate nanoparticles before the undergoing photovoltaic property test as catalysts to photodegrade organic dye rhodamine B (RB). Figure 8 displays the photocatalysis performance of these stannate nanoparticles to degrade/bleach (UV light illumination λ = 365 nm). For different stannate nanocomposites obtained from the thermal engineering of ZHS, the color change before and after UV irridation can be used to judge their activity as photocatalysts. There is nearly no color change for as- synthesized ZHS nanoparticle powder after 200 minutes. While, the color of RB solution change from bright pink to colorless solution photodegradation in the presence of amorphous ZS nanoparticle after same period of time. Catalyzed by crystal Zn_2SnO_4/SnO_2 nanoparticles for 200 minutes, bright pink RB solution was bleached to very pale pink.

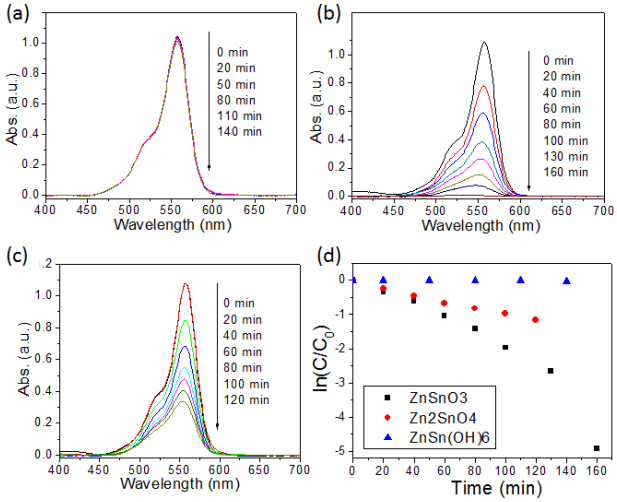

Fig. 8 Absorption spectral changes in RB during irradiation with UV light (λ = 365 nm) in the presence of the $ZnSnO_3.3H_2O$ (a), $ZnSnO_3$ (b), Zn_2SnO_4/SnO_2 (c) nanoparticles and first-order reaction kinetic plots for photocatalytic degradation in the presence of above nanomaterials(d). (The experiment was performed using 20 mL RB aqueous with initial concentrations of 1×10^{-5} mg/ml and 20 mg catalyst. C_0 is the initial RB concentration, and C is the final RB concentration at a given elapsed time.)

Absorption spectral changes in RB during irradiation can be used to both qualitatively and quantitatively measure the activity of these photocatalysts. Figure 8a-c illustrated the RB abs. spectra evolution in the presence of the $ZnSnO_3.3H_2O$, $ZnSnO_3$, Zn_2SnO_4/SnO_2 nanoparticles under UV irradiation respectively. As shown in Figure 8, $ZnSnO_3.3H_2O$ barely show the activity in catalysis of photo degradation of RB, while $ZnSnO_3$ was the most effective sample, followed by mixture crystal of Zn_2SnO_4 and SnO_2. From those absorption spectra, the degradation rate of RB can be calculated and hence the relationship between degradation rate and irradiation time, i.e. reaction kinetics, can be achieved.

Most of photo degradation reactions of dyes obey first order reaction kinetics. The plots of $-\ln(C/C_0)$ verse irradiation time (t) have been drawn in Figure 8d to reveal the relationship between sample composition

and photocatalytic efficiency. Since straight lines can be fitted for the curves of as-prepared $ZnSnO_3.3H_2O$ and Zn_2SnO_4/SnO_2, the first-order reaction kinetic of the photo degradation of RB shows in the presence of the above catalysts (shown in Figure 8d). While for amorphous $ZnSnO_3$ nanoparticle, it's much more efficient than the others and follows non-first order reaction kinetics. The improved catalytic activity should be attributed to the position of conduction/valence bands. And the unusual non-first order and non-zero order reaction kinetics for $ZnSnO_3$ may arise by its amorphous structure. It is well-known that crystallinity plays an important role in the optimization of the photo degradation efficiency for most metal oxide photo catalysts. They show nearly no photocatalytic activity when they are in amorphous structure, while activities become higher when getting better crystalline structures to certain extent. So, it is interesting to find an amorphous semiconductor that keeps high photocatalytic activity. It implies that the crystal $ZnSnO_3$ may have even higher activity.

Publications / Patents / Presentations:

1. C.H. Liu, G. Wrobel, P.X. Gao, Thermal Decomposition of Hydroxystannate Cubes into Stannate-based Semiconductor Nanocomposites for Energy Harvesting and Utilization. MRS Fall meeting 2011, Boston, Nov., 2011. (oral)
2. K.T. Liao, P. Shimpi, P.X. Gao, Scale-up Synthesis of nanostructured copper hydroxystannates and Cu-Sn dendrite alloys on selected substrates, MRS Fall meeting 2011, Boston, Nov., 2011. (poster)
3. G. Wrobel, C.H. Liu, M. Piech, S. Dardona, P.X. Gao, "Synthesis and Fire Retardant Property of Zinc Hydroxystannate coated microfibers," *Sci. Adv. Mater.,* 2012, 4, 819-824.
4. P.X. Gao, P. Shimpi, et al., "Multifunctional Composite Nanostructures for Energy and Environmental Applications," *Int. J. Mole. Sci.,* 2012, 13(6), 7393-7423. (invited)

Project Title: Optimization of FCC Selectivity Through Detailed Modeling of Catalyst Evaluation Experiments and the Contributions of Catalyst Components
Partner: W.R. Grace & Co.
PI: George M. Bollas

Abstract

In this report detailed models of state-of-the-art catalyst evaluation procedures for the Fluid Catalytic Cracking (FCC) process are presented. Two different approaches are used for calculations, the first utilizes a kinetic network scheme to simulate FCC kinetics, regardless of the laboratory unit used for catalyst evaluation (the Kinetics-Based Model, KBm); and the second uses the same kinetic scheme implemented in comprehensive process models of the catalyst evaluation units used (the Real-Process-Based model, RPBm). Four types of reactors are studied as catalyst testing reactors, with the data provided by W.R. Grace & Co.: Micro Activity Test (MAT), Short-Contact Micro Activity Test (SCT-MAT), Advanced Catalyst Evaluation (ACE) and Davison Circulating Riser (DCR) units. The MAT and SCT-MAT units are modeled as fixed bed reactors, while fluidized bed reactor models are used to study the behavior of the ACE and DCR units. All models developed were deployed as part of a tool in Microsoft Excel with a user-friendly interface that allows W.R. Grace & Co. to incorporate their usage as part of everyday catalyst evaluation procedures. The models use the same reaction kinetic network and catalyst deactivation function(s) for different catalyst testing reactors, to facilitate the analysis of laboratory catalyst testing results, the understanding of unit effects and the scaling-up of catalyst selectivity measured in laboratory unit reactors, by allowing the calculation of metrics based on which catalysts can be examined and compared on the same basis.

Project Tasks

This project addressed these particular research needs: analysis of laboratory catalyst testing results, understanding of unit effects and scaling-up catalyst selectivity measured in laboratory units to riser reactors, model of the particular effects of zeolite diffusional properties and matrix activity by developing separate reaction networks for each and study of the deactivation of zeolite and matrix.

In task 1 hydrodynamic models were developed for the different types of catalyst testing reactors used by the industrial partner: the SCT-MAT unit, the ACE unit and the DCR unit. Key characteristics of catalyst testing reactors were identified and existing models were analyzed.

In task 2, several different reaction kinetics networks were examined, regarding their applicability to FCC. The lumping strategy was adopted for the kinetic model. Performance of catalyst decay functions was examined, existing kinetic networks were surveyed, and algorithms for estimation of parameters and kinetic networks were developed. All models have been integrated into a user-friendly interface and the model was validated with experimental data provided by the industrial partner.

In task 3 the effect of matrix type, zeolite content and diffusion characteristics, such as the crystal size, on the kinetic constants of the lumped kinetic network were explored. Separate reaction networks with different kinetic constants were developed for the reactions occurring on the matrix and zeolite surfaces. Validation tests were taken using experimental data from the industrial partner.

Project Objectives & Research Schedule

Specific objectives involved:

a. Decoupling of reaction kinetics and catalyst deactivation from reactor design.
b. Development of models for different catalyst evaluation reactors.
c. Development of detailed reaction kinetics networks.
d. Separation of the effects of zeolite and matrix on catalyst activity and selectivity.
e. Achievement of model-based optimization of catalyst testing.
f. Achievement of model-based optimization of catalyst formulation.
g. Improvement of refinery efficiency.

Milestone / Task Description	Planned Completion Date	Completion
Modeling catalyst testing reactors		
Identify key characteristics of catalyst testing reactors	01/01/11	100 %
Survey existing models	01/01/11	100 %
Develop and validate models with available data	04/01/11	100 %
Reaction network and catalyst deactivation		
Examine performance of catalyst decay functions	01/01/11	100 %
Survey existing kinetic networks	04/01/11	100 %
Develop kinetic network and parameter estimation algorithm	06/01/11	100 %
Integrate all models into a user friendly interface	09/01/11	100 %
Validate model with experimental results	10/01/11	100 %
Effect of catalyst properties (zeolite and matrix)		
Literature survey of the reactions occurring on matrix	12/01/11	100 %
Develop separate kinetic networks for matrix and zeolite	12/01/11	100 %
Incorporate effectiveness factors	03/01/12	100 %
Integrate all models	06/31/12	100 %
Validate model with experimental data	07/31/12	100 %
Streamline the process of improving models with new experimental data and understanding	09/31/12	100 %

1. Introduction

Fluid Catalytic Cracking (FCC) is still a key oil refinery process in the petroleum industry, converting high molecular weight petroleum fractions into lighter more valuable products. Due to its complexity and associated economic incentives, modeling of FCC units is of pivotal interest. The effective simulation of FCC units requires a thorough understanding of the combined kinetics and hydrodynamics of the reactor used in this process, a riser (entrained-flow), in which the gas and catalyst concurrently flow upward, the catalyst concentration is low and the solids-feed contact time is short [1–3]. To predict the performance of commercial FCC units under different operating conditions, feed properties, and catalyst activity and selectivity, catalyst evaluation procedures at bench level are used [2].

Two common laboratory techniques used to evaluate the performance of FCC catalysts include microactivity testing and circulating riser pilot plants. Both units are able to evaluate equilibrium catalysts and laboratory deactivated catalysts, and each has its own set of advantages and disadvantages. The Micro Activity Test (MAT) is a convenient approach for evaluating the catalytic performance of FCC catalysts, as described originally in the ASTM D3907 procedure. The version of the procedure used by W.R. Grace & Co. consists of a fixed bed reactor that requires only a small amount of catalyst and feed, gives excellent reproducibility and can process a wide range of feedstocks. The Davison Circulating Riser (DCR), developed by W.R. Grace & Co.[4–6], operates as a fully circulating pilot unit. Testing catalyst in the DCR unit is more time consuming, requires more catalyst and feed and it is more expensive than the MAT unit; however, the operation of the DCR unit better resembles a commercial FCC unit, with similar product selectivities [6].

The principal shortcoming of MAT procedures is the catalyst contact-time of 75 s, which is not representative of commercial operations, where contact-times between 2s and 10 s are employed [7]. To avoid this shortcoming, among others encountered with the traditional MAT technique, the Short Contact Time Micro Activity Test (SCT-MAT) was developed by W.R. Grace & Co., and its reliability and accuracy was improved [8–10]. Another, more recent development related to FCC laboratory-testing is the Advanced Catalyst Evaluation (ACE) technique. ACE-testing is performed in a fluidized bed reactor, where a vaporized stream of a heavy oil fraction is forced to flow through a fluidized catalyst bed at short contact times [11].

Modeling of laboratory units used for catalyst evaluation, as presented in this report, poses many difficulties and research challenges. Several different unit types have to be modeled in a way consistent, so that catalyst evaluation results can be used for realizing potential benefits in commercial operations. For the simulation of the effect of laboratory reactors operating conditions on product selectivity, an analysis of reactor hydrodynamics and feedstock cracking reaction kinetics has to be performed. The riser reactor can be simulated as a circulating fluidized bed [2]. Fixed bed reactors, such as the SCT-MAT unit [10], can be modeled as ideal plug flow reactors. Fluid bed batch reactors, such as the ACE unit [12] can be modeled as bubbling bed or even spouted bed reactors where the catalyst-hydrocarbons contact efficiency needs to be calculated in detail. Hydrodynamic analysis of these reactors can lead to accurately calculating the catalyst - feedstock contact time and the catalyst activity as a function of time.

The complexity of gas oil mixtures, which are typical FCC feeds, and the different product slates of the FCC process (a direct consequence of the complex interplay between reactions such as cracking, isomerization, hydrogen transfer, oligomerization, etc.) makes it extremely difficult to characterize and describe the inherent kinetics of the process at a molecular level. Hence, one is forced to examine generalities rather than details. One of the methods used to do this is to consider the behavior of groups of compounds as a unit. In this way similar components are grouped into a few “cuts” or “lumps”. The number of lumps of the models proposed in the literature for catalytic cracking reactions have been consecutively increasing to obtain a more detailed prediction of product distribution. In the first kinetic

model (3-lump), proposed by Weekman [13], reactants and products were lumped into three major groups: gas oil, gasoline, and light gas plus coke. Yen et al. [14] and Lee et al. [15] took one step forward by dividing the light gas plus coke lump into two different lumps C_1-C_4 gas and coke, developing the first 4-lump models for fluid catalytic cracking. Advancing the lumping methodology, Corella and Frances [16] developed a 5-lump model, in which the gas-oil lump was divided into its heavy and light fractions. Dupain et al. [17] simplified the 5-lump model of Corella and Frances [16] for the specific case of the catalytic cracking of aromatic gas oil, by reducing the reactions involved in the lumping scheme. Another 5-lump model was developed by Larocca et al. [18], in which the 3-lump model of Weekman [13] was modified by splitting the gas oil lump into aromatic, paraffinic, and naphthtenic lumps. Ancheyta-Juarez et al. [19] followed a different approach in their 5-lump models development, in which they considered the gas oil as one lump, but divided the gas lump into two lumps (liquefied product gas and dry gas). 6-lump models were developed by Takatsuka et al. [20] (including the resid as a separate lump to predict the catalytic cracking of residual oil), and Oliveira and Biscaia [21] (emphasizing in the catalytic cracking of gasoline and paraffinic gas oils). Hagelberg et al. [9] expanded the 5-lump model of Ancheyta-Juarez et al. [19] to an 8-lump model by dividing the gasoline fraction into paraffins, olefins, naphthenes and aromatics. Wojciechowski and Corma [22] proposed a 12-lump reaction scheme for catalytic cracking in which the gas composition was considered in detail. Jacob et al. [23] proposed a 10-lump model (light and heavy gas oil paraffinic, naphthenic and aromatic rings and substituents). On the basis of the 10-lump model of Jacob et al. [23], Ellis et al. [24] developed a more advanced model capable of predicting the light gas product slate, using empirical algebraic equations. Different models have been reviewed recently, and more information can be found therein [25], [26].

In the study of the reactions involved in the catalytic cracking process, in addition to the difficulties mentioned in modeling the catalytic cracking kinetics, particular attention needs to be paid on the function used in the model to describe catalyst deactivation. A large number of catalyst decay functions have been proposed in the literature. They are summarized in the time on stream theory [27] as time-based models and coke-on-catalyst models [28]. The first efforts in modeling coke formation were made by Voorhies [29] who showed that the rate of carbon formation is largely a function of catalyst residence time. Although easier to implement, time-based models do not recognize the effect of feed rate in the deactivation. Coke-on-catalyst models appear more accurate, but more complex; the so-called soft coke or strippable coke needs to be accounted for, which typically is not measured). Soft coke consists of polar molecules that strongly absorb on the catalyst surface, blocking active sites, which can be desorbed during stripping. It can be measured in laboratory units by repeating the same experiment with and without catalyst stripping. Soft coke may transform to hard coke (the coke burned in the regenerator of a commercial plant) at higher residence times [3]. This is a factor that needs to be accounted for when modeling reactors with large differences in catalyst residence time (for instance ACE unit to DCR).

In this report, detailed models of state-of-the-art catalyst evaluation procedures for the FCC process were developed, following two different approaches. Key properties of the models are that they can be practically implemented in everyday catalyst evaluation procedures and that they use the same reaction kinetics network and catalyst deactivation function(s) for different catalyst testing reactors (MAT, SCT-MAT, ACE unit and DCR unit). In this work, lumping kinetic network schemes were used for the models, as well as deactivation functions using the coke-on-catalyst approach. The structure of this report is as follows: the methodology used to develop the algorithms is presented in Section 2. Section 3 presents the results found for the first two tasks of the project, using the models developed and the comparison against experimental data. Section 4 presents the results for the last task of the project, related to the effects of matrix and zeolite effects on catalyst properties. Finally, on Section 5 the conclusions of the project are summarized.

2. Methodology

The development of state-of-the-art models for catalyst testing procedures involves the study of fixed bed and fluidized bed catalytic reactors. Two different approaches have been used to model the behavior of both types of reactors: The Kinetics-Based model (KBm) and the Real-Process-Based model (RPBm). For both approaches, the kinetic network used to represent the reactions that occur inside the reactors, as well as the deactivation of the catalyst used, need to be modeled. We start by describing the different kinetic networks used, to later establish the particular characteristics of both the KBm and the RPBm. In general, we assume that there is no temperature gradient inside the catalyst particles, since they are microspheres and catalytic reactions are mild endothermic [31]. We also assume that particle diffusion, if important, can be accounted for by effectiveness factors that would have been multipliers to the kinetic constants estimated; therefore, they would be reflected in the selectivity of a catalyst estimated by lumped kinetic constants of a broader meaning (kinetics and diffusional effects). Thus, we developed pseudo-homogeneous, one-dimensional models for the different catalyst evaluation units studied in this work.

2.1. Kinetic networks & Catalyst Deactivation

In the study of the reactions involved in the catalytic process we follow a lumping methodology. Lumping of many components together has always been a necessity in the petroleum industry where thousands of individual molecular species are present in even relatively narrow boiling range cuts [23]. Since the work by Weekman and Nace [30], it has been shown that even a three-lump system could adequately describe gasoline selectivity behavior in catalytic cracking. However, more detailed schemes (like the one developed by Jcob et al. [23], using 10-lumps) allow the estimation of rate constants that are independent of the initial composition of the feedstock. In this report we present results obtained while using different lumping kinetic network schemes, ranging from four to six lumps, and presented later on.

Coupled to the kinetic network scheme, the deactivation function used in models for catalyst testing reactors has to be specified. In general, there are two approaches to model the complex phenomenon of catalyst deactivation: time-based models and coke-on-catalyst models [28]. For the time-based models, different decay functions used in the literature are summarized in the time-on-stream theory [27], which states that the catalyst activity ( ) can be represented through:

$$-\frac{d\phi}{dt} = k_d \phi^m \quad (1)$$

where t is time-on-stream, k_d is the deactivation constant and m the number of active sites implicated in each deactivation event.

In an analogous way as for the time-on-stream theory, the catalyst deactivation has been related to coke content through the following rate equation

$$-\frac{d\phi}{dCoC} = k_d \phi^m \quad (1)$$

where CoC is defined as coke-on-catalyst [28]. Coke production, and thus the ability to predict the coke yield, is of crucial importance during FCC operation, because it impacts the overall heat balance of the FCC unit by determining the heat production by coke combustion in the regenerator and in consequence, the catalyst circulation rate in the unit. FCC coke can be subdivided according to origin into four types: catalytic coke formed as a byproduct of catalytic cracking, carbon residue coke formed via thermal (non-catalytic) reactions, contaminant coke formed as a result of catalyst poisoning, and catalyst-to-oil coke yielded by incomplete stripping [3]. Considering that the coke yield due to incomplete stripping is negligible, the total coke yield can be predicted by adding the noncatalytic coke (residue and contaminant) to the catalytic coke. Results are reported using the catalyst decay function of the coke-on-catalyst, which better represents the physics behind the catalyst deactivation process in FCC units.

2.2. Kinetics-based Model (KBm)

In this approach, a system of ODEs based only on a lumping reaction kinetic network is solved for all types of catalyst evaluation units modeled (MAT, SCT-MAT, ACE and DCR units) and used in W.R. Grace & Co. The system of ODEs to solve is described by:

$$\frac{dy_i}{dt} = \sum_{j=1}^{i-1} k_{ji} y_j^{\alpha} \phi - \sum_{j=i+1}^{N} k_{ij} y_i^{\alpha} \phi \qquad (1)$$

where y_i corresponds to the mass fraction of component i $(i=1…n)$ in the mixture, t is the gas residence time in the unit, ϕ is the deactivation function and k_{ij} are the reaction kinetic network constants corresponding to a lumping kinetic network scheme. In the expression α indicates the order of the reactions. As in many other kinetic models described in the literature [27], a second order of reaction has been used for gasoil cracking, to take into account the ample range of feedstock cracking rate, while the cracking of products has been described with a first order reaction rate.

Under this approach, the system of equations to solve is the same for all the catalyst testing units studied. The model will only change depending on the kinetic network defined to represent the system. As an example, in the case of a four-lump scheme for the reaction kinetic network (shown in Figure 1) the system of equations to be solved is described by:

$$\frac{dy_1}{dt} = -k_{12} y_1^2 \phi - k_{13} y_1^2 \phi - k_{14} y_1^2 \phi \qquad (1)$$

$$\frac{dy_2}{dt} = k_{12} y_1^2 \phi - k_{23} y_2 \phi - k_{24} y_2 \phi \qquad (1)$$

$$\frac{dy_3}{dt} = k_{13} y_1^2 \phi + k_{23} y_2 \phi - k_{34} y_3 \phi \qquad (1)$$

$$\frac{dy_4}{dt} = k_{14} y_1^2 \phi + k_{24} y_2 \phi + k_{34} y_3 \phi \qquad (1)$$

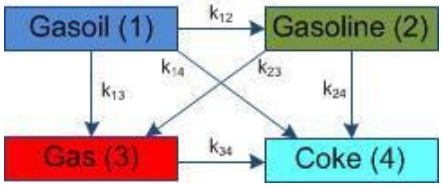

Figure 1 – Four-lump kinetic network [14], [15]

2.3. Real-process-based Model (RPBm)

In this approach, beyond the reaction kinetic network used, characteristics inherent to the specific reactors modeled are incorporated in the system of ODEs to be solved. Thus, the system of ODEs used depends on the type of reactor being modeled. In general, we start from the continuity equation of a multicomponent mixture, in its general and by-component form, as follows:

$$\frac{\partial C}{\partial t} = -(\nabla \cdot (C\, u_{SG})) - (\nabla \cdot J) + \rho_{bed} \sum_{j=1}^{N} R_j \qquad (1)$$

$$\frac{\partial C_i}{\partial t} = -\left(\nabla \cdot (C_i\, u_{SG,i})\right) - (\nabla \cdot J_i) + \rho_{bed} R_i \qquad (1)$$

The first term in the equations corresponds to the rate of increase in moles per unit volume. The second term corresponds to the net rate of addition in moles per unit volume by convection, the third term to the rate of addition of moles per unit volume by diffusion and the last one to the rate of production of moles per unit volume per reaction. C is the total molar concentration of the mixture, C_i is the molar concentration of component i, u_{SG} is the molar average velocity (not the interstitial velocity) of the mixture and ρ_{bed} is the packing bed density of the reactor. In our models we take into account only the

axial concentration profile and work with pseudo-homogeneous assumptions. The specific details for the different types of units modeled follow.

2.4.Fixed Bed Units

The equations described here apply to the models of MAT and SCT-MAT units. For these units, we consider that (a) there is a concentration profile only in the axial direction of the reactor, (b) the porosity of the bed inside the reactor and (c) only the gas phase (as an isobaric and isothermal ideal gas mixture), velocity is equal for all the gaseous components in the mixture, we get that:

$$\varepsilon \frac{\partial C_i}{\partial t} + u_{SG} \frac{\partial C_i}{\partial z} = -\rho_{bed} \frac{C_i}{C} \sum_{j=1}^{N} R_j + \rho_{bed} R_i \qquad (1)$$

Where R_i (the reaction rate) is defined (in terms of a lumping reaction kinetic network) by

$$R_i = \sum_{j=1}^{i-1} k_{ji} C_j^{\alpha} \phi - \sum_{j=i+1}^{N} k_{ij} C_i^{\alpha} \phi \qquad (1)$$

2.5.ACE Unit

For the ACE unit, modeled as a fluidized bed reactor, we follow the simple three-region model for the gas flow through fluidized beds as described by Kunii and Levenspiel [32] (shown in Figure 2). In the model, uniformly sized bubbles, surrounded by clouds and followed by wakes, rise through an emulsion of downward moving solids. Interchange of gas occurs continuously among bubble, cloud-wake, and emulsion regions. All internal flows and interchanges in the bed are derived from the effective bubble size.

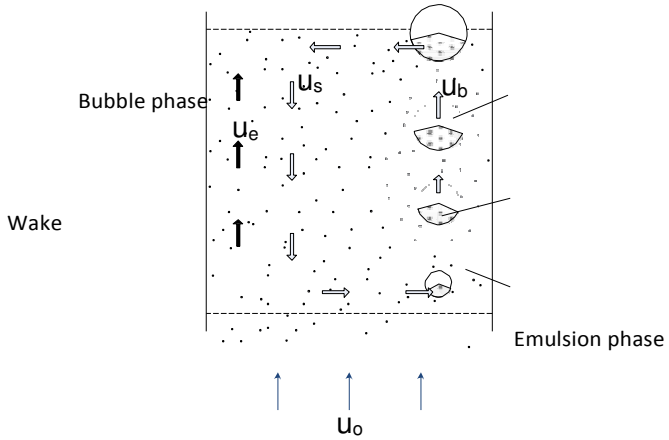

Figure 2.- Bubbling bed model for a fluidized bed reactor

Considering that:

□ : fraction of bed in bubbles

□□ : fraction of bed as wake

□$_{mf}$: minimum fluidization porosity

$_{mf}$: amount of gas in bubble+wake phase

$_{mf}$) : amount of solids in bubble+wake phase

□□□□□□□□□ : fraction of bed as emulsion

□□□□□□□□□□□□□$_{mf}$: amount of gas in the emulsion

□□□□□□□□□□□□□□□□□□□□$_{mf}$) : amount of solids in the emulsion

Bubble diameter:

$$d_{bo} = 3.77 \frac{(u_{SG} - u_{mf})^2}{g} \quad (1)$$

$$d_{bmax} = 2.59\, g^{-0.2} ((u_{SG} - u_{mf})A)^{0.4} \quad (1)$$

$$d_b = d_{bmax} - (d_{bmax} - d_{bo}) \exp\left(\frac{-0.3\, z}{D}\right) \quad (1)$$

Bubble velocity:

$$u_b = u_{SG} - u_{mf} + 0.711(g\ d_b)^{0.5} \quad (1)$$

Fraction of bed in bubbles:

$$\delta = \frac{(u_{SG} - u_{mf})}{u_b} \quad (1)$$

Downward solid velocity in emulsion:

$$u_s = \frac{\alpha\delta u_b}{(1 - \delta - \alpha\delta)} \quad (1)$$

Emulsion velocity:

$$u_e = \frac{u_{mf}}{\varepsilon_{mf}} - u_s \quad (1)$$

Mass transfer coefficients:

$$K_{i,bc} = 4.5\frac{u_{mf}}{d_b} + 5.85\frac{D_i^{0.5}\ g^{0.25}}{d_b^{5/4}} \quad (1)$$

$$K_{i,ce} = 6.78\left(\frac{\varepsilon_{mf}\ D_i\ u_b}{d_b^3}\right)^{0.5} \quad (1)$$

$$\frac{1}{K_{i,be}} = \frac{1}{K_{i,bc}} + \frac{1}{K_{i,ce}} \quad (1)$$

$$K_{i,sb} = K_{i,be}\frac{(\delta + \delta\alpha\varepsilon_{mf})}{(1 - \delta - \alpha\delta)\varepsilon_{mf}} \quad (1)$$

$$\text{if } \frac{u_{SG}}{u_{mf}} \leq 3 \text{ then } K_{i,we} = \frac{0.075\ (u_{SG} - u_{mf})}{u_{mf}\ d_b}$$

$$\text{if } \frac{u_{SG}}{u_{mf}} > 3 \text{ then } K_{i,we} = \frac{0.15}{d_b} \quad (1)$$

$$K_{i,sw} = K_{i,we}\frac{\alpha\delta}{(1 - \delta - \alpha\delta)} \quad (1)$$

From the continuity equation, we get the following equations for the different phases in the model:

Bubble+wake phase, gas:

$$\frac{\partial[(\delta + \alpha\delta\varepsilon_{mf})C_{i,b}]}{\partial t} = -\frac{\partial(\delta + \alpha\delta\varepsilon_{mf})C_{i,b}\ u_b}{\partial z} + (\delta + \alpha\delta\varepsilon_{mf})K_{i,be}\ (C_{i,e} - C_{i,b}) + (\lambda_1 C_{i,b} + \lambda_2 C_{i,e})\frac{\partial[(\delta + \alpha\delta\varepsilon_{mf})\ u_b]}{\partial z} + \alpha\delta(1 - \varepsilon_{mf})\rho_p\ R_{i,b} \quad (1)$$

Bubble+wake phase, solids:

$$\frac{\partial[\alpha\delta\,(1-\varepsilon_{mf})\,\rho_p\,C_{c,w}]}{\partial t} = -\frac{\partial[\alpha\delta\,(1-\varepsilon_{mf})\,\rho_p\,C_{c,w}u_b]}{\partial z} + \alpha\delta\,(1-\varepsilon_{mf})\,\rho_p\,K_{i,we}\,(C_{c,e}-C_{c,w}) + (\lambda_1 C_{c,w}+\lambda_2 C_{c,e})\,\frac{\partial[\alpha\delta\,(1-\varepsilon_{mf})\,\rho_p u_b]}{\partial z} + \alpha\delta\,(1-\varepsilon_{mf})\,\rho_p\,R_{c,w}M_c \qquad (1)$$

Emulsion, gas:

$$\frac{\partial[(1-\delta-\alpha\delta)\varepsilon_{mf}C_{i,e}]}{\partial t} = -\frac{\partial[(1-\delta-\alpha\delta)\,\varepsilon_{mf}\,C_{i,e}\,u_e]}{\partial z} + (1-\delta-\alpha\delta)\,\varepsilon_{mf}\,K_{i,eb}(C_{i,b}-C_{i,e}) - (\lambda_1 C_{i,b}+\lambda_2 C_{i,e})\frac{\partial[(\delta+\alpha\delta\varepsilon_{mf})\,u_b]}{\partial z} + (1-\delta-\alpha\delta)(1-\varepsilon_{mf})\rho_p\,R_{i,e} \qquad (1)$$

Emulsion phase, solids:

$$\frac{\partial[(1-\delta-\alpha\delta)(1-\varepsilon_{mf})\,\rho_p\,C_{c,e}]}{\partial t} = -\frac{\partial[(1-\delta-\alpha\delta)\,(1-\varepsilon_{mf})\,\rho_p\,C_{c,e}u_s]}{\partial z} + (1-\delta-\alpha\delta)\,(1-\varepsilon_{mf})\,\rho_p\,K_{i,ew}\,(C_{c,w}-C_{c,e}) + (\lambda_1 C_{c,w}+\lambda_2 C_{c,e})\,\frac{\partial[\alpha\delta\,(1-\varepsilon_{mf})\,\rho_p u_b]}{\partial z} + (1-\delta-\alpha\delta)\,(1-\varepsilon_{mf})\,\rho_p\,R_{c,e}M_c \qquad (1)$$

2.6.**DCR Unit**

For DCR unit the model we follow is a pseudo-steady state model of a riser. Thus, starting from steady state and rearranging we get that:

$$\frac{\partial C_i}{\partial z} = -\frac{\rho_{bed}\,\varepsilon}{u_{SG}}\left[\frac{C_i}{C}\sum_{j=1}^{N} R_j + R_i\right] \qquad (1)$$

3. Results and Discussion

3.1 Modeling Testing Reactors & Reaction Network and Catalyst Deactivation

3.1.1.*Interface*

The models described in this report have been deployed as part of an Add-In for Microsoft Excel (Figure 3), in order to make the calculations available for everyday catalyst evaluation procedures. For the Add-In to work, information on the feedstock, catalyst and reactor are necessary, coupled with the experimental data. Different reaction kinetic networks are available for calculations. Both models are available to run calculations from experimental data and to make predictions from known kinetic network constants. All calculations behind the Add-In are executed in MATLAB, through an accessible executable file. After calculations are done, a plot with the products yields as a function of conversion is shown (Figure 4). All information is saved in a workbook in Microsoft Excel. It is important to note that the interface has

evolved through feedback from the final users, which will facilitate its incorporation as part of daily catalyst evaluation procedures.

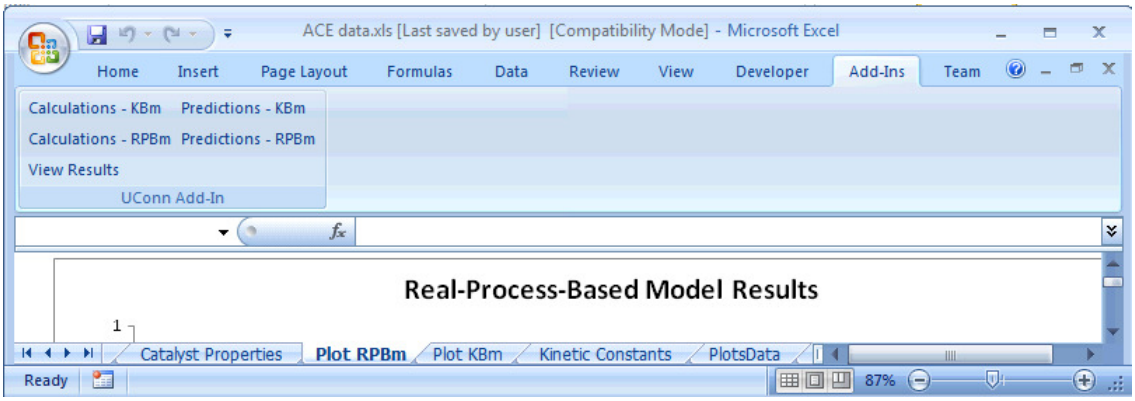

Figure 3 - Interface: Add-In in Microsoft Excel

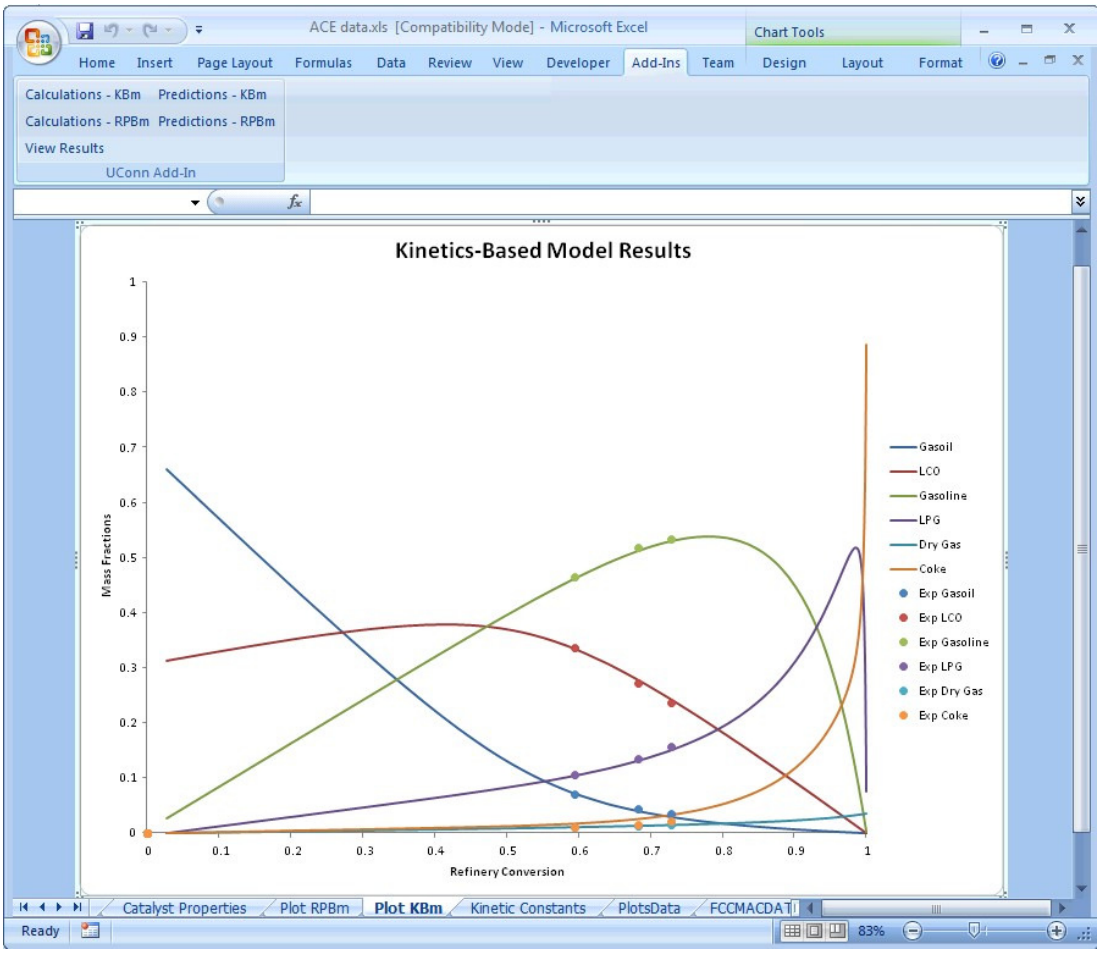

Figure 4 .- Results in Microsoft Excel

3.1.2.*Model Calculations*

At W.R. Grace & Co. four different types of units are used for catalyst testing procedures: MAT, SCT-MAT, ACE and DCR. We compare the most relevant characteristics of these units. Given that access to experimental data was provided by W.R. Grace & Co. from an extensive database, the first objective of this report was to prove that both, the Kinetics-Based model (KBm) and the Real-Process-Based model (RPBm) predictions agree with experimental data.

In order to do calculations with the models developed, the first step was to select a kinetic network scheme and the catalyst deactivation function to use. Three different lumping schemes (4-lumps, 5-lumps and 6-lumps) were selected for the calculations, as shown in Figure 5. In terms of the catalyst deactivation function, the coke-on-catalyst approach was selected,

Table 1.- Main features of the catalyst testing units studied in this work.

	MAT	SCT-MAT	ACE	DCR
Type of Reactor	Fixed bed	Fixed bed	Fluidized bed	Fluidized bed
Operation	transient	Transient	transient	transient
Catalyst residence time (s)	75	9	30	2
Catalyst to Oil range	1-7	2-3	2-7	5-8

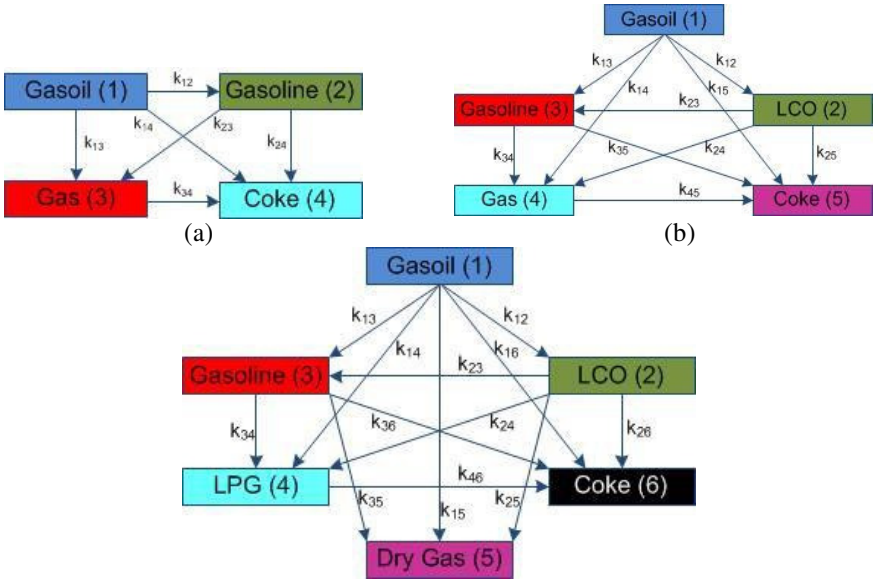

(c)

Figure 5 .- Kinetic network schemes used in this report: (a) 4-lumps, (b) 5-lumps and (c) 6-lumps.

In Figure 6 results for three different lumping schemes used as kinetic networks (Figure 5) are shown, for the four different reactors studied (MAT, SCT-MAT, ACE and DCE), using the Kinetics-Based model. In the plots, where the variation of the products yields against the refinery conversion (defined as the sum of the yields to gasoline, LPG, dry gas and coke) is presented, the agreement between experimental data and modeling results is clear for all the cases.

For catalyst testing reactors, experimental data is available only for a limited range of conversion (especially for ACE reactors). Thus, it is difficult to predict the behavior of each reactor for conversions distant from the experimental data provided. Also, as the range of conversion of the experimental data is different for all reactors, it is difficult to compare, for example, the behavior of the same catalyst for different reactors. As shown in Figure 6, predictions of the KBm cover a wide range of conversion. Therefore, even with scarce experimental data, it is possible to study the behavior of the products yields for a wide range of conversion, for any type of reactor. Moreover, a comparison of the products yields of different reactors is possible, under the same operational conditions (same feedstock and catalyst) and the same assumptions (same reaction kinetic network and catalyst deactivation function).

Besides providing products yields as a function of conversion (as shown in Figure 6), calculations using the KBm provide values for the kinetic network constants related to the reaction kinetic network scheme selected. In Table 2, examples of kinetic network constants are shown (corresponding to the curves presented in Figure 6(c)). The table shows the similarities between the values of the kinetic constants for different reactors. Moreover, it evidences the possibility of predicting the behavior of products for any of the reactors starting from the kinetic network constants calculated from experimental data of another type of reactor. As an example, in Figure 7 predictions using the KBm are presented for a DCR unit. On one side (Figure 7(a)), predictions using the experimental data of the DCR unit are shown. On the other side (Figure 7(b)), predictions using kinetic network constants calculated from experimental data of an ACE unit (under the same conditions) are shown. As it was expected, the predictions of the KBm for the DCR unit based on the kinetic constants calculated from experimental data of the ACE unit, are very close to the experimental data for the DCR unit.

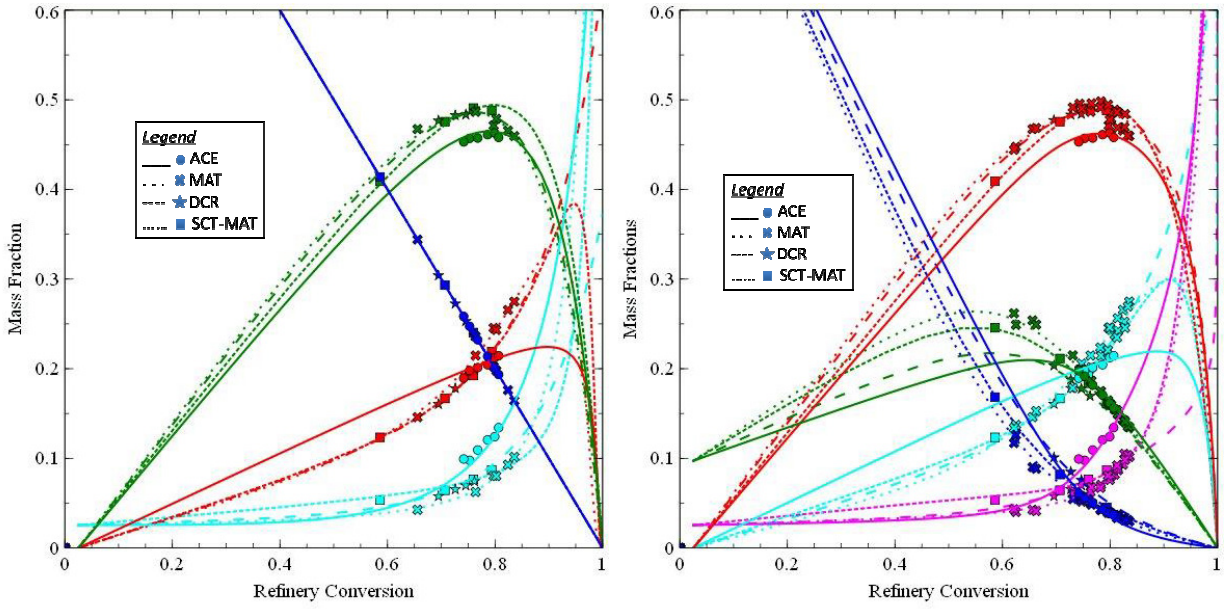

(a) (b)

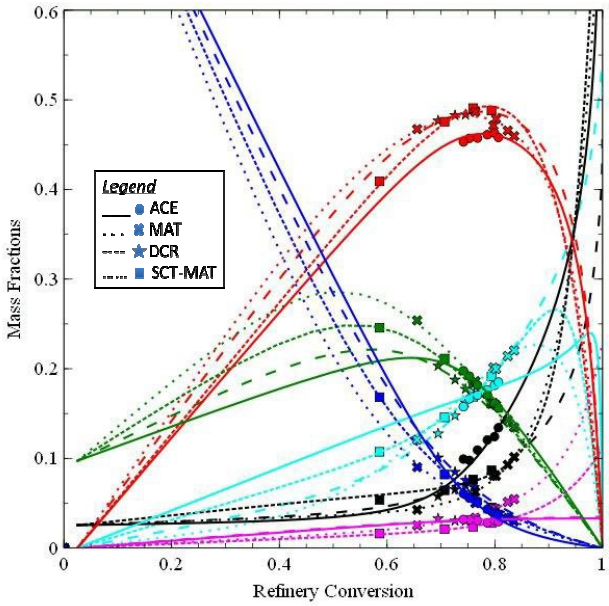

(c)

Figure 6.- Experimental and model results for different kinetic network schemes (as shown in Fig 5) and different reactors (MAT, SCT-MAT, ACE and DCR units): (a) 4-lumps, (b) 5-lumps and (c) 6-lumps. Experimental data was collected for all the reactors under the same conditions (same catalyst and same feedstock). A catalyst decay function related to the amount of Coke-on-catalyst was used.

Table 2.- Kinetic network constants for different reactors under the same conditions (same catalyst and feedstock), using a 6-lump reaction kinetic network scheme (Figure 5(c)), and the same catalyst decay function.

Reactor	Lump	LCO	Gasoline	LPG	Dry Gas	Coke
MAT	**Gasoil**	8.5871	14.5911	1.1289	0.5321	0.3698
	LCO	0	1.3438	2.9503	0.0004	0.0022
	Gasoline	0	0	0.2003	0.1323	0.0628
	LPG	0	0	0	0	1.3447
SCT-MAT	**Gasoil**	10.6144	20.0000	4.9124	0.7323	1.7257
	LCO	0	6.6285	0.8997	0.0000	0.0000
	Gasoline	0	0	0.8202	0.1168	0.0000
	LPG	0	0	0	0	1.8314
ACE	**Gasoil**	5.2418	16.7099	5.6680	1.0905	0.1905
	LCO	0	0.0001	0.2038	0.0000	2.2087
	Gasoline	0	0	0.0411	0.0000	0.1042
	LPG	0	0	0	0	0.0361
DCR	**Gasoil**	4.0196	11.0681	1.5054	0.6592	0.2825
	LCO	0	0.0842	2.7841	0.0226	0.6599
	Gasoline	0	0	0.0789	0.0000	0.1057
	LPG	0	0	0	0	0.0001

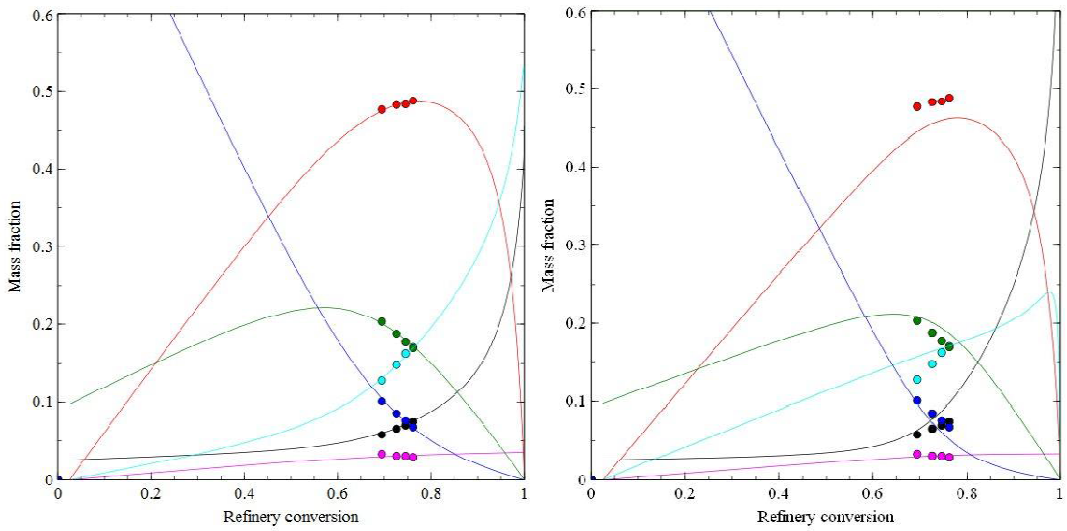

(a) (b)

Figure 7.- KBm predictions for a DCR unit, using a 6-lump (Figure 5(c)) reaction kinetic network. On the left, predictions from DCR experimental data. On the right, predictions for the DCR unit using kinetic network constants calculated with experimental data (under the same conditions) for an ACE unit.

Using a more detailed approach than the one in the KBm, the RPBm was developed. As described in the methodology, this model incorporates hydrodynamic details of the reactors in the calculations. In Figure 8 results of the predictions of the RPBm and experimental data for ACE and DCR units are presented, using a 6-lump reaction kinetic network (Figure 5(c)). The agreement between the experimental data and the model predictions is evident. Prediction of products yields for a wide range of conversion is possible from the RPBm, as it was for the KBm. Comparison between curves from different reactors is again possible, as with the KBm, as all calculations use the same assumptions (same reaction kinetic network and deactivation function) and the same operational conditions (same feedstock and catalyst).

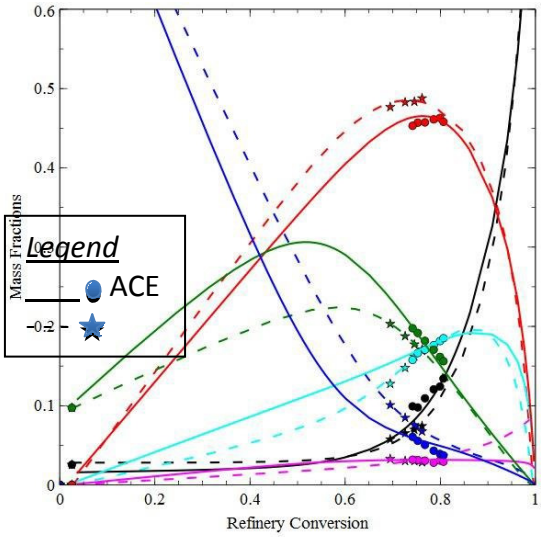

Figure 8.- Experimental and model results for the RPBm for a 6-lump reaction kinetic network (Fig 5(c)) for ACE and DCR units. Experimental data was collected for both reactors under the same conditions (same catalyst and same feedstock). A catalyst decay function related to the amount of Coke-on-catalyst was used.

Figure 9 shows the curves of the products yields as a function of the conversion for the same reactor (under the same conditions) for both models (KBm and RPBm). From the plots, several conclusions can be drawn: the overcracking conversion for gasoline is lower for the RPBm, the yields of LPG & Dry Gas decrease after a maximum for the RPBm and the yield of coke increases more rapidly for the RPBm. From general knowledge, this behavior was expected. Thus, introduction of hydrodynamic details in the calculations improve the prediction of the behavior of the products yields for catalyst evaluation units. Therefore, for fast and accurate predictions of products yields in terms of conversion, the KBm is a reliable tool. For more accurate studies involving a less empirical analysis of the data and more realistic predictions, the RPBm is the best tool to use.

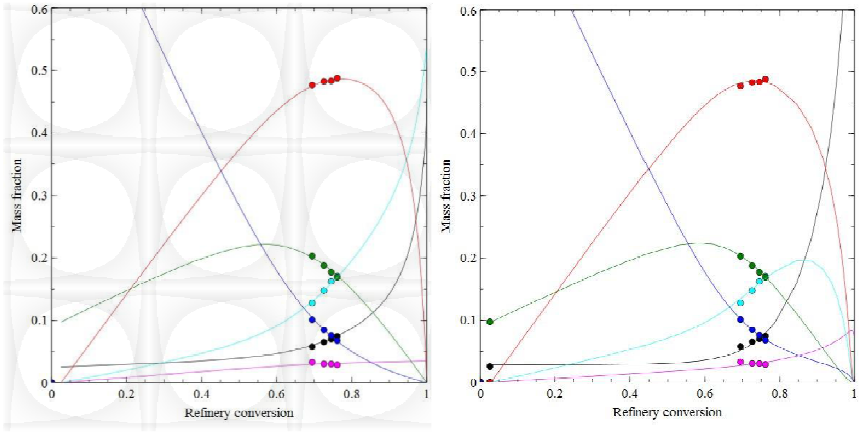

(a) KBm (b) RPBm

Figure 9 .- Predictions of both models (KBm on the left and RPBm on the right) for a DCR unit, using the 6-lump reaction kinetic network (Figure 5(c)) and a deactivation function relate to the amount of coke-on-catalyst.

Kinetic network constants for DCR and ACE units (corresponding to the plot in Figure 8) are shown. As it was the case for the KBm, the similarities among the kinetic constants evidences the possibility of predicting the behavior of one reactor based on the kinetic network constants calculated from another unit (under the same conditions and assumptions). In Figure 10, predictions using the RPBm model for a DCR unit are shown. On one hand (Figure 10(a)), predictions using experimental data for a DCR unit are presented. On the other hand (Figure 10(b)), predictions for the DCR unit using experimental data of an ACE unit, under the same conditions (same catalyst and feedstock) and using the same assumptions (6-lump reaction kinetic network and coke-on- catalyst dependent catalyst decay function), are presented. As it was expected, the predictions of the RPBm for the DCR unit based on the kinetic constants calculated from experimental data of the ACE unit, are very close to the experimental data for the DCR unit.

Table 3.- Kinetic network constants for DCR and ACE units under the same conditions (same catalyst and feedstock), using a 6-lump reaction kinetic network scheme (Figure 5(c)), and the same catalyst decay function.

Reactor	Lump	LCO	Gasoline	LPG	Dry Gas	Coke
ACE	Gasoil	42.0440	121.7477	14.2766	2.5891	0.0000
	LCO	0	0.0285	0.0288	0.0038	0.0019
	Gasoline	0	0	0.0238	0.0023	0.0000
	LPG	0	0	0	0	0.0179
DCR	Gasoil	32.4918	94.7160	15.2444	4.0761	0.0000
	LCO	0	0.0211	0.0086	0.0021	0.0059
	Gasoline	0	0	0.0211	0.0000	0.0000
	LPG	0	0	0	0	0.0583

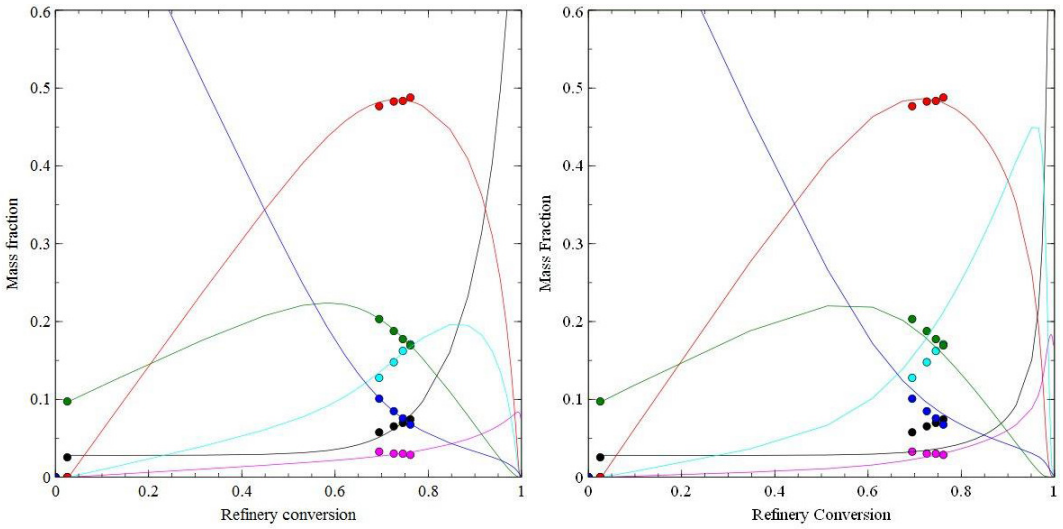

(a) (b)

Figure 10.- RPBm predictions for DCR unit, using a 6-lump (Figure 5(c)) reaction kinetic network. On the left, predictions from DCR experimental data. On the right, predictions for the DCR unit using kinetic network constants calculated with experimental data (under the same conditions) for an ACE unit.

3.2.**Effect of Matrix and Zeolite and Decoupling of the Contribution of Catalyst Components**

The third task of this work was to develop a predictive model for fluid catalytic cracking units, by utilizing the kinetic parameters estimated for single component catalytic systems in the prediction of multicomponent catalyst behavior. Fluid catalytic cracking selectivity is affected by both the zeolite and the matrix (support) of the catalyst. The zeolite is dispersed throughout the alumina silicate matrix and clay binder. Typical FCC catalysts consist of microporous zeolite, and macroporous support at various weight or surface area fractions. Each component of the catalyst contributes differently to the selectivity of the process towards valuable products such as gasoline, light cycle oil, liquid petroleum gas and less valuable byproducts such as dry gas and coke. Moreover, in industrial applications blends of catalysts of different compositions are often used to improve the overall activity and selectivity of the process. A computational model was developed to predict yields and conversion of cracking products through lumping of FCC components. The model incorporates different set of kinetics to account for multicomponent catalyst mixtures and accounts for differing yields of coke in a multicomponent catalyst mixture (i.e., a single blend of zeolite and matrix (support) in the same catalyst formulation, or blends of catalysts of different formulations). The model successfully uses the 6-lump KBm model to predict effects of changing zeolite to matrix ratios as well as mixing of two entirely different catalysts, without additional fitting of its kinetic parameters. Application of the model to laboratory-scale data of catalysts blends and to catalysts of different zeolite/matrix compositions is shown, analyzed, and explained using the model. Non-linearities in the experimental results and selectivity trends that would otherwise be impossible to understand are explained by analyzing the model predictions for the individual catalyst components. The model-based analysis of a large database of experiments performed by W.R. Grace & Co. was based on the following criteria and assumptions:

- The Kinetics-based model (KBm) was used.
- For the catalyst blends the same reaction network was employed twice (for each catalyst independently) assuming perfect mixing in the catalyst phase (ACE and DCR runs studied).
- Space time was split into time and catalyst-to-oil ratios times the fraction of each catalyst.
- Only catalyst deactivation functions based on coke-on-catalyst were used.

- For all the experimental data with catalyst blends the kinetic parameters and the catalyst decay constant were fitted using the experiments with each catalyst.
- In all the data shown, the blends have not been taken into consideration when fitting the kinetic constants and decay constants.
- Conradson Carbon Residue in the feed was not considered to affect catalyst activity (explained in detail later on).
- Same principles were applied to the Zeolite/Matrix study (considered as a mixture of two catalysts)
- Overall, the approach taken was that catalyst mixtures result in two kinetic networks in parallel (reactions in parallel).
- In a riser reactor the "time of experiment" is approximately equal to the residence time of the catalyst (neglect gas/solids slip, the residence time of the catalyst equals that of the gas phase).
- The time of experiment is an input (SCT-MAT: 9s, ACE: 30s, old MAT: 75s). A constant residence time of 5s for all the DCR experiments was assumed. Using the process model would make the following observations better and more accurate.
- Dry gas in risers is severely affected by the residence time in the disengager and the temperature of the regenerated catalyst. The prediction of dry gas is relatively inaccurate, but this is not the objective of this study.
- Coke on regenerated catalyst was assumed to be zero in all experiments. With an efficient regenerator this is a good approximation.

3.2.1.*Catalyst Blends in the DCR unit*

W.R. Grace & Co. DCR experiments with three feedstocks (Code Names: Feed I, II, and III) and two catalysts (Code Names: Cat A and Cat B) were used in the analysis of the performance of catalyst blends. The properties of the catalysts are shown in Table 4. The major difference between the two catalysts studied was the zeolite to matrix ratio, as Catalyst B had a high-surface area (mesoporous) matrix. Therefore, comparison between Catalysts A and B in this analysis is equivalent to comparing the contribution of the crystallic microporosity of the high-zeolite content Catalyst A with the amorphous mesoporosity of the matrix of Catalyst B.

Table 4.- Properties of catalysts used for the study of catalyst blends

	Catalyst A	**Catalyst B**	**Blend**
SA (m^2/g)	187	175	181
Zeolite (m^2/g)	149	92	122
Matrix (m^2/g)	38	83	59
Unit Cell	24.28	24.29	

Experiments with Catalysts A and B were performed in W.R. Grace & Co. in the DCR unit using similar conditions (riser temperature and catalyst to oil ratio for the three different feedstocks). The model developed splits the kinetic network for each catalyst (6-lump kinetic network in this case, as described in Section 2.2) and predicts the performance of the blend, using the kinetic constants estimated for the pure Catalysts A and B. Figure 11 shows the simulation of the DCR results for Catalysts A and B and the prediction of the selectivity of their blend; no fitting or model adjustment has been performed for the prediction of the DCR selectivity using the catalyst blend. The blend exhibits an overall average behavior. The blend behaves more like Catalyst B for bottoms, LCO and gasoline selectivity and more like Catalyst A for LPG and Coke selectivity. The model predicts all these trends very accurately.

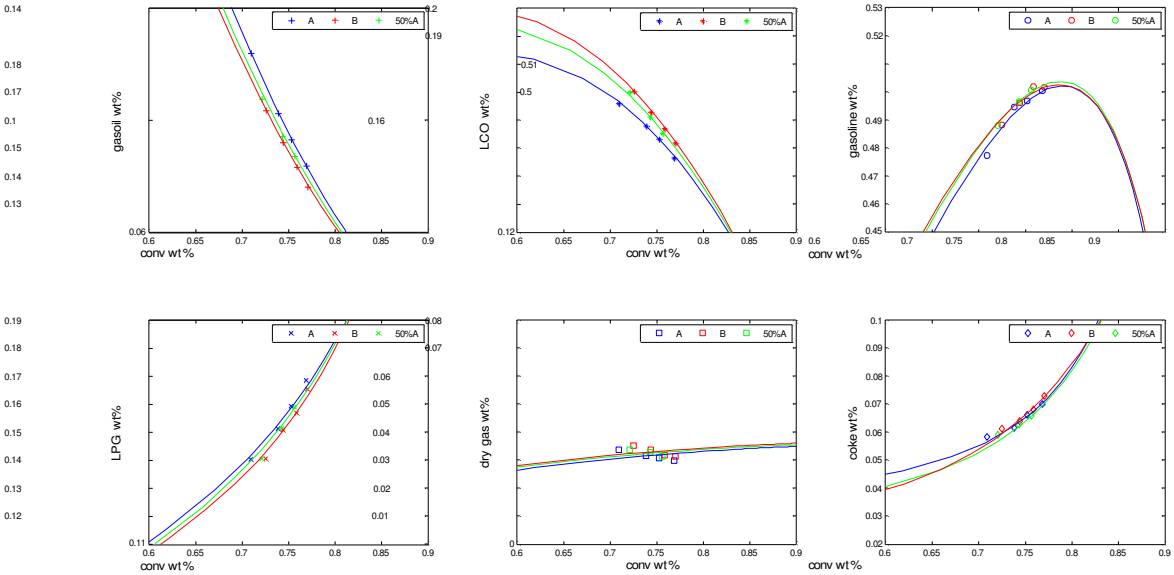

Figure 11.- KBm prediction for DCR tests with Catalysts A, B and their respective 50/50 blend for Feed I.

Feed I has a 5.1wt% Conradson Carbon Residue (CCR). The KBm uses 50% of the CCR as an initial value for the coke lump, while the remaining is assumed to yield bottoms (unconverted feed). However, in this model the catalyst deactivation function is an exponential function of the coke on catalyst. Using the initial coke yield (derived from the CCR) in the catalyst deactivation function resulted in much deactivated catalysts, low conversions and poor predictions (even for the pure catalysts). Therefore, it was assumed that CCR is not responsible for catalyst deactivation. *What this is implying is that CCR forms coke on any surface. It is not a catalytic product and as such it is formed on the matrix where deactivation is not important, instead of the zeolite where coke formation results in deactivation.* This novel finding resulted in improving all the predictions with the KBm for feedstocks with high CCR, while the prediction of testing results with low-CCR feedstocks were not affected by this assumption.

Because most of the coke yield comes from the CCR, the actual catalytic coke is smaller. Hence, deactivation of the catalyst is less significant and the overall behavior of the two catalysts and their blend is very similar. The analysis of the coke on catalyst content and the corresponding catalyst activity for the cases studied (Catalyst A, Catalyst B and the corresponding 50% blend) is shown in Figure 12. Evidently, the performance of each catalyst in the blend remains similar to the respective performance of the pure catalyst.

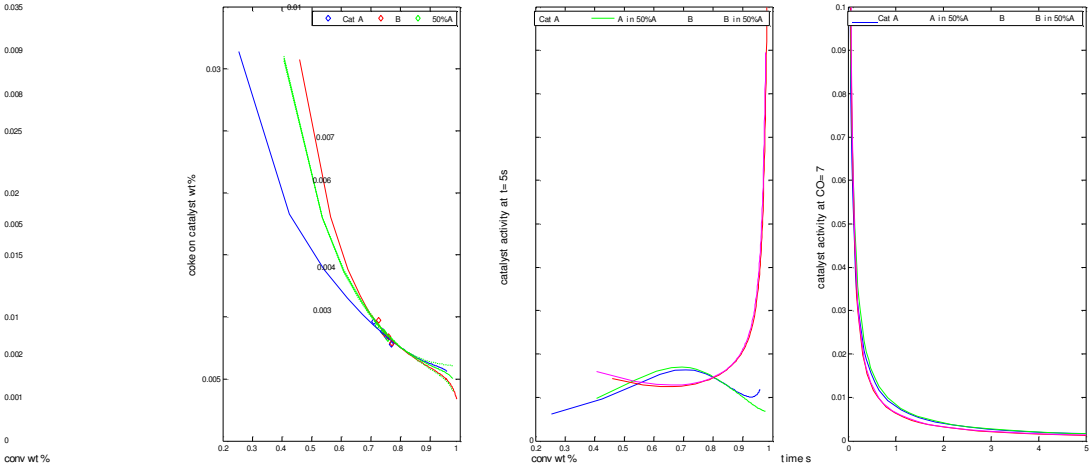

Figure 12.- KBm predictions of the coke on catalyst and catalyst activity for the experiments of Figure 11.

Figure 13 presents experimental and simulation results of the two catalysts in the DCR using Feed II. Observation of the experimental results *in conjunction with the model predictions*, tells a different story than trying to explain the results without the model. From the data one gets the impression that the gasoline selectivity of the blend is better than any of the pure catalysts. However, the results are actually an average of the two catalysts, but because the overcracking points of the two catalysts are very different, the bounds of the average switch (Catalyst B is more selective to gasoline at conversions below ~75wt% and Catalyst A is more gasoline selective at conversions >~75wt%). Coke yield and LPG predictions are almost perfect, and the model is able to predict that the blend will be more selective to LPG than the average of the two catalysts. Dry gas prediction is less accurate, which can be attributed to thermal cracking reactions and cracking in the disengager that were not taken into account. At small C/O ratios the model prediction is slightly off and this can be attributed to fluidization effects (less catalyst is used to establish the lower C/O ratios; thus, affecting the riser void fraction and contact efficiency). The major conclusion of this study is that t*he differences in the gasoline overcracking points between Catalysts A and B, give the impression of a strange (non-linear) behavior for their blend, but the model shows a simple close to average behavior for the blend.*

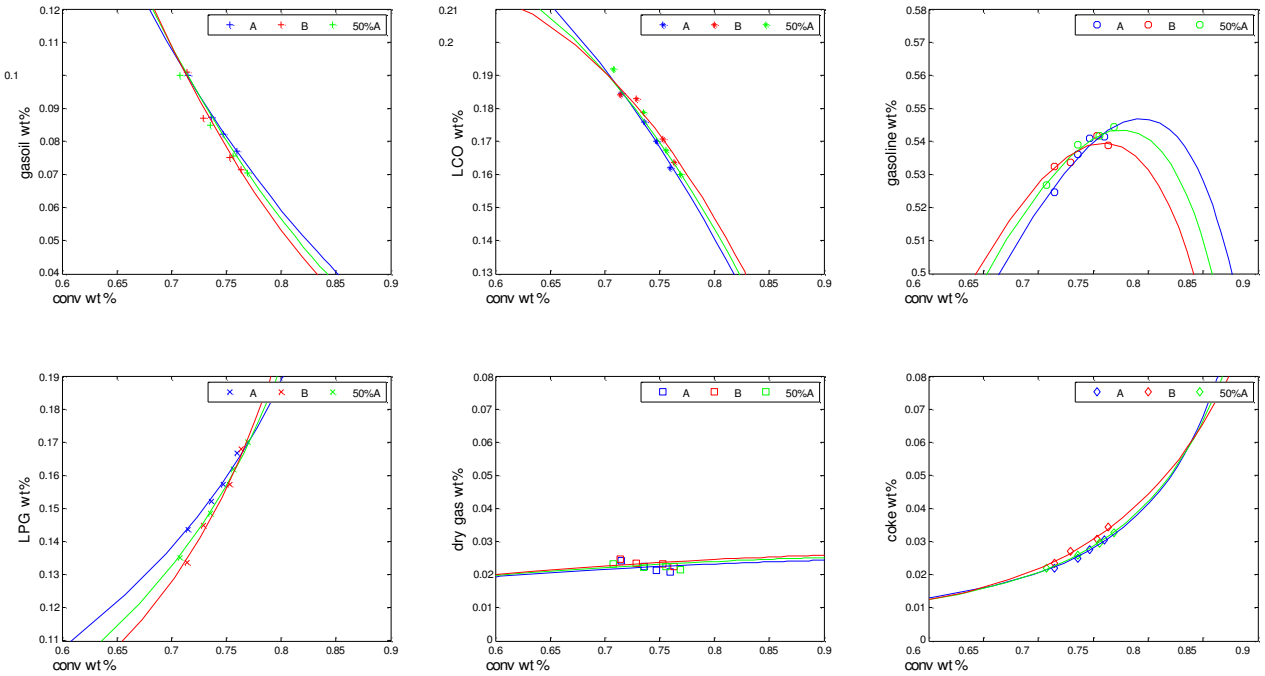

Figure 13.- KBm prediction of DCR test with Catalysts A and B and their respective 50% blend for Feed II.

Figure 14 presents coke on catalyst and catalyst decay profiles for Catalyst A and B and their respective blend. Catalyst A has a higher decay constant (higher catalyst activity retention) than Catalyst B. Again the activity of each catalyst in the blend is similar to the respective activity in the pure catalyst runs.

Figure 15 presents the prediction of the model for DCR experiments with Feed III. Remarkably, the prediction of the 50% blend is very accurate. *The model identifies that the blend will behave more like Catalyst A in terms of gasoline and coke yields, more like an average of the two for LCO and bottoms and that there will not be significant differences in LPG and dry gas.* Prediction of dry gas is also very good in this case. Feed III is a ~40vol% LCO feedstock. This value is used as initial in the model, and it is impressive how well the yields are predicted for such a light feed.

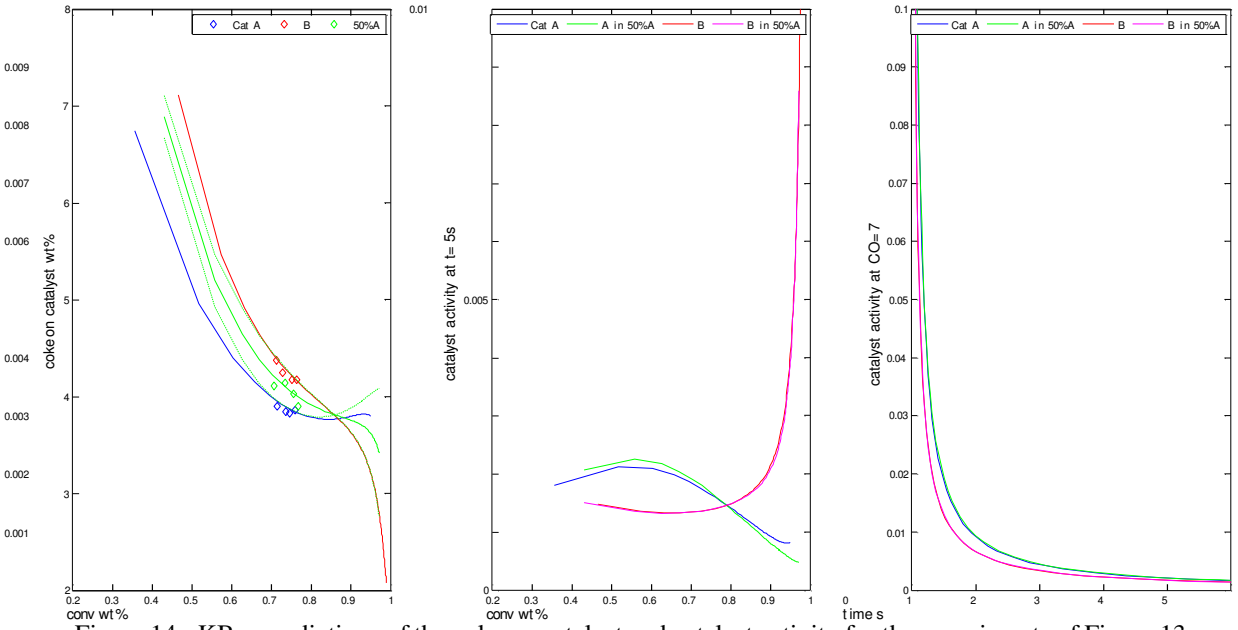

Figure 14.- KBm predictions of the coke on catalyst and catalyst activity for the experiments of Figure 13.

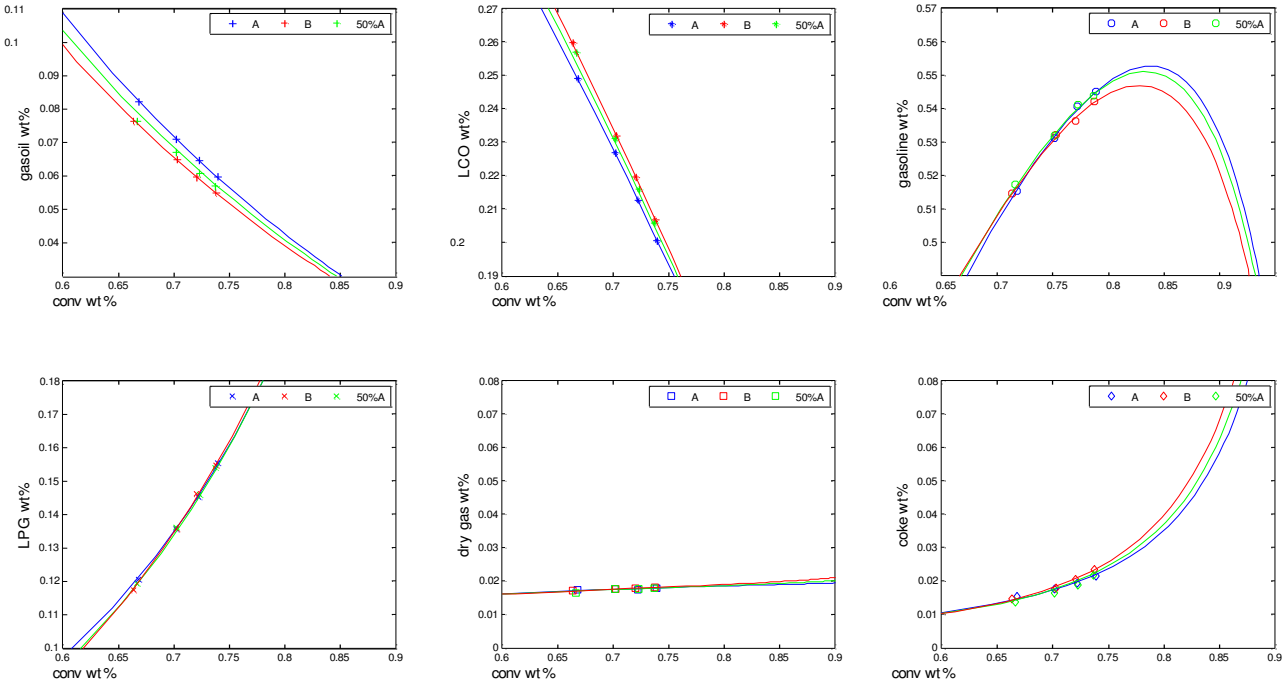

Figure 15.- KBm prediction for DCR tests with Catalysts A and B and their respective 50% blend for Feed III.

Figure 16 presents the profiles of coke on catalyst ad catalyst activity for the DCR experiment with Feed III. Overall (this is consistent in all the feedstocks and all the experiments), Catalyst A has a higher catalyst decay constant (*i.e.*, does not deactivate as quickly) than Catalyst B. This was clearly evident in the gasoline selectivity plot. *The blend forms more coke on Catalyst B, thus retaining the activity and selectivity of Catalyst A, resulting in a behavior that looks more like that of Catalyst A than an average of the two catalysts.*

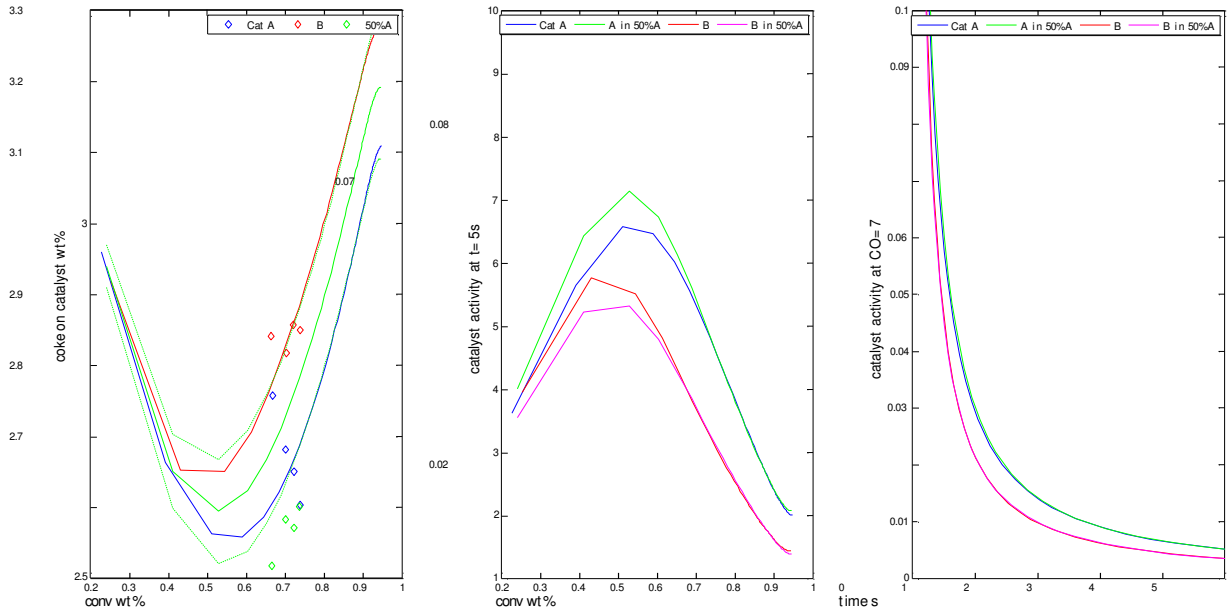

Figure 16.- KBm predictions of the coke on catalyst and catalyst activity for the experiments of Figure 15.

In summary, the model was capable of *predicting* the behavior of the blends very accurately *without additional fitting*. It seems that the behavior of the blends is not straight forward. Different conclusions are drawn from the different data, but from the behavior of the pure catalysts we are clearly able to explain the behavior of their blends and hopefully predict the behavior of future blends. The insights obtained from this work in combination with the model are valuable (for instance the remark about the lack of CCR contribution on catalyst deactivation from studying the data with Feed I). Application of the same concepts to the real process model, would eliminate a few of the assumptions used here and should improve the predictive capability of the model.

3.2.2.*Effect of zeolite and matrix (DCR unit study)*

To study the contributions of zeolite and matrix on catalyst selectivity, W.R. Grace & Co. performed experiments in the DCR with catalysts of varying zeolite/matrix ratios. As shown in Table 5, catalysts of progressively reducing zeolite content were prepared and evaluated.

Table 5.- Properties of catalysts used for the study of effects of zeolite and matrix

	Catalyst I	Catalyst II	Catalyst III	Catalyst IV
Zeolite	Base	Base - 5%	Base - 10%	Base - 15%
Matrix	Base	Base	Base	Base
Clay	Base	Base + 5%	Base + 10%	Base + 15%
Zeolite	40	35	30	25
Matrix	50	50	50	50
Clay	10	15	20	25

In the modeling of these data Catalysts I and IV were fitted to experimental data and all other catalyst performances were predicted (no other fitting or adjustments) using the KBm. The results of this analysis are shown in Figure 17. Overall, the model is shown to be predictive (when we fit one of the mixtures; in the absence of pure matrix experiments). However, due to the small differences in the catalysts prepared,

the available data are not ideal for this study. In general, decreasing the zeolite content, results in increased LCO yields, higher conversions, and only minor selectivity differences for the other lumps. The model was able to predict this behavior quite accurately.

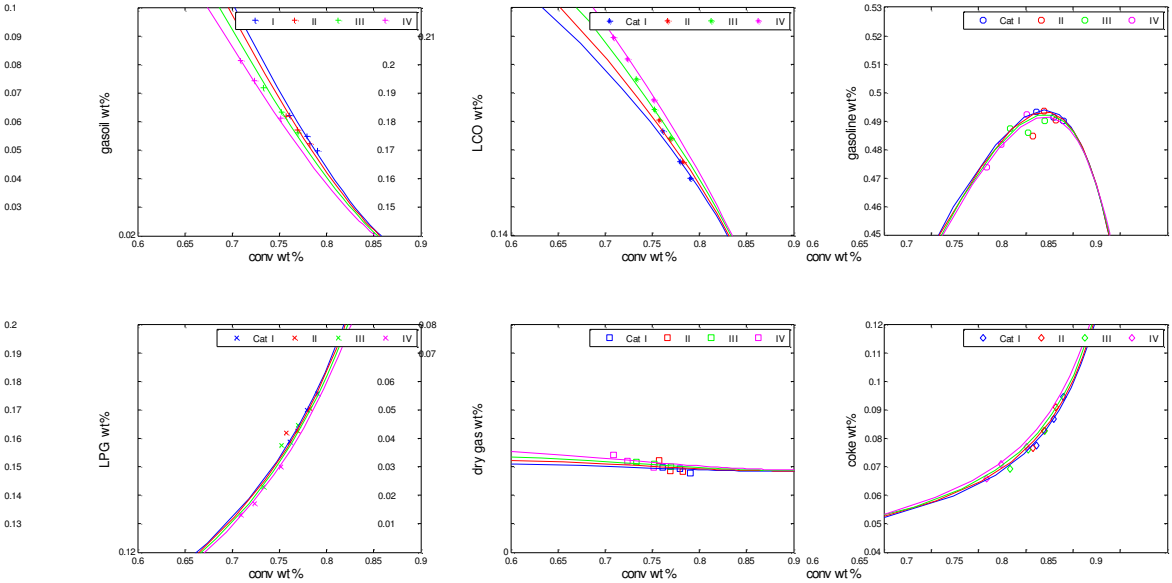

Figure 17.- **KBm prediction for DCR tests with catalysts of varying zeolite content.**

Of significance in this case are the kinetic constants that the model used to simulate the experimental data. Table 6 presents the kinetic constants estimated for the zeolite and the matrix for all the reactions of the 6-lump model, as well as the catalyst decay constant (exponential catalyst deactivation function of coke-on-catalyst used). Kinetic constants are in agreement with common know-how of FCC selectivity (matrix is responsible for pre-cracking and large molecules cracking). The model clearly predicts the pre-cracking since the only case where the kinetic constant of the matrix is higher than that of the zeolite is in the case of GO (gasoil) ->LCO (light cycle oil) reaction. The model also predicts that GO->DRY is an important reaction, which indicates that dry gas is mostly a thermal cracking product. Finally, LCO to GSL (gasoline) and LPG (light product gas) to COK (coke) are not negligible reactions.

Table 6.- Kinetic constants estimated for zeolite and matrix, using a 6-lump model and a decay function in terms of coke-on-catalyst

Reactant	Product	K_{ij} Zeolite	K_{ij} Matrx
GO	LCO	2.74E-02	1.53E-01
	GSL	1.03E+00	2.16E-02
	LPG	2.44E-01	1.43E-04
	DRY	4.76E-02	2.42E-02
	COK	3.68E-02	6.93E-08
LCO	GSL	3.10E-02	5.13E-03
	LPG	1.57E-06	3.66E-05
	DRY	5.31E-07	4.52E-05
	COK	5.71E-02	1.79E-07
GSL	LPG	1.59E-02	2.35E-09
	DRY	4.87E-06	2.58E-08
	COK	2.35E-08	7.42E-10
LPG	COK	1.46E-02	1.67E-03
α		4.24E+02	0.00E+00

4. Conclusions:

In this work, two different models have been developed to optimize FCC catalyst evaluation procedures. In the first approach (Kinetics-Based model, KBm), predictions of products yields in terms of conversion are calculated by solving sets of differential equations that depend on the reaction kinetic network scheme selected. For the second approach (Real-Process-Based model, RPBm), the system of differential equations solved, beyond involving the reaction kinetic network scheme selected, deals with hydrodynamic details of the units studied. For both approaches, a catalyst decay function that depends on the amount of coke-on-catalyst was used. The models have been developed for four different units: MAT, SCT-MAT, ACE and DCR units, widely used at W.R. Grace & Co.

Predictions of the models were compared against experimental data provided by W.R. Grace & Co. and very good agreements were found, for both the KBm and the RPBm. To study the behavior of different units for catalyst testing experiments, both models predict products yields for a wide range of conversion and allow a basis of comparison for different reactors under the same operational conditions (same feedstock and catalyst) and using the same assumptions (same reaction kinetic network and catalyst decay function). Thus, both models provide comparison of different units using the same metrics, which was not possible before. For fast and accurate predictions of products yields in terms of conversion, the KBm is a reliable tool. For more accurate studies involving a less empirical analysis of the data and more realistic predictions, the RPBm is the best tool to use.

The advantages of the models go beyond prediction of products yields for wider ranges of conversion than the experimental data. The models allow the prediction of products yields for one type of reactor using the kinetic network constants calculated for another type of reactor: (a) similar kinetic constants for different types of reactors (under the same conditions) were shown (b) predictions (using both models) for DCR units, using experimental data of ACE units, were proven to be similar to DCR experimental data. Finally, as the models have been deployed behind a friendly interface in Microsoft Excel, their usage will be incorporated in daily procedures at W.R. Grace & Co.

For the second part of the project, the model was capable of predicting the behavior of the blends very accurately without additional fitting. It seems that the behavior of the blends is not straight forward. Different conclusions are drawn from the different data, but from the behavior of the pure catalysts we are clearly able to explain the behavior of their blends and hopefully predict the behavior of future blends. The insights obtained from this work in combination with the model are valuable. Application of the same concepts to the real process model, would eliminate a few of the assumptions used during this project and should improve the predictive capability of the model. Moreover, it was shown that in general, decreasing the zeolite content results in increased LCO yields, higher conversions, and only minor selectivity differences for the other lumps. And again, the model was able to predict this behavior quite accurately.

Presentations:

1. George M. Bollas, Dariusz Orlicki, Hongbo Ma, *FCC selectivity studied in lab-scale units and pilot plants*, ACS Annual Meeting, August 2010, Boston MA USA
2. George M. Bollas, Dariusz Orlicki, Hongbo Ma, *Some uses and misuses of FCC catalyst testing experimental data*, AIChE Annual Meeting, November 2010, Salt Lake City UT USA
3. Monica Navarro, Dariusz Orlicki , George M. Bollas, *Detailed modeling of FCC selectivity in catalyst evaluation experiments. ACS National Meeting, San Diego, CA, March 25-29, 2012.*

Acknowledges:

Financial support from the Department of Energy (Sustainable Energy and Resources Utilization program) is gratefully acknowledged. Also, the authors thank W.R. Grace & Co. for financial support and permission to publish this work.

References:

1. G. M. Bollas, S. Papadokonstadakis, J. Michalopoulos, G. Arampatzis, A. A. Lappas, I. A. Vasalos, and A. Lygeros, "Using hybrid neural networks in scaling up an FCC model from a pilot plant to an industrial unit," *Chemical Engineering and Processing*, vol. 42, no. 8–9, pp. 697–713, Aug. 2003.
2. G. M. Bollas, I. A. Vasalos, A. A. Lappas, and D. Iatridis, "Modeling Small-Diameter FCC Riser Reactors. A Hydrodynamic and Kinetic Approach," *Industrial & Engineering Chemistry Research*, vol. 41, no. 22, pp. 5410–5419, Oct. 2002.
3. G. M. Bollas, I. A. Vasalos, A. A. Lappas, D. K. Iatridis, and G. K. Tsioni, "Bulk Molecular Characterization Approach for the Simulation of FCC Feedstocks," *Industrial & Engineering Chemistry Research*, vol. 43, no. 13, pp. 3270–3281, Jun. 2004.
4. G. W. Young and G. D. Weatherbee, "FCCU Studies with an Adiabatic Circulating Pilot Unit," in *AIChE Annual Meeting in San Francisco, CA*, 1989.
5. G. W. Young and G. D. Weatherbee, "FCCU Studies with an Adiabatic Circulating Pilot Unit," in *AIChE Annual Meeting in San Francisco, CA*, 1989.
6. L. T. Boock and X. Zhao, "Recent Advances in FCC Catalyst Evaluations: MAT vs. DCR Pilot Plant Results," in *Fluid Cracking Catalysts*, Occelli Mario L. and P. O'connor, Eds. 1998.
7. D. Wallenstein, R. H. Harding, J. Witzler, and X. Zhao, "Rational assessment of FCC catalyst performance by utilization of micro-activity testing," *Applied catalysis. A, General*, vol. 167, no. 1, pp. 141–155, 1998.
8. R. H. Harding, A. W. Peters, and J. R. D. Nee, "New developments in FCC catalyst technology," *Applied Catalysis A: General*, vol. 221, no. 1–2, pp. 389–396, Nov. 2001.
9. P. Hagelberg, I. Eilos, J. Hiltunen, K. Lipiäinen, V. M. Niemi, J. Aittamaa, and A. O. I. Krause, "Kinetics of catalytic cracking with short contact times," *Applied Catalysis A: General*, vol. 223, no. 1–2, pp. 73–84, Jan. 2002.
10. D. Wallenstein, M. Seese, and X. Zhao, "A novel selectivity test for the evaluation of FCC catalysts," *Applied Catalysis A: General*, vol. 231, no. 1–2, pp. 227–242, May 2002.
11. R. C. Vieira, J. C. Pinto, E. C. Biscaia, C. M. L. A. Baptista, and H. S. Cerqueira, "Simulation of Catalytic Cracking in a Fixed-Fluidized-Bed Unit," *Industrial & Engineering Chemistry Research*, vol. 43, no. 19, pp. 6027–6034, Sep. 2004.
12. "Kayser Technology, Inc." [Online]. Available: http://kaysertech.com/downloads.htm.
13. V. W. Weekman, "Model of Catalytic Cracking Conversion in Fixed, Moving, and Fluid-Bed Reactors," *Industrial & Engineering Chemistry Process Design and Development*, vol. 7, no. 1, pp. 90–95, Jan. 1968.
14. L. C. Yen, R. E. Wrench, and A. S. Ong, "Reaction kinetic correlation equation predicts fluid catalytic cracking coke yields," *Oil & Gas Journal*, pp. 1–5, 1988.
15. L.-S. Lee, Y.-W. Chen, T.-N. Huang, and W.-Y. Pan, "Four-lump kinetic model for fluid catalytic cracking process," *The Canadian Journal of Chemical Engineering*, vol. 67, no. 4, pp. 615–619, Aug. 1989.
16. J. Corella and E. Frances, *Fluid Catalytic Cracking II*, vol. 452. Washington, DC: American Chemical Society, 1991, pp. 165–182.
17. X. Dupain, E. D. Gamas, R. Madon, C. P. Kelkar, M. Makkee, and J. A. Mouli n, "Aromatic gas oil cracking under realistic FCC conditions in a microriser reactor☆," *Fuel*, vol. 82, no. 13, pp. 1559–1569, Sep. 2003.
18. M. Larocca, S. Ng, and H. I. de Lasa, "Fast catalytic cracking of heavy gas oils: modeling coke deactivation," *Industrial & Engineering Chemistry Research*, vol. 29, no. 2, pp. 171–180, Feb. 1990.
19. J. Ancheyta-Juarez, F. Lopez-Isunza, and E. Aguilar-Rodriguez, "5-Lump kinetic model for gas oil catalytic cracking," *Applied Catalysis A: General*, vol. 177, no. 2, pp. 227–235, Feb. 1999.
20. T. Takatsuka, S. Sato, Y. Morimoto, and H. Hashimoto, "A Reaction Model for Fluidized-Bed Catalytic Cracking of Residual Oil," *International Chemical Engineering*, no. 27, pp. 107–116, 1987.

21. L. L. Oliveira and E. C. Biscaia, “Catalytic cracking kinetic models. Parameter estimation and model evaluation,” *Industrial & Engineering Chemistry Research*, vol. 28, no. 3, pp. 264–271, Mar. 1989.
22. B. W. Wo ciechowski and A. Corma, “Catalytic cracking: Catalysts, chemistry, and kinetics,” Jan. 1986.
23. S. M. Jacob, B. Gross, S. E. Voltz, and V. W. Weekman, “A lumping and reaction scheme for catalytic cracking,” *AIChE Journal*, vol. 22, no. 4, pp. 701–713, Jul. 1976.
24. R. C. Ellis, X. Li, and J. B. Riggs, “Modeling and Optimization of a Model IV Fluidized Catalytic Cracking Unit,” *AIChE Journal*, vol. 44, no. 9, pp. 2068–2068, 2004.
25. C. I. C. Pinheiro, J. L. Fernandes, L. Domingues, A. J. S. Chambel, I. Graça, N. M. C. Oliveira, H. S. Cerqueira, and F. R. Ribeiro, “Fluid Catalytic Cracking (FCC) Process Modeling, Simulation, and Control,” *Industrial & Engineering Chemistry Research*, vol. 51, no. 1, pp. 1–29, Jan. 2012.
26. J. Singh, S. Kumar, and M. O. Garg, “Kinetic modelling of thermal cracking of petroleum residues: A critique,” *Fuel Processing Technology*, vol. 94, no. 1, pp. 131–144, Feb. 2012.
27. M. R. Viner and B. W. Wo ciechowski, “The chemistry of catalyst poisoning and the time on stream theory,” *The Canadian Journal of Chemical Engineering*, vol. 60, no. 1, pp. 127–135, Feb. 1982.
28. A. Corma, F. V. Melo, and L. Sauvanaud, “Kinetic and decay cracking model for a MicroDowner unit,” *Applied Catalysis A: General*, vol. 287, no. 1, pp. 34–46, Jun. 2005.
29. A. Voorhies, “Carbon Formation in Catalytic Cracking,” *Industrial and Engineering Chemistry*, vol. 37, no. 4, pp. 318–322, 1945.
30. V. W. Weekman and D. M. Nace, “Kinetics of catalytic cracking selectivity in fixed, moving, and fluid bed reactors,” *AIChE Journal*, vol. 16, no. 3, pp. 397–404, May 1970.
31. G. Jimenez-Garcia, R. Quintana-Solorzano, R. Aguilar-Lopez, and R. Maya-Yescas, “Modelling Catalyst Deactivation by External Coke Deposition during Fluid Catalytic Cracking,” *International Journal of Chemical Reactor Engineering*, vol. 8, no. 1, 2010.
32. D. Kunii and O. Levenspiel, “Bubbling Bed Model. Model for Flow of Gas through a Fluidized Bed,” *Industrial & Engineering Chemistry Fundamentals*, vol. 7, no. 3, pp. 446–452, Aug. 1968.

Project Title: Evaluation of the performance of rapidly quenched YSZ electrolyte in a SOFC and its comparison with conventional SOFC architecture. Development of Micro Direct Methanol Solid Oxide Fuel Cells for Portable Electronic Applications.
Partner: NanoCell systems Inc.
PI: Radenka Maric

1. Introduction

The objective of the work described herein is to establish an R&D base for the energy efficient manufacture of micro-Solid Oxide Fuel Cells in an integrated production line. In the current research program, emphasis has been on the morphological and electrochemical properties of 8Mol% yttria-stabilized-zirconia (8YSZ) synthesized by rapid quenching from high enthalpy thermal plasma. This technology attractiveness is in producing “far-from-equilibrium” nanostructured YSZ layers and thin films using simple aqueous precursors as a part of an integrated fabrication process. In the project as reported previously, research findings were presented on agglomerated YSZ nano powder synthesized by rapid water quenching from DC thermal plasma. This part of the investigation included analysis of crystal structure, and morphology following thermal treatment. Additionally, the investigation included a study of crystal structure, morphology, and electrical conductivity in consolidated YSZ material. In what follows, we describe continued work on structural and kinetic properties as determined by Raman spectroscopy and differential scanning calorimetry (DSC). In analyzing this work, it has proved to be instructive to compare the results with those obtained by other technologies, specifically spray pyrolysis and wet chemistry synthesis.

2. Experimental

2.1 Raman Spectroscopy

As has been pointed out (1), Raman spectroscopy, in contrast to X-ray diffraction, is especially sensitive to the local symmetry and sensitive both to oxygen ion displacements due to large polarizability (1) and to localized order. As discussed in the literature, the Raman spectra for the cubic phase exhibits a single peak at 617cm^{-1} attributable to the O-Zr–O stretching mode in F2g symmetry. Displacement of the oxygen ions along the [100] direction results in a transition from cubic to tetragonal symmetry. As a result of lower symmetry tetragonal zirconia and 8YSZ exhibit peaks around 474 cm^{-1} and 647 cm^{-1} (assigned to the E_g symmetry), and around 260cm^{-1}, 346$cm^{-1}$and 600cm^{-1} attributed to an $A1_g$ or $B1_g$ symmetry, see Table I.

Table I

YSZ Phase	Raman shift (cm^{-1})	Mode
cubic	617.2	F_{2g} symmetric O-Zr-O stretching
tetragonal	256.5	E_g O_{II}-Zr-O_{II} stretching
"	318.2	B_{1g} coupled Zr-O bending & stretching
"	460.7	E_g coupled Zr-O bending & stretching
"	603.4	A_{1g} symmetric O-Zr-O stretching
"	640.0	E_g asymmetric O-Zr-O stretching

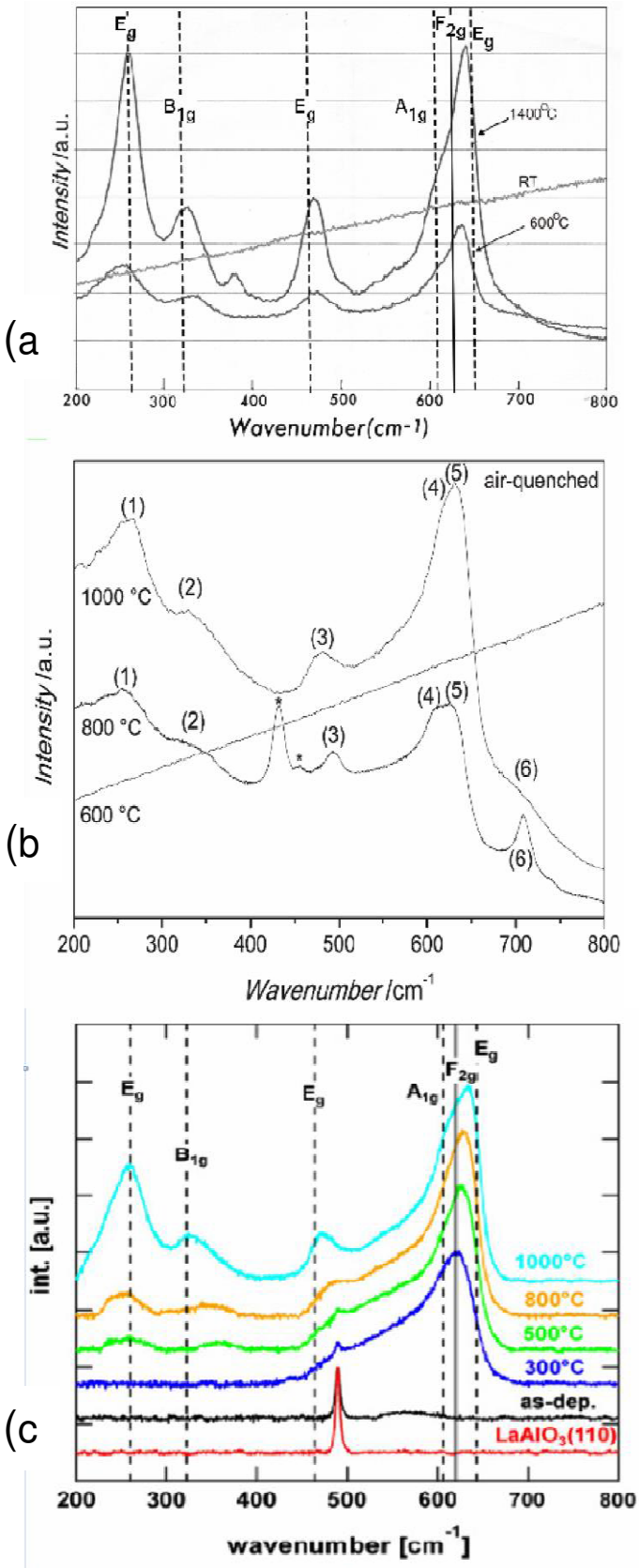

Figure1(a) shows recently obtained Raman spectra from plasma quenched 8YSZ, in Figs.1(b&c) this data is compared with spectra obtained from nanostructured 8YSZ synthesized by spray deposition (2) and laser sputtering (3). As noted in Fig.1(a), there is no detectable spectra at room temperature for as-synthesized material. We note that a similar situation was obtained by Scherrer et al (2) in Raman spectra of YSZ powders synthesized by spray pyrolysis and following 600°C heat treatment, see Fig.1(b). In the case of plasma quenched material however (see Fig1 (a)} clearly defined tetragonal peak are evident. This feature is clearly indicative of the preference of plasma quenching over spray pyrolysis. As seen in the spectra for 8YSZ thermally treated for two hours at 1400°C a particularly well-defined tetragonal structure is evident. This result is consistent with previous XRD studies. Finally, it is significant to note the Raman spectra in plasma quenched material to that synthesized by laser sputtering as shown in Fig.1(c). However, as will be discussed, the plasma quenching methodology has the distinctive advantage of scalability for large-scale manufacture. An incidental feature of Raman spectroscopy, it is noted, is its amenability for monitoring reactive species during plasma and flame synthesis. This has significant potential for feed back control for quality assurance purposes

Fig.1 Raman spectra for (a) plasma quenched nanostructured YSZ in the as-synthesized condition & after 2 hours treatment at 600°C & 1400°C. Comparative spectra from the literature (2,3) for materials synthesized by spray pyrolysis & laser sputtering are shown in (b) & (c).

2.2 DSC Kinetics Study

For further elucidation of crystallization kinetics in plasma quenched YSZ, DSC data was collected at different heating rates. As shown in Fig. 2 two exothermic processes are observed with peak temperatures (T_{C1}, T_{C2}) between 400°C and 900°C. From this data the Kissinger equation was used to obtain the plot shown in Fig.3 where the linear slope gives the activation energy. For the first reaction in the region of 400°C, the activation energy is 69.4kJ.mol^{-1}. For the second reaction between 650°C-700°C the activation energy is 125.5kJ.mol^{-1}. The T_{C1} peak temperature of the first reaction at 400°C corresponds to crystallization, as reported in literature, that occurs between 320°C to 540°C with activation energies ranging from 119kJ.mol^{-1} and 32 kJ.mol^{-1}. (4-6,14). The T_{C2} peak temperatures shown in Fig.2 appears to correspond to that described by Scherrer et al (ref) that is discussed below.

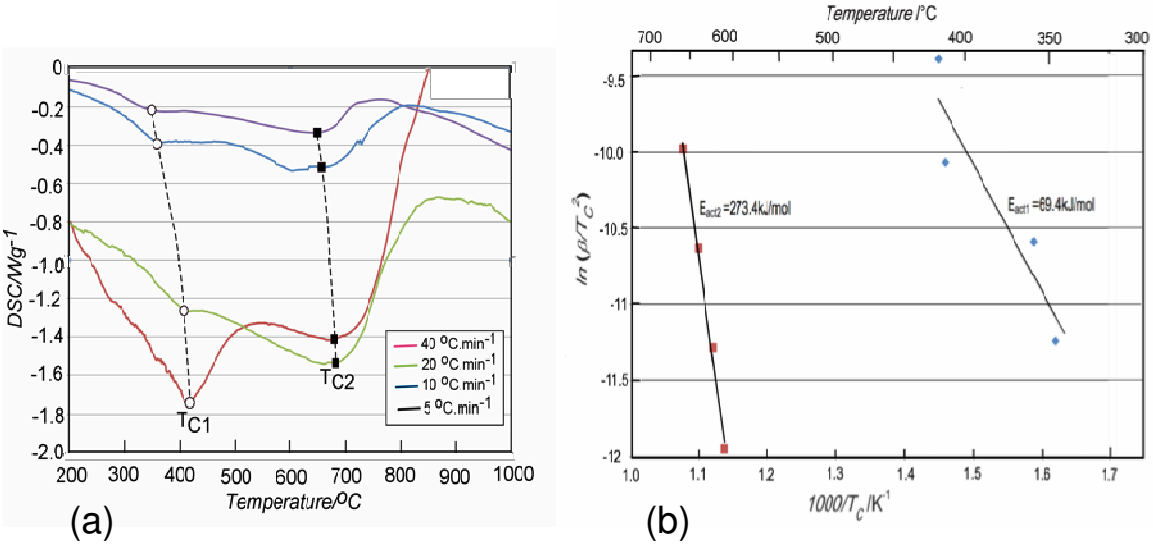

Fig.2 (a) Non-isothermal crystallization of plasma quenched YSZ in static air displaying exothermic DSC heat release. (b) Kissinger (7) plot of the data peaks T_{C1} and T_{C2} displayed in (a) to determine the activation energies.

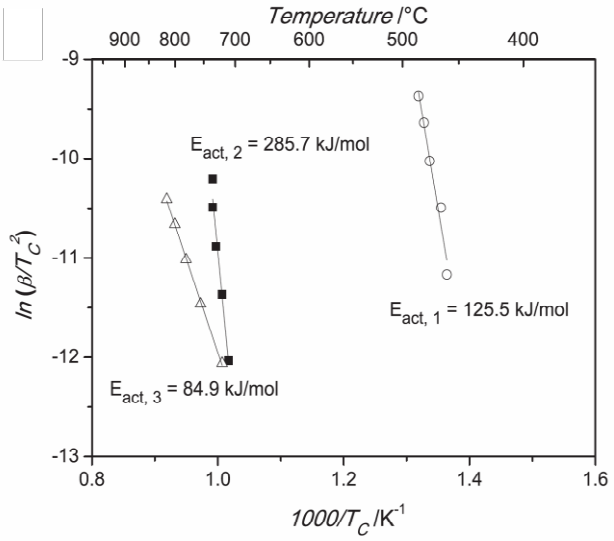

A noticeable feature in comparing data presented in Fig. 2 with that for spray deposited nanostructured YSZ is a shift of reactions to a lower temperature. This is evident in comparing data in Fig.2(b) with that of Scherrer feature is the absence of evidence of a third reaction peak at a temperature beyond 700°C with an activation energy of 84.9kJ/mol. that Scherrer et al (2) assign to the release of carbon dioxide and water.

Fig.3 Kissinger (7) plot of the data peaks obtained by Scherrer et al (2) for spray deposited nanostructured YSZ obtained by non-isothermal heat treatment.

3. Discussion

Pursuit of the research described above complements and confirms previous research findings on nanostructured YSZ synthesized by far-from-equilibrium processing. This includes the production of a non-transformable tetragonal material retaining its crystal structure of nanocrystalline dimensions up to at least 1400°C. From an industrial standpoint, the thermal spray rapid quenching clearly offers a viable route for producing large amounts of nanopowder material at low cost. Additionally, it has the potential for forming micro and nano-layers over large areas in the manufacture of micro-SOFCs.

It is noted that documented crystallization kinetic data is a necessary prerequisite for establishing a reliable and optimized processing methodology. To date, only gels and powders synthesized by wet chemistry that crystallization characteristics have received detailed attention (8–13). In these cases crystallization consistently occurs at temperatures ranging from 400–500°C following solvent evaporation at lower temperatures. A notable feature of these studies is the significant scatter in values of the activation energies with values ranging from as small as ~13 kJ/mol (14) up to 232 kJ/mol (11). As noted by Heiroth et al (3), this feature appears to indicate how precursor and solvent selection in chemical processing may strongly influence phase transformation and grain growth mechanisms. Concerning the activation energies, it is also noted that values in the range of ~500kJ/mol are characteristic of those for bulk diffusion controlled processes, whereas surface or grain boundary diffusion control typically yields lower values ranging from 10 to 100kJ/mol. For comparison Chien and Heuer (15) report an activation energy of 511.4±10 kJ/mol for the Zr diffusion in single crystalline YSZ vacancy exchange.

From consideration described above, the characterization studies conducted in the present program provide a base for industrial development of plasma quenched material. This may be either as a powder or deposited layers for use in fabricating micro-SOFCs and other devices. Distinctive methodological advantages include (i) negligible weight loss during heat treatment, (ii) a durable non-transformable tetragonal nanostructured YSZ base, and (iii) crystallization kinetics occurring at a relatively low temperature. These considerations are highly pertinent in considering SOFC architecture using the methodology proposed by Maric, Furusaki, Nishijima, & Neagu (16). Conceptually, this facilitates fabrication of a planar micro-SOFC array assemblies on a durable porous Ni-YSZ base-anode surmounted with a thin YSZ electrolyte layer of microscale or nanoscale thickness. In principle, this methodology is envisaged to facilitate fully integrated fabrication with continuous in-line production sequence utilizing thermal plasma or flame sequential layer deposition. As mentioned previously, using Raman diagnostics it becomes possible, in this system, to continuously monitor reactive species in the f flame, and then employ feedback control to maintain product consistency.

4. References

1. C. Viazzi, Bonino, J.-P., Ansart, F., & Barnabé, A. (2008). *Journal of Alloys and Compounds*, *452*(2), 377
2. B. Scherrer, Heiroth, S., Hafner, R., Martynczuk, J., Bieberle-Hütter, A., Rupp, J. L. M., & Gauckler, L. J. (2011) *Advanced Functional Materials*, *21*(20), 3967
3. S, Heiroth, Frison, R., Rupp, J. L. M., Lippert, T., Barthazy Meier, E. J., Müller Gubler, E., Döbeli, M., et al. (2011). *Solid State Ionics*, *191*(1), 12
4. J. L. M. Rupp, Scherrer, B., Harvey, A. S., & Gauckler, L. J. (2009). *Advanced Functional Materials*, *19*(17), 2790
5. Y.Z. Jiang, H.Z. Song, J.F. Gao, G.Y. Meng, J. Electrochem. Soc. 152 (2005), C498
6. D. Perednis, O. Wilhelm, S.E. Pratsinis, L.J. Gauckler, Thin Solid Films 474 (2005) 84.

7. H. E. Kissinger , Anal. Chem. 1957, 29, 1702 .
8. A. Aronne, A. Marotta, P. Pernice, M. Catauro, Thermochim. Acta 275 (1996) 75–82.
9. D.Y. Chen, E. Jordan, M. Gell, J. Mater. Sci. 42 (2007) 5576–5580.
10. A. Ghosh, D.D. Upadhyaya, R. Prasad, J. Am. Ceram. Soc. 85 (2002) 2399–2403.
11. C.W. Kuo, Y.H. Lee, I.M. Hung, M.C. Wang, S.B. Wen, K.Z. Fung, C.J. Shih, J. Alloy Compd. 453 (2008) 470–475.
12. S. Ramanathan, R.V. Muraleedharan, S.K. Roy, P.K.K. Nayar, J. Am. Ceram. Soc. 78 (1995) 429–432.
13. S. Ramanathan, N.C. Soni, R. Prasad, J. Mater. Sci. Lett. 12 (1993) 122–124.
14. S. Shukla, S. Seal, R. Vij, S. Bandyopadhyay, Nano Lett. 3 (2003) 397–401.
15. F.R. Chien, A.H. Heuer, Philos. Mag. A 73 (1996) 681
16. R. Maric, Furusaki, K., Nishijima, D., & Neagu, R. (2011). ECS Trans. 2011, Volume 35, Issue 1, 473

Project Title: Gasification Technology and Clean-Up for Integration with Solid Oxide Fuel Cell
PI: Radenka Maric

Introduction:
Sustainable management of biosolids remains a challenge for wastewater utilities and agencies across North America. Traditional practices such as agricultural land application are becoming increasingly more difficult because of rising costs, regulatory uncertainty and public opposition. With growing awareness of climate change and with the growing need to reduce dependence on foreign oil, utilizing renewable fuels for energy is increasing in importance.

The agriculture and food processing industries as well as the wastewater treatment industry have realized there are significant energy resources contained in those waste products. Globally, there is an ever increasing demand for energy especially as population density increases in urban areas which is now the trend. Energy consumption and production to meet that demand may be the most significant challenge of the 21st Century. Global energy demand is increasing at an incredibly fast rate - the Energy Information Agency (EIA) of the U.S. Department of Energy (DOE) estimated that world energy use will climb 50% over a predicted period from 2009 to 2035. Coupled with the growing energy demand is the high use of energy for treatment of waste products. For example, in the United States, wastewater treatment plants use 3% of all of the energy generated. It is one of the highest energy dependent industries.

Wastewater residuals are a significant renewable energy source. Domestic primary and secondary biosolids (wastewater residuals), prior to any type of stabilization such as anaerobic digestion, contain 16-20 MJ/kg (8000-9000 BTU/lb). This is equivalent to 2.3-2.6 kWh/lb about the same energy value as low grade coal (NACWA, 2010).

The goal is to capture as much of these resources as possible. Organizations such as the Water Environment Federation (WEF.org) have issued position statements on resource recovery from wastewater and have identified wastewater treatment plants as “Resource Recovery Facilities” (WEF, 2011). WEF’s position statement states that “wastewater treatment plants are not waste disposal facilities, but rather water resource recovery facilities that produce clean water, recover nutrients (such as phosphorus and nitrogen), and have the potential to reduce the nation’s dependence upon fossil fuel through the production and use of renewable energy. Energy derived from wastewater treatment is a renewable energy resource”. Furthermore, agricultural waste contributes to the continued degradation of rivers and other waterways, so the agricultural industry is looking at improved methods of disposal and food processor are investigating ways of capturing energy from their waste products.

With this in mind, the Center for Clean Energy Engineering (C2E2) is investigating ways of capturing energy from wastewater biosolids, agricultural waste (chicken manure) and food waste (cafeteria). The process chosen for this is gasification. Gasification is the thermochemical conversion of carbon based fuels. The product of gasification is a synthesis or producer gas commonly called syngas which is composed of hydrogen, carbon monoxide and other gases depending on the fuel. Syngas can be used to provide heat energy or as a fuel in internal combustion engines or fuel cells to generate electricity and provide heat (combined heat and power, CHP). The ash produced from biosolids or chicken manure in the gasification process can be used as a soil conditioner since it contains a fairly high concentration of phosphorus or it can be used as an aggregate in asphalt and concrete or in the manufacture of engineered tiles and stones.

One of the biggest disadvantages of gasification is the formation of tars, such as, benzene, naphthalene, acenapthalene, fluorine, phenanthrene, pyrene and chrysene. Because of the presence of these tars, significant gas clean-up is required before the gas can be used as a fuel in internal combustion engines or fuel cells. In order for these waste products to be used as a renewable energy source, it is critical to understand how the materials gasify, the quantity and quality of syngas produced, the quantity and characteristics of the tars and the quantity of ash and condensate produced. Most important is to determine methods for gas cleanup for either internal combustion (IC) engines or fuel cells. Fuel cells have higher energy conversion efficiency than IC engines and a much cleaner exhaust and would be the preferred way of generating power.

Figure 1 Plot Gasification Unit

The City of Stamford Water Pollution Control Authority (WPCA) under a grant from the Department of Energy, designed and built a mobile pilot gasifier. This unit was no longer being used by the WPCA and they donated it to C2E2 for further gasification research. The following report describes the project, discusses refurbishing and modifications of the pilot unit, operating procedures, results to date and future work.

Figure 2 Feed Hopper

Project Description

The project involve the use of the pilot gasification system (Figure 1) to develop information relating to gasification of various waste products so as to understand the characteristics of synthetic gas and tars produced from these waste materials and develop methods to clean the gas making it suitable for use in either internal combustion engines or fuel cells to generate power.

Figure 3 Particulate Separator

Process Description: The gasification system used for this project is classified as a downdraft gasifier. Feedstock is introduced through a hopper (Figure 2) at the top of the reactor. Air is forced through the reactor using an air compressor. The tar laden syngas flows from the reactor to a cyclone particle separator (Figure 3) where particulates and condensate are removed. The hot syngas then flows through a heat exchanger (Figure 4) which consists of an inner stainless steel coil and an outer copper coil. A mixture of water and glycol, externally cooled using an air conditioning unit, flows through these coils while the syngas passes around the coils. As the gas is cooled, water and some tar condense along the coils and walls of the heat exchanger.

Figure 4 Heat Exchanger

After the heat exchanger, the gas stream passes through a series of filters to remove tar and moisture. The first filter is the coarse filter (Figure 5) containing a perforated basket filled with charcoal on which the tars condense. This tar-covered charcoal may then be used as a high energy feedstock since the tars have a high BTU value. The basket is tightly wrapped with household insulation to insure a tight fit within the filter and act as an additional tar and moisture filter.

Figure 5 Coarse and Moisture Filters

The next filter is the moisture filter (Figure 5). Similarly to the coarse filter, the moisture filter contains a perforated basket wrapped in insulation. The bottom layer of the basket is a floor buffer pad. Above the buffer pad is a six-inch layer of wood stove pellets. The final layer is charcoal briquettes. The tar covered wood and charcoal can also be used as a high BTU feedstock. The syngas then flows through a fine filter (Figure 6) composed of a sheet of steel wool rolled into a cylinder. After the fine filter, the syngas then flows through the elevated biofilter and then to a flare where it is burned. A propane fired generator is used to provide power to all of the electrical motors and systems.

Figure 6 Fine Filter

Work Plan: The initial work plan include the following steps:

- Disassemble and clean all components including gasifier, heat exchanger, filters, piping, etc.
- Install forced air system
- Install instrumentation
- Install new air pollution and flare system
- Develop sampling, testing, start-up and safety plans
- Startup unit to become familiar with operation and troubleshoot operation
- Collect gas and condensate samples for initial analysis

Disassembly, Inspection and Cleaning: The unit was completely disassembled. Each piece of equipment and piping was inspected. The interior of the gasifier had accumulated ash, tar and vitrified material (Figure 7). Much of the piping had accumulations of tars and soot (Figure 8). Prior to cleaning the unit, we developed a protocol which included providing MSDS for each potential product, personal protective equipment, sealed containers for waste materials as well as disposal criteria for these materials meeting all environment regulations.

Figure 7 Ash and tar in gasifier

Figure 8 Tar accumulations in piping

Over about an eight-week period, the gasifier interior and all piping was cleaned. Some valves were replaced or repaired, all gaskets were replaced, the gasifier and much of the piping leading to the cyclone was insulated, new components were purchased and/or fabricated and the entire system reassembled.

An air purging system was added to the site glass to ensure continuous visibility during operation. Additionally, the electrical system was inspected and rewired and the generator was modified, repaired and tested.

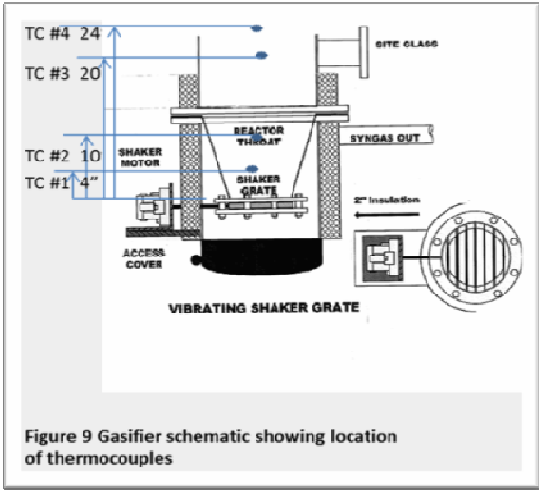

Figure 9 Gasifier schematic showing location of thermocouples

Air System Modification: The original pilot unit was operated with an induced draft system. After consideration, the project team recommended a forced air system. The draft fan was removed and a new piping configuration was installed along with two compressors; 1/3 hp and 1.8 hp. The total airflow through the system from these compressors is 12 cfm.

Instrumentation: The existing four thermocouples in the gasifier were replaced using the same locations as the existing ones (Figure 9). In addition to these four, a thermocouple was placed at each gas sampling port. Pressure sensors were also installed at various locations throughout the process such as before and after the filters to determine pressure loss due to accumulated material. A schematic of all instruments and their locations is depicted in Figure 10.

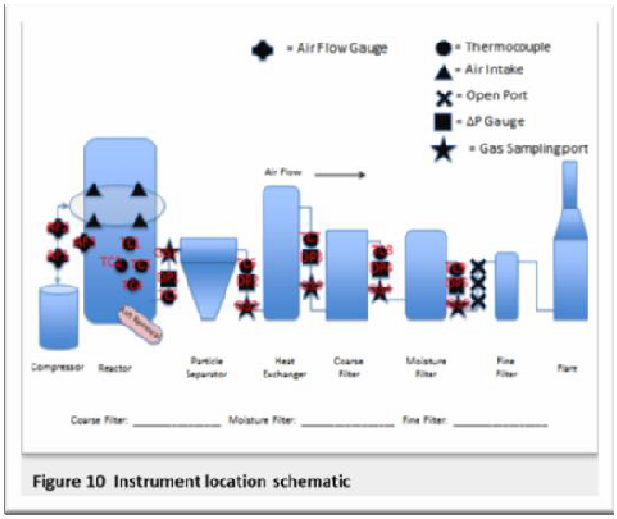

Figure 10 Instrument location schematic

Figure 11 Biofilter and flare

Air Pollution and Flare System: A biofilter was built for air pollution control (Figure 11). When the pilot unit is in operation, syngas passes through a layer of wood chip and activated carbon (charcoal) to remove particulates and remaining tar. The gas is then goes to a flare with an automatic ignition system. Once an ignitable gas is produced, the ignition system is activated.

Gasifier Throat Modification: Based on the results from numerous process runs, it appeared that the feed rate for the existing design would require a considerable amount of fuel. By reducing the size of the throat, the feed rate would be significantly lower and makes the pilot unit more practical. An insert was designed by Leonard Bonville and is shown in schematic in Figures 12. The insert was made from a 4.5 inch steel pipe with six- ½ inch steel air tubes and a 1.5 inch hole in bottom plate and was installed in the gasifier unit. The modified unit was placed in service on November 28 and performance was very good. The modified unit was used from November 28 through December 12. Figure 13 shows the insert in place in the gasifier after the December 3 run. This modification will be used for all future runs.

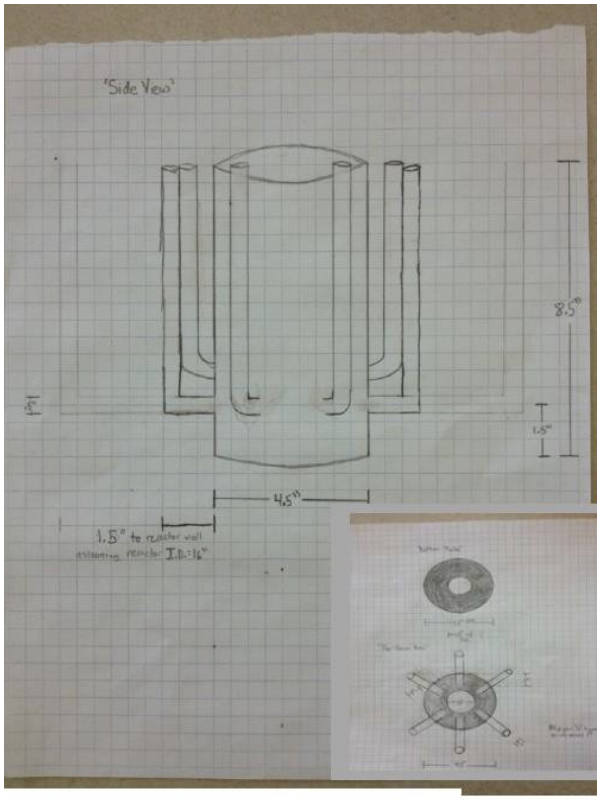

Figure 12 Throat Modification

Sampling and Testing Plans: The purpose of the sampling and testing plan was to establish a standard procedure for collection and analysis of all samples associated with the gasification process with the objective of generating accurate and reproducible data which can be used to

- correlate operating conditions with gas quality,
- optimize process and
- calculate mass balances

The current sampling locations (Figure 10) include: Ash (bottom of gasifier); Condensate (from particulate separator, drain from heat exchanger, drain from filters and bottom of biofilter); Gas (after particulate separator and before heat exchanger, after heat exchanger and before filters, between moisture filter and coarse filter, after coarse filter and before fine filter, and after fine filter). An example of a gas sampling port is shown in Figure 14.

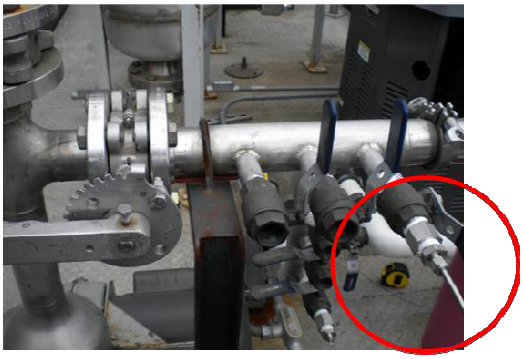

Figure 14 Gas sampling port

Gas samples are taken in Tedlar bags (Figure 15). Gas is sampled by connecting the valve on the gas bag to a pump which is connected to the valve at the sampling point (Figure 16). The valves on the gas bag are opened to allow gas to fill the bag. The valve on the bag is closed, removed and sent for chromatographic analysis.

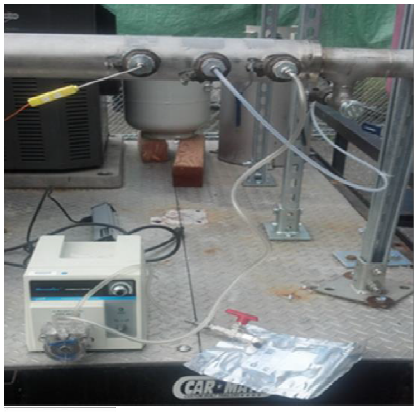

Figure 15 Gas Sampling

Figure 16 Tedlar gas sample bag

in bottles and ash in metal trays. The moisture content in the feedstock is determined using thermogravimetric analysis (TGA) and gas chromatography is used for gas and condensate samples. Samples are collected periodically during each run and the operating conditions will be modified based on analytical results.

Safety Plans: A safety plan was developed prior to activating the unit. The safety plan included discussion on required personal protective equipment, training of personnel on safe operating procedures, fencing and security for the pilot unit and safe handling of feedstock, samples and by-products. The following safety precautions are used when the pilot unit is in operation:

- Rubber gloves and safety goggles are used when feeding fuel to the unit
- High temperature protective gloves and safety goggles are used when removing ash, condensate or other materials or when working around the gasifier and piping.

The pilot unit and storage area are completely fenced in with limited access. Signage is posted along the enclosure stating safety precautions.

Start-up Plan: A start-up plan was developed which outlined procedures and methodology for operating the pilot unit. The initial plan used charcoal and wood stove pellets; however, based on experience with start-up, charcoal was replaced with ceramic briquettes to form the initial reactor bed (Figure 17). Charcoal is still used to initiate the reaction with wood pellets as fuel. This plan was used for the first few operations of the pilot unit and was modified as necessary throughout the testing period. When the new insert was placed into service, the startup process was modified using a significant quantity of wood pellets (about 40 lbs) during the start-up process.

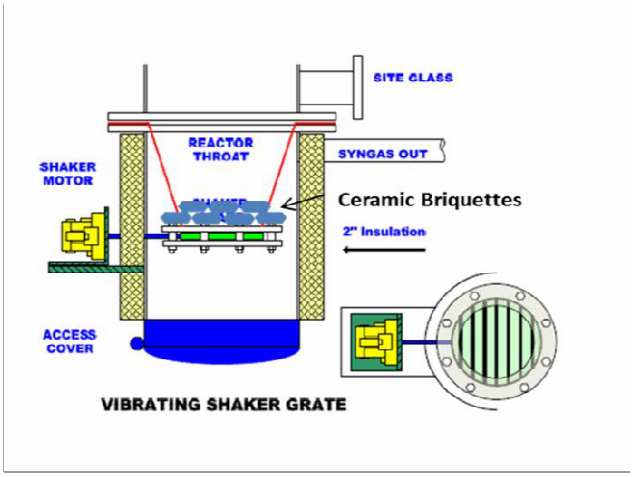

Figure 17 Schematic of gasifier showing briquette bed

Operation and Results:

Operation 2012: In early September 2012, rehabilitation of the pilot unit was completed. From September 12 to December 13, eighteen individual operational runs were made. The tests run from September 12 to December 3 used wood pellets as fuel and the ones in December used dried, pelletized wastewater biosolids. The test runs from November 30 through December 13 used the modified gasifier throat insert. Table 1 is a summary of each of the runs. During these test runs, there were some equipment malfunctions such as leaking gaskets, thermocouple wiring, clogged filters, and generator malfunctions. All of these were correctable and did not impact the ability to conduct further test runs.

Table 1: Summary of Gasifier Test Runs

Date	Feedstoc	Feed Rat	Syngas	Samples Collecte	Comments
12-Sep	Wood Pellets	2 lbs/12 min	Yes	None	Two problems occurred with this run; the propane valve on the generator froze and the gasket on the gasifier port leaked. The run was terminated to make repairs.
24-Sep	Wood Pellets	2 lbs/12 min make repair.	No	None	Discover problems with thermocouple wiring. Run was terminated to
26-Sep	Wood Pellets	2lbs/12 min; 2 lbs/6min	Yes	Condensate, gas	At the 2 lbs/12 min feed rate, the temperature dropped from 900 C to 825 C. Feed rate changed to every six minutes which increased the rate of temperature change (30 degrees over 12 minutes). Feed rate changed back to every twelve minutes. Demonstrated the effect of feed rate on temperature.
3-Oct	Wood Pellets	2 lbs/12 min	No	Condensate	
8-Oct	Wood Pellets	2 lbs/12 min after initial startup with wood pellets	No	Condensate	Changed to ceramic bricks instead of charcoal for bed, covered with wood pellets. Purpose of run was to bring gasifier to temperature without using charcoal. Successful in reaching temperature but it took a significant time to accomplish this.
10-Oct	Wood Pellets		No	None	The test was ended almost immediately due to the bottom hopper gasket leaking.
15-Oct	Wood Pellets	1 lb@varing intervals	No	Condensate	Five-hour run starting at 0820 and ending at 1340. One pound of feedstack added beginning at 1050. Wood pellets feed at various intervals ranging from about 20 minutes to 10 minutes. Ash a level of second thermocouple.
17-Oct	Wood Pellets	1 lb@varing intervals	No	Condensate, gas	Feed rates varied based on maintaining a constant temperature. Temperature in pyrolysis zone maintained between 928 and 950 C. Three to four gallons on condensate were formed during this run.
22-Oct	Wood Pellets	Various mass and intervals	No	Condensate, gas	Total of 28 lbs of wood pellets were added during this run; two ten lbs additions and then 2 lbs/12 minutes. Charcoal used during startup until the temperature at thermocouple 2 reached 950 C.
24-Oct	Wood Pellets	Various mass and intervals	No	None	About 40 pounds of wood pellets were added when the gasifier reached operating temperatures. Temperature dropped as low as 485 C. Airflow was varied to see if temperature could be increased.
7-Nov Wood	Pellets	20 lbs @varying intervals	No	None	Used shop vacuum to induce more airflow to increase temperature. Changed feed rate to 20 lbs at each addition. Temperatures remained low. Highest temperature 773 C. Run was terminated due to a clogged filter.
14-Nov	Wood	Various mass and intervals	Yes	Condensate, gas	Used shop vacuum to induce more airflow to increase temperature. Feed rate varied as did mass of feed. With increased airflow temperature reached 929 C and syngas was produced. As more material was fed, temperature dropped and gas production was lost. Feedstock was then added at a rate of 10 lbs. Temperature increased and syngas was produced.
Pellets					
29-Nov	Wood	20 lbs	No	None	First use of modified reactor. The insert was filled with charcoal and below the insert was 20 pounds of charcoal, a layer of ceramic briquettes and 10 pounds of charcoal. Temperatures ranged from 614 C to 791 C.
Pellets					
30-Nov	Wood	2 lbs/6 min during 75% of the run time.	Yes	Condensate, gas	Temperatures ranged from 840 C to 1024 C with syngas being produced
Pellets					
3-Dec Wood		4 lbs/6 min;	Yes	None	During this run, temperatures were relatively stable with the temperature in the pyrolysis zone fluctuating only 62°C during the last two hours of the run (701°C-763°C), while the upper middle zone fluctuated 104°C (1031°C-1135°C).
Pellets		2 lbs/6 minutes			
5-Dec	Biosolids	4 lbs/6 min	Yes	Condensate, gas	Clogged finalfilter caused system to be shut down and then restarted after cleaning. Syngas production was intermittant during this run.
10-Dec	Biosolids	2 lbs/6 min	Yes	None	Syngas production at about 908 C
12-Dec	Wood Pellets and Biosolids	2 lbs/6 min; 6 lbs/6 min	Yes	None	Final filter clogged with tars. Removed from the system and then restarted. Syngas was produced at about 840 C

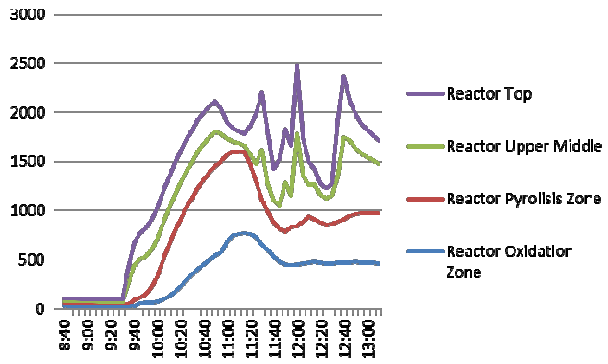

Figure 18 November 14 Temperature Profile

temperature profiles for two different test runs. The November 14 and December 3 run used wood pellets. Both runs produced syngas. It is important to note the temperature decrease when feedstock is added.

Only a relatively few test runs produced syngas. This was an unexpected result since when the pilot unit was in Stamford each test run produced a significant quantity of syngas. During every one of the test runs, each time feedstock was added the temperature dropped. In instances when the temperature dropped below the experimental temperature, pellets were added at a different rate. Also airflow was varied to try to establish a constant temperature. Of the entire test run period, the most stability in operating temperature occurred on December 3. Figures 18 and 19 show the

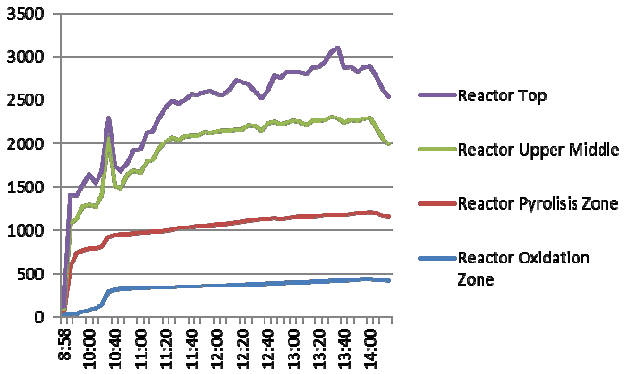

Figure 19 December 3 Temperature profile

Gas Analysis: Gas samples were collected during various runs. The gas analysis is performed using a Gas Chromatographer equipped with Thermal Conductivity Detector (GC/TCD) Agilent Model6890N. Table 2 shows the gas composition of six gas samples taken on different days or at different times during a given test run. The sample labeled R-11-14 was with the pilot gasifier prior to modifying the throat. All of the rest of the samples were collected from runs using the throat insert. Additionally, the gas samples taken on 11-14, 11-30 and 12-3 were with wood pellets as a feedstock.

There does not appear to be significant differences in the gas composition relative to feedstock (Figure 20). The heating value for these runs is shown in Table 3. The values for two of the three runs with the insert are higher than those runs without the insert; however, the reasons for that are unknown at this time. The values obtained in these runs correlate well with literature values for syngas produced from biomass.

Run	H2, %	N2, %	CO, %	CH4, %	CO2, %
R-11/14	11.24	46.75	27.05	2.37	7.39
R-11/30a	9.06	49.44	28.53	1.91	7.39
R-11/30b	15.72	35.05	27.43	4.72	14.50
R-12-03a	7.99	48.25	30.04	1.93	1.04
R-12-03b	12.13	43.51	31.9	2.38	6.32
R-12-03c	10.92	42.99	29.46	2.92	10.04

Table 2-Gas composition of various syngas samples

It is important to note the high concentration of nitrogen (Table 2). Nitrogen makes up about 50% of the total gas volume and nitrogen has no energy value. Much of the nitrogen comes from the air used in the gasifier and some from the feedstock itself. It

will be important as this research continues to look at ways to reduce the nitrogen content. This will result in a higher syngas energy value. Ways of achieving this include using synthetic air mixtures with higher concentrations of oxygen or oxygen containing products.

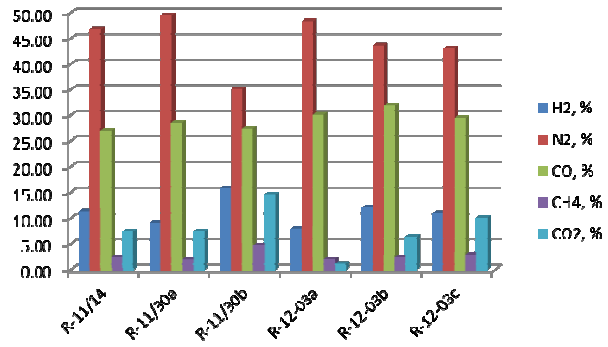

Figure 20 Gas composition of various syngas samples

Run	BTU/ft³	Mj/m³
R-11/14	148	5.51
R-11/30a	131	4.87
R-11/30b	144	5.39
R-12-03a	143	5.32
R-12-03b	167	6.21
R-12-03c	160	5.97

Table 3 Energy Value of Syngas

Condensate: The analysis of the condensate is a complicated task. The condensate is a black liquor, which is composed mainly of poly-aromatic hydrocarbons (PAH). The qualitative determination of the PAH requires GC equipped with Mass Detector (GC/MS). At C2E2 this analysis will be performed using existing GC/MS Agilent Model 5973. At this point this analysis is not feasible due to the presence of significant amounts of water and particulates in the condensate. Our plans include the installation of impinger bottles (Figure 21) in the outlet of the filters, where the condensate will be collected and separated into fractions. The usage of impinger bottles is a common and widely acceptable practice for the sampling of tars and particulates in syngas derived from biomass gasification. The impinger bottles already exist in the lab and were actually part of the gasifier. However, they were never used because of the complexity involved with the sampling procedure.

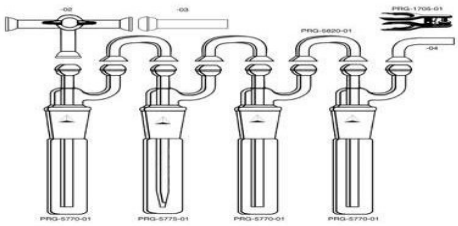

Figure 21: Impingers bottles for condensate sampling, fractionation and collection.

To verify the presence of heavy hydrocarbons in the produced syngas, some preliminary analysis has been performed using a Gas Chromatographer equipped with a Simulated Distillation and Flame Ionization Detector (GC/SimDist with FID), Agilent Model 7890A. SimDist is a GC technique which separates individual hydrocarbon components in the order of their boiling points. The result of SimDist analysis provides a quantitative percent mass yield as a function of boiling point of the hydrocarbon components of the sample, but the qualitative determination of the components is difficult. Figure 22 shows the GC/SimDist chromatograph of a condensate sample received from one of the gasifier runs.

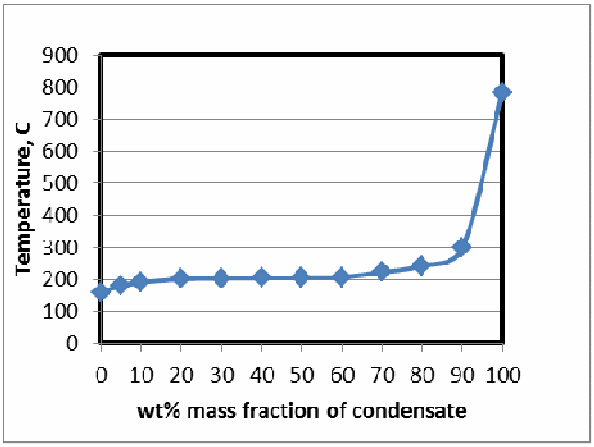

Figure 22: Simulated Distillation curve of the liquid condensate

From Figure 23 it appears that the condensate boils between 160 to 800°C. Actually most of the condensate has a boiling point higher than 200°C and lower than 300°C. Most likely the condensate contains primarily naphthalene (2 aromatic rings) derivatives, (naphthalene b.p. 218°C).

Operation 2013: The goals for 2013 were to:

- Standardize feedstock preparation
- Use biosolids, chicken manure and food waste as feed stocks and develop gas and tar characteristics
- Analyze gas and clinkers to determine characteristics and relate to operating conditions

Standardize feedstock preparation/pelletization

During April and May, efforts were concentrated on creating a consistent pellet with desirable mechanical properties. Each feedstock was combined with a portion of deionized (DI) water, mixed using a commercial dough mixer and then extruded. Pellets ranged in size from about 0.5 inches to 1 inch and about 0.5 inches in diameter. The following is a description of the specific water to feedstock ratio and extrusion conditions for each feedstock:

BIOSOLIDS

1000 grams of biosolids to 225 mL of DI water; pressure 10 tons

DINING HALL BIOMASS

400 grams of dining hall biomass to 25 mL DI water; Pressure 5-8 tons
Required a larger extrusion die than biosolids

COW MANURE

Cow manure was problematic since it arrived as a mixture of manure, plant life, straw, and wood chips. The cow manure had to be separated and broken apart. In addition, the water content of the "as received" manure was too high and a significant amount of liquid sprayed/dripped during the extrusion. The manure was solar dried to reduce the water content. Unfortunately, the dry cow manure also failed to pelletize. It is likely due to the material properties of the manure as it is composed of many strands of semi-digested grass. Once the manure passed through the die, the compressed manure sprung back into shape like popcorn. The next step is to grind up the dried manure and reattempt to pelletize it.

Biosolids, chicken manure and food waste as feedstock to develop gas, and tar characteristics: During this period, there were eight separate gasifier runs using three different feedstock; biosolids (wastewater residuals), dining hall food waste and wood. See Appendix A for detailed run reports. Table 1 is a summary of the conditions and results from each test run. Reports from each of these runs are contained in Appendix A.

Table 4 Summary of Eight Test Runs (2013)

			*Pyrolysis Zone					
Run No.	Date	Run Duration	Feedstock	Airflow,SCFM	Temperature, C	Combustible Gas	Tars	Clinkers
1	10-Jun-13	77.00	Biosolids	~3	921-1048	No	yes	No
2	12-Jun-13	191.00	Food Waste	~3	421-471	Yes-20 min	yes	Yes
3	19-Jun-13	120.00	Wood	~2.5	497-532	Yes, intermittant-42 min	yes	Yes
4	20-Jun-13	88.00	Wood	~3	669-735	Yes-6 min	yes	Yes
5	24-Jun-13	177.00	Wood	~2	455-753	Yes- 132 min	yes	Yes
6	8-Jul-13	55.00	DHW	~3.5	450-505	Yes	yes	yes
7	8-Jul-13	300.00	DHW	~3.5	516-1005	Yes	yes	** yes
8	16-Jul-13	192.00	DHW	~10	501-1084	Yes	yes	

** Along with clinkers, a dough-like carbonanceus material was formed

* Pyrolysis zone temperature when gas was produced

These data indicate that dining hall waste (DHW) shows good promise as a feedstock in a gasifier.

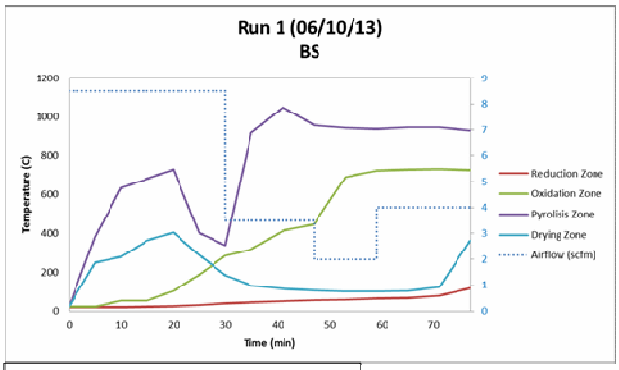

Figure 23 Run 1-Temperature Profile

Temperature Profiles: It is difficult to control temperature in the gasifier since it does not have sufficient instrumentation and control over airflow. Airflow and feed rate have a direct impact on temperature. The following graphs show the variability of temperature in all zones during each run (Note that the shaded area indicates the period a combustible gas production).

Figure 23 shows the temperature profile for Run-1 using biosolids as fuel. The run lasted 77 minutes and only produced small amounts of combustible gas. Figure 24 shows the temperature profile for Run-2 lasting 191 minutes using food waste as fuel and producing a combustible gas for a period of about 20 minutes. Figure 25 to 27 (Run-3 to Run-5) shows the temperature profile using wood pellets as fuel. Run-3 and Run-5 produced a combustible gas for 42 and 132 minutes respectively; whereas Run 4 only produced gas for about 6 minutes.

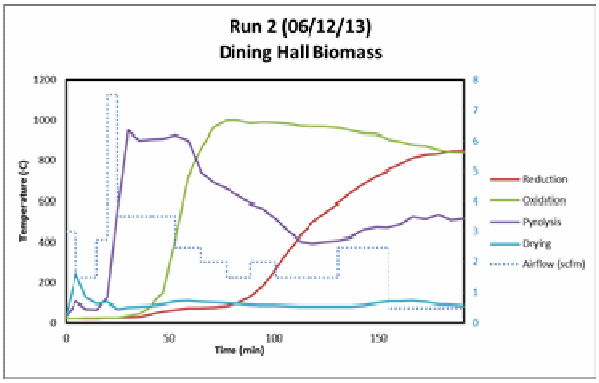

Figure 24- Run 2 Temperature Profile

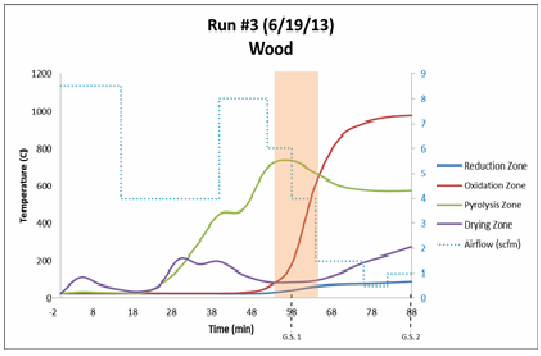

Figure 25- Run 3 Temperature Profile

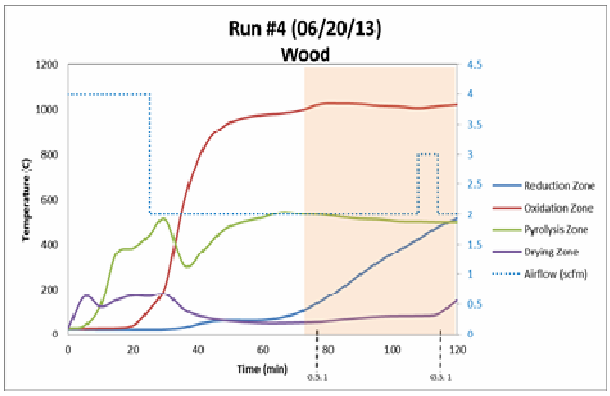

Figure 26- Run 4 Temperature Profile

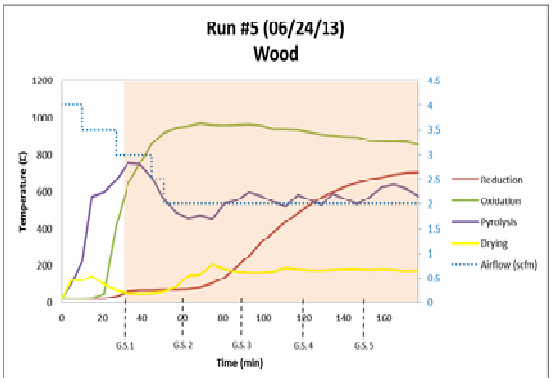

Figure 27-Run 5 Temperature Profile

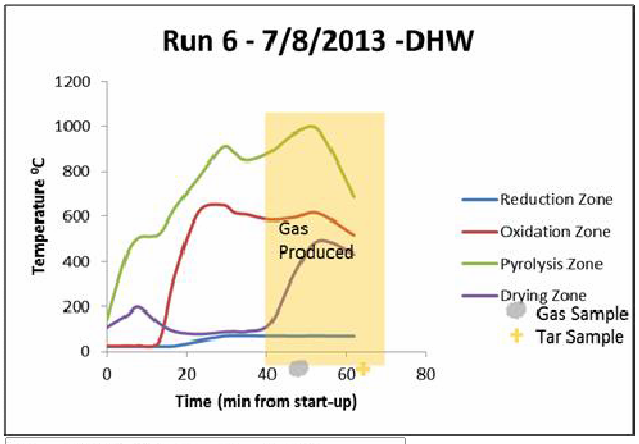

Figure 28- Run 6 Temperature Profile

The temperature profiles for Run-6 to Run-8, shown in Figures 28 to 30, used dining hall waste as the fuel and all produced a combustible gas. They were also the longest duration of all eight runs.

The best gas production in general appears to be when the temperature is above 500° C, although there are some exceptions. It will be necessary to do further tests to correlate temperature, feed rate and gas production.

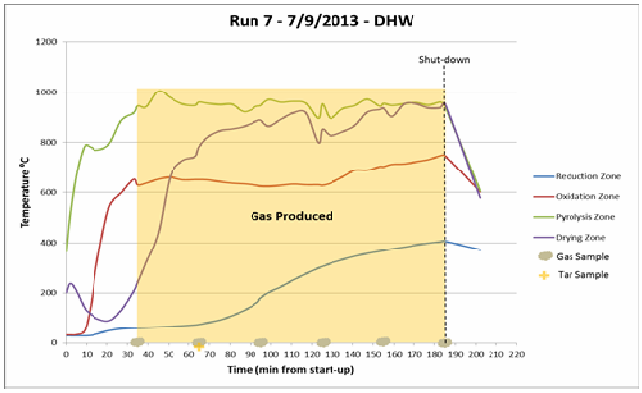

Figure 29- Run 7 Temperature Profile

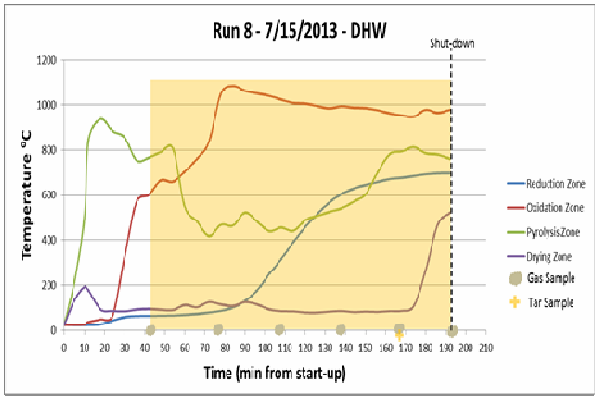

Figure 30 Run 8 Temperature Profile

Clinkers Production:

A clinker is a partially vitrified mass of fuel. Clinkers typically form when the temperature in the gasifier is higher than the fusion point of the material. It was important to correlate the production of clinkers

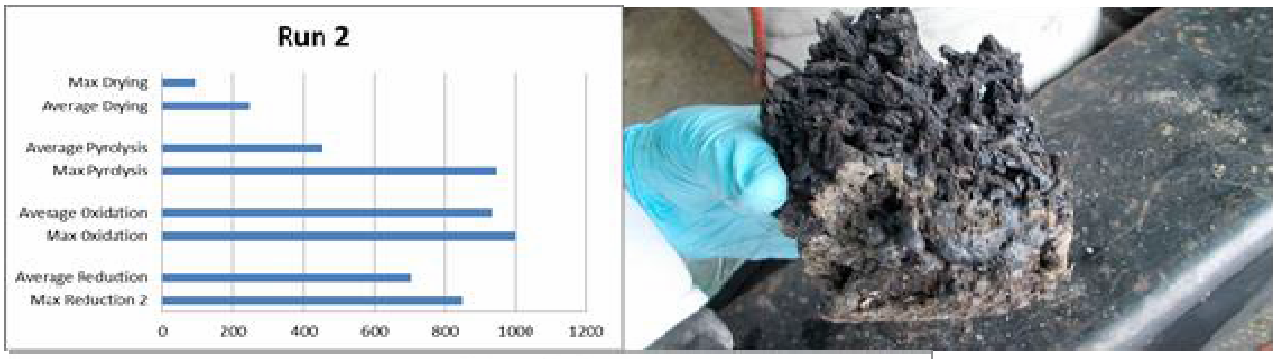

Figure 31 Run-2 Temperature profile and Clinker

with feedstock, temperature, airflow and other operating characteristics. Run-2 (Figure 31) produced the largest clinker encountered with respect to all of the other 2013 runs. The feedstock for this run was

biosolids with screens in place in the insert. The duration of the run was 191 minutes and during this time, the maximum temperatures achieved were 853°C in the reduction zone, 1001°C in the oxidation zone, 951°C in the pyrolysis zone and 245°C in the drying zone. During this period, the average temperature was 703°C in the reduction zone, 932°C in the oxidation zone, 455°C in the pyrolysis zone, and 92.7°C in the drying zone and a combustible gas was produced for about 18 minutes.

Run-5 (Figure 32) produced two small clinkers with the larger clinker measuring ~1.5 inches along its major axis. The feedstock for this run was wood pellets with no screens in the insert. The duration of the run was 174 minutes and during this time, the maximum temperatures achieved were 705°C in the reduction zone, 966°C in the oxidation zone, 753°C in the pyrolysis zone and 205°C in the drying zone. During this period, the average temperature was 383°C in the reduction zone, 911°C in the oxidation zone, 565°C in the pyrolysis zone, and 156°C in the drying zone and a combustible gas was produced for 123 minutes.

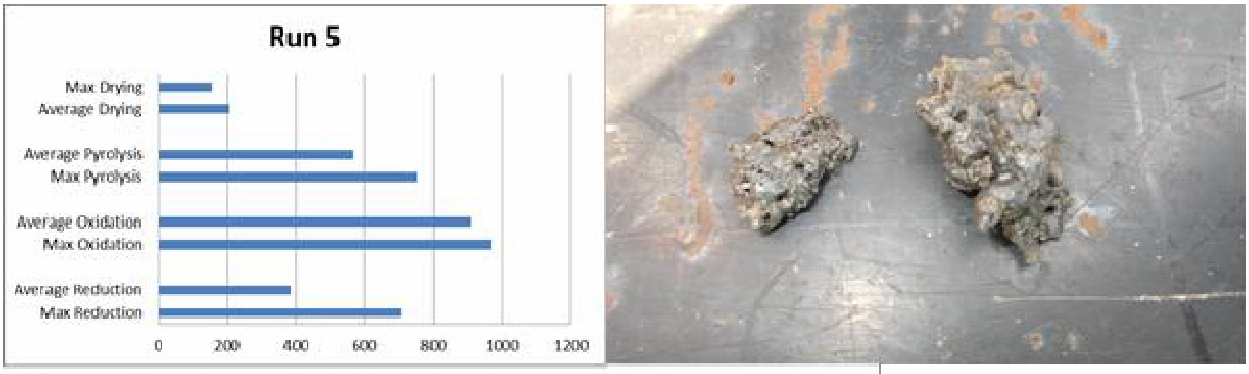

Figure 32 Run-5 Temperature profile and Clinker

Run-8 (Figure 33) produced a flat, cylindrical clinker measuring ~3 in diameter. The feedstock for this run was dining hall waste with no screens in the insert. The duration of the run was 192 minutes and during this time, the maximum temperatures achieved were 697°C in the reduction zone, 1084°C in the oxidation zone, 937°C in the pyrolysis zone and 133°C in the drying zone. During this period, the average temperature was 387°C in the reduction zone, 933°C in the oxidation zone, 605°C in the pyrolysis zone, and 133°C in the drying zone and a combustible gas was produced for 150 minutes.

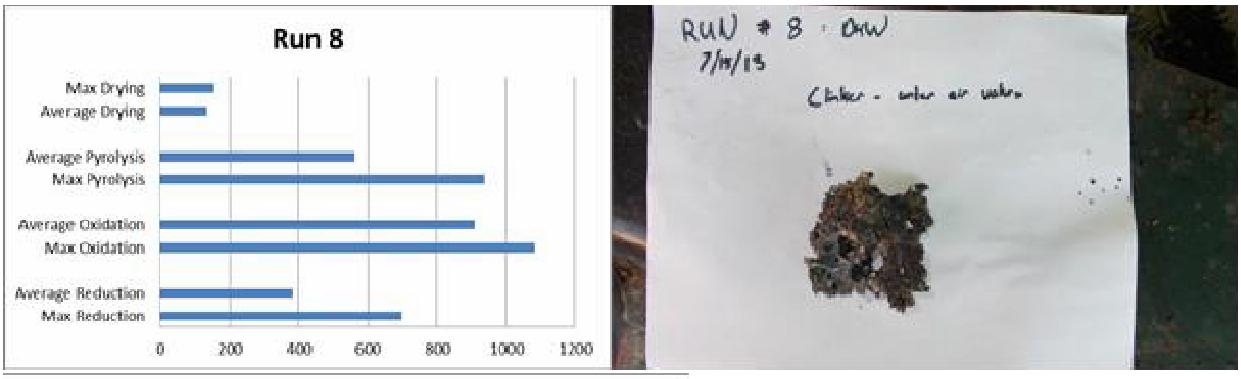

Figure 33 Run-8 Temperature profile and Clinker

Run 9 (Figure 34) produced a large clinker only marginally smaller than the clinker found in Run 2. However, this clinker was both harder and denser than all clinkers produced previously. The feedstock used for this run was Mix #1 with no screens in the insert. The duration of this run was 195 minutes and during this time, the maximum temperatures achieved were 685°C in the reduction zone, 1057°C in the oxidation zone, 887°C in the pyrolysis zone and 563°C in the drying zone.

During this period, the average temperature was 398°C in the reduction zone, 953°C in the oxidation zone, 522°C in the pyrolysis zone, and 207°C in the drying zone and a combustible gas was produced for 152 minutes. Clinker formation appears to be temperature and feedstock related and correlates to the fusion point of the feedstock; biosolids has a lower fusion point than food waste and therefore is more likely to produce clinkers.

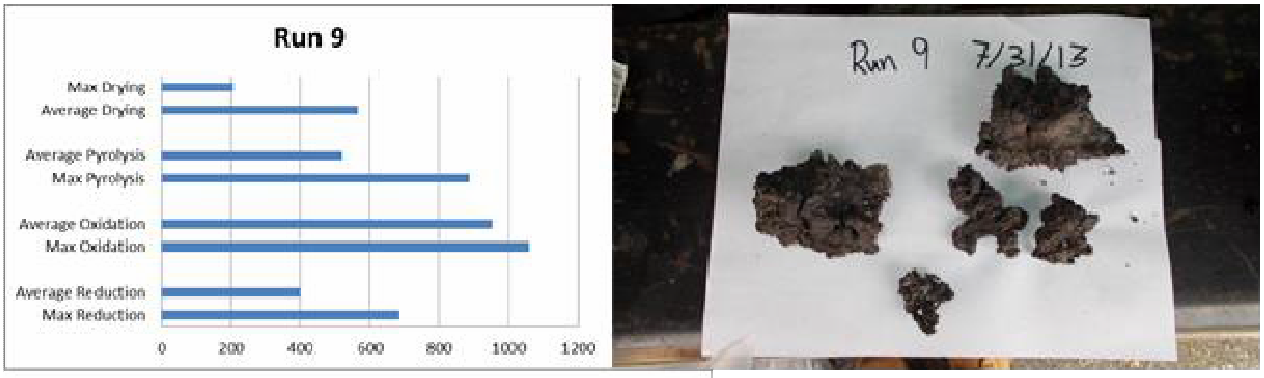

Figure 34 Run-9 Temperature profile and Clinker

Gas Production: Gas samples were taken during Run-7 and Run-8, which used dining hall waste as a feedstock. Table 5 shows the composition of the gas and the energy value associated with each sample. Although the gas was combustible, the energy value was low relative to the literature and values obtained during this project on biosolids, which ranged from 132 to 167 BTUs/ft^3.

Whether the low energy value of the gas was due to the feedstock or to the operating conditions is unknown at this time. Further research is needed to identify and optimize airflow, temperature and feed rate to produce the highest energy value possible. Theoretically, the energy value of the gas should be between 130 and 200 BTUs/ft^3.

Table 5 Gas Analysis DHW

Test	H2,	N2, %	CO,	CH4,	CO2,	BTU Va
7-1	4%	70%	12%	1%	8%	62
7-2	9%	58%	10%	2%	15%	82
7-3	3%	71%	9%	1%	10%	49
8-1	4%	65%	12%	2%	13%	72
8-2	2%	91%	3%	0%	2%	16
8-3	8%	52%	16%	2%	11%	98

Summary and Recommendations

Gasification of carbon containing waste products shows promise. The results of this research project have shown that various waste products (biosolids, cow manure and food waste) can be successfully gasified and produce a combustible gas. With continued research, it will be possible to determine optimum conditions within the gasifier to produce high levels of hydrogen and carbon monoxide with the concept of using these gases in highly efficient solid oxide fuel cells or converting them to liquid fuels. More work is needed in evaluating methods of cleaning the syngas and removing or cracking tars.

There is a high level of interest in the wastewater and solid waste industries in gasification as a means to dispose of waste products in a safe and environmentally sound manner while capturing the energy embedded in these products.

Appendix A - 2013-Run reports from each gasifier run

Season #2 Run #1 (6/10/2013)
Batch #35 BS Pellets

The gasifier run was performed on June 10th, 2013 and was the second run performed in 2013. The feedstock used was Biosolid pellets from batch #35. Biosolids mixed with deionized water and extruded through a ½ inch diameter die. These pellets were mixed, compressed, and separated into bags in June 2013.

The run began at 10:05 AM, the weather was windy. The manhole cover on the reactor was removed; lighter fluid was sprayed on the charcoal bed and was lit. The airflow through the system was set to ~ 3 SCFM (Standard cubic feet per minute) using 0 SCFM from the large compressor; 3 SCFM from the small compressor, and 0 SCFM through the sight glass). At 10:25, 40 lbs of SSW pellets was added to the reactor. The airflow in the system was changed to 8 SCFM (6 SCHM from the large compressor, 1 SCFM from the small compressor, and 1 SCFM from the eyeglass). After 6 minutes, the airflow was reduced to ~4 SCFM (0 SCFM from the large compressor, 3SCFM from the small compressor, and ~1SCFM from the eyeglass).

From 10:48 to 1:06, 2 lbs of SSW pellets were added every 6 minutes. When the first 2 pounds of feedstock was added to the reactor the temperature in the reduction zone was 46°C, the oxidation zone was at 85°C, the pyrolysis zone was at 907°C, and the drying zone was at 84.6°C. The airflow was adjusted several times throughout the run to control the temperature within the reactor (see run notes).

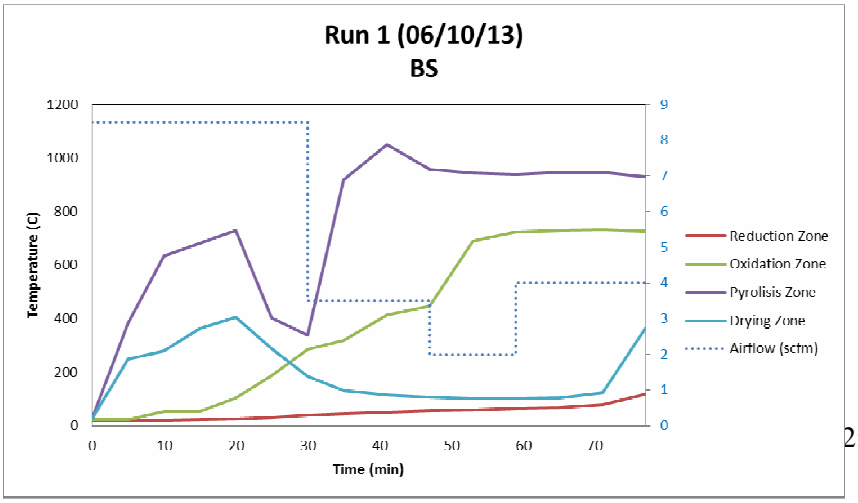

Gas was produced intermittently throughout the run. At 11:36, the flare was initially lit but would not remain lit. At this time the temperature in the reduction zone was at 128°C, the oxidation zone was at 985°C, the pyrolysis zone zone was at 589°C, and the drying zone was at 89.4°C. Gas sample #1 was taken at 11:54.

2:24, the flare was lit and

remained lit until 12:42. During

this period the temperature of the of the reduction zone ranged between 642°C-755°C, the oxidation zone ranged between 909°C and 950°C, the pyrolysis zone ranged between 421°C-471°C, and the drying zone ranged between 81.8°C-105°C. During this period, the airflow in the reactor was at ~3 SCHM (0 SCHM from the large compressor, 2 SCHM from the small compressor, and 1 SCHM from the eyeglass). Gas sample #2 was taken at 12:30.

The flare was periodically tested to see if it would ignite again, however the gas stream never stayed lit for the remainder of the run. A final gas sample (Gas Sample #3) was taken at 1:06. The run was aborted at 1:18; however, the gasifier temperature program was allowed to run for 20-30 minutes after the run was aborted.

Season #2 Run #2 (6/12/2013)
Batch #50 DHW Pellet

The gasifier run was performed on June 12th, 2013 and was the second run performed in 2013. The feedstock used was pellets from batch #50. Filtered dining hall biomass was mixed with deionized water and extruded through a ½ inch diameter die. These pellets were separated into two pound bags in June 2013. A total of 64 pounds of DHW pellets were used in this run. The vibrator was on through the entirety of the run.

The run began at 9:30 AM using 3 pounds of charcoal as the initial fuel. The charcoal was lit using lighter fluid. The airflow through the system was set to ~8 SCFM (6 sfrom the large compressor, 2 SCFM from the small compressor, and 30 scfh through the sight glass). The water pressure in the tuyere was at 5 in.

At 9:55 AM, 40 pounds of the feedstock pellets were added to the reactor. The airflow through the system remained at ~8 SCFM. At the time the initial feedstock was added, the temperature of the reduction zone was 26.6°C, oxidation zone was at 292°C, the pyrolysis zone was at 346.6°C, and the drying zone was at 267.4°C. The water pressure remained at 5 in.

At 10:10 AM, the airflow through the system was changed to ~4 SCFM (0 scfm from the large compressor, 3 SCFM from the small compressor, and 27 s SCFM from the sight glass. At this time the temperature was 46°C in the reduction zone, 565°C in the oxidation zone, 1048°C in the pyrolysis zone, and the drying zone was at 114°C. The water pressure decreased to 1.6 in.

Between 10:15 and 10:45, 4 pounds of feedstock was added at six minute intervals. During this period, the reduction zone temperature varied from 50.7°C to 72.6°C, the oxidation zone varied between 684°C and 732°C, the pyrolysis zone varied between 940°C and 959°C, and the drying zone varied between 105.8°C and 144°C. The water pressure remained to 1.6 in. Throughout this period, the flare was periodically tested to see if the gas stream would stay lit. The run was aborted at 11:03 and the flare never stayed lit.

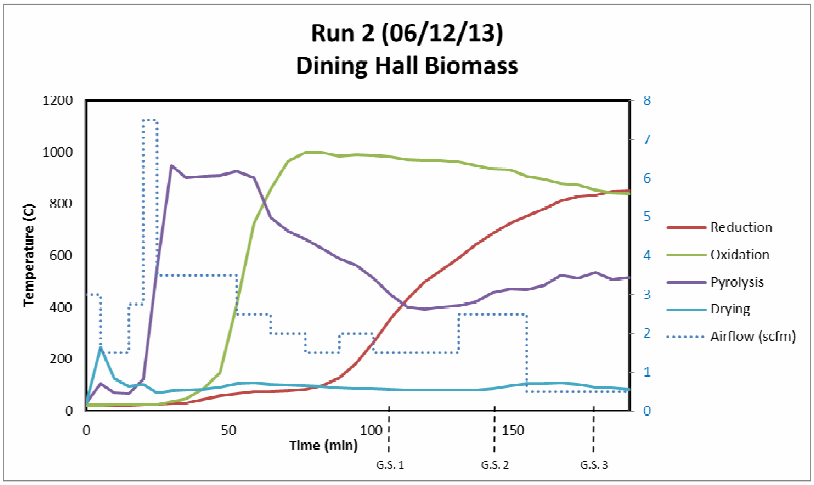

Run #3 (6/19/2013)
VIBRATOR ON
3 lb Charcoal
40 lb Wood Pellets
Feedstock: Wood
The run began at 9:00 when the charcoal was lit. The airflow was initially set at a total of ~8.5 scfm (6.5 scfm from the large compressor, 1.5 scfm from the small compressor, and 30 scfh from the eyeglass). The flame went out, at the charcoal was relit at 9:15 with the airflow lowered to ~4 scfm (0 scfm from the large compressor, 3.5 scfm from the small compressor, and 22 scfh from the eyeglass).

At 9:40, 40 lb of feedstock was added to the reactor, at this point the temperature in the reduction zone was 23.8°C, the oxidation zone was at 30.2°C, the pyrolysis zone was at 476°C and the drying zone was at 125°C. The airflow was increased to ~8 scfm (6 scfm from the large compressor, 1.5 scfm from the small compressor, and 22 scfh from the eyeglass). Beginning at 9:46, 2 lb bags of feedstock were added to the reactor every 6 minutes.

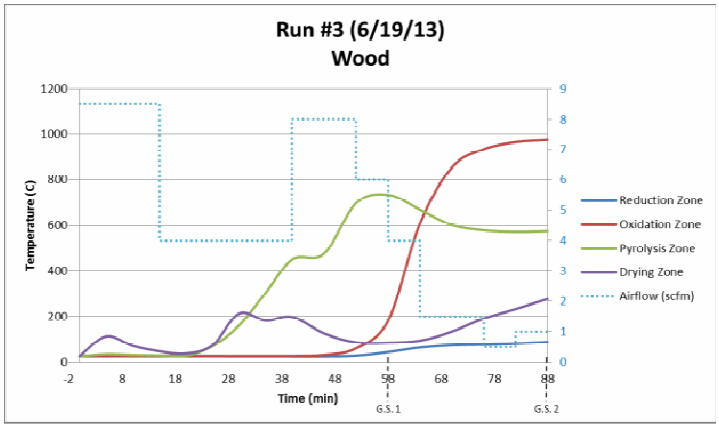

The flare was lit at 9:52, the temperature at this point was 42.7°C at the reduction zone, 180°C at the oxidation zone, 735°C at the pyrolysis at 83.8°C at the drying. The airflow was decreased to ~6 scfm (4.5 scfm from the large compressor, 1 scfm from the small compressor and 30 scfh from the eyeglass). At 9:58 the flare went out and could not be relit. When the flare went out the temperature was 73.8°C at the reduction zone, 855°C at the oxidation zone, 602°C at the pyrolysis zone, and 133°C at the drying zone. The airflow was decreased several times between 9:58-10:22 from 6 scfm to .5 scfm. During this period the temperature in the reduction zone stayed between 63.3°C to 87.4°C, the temperature in the oxidation zone increased from 855°C-977°C, the pyrolysis zone temperature decreased from 669°C-574°C, and the drying zone temperature increased from 93.4°C-277°C.

While cleaning the reactor, the evidence suggested the burn occurred as expected. All the burnt remains were situated within the insert. The coal and feedstock outside the insert did not get burned. There were no clinkers found in the reactor and the air valves were clear.

Run #4 (6/20/2013)
VIBRATOR ON
3 lb Charcoal
40 lb Wood Pellets
Feedstock: Wood
The run began at 9:28 with an initial air flow of ~4 scfm(0 from the large compressor, 3.4 scfm from the small compressor and 22 scfh from the eyeglass). The temperature was allowed to climb until the pyrolysis zone reached ~500C.

At 9:58, 40 lb of the feedstock was added to the reactor. At this time, the temperature in the reduction zone was 23°C, the oxidation zone was at 215°C, the pyrolysis zone was at 303°C and the drying zone was at 178°C. The airflow was reduced to ~2 scfm (0 scfm from the large compressor, 1.5 scfm from the small compressor, and 30 scfh from the eyeglass). From this point on, 2 lb of feedstock was added to the reactor every 6 minutes.

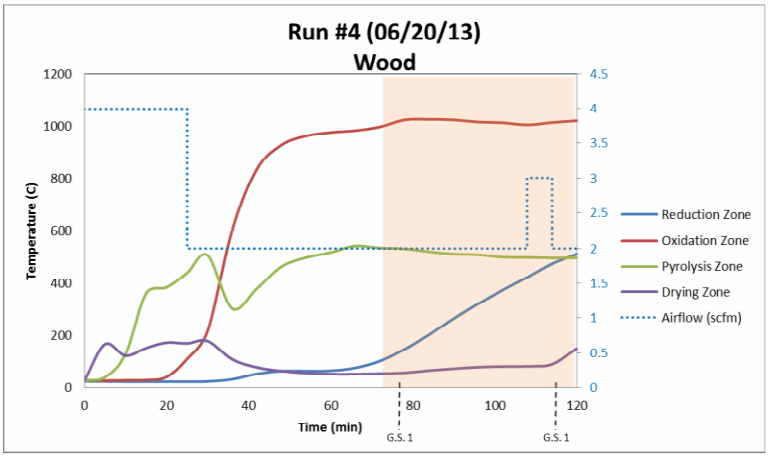

Between 9:58 to 10:46, the flare could not be lit. The temperature in the reduction zone increased from 23°C to 101°C, the oxidation zone increased from 216°C to 1023°C, the pyrolysis zone increased from 507°C to 532°C, and the drying zone decreased from 178°C to 58°C. At 10:46 the flare was lit for the first time, but the flame went out quickly. Gas sample #1 was taken at 10:53.

The flare was lit several times between 10:52 to 10:16, but was unable to remain lit for a significant amount of time. During this period, the temperature ranged between 147°C -423°C in the reduction zone, 1024°C -1013°C in the oxidation zone, 532°C -499°C in the pyrolysis, and 58.6-81°C in the drying zone. At 10:16 the airflow was increased to ~3 scfm (0 scfm from the large compressor, 2.5 scfm from the small compressor and 30 scfh from the eyeglass). The flare was lit again and remained lit. At this time the temperature was 479°C in the reduction zone, 1013°C in the oxidation zone, 497°C in the pyrolysis zone, and 89°C in the drying zone.

At 10:22 the airflow was decreased to ~3scfm (0 scfm from the large compressor, 1.5 scfm from the small compressor, and 30 scfh from the eyeglass). The flare went out ~1 minute after the airflow was decreased. The run was aborted at 10:34.

Run #5 (6/24/2013)
NO SCREENS
VIBRATOR ON
3 lb Charcoal
40 lb Wood Pellets
Feedstock: Wood

The run began at 9:32 with an initial air flow of ~scfm (0 from the large compressor, 3.3 scfm from the small compressor, and 22 scfh from the eyeglass). The temperature was allowed to climb until the pyrolysis zone reached ~500°C.

At 9:43, 40 lb of the feedstock was added to the reactor. At this time the temperature was 23°C in the reduction zone, 25°C in the oxidation zone, 574°C in the pyrolysis zone, and 193°C in the drying zone. The airflow was reduced to ~3.5 scfm (0 scfm from the large compressor, 3.3 scfm from the small compressor, and 20 scfh from the eyeglass).

At 10:07, the flare was lit and remained lit. At this time the temperature was 69°C in the reduction zone, 751°C in the oxidation zone, 748°C in the pyrolysis zone, and 51°C in the drying zone. Gas Sample 1 was taken at 11:07 and subsequent gas samples were taken every 30 minutes (11:07, 11:31, 12:01).

The flare remained lit for the remainder of the run. The airflow was lowered to ~2 scfm at 10:25 (0 scfm from the large compressor, 1.5 scfm from the small compressor, and 30 scfh from the eyeglass). The airflow was not changed for the remainder of the run. During this period the temperature in the reduction zone ranged from 79°C-702°C, the oxidation zone ranged between 751°C-966°C, the pyrolysis zone ranged between 748°C-455°C, and the drying zone ranged between 55°C-205°C. The run was aborted at 12:21 because the vibrator broke off

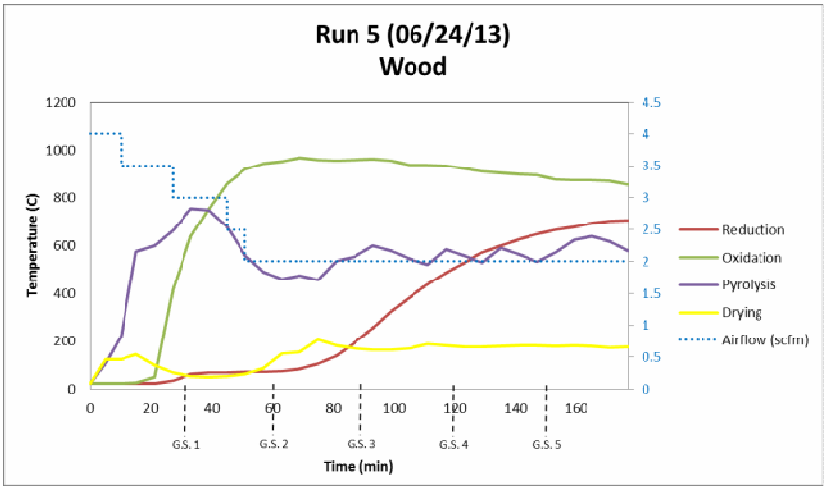

The following day, the reactor was cleaned. The majority of the burnt material was contained within the insert; a chimney was formed directly above the insert. Two small clinkers (<2" in diameter) were found several inches below the insert. However, the air valves were clean and no clinkers were found within the insert itself.

Run #6 (7/08/2013)
NO SCREENS
VIBRATOR ON
3 lb Charcoal
40 lb DHW
Feedstock: DHW

The small compressor did not initially run during the pre-run inspection. After some adjustments, the small compressor was repaired. The run began at 9:00 with an initial air flow of ~4 scfm (0 from the large compressor, 3.4 scfm from the small compressor, and 22 scfh from the eyeglass). The temperature was allowed to climb until the pyrolysis zone reached ~500°C.

At 9:08, the temperature was 23.9°C in the reduction zone, 27.8°C in the oxidation zone, 505°C in the pyrolysis zone, and 197°C in the drying zone. At this point, 40 lb of DHW was added to the reactor and 6 lbs were added at 6 minute intervals. At 9:39 the airflow was reduced to ~2 scfm (0 from the large compressor, 1.5 from the small compressor, and 30 scfh from the eyeglass.).

The flare was lit at 9:32 and remained lit for the remainder of the run. During this period the temperature ranged between 68.2°C-67.2°C in the reduction zone, 585°C -617°C in the oxidation zone, 883°C-983°C in the pyrolysis zone, and 87.2°C-490°C in the drying zone. Gas Sample 1 was taken at 9:39.

The end was aborted premature due to a failure from the air compressors. The large and small air compressors stopped working at 9:55 and could not be restarted. At the time of failure, the shop-vac was being run off the generator.

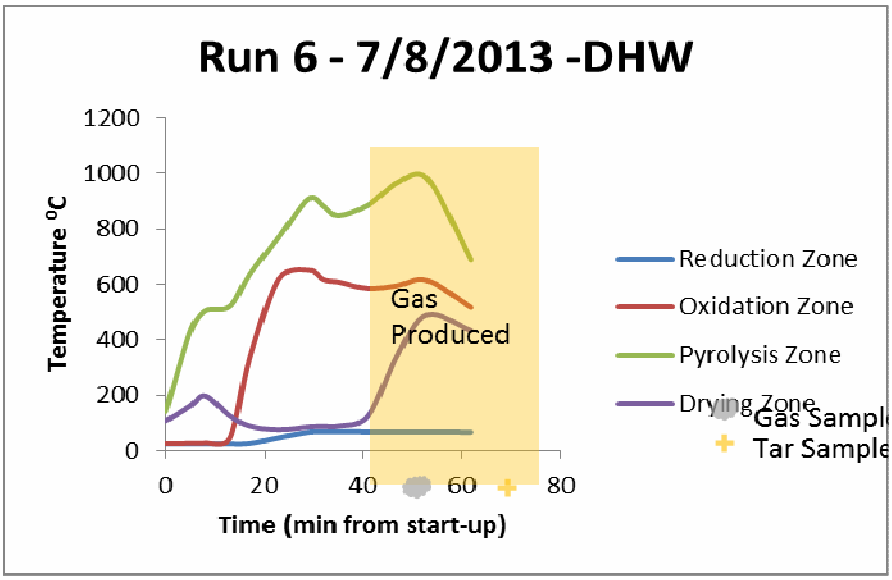

Run 6 – Post-Run Report

Figure 1

Figure 2

The post-run cleaning was typical, with most of the burnt material located within the center of the reactor. The dining hall waste pellets had swelled in size and had become weaker. The reactor was filled to a height just above the rim of the manhole cover (Fig 1). Once again, a shell was formed in the shape of a dome over the insert (Fig. 2). A large circular clinker was found at the bottom of the insert just below the air valves. Furthermore, the air valves were clogged with clinkers and a drill bit was used to clear them.

Run #7 (07/09/2013)
NO SCREENS
VIBRATOR ON
3 lb CharcoalRun
40 lb DHW
Feedstock: DHW

The run began at 9:10 with an initial airflow of ~4 scfm (0 from the large compressor, ~3.4 scfm from the small compressor and ~22scfh from the eyeglass). The temperature was allowed to climb until the pyrolysis zone reached 500°C.

At 9:17 40 lb of the feedstock was added to the reactor. At this time, the temperature in the drying zone was 238°C, the pyrolysis zone was 516°C, the oxidation zone was at 31.9°C, and the reduction was at 28.2°C. 2 lb of feedstock was added into the reactor at 6 minute intervals. At 9:27 the airflow was decreased from ~3.4 scfm to ~2 scfm (0 scfm from the large compressor, ~1.5 scfm from the small compressor, and ~30 scfh from the eyeglass). The airflow was not changed for the remainder of the run.

The flare was lit and stayed lit at 9:50 and Gas Sample 1 was taken. The temperature was 244°C in the drying zone, 945°C in the pyrolysis zone, 629°C in the oxidation zone, and 60°C in the reduction zone. The flare remained lit for the remainder of the run. While the flare was lit, the temperature in the oxidation zone quickly increased but stabilized between 850°C-950°C. The temperature in the pyrolysis zone increased to a maximum of 1005°C (45 min) but stabilized between 850°C-950°C. The oxidation zone increased slowly throughout the duration of the run from 629°C to 748°C when the run was aborted. The temperature in the reduction zone also increased through the duration of the run to a maximum of 407°C. Six gas samples were taken at 30 minute intervals starting at 9:50. A single tar sample from the heat exchanger was taken at 10:20. Starting at approximately 1.5 hours through the run, it was noted that there was a significant amount of smoke coming through the hopper when the feedstock was poured in. The proper feeding procedure was followed; however there was a significantly greater amount of smoke when compared to previous runs. At 2:15 the run was terminated voluntarily.

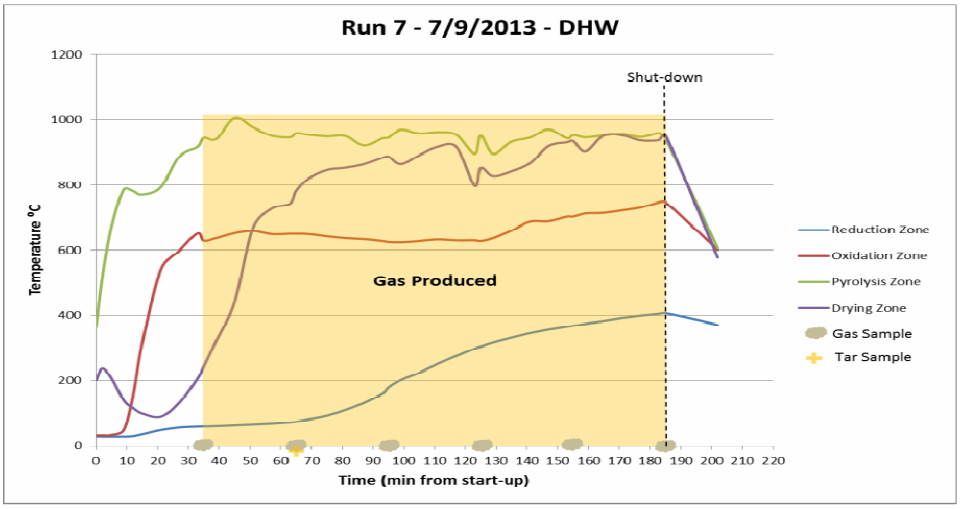

Run 7 Post-Run Report

Figure 1

The post-run cleaning was typical, with most of the burnt material located within the center of the reactor (Fig 1). The dining hall waste pellets had swelled in size and had become weaker. The reactor was very full; it was filled well above the top of the opening.

Figure 2

Figure 3

There was a large amount of caked DHW on the upper walls of the reactor (Fig 2). It was a darker shade of brown when compared to the pellets and had a doughy consistency. This has not been seen in the previous 6 runs. There was a large circular clinker located just below the air valves. The size and location were very similar to the previous run. The air valves were clear and free of clinkers/debris.

Run #8 (07/15/2013)
NO SCREENS
VIBRATOR ON
3 lb Charcoal
40 lb DHW
Feedstock: DHW
Run #8 began at 9:10 with an initial airflow of ~4 scfm (0 from the large compressor, ~3.4 scfm from the small compressor and ~22 scfh from the eyeglass). The temperature was allowed to climb until the pyrolysis zone reached 500°C.
At 9:22, 40 lb of the feedstock was added to the reactor. At this time, the temperature was 193.3°C in the drying zone, 501.1°C in the pyrolysis zone, 26.3°C in the oxidation zone, and 23.7°C in the reduction zone. Immediately after adding the initial 40 lb of feedstock, the airflow was decreased to ~ 2scfm (0

scfm from the large compressor, ~1.5 scfm from the small compressor, and ~30 scfh from the eyeglass). 2 lb of the feedstock was added into the reactor at 6 minute intervals.

In previous runs, the airflow was reduced ~10 minutes after the initial 40 lb of feedstock was added. In this run, the airflow was decreased immediately after the initial feedstock was added. The intention of this change was to decrease the temperature in the oxidation zone.

The flare was lit and stayed lit at 9:53 and Gas Sample 1 was taken. The temperature was 95.2°C in the drying zone, 766°C in the pyrolysis zone, 601°C in the oxidation zone, and 64.3°C in the reduction zone. The flare remained lit for the remainder of the run. The temperature in the drying zone peaked at 126°C, but remained below 100°C for the majority of the run. The temperature in the pyrolysis slowly climbed through the duration of the run to a peak of 812°C. The oxidation zone peaked halfway through the run at a temperature of 1084°C, but decreased between 900°C-1000°C for the remainder of the run. The temperature in the reduction zone increased throughout the run to a maximum of 697°C.

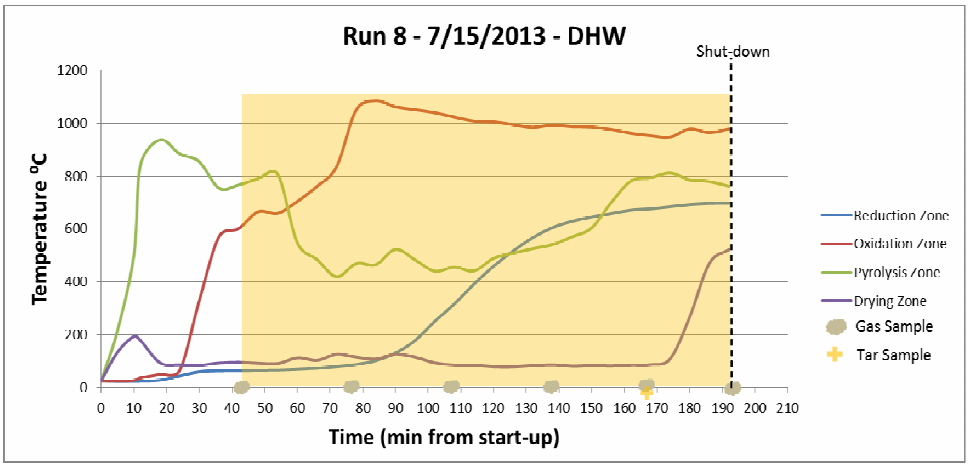

Six gas samples were taken at 30 minute intervals starting at 9:53. A single tar sample from the heat exchanger was taken at 10:58. At 12:22 the run was terminated voluntarily.

Run 8-Post-Run Report

Figure 1

Figure 2

The reactor was full of non-burnt feedstock (Fig 1); it was filled several inches above the top of the manhole. The burnt material was not confined to the center as seen in Figure 2 (Fig 2). Burnt feedstock was found throughout the interior within a few inches above the insert.

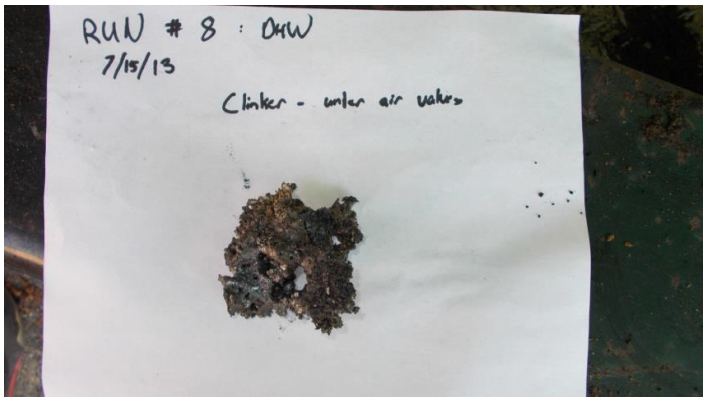

Figure 3

A large clinker was found just below the air valves similar to the previous runs. Three of the air valves were clogged with clinkers with one of the air valves being severely clogged.

Project Title: Nanostructured Catalyst-Support Systems for Next Generation Electrolyzers
Industrial Partner: Proton OnSite (formerly Proton Energy Systems)
PI: William Mustain; Co-PI's Radenka Maric; C. Barry Carter

1. Project Objective and Goals:

The objective of this proposed effort was to elucidate the effects of catalyst-support interactions on the activity, stability and utilization of supported Pt clusters for both water and oxygen evolution reactions in a proton exchange membrane electrolysis cell (PEMEC). In this study, four electrocatalyst systems were investigated: Pt black, Vulcan XC-72 supported Pt, Platinized tungsten carbide, and Pt supported on Magneli phase titania, Ti_4O_7. Each system was prepared in high surface area form and both physically and electrochemically characterized. Electrocatalytically active nanosized Pt clusters were deposited on each catalyst support and the resulting electrocatalyst was exposed to a series of electrochemical and materials analysis techniques including: Transmission Electron Spectroscopy, X-Ray Photoelectron Spectroscopy, X-Ray Diffraction, Scanning Electron Microscopy, Brunauer, Emmet and Teller gas adsorption, Cyclic Voltammetry and Linear Sweep Voltammetry on thin-film rotating disk electrodes.

2. Background

In recent years, hydrogen has received a considerable amount of attention due to its potential as a clean fuel for several devices and processes including proton exchange membrane fuel cells [1, 2]. Currently, the most common hydrogen source is hydrocarbons; however, it has been proposed that water electrolysis from renewable energy sources (i.e. PV solar) would represent a truly sustainable route for H_2. In proton exchange membrane (PEM)-based electrolyzers, water is fed to the anode where it is oxidized to molecular oxygen, protons and electrons (OER, Equation 1).

$$H_2O \rightarrow \frac{1}{2}O_2 + 2H^+ + 2e^-, \; E^o = 1.229\text{V} \quad (1)$$

The resulting protons travel through the PEM, electrons through the external power supply to the cathode where they combine to form the molecular hydrogen, (HER, Equation 2) [3, 4].

$$2H^+ + 2e^- \rightarrow H_2, \; E^o = 0.0\text{V} \quad (2)$$

This yields a total cell reaction of:

$$H_2O \rightarrow \frac{1}{2}O_2 + H_2, \; V_{thermo} = 1.229\text{ V} \quad (3)$$

Though the thermodynamically derived voltage for this cell is 1.229V, significant polarization losses at both the anode and cathode, coupled with transport losses in the electrolyte drive the true operating voltage in excess of 2.0V in commercial devices [5], with the hydrogen electrode seeing potentials as low as -0.4 V. Therefore, it is imperative for researchers to develop efficient electrocatalysts for the OER and HER.

In addition, reversible electrolyzer/fuel cell architectures have been recently proposed for compact energy storage/on-demand energy generation [6, 7], typically for remote or off-grid applications. For these devices, the operating voltage for the hydrogen oxidation electrode, Equation 4, during fuel cell operation can be nearly 0.2 V. These operating environments place a premium on the stability of the selected electrocatalyst between -0.4 and 0.2 V.

$$H_2 \rightarrow 2H^+ + 2e^-, E^o=0.0V \quad (4)$$

Supported Pt electrocatalysts are the most commonly implemented electrocatalyst for the HER. Pt is active for the HER, though quite expensive, which leads to high capital investment costs in electrolytic commercial hydrogen production [8, 9]. This has led researchers to search for HER electrocatalysts that either enhance the electrocatalytic activity of Pt or remove Pt completely. One way to achieve high activity is to manipulate the Pt electronic structure [10-12]; a comprehensive enhancement mechanism has yet to be proposed, which limits the rational design of next generation materials [13-15]. One additional mechanism to increase Pt activity is to improve dispersion and utilization, effectively increasing the electrochemically active surface area of the electrode. For Pt free catalysts, the most notable catalyst to date is Raney Ni, which has been reported to have a good performance [16], however, its limited stability in acid media due to dissolution has prevented widespread deployment.

Therefore, the purpose of this study was to develop new electrocatalyst support materials for the HER that have high stability and high electrochemical activity, whilst lowering the Pt loading to reduce cost.

3. Progress:

A significant amount of progress was made during our work. However, in each section below, only a small sampling of the results are shown, highlighting the most significant findings.

3.1 Evaluating the Proton Catalyst

The Proton catalyst was physically and electrochemically characterized. As expected (based on conversations with the sponsor), a pure Pt catalyst was found by SEM/EDX and TEM images, Figure 1, show fairly large agglomerated particles that are well faceted.

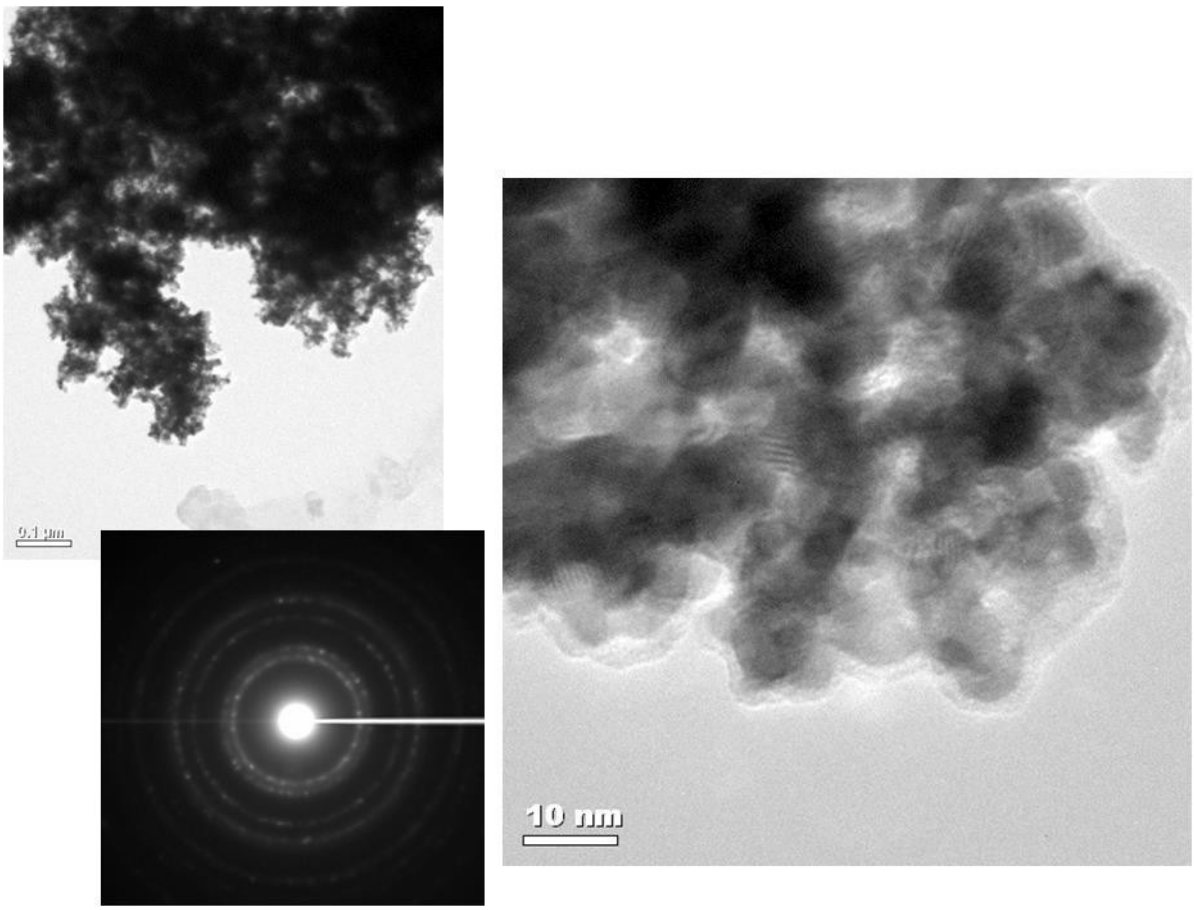

Figure 1: TEM Images of the Proton Catalyst

The Proton Pt catalyst was then coated on a 5 cm^2 glassy carbon disk electrode by preparing a 3 mg/ml aqueous dispersion and depositing 20µL of the dispersion on the electrode and allowing it to dry. Then, a 20µL aliquot of 100X diluted Nafion ® DE-520 solution was placed over the particle and allowed to dry. The dispersed catalyst was investigated in a 0.1 M $HClO_4$ electrolyte by cyclic voltammetry. Figure 2 shows a cyclic voltammogram (CV) for the Proton catalyst over cycles between 0 and 1.4 V vs. NHE in N_2 saturated electrolyte.

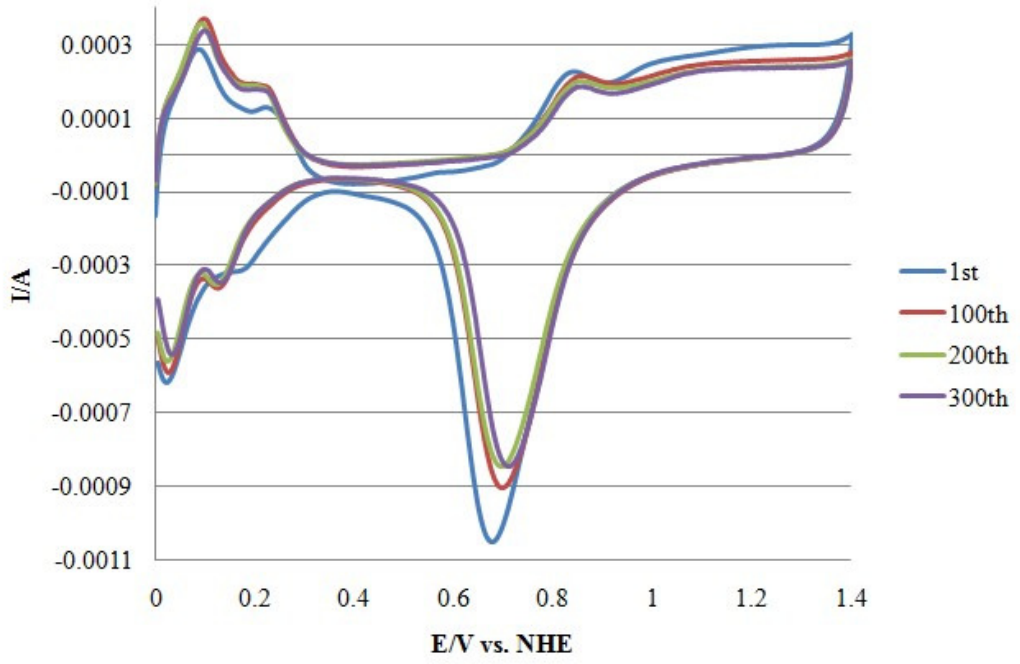

Figure 2: CV of Proton catalyst in N_2 saturated 0.1M $HClO_4$

The HER was also studied for 300 cycles between 0.2 V and -0.25 V vs. NHE. This also showed excellent cycling stability. This is shown in Figure 3.

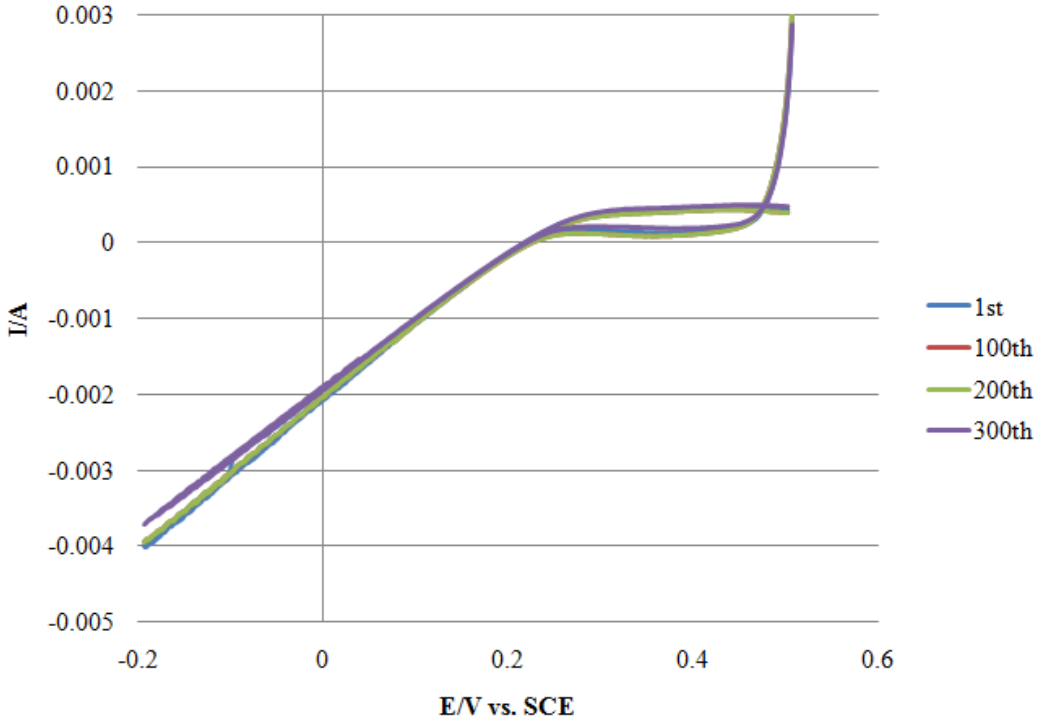

Figure 3: HER stability of the Proton catalyst.

The proton catalyst was then looked at by TEM and there was no noticeable difference in the catalyst structure after electrochemical treatment.

3.2 Synthesis and Characterization of Pt/WC

In short, WC was prepared by mixing tungsten oxide, carbon powder, KCl, and Ni powder in a ceramic boat and heated in a tube furnace at 1300^{o}C for 2h. The resulting powder was rinsed with copious amounts of HCl and 18MΩ Millipore DI water and dried. The WC support was platinized by first dispersing on a mirror-polished glassy carbon working electrode. Then, the WC was coated with an electrochemically deposited Cu monolayer by potential scanning in a $H_2SO_4/CuSO_4$ solution. The resulting electrode was rinsed with Millipore water and transferred to a dilute K_2PtCl_4/H_2SO_4 solution, which facilitated the galvanic displacement of Cu by Pt. Finally, the electrode was rinsed thoroughly with Millipore water. The resulting catalyst is shown in Figure 4.

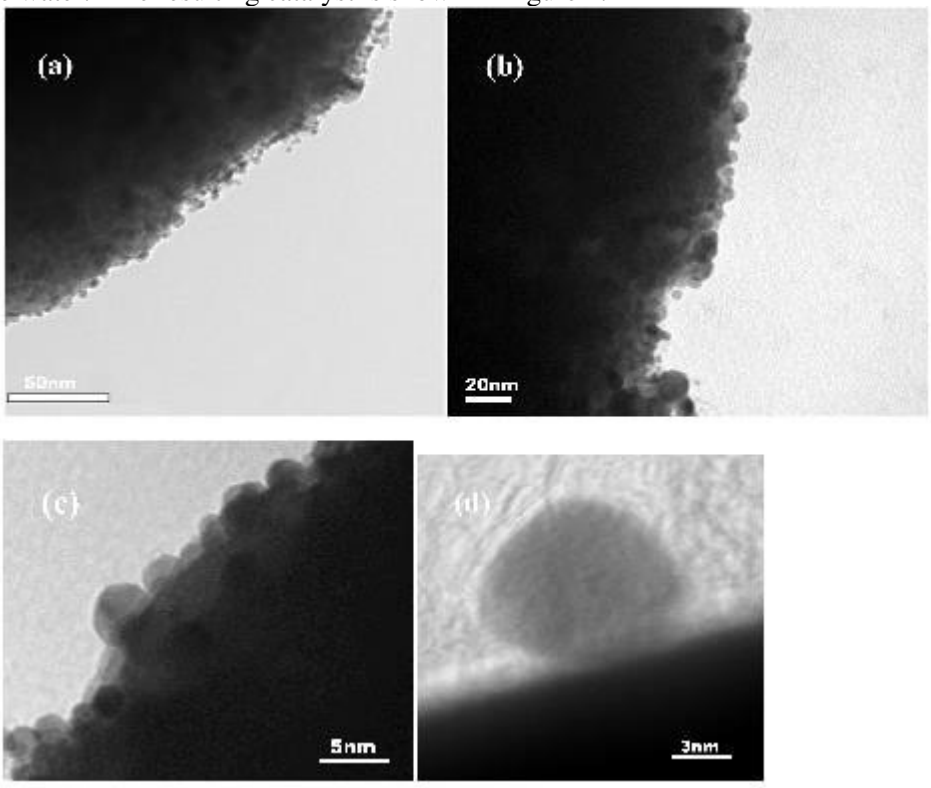

Figure 4: TEM images of Pt/WC

Clearly, the Pt particles were well dispersed on the new support material. Next, the catalyst's stability for the HER was investigated in the same way as the Proton catalyst, Figure 5.

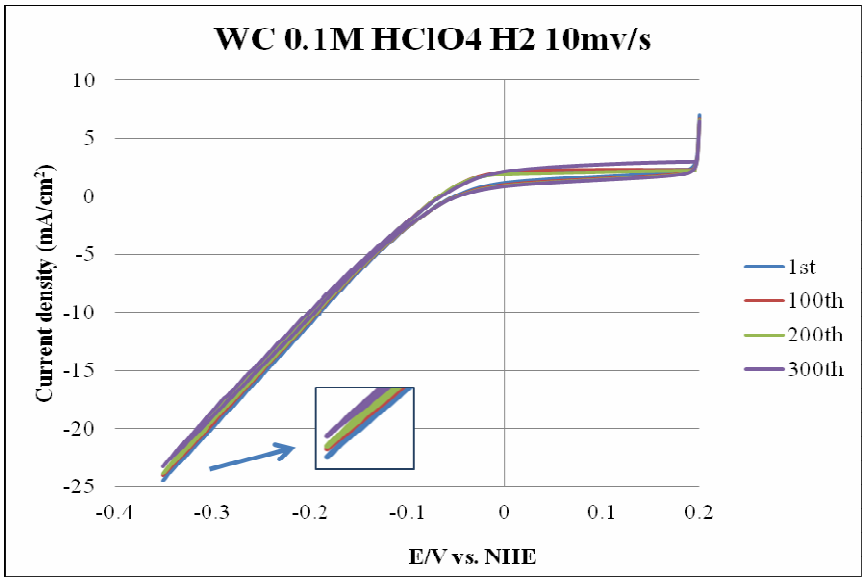

Figure 5: HER stability tests for Pt/WC

The Pt/WC catalyst showed excellent stability, comparable to the Proton catalyst. The activity was also comparable. These are very promising results as the Pt/WC catalyst has approximately 1/5 the loading of the conventional Proton catalyst. This is in stark contrast to commercial Pt/C catalysts whose performance degraded significantly, > 20 %, over the same number of scans (Figure not shown).

3.3 Completing the RSDT System and Demonstrating its Operation

As planned, the assembly of the laboratory scale RSDT setup was completed during the first quarter of the project. It is shown in Figure 6.

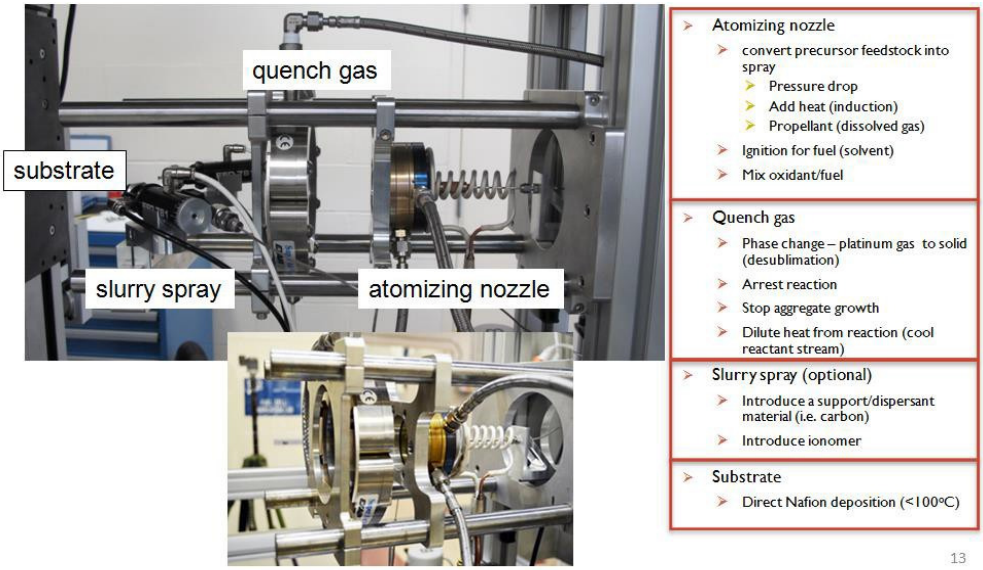

Figure 6: Photograph of the UConn RSDT Setup

The RSDT system was used to make Pt/Nafion electrodes that were well dispersed and high quality with only a few defects. This can be seen from a top view in Figure 7. A cross sectional view of one defect is shown in Figure 8.

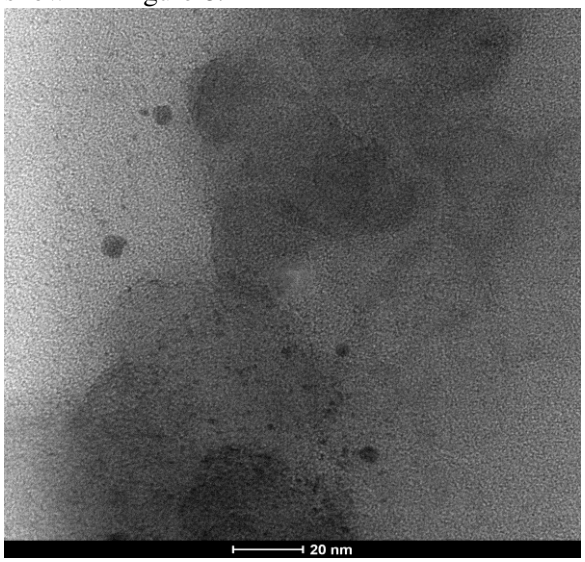

Figure 7: Top view of RSDT film

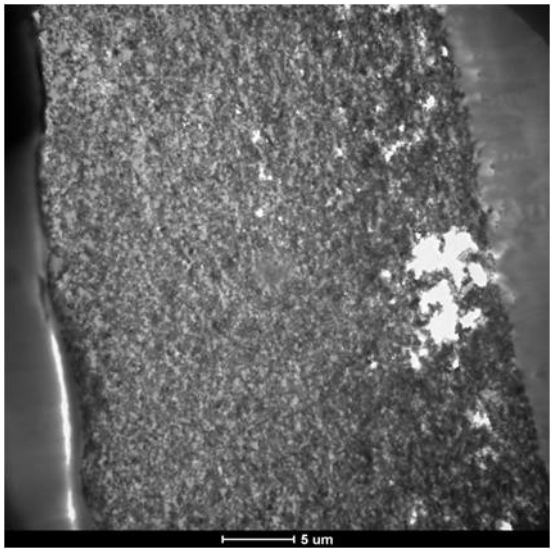

Figure 8: Image of one RSDT defect

These high quality films also showed excellent electrochemical performance, with similar electrochemically active area and Pt mass activity as state of the art commercial catalysts. The behavior of these films is summarized in the Table below.

	L_{Pt}	ECA	i_s @ 0.9V	i_m @ 0.9V
	mg_{Pt}/cm^2	m_{Pt}^2/g_{Pt}	mA/cm_{Pt}^2	A/mg_{Pt}
ink prepared				
40% Pt/Vu (ETEK)	13.7	31	190	190
20% Pt/Vu (ETEK)	14.3	65	230	230
45.9% Pt/HSC-E (TKK)	12.7	78	190	190
27% Pt/Ketjen	16.1	120	150	200
RSDT				
PT-1	4.9	92	220	201
PCI-1	6.1	120	152	143

Table 1: Comparison of RSDT and commercial catalyst films.

3.4 RSDT Deposition of Pt/Ti_4O_7

The RSDT setup in Figure 6 was modified to include a secondary set of nozzles whose purpose was to inject the catalyst support into the Pt field following the condensation and reduction of Pt in the flame. The resulting Pt/Ti_4O_7 particles deposited directly onto Nafion® 117 is shown in Figure 9.

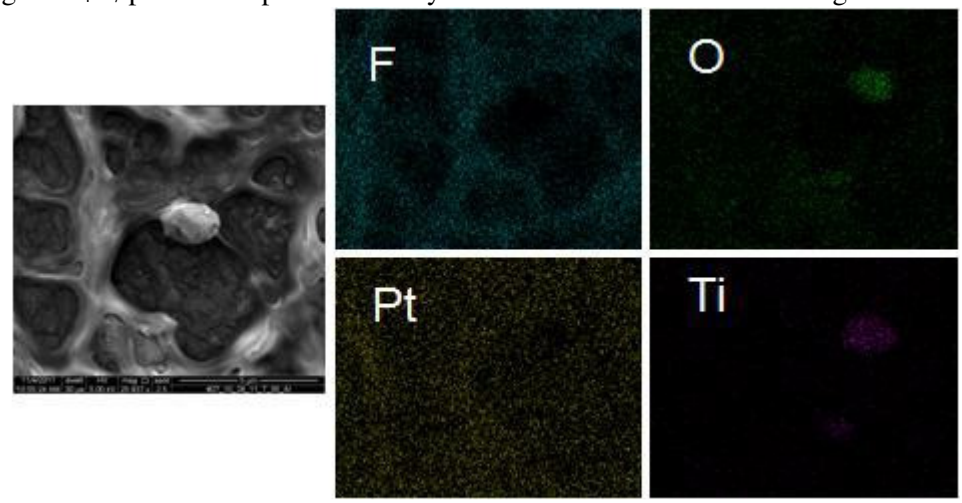

Figure 9: Pt/Ti_4O_7 particles deposited onto Nafion® 117.

One of the limitations of the Ebonex® Magneli phase titanate that was used was its large particle size. The team developed a ball milling procedure to reduce the primary particle size to the nm scale, a significant reduction from the commercial size.

3.5 Electrolyzer Testing

The team has taken the catalyst coated membranes (CCMs) prepared by RSDT and loaded them into a 25 cm^2 PEMEC. The PEMEC performance for Pt-anode, Pt-cathode cells prepared by RSDT have shown very good performance, shown in Figure 10.

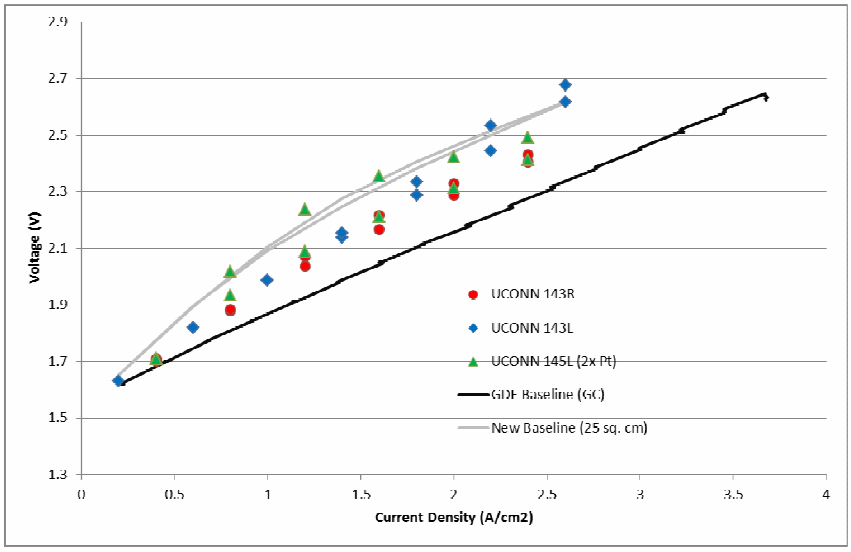

Figure 10: UConn-Proton PEMEC performance.

4. Collaborative Outcomes

Since the completion of this program, the interaction between UConn and Proton Onsite has increased significantly. There have been several proposals submitted by the team in this proposal to DOE and NSF, whose initial data resulted from this project. To date, one DOE STTR Phase-I proposal has been funded (DOE-EC-013088-03) and a few are currently under review.

References:

1. Armor, J.N., *Catalysis and the hydrogen economy.* Catalysis Letters, 2005. **101**(3-4): p. 131-135.
2. Holladay, J.D., et al., *An overview of hydrogen production technologies.* Catalysis Today, 2009. **139**(4): p. 244-260.
3. Manzoli, M., A. Chiorino, and F. Boccuzzi, *Decomposition and combined reforming of methanol to hydrogen: a FTIR and QMS study on Cu and Au catalysts supported on ZnO and TiO2.* Applied Catalysis B: Environmental, 2005. **57**(3): p. 201-209.
4. Hwu, H.H. and J.G. Chen, *Potential Application of Tungsten Carbides as Electrocatalysts: 4. Reactions of Methanol, Water, and Carbon Monoxide over Carbide-Modified W(110).* The Journal of Physical Chemistry B, 2003. **107**(9): p. 2029-2039.
5. Naik, S.P. and J.B. Fernandes, *Synthesis of an active zinc oxide and evaluation of catalytic activity towards decomposition of propan-2-ol*, in *Studies in Surface Science and Catalysis*, T.S.R.P. Rao and G.M. Dhar, Editors. 1998, Elsevier. p. 513-517.
6. W, S., *The role of fuel cells in energy storage.* Journal of Power Sources, 2000. **86**(1-2): p. 74-83.
7. Baldwin, R., et al., *Hydrogen□oxygen proton-exchange membrane fuel cells and electrolyzers.* Journal of Power Sources, 1990. **29**(3-4): p. 399-412.
8. Z. Mme, H.A., J. Pagetti, J. Talbot, Mater. Chem., 1977. **2**: p. 83.
9. K. Ashok, V., Mater. Chem. , 1979. **4**: p. 51.
10. Miles, M.H. and M.A. Thomason, *Periodic Variations of Overvoltages for Water Electrolysis in Acid Solutions from Cyclic Voltammetric Studies.* Journal of The Electrochemical Society, 1976. **123**(10): p. 1459-1461.
11. Conway, B.E. and J. O'M Bockris, *Electrolytic hydrogen evolution kinetics and its relation to the electronic and adsorptive properties of the metal.* The Journal of Chemical Physics, 1957. **26**(3): p. 532-541.
12. Sergio, T., *Work function, electronegativity, and electrochemical behaviour of metals: III. Electrolytic hydrogen evolution in acid solutions.* Journal of Electroanalytical Chemistry and Interfacial Electrochemistry, 1972. **39**(1): p. 163-184.
13. Al-Odail, F.A., A. Anastasopoulos, and B.E. Hayden, *The hydrogen evolution reaction and hydrogen oxidation reaction on thin film PdAu alloy surfaces.* Physical Chemistry Chemical Physics, 2010. **12**(37): p. 11398-11406.
14. Pašti, I. and S. Mentus, *Electronic properties of the PtxMe1−x/Pt(1 1 1) (Me = Au, Bi, In, Pb, Pd, Sn and Cu) surface alloys: DFT study.* Materials Chemistry and Physics, 2009. **116**(1): p. 94-101.
15. Greeley, J. and J.K. Nørskov, *Large-scale, density functional theory-based screening of alloys for hydrogen evolution.* Surface Science, 2007. **601**(6): p. 1590-1598.
16. Tanaka, S., N. Hirose, and T. Tanaki, *Evaluation of Raney–nickel cathodes prepared with aluminum powder and tin powder.* International Journal of Hydrogen Energy, 2000. **25**(5): p. 481-485.

Project Title: Reliability Evaluation and Enhancement of Synchronized Phasor Network
Industrial Partner: BC Hydro
PI: Peng Zhang

Project Objective and Goals:
The goals of this project are two folds including (1) reliability evaluation for a real large synchrophasor network and (2) enhancing the reliability of synchrophasor network through new robust measurement technologies.

First, we aim at quantifying and enhancing the reliability of BC Hydro's synchronized phasor (synchrophasor) network which is planned to be connected as part of the WECC wide area measurement system. Failures in the synchrophasor network will expose BC Hydro's transmission system to serious potential risks because of its widespread effect. To effectively quantify the reliability of a synchropahsor network, a hierarchical approach has been proposed. At the hierarchical level I, the reliability of a single phasor measurement unit (PMU) is analyzed. Hierarchical level II deals with the reliability of a PMUs-PDC working group constituted by one PDC and its subordinate PMUs. Hierarchical level III focuses on the assessment of the overall reliability of a backbone network to which multiple PMUs-PDC groups are interconnected. This approach has been used to assess the reliability of BC Hydro's synchrophasor network. Further, extensive sensitivity studies have been performed to identify the vulnerabilities in BC Hydro's synchrophasor network so as to provide the most cost-effective strategy to reinforce the network. Second, an Enhanced Subspace Least Mean Square (ESLMS) method has been presented for reliable and efficient power system phasor measurement. The high accuracy and high resolution of our Subspace Least Mean Square (SLMS) method are achieved at the cost of being computationally expensive. In this report the SLMS method is enhanced in two aspects: speed, and accuracy. The computation burden of SLMS is significantly reduced in three ways: (1) exploring the sparsity of power system signals, (2) using an iterative multi-sectional search scheme, and (3) the combination of the two techniques. These enhancements lead to speedup of about 100 times. Further, detection of the harmonic components based on the fact that they possess multiples of the fundamental frequency has been effectively employed, resulting in a more accurate and robust algorithm for fundamental and harmonic estimation in presence of noise. The enhanced SLMS algorithm, which detects harmonics more accurately, is more than 150 times faster than the original SLMS if interharmonic level is negligibly low. Moreover, the effect of signal noise on the estimation of phasor, frequency, and rate of change of frequency (RCF) has been presented in terms of the estimation of variance. The variance of the magnitude and phase has been presented as well. The analysis facilitate to eliminate measurement errors for Fourier-based measurement technologies.

2. Introduction

PMU networks are being developed in North American power utilities to serve as the next generation data communication infrastructures, especially for protection and control of bulk power transmission systems (1). A PMU network is also called a synchrophasor network, or a Wide Area Measurement System (WAMS), which is a geographically large system consisting of networked PMUs, phasor data concentrator (PDC), control center, high-speed data communication networks, as well as associated measurement, protection and/or control software applications. PMU is a crucial smart grid technology that is able to monitor and control power systems in real time by utilizing a highly precise synchronous clock system--global positioning system (GPS)--to build a unified time-space ordinate for the whole grid. PMUs are normally installed at key locations in the power network to acquire highly accurate voltage, current and phase angle snapshots of the instantaneous state of power systems (2), and updated no less than 30 times per second (3). Real-time synchrophasors can be integrated into control center state estimator for improving the accuracy of both steady state and dynamic security assessment,

thus enabling the power

systems to be operated closer to the design limits safely and securely (4-12). WAMS is expected to provide insights into the monitoring and control of the power system in real time, which were previously unavailable (13). In the near future, WAMS will reshape the transmission system through highly accurate computer applications for predicting, detecting and visualizing the onset of instability and intelligent controllers that will take automatic action to stabilize grid dynamics on a region-wide basis 14-17. Through WAMS, the transfer capability of power grid will be maximized without risking system performance.

BC Hydro has pioneered the implementation of Synchrophasor technologies in its Fraser Valley Office (FVO) and has installed PMUs in substations and major power plants. In the existing network, BC Hydro system states are sampled and transmitted to BPA's Phasor Data Concentrator (PDC) and then relayed to the Energy Management System at FVO for situational awareness purpose. Once integrated into the Western Interconnection Synchrophasor Program (WISP), BC Hydro PMU network will be linked with other PMU networks in neighboring US utilities through WECC's backbone WAMS network. Eventually, the Synchrophasor networks in North America could evolve into a continent–wide system. Geographically and physically, this interconnected PMU network will become a large-scale system as complex as the object that it monitors and controls—the North American Power Grid.

Similar to any other large cyber-physical systems, a WAMS can fail due to accidental errors and occasional failures in its components even though it is designed to guarantee and enhance security and stability of power systems. WAMS provides continuous information to system control centers for security of the grid. Therefore, it is the information source and system control channel in a wide area and integrated manner for state estimator, RAS, SCADA, and other essential components of the Energy Management System (EMS). Obviously, the observability and controllability of bulk power system are highly dependent on the availability and survivability of the WAMS. The consequence of WAMS failure is severe and even catastrophic. If protection/control functions are implemented in WAMS, unavailability of PMUs, spurious phasor data, and communication interruption will expose the power system to serious potential risks and may cause large blackouts because these adverse events will have wide-area impacts on the monitoring, control, and operation functions of system control centers.

WAMS reliability and its impact on power system security have been of great concern to power utilities including BC Hydro. The reliability evaluation of a real-life complex WAMS is still an open problem, despite emerging literature on the theoretical studies of WAMS reliability (24,25). In this project, we aim at building models, measures, evaluation methods for the reliability of BC Hydro's WAMS. In particular, two fundamental questions will be answered: (1) How to quantitatively analyze the reliability of WAMS considering parametric uncertainties and network quality? (2) How to identify the vulnerabilities in WAMS configuration so as to find most cost-effective strategies to enhance reliability with limited budget? WAMS is a vast network of electronic devices and communication links. Thus the WAMS reliability will have to deal with many risks in both systems, including hardware failure and software failure and other aspects 26-28. To tackle the challenges, we propose systematic methods for assessing and enhancing reliability of the synchronized phasor networks.

3. Reliability Analysis Method

Synchronized phasor network is a complex communication and control infrastructure designed to improve electric power system reliability, prevent the cascading outages, and support the grid integration of renewable resources 29-44. Figure 2.1 shows a schematic of a Synchronized phasor network. A typical example is the synchrophasor network to be built by the Western Interconnection Synchrophasor Program sponsored by DOE 45- 48.

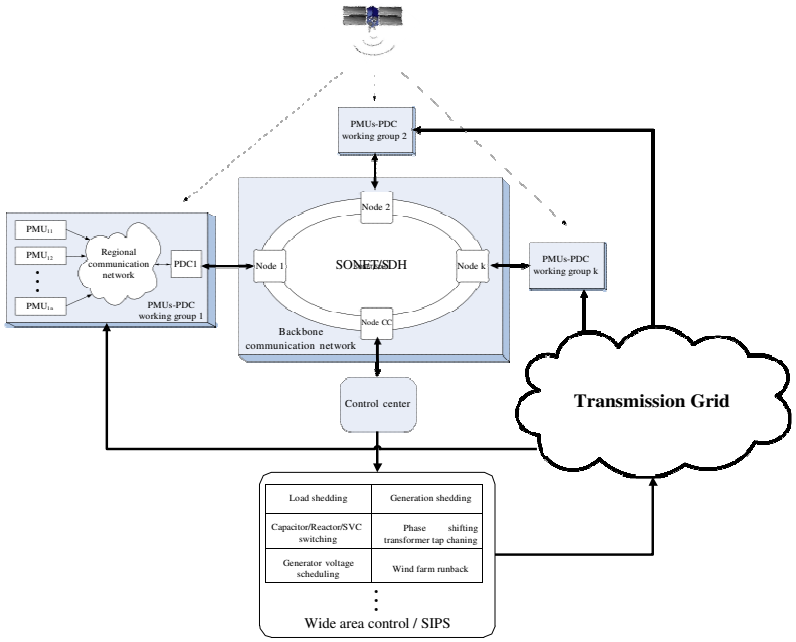

Figure 2.1 Hierarchical schematic structure of Synchronized phasor network

A hierarchical approach is adopted to evaluate the reliability of a WAMS. First, a Markov method is developed to analyze phasor measurement unit considering data uncertainty; Second, a method of calculating multiple reliability indices of PMU networks in the protection and recovery survival mechanisms is developed and an equivalent two-state model of a PMU network is presented.

4. Reliability Analysis Method

Phasor measurement units (PMUs) have been increasingly deployed in North American power industry for increasing controllability and observability of power systems. A total of over 1000 PMUs, five times of the existing PMUs, will be installed in the upcoming years. PMUs are the most fundamental devices in a WAMS. Thus, reliability analysis of PMU is the foundation and first step towards the reliability quantification and enhancement of WAMS.

Data uncertainty is a major challenge for PMU reliability assessment. PMUs have been installed in power systems only in recent years. The statistical failure data of PMUs are still sparse, which introduces imprecision in estimation of reliability parameters of PMU's components. Moreover, due to uncertainties in statistical data, it is necessary to estimate a range of a reliability parameter rather than a single value. On the one hand, statistical data of PMU components' failure records can be used, and on the other hand, the estimated ranges of reliability parameters may need to be adjusted on the basis of engineering judgments or field experiences that are generally characterized by vague linguistic descriptions. Traditional probabilistic methods are unable to properly handle fuzziness in data uncertainties. To tackle this challenge in real-world power systems, we propose combined statistic and fuzzy models for component's parameters and a generalized fuzzy hierarchical Markov method that is able to deal with data uncertainties in evaluating the entire PMU reliability.

Following our previous work, a PMU is broken down into seven functional modules as shown in Fig. 2.2,

including the voltage/current transformation module (M1), low-pass/band-pass filter module (M2), analog/digital sampling module (M3), CPU module (M4), GPS module (M5), communication module (M6) and power supply module (M0).

We have developed the fuzzy models of all the modules to cope with data uncertainties. The combined statistic-fuzzy models for different reliability parameters of components in each module are presented. Different fuzzy reliability modeling techniques are applied to different modules depending on their configurations and failure modes. A fuzzy series, or parallel, or series-parallel network model is used to represent the module M0, M1, M2, M3, M4 or M6, whereas a fuzzy Markov state space model is applied to represent the module M5 with more complex multiple failure modes. The reliability models for individual modules are converted into two-state Markov equivalents in series to facilitate the reliability evaluation of the entire PMU. In addition, a fuzzy sensitivity-analysis index is developed to quantify the impacts of parameters' uncertainties on the uncertainty of PMU reliability.

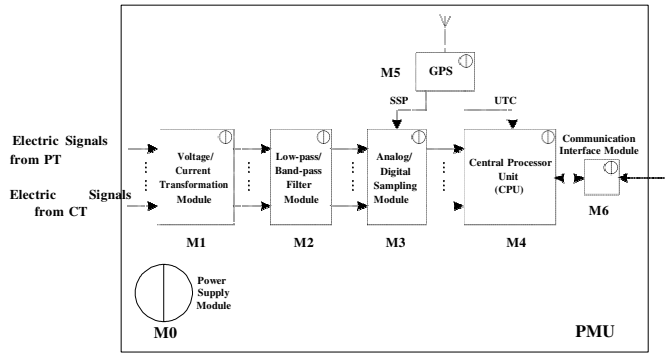

Figure 2.2 Structure of PMU

2.1.1 Statistic-Fuzzy Models for Reliability Parameters of Components in PMU

Results of fuzzy reliability evaluation of PMU depend on reasonable fuzzy membership functions of reliability parameters of its components. As mentioned earlier, a range of a parameter rather than a single value should be used in PMU reliability evaluation to cover the uncertainty of the parameter. The concept of a range is consistent with the cut-set in a membership function of fuzzy variable. A new fuzzy membership model named Pseudo-Gauss (PG) function is presented first in this section. The proposed model can take into account of statistical characteristic of reliability parameters of components in PMU. The presented membership function has the following general form:

$$u(x)=\begin{cases} L(x)=\exp\left[-\dfrac{(x-m)^2}{\sigma_L^{\,2}}\right] & x<m \\ R(x)=\exp\left[-\dfrac{(x-m)^2}{\sigma_R^{\,2}}\right] & x\geq m \end{cases} \qquad (2.1)$$

where x represents a reliability parameter of a component in PMU; m is the mean estimate of x; $L(x)$ and $R(x)$ are the left and right parts of $u(x)$. The shapes of $L(x)$ and $R(x)$ are mainly dependent on the scale parameters σ_L and σ_R.

The reliability parameters of a component in PMU reliability evaluation include repair time (r) and failure rate (λ). A switching component requires a parameter of unsuccessful switching probability (q). Given a set of statistical data of each parameter, the mean and interval estimates (upper and lower bounds) can be calculated using a statistical parameter estimation method. Once the mean, upper bound and lower bound of a component's reliability parameter are obtained, the scale parameters σ_L and σ_R in the membership function can be estimated.

A. Repair time r

The mean of repair time and its upper and lower bounds can be estimated using the *t*-distribution as follows:

$$\bar{r} = \sum_{i=1}^{n} r_i / n \tag{2.2}$$

$$[r_{\min}, r_{\max}] = [\bar{r} - t_{\alpha_0/2}(n-1)\frac{s}{\sqrt{n}}, \bar{r} + t_{\alpha_0/2}(n-1)\frac{s}{\sqrt{n}}] \tag{2.3}$$

where r_i is the repair time of a component in the *i*th outage; $\bar{r}$ denotes the mean estimate of the repair time; *n* is the number of repair time samples in the data set; *s* is the sample standard deviation; and $t_{\alpha 0/2}$ is chosen in such a way that the integral of the *t*-distribution density function with *n*-1 degrees of freedom from $t_{\alpha 0/2}$ to ∞ equals $\alpha_{0/2}$ where α_0 is a given significant level and is often specified to be 2.5-5%.

B. Failure rate λ

The mean of failure rate and its upper and lower bounds can be estimated using the $\chi^2 x2$-distribution as follows:

$$\bar{\lambda} = n/T \tag{2.4}$$

$$[\lambda^{\alpha_0}_{\min}, \lambda^{\alpha_0}_{\max}] = [\chi^2_{1-\alpha_0/2}(2n)/2T, \chi^2_{\alpha_0/2}(2n+2)/2T] \tag{2.5}$$

where *n* is the number of outages in the duration for statistical data set (e.g. one year); *T* is the length of the duration; $\bar{\lambda}$ is the mean estimate of failure rate; and $^2\chi_{\alpha_0/2}(2n+2)$ is chosen in such a way that the integral of the Chi-square distribution density function with degree of freedom 2n+2 from $^2\chi_{\alpha_0/2}(2n+2)$ to ∞ equals $\alpha_0/2$, whereas $^2\chi_{1-\alpha_0/2}(2n)$ is chosen that the integral of the Chi-square distribution density function with 2*n* degree of freedom from 0 to $\chi^2_{1-\alpha_0/2}(2n)$ equals $\alpha_0/2$ where α_0 is a given significant level.

C. Unsuccessful switching probability q

The mean of unsuccessful switching probability and its upper and lower bounds can be estimated using the binomial distribution as follows:

$$q = \frac{y}{n} \tag{2.6}$$

$$[q_{\min}, q_{\max}] = [q - z_{\alpha_0/2}\sqrt{q(1-q)/n}, q + z_{\alpha_0/2}\sqrt{q(1-q)/n}] \tag{2.7}$$

where *n* is the total number of switching actions; *y* is the number of unsuccessful switching events; and $z_{\alpha_0/2}$ is chosen in such a way that the integral of the standard normal distribution density function from $z_{\alpha_0/2}$ to ∞ equals $\alpha_0/2$ where α_0 is a given significant level.

D. Estimating the scale parameters σ_L and σ_R

The concept of the significant level is somewhat similar to the fuzzy degree in the membership function since both of them reflect a subjective confidence degree. Therefore it can be assumed that the upper and lower bounds calculated in Equation (2.3), (2.5) or (2.7) correspond to the two bounds at the α_0-cut of the fuzzy membership function where α_0 is a small percentage such as 5%. Therefore σ_L and σ_R can be estimated using the following formulas:

$$\begin{cases} \alpha_0 = \exp[-\frac{(x^{\alpha_0}_{\min} - m)^2}{\sigma_L^2}] \\ \alpha_0 = \exp[-\frac{(x_{\max} - m)^2}{\sigma_R^2}] \end{cases} \Rightarrow \begin{cases} \sigma_L = -(x^{\alpha_0}_{\min} - m)/\sqrt{-\ln \alpha_0} \\ \sigma_R = (x^{\alpha_0}_{\max} - m)/\sqrt{-\ln \alpha_0} \end{cases} \tag{2.8}$$

where *m* is the mean estimate of a reliability parameter of a component which is calculated from Equation

(2.2), (2.4) or (2.6), and $[x^{\alpha_0}_{\min}, x^{\alpha_0}_{\max}]$ is its interval estimate which is calculated from Equation (2.3), (2.5) or (2.7) at the given α_0 significant level.

By substituting the calculated σ_L and σ_R into (2.1), the PG membership function $u(x)$ of a reliability parameter of a component is created and can be plotted as shown in Figure 2.3.

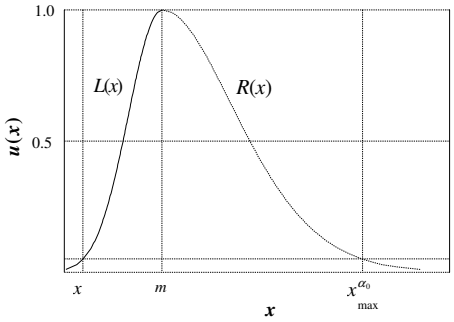

Figure 2.3 PG membership function of a reliability parameter

Note that the membership functions of repair time and unsuccessful switching probability are symmetric because the *t*-distribution and normal distribution in the interval estimation of these two reliability parameters are symmetric, whereas the membership function of failure rate is asymmetric because of the asymmetric characteristic of chi-square distribution for failure rate.

The proposed PG fuzzy membership function is a convex function in the real number domain. The most basic calculations in the fuzzy numbers are interval calculations at any cut-set. For a specified α_i, the α_i-cut interval $[x^{\alpha_i}_{\min}, x^{\alpha_i}_{\max}]$ of the PG membership function $u(x)$ can be obtained from Equation (2.8):

$$\begin{aligned} x^{\alpha_i}_{\min} &= m - \sigma_L \sqrt{-\ln \alpha_i} \\ x^{\alpha_i}_{\max} &= m + \sigma_R \sqrt{-\ln \alpha_i} \end{aligned} \tag{2.9}$$

For each module (M0-M6) of PMU shown in Figure 2.2, the membership functions of reliability parameters of its components are inputs and the membership functions of reliability indices of a two-state equivalent Markov model for each module are outputs. The reliability indices of the entire PMU can be evaluated using the equivalent Markov models of the seven modules and fuzzy interval calculations. These are discussed in the next section.

2.1.2 Fuzzy Models of Modules and Interval Calculations

The essential difference between crisp and fuzzy models of the modules is that all variables in a fuzzy model are expressed using their membership functions and require interval calculations at fuzzy grades (cut-sets). Simple operation rules for addition, subtraction, multiplication and division of fuzzy intervals, unfortunately, cannot be directly used when there is a dependency relationship between fuzzy numbers, which exists in some relatively complex reliability models of PMU modules. In the case of containing dependent fuzzy numbers, using the simple operation rules can lead to catastrophic overestimation in the reliability analysis. A suite of fuzzy interval calculation methods for the different reliability modules in PMU are proposed as follows.

A. Parallel models for M0 and M6

The power supply module (M0) and communication module (M6) in Fig. 2.2 are assumed to have two units in parallel-connection for redundancy. Therefore, using the parallel network concept, we have the following approximate formulas for M0:

$$\lambda_{M0} = \lambda_{1s}\lambda_{2s}(r_{1s} + r_{2s}) \quad (2.10)$$

$$r_{M0} = 1/(\frac{1}{r_{1s}} + \frac{1}{r_{2s}}) \quad (2.11)$$

$$U_{M0} = \lambda_{1s} r_{1s} \lambda_{2s} r_{2s} \quad (2.12)$$

where λ_{M0}, r_{M0} and U_{M0} are the failure rate, repair time and unavailability of an equivalent two-state model for M0 respectively; λ_{1s}, λ_{2s} and, r_{1s}, r_{2s} are the failure rates and repair times of the two parallel DC power sources, respectively.

The simple arithmetic operation rules of fuzzy intervals can be applied to Equations (2.10), (2.11) and (2.12). The α_i-cut intervals of λ_{M0}, r_{M0} and U_{M0} are calculated by

$$[\lambda_{M0}^{\alpha_i}] = [\lambda_{1s\min}^{\alpha_i}\lambda_{2s\min}^{\alpha_i}(r_{1s\min}^{\alpha_i} + r_{2s\min}^{\alpha_i}), \lambda_{1s\max}^{\alpha_i}\lambda_{2s\max}^{\alpha_i}(r_{1s\max}^{\alpha_i} + r_{2s\max}^{\alpha_i})] \quad (2.13)$$

$$[r_{M0}^{\alpha}] = [1/(\frac{1}{r_{1s\min}^{\alpha_i}} + \frac{1}{r_{2s\min}^{\alpha_i}}), 1/(\frac{1}{r_{1s\max}^{\alpha_i}} + \frac{1}{r_{2s\max}^{\alpha_i}})] \quad (2.14)$$

$$U_M^{\alpha_i} = \lambda_s^{\alpha_i} r_s^{\alpha_i} \lambda_s^{\alpha_i} r_s^{\alpha_i} \lambda_s^{\alpha_i} r_s^{\alpha_i} \lambda_s^{\alpha_i} r_s^{\alpha_i} \quad (2.15)$$

where $\lambda_{1s\min}^{\alpha_i}$, $\lambda_{2s\min}^{\alpha_i}$, $r_{1s\min}^{\alpha_i}$, $r_{2s\min}^{\alpha_i}$, $\lambda_{1s\max}^{\alpha_i}$, $\lambda_{2s\max}^{\alpha_i}$, $r_{1s\max}^{\alpha_i}$ and $r_{2s\max}^{\alpha_i}$ are the lower and upper bounds of the α_i-cut intervals for the failure rate and repair time of each of the two parallel DC power sources, which are estimated using Equation (2.9).

Similarly, the α_i-cut intervals ($[\lambda_{M6}^{\alpha_i}]$, $[r_{M6}^{\alpha_i}]$ and $[U_{M6}^{\alpha_i}]$) for the failure rate, repair time and unavailability of the module 6 which is composed of two parallel communication interfaces can be calculated using the equations similar to (2.10)-(2.15) except that the failure rates and repair times of the two parallel components are expressed by λ_{1c}, λ_{2c} and r_{1c} r_{2c} respectively and therefore the subscripts 1*s* and 2*s* are replaced by 1*c* and 2*c*. ,

B. Series model for M4

A serial network model is appropriate for the two-state Markov model of the CPU module M4 since it contains one software unit and one hardware unit where the failure of either one will result in outage of the whole module.

According to the series network concept, the failure rate λ_{M4}, repair time r_{M4} and unavailability U_{M4} of M4 are calculated by

$$\lambda_{M4} = \lambda_{hw} + \lambda_{sw} \quad (2.16)$$

$$r_{M4} = (\lambda_{hw} r_{sw} + \lambda_{sw} r_{sw}) / (\lambda_{hw} + \lambda_{sw}) \quad (2.17)$$

$$U_{M4} = \lambda_{hw} r_{hw} + \lambda_{sw} r_{sw} \quad (2.18)$$

where λ_{M4}, r_{M4} and U_{M4} are the failure rate, repair time and unavailability of the two-state model for M4 respectively; $\lambda_{sw}, \lambda_{hw}$ and r_{sw}, r_{hw} are the failure rates and repair times of hardware and software units, respectively. Note that Equation (2.18) is approximate since the overlapping term $-\lambda_{hw} r_{hw} \lambda_{sw} r_{sw}$ which has a very small value has been ignored.

By using the addition and multiplication rules of interval calculations, the intervals of failure rate and unavailability of M4 at the α_i-cut grade are given by

$$[\lambda_{M4}^{\alpha_i}] = [\lambda_{sw}^{\alpha_i}{}_{\min} + \lambda_{hw}^{\alpha_i}{}_{\min}, \lambda_{sw}^{\alpha_i}{}_{\max} + \lambda_{hw}^{\alpha_i}{}_{\max}] \quad (2.19)$$

$$U_M = \lambda_{hw} \left(\frac{r_h}{w} + \frac{\lambda_w}{\lambda_{sw}} \right) \left(\frac{r_{hw}}{2} + \frac{r_{sw}}{2} \right)$$

$$[r_{M4}^{\alpha_i}] = [\min\{f(r_{sw\min}^{\alpha_i}, r_{hw\min}^{\alpha_i}, Z_{\min}^{\alpha_i}), f(r_{sw\min}^{\alpha_i}, r_{hw\min}^{\alpha_i}, Z_{\max}^{\alpha_i})\}, \max\{f(r_{sw\max}^{\alpha_i}, r_{hw\max}^{\alpha_i}, Z_{\min}^{\alpha_i}), f(r_{sw\max}^{\alpha_i}, r_{hw\max}^{\alpha_i}, Z_{\max}^{\alpha_i})\}]$$

where $\lambda_{sw\min}^{\alpha_i}$, $\lambda_{sw\max}^{\alpha_i}$, $\lambda_{hw\min}^{\alpha_i}$, $\lambda_{hw\max}^{\alpha_i}$, $r_{sw\min}^{\alpha_i}$, $r_{sw\max}^{\alpha_i}$, $r_{hw\min}^{\alpha_i}$ and $r_{hw\max}^{\alpha_i}$ represent the lower and upper bounds of the α_i-cut intervals for the failure rates and repair times of software and hardware units in M4, respectively.

Unfortunately, the simple arithmetic operation rules of intervals cannot be directly applied to the interval calculation of the repair time r_{M4} as the λ_{sw} and λ_{hw} exist in both numerator and denominator of Equation (2.17). In other words, the relationships between fuzzy terms in the calculation are not "independent".

To deal with this problem, an intermediate variable $Z = \lambda_{sw} / \lambda_{hw}$ is introduced into (2.17) to yield

$$r_{M4} = \frac{\lambda_{sw} r_{sw} + \lambda_{hw} r_{hw}}{\lambda_{sw} + \lambda_{hw}} = \frac{\lambda_{hw} \left(\frac{\lambda_{sw}}{\lambda_{hw}} r_{sw} + r_{hw} \right)}{\lambda_{hw} \left(\frac{\lambda_{sw}}{\lambda_{hw}} + 1 \right)} = \frac{Z r_{sw} + r_{hw}}{Z + 1} \tag{2.21}$$

Z is independent of r_{sw} or r_{hw} but there is the same Z in the numerator and denominator. If Z is given, the α_i-cut interval $[r_{M4}^{\alpha_i}]$ can be obtained when r_{sw} or r_{hw} reaches its maximum and minimum. It can be observed that r_{M4} is a monotonous function of Z if r_{sw} and r_{hw} are given. Therefore, $[r_{M4}^{\alpha_i}]$ can be derived by using the simplified enumeration technique:

$$[r_{M4}^{\alpha_i}] = [\min\{f(r_{sw\min}^{\alpha_i}, r_{hw\min}^{\alpha_i}, Z_{\min}^{\alpha_i}), f(r_{sw\min}^{\alpha_i}, r_{hw\min}^{\alpha_i}, Z_{\max}^{\alpha_i})\}, \max\{f(r_{sw\max}^{\alpha_i}, r_{hw\max}^{\alpha_i}, Z_{\min}^{\alpha_i}), f(r_{sw\max}^{\alpha_i}, r_{hw\max}^{\alpha_i}, Z_{\max}^{\alpha_i})\}] \tag{2.22}$$

where $r_{sw\min}^{\alpha_i}$, $r_{hw\min}^{\alpha_i}$, $Z_{\min}^{\alpha_i}$ and $r_{sw\max}^{\alpha_i}$, $r_{hw\max}^{\alpha_i}$, $Z_{\max}^{\alpha_i}$ are the minimums and maximums of r_{sw}, r_{hw} and Z at the α_i-cut grade; f denotes the function expressed by Equation (2.21).

Note that the α_i -cut interval of Z is calculated by

$$[Z^{\alpha_i}] = [\frac{\lambda_{sw\min}^{\alpha_i}}{\lambda_{hw\max}^{\alpha_i}}, \frac{\lambda_{sw\max}^{\alpha_i}}{\lambda_{hw\min}^{\alpha_i}}] \tag{2.23}$$

C. Serials-Parallel models for M1, M2 and M3

The voltage/current transformation module (M1), low-pass/band-pass filter module (M2) and analog/digital sampling module (M3) have the same structure in which two circuit boards (B1 and B2) are in parallel and each of them consists of three single-phase voltage circuits and three single-phase current circuits in series from a reliability viewpoint since a board fails if any voltage or current circuit fails.

It is assumed that each voltage (or current) circuit has an identical failure rate and each circuit board has a total repair (replacement) rate since the whole board will be replaced no matter which circuit has failed. A two-state Markov model for M1, M2 or M3 can be obtained using combined serials and parallel network concepts.

For example, the α_i-cut intervals of the failure rate λ_{M1}, repair time r_{M1} and unavailability U_{M1} of M1 are calculated by

$$[\lambda_{M1}^{\alpha_i}] = [\lambda_{B1\min}^{\alpha_i} \lambda_{B2\min}^{\alpha_i} (r_{B1\min}^{\alpha_i} + r_{B2\min}^{\alpha_i}), \lambda_{B1\max}^{\alpha_i} \lambda_{B2\max}^{\alpha_i} (r_{B1\max}^{\alpha_i} + r_{B2\max}^{\alpha_i})] \tag{2.24}$$

$$[r_{M1}^{\alpha_i}]=[1/(\frac{1}{r_{B1\min}^{\alpha_i}}+\alpha_i\frac{1}{r_{B2\min}}(\quad),1/\ \frac{1}{r_{B1\max}^{\alpha_i}}{}_{i}+\frac{1}{r_{B2\max}^{\alpha}})] \tag{2.25}$$

$$U_M^{\alpha_i} = \lambda_B^{\alpha_i} r_B^{\alpha_i} \lambda_B^{\alpha_i} r_B^{\alpha_i} \lambda_B^{\alpha_i} r_B^{\alpha_i} \lambda_B^{\alpha_i} r_B^{\alpha_i} \quad (2.26)$$

where

$$\lambda^{\alpha_i} = 4^{U} {}^{\alpha_i} \lambda^{I} {}^{\alpha_i} \lambda^{U} {}^{\alpha_i} + \lambda^{I} {}^{\alpha_i} \quad (2.27)$$

$$[\ _{B1}] \quad [3(\ _{B1})_{\min} \quad 3(\ _{B1})_{\min}, 3(\ _{B1})_{\max} \quad 3(\lambda^{I}_{B1})^{\alpha_i}_{\max}]$$

$$\lambda^{\alpha_i} = \quad (2.28)$$

$$[\ _{B2}] \quad [3(\lambda^{U}_{B2})^{\alpha_i}_{\min} + 3(\lambda^{I}_{B2})^{\alpha_i}_{\min}, 3(\lambda^{U}_{B2})^{\alpha_i}_{\max} + 3(\lambda^{I}_{B2})^{\alpha_i}_{\max}]$$

In Equations (2.27) and (2.28), λ^{U}_{B1}, λ^{I}_{B1} and λ^{U}_{B2}, λ^{I}_{B2} represent the failure rates of the voltage circuit and current circuit in B1 and B2 boards, respectively; r_{B1} and r_{B2} represent the repair times of B1 and B2 boards. The lower and upper bounds of the α_i-cut interval for the component reliability parameter λ^{U}_{B1}, λ^{I}_{B1}, λ^{U}_{B2}, λ^{I}_{B2}, r_{B1} or r_{B2} are estimated using Equation (2.9).

Similarly, the α_i-cut interval of the failure rate, repair rate, or unavailability of the two-state model for M2 or M3, which is expressed by $[\lambda^{\alpha_i}_{M2}], [\lambda^{\alpha_i}_{M3}], [r^{\alpha_i}_{M2}], [r^{\alpha_i}_{M3}], [U^{\alpha_i}_{M2}]$ or $[U^{\alpha_i}_{M3}]$ is estimated in the same way.

D. Markov Model for M5

The GPS module (M5) has a high-precision crystal oscillator and a GPS receiver for producing high-precision clock signals. Normally, the crystal oscillator works in a track mode, where it traces the GPS signals (Pulses per Second (PPS)) and compensates any time error between the quartz oscillator frequency and PPS. The crystal oscillator will switch to the replacement mode to substitute the GPS receiver and to provide synchronous time signal when the GPS receiver fails. This switching is called functional switching.

The Markov model as shown in Figure 4.3 is developed to represent the reliability of GPS module.

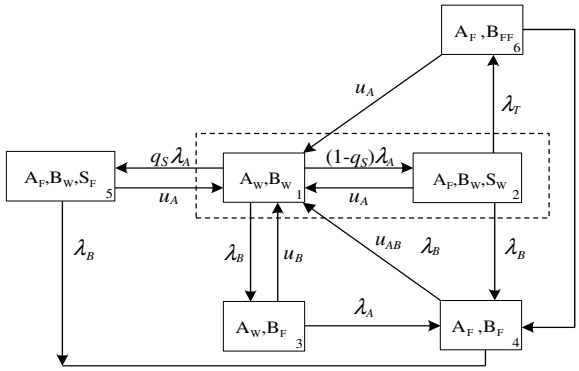

Figure 2.4 Markov state space model of GPS module

Here, A, B and S represent the GPS receiver, crystal oscillator and switching respectively. The subscript W and F denote that the unit is in an operation or physical failure state, respectively. The subscript FF denotes the crystal oscillator in a functional failure state where the failure is due to a large cumulative time error when the crystal oscillator operates alone without the GPS receiver. λ_T is the transition rate at which the functional failure of the crystal oscillator occurs and can be calculated using the reciprocal of the average duration required to reach the maximum cumulative time error. Additionally, q_S is the probability of unsuccessful functional switching and λ_A, u_A, and λ_B, u_B represent the failure rates and repair rates of the GPS receiver and crystal oscillator respectively. If the failed components are repaired one by one, the repair rate u_{AB} of two components fault can be calculated as $u_A u_B/(u_A + u_B)$. Note that the repair rate equals the reciprocal of repair time.

Using the frequency balance technique, the equivalent failure rate $\lambda_{M5,}$, repair time r_{M5} and unavailability U_{M5} of M5 can be obtained and expressed by

$$\lambda_{M5} = \frac{P_1(q_S\lambda_A + \lambda_B) + P_2(\lambda_T + \lambda_B)}{P_1 + P_2} \quad (2.29)$$

$$P_1(\quad r_{M5} = \frac{P_3 + P_4 + P_5 + P_6}{q_S\lambda_A + \lambda_B) + P_2(\lambda_T + \lambda_B)} \quad (2.30)$$

$$U_{M5} = P_3 + P_4 + P_5 + P_6 \quad (2.31)$$

However, this is not a crisp Markov model but a fuzzy Markov model since all reliability parameters in the model are represented by membership functions that require interval calculations at fuzzy grades (cut-sets). Particularly, the state probabilities P_i (i=1,…,6) are results of the Markov model and thus are implicit functions of reliability parameters of components. Interval calculation rules cannot deal with this complex reliability model. The following optimization model can be used to compute the fuzzy intervals of the unavailability U_{M5} at any α_i-cut:

$$\underline{U_{M5}(\alpha_i)} = \min \sum_{j=3}^{6} P_j \text{ and } \overline{U_{M5}(\alpha_i)} = \max \sum_{j=3}^{6} P_j \quad (2.32)$$

Subject to

$$(\boldsymbol{T}^T - \boldsymbol{I})\boldsymbol{P}^T = 0 \quad (2.33)$$

$$P_1 + \cdots + P_6 = 1 \quad (2.34)$$

$$\lambda_{j\min}^{\alpha_i} \le \lambda_j \le \lambda_{j\max}^{\alpha_i} \quad (j = 1,\ldots,6) \quad (2.35)$$

As shown in Fig. 2.4, the Markov model of GPS has 6 states with 2 working states (states 1 and 2 in the dot-dashed frame),five independent transition rates expressed by λ_A, λ_B, u_A, u_B, λ_T, and the unsuccessful switching probability q_S. $\boldsymbol{P}$ is the probability row vector of limiting states and P_i is its element for the probability of each limiting state; $\boldsymbol{I}$ is the unit matrix; $\boldsymbol{T}$ is the state transition matrix and the superscript T represents transposition of a matrix or vector; $\underline{U_{M5}(\alpha_i)}$ and $\overline{U_{M5}(\alpha_i)}$ are the lower and upper bounds of the sum of probabilities of 4 failure states 3, 4 5 and 6. $\lambda_{j\min}^{\alpha_i}$ and $\lambda_{j\max}^{\alpha_i}$ are the minimum and maximum of transition rate j at the α_i-cut grade. Equation (2.33) represents the Markov equations, and Equation (2.34) is the total probability condition.

By solving the two optimization problems (minimization and maximization of the objective function) with the same constraints respectively, the lower and upper bounds of the probability interval of the unavailability U_{M5} are obtained. The similar concept can be extended to calculate the fuzzy intervals for the failure rate $\lambda_{M5,}$ and repair time r_{M5} of the two-state model for M5. The α_i-cut intervals for $\lambda_{M5,}$ ($\underline{\lambda_{M5}(\alpha_i)}$ and $\overline{\lambda_{M5}(\alpha_i)}$)and those for r_{M5} ($\underline{r_{M5}(\alpha_i)}$ and $\overline{r_{M5}(\alpha_i)}$) are obtained by solving the optimization models with the objective functions in Equations (2.36) - (2.39) respectively and with the same constraints (2.33), (2.34) and (2.35).

$$\underline{\lambda_{M5}(\alpha_i)} = \min \frac{P_1(q_S\lambda_A + \lambda_B) + P_2(\lambda_T + \lambda_B)}{P_1 + P_2} \quad (2.36)$$

$$\lambda_{M5} \quad \overline{\quad}(\alpha_i) = \max \frac{P_1(q_S\lambda_A + \lambda_B) + P_2(\lambda_T + \lambda_B)}{P_1 + P_2} \quad (2.37)$$

$$M5 \quad i \quad r \quad (\alpha) = \min \frac{P_3 + P_4 + P_5 + P_6}{\overline{\quad}P_1(\quad q_S\lambda_A + \lambda_B) + P_2(\lambda_T + \lambda_B)} \quad (2.38)$$

$$M5 \quad i \qquad \overline{r}(\alpha) = \max_{P_1(} \frac{P_3 + P_4 + P_5 + P_6}{q_S\lambda_A + \lambda_B) + P_2(\lambda_T + \lambda_B)} \tag{2.39}$$

F. Equivalent two-state fuzzy Markov model of PMU

So far, the α_i-cut interval calculation models of failure rate, repair time and unavailability for each of the seven modules have been developed. As shown in Figure 2.2, the PMU can be represented using the seven two-state Markov models connected in series. By applying the series concept again, the reliability indices (failure rate, repair time and unavailability) for the whole PMU are calculated by

$$\lambda_{PMU} = \sum_{i=0}^{6} \lambda_{Mi} \tag{2.40}$$

$$r_{PMU} = (\sum_{i=0}^{6} \lambda_{Mi} r_{Mi}) / (\sum_{i=0}^{6} \lambda_{Mi}) \tag{2.41}$$

$$U_{PMU} = 1 - \prod_{i=0}^{6} (1 - U_{Mi}) \tag{2.42}$$

The α_i-cut intervals of the failure rate and repair time for the whole PMU can be calculated by repeatedly using equations similar to (2.19) and (2.21)-(2.23) respectively, whereas the α_i-cut intervals of the unavailability for the whole PMU can be computed by directly using the subtraction and multiplication rules for interval calculations. The fuzzy membership functions of the three reliability indices for the whole PMU are built by the fuzzy interval calculations at different α_i–cuts from 0.0 to 1.0.

2.1.3 Fuzzy Reliability Indices of PMU

The estimated means and upper and lower bounds of the reliability parameters for components in the PMU modules have been calculated by using typical data (49). The membership functions of three reliability indices (unavailability *U,* failure rate λ and repair time *r*) of the whole PMU are plotted in Figures 2.5-2.7.

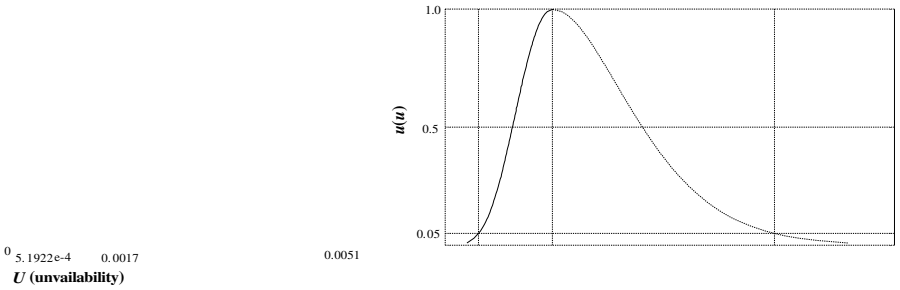

Figure 2.5 Membership function of unavailability of PMU

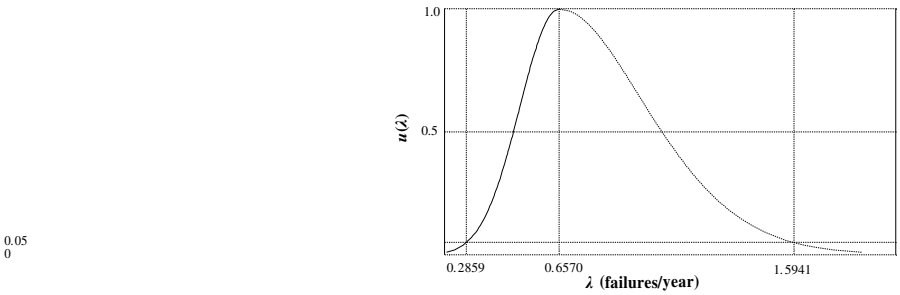

Figure 2.6 Membership function of failure rate of PMU

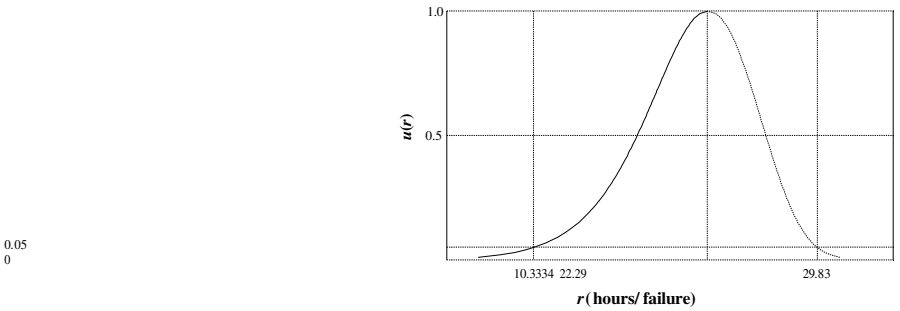

Figure 2.7 Membership function of repair time of PMU

The following observations can be made:

- The fuzzy membership functions of the reliability indices quantitatively indicate the ranges of the indices representing PMU reliability. For instance, it can be seen from Figure 2.5 that the unavailability of PMU is 0.17% with the maximal possibility at the fuzzy grade of 1.0 but could be as low as 0.052% and as high as 0.51% with the minimal possibility at the fuzzy grades of 0.05. The different ranges of failure rate and repair time of PMU at different fuzzy grades can be observed from Figure 2.6 and 2.7 respectively.
- The fuzzy membership functions of reliability indices of PMU are still convex and have an asymmetric shape similar to that of a Pseudo-Gauss membership function being deformed leftward (U and λ) or rightward (r).
- The indices with maximal possibility at the fuzzy grade of 1.0 are the same as those obtained using the crisp Markov model (49) and setting the reliability parameters of components to be the mean estimates. This indicates that the fuzzy Markov model of PMU includes the information of the crisp Markov model of PMU and provides a wider insight into reliability indices and their uncertain ranges at different confidence levels.

2.1.4 Fuzzy Sensitivity Analysis of PMU

Uncertainties of different reliability parameters of different components have different impacts on the uncertainty of PMU reliability indices. The fuzzy sensitivity analysis can be performed to identify the most sensitive fuzzy parameter impacting the uncertainty of PMU reliability and to quantify the change range of a fuzzy reliability index of PMU with the variation in the uncertain range of a specific reliability parameter at the (1-α_0) confidence level. The unavailability index is used as an example in the following and the fuzzy sensitivity analyses for other two indices are similar. For this purpose, the sensitivity index named Weighted Fuzzy Closeness (*WFC*) index is proposed as follows:

$$WFC(u_1,u_2)=\frac{\sum_{i=1}^{n}[(|(u_1)_L^{\alpha_i}-(u_2)_L^{\alpha_i}|+|(u_1)_U^{\alpha_i}-(u_2)_U^{\alpha_i}|)\times\alpha_i]}{\sum_{i=1}^{n}\alpha_i} \tag{2.43}$$

where u_1 and u_2 represent the two membership functions of PMU unavailability before and after the uncertain range of a specific reliability parameter is changed; $(u_1)_L^{\alpha_i}$ and $(u_1)_U^{\alpha_i}$ represent the lower and upper bounds of u_1 at the α_i-cut set; $(u_2)_L^{\alpha_i}$ and $(u_2)_U^{\alpha_i}$ represent the bounds of u_2 at the α_i-cut set; n is the number of α_i-cut sets. Obviously, the *WFC* reflects the weighted average distance between two membership functions. A greater index value denotes a higher sensitivity.

The previous studies identified 5 failure rates in M4 and M5 modules that have the largest impacts on

PMU reliability. The *WFC* indices of these five failure rates with their fuzzy sensitivity ranking order are given in Table 2.1. In each case, the confidence interval of only one failure rate is decreased or increased by 20% from the initial value but its mean estimate is kept as unchanged.

Table 2.1 Fuzzy sensitivity analysis for PMU parameters

Indices & Order / **Parameters**	***WFC* (80%)**	***WFC* (120%)**	***Fuzzy Sensitivity***
λ_{hw}**(M4)**	4.8296e-5	4.8296e-5	2
λ_{sw}**(M4)**	3.3190e-6	3.3190e-6	5
λ_T**(M5)**	3.8715e-5	3.7321e-5	3
λ_B**(M5)**	5.2961e-6	5.2458e-6	4
λ_A**(M5)**	1.3389e-4	1.3380e-4	1

The *WFC* values indicate that λ_A is the most sensitive parameter impacting the uncertainty of PMU reliability, followed by λ_{hw}, λ_T and then by λ_B and λ_{sw}. In other words, the uncertainty of PMU reliability can be effectively decreased if the most sensitive reliability parameter of a key component such as λ_A can be more exactly estimated.

The membership functions of the most sensitive parameter λ_A for the initial (1-α_0) confidence interval, 80% and 120% of the initial interval are shown in Fig.2.8-(a). The three membership functions of PMU unavailability corresponding to the three intervals of λ_A are shown in Fig.2.8-(b). Note that 80% means that the range between the mean point and upper bound point or between the mean point and lower bound point is 80% of its original range. The 120% has a similar significance.

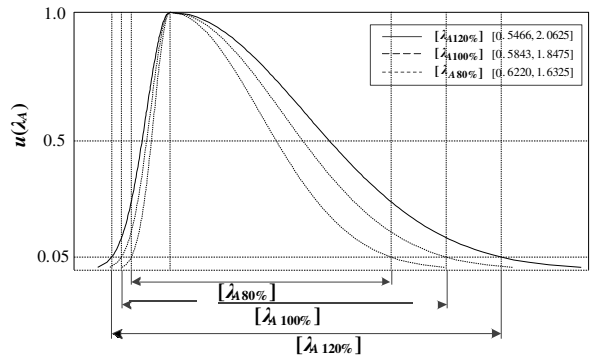

(a) Membership functions of λ_A for the three confidence intervals

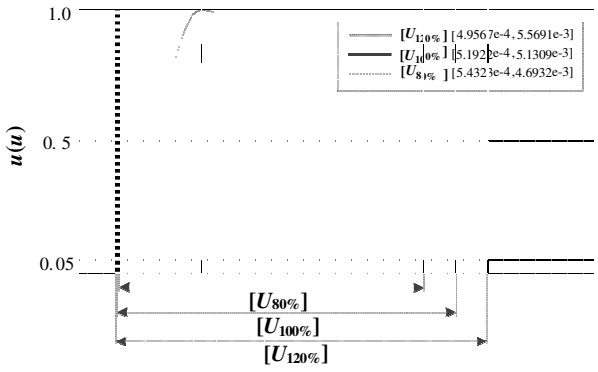

(b) Membership functions of PMU unavailability for the three confidence intervals

Figure 2.8 Sensitivity analysis of λ_A in M5 to PMU reliability

The following observations can be made:

- A relatively large percentage variation of λ_A creates a relatively small percentage change of PMU unavailability. The 20% variation of the confidence interval of λ_A in both upper bound (increase) and lower bound (decrease) leads to only about 13% increase of PMU unavailability in the upper bound and only 2-3% decrease in the lower bound. This indicates that the uncertainty of unavailability of the whole PMU is not so sensitive even to the most sensitive parameter. This is a positive feature.
- However, the sensitivity of the PMU unavailability is of asymmetry. It is much more sensitive at its upper bound than its lower bound. This means that the PMU unavailability will have a larger "bad" error (increased unavailability) than a "good" error (decreased unavailability) due to uncertainty of component's reliability parameter.

Identification of sensitive components or parameters provides useful information in the quality control of reliability data of PMU components.

2.2 Reliability Analysis of PMU networks

Any existing communication and data transfer network in power systems has a complicated structure because of its geographically large scale and complexity in connections. Different random factors in such a complex network make it very difficult to exactly predict communication latency and possible contingencies. The existing communication and data transfer network cannot meet the requirement of real-time PMU data transmission [50]. A hierarchical structure of WAMS is presented as shown in Figure 2.1. In the proposed hierarchical structure, not only the backbone network (which may be a single-direction, ring-structure and dual-passage optic fiber network) can restore communication within 50ms, but also each regional PMU network can recover the communication within the same time range after any outage occurs [51]. In other words, this hierarchical structure can satisfy the time requirement of data transfer in the whole WAMS that has a very wide coverage geographically.

At the initial stage of PMU network, a simple parallel redundancy structure for data transfer between each PMU and Phasor Data Center (PDC) may be enough because only very few PMUs are installed at the beginning [52], [53]. With the growth of WAMS and increased number of PMUs, however, a PMU network in WAMS will definitely become a complex mesh net due to economic and reliability considerations. This section develops the methods of calculating multiple reliability indices for a meshed WAMS PMU network.

In this section, we will first discuss the hierarchical structure of WAMS and two survival mechanisms of PMU networks to meet the service quality requirements. Then, we will present the methods to evaluate multiple reliability indices for WAMS PMU networks with the two different survival mechanisms. Finally, a numerical example will be provided.

2.2.1 Survival Mechanisms of PMU Networks

A network survival mechanism refers to the way of recovering the normal data transfer in the network after a contingency event such as a link failure. The network survival mechanisms could be classified into dynamic restoration and static protection [54-56]. In the dynamic restoration, no backup path is pre-specified. When a contingency happens, a search process starts to dynamically find a possible backup path. If no backup path can be found, the network fails with data transfer lost. This mechanism can allow better resource utilization and save investments because it does not need pre-specified backup paths for each of all PMUs. Its disadvantage is a longer recovery time as additional routing and signaling messages are required to select and set up backup paths when an outage occurs. In the static protection, a backup path is pre-established together with the primary path for each PMU. When a contingency occurs on the primary path, the data transfer is switched to the backup path immediately. This mechanism assures a fast recovery of data transfer interruption. Its demerit is the need of more resources resulting in a relatively high investment cost.

The Resilience-Differentiated Quality of Services (RD-QoS) model proposed in Reference [57] can be used as the criteria to analyze the survival requirements of WAMS PMU networks. The RD-QoS model includes four resilience classes primarily distinguished by recovery time requirements. Traffic flows of Resilience Class 1 (RC1) have the highest resilience requirement and require service recovery within 100ms. The proposed resilience scheme for RC1 services is the static protection. Traffic flows of Resilience Class 2 (RC2) have the medium resilience requirement with the recovery time between 100ms and 1s. A fast dynamic restoration, in which a recovery path is established right after a failure is detected, is needed for RC2 services. Traffic flows of Resilience Class 3 (RC3) correspond to the lower resilience requirement with the recovery time between 1 and 10 seconds. Data packets may be forwarded after a rerouting is established following data transfers needing RC2 services. Resilience Class 4 (RC4) is defined for traffic flows with no resilience requirement.

WAMS could be applied into the three main areas: (1) real time wide-area monitoring and analysis; (2)

real time wide-area control; and (3) real time wide-area protection. Additionally, the control action of power system primary protection is required to be within 20ms and the time requirement of transient stability control ranges from 150ms to 2s. In contrast with the RD-QoS model, it can be seen that the communication restoration requirements for the three applications of WAMS simply correspond to the traffic flows in RC1, RC2 and RC3 services. Therefore, both static protection and dynamic recovery mechanisms should be adopted in the WAMS PMU network.

2.2.2 Reliability Evaluation of PMU Networks

It is assumed that all optic fiber links in the PMU network are independent of each other. Each optic fiber has two states of working and failure with the constant failure and repair rates. The availability and unavailability of each link can be calculated as follows:

$$R_i = \frac{\lambda_i}{\lambda + u} \qquad (2.44)$$

i

$$Q_i = \frac{u_i}{\lambda_i + u_i}$$

where λ_i and u_i are the failure and repair rates of the ith optic fiber link in the PMU network, respectively. The repair time r_i is the reciprocal of u_i. λ_i and r_i can be estimated using historical statistic data.

1. Reliability evaluation in the protection mechanism

Unlike a single-input and single-output network that is often discussed in general reliability engineering, the PMU network in the proposed WAMS structure is a multi-input (several or many PMUs) and single-output (one PDC) network. Locations of PMUs geographically spread in the PMU network because PMUs are installed at substations and generator plants in a power system. The *Dijkstra* shortest path algorithm can be used to determine two disjoint paths (without common links) in the PMU network as the 1+1 protection routes for each PMU. When the primary path fails, the backup one is switched in service immediately. Reference [58] investigated the relationship between the number of possible disjoint paths of node-pairs and the average number of links connected to nodes (called nodal degree) using a random graph generator approach. According to the simulation results in the reference, the probability of having two disjoint paths between any node-pairs is near 100% when the nodal degree is greater than 3.

A PMU network in WAMS is in the normal working state if every PMU can normally communicate with the PDC. Thus we have

$$A = \bigcap_{i=1}^{n} A_i \tag{2.45}$$

where A represents the normal operation state of the PMU network and A_i represents the normal path state on which data can be transferred from the ith PMU to the PDC. n is the number of PMUs. Using the concept of union and intersection of the set theory yields

$$A_i = A_i^P \bigcup A_i^S = (\bigcap_{x_{i,p} \in A_i^P} x_{i,p}) \bigcup (\bigcap_{x_{i,s} \in A_i^S} x_{i,s}) \tag{2.46}$$

where A_i^P and A_i^S denote the optic fiber link sets on the primary path and backup path of the ith PMU in the normal state respectively; $x_{i,p}$ indicates that the pth link on the primary path of the ith PMU is good and $x_{i,s}$ indicates that the sth link belonging to the backup path of the ith PMU is good.

Equation (2.45) is equivalent to

$$\overline{A} = \bigcup_{i=1}^{n} \overline{A_i} \tag{2.47}$$

In general, there are common optic fiber links among the communication paths of different PMUs although the two protection routes of each PMU are disjoint. The unavailability of the PMU network is the probability of the state defined by Equation (2.47). By using the union concept again and ignoring the events in which three or more communication channels of PMUs fail at the same time, the unavailability of the PMU network can be approximately expanded to include only the first and second order terms as follows:

$$P(\overline{A}) = \sum_{i=1}^{n} P(\overline{A_i}) - \sum_{i<j=2}^{n} P(\overline{A_i} \cap \overline{A_j}) \tag{2.48}$$

Note that the primary path and backup path of a PMU are disjointed to each other in any first order term and therefore by substituting Equation (2.46) into Equation (2.48), we have

$$P(\overline{A_i}) = 1 - P(A_i) = 1 - P(A_i^P \bigcup A_i^S) = 1 - [P(A_i^P) + P(A_i^S) - P(A_i^P)P(A_i^S)]$$
$$= 1 - P(\prod_{x_{i,p} \in A_i^P} x_{i,p}) - P(\prod_{x_{i,s} \in A_i^S} x_{i,s}) + P(\prod_{x_{i,p} \in A_i^P} x_{i,p})P(\prod_{x_{i,s} \in A_i^S} x_{i,s}) \tag{2.49}$$

For any second order term, we have

$$P(\overline{A}_i \bigcap \overline{A}_j) = P(\overline{A_i \bigcup A_j}) = 1 - P(A_i \bigcup A_j)$$
$$= 1 - P(A_i^P \bigcup A_i^S \bigcup A_j^P \bigcup A_j^S) \quad (2.50)$$

According to the covering law of the set theory, Equation (2.50) can be expanded as:

$$P(\overline{A}_i \bigcap \overline{A}_j) = 1 - P(A_i^P + \overline{A_i^P}\ A_i^S + \overline{A_i^P}\ \overline{A_i^S}\ A_j^P + \overline{A_i^P}\ \overline{A_i^S}\ \overline{A_j^P}\ A_j^S) \quad (2.51)$$

In Equation (2.51), A_i^P and A_i^S are disjoint, and so are A_j^P and A_j^S. By eliminating the common links using the absorbing law of the set theory, Equation (2.51) can be expressed as:

$$P(\overline{A}_i \bigcap \overline{A}_j) = 1 - P(\prod_{x_{i,p} \in A_i^P} x_{i,p} + \overline{\prod_{x_{i,p} \in A_i^P} x_{i,p}} \cdot \prod_{x_{i,s} \in A_i^S} x_{i,s} + \overline{\prod_{x_{i,p} \in A_i^P \leftarrow A_j^P} x_{i,p}} \cdot \overline{\prod_{x_{i,s} \in A_i^S \leftarrow A_j^P} x_{i,s}} \cdot \prod_{x_{j,p} \in A_j^P} x_{j,p}$$
$$+ \overline{\prod_{x_{i,p} \in A_i^P \leftarrow A^S} x_{i,p}} \cdot \overline{\prod_{x_{i,s} \in A_i^S \leftarrow A_j^S} x_{i,s}} \cdot \overline{\prod_{x_{j,p} \in A_j^P} x_{j,p}} \cdot \prod_{x_{j,s} \in A_j^S} x_{j,s}) \quad (2.52)$$

Here, $A_i^P \leftarrow A_j^P$ represents the residual A_i^P in which the overlapping links between A_i^P and A_j^P have been eliminated. Other residual sets in Equation (2.52) have the same significance.

Every complement set in Equation (2.52) can be further expanded using the covering law again. For example, $\overline{\prod_{x_{i,p} \in A_i^P} x_{i,p}}$ can be expanded as:

$$\overline{\prod_{x_{i,p} \in A_i^P} x_{i,p}} = \overline{x}_{i,1} + (x_{i,1}\overline{x_{i,2}}) + (x_{i,1}x_{i,2}\overline{x_{i,3}}) + \cdots + (x_{i,1}x_{i,2} \cdots x_{i,l-1}\overline{x_{i,l}}) \quad (2.53)$$

Here, l is the number of elements (links) in A_i^P.

Note that the expanded terms in Equation (2.53) are non-intersected sets. By substituting Equation (2.53) into Equation (2.52) and absorbing the overlapping links, and then re-substituting Equation (2.49) and (2.52) into Equation (2.48), the unavailability of the PMU network can be expressed as an algebraic sum of multiple terms with each term being a product of unavailability of optic fiber links. The availability of the PMU network can be also expressed as an algebraic sum of multiple terms with each term being a product of availability of optic fiber links through a simple transformation. By substituting Equation (2.44) into the equation for the availability *P(A)* or unavailability $P(\overline{A})$ of the PMU network, *P(A)* or $P(\overline{A})$ can be easily calculated using failure and repair rates of optic fiber links.

2. Reliability evaluation in the recovery mechanism

According to the definition of recovery mechanism, the communication reliability of the PMU network depends on the dynamic connectivity of node pairs between each PMU and PDC. The reliability evaluation approaches for network connectivity include the cut-set and tie-set techniques. Generally speaking, a cut-set technique is faster than a tie-set technique [59]. The minimal cut-set approach [60] is used to identify all minimum cut sets between each PMU and PDC. Then the following method is used to evaluate reliability of PMU network in the recovery survival mechanism.

From a viewpoint of PMU network reliability, the minimum cut sets between each PMU and PDC in the recovery mechanism are similar to the primary and backup paths of each PMU in the protection mechanism. Therefore, there are similar expressions in the recovery mechanism as long as cut sets are used to replace the states defined by paths in Equations (2.45) and (2.47). The data transfer failure of the

*i*th PMU can be expressed using the union of the cut sets as follows:

$$\overline{A_i} = \bigcup_{j=1}^{m} C_{ij} \tag{2.54}$$

where m is the number of minimum cut sets between the ith PMU and the PDC; C_{ij} refers to the failure event of the jth cut set of the ith PMU, which can be calculated by

$$C_{ij} = \bigcap_{k=1}^{l} \overline{x}_{ijk} \tag{2.55}$$

$\overline{x}_{ijk}$ denotes the failure state of the kth link in C_{ij} and l is the number of links in the cut set.

Substituting Equation (2.55) into Equation (2.47) yields

$$\overline{A} = \bigcup_{i=1}^{n} (\bigcup_{j=1}^{m} C_{ij}) \tag{2.56}$$

By re-ordering these cut sets, Equation (2.46) can be re-written as:

$$\overline{A} = \bigcup_{i=1}^{g} C_i \tag{2.57}$$

where g is the total number of all minimum cut sets between each PMU and PDC in the PMU network.

Similarly, by applying the concept of union and keeping only up to the second order terms, the unavailability of the PMU network is calculated by

$$P(\overline{A}) = \sum_{i=1}^{g} P(C_i) - \sum_{i<j=2}^{g} P(C_i \cap C_j) \tag{2.58}$$

For any term of single minimal cut set, we have

$$P(C_i) = P(\bigcap_{x_{ik} \in C_i} \overline{x}_{ik}) = P(\prod_{x_{ik} \in C_i} \overline{x}_{ik}) \tag{2.59}$$

For any term of two minimal cut sets, we have

$$\begin{aligned} P(C_i \cap C_j) &= P[(\bigcap_{x_{ik} \in C_i} \overline{x}_{ik}) \bigcap (\bigcap_{x_{jk} \in C_j} \overline{x}_{jk})] \\ &= P(\prod_{x_{ik} \in C_i \leftarrow C_j} \overline{x}_{ik}) \cdot P(\prod_{x_{jk} \in C_j} \overline{x}_{jk}) \end{aligned} \tag{2.60}$$

Here, $C_i \leftarrow C_j$ represents the residual C_i in which the overlapping links between C_i and C_j have been eliminated. $\overline{x}_{ik}$ and $\overline{x}_{jk}$ represent the failure link in C_i and C_j, respectively.

By substituting Equation (2.44) into the equation for the availability $P(A)$ or unavailability $P(\overline{A})$ of WAMS PMU network in the recovery mechanism, $P(A)$ or $P(\overline{A})$ can be calculated using failure and repair rates of optic fiber links.

3. Sensitivity analysis

The availability $P(A)$ (or unavailability $P(\overline{A})$) of PMU network has been expressed as a function of the optic fiber link availability R_k (or link unavailability Q_k) in either of the two survival mechanisms, i.e.

$$\begin{aligned} P(A) &= f_R(R_1, R_2, \cdots, R_l) \\ P(\overline{A}) &= f_Q(Q_1, Q_2, \cdots, Q_l) \end{aligned} \tag{2.61}$$

Therefore the reliability sensitivity of the PMU network to each link can be obtained as follows:

$$S_k = \frac{\partial P(A)}{\partial R_k} = \frac{\partial P(\overline{A})}{\partial Q_k} \qquad k = 1, 2, \cdots, l \tag{2.62}$$

where R_k (or Q_k) is the availability (or unavailability) of the kth optic fiber link, l is the number of optic fiber links in the PMU network.

Based on results of sensitivity analysis, crucial link(s) can be identified and so can the measures of improving the reliability of each PMU network in WAMS.

4. Other reliability indices and equivalent two-state model of WAMS PMU network

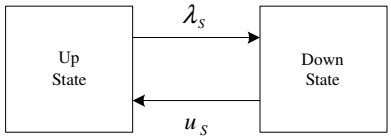

Fig. 2.9 Equivalent two-state model of the regional network in WAMS

There may be many PMU networks in a WAMS depending on the geographical size. If each PMU network can be represented using an equivalent two-state model as shown in Fig. 2.9, it will be modeled as a two-state component in reliability evaluation of the whole WAMS, resulting in great simplification.

In the discussions earlier, the availability and unavailability of PMU network have been deduced. This section presents a method to calculate the failure frequency of PMU network. The failure rate and repair rate of the two-state model can be calculated easily once the failure frequency is obtained. Additionally, the reciprocal of repair rate is the average repair time of PMU network. Thus multiple reliability indices of PMU network will be developed.

In the reliability evaluation of general engineering systems, the network failure frequency is usually calculated using either the Markov state approach or the frequency-duration approach [57]. The essence of these two methods is state enumeration (state space representation), which leads to a huge computing burden, particularly for a relatively large network. Reference [61] proves a method of calculating the network failure frequency for a single input and single output network using a disjoint formula. This method is generalized in this paper to calculate the failure frequency of the multi-input and single-output PMU network in WAMS in the following. As mentioned earlier, by using the disjoint concept, the availability (or unavailability) of PMU network can be expressed as an algebraic sum of multiple terms with each term being a product of availability (or unavailability) of corresponding optic fiber links, i.e.

$$P(A) = \sum_{i=1}^{NR} \left(\prod_{j \in SR_i} R_j \right)$$
$$P(\overline{A}) = \sum_{i=1}^{NQ} \left(\prod_{j \in SQ_i} Q_j \right) \tag{2.63}$$

Here, R_j (or Q_j) is the availability (or unavailability) of optic fiber links; SR_i (or SQ_i) denotes the set of subscripts of independent optic fiber links in the ith product term; NR (or NQ) is the number of product terms in the availability (or unavailability) equation of PMU network.

As well known, the transition frequency is the product of state probability and transition rate in a state space representation [57]. It can be proved using the same concept in Reference [61] that the failure or repair frequency of the PMU network in WAMS can be calculated using equivalent transition frequencies of the state sets represented by elements in the product terms. It can be expressed as follows:

$$f_A = \sum_{i=1}^{NR} \left(\prod_{j \in SR_i} R_j \cdot \sum_{j \in SR_i} \lambda_j \right)$$
$$f_U = \sum_{i=1}^{NQ} \left(\prod_{j \in SQ_i} Q_j \cdot \sum_{j \in SQ_i} \mu_j \right) \quad (2.64)$$

Here λ_j and u_j are the failure rate and repair rate of optic fiber links; f_A and f_U denote the failure and repair frequencies of PMU network. Obviously, they are both equal to the transition frequency f_S in the equivalent two-state model.

$$f_S = f_A = f_U \quad (2.65)$$

The failure rate λ_s, average repair time r_s and the repair rate μ_s of the equivalent two-state model for the WAMS PMU network can be calculated as follows:

$$\lambda_s = \frac{f_s}{P(A)} \quad (2.66)$$

$$r_s = \frac{1}{\mu_s} = \frac{P(\overline{A})}{f_s} \quad (2.67)$$

2.2.3 Numerical Example of a PMU Network

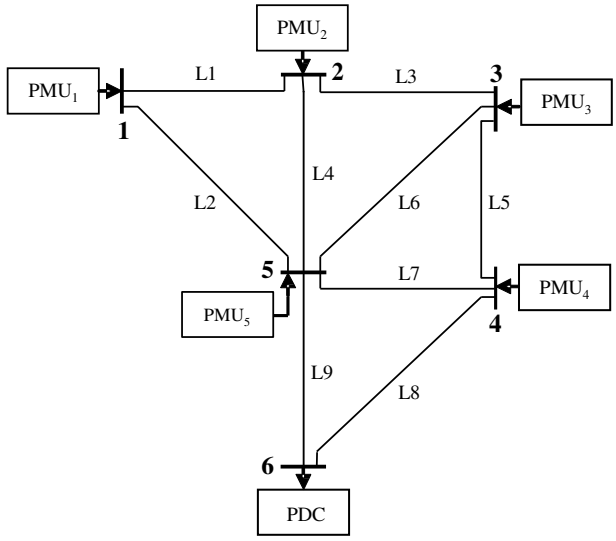

Fig. 2.10 A regional network in WAMS

Fig. 2.10 shows a regional network in WAMS with 6 nodes and 9 optic fiber links. The parameters of the links are listed in Table 2.2. Tables 2.3-2.5 present the reliability indices of the regional network obtained using the presented method in the following three cases.

- Arrangement 1: The PMUs are located at Nodes 1 and 2 and the PDC at Node 6;
- Arrangement 2: The number of PMUs is increased. The PMUs are located at Nodes 1-5 and the PDC is still located at Node 6. This may represent a situation of development of the regional network in WAMS. Note that the PMUs and PDC in this arrangement are shown in Fig. 2.10.
- Arrangement 3: This case is the same as Arrangement 2 except that Node 5 becomes a PDC node and

Node 6 becomes a PMU node.

Table 2.2 Parameters of optic fiber links

Parameters / Links(start node/end node)	Length (km)	Failure rate (failures/year)	Repair time (hours)
L1(1/2) λ_{Li}	228	5.9918	38
L2(1/5)	108	2.8382	18
L3(2/3)	124	3.2587	20
L4(2/5)	172	4.5202	32
L5(3/4)	128	3.3638	22
L6(3/5)	68	1.787	12
L7(4/5)	112	2.9434	18
L8(4/6)	44	1.1563	6
L9(5/6)	148	3.8894	36

Table 2.3 Reliability indices of the regional network in WAMS (Arrangement 1)

Reliability indices / Survival Mechanisms	Availability	Unavailability	Failure frequency (failures/year)	Failure rate (failures/year)	Repair time (hours)	Sensitivity of the most crucial link
Static protection	0.9986	1.4102e-3	0.9324	0.9337	13.2491	5.7367e-2(L9)
Dynamic recovery	0.9998	1.6388e-4	0.1312	0.1312	10.9409	2.5454e-2(L2)

Table 2.4 Reliability indices of the regional network in WAMS (Arrangement 2)

Reliability indices / Survival Mechanisms	Availability	Unavailability	Failure frequency (failures/year)	Failure rate (failures/year)	Repair time (hours)	Sensitivity of the most crucial link
Static protection	0.9983	1.7005e-3	1.1851	1.1872	12.5697	1.0706e-1(L8)
Dynamic recovery	0.9998	1.6407e-4	0.1315	0.1315	10.9261	2.5454e-2(L2)

Table 2.5 Reliability indices of the regional network in WAMS (Arrangement 3)

Reliability indices / Survival Mechanisms	Availability	Unavailability	Failure frequency (failures/year)	Failure rate (failures/year)	Repair time (hours)	Sensitivity of the most crucial link
Static protection	0.9994	6.3925e-4	0.5083	0.5087	11.0158	3.4653e-2 (L7)
Dynamic recovery	0.9998	1.6407e-4	0.1315	0.1315	10.9263	2.5454e-2(L2)

The following observations can be made from the reliability indices in Tables 2.3-2.5:
Protection mechanism:

- Even in the protection mechanism, the regional network can reach a sufficiently high reliability level and provide good expansibility of WAMS.
- The increased number of PMUs has very little impact on the reliability of the regional network as all PMUs have their own primary and backup protection routes, which are relatively independent in the mesh network. On the other hand, the reliability the regional network can be improved by selecting a better location of PDC.
- The most crucial optic fiber link varies with different arrangements. This indicates that the reliability of the regional network can be enhanced by improving availability of crucial link(s) and/or selecting better protection routes.

Recovery mechanism:

- The reliability of the regional network in the recovery mechanism is extremely high (near to 1).
- The sensitivity analysis indicates that the most crucial optic fiber link with its sensitivity value remains unchanged in the different arrangements. This suggests that improving availability of crucial link(s) may not be effective for improving the reliability of the regional network in the recovery mechanism.
- Both the number of PMUs and the location of PDC have almost no impact on the reliability of the regional network in the recovery mechanism. Hence, a key consideration in this mechanism should focus on how to timely restore data transfer after a contingency occurs.

In addition, it can be also seen that, in the two survival mechanisms, the most sensitive optic fiber link is not the link with the highest failure rate. The most crucial link can be determined only by a network reliability sensitivity analysis.

The presented method provides not only the availability and unavailability of WAMS regional network but also the indices of failure frequency, failure rate, repair rate and repair time. The multiple indices can be used to build the equivalent two-state model of the regional network, which is extremely useful for reliability evaluation of the whole WAMS.

3. Reliability Analysis of BC Hydro PMU/RTU Network

Currently, BC Hydro has 9 PMUs installed at major generation stations and substations. Phasor data sampled by PMUs are routed to BC Hydro's Fraser Valley control center (FVO) through a microwave communication network. In order to explore the reliability of the PMU network, the communication network is modeled as a two-layer graph based on the geographic locations of the PMUs and the control center, as shown in Fig. 3.1. The main graph in Fig. 3.1 (a) consists of 20 nodes and 23 lines, and the lower mainland graph in Fig. 3.1 (b) is composed by 12 nodes and 15 lines. The 9 PMUs locate at nodes 1, 2, 4, 5, 11, 17, 19, 20, and 26, and the control center is represented by node 25. Apart from the PMU nodes, some necessary intermediate nodes including the microwave relays and optic fiber stations are also included in the two-layer graph.

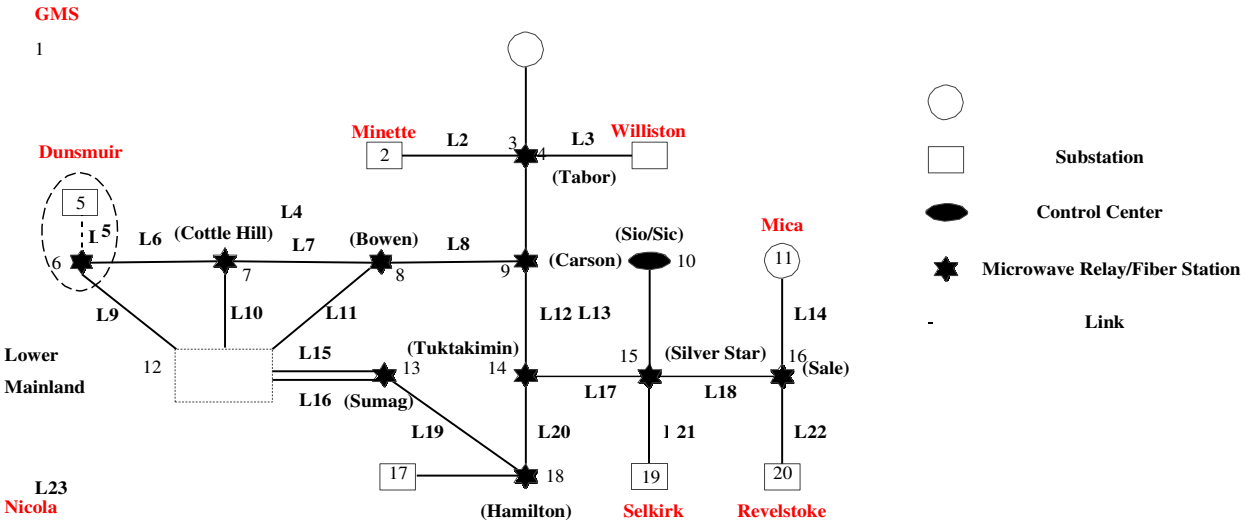

(a) Main Graph (MN)

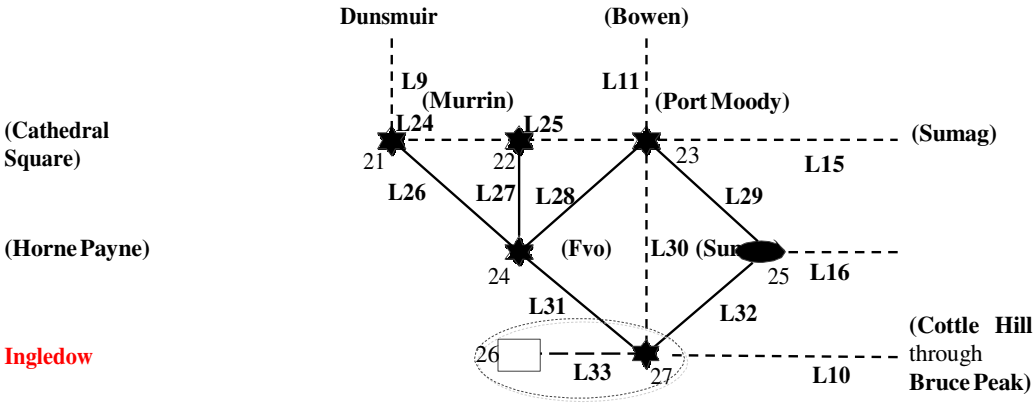

(b) Lower Mainland Graph (LMN)

Figure 3.1 Two Layer Graph for PMU Network

3.1 Reliability Parameters of Components

The first step for evaluating reliability of the PMU network is to obtain component reliability parameters. The focus is to identify the reliability parameters of PMUs and communication components. In this report, RTU network will also be evaluated in order to compare the reliability performance between a PMU network and a RTU counterpart. Therefore, statistical analysis has been performed to decide the component reliability parameters for RTUs, PMUs as well as the components in the telecommunication network.

3.1.1 RTU Reliability Parameters

According to the 6-year (2006~2011) event records for RTUs in BC Hydro transmission system, a total of five RTUs at various substations have experienced some outage events. For instance, the RTUs in substation GMS had 2 forced outages within the 6 years. The total duration of the two outages is 547.0 hours. Thus, the failure rate and repair time of the RTU can be estimated by

$$\lambda_{Ci,RTU} = \frac{\text{Forced outages}}{\text{(Number of RTUs)} \times \text{(years)}} = \frac{2}{1 \times 6} = 0.3333 \text{ (failures/year)} \qquad (3.1)$$

$$r_{i,RTU} = \frac{\text{Total duration}}{\text{Forced outages}} = \frac{547.0}{2} = 273.5 \text{ (hours)} \quad (3.2)$$

The failure rate and repair time of other RTUs can be calculated in the same way.

3.1.2 PMU Reliability Parameters

No statistical data for PMUs is available from BC Hydro. Therefore, typical PMU reliability parameters in 69 are adopted, as given in Table 3.2.

Table 3.1 PMU reliability parameters

Parameters / Component (Number)	Availability	Unavailability	λ_{Ci} (failures/year)	r_{Ci} (hours)
PMU	0.99550	4.5003e-3	0.1868	212.0

3.1.3 Communication Component Reliability Parameters

BC Hydro has recorded the failure events happened in the telecommunication system. Unlike the RTUs records which are associated with substations where those RTUs are installed, the forced outages and durations of different types of communication components are aggregated records for the whole BC Hydro telecommunication system. For example, there are 184 digital access cross connect systems (DACS) in the telecommunication system. According to the 6 years records, there were 68 forced outages and a total of 1097.5 hours of repair time for DACS. As such, the failure rate and repair time of DACS can be estimated by

$$\lambda_{Ci,RACS} = \frac{\text{Forced outages}}{(\text{Number of Components}) \times (\text{Total years})} = \frac{68}{184 \times 6} = 0.0616 \text{ (failures/year)} \quad (3.3)$$

$$r_{Ci,RACS} = \frac{\text{Total duration}}{\text{Forced outages}} = \frac{1097.5}{68} = 16.14 \text{ (hours)} \quad (3.4)$$

Using the same method, the reliability parameters of other communication components can be obtained.

In BC Hydro telecommunication system, although the majority of communication between substations relies on microwave channel, there are a few substations connected by optic fibers. The major difference between optic fibers and microwave is that optic fibers have physical communication link in between, whereas microwave signals are transferred in air. Therefore, the failures of optic fibers link should be counted. The failure rate of an optic fiber link is proportional to its length. In this report, the typical parameters of optic fibers are adopted 70 (see Table 3.2 below).

Table 3.2 Reliability parameters of optic fibers

Parameters / Component	λ_{Ci} (failures/year)	r_{Ci} (hours)
Optic fiber port	0.0053	7.23
Fiber	0.0026/(km)	13.33/(km)

3.2 Reliability Analysis of the BC Hydro PMU and RTU Networks

3.2.1 Assumptions

In the reliability analysis of the BC Hydro PMU and RTU networks, the following assumptions are made:

2. Any RTU at a major generation stations or substation has a backup. The two RTUs provide same measurements.

3. All major microwave terminal devices including DACS, FOMUX, microwave radios, power supply sources and main auxiliaries, are redundant.

4. Due to economic consideration, no redundancy is provided for PMU and optic fiber link in BC Hydro network.

Therefore, each component has two paralleled units, except for the PMUs and optic fibers. The line reliability parameters can be calculated using the parallel and series network concepts as follows:
1) For paralleled components, we have

$$\lambda_{Ci}^{p} = \lambda_{C1}\lambda_{C2}(r_{C1} + r_{C2}) \tag{3.5}$$

$$r_{Ci}^{p} = \frac{r_{C1}r_{C2}}{r_{C1} + r_{C2}} \tag{3.6}$$

where λ_1, λ_1, r_1 and r_2 are failure rates and repair times of the paralleled components 1 and 2, respectively.

2) For a line with N series components, we have

$$\lambda_{Lj} = \sum_{i=1}^{N} \lambda_{Ci}^{p} \tag{3.7}$$

$$r_{Lj} = \frac{1 - \prod_{i=1}^{N} \left(\frac{1}{1 + \lambda_{Ci}^{p} r_{Ci}^{p}}\right)}{\left[\prod_{i=1}^{N} \left(\frac{1}{1 + \lambda_{Ci}^{p} r_{Ci}^{p}}\right)\right] \cdot \sum_{i=1}^{N} \lambda_{Ci}^{p}} \tag{3.8}$$

Note that if some optic fiber links are included in a line, they should be added to (3.7) and (3.8) as series components. It is worth pointing out that failure rate and repair time of optic fiber are in proportion to the length of the link.

3.2.2 Reliability Analysis

(1) A typical communication path between GMS and ING
Two PMUs at substations GMS and ING are used to monitor system oscillation in BC Hydro. There are 16 relay stations between the two PMUs. Therefore, the communication line between GMS and ING consists of a series of components. The corresponding reliability parameters of the communication line can be calculated using the concepts of parallel and series networks and the results are shown in Table 3.3. Note that the two PMUs in GMS and ING do not have redundancy.

Table 3.3 Reliability of line GMS-ING

Parameters / Lines(from-to)	Serial components PMU/DACS/FOMUX/RADIO//OFP /AUX/AC	Availability	Unavailability	λ_{Li} (failures/year)	r_{Li} (hours)
Line (GMS-ING)	2/2/15/30/0/16/16	0.99099	9.009e-3	0.3785	210.4

(2) Swing monitoring at the Control Center

The function of oscillation monitoring can be realized either by particular communication path between GMS and ING, or by sending the PMU measurements at GMS and ING to FVO through the telecommunication system. For the second approach, PMU signals should be delivered in the complex mesh network. So, the minimal cut-set approach is used to calculate reliability parameters for swing monitoring at the control center. The procedures for minimal-cut-set-based reliability estimation are given below. Further details can be found in reference 71.

- Step 1: Using the minimal cut-set approach to identify all the minimal cut sets between the PMUs and the control center in the two-layer PMU networks in Fig. 3.2.
- Step 2: Applying the concept of union and neglecting the 3rd and higher order cut-set combinations, the unavailability of the PMU network can be approximately assessed.
- Step 3: Using the covering law to eliminate the overlapping lines, and then substituting the line reliability parameters by the simple expression, the reliability parameters of the two networks in Fig. 3.2 can be calculated.
- Step 4: Using the series connection concept for the two PMU networks, the reliability parameters of the entire system can be obtained, which are shown in Table 3.7.

Table 3.4 Reliability parameters for monitoring oscillation at the control center

Nodes / Parameters	Availability	Unavailability	λ_{Li} (failures/year)	r_{Li} (hours)
GMS and ING	0.99100	9.002e-3	0.3746	212.5

It is observed that placing the oscillation monitor at the control center will not significantly improve the reliability, because the reliability of this oscillation monitoring system is largely determined by the two PMUs which do not have redundancy.

(3) Comparison for the PMU and RTU Networks

The only difference between the PMU and RTU networks are the measurement units, i.e., PMUs and RTUs. Because no redundancy is provided for PMUs, the failure rates of the links with PMUs in the PMU network are much higher than those for the corresponding lines in the RTU network.

As aforementioned, the cut-set approach is used to compute the reliability indexes for the two networks, shown in Table 3.5. In this table, an assumed case with PMU redundancy is also caculated. From Table 3.5, the following observations can be obtained.

- The reliability of the BC Hydro PMU network is low. Thus, without backup PMUs, it is not recommended to use more than two PMU measurements for protection or control purposes.
- With backup PMUs, the reliability of the PMU network could be as high as 99.974%. This reliability will meet the requirement of controls and protections.
- The reliability of current RTU network is relatively high. Therefore, the RTU network suffices for protection or control that only requires asynchronous measurements.

Table 3.5 Reliability of the PMU and RTU networks

Network \ Parameters		Availability	Unavailability	λ (failures/year)	r (hours)
PMU Network	without backup	0.95961	4.0393-2	1.7405	211.9
	with backup	0.99977	2.3463e-4	0.0251	81.8
RTU Network		0.99961	3.8832e-4	0.0334	10

3.2.3 Sensitivity Analyses

In an actual PMU (or RTU) network, the reliability data of the network components may have large variations, due to various manufacturing and operating conditions. Sensitivity analyses are conducted to investigate the impacts of different component parameters on the reliability of the entire network. In each case, only one type of parameters vary from one tenth to ten times of its base value. It should be noted that from the expression of component availability $A=1/(1+\lambda r)$, the effect of failure rate (λ) on component availability is the same as the repair time (r). Therefore, only the changes of component failure rate are considered in sensitivity analysis in this report.

(1) Sensitivity Analysis for the PMU Network

We first conduct the sensitivity analysis for the PMU network. The results are listed in Tables 3.6-3.23. Because no backup is provided for PMUs in the PMU network, the reliability parameters of PMUs significantly will affect the reliability of the entire network. In Table 3.6, the availability of PMU network decreases from 0.99588 to 0.62565 when the failure rate of PMUs changes from 0.1x of base value to 10x of base value. Therefore, PMUs are the most critical components in this network. Any reliability enhancement for PMUs will greatly improve the reliability of the whole network. Following PMUs are the FONUX and AC station service (see Tables 3.8 and 3.13). The sensitivity analyses for the three components are shown in Fig. 3.2. Again, this figure shows that PMUs are the most sensitive components which have great impact on the availability of the whole PMU network. Compared to PMUs, the other components only have trivial effect on the reliability of PMU network because these components all have backup and are of very high reliabilities.

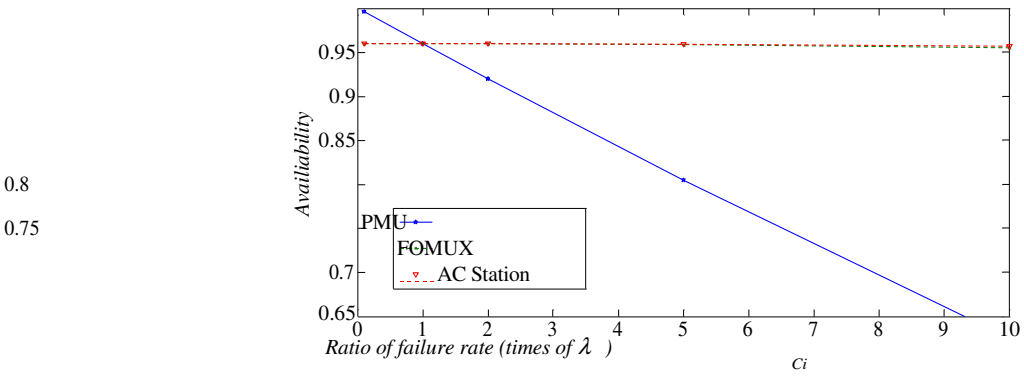

Figure 3.2 Sensitivity analysis for PMU network availability

Table 3.6 Sensitivity of PMU

Component	Parameters	$0.1\lambda_{Ci}$	λ_{Ci}	$2.0\lambda_{Ci}$	$5.0\lambda_{Ci}$	$10\lambda_{Ci}$
PMU	Availability	0.99588	0.95961	0.91995	0.80492	0.62565
	Unavailability	4.1175E-03	4.0393E-02	8.0053E-02	1.9508E-01	3.7435E-01
	λN(failures/year)	0.1787	1.7405	3.5753	9.8231	23.7469
	rN(hours)	202.7	211.9	213.2	216.1	220.7

Table 3.7 Sensitivity of DACS

Component	Parameters	$0.1\lambda_{Ci}$	λ_{Ci}	$2.0\lambda_{Ci}$	$5.0\lambda_{Ci}$	$10\lambda_{Ci}$
DACS	Availability	0.95961	0.95961	0.95961	0.95960	0.95960
	Unavailability	4.0393E-02	4.0393E-02	4.0394E-02	4.0396E-02	4.0405E-02
	λ_N(failures/year)	1.7404	1.7405	1.7409	1.7437	1.7534
	r_N(hours)	211.9	211.9	211.8	211.5	210.4

Table 3.8 Sensitivity of FOMUX

Component	Parameters	$0.1\lambda_{Ci}$	λ_{Ci}	$2.0\lambda_{Ci}$	$5.0\lambda_{Ci}$	$10\lambda_{Ci}$
FOMUX	Availability	0.95965	0.95961	0.95947	0.95849	0.95503
	Unavailability	4.0347E-02	4.0393E-02	4.0534E-02	4.1515E-02	4.4973E-02
	λ_N(failures/year)	1.7347	1.7405	1.7580	1.8795	2.3122
	r_N(hours)	212.3	211.9	210.5	201.9	178.4

Table 3.9 Sensitivity of Microwave Radio

Component	Parameters	$0.1\lambda_{Ci}$	λ_{Ci}	$2.0\lambda_{Ci}$	$5.0\lambda_{Ci}$	$10\lambda_{Ci}$
Microwave Radio	Availability	0.95961	0.95961	0.95961	0.95960	0.95959
	Unavailability	4.0393E-02	4.0393E-02	4.0394E-02	4.0396E-02	4.0406E-02
	λ_N(failures/year)	1.7402	1.7405	1.7414	1.7480	1.7713
	r_N(hours)	211.9	211.9	211.7	211.0	208.2

Table 3.10 Sensitivity of Diesel/Auxiliary

Component	Parameters	$0.1\lambda_{Ci}$	λ_{Ci}	$2.0\lambda_{Ci}$	$5.0\lambda_{Ci}$	$10\lambda_{Ci}$
Diesel/Auxiliary	Availability	0.95961	0.95961	0.95960	0.95957	0.95948
	Unavailability	4.0392E-02	4.0393E-02	4.0397E-02	4.0425E-02	4.0525E-02
	λ_N(failures/year)	1.7401	1.7405	1.7417	1.7500	1.7794
	r_N(hours)	211.9	211.9	211.7	210.9	207.9

Table 3.11 Sensitivity of AC Station

Component	Parameters	$0.1\lambda_{Ci}$	λ_{Ci}	$0\lambda_{Ci}$ 2.0λ_{Ci}	$5.0\lambda_{Ci}$	1
AC Station	Availability	0.95961	0.95961	0.95960	0.95955	0.95937
	Unavailability	4.0391E-02	4.0393E-02	4.0401E-02	4.0452E-02	4.0634E-02

	λ_N(failures/year)	1.7368	1.7405	1.7517	1.8300	2.1087
	r_N(hours)	212.3	211.9	210.5	201.8	175.9

Table 3.12 Sensitivity of Optic Fiber Port

Component \ Parameters		$0.1\lambda_{Ci}$	λ_{Ci}	$2.0\lambda_{Ci}$	$5.0\lambda_{Ci}$	$10\lambda_{Ci}$
Optic fiber port	Availability	0.95961	0.95961	0.95961	0.95961	0.95961
	Unavailability	4.0393E-02	4.0393E-02	4.0393E-02	4.0393E-02	4.0393E-02
	λ_N(failures/year)	1.7405	1.7405	1.7405	1.7405	1.7405
	r_N(hours)	211.9	211.9	211.9	211.9	211.9

Table 3.13 Sensitivity of Optic Fiber

Component \ Parameters		$0.1\lambda_{Ci}$	λ_{Ci}	$2.0\lambda_{Ci}$	$5.0\lambda_{Ci}$	$10\lambda_{Ci}$
Optic Fiber	Availability	0.95961	0.95961	0.95960	0.95959	0.95951
	Unavailability	4.0392E-02	4.0393E-02	4.0396E-02	4.0415E-02	4.0492E-02
	λ_N(failures/year)	1.7404	1.7405	1.7408	1.7426	1.7499
	r_N(hours)	211.9	211.9	211.8	211.7	211.3

(2) Sensitivity Analysis for the RTU Network

The sensitivity analysis results for the RTU network are shown in Tables 3.18-3.25. The RTU, FOMUX and AC station service are found to be the three most important components that affect the network availability, which is illustrated in Fig. 3.3. Although the backup of RTUs has been considered in the RTU network, RTU reliability are still the most critical factor for the overall network reliability. The availability of RTU network will vary from 0.99992 to 0.97057 when the failure rate of RTUs changes from 0.1 to 10 times of the base value.

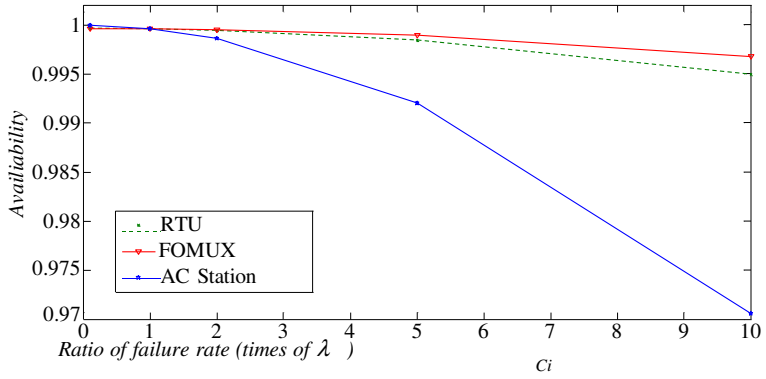

Figure 3.3 Sensitivity analysis in the RTU network.

Table 3.14 Sensitivity of RTU

	Parameters changes	$0.1\lambda_{Ci}$	λ_{Ci}	$2.0\lambda_{Ci}$	$5.0\lambda_{Ci}$	$10\lambda_{Ci}$
RTU	Availability	0.99994	0.99961	0.99862	0.99205	0.97060
	Unavailability	5.5762E-05	3.8832E-04	1.3754E-03	7.9506E-03	2.9402E-02
	λ_N(failures/year)	0.0103	0.0334	0.1021	0.5646	2.1250
	r_N(hours)	47.5	102.0	118.2	124.4	124.9

Table 3.15 Sensitivity of DACS

Component	Parameters changes	$0.1\lambda_{Ci}$	λ_{Ci}	$2.0\lambda_{Ci}$	$5.0\lambda_{Ci}$	$10\lambda_{Ci}$
DACS	Availability	0.99961	0.99961	0.99961	0.99961	0.99960
	Unavailability	3.8821E-04	3.8832E-04	3.8868E-04	3.9113E-04	3.9988E-04
	λ_N(failures/year)	0.0333	0.0334	0.0338	0.0364	0.0459
	r_N(hours)	102.3	102.0	100.9	94.1	76.3

Table 3.16 Sensitivity of FOMUX

Component	Parameters changes	$0.1\lambda_{Ci}$	λ_{Ci}	$2.0\lambda_{Ci}$	$0\lambda_{Ci}$ $5.0\lambda_{Ci}$	1
FOMUX	Availability	0.99966	0.99961	0.99947	0.99848	0.99500
	Unavailability	3.4130E-04	3.8832E-04	5.3036E-04	1.5171E-03	4.9993E-03

	λ_N(failures/year)	0.0279	0.0334	0.0500	0.1661	0.5793
	r_N(hours)	107.3	102.0	92.9	80.1	76.0

Table 3.17 Sensitivity of Microwave Radio

Component \ Parameters changes		$0.1\lambda_{Ci}$	λ_{Ci}		$2.0\lambda_{Ci}$	$5.0\lambda_{Ci}$	$10\lambda_{Ci}$
Microwave Radio	Availability	0.99961	0.99961	0.99961	0.99961	0.99960	
	Unavailability	3.8820E-04	3.8832E-04	3.8870E-04	3.9131E-04	4.0062E-04	
	λ_N(failures/year)	0.0331	0.0334	0.0343	0.0406	0.0632	
	r_N(hours)	102.8	102.0	99.4	84.5	55.6	

Table 3.18 Sensitivity of Diesel/Auxiliary

Component \ Parameters changes		$0.1\lambda_{Ci}$	λ_{Ci}		$2.0\lambda_{Ci}$	$5.0\lambda_{Ci}$	$10\lambda_{Ci}$
Diesel/Auxiliary	Availability	0.99961	0.99961	0.99961	0.99958	0.99948	
	Unavailability	3.8700E-04	3.8832E-04	3.9234E-04	4.2044E-04	5.2057E-04	
	λ_N(failures/year)	0.0330	0.0334	0.0345	0.0425	0.0708	
	r_N(hours)	102.8	102.0	99.6	86.8	64.5	

Table 3.19 Sensitivity of AC Station

Component \ Parameters changes		$0.1\lambda_{Ci}$	λ_{Ci}		$2.0\lambda_{Ci}$	$5.0\lambda_{Ci}$	$10\lambda_{Ci}$
AC Station	Availability	0.99961	0.99961	0.99960	0.99955	0.99937	
	Unavailability	3.8589E-04	3.8832E-04	3.9569E-04	4.4717E-04	6.3052E-04	
	λ_N(failures/year)	0.0298	0.0334	0.0442	0.1198	0.3891	
	r_N(hours)	113.5	102.0	78.5	32.7	14.2	

Table 3.20 Sensitivity of Optic Fiber Port

Component \ Parameters changes		$0.1\lambda_{Ci}$	λ_{Ci}	$2.0\lambda_{Ci}$	$5.0\lambda_{Ci}$	$10\lambda_{Ci}$
Optic fiber port	Availability	0.99961	0.99961	0.99961	0.99961	0.99961
	Unavailability	3.8832E-04	3.8832E-04	3.8832E-04	3.8832E-04	3.8832E-04
	λ_N(failures/year)	0.0334	0.0334	0.0334	0.0334	0.0334
	r_N(hours)	102.0	102.0	102.0	102.0	102.0

Table 3.21 Sensitivity of Optic Fiber

Component \ Parameter changes		$0.1\lambda_{Ci}$	λ_{Ci}	$2.0\lambda_{Ci}$	$5.0\lambda_{Ci}$	$10\lambda_{Ci}$
Optic Fiber	Availability	0.99961	0.99961	0.99961	0.99959	0.99951
	Unavailability	3.8724E-04	3.8832E-04	3.9110E-04	4.1027E-04	4.9026E-04
	λ_N(failures/year)	0.0332	0.0334	0.0337	0.0355	0.0427
	r_N(hours)	102.1	102.0	101.8	101.4	100.5

(3) Identification of the Critical Lines

The sensitivity analysis method can be used not only to identify critical components, but also to search critical lines in the PMU and RTU networks. As mentioned before, the difference of PMU and RTU network lies in the different types of measurement devices. Therefore, in order to exclude the effect of various measurement units, it is assumed that PMUs and RTUs are 100% reliable. Then, sensitivity analysis can be used to identify the critical communication lines in both PMU and RTU networks which share the same structure. Note that all components of a communication line are treated as a whole in the structural sensitivity analysis.

In each case, the failure rate of a specific line will vary from 0.1 times to 10 times of its base values while keeping the parameters of other lines constant. The final results are summarized in Table 3.22. According to the sensitivity analysis, lines 4, 2, 17 and 21 are ranked as the most critical lines. Their complete sensitivy results are listed in Tables 3.22-3.26. The availability results for these five lines are illustrated in Fig. 3.4.

For the network structure in Fig.3.1, it is observed that the top ranked lines are either those connecting to several PMUs (e.g. lines 4 and 17) or the longer lines which contain more communication components (e.g. lines 2 and 21). The results of structure sensitivity analysis provide valuable heuristics for finding cost-effective hardening schemes for BC Hydro's communication network.

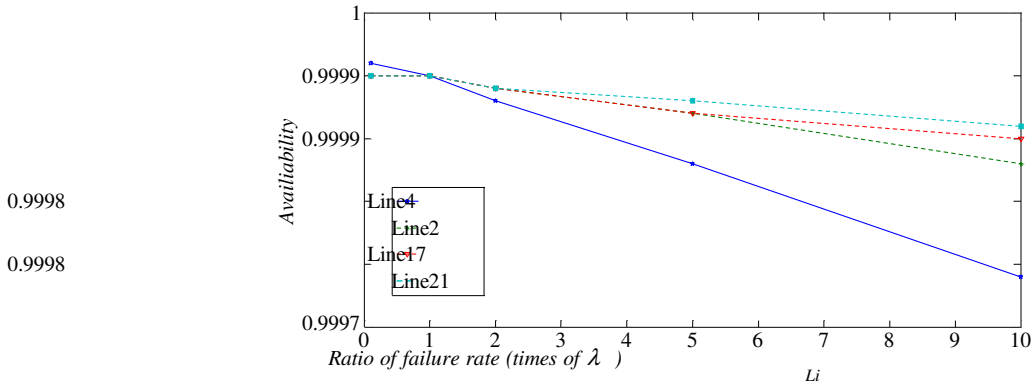

Figure 3.4 Sensitivities of the top five lines.

Table 3.22 Line Sensitivity Analysis to Identify Critical Lines

Changes / Lines(rank)	$0.1\lambda_{Li}$	λ_{Li}	$2.0\lambda_{Li}$	$5.0\lambda_{Li}$	$10\lambda_{Li}$
L1(5th)	4.8724E-05	5.2355E-05	5.6389E-05	6.8492E-05	8.8663E-05
L2(2nd)	4.5104E-05	5.2355E-05	6.0410E-05	8.4577E-05	1.2485E-04
L3(10th)	5.0621E-05	5.2355E-05	5.4281E-05	6.0059E-05	6.9688E-05
L4(1st)	3.6595E-05	5.2355E-05	6.9865E-05	1.2240E-04	2.0995E-04
L5(15th)	5.2343E-05	5.2355E-05	5.2367E-05	5.2406E-05	5.2470E-05
L6(27th)	5.2355E-05	5.2355E-05	5.2355E-05	5.2355E-05	5.2355E-05
L7(30th)	5.2355E-05	5.2355E-05	5.2355E-05	5.2355E-05	5.2355E-05
L8(20th)	5.2354E-05	5.2355E-05	5.2356E-05	5.2359E-05	5.2364E-05
L9(26th)	5.2355E-05	5.2355E-05	5.2355E-05	5.2355E-05	5.2355E-05
L10(31th)	5.2355E-05	5.2355E-05	5.2355E-05	5.2355E-05	5.2355E-05
L11(32th)	5.2355E-05	5.2355E-05	5.2355E-05	5.2355E-05	5.2355E-05
L12(22th)	5.2354E-05	5.2355E-05	5.2355E-05	5.2356E-05	5.2358E-05
L13(33th)	5.2355E-05	5.2355E-05	5.2355E-05	5.2355E-05	5.2355E-05
L14(7th)	5.0445E-05	5.2355E-05	5.4476E-05	6.0840E-05	7.1446E-05

L15(29th)	5.2355E-05	5.2355E-05	5.2355E-05	5.2355E-05	5.2355E-05
L16(28th)	5.2355E-05	5.2355E-05	5.2355E-05	5.2355E-05	5.2355E-05
L17(3rd)	4.7189E-05	5.2355E-05	5.8094E-05	7.5312E-05	1.0401E-04
L18(6th)	4.8911E-05	5.2355E-05	5.6181E-05	6.7660E-05	8.6790E-05
L19(8th)	5.2354E-05	5.2355E-05	5.2355E-05	5.2358E-05	5.2363E-05
L20(23th)	5.2354E-05	5.2355E-05	5.2355E-05	5.2356E-05	5.2357E-05
L21(4th)	4.8636E-05	5.2355E-05	5.6487E-05	6.8882E-05	8.9541E-05
L22(9th)	5.0621E-05	5.2355E-05	5.4281E-05	6.0059E-05	6.9688E-05
L23(8th)	5.0621E-05	5.2355E-05	5.4281E-05	6.0059E-05	6.9688E-05
L24(12th)	5.1622E-05	5.2355E-05	5.3168E-05	5.5598E-05	5.9620E-05
L25(17th)	5.2352E-05	5.2355E-05	5.2357E-05	5.2365E-05	5.2378E-05
L26(11th)	5.1621E-05	5.2355E-05	5.3168E-05	5.5598E-05	5.9620E-05
L27(25th)	5.2355E-05	5.2355E-05	5.2355E-05	5.2355E-05	5.2355E-05
L28(18th)	5.2352E-05	5.2355E-05	5.2357E-05	5.2365E-05	5.2377E-05
L29(13th)	5.2074E-05	5.2355E-05	5.2666E-05	5.3601E-05	5.5159E-05
L30(24th)	5.2354E-05	5.2355E-05	5.2355E-05	5.2355E-05	5.2355E-05
L31(19th)	5.2352E-05	5.2355E-05	5.2357E-05	5.2364E-05	5.2375E-05
L32(14th)	5.2072E-05	5.2355E-05	5.2668E-05	5.3606E-05	5.5157E-05
L33(16th)	5.2343E-05	5.2355E-05	5.2367E-05	5.2406E-05	5.2470E-05

Table 3.23 Sensitivity of Line 4

Line \ Parameters changes		$0.1\lambda_{Ci}$	λ_{Ci}	$2.0\lambda_{Ci}$	$5.0\lambda_{Ci}$	$10\lambda_{Ci}$
L4	Availability	0.99996	0.99995	0.99993	0.99988	0.99979
	Unavailability	3.6595E-05	5.2355E-05	6.9865E-05	1.2240E-04	2.0995E-04
	λ_N(failures/year)	0.0072	0.0101	0.0132	0.0228	0.0388
	r_N(hours)	44.6	45.6	46.2	47.0	47.4

Table 3.24 Sensitivity of Line 2

Line \ Parameters changes		$0.1\lambda_{Ci}$	λ_{Ci}	$2.0\lambda_{Ci}$	$5.0\lambda_{Ci}$	$10\lambda_{Ci}$
L2	Availability	0.99995	0.99995	0.99994	0.99992	0.99988
	Unavailability	4.5104E-05	5.2355E-05	6.0410E-05	8.4577E-05	1.2485E-04
	λ_N(failures/year)	0.0085	0.0101	0.0118	0.0169	0.0255
	r_N(hours)	46.4	45.6	45.0	43.8	42.9

Table 3.25 Sensitivity of Line 17

Line \ Parameters changes		$0.1\lambda_{Ci}$	λ_{Ci}	$2.0\lambda_{Ci}$	$5.0\lambda_{Ci}$	$10\lambda_{Ci}$
L17	Availability	0.99995	0.99995	0.99994	0.99992	0.99990
	Unavailability	4.7189E-05	5.2355E-05	5.8094E-05	7.5312E-05	1.0401E-04
	λ_N(failures/year)	0.0092	0.0101	0.0110	0.0139	0.0187
	r_N(hours)	45.0	45.6	46.2	47.5	48.8

Table 3.26 Sensitivity of Line 21

Line \ Parameters changes		$0.1\lambda_{Ci}$	λ_{Ci}	$2.0\lambda_{Ci}$	$5.0\lambda_{Ci}$	$10\lambda_{Ci}$
L21	Availability	0.99995	0.99995	0.99994	0.99993	0.99991
	Unavailability	4.8724E-05	5.2355E-05	5.6389E-05	6.8492E-05	8.8663E-05
	λ_N(failures/year)	0.0093	0.0101	0.0109	0.0135	0.0178
	r_N(hours)	46.0	45.6	45.2	44.4	43.5

3.3 Reliability Analysis of BC Hydro PMU/RTU Network

3.3.1 Reliability Analysis for Future BC Hydro PMU Network Covering 500kV Buses and Important 220kV Buses

In previous subsection, it has been introduced that BC Hydro has a PMU network including 9 PMUs at major stations. If each PMU has a backup unit, the availability of the PMU network can be as high as 0.99974 (see Table 3.5). Considering that PMUs may be eventually installed at all 500kV buses and important 220kV buses, one may ask this question: how reliable the future BC Hydro PMU network could be? To provide the answer, it is assumed that PMUs would be deployed at all four generation stations and 17 of 18 substations (because no associated communication node was identified in BC Hydro telecommunication map for substation NTL-Natal). Here each PMU is assumed to have a backup and PMU measurements are transmitted to FVO through the microwave communication network, namely the BC Hydro telecommunication network. Fig. 3.6 illustrates this future PMU network design where a total of 53 lines and 46 nodes are included.

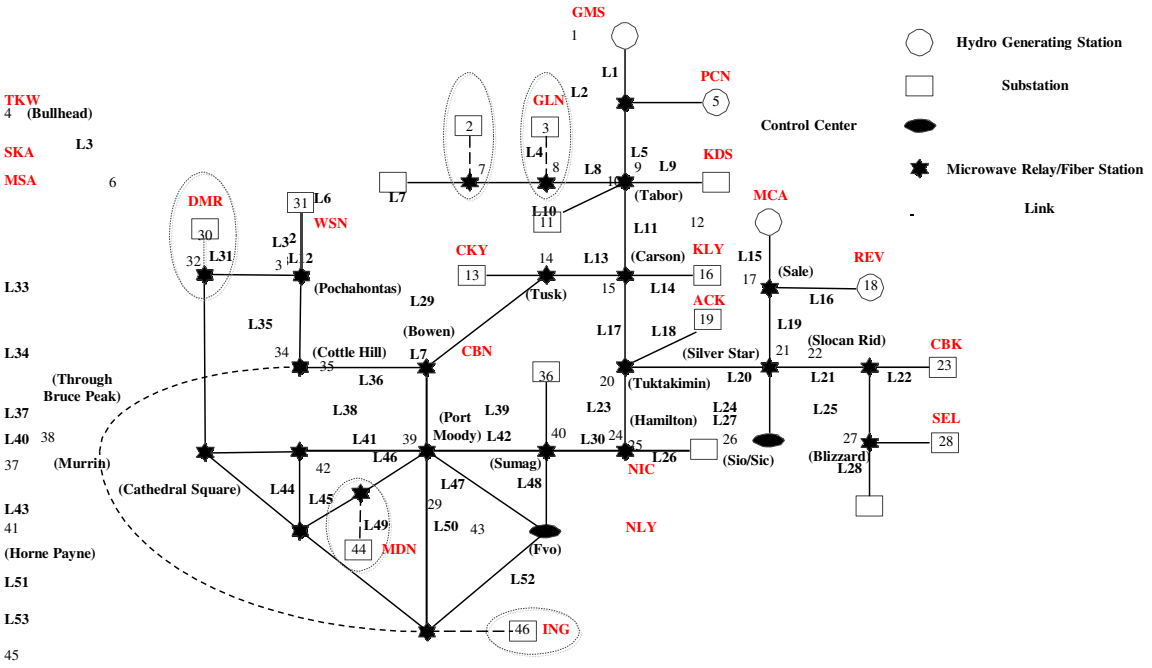

Figure 3.5 An envisioned future PMU network.

Similarly, each line in this figure is composed of a group of measurement components and communication components. The reliability parameters of the envisioned PMU network are shown in Table 3.27. The final results show that the availability of the PMU network can be as high as 99.9% even for a control (or protection) function which needs synchronized measurements from all 21 PMUs in the system. This is largely due to the availability of the PMU backups. Such a high reliability level will satisfy the reliability requirements in implementing system control and protection functions in BC Hydro's Energy Management Systems.

Table 3.27 Reliability of the Extended PMU networks

Parameters / Network	Availability	Unavailability	λ (failures/year)	r (hours)
PMU Network	0.99933	6.7300E-04	0.0745	79.2

3.3.2 Sensitivity Analysis for the Envisioned PMU Network

Sensitivity analysis has been applied for the envisioned PMU network. For each component or communication line, the failure rate varies from one tenth up to ten times of the base value while keeping other parameters constant. The results are illustrated in Fig. 3.6 and are summarized in Tables 28-35. Once again, it is found that the PMUs are the most sensitive components in the network, followed by FOMUX and AC station service.

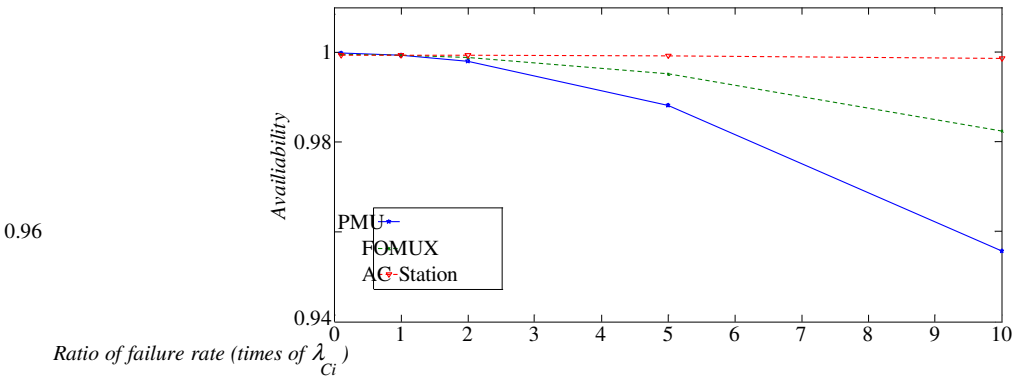

Figure 3.6 Sensitivity analysis in the extended PMU network.

Table 3.28 Sensitivity of PMU

Component \ Parameters		$0.1\lambda_{Ci}$	λ_{Ci}	$2.0\lambda_{Ci}$	$5.0\lambda_{Ci}$	$10\lambda_{Ci}$
PMU	Availability	0.99981	0.99933	0.99789	0.98814	0.95564
	Unavailability	1.9197E-04	6.7300E-04	2.1124E-03	1.1862E-02	4.4359E-02
	λN(failures/year)	0.0347	0.0745	0.1936	1.0067	3.7928
	rN(hours)	48.5	79.2	95.8	104.5	107.2

Table 3.29 Sensitivity of DACS

Component \ Parameters		$0.1\lambda_{Ci}$	λ_{Ci}	$2.0\lambda_{Ci}$	$5.0\lambda_{Ci}$	$10\lambda_{Ci}$
DACS	Availability	0.99933	0.99933	0.99933	0.99932	0.99930
	Unavailability	6.7269E-04	6.7300E-04	6.7393E-04	6.8041E-04	7.0352E-04
	λ_N(failures/year)	0.0741	0.0745	0.0755	0.0825	0.1076
	r_N(hours)	79.5	79.2	78.3	72.3	57.3

Table 3.30 Sensitivity of FOMUX

Component \ Parameters		$0.1\lambda_{Ci}$	λ_{Ci}	$2.0\lambda_{Ci}$	$5.0\lambda_{Ci}$	$10\lambda_{Ci}$
FOMUX	Availability	0.99950	0.99933	0.99881	0.99519	0.98246
	Unavailability	5.0045E-04	6.7300E-04	1.1940E-03	4.8113E-03	1.7540E-02
	λ_N(failures/year)	0.0543	0.0745	0.1355	0.5612	2.0865
	r_N(hours)	80.8	79.2	77.3	75.5	75.0

Table 3.31 Sensitivity of Microwave Radio

Component	Parameters	$0.1\lambda_{Ci}$	λ_{Ci}	$2.0\lambda_{Ci}$	$5.0\lambda_{Ci}$	$10\lambda_{Ci}$
Microwave Radio	Availability	0.99933	0.99933	0.99933	0.99932	0.99929
	Unavailability	6.7261E-04	6.7300E-04	6.7417E-04	6.8237E-04	7.1163E-04
	λ_N(failures/year)	0.0735	0.0745	0.0773	0.0972	0.1681
	r_N(hours)	80.2	79.2	76.4	61.6	37.1

Table 3.32 Sensitivity of Diesel/Auxiliary

Component	Parameters	$0.1\lambda_{Ci}$	λ_{Ci}	$2.0\lambda_{Ci}$	$5.0\lambda_{Ci}$	$10\lambda_{Ci}$
Diesel/Auxiliary	Availability	0.99933	0.99933	0.99931	0.99923	0.99891
	Unavailability	6.6880E-04	6.7300E-04	6.8570E-04	7.7453E-04	1.0910E-03
	λ_N(failures/year)	0.0733	0.0745	0.0781	0.1032	0.1927
	r_N(hours)	80.0	79.2	77.0	65.8	49.7

Table 3.33 Sensitivity of AC Station

Component	Parameters	$0.1\lambda_{Ci}$	λ_{Ci}	$2.0\lambda_{Ci}$	$5.0\lambda_{Ci}$	$10\lambda_{Ci}$
AC Station	Availability	0.99933	0.99933	0.99930	0.99914	0.99856
	Unavailability	6.6531E-04	6.7300E-04	6.9629E-04	8.5904E-04	1.4385E-03
	λ_N(failures/year)	0.0632	0.0745	0.1087	0.3477	1.1993
	r_N(hours)	92.3	79.2	56.2	21.7	10.5

Table 3.34 Sensitivity of Optic Fiber Port

Component \ Parameters		$0.1\lambda_{Ci}$	λ_{Ci}	$2.0\lambda_{Ci}$	$5.0\lambda_{Ci}$	$10\lambda_{Ci}$
Optic fiber port	Availability	0.99933	0.99933	0.99933	0.99933	0.99933
	Unavailability	6.7300E-04	6.7300E-04	6.7300E-04	6.7300E-04	6.7300E-04
	λ_N(failures/year)	0.0745	0.0745	0.0745	0.0745	0.0745
	r_N(hours)	79.2	79.2	79.2	79.2	79.2

Table 3.35 Sensitivity of Optic Fiber

Component \ Parameters		$0.1\lambda_{Ci}$	λ_{Ci}	$2.0\lambda_{Ci}$	$5.0\lambda_{Ci}$	$10\lambda_{Ci}$
Optic Fiber	Availability	0.99933	0.99933	0.99933	0.99933	0.99933
	Unavailability	6.7294E-04	6.7300E-04	6.7307E-04	6.7327E-04	6.7359E-04
	λ_N(failures/year)	0.0745	0.0745	0.0745	0.0745	0.0746
	r_N(hours)	79.2	79.2	79.2	79.2	79.2

4. Stochastic Signal Processing for Enhancing PMU Reliability

4.1 Background

Accurate and efficient measurement of fundamental frequency, harmonic and interharmonic phasors is of prime importance for power system planning, operation, maintenance and control. Modern power systems have high penetration of renewables, power electronic devices and nonlinear loads. Thus the power signals (voltage or current) are more polluted by harmonics, interharmonic and noises. This necessitates more robust and accurate estimation techniques.

Different approaches have been used for power signal frequency estimation including zero-crossing or level-crossing approaches [72] and related modified versions [73], least squares [74-75], Kalman filter [76-79], $\alpha\beta$-transformation [80], Clark-transformation [81], orthogonal FIR-based approaches [82-83], DFT-based methods [84-87], Prony [88], Newton-type method [89-90], PLL [91], neural network [92], adaptive filtering [93], wavelet [94], notch filter [95], and subspace-based methods [88, 96, 97]. Zero crossing is sensitive to noise and harmonics. Curve fitting based methods rely on the model that has been used for the signal; the signal in general may not fit that model and hence introduce some error into estimation. The reliance on the model is the case for Kalman-filter based and proxy methods. Orthogonal approaches such as $\alpha\beta$-transformation, Clark-transformation need three phase signals and also assume symmetric signals. DFT suffers from leakage effect and introduce errors in the off-nominal condition. Also literature lacks a method which is capable of accurate estimation of fundamental, harmonic, and interharmonic frequencies and phasors in a single method.

Recently, a Subspace Least Mean Square (SLMS) method [98] has been developed for fundamental, harmonic and interharmonic frequency and phasor measurement in power systems. SLMS provides a high-resolution and highly accurate estimation of fundamental frequency, harmonics, interharmonics and their corresponding amplitudes and phases. SLMS is highly resilient to noise, and its superiority to other enhanced methods has been discussed in [98]. SLMS, however, similar to other subspace-based methods, is computationally expensive.

This report has two main contributions. First, three schemes are proposed to improve the speed of SLMS. Scheme I explores the sparsity in real power system signals to reduce the searching load. Scheme II uses an iterative multisectional search approach to accelerate the location of harmonics and interharmonics. Scheme III combines Schemes I and II to achieve further speedup. The computation burden is significantly reduced, leading to speedup of more than 150 times. These three schemes need to calculate the multiplications of signal vectors and noise vectors. Signal vectors and noise vectors are in general complex-valued. As will be discussed, it is sufficient to use only the real part of these complex vectors to locate signal frequencies. Therefore, the computation burden is further reduced by adopting only the real parts of these vectors in frequency screening process. Therefore, three real-implemented versions of the foregoing schemes are proposed as well. The speed and accuracy of these six different schemes are thoroughly assessed.

The second contribution is to enhance the accuracy of harmonics measurement for high voltage power systems where interharmonics are often negligible. By using the sparsity of power system signals, the enhanced schemes are shown to be not only faster but also more accurate and more robust compared to the original SLMS. This accuracy stems from effective use of two facts: the prior knowledge that harmonic frequencies are multiples of the fundamental frequency, and the fact that estimation of fundamental frequency is less affected by noise (because of high amplitude of fundamental tone) than that of harmonics. By using this heuristic knowledge, harmonic components can be directly captured by simply testing the orthogonality of candidate frequencies which are multiple of fundamental frequency, instead of estimating harmonics exhaustively from finding the local minima of subspace function.

4.2 Methodology

We present enhancements to Subspace Least Mean Square which is used for accurate measurement of power system frequency, harmonic and interharmonic components.

4.2.1 Subspace Least Mean Square Method

In this section the fundamentals of subspace least mean square (SLMS) algorithm [98] is reviewed and it is reasoned how only the real parts of the signal and noise vectors could be used for construction of subspace function.

Subspace least mean square (SLMS) algorithm is based on the orthogonality of signal and noise subspaces. The procedure is as follows. Out of a data window of signal samples the autocorrelation matrix is constructed and used for extracting the signal and noise subspaces. The eigenvectors of the autocorrelation matrix span the whole signal and noise subspaces: eigenvectors corresponding to bigger

eigenvalues span the signal subspace, and those corresponding to smaller eigenvalues span the noise subspace. The whole possible spectrum (from dc to Nyquist frequency) with a small-frequency step (e.g. 0.01 Hz) is scanned and the presence of each single candidate frequency is validated if it is orthogonal to all noise eigenvectors. In other words, a candidate signal vector orthogonal to noise eigenvectors resides in signal subspace and hence that frequency exists in the original signal.

SLMS assumes that the signal is composed of different complex sinusoidal signals; hence, it is a complex-number-based algorithm. However, for power system, we deal with real-valued sinusoidal signals and the algorithm could be simplified. Here we present a revised version of SLMS method in which construction of subspace function is real-based.

Consider a sampled power system signal x(n) that consists of L spectral components and additive white Gaussian noise (AWGN) w(n):

$$x(n) = \sum_{i=1}^{L} A_i e^{jn\omega_i} + w(n) \qquad (4.1)$$

where $A_i = |A_i| e^{j\phi_i}$, $|A_i|$ is the amplitude, ϕ_i is the phase angle, and ω_i is the frequency of i-th component. The next step is constructing an autocorrelation matrix for the signal. A highly accurate estimate of the autocorrelation matrix can be constructed using two cycles of data samples.

Once the autocorrelation matrix is constructed the next step is to calculate the signal and noise subspaces. Since the energy of a signal component is by far more than that of a noise component, signal eigenvectors correspond to big eigenvalues and noise eigenvectors correspond to small eigenvalues. The separation between these two subspaces is performed by a wise selection of an eigenthreshold which is determined experimentally and offline. Experimental results show that the eigenthreshold of 1e-7 distinguishes well between the signal and noise subspaces [98].

The fundamental property of signal and noise subspaces is that they are orthogonal. Since a signal vector lies in the signal subspace, it could be decomposed into linear combination of signal eigenvectors; thus a signal vector should be orthogonal to all noise eigenvectors.

To find the existing frequencies of the signal a subspace function based on candidate signal vectors is constructed [98]. A candidate signal vector is represented as $\mathbf{e}(\omega) = [1 \quad e^{j\omega} \quad \cdots \quad e^{j(N-1)\omega}]^T$. In original SLMS [98] an entry of subspace function is constructed by summation of magnitudes of the inner product of a candidate signal by all noise vectors. Power signals, however, contain real-valued signals; therefore if $\mathbf{e}(\omega)$ exists in the original signal, so do $\mathbf{e}(-\omega)$, and consequently their linear combination exists in the original signal as well. Thus the candidate signal could be selected as $\mathbf{e}_r(\omega) = (\mathbf{e}(\omega) + \mathbf{e}(-\omega))/2 = [1 \quad \cos(\omega) \quad \cdots \quad \cos((N-1)\omega)]^T$. Also note that instead of inner product of the signal vector by a noise vector, we can just calculate the inner product of signal vector by the real part of that noise vector. Therefore we can use the summation of absolute of inner product of $\mathbf{e}_r(\omega)$ by real part of noise vectors to calculate an entry of the subspace function.
The zeros of $H(\omega)$ are then sought to determine the existing frequencies in the power signal.

Once the signal frequencies are obtained a least mean squares (LMS) approach is used to compute the amplitude and phase of each tone [98]. If some spurious frequencies (due to noisy samples) are detected, their resulting amplitudes would be too small and be discarded. The threshold of 0.001 times of the amplitude of the fundamental component is found satisfactory in discarding spurious frequencies.

4.2.2 Techniques to Enhance the Speed of the Algorithm

4.2.2.1 Sparsity Technique Using the Unique Characteristics of Power System Signals

Searching for the whole frequencies from dc to Nyquist frequency is a time-consuming task especially when a small frequency step size (high resolution) is practiced. Fortunately, when dealing with power system signals (current or voltage signals), prior knowledge about the characteristics of the signal can be applied.

Power system signals at any condition have a great energy at the fundamental frequency which is at or around the nominal frequency; thus the fundamental frequency could be simply found by selecting high resolution candidate frequencies around the nominal frequency.

Another unique feature of power system signals is that they may contain some harmonics which are integer multiples of the fundamental frequency (either the fundamental frequency is nominal or off-nominal). Once the fundamental frequency is estimated, the only potential candidates for the harmonics are the integer-multiples of that fundamental frequency. Therefore, instead of using a series of candidate frequencies around each possible harmonic, only one candidate which is an integer-multiple of the fundamental frequency (already determined in the first step) has to be tested. In other words, for each harmonic, one single candidate is tested to check whether it is orthogonal to noise vectors or not. If the orthogonality condition is met, it is an existing harmonic in the original signal; otherwise that harmonic is not a component of the signal. In fact using this scheme, instead of scanning a large number of candidate frequencies (as in original algorithm [98]), only a very sparse number of frequencies need to be scanned. This sparsity technique enormously eliminate the computation effort for finding harmonic components.

Figure 4.1 shows the pictorial representation of this scheme. As Figure 4.1(a) shows, in the original algorithm, all frequencies from dc to Nyquist frequency are among the candidate frequencies. In Figure 4.1(b), however, only around the nominal frequency a full scan is performed. Once the fundamental frequency is detected, in the next step just its multiples are tested for orthogonality condition. As pictorially can be perceived, the computation burden of the algorithm is significantly cut by using this characteristic of power system signals.

The computation burden of calculating the subspace function $H(\omega)$ can be roughly (assuming that the calculations are linearly dependent on the number of candidate signals) represented as follows. Assuming the frequency resolution to be δf, the number of calculations would be

$$n_{\text{original}} = \frac{f_{\text{Nyq}}}{\delta f} = \frac{f_s}{2\delta f} \tag{4.2}$$

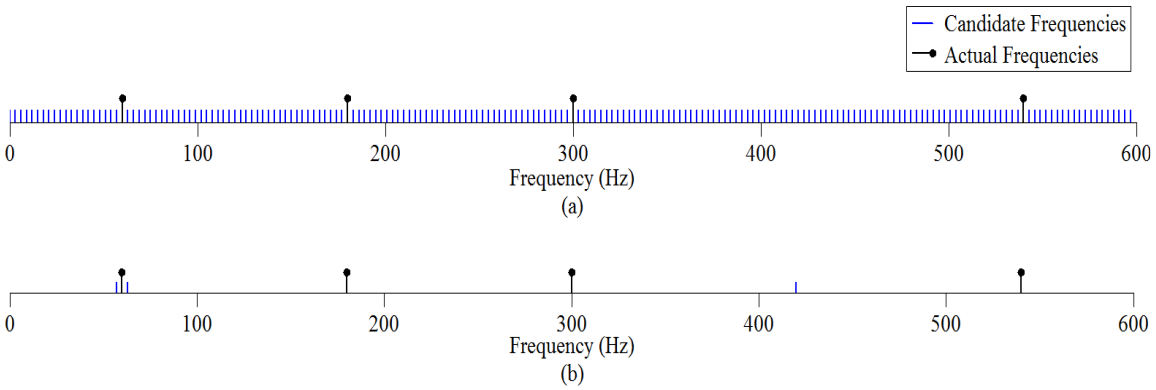

Figure 4.1 (a) Original algorithm with all frequencies from 0 to Nyquist frequency scanned (b) Enhanced algorithm applying sparsity technique

In the sparsity scheme only the data around the nominal frequency of f_0 and within a limited domain of $2\Delta f$ are sought. For example for $\Delta f = 5\text{Hz}$ the domain of search is $[f_0 - \Delta f, f_0 + \Delta f] = [55\text{Hz}, 65\text{Hz}]$. Therefore

$$n_{\text{sparsity}} = \frac{2\Delta f}{\delta f} = \frac{2\Delta f}{\delta f} \tag{4.3}$$

Hence the ratio would be

$$r = \frac{n_{\text{original}}}{n_{\text{sparsity}}} = \frac{f_s / 2 / \delta f}{2\Delta f / \delta f} = \frac{f_s}{4\Delta f} \tag{4.4}$$

which is in fact the ratio of whole possible signals, i.e, f_{Nyq}, to the region around fundamental frequency in which the fundamental frequency is sought, i.e, $2\Delta f$. For example, if $f_s = 3840\text{Hz}$ and $\Delta f = 5\text{Hz}$, then $r = 192$.

The significance of the foregoing heuristic method is not restricted to cutting the computation burden; it makes the estimation of harmonic frequencies more resilient to noise too. Where does this noise-resilient harmonic estimation stem from? In the original algorithm detection of the fundamental and harmonic frequencies is performed by searching the local minima of the subspace function. When the signal samples are noisy, these local minima are disturbed and they deviate from their true positions. Since the fundamental frequency always has a big amplitude, its corresponding local minimum deviates insignificantly compared to the deviation of the local minima of the harmonics. Therefore, in original SLMS, estimation of harmonic frequencies is not as resilient to noise as the estimation of fundamental frequency is (Figure 4.2).

It shows the subspace function around the nominal frequency and two other harmonics (5th harmonic and 7th harmonic), for the following signal.

$$\begin{aligned} x(t) &= \cos(2\pi 60t) \\ &+ 0.005\cos(2\pi 300t + 30°) \\ &+ 0.002\cos(2\pi 420t + 25°) \end{aligned} \tag{4.5}$$

The subspace function is plotted in two cases: noise-free signal, and noisy signal (SNR=60dB). As it is perceived from Figure 4.2, in the noise-free case, the local minimum of subspace function around the nominal frequency provides exact estimation of the fundamental frequency. In the case of noisy signal, the subspace function around the nominal frequency is disturbed insignificantly, and more importantly its

pattern is preserved, i.e. the minimum of the subspace function still occurs at 60 Hz. On the other hand, the subspace function around the harmonic frequencies have been disturbed more, and more importantly, the local minima of the subspace function have deviated from the true frequencies of 300 Hz and 420 Hz, resulting in some error in harmonic estimation. Note that the minimum of subspace function for the 7th harmonic is affected more by noise than that of the 5th harmonic. This is because the amplitude of the 5th harmonic is bigger than the amplitude of the 7th harmonic.

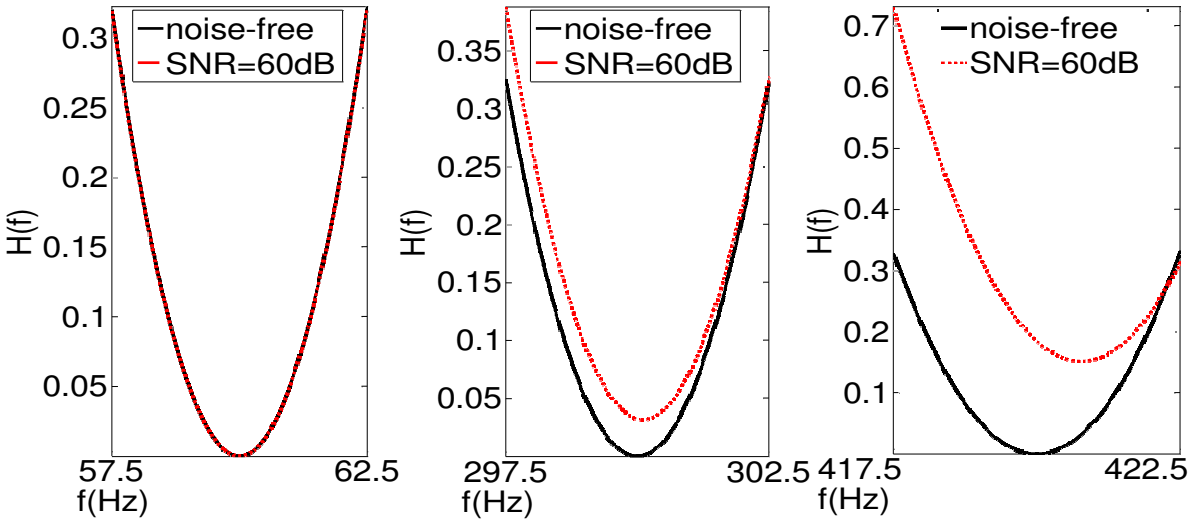

Figure 4.2 Residence to noise of subspace function around the fundamental frequency

When the foregoing heuristic approach is applied, however, the estimation of harmonic frequencies, instead of being based on the local minima of subspace function, is based on checking the orthogonality condition of integer multiples of fundamental frequency (already estimated); thus the accuracy of detecting the harmonics becomes as resilient to noise as that of the fundamental.

4.2.2.2 Catch and Pinpoint Scheme

This scheme starts from a bird's view broad scan with a rough estimate (e.g. accuracy of 5 Hz) of existing frequencies and continues with an iterative fine-tuning around the suspected signals caught in the broad scan. In first iteration (bird's view step) candidate frequencies are selected over all possible spectrum (from dc to Nyquist frequency) but with a very low resolution (e.g. 5 Hz) so that the computation burden becomes very low. Once very rough estimates of existing frequencies are obtained, in the next iteration the candidate frequencies are selected with higher resolution and around the existing rough-resolution caught frequencies. This iterative approach is continued until frequency components are determined with desired accuracy.

Figure 4.3 shows the flowchart of catch-and-pinpoint scheme. In this flowchart δf is the resolution of candidate frequencies (CF). Candidate frequencies (CF) at the first iteration span the whole spectrum from dc to Nyquist frequency (f_{NYQ}) with δf initialized by a big step size frequency, e.g. 5 Hz. In the next iteration the step size for creating the candidate frequencies is a downscaled version of the δf^{old} (δf of the previous iteration), i.e., $\delta f^{new} = \delta f^{old} / SC$, where the scaling factor $SC > 1$ (in simulations $SC = 10$). At each iteration the orthogonality of each candidate frequency to the noise vectors is tested (denoted by $V(f_k) \perp V_n$ in the flowchart), and if the candidate signal is orthogonal to the noise vectors it is considered as a signal frequency at that iteration. Despite the first iteration in which the CF includes

all frequencies from dc to Nyquist frequency, other iterations include the union of $(\delta f^{old} + 2\delta f^{new})$-neighborhood of each frequency which is detected as a signal frequency in the previous iteration. A $2\delta f^{new}$ overlap between the prospective frequency intervals is adopted to block the possibility of missing interharmonics. Finally, it should be noted that though represented by $V(f_k) \perp V_n$ in the flowchart, the orthogonally test is actually performed by finding the minima of sum of magnitude of dot product of candidate signal frequencies by all noise vectors.

The values used in simulations in this report are as follows: ITR=4, SC=10, and the initialization of $\delta f = 5\text{Hz}$. These values result in the final resolution of $\delta f = 0.005\text{Hz}$ at the end of last iteration.

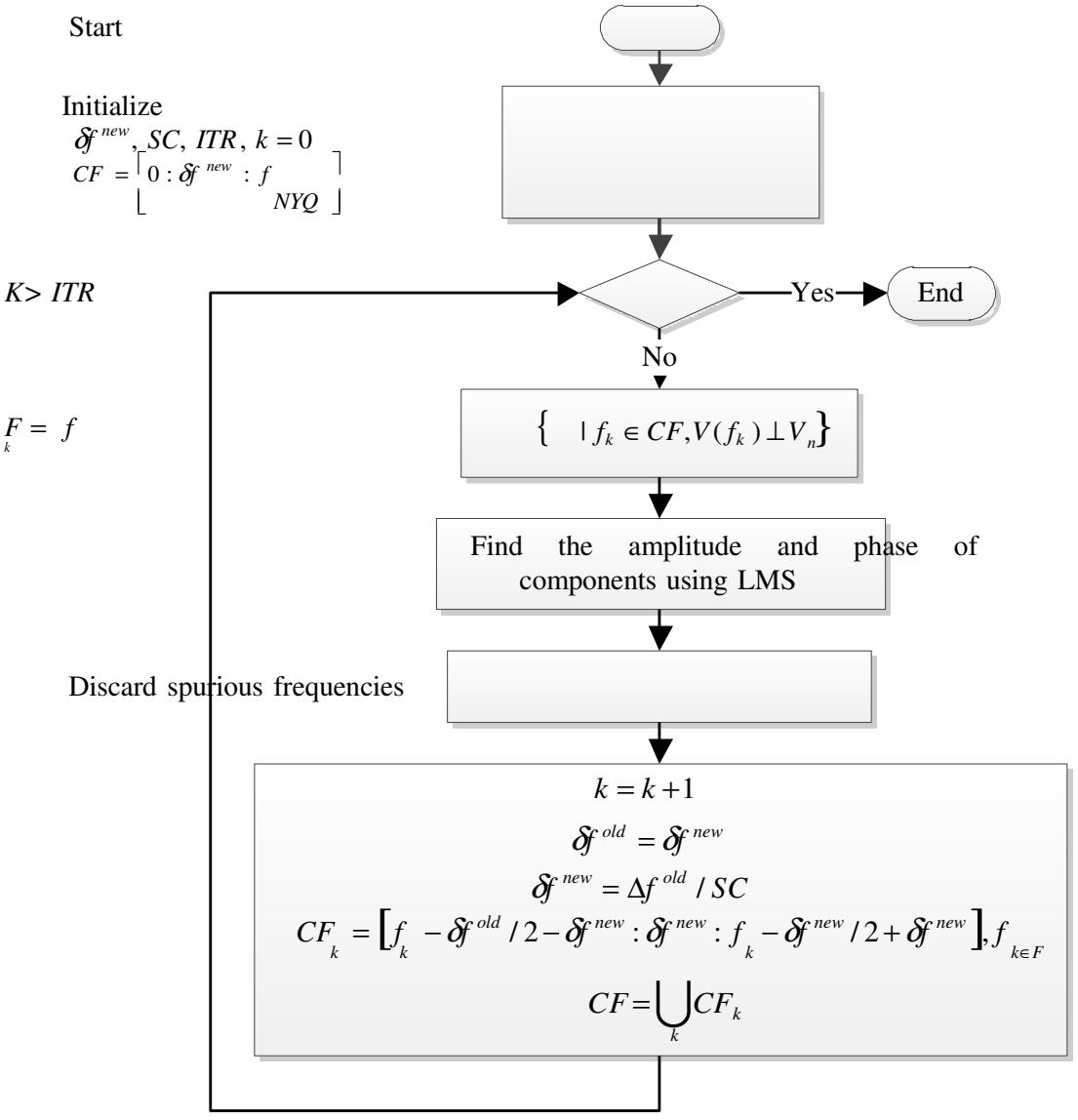

Figure 4.3 Flowchart of catch-and-pinpoint scheme

Note that in each iteration, after detecting the existing frequencies, the LMS algorithm is applied to find the amplitude and phase of those tones. If the amplitude of an existing frequency is less than a threshold value, that tone is considered as a spurious frequency and discarded.

The following example demonstrates how the catch and pinpoint scheme works. The test signal is composed of the fundamental frequency and two interharmonics.

$$\begin{aligned} x(t) &= \cos(2\pi 60t) \\ &+ 0.003\cos(2\pi 252t + 30°) \\ &+ 0.002\cos(2\pi 457.23t + 25°) \end{aligned} \qquad (4.6)$$

The catch and pinpoint scheme with parameters $\delta f = 5Hz$, $SC = 10$, $ITR = 4$ is employed. This means that the algorithm has four iterations; in the first iteration the whole spectrum from dc to Nyquist frequency is scanned with a coarse frequency step size of $\delta f = 5Hz$. Since $SC = 10$, in the second, third, and fourth iterations the frequency step sizes are, correspondingly, $\delta f = 0.5Hz$, $\delta f = 0.05Hz$, and $\delta f = 0.005Hz$.

Figures 4.4 to 4.7 show the subspace function $H(f)$ in the four iterations. Note that except in the first iteration in which the candidate frequencies span the whole spectrum, in the other iterations the candidate frequencies are a union of some separate intervals of candidate frequencies. Here since there are three tones, the candidate signals are a union of three frequency intervals.

Figure 4.4 shows the graph of $H(f)$ computed for the whole spectrum with the coarse resolution of 5 Hz. This rough resolution is sufficient to find a rough estimate of existing frequencies. The local minima of the subspace function of $H(f)$ in the first iteration are 60 Hz, 250 Hz, and 455 Hz.

In the second iteration . Therefore, as shown in Figure 4.5, the candidate frequencies are a union of three separate frequency intervals of $[57, 63]$, $[247, 253]$, and $[452, 458]$. Then the minimum of subspace function of $H(f)$ with precision of 0.5 Hz is found in each interval, which respectively is, 60.0 Hz, 252.0 Hz, and 457.0 Hz.

In the third iteration $\delta f^{new} = \delta f^{old} / SC = 0.05\,\text{Hz}$. Therefore, as shown in Figure 4.6, the candidate frequencies are a union of three separate frequency intervals of $[59.7, 60.3]$, $[251.7, 252.3]$, and $[456.7, 457.3]$. Then the minimum of subspace function of $H(f)$ with precision of 0.05 Hz is found in each interval, which respectively is, is 60.00 Hz, 252.00 Hz, and 457.25 Hz.

In the fourth iteration $\delta f^{new} = \delta f^{old} / SC = 0.005\,\text{Hz}$. Therefore as shown in Figure 4.6, the candidate are a union of three separate frequency intervals of $[59.97, 60.03]$, $[251.97, 252.03]$, $[457.22, 457.28]$. Finally the minimum of subspace function of $H(f)$ with precision of 0.005 Hz is found in each interval, which respectively is 60.000 Hz, 252.000 Hz, and 457.230 Hz.

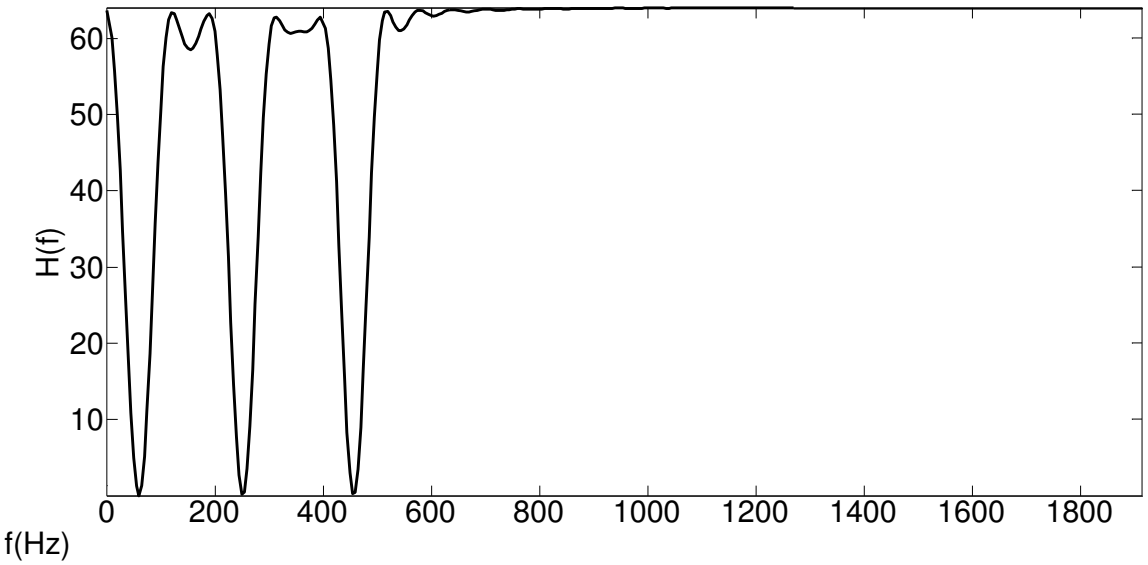

Figure 4.4 Subspace function of catch-and-pinpoint scheme - first iteration

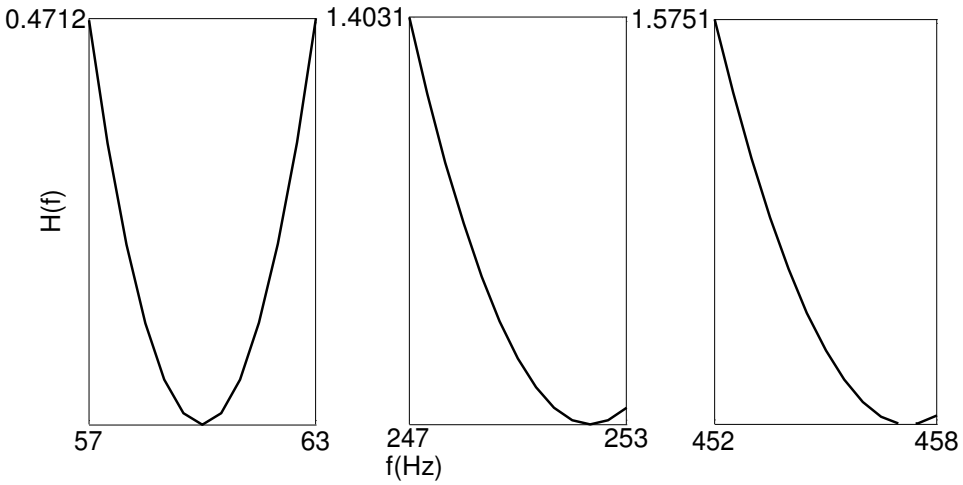

Figure 4.5 Subspace function of catch-and-pinpoint scheme - second iteration

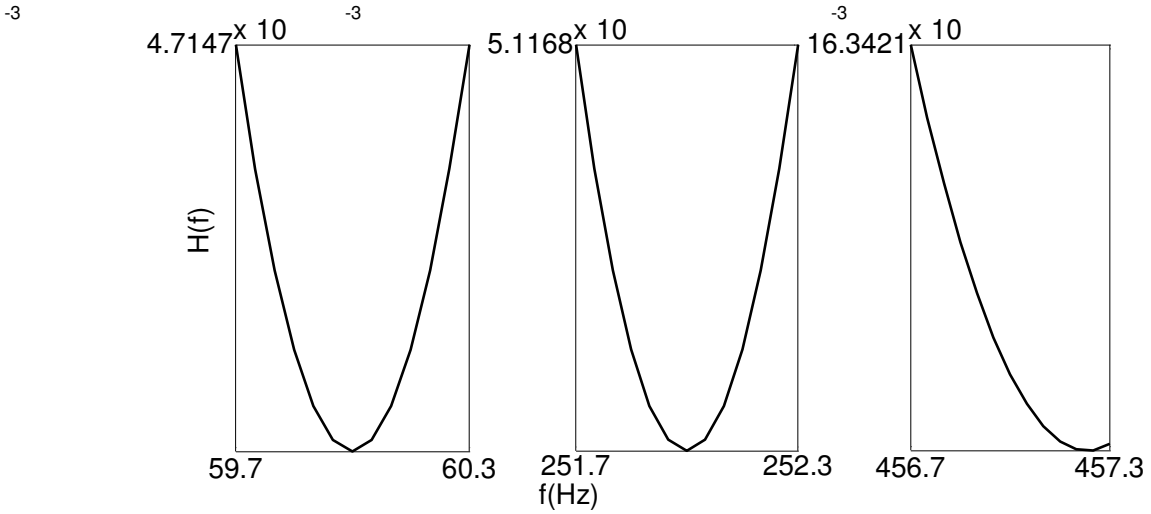

Figure 4.6 Subspace function of catch-and-pinpoint scheme - third iteration

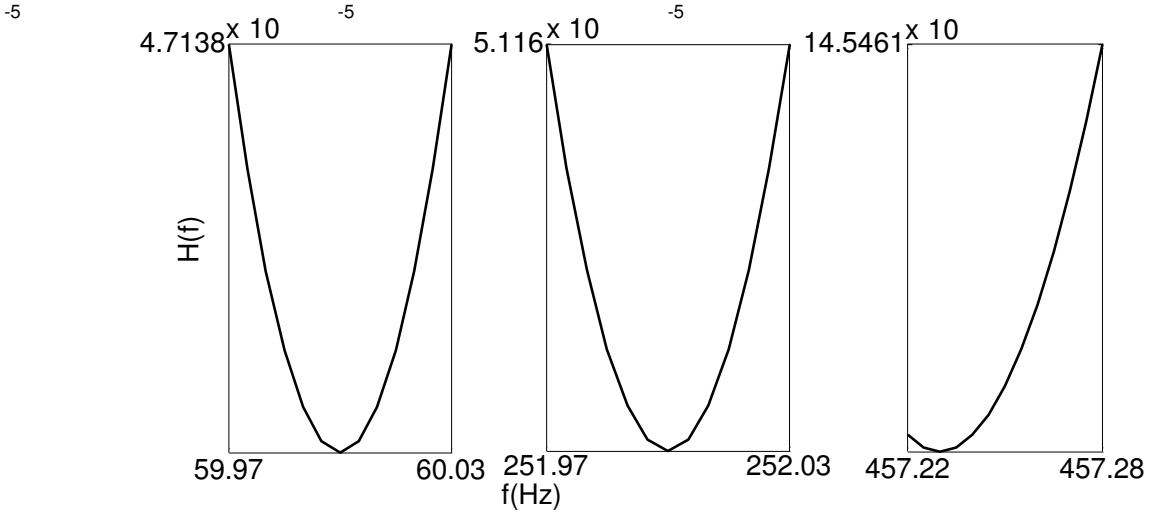

Figure 4.7 Subspace function of catch-and-pinpoint scheme - fourth iteration

It is interesting to note that the higher the amplitude of a tone the lower the subspace function values in the neighborhood of that tone. This could be seen by inspection of Figures 4.5 to 4.7 in which the subspace function has smaller values in the neighborhood of the fundamental frequency and it increases in the neighborhood of 252 Hz tone and 457.23 Hz tone.

Table 4.1 Iteration Results of the Catch-and-Pinpoint Example

(A) FUNDAMENTAL FREQUENCY

Iteration	Frequency	Amplitude	Phase (degree)
1	60	1.0000	0.0004
2	60.0	1.0000	0.0000
3	60.00	1.0000	0.0000
4	60.000	1.0000	0.0000

(B) F=252 HZ TONE

Iteration	Frequency	Amplitude	Phase (degree)
1	250	0.003	35.8918
2	252.0	0.003	30.0092
3	252.00	0.003	29.9992
4	252.000	0.003	30.0000

(C) F=457.23 HZ TONE

Iteration	Frequency	Amplitude	Phase (degree)
1	455	0.002	31.7456
2	457.0	0.002	25.6719
3	457.25	0.002	24.9416
4	457.23	0.002	25.0000

Table 4.1 shows the frequency, amplitude, and phase of all three tones in the four iterations. As the following table shows the frequency as well as amplitude and phase are detected roughly in the first iteration and then tuned to the true values in the next iterations. Table I also demonstrates that, despite frequency and phase which need several iterations to be tuned to the true values, amplitude is less sensitive to the resolution of frequency used in the algorithm and the exact amplitude is obtained in the first iteration.

4.2.2.3 Hybrid Scheme

The hybrid scheme is a combination of the sparsity and the catch-and-pinpoint schemes. In the hybrid scheme, first the fundamental frequency is sought by catch-and-pinpoint scheme; since at the first step we are only interested in finding the fundamental frequency, the first iteration of catch –and-pinpoint spans only the neighborhood of the fundamental frequency. Once the fundamental frequency is detected, the existence of any harmonic frequency is tested by investigating whether its corresponding signal vector is orthogonal to the noise vectors or not.

4.3 Simulation Results

In this section, the speed and accuracy are compared to that of the original SLMS algorithm.

The following signal is used as the test signal. It includes the fundamental frequency which is off-nominal and the 5th harmonic and an interharmonic component.

$$x(t) = \cos(2\pi 60.1t) + 0.005\cos(2\pi 300.5t + 30°) + 0.002\cos(2\pi 457.23t + 10°) \quad (4.7)$$

The following schemes have been implemented and tested.

- Heu: Heuristic approach
- CP: Catch and pinpoint
- Hyb: Hybrid scheme

- HR, CPR, and HybR: respectively real counterparts of Heu, CP, and Hyb, with real-valued construction of the subspace function $H(f)$.

4.3.1 Speed Assessment

Figure 4.8 shows the result of mean processing time for different schemes of implementation. The mean processing time is shown in millisecond and also in terms of cycles in each scheme. Since the mean processing time of the original SLMS algorithm (about 371 ms or equivalently 22.24 cycles) is by far larger than that of the proposed schemes, it has not been shown in the figure. As Figure 4.8 shows, the heuristic (sparsity) algorithm is the most time-consuming proposed algorithm with mean processing time of 4.5 ms or equivalently 0.27 cycles, and the real-implemented hybrid algorithm (HbR) is the best algorithm in terms of speed with mean processing time of 2.2 ms or 0.13 cycles.

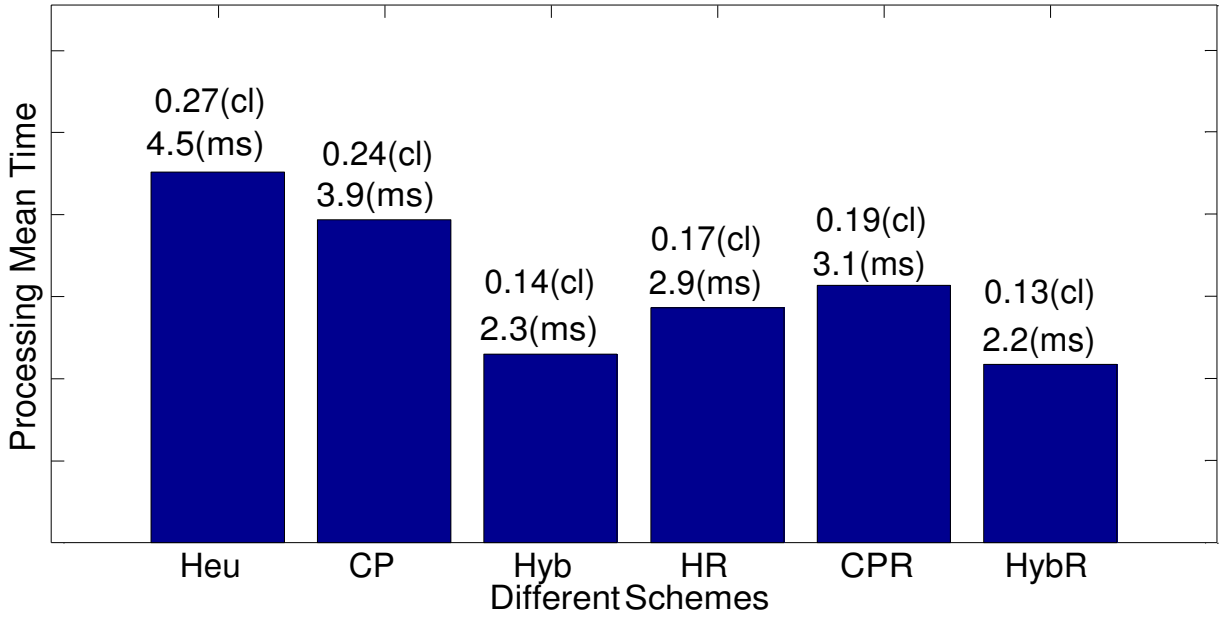

Figure 4.8 Comparison of mean processing time for different schemes (original algorithm, which has not shown in this histogram, consumes 371 ms or 22.24 cycles)

Figure 4.9 shows the ratio of speed enhancement of each algorithm compared to the original algorithm. As illustrated in this figure, the heuristic (sparsity) algorithm provides 84 times improvement, catch and pinpoint (CP) 96 times improvement; HbR with 172 times improvement has the highest speed.

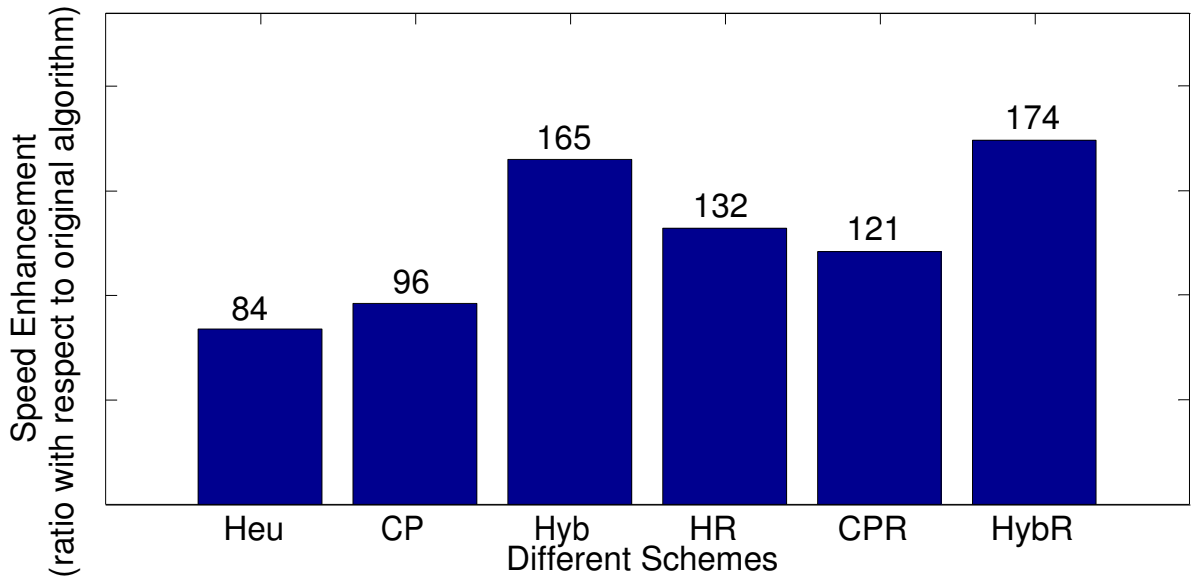

Figure 4.9 Comparison of speed enhancement in different schemes (ratio with respect to the original algorithm)

4.3.2 Accuracy Assessment

In this section the accuracy of the proposed algorithms in terms of frequency, phase and amplitude is discussed. First we compare the accuracy of the approaches using noise-free signal. Then noisy signals are used for accuracy assessment.

Table 4.2 shows the result of measurements of different algorithms in the noise-free environment. As this table shows, the result of original SLMS (Org) and CP are the same and both can detect all the existing tones in the signal. Schemes Heu, Hyb, HR, and HbR can detect the fundamental and harmonic component. As they are not designed to detect interharmonics, they cannot detect interharmonic component. CPR fails to detect the interharmonic component. Besides Org and CP, other schemes estimate the fundamental component correctly as well; they also estimate the frequency and amplitude of harmonic component correctly. However, there is a slight error (2.1 degrees) in measuring the phase of harmonic component. As perceived from Table 4.2, the CP algorithm, the same as the original algorithm, is capable of measuring frequency, phasor and amplitude of the fundamental, harmonic, and interharmonic components without any error.

Table 4.2 Signal parameters and measurement results in Noise-Free Environment

	1			2			3		
	f_i (HZ)	A_i (PU)	ϕ_i (°)	f_i (HZ)	A_i (PU)	ϕ_i (°)	f_i (HZ)	A_i (PU)	ϕ_i (°)
ACTUAL VALUE	60.1	1.00	0.0	300.5	0.005	30.0	457.23	0.002	10.0
ORG	60.1	1.00	0.0	300.5	0.005	30.0	457.23	0.002	10.0
HEU	60.1	1.00	0.0	300.5	0.005	32.1	-	-	-
CP	60.1	1.00	0.0	300.5	0.005	30.0	457.23	0.002	10.0
HYB	60.1	1.00	0.0	300.5	0.005	32.1	-	-	-
HEUR	60.1	1.00	0.0	300.5	0.005	32.1	-	-	-
CPR	60.1	1.00	0.0	300.5	0.005	32.1	-	-	-
HYBR	60.1	1.00	0.0	300.5	0.005	32.1	-	-	-

Table 4.3 shows the result of measurements of different algorithms in a noisy environment of SNR = 60 dB. As this table shows, as long as the fundamental tone is considered, all schemes provide exact estimations in terms of frequency, amplitude and phase. Only Org and CP can detect the interharmonic component. The errors of estimation of the interharmonic is 0.04 Hz in frequency, 5% in amplitude and 2.48 degrees in phase. All schemes can detect the harmonic component. Org and CP provide better estimation in phase (4 degrees error vs. 5.2 degrees for other schemes). The frequency estimation of the harmonic component for Heu, Hyb, HR, CPR, and HybR is better than that of Org and CP (0 Hz error compared to 0.3 Hz error).

Based on Table 4.3 we can conclude that if the detection of the all tones including the interharmonic is considered it is better to use CP scheme, which provides the same result as Org but with less computation burden. However, if only detection of fundamental and harmonics is considered, schemes Heu, Hyb, HR, CPR, and HybR could be used which have less computation burden and among which HybR has the least computation burden.

Table 4.3 Signal parameters and measurement results in Noisy Environment (SNR: 60 DB)

	1			2			3		
	f_i (HZ)	A_i (PU)	ϕ_i (°)	f_i (HZ)	A_i (PU)	ϕ_i (°)	f_i (HZ)	A_i (PU)	ϕ_i (°)
ACTUAL VALUE	60.1	1.00	0.0	300.5	0.005	30.0	457.23	0.002	10.0
ORG	60.1	1.00	0.0	300.2	0.005	34.0	457.19	0.0019	12.48
HEU	60.1	1.00	0.0	300.5	0.005	35.2	-	-	-
CP	60.1	1.00	0.0	300.2	0.005	34.0	457.19	0.0019	12.48
HYB	60.1	1.00	0.0	300.5	0.005	35.2	-	-	-
HEUR	60.1	1.00	0.0	300.5	0.005	35.2	-	-	-
CPR	60.1	1.00	0.0	300.2	0.005	35.9	-	-	-
HYBR	60.1	1.00	0	300.5	0.005	35.2	-	-	-

Table 4.4 Signal parameters and measurement results in Noisy Environment (SNR: 50 DB)

	1			2			3		
	f_i (Hz)	A_i (pu)	ϕ_i (°)	f_i (Hz)	A_i (pu)	ϕ_i (°)	f_i (Hz)	A_i (pu)	ϕ_i (°)
Actual value	60.1	1.00	0.0	300.5	0.005	30.0	457.23	0.002	10.0
Org	60.1	1.00	0.0	299.9	0.0051	41.8	453.7	0.0018	27.5
Heu	60.1	1.00	0.0	300.5	0.0051	41.8	-	-	-
CP	60.1	1.00	0.0	299.9	0.0051	41.6	453.7	0.0018	28.3
Hyb	60.1	1.00	0.0	300.5	0.0051	41.8	-	-	-
HeuR	60.1	1.00	0.0	300.5	0.0051	41.8	-	-	-
CPR	60.1	1.00	0.0	-	-	-	-	-	-
HybR	60.1	1.00	0.0	300.5	0.0051	41.8	-	-	-

Table 4.4 shows the result of measurements when the environment is more noisy (SNR=50 dB). As this table shows, Org and CP can detect the fundamental, harmonic and interharmonic components. However, due to noisy signal, the estimation of the harmonic in Org and CP has 0.6 Hz error and that of interharmonic is 3.53 Hz. The estimations of amplitudes are respectively 2% and 5%, while the errors in phase are respectively 11.75 and 17.52 degrees. On the other hand, Heu, Hyb, HR, and HybR can detect both fundamental and harmonic frequency without error. There is 2% error in the amplitude of harmonic, and 11.8 degrees error in the phase of harmonic. CPR, however, fails to detect the interharmonic and the harmonic.

The reason that Heu, Hyb, HR, and HybR have better accuracies in detecting the fundamental and interharmonic frequencies than Org and CP can be justified as follows. Despite Org and CP which search the whole frequency spectrum, to find the fundamental and non-fundamental frequencies, sparsity-based schemes scan only the interval around the fundamental frequency. Since fundamental frequency always has a big amplitude in any noisy environment, its detection is affected by noise insignificantly. But since harmonic components have by far smaller amplitudes than the fundamental, their detection is affected by noise to a great extent. In sparsity-based schemes, however, the detection of harmonics is based on the detection of the fundamental frequency, hence the detection of the harmonics is as resilient to noise as the detection of the fundamental frequency is.

4.3.3 Assessment Conclusion

Based on the foregoing results and discussion in previous subsections, the following statements are concluded for different SLMS schemes:

- CPR scheme should be avoided as it cannot detect interharmonics and harmonics in a very noisy environment.
- Org and CP could be used when interharmonic components should necessarily be detected. CP is the desired approach in this case as it has less computation burden.
- Estimation of the fundamental frequency is highly resilient to noise.
- Heu, Hyb, HR, HybR provide exact estimation of frequencies of the fundamental and harmonics. The preferred scheme, taking the computation burden also into account, is HybR.

5. Noise Analytics for PMU Accuracy

5.1 Analysis of Noise Effect in DFT Algorithm: Theory

Noise remains a concern in any measurement system and results in random fluctuation of estimation around the expectation of the parameter. The behavior of these random fluctuations in estimation is dependent on the behavior of noise signal. One of the insightful measures in probabilistic phenomena is the variance which is the yardstick of variation of the signal around it expected value. Finding the exact variance of an estimated parameter is, in general, a tough task. Cramer-Rao Lower Bound (CRLB), however, provides a lower bound for estimation variance which no estimation algorithm is able to present less variance than [99-100] and an estimation method touching CRLB is called efficient. CRLB is a general bound regardless of the estimation algorithm. To analyze the behavior of a specific algorithm in dealing with noise, tracking the noise effect from the source through the algorithm steps toward the parameter estimation provides insightful results for that specific algorithm.

Frequency is an important parameter of the signal and there are different approaches for its estimation in the literature [101-13]. In power system measurement, phasor, frequency, and rate of change of frequency are among the most important parameters of interest. Power system literature abounds with algorithms tackling the estimation of these parameters [104]. Many papers have primarily focused on estimation of the forgoing parameters and to justify the algorithm resilience to noise they have used simulation. Simulation is a standard approach in noise analysis and especially in comparing different algorithms to assess their noise resilience. On the other hand, an analytical approach, even if approximate, can show the share of different parameters in contributing to estimation uncertainty and provide insight into the effect of different parameters of the algorithm on the resilience of estimation to noise.

In many measurement systems, including power system measurement, noise could be modeled as additive random variable with zero-mean Gaussian distribution. Because of the nonlinear transformations used in estimation algorithm, the estimated parameter would have a non-Gaussian distribution. However, it often could be approximated with a Gaussian one.

In this report, we present the effect of noise on estimation of frequency and rate of change of frequency (RCF) in power system measurement. To make the flow of the report fluent we present the effect of noise on estimation of magnitude and phase as well. We assume the power system signal (voltage or current) is sinusoidal. Due to widespread use of DFT in academic research and industrial implementations, we focus on DFT algorithm.

5.1.1 Variance Estimation for Magnitude and Phase

In this section we approximate the variance of magnitude and phase. Assume the given signal is, as follows, sinusoidal:

$$x(t) = \sqrt{2}A\cos(2\pi f_0 t + \phi_0) \tag{5.1}$$

where A is the rms value of the signal, f_0 the nominal frequency (50, or 60 Hz), and ϕ_0 the initial phase. The phasor of the signal is

$$\bar{A} = A\exp(j\phi_0). \tag{5.2}$$

To obtain (5.2), DFT method may be used as follows. Let's sample the signal with sampling frequency of $f_s = Nf_0$, an integer multiple of the nominal frequency. Therefore:

$$x_k = \sqrt{2}A\cos\left(\frac{2\pi}{N}k + \phi_0\right) \tag{5.3}$$

Taking DFT of (5.3) yields (note that in this report by DFT we mean the fundamental-bin entry of the DFT vector):

$$\bar{X} = \frac{\sqrt{2}}{N}\sum_{k=0}^{N-1} x_k \exp\left(-j\frac{2\pi}{N}k\right) \tag{5.4}$$

which in rectangular form is represented as:

$$X_r = \frac{\sqrt{2}}{N}\sum_{k=0}^{N-1} a_k x_k, \qquad a_k = \cos\left(\frac{2\pi}{N}k\right) \tag{5.5a}$$

$$X_i = -\frac{\sqrt{2}}{N}\sum_{k=0}^{N-1} b_k x_k, \qquad b_k = \sin\left(\frac{2\pi}{N}k\right) \tag{5.5b}$$

$$\bar{X} = X_r + jX_i \tag{5.5c}$$

It can be shown that

$$\bar{X} = \bar{A} \tag{5.6}$$

Therefore the magnitude and phase of $\bar{A}$ are as follows.

$$A = \left|\bar{A}\right| = \sqrt{X_r^2 + X_i^2} \tag{5.7a}$$

$$\phi_0 = \angle\bar{A} = \tan^{-1}\left(\frac{X_i}{X_r}\right) \tag{5.7b}$$

In above we assumed the signal is noise-free. Now consider the signal is noisy:

$$\mathbf{z}_k = x_k + \boldsymbol{\upsilon}_k \tag{5.8}$$

where at each time instance k, noise is assumed to be a zero-mean Gaussian random variable, i.e. $\boldsymbol{\upsilon}_k \sim \mathrm{N}(0,\sigma^2)$. Random variables of noise at different time instances are assumed to be mutually independent. Applying rectangular DFT to $\mathbf{z}_k$, we introduce the random variables $\mathbf{r}$ and $\mathbf{i}$ as follows:

$$\mathbf{r} = \frac{\sqrt{2}}{N}\sum_{k=0}^{N-1} a_k \mathbf{z}_k \tag{5.9a}$$

$$\mathbf{i} = -\frac{\sqrt{2}}{N}\sum_{k=0}^{N-1} b_k \mathbf{z}_k \tag{5.9b}$$

Simplifying (5.9a) and (5.9b) yields

$$\mathbf{r} = X_r + \boldsymbol{\xi}_r \quad \mathbf{i} = X_i + \boldsymbol{\xi}_i \tag{5.10}$$

where

$$\boldsymbol{\xi}_r = \frac{\sqrt{2}}{N}\sum_{k=0}^{N-1} a_k \boldsymbol{\upsilon}_k, \quad \boldsymbol{\xi}_i = -\frac{\sqrt{2}}{N}\sum_{k=0}^{N-1} b_k \boldsymbol{\upsilon}_k \tag{5.11}$$

It can be easily shown that

$$\boldsymbol{\xi}_r \sim \mathrm{N}(0,\sigma_\xi^2), \quad \boldsymbol{\xi}_i \sim \mathrm{N}(0,\sigma_\xi^2), \quad \sigma_\xi^2 = \frac{\sigma^2}{N} \tag{5.12}$$

Using (5.10) and (5.12) we can write

$$\mathbf{r} \sim \mathrm{N}(X_r,\sigma_\xi^2) \quad \mathbf{i} \sim \mathrm{N}(X_i,\sigma_\xi^2) \tag{5.13}$$

Next we introduce random variables of magnitude ($\mathbf{w}$) and phase ($\boldsymbol{\varphi}$) as follows.

$$\mathbf{w} = \sqrt{\mathbf{r}^2 + \mathbf{i}^2} \tag{5.14a}$$

$$\boldsymbol{\varphi} = \tan^{-1}(\mathbf{h}) \tag{5.14b}$$

$$\mathbf{h} = \frac{\mathbf{i}}{\mathbf{r}} \tag{5.14c}$$

We insert (5.10) into (5.14a), expand it, ignore the nonlinear error terms of $\boldsymbol{\xi}_r^2$ and $\boldsymbol{\xi}_i^2$, and employ the

approximation of $\sqrt{1+x} \cong 1+\frac{x}{2}$ to obtain the following approximate relation.

$$\mathbf{w} \cong A + \frac{X_r}{A}\xi_r + \frac{X_i}{A}\xi_i \tag{5.15}$$

To find the variance of magnitude $\mathbf{w}$ we need to know whether ξ_r and ξ_i are independent. We prove they are. For this end it is sufficient to show that $\mathrm{Cov}(\xi_r, \xi_i) = 0$.

$$N\mathrm{Cov}(\xi_r,\xi_i) = \mathrm{E}[\xi_r\xi_i] = E\left[\left(\frac{\sqrt{2}}{N}\sum_{k=0}^{N-1} a_k \upsilon_k\right)\left(\frac{\sqrt{2}}{N}\sum_{k=0}^{N-1} b_k \upsilon_k\right)\right] \tag{5.16}$$

$$= \frac{2}{N^2}\sum_{k=0}^{N-1} a_k b_k E[\upsilon_k^2] + \frac{2}{N^2}\sum_{\substack{m=0 \\ m\neq n}}^{N-1}\sum_{n=0}^{N-1} a_m b_n E[\upsilon_m \upsilon_n]$$

Since we assumed υ_k variable be mutually independent with variance σ^2, therefore

$$E[\upsilon_m \upsilon_n] = 0 \quad m \neq n \tag{5.17a}$$

$$E[\upsilon_k^2] = \sigma^2 \tag{5.17b}$$

Using (5.17) we can write (5.16) as

$$N\mathrm{Cov}(\xi_r,\xi_i) = \frac{2\sigma^2}{2}\sum_{k=0}^{N-1} a_k b_k \tag{5.18}$$

Since a_k and b_k are orthogonal signals, $\sum_{k=0}^{N-1} a_k b_k = 0$; thus

$$\mathrm{Cov}(\xi_r,\xi_i) = 0 \tag{5.19}$$

meaning that ξ_r and ξ_i are independent.

Since ξ_r and ξ_i are independent, we conclude that:

$$\mathbf{w} \sim \mathrm{N}\left(A, \sigma_w^2\right), \quad \sigma_w^2 = \sigma_\xi^2 = \frac{\sigma^2}{N} = \sigma^2\frac{f_0}{f_s} \tag{5.20}$$

Equation (5.20) represents the approximate variance for magnitude estimation using DFT. It is inversely proportional to N or f_s.

Next we find the approximate variance for phase. We first find the variance of $\mathbf{h}$. We expand (5.14c) as follows:

$$\mathbf{h} = \frac{\mathbf{i}}{\mathbf{r}} = \frac{X_i + \xi_i}{X_r + \xi_r} = \frac{X_i + \xi_i}{X_r\left(1 + \frac{\xi_r}{X_r}\right)} \tag{5.21}$$

To simplify the expression in the denominator we may use the approximation $\frac{1}{1+\varepsilon} \cong 1-\varepsilon$ which is valid when ε is very small. Therefore we should make sure $\frac{\xi_r}{X_r}$ is very small. Since $\xi_r \sim \mathrm{N}\left(0, \frac{\sigma^2}{N}\right)$, and σ practically is a small fraction of A, the expression $\frac{\xi_r}{X_r}$ is a small fraction, unless X_r is small. To force X_r not to have a small value, we assume $\phi_0 \in \mathbf{B}$, where $\mathbf{B} = \left[-\frac{\pi}{4}, \frac{\pi}{4}\right]$. With this restriction on ϕ_0 we

will be sure that in the worst case, i.e., when ϕ_0 equals $\frac{\pi}{4}$ or $-\frac{\pi}{4}$, still X_r is $\frac{A}{2}$, big enough for our purpose. Therefore (5.21) is approximated using $\frac{1}{1+\varepsilon} \cong 1-\varepsilon$.

$$\mathbf{h} \cong \frac{X_i}{X_r} - \frac{X_i}{X_r^2}\xi_r + \frac{1}{X_r}\xi_i \tag{5.22}$$

Due to independence of ξ_r and ξ_i we conclude that

$$\mathbf{h} \approx \mathrm{N}(\mu_h, \sigma_h^2) \tag{5.23}$$

where

$$\mu_h = \frac{X_i}{X_r} \tag{5.24}$$

$$\sigma_h^2 = \left(\frac{X_i}{X_r^2}\right)^2 \sigma_\xi^2 + \left(\frac{1}{X_r}\right)^2 \sigma_\xi^2 \tag{5.25}$$

$$\sigma_i^2 = \sigma_\xi^2 \frac{X_r^2 + X_r^2}{X_r^4} = \sigma_\xi^2 \frac{A^2}{X_r^2} = \frac{A^2\sigma^2}{X_r^2 N}$$

Since $\cos(\phi_0) = \frac{X_r}{A}$, (5.25) may be written as follows.

$$\sigma_h^2 = \frac{\sigma^2}{A^2 \cos^4(\phi_0) N} \tag{5.26}$$

Note that we found that $\mathbf{h}$ has approximately a normal pdf with mean μ_h and variance σ_h^2, provided that $\phi_0 \in \mathbf{B}$. In other words

$$f_{\mathbf{H}}(h \mid \phi_0 \in \mathbf{B}) = \frac{1}{\sqrt{2\pi}\sigma_h} \exp\left(-\frac{(h-\mu_h)^2}{2\sigma_h^2}\right) \tag{5.27}$$

We can assume that ϕ_0 has a uniform distribution in $\left[-\frac{\pi}{2}, \frac{\pi}{2}\right]$. If $\phi_0 \in \bar{\mathbf{B}}$, because of big values of $\frac{\xi_r}{X_r}$, approximation of $\frac{1}{1+\frac{\xi_r}{X_r}} \cong 1 - \frac{\xi_r}{X_r}$ is no longer valid, resulting in invalidity of approximation of (5.22).

In this case we redefine $\mathbf{h}$ as $\frac{\mathbf{r}}{\mathbf{i}}$, and use $\cot^{-1}(\mathbf{h})$ to calculate phase. Then we argue similarly to the previous case to conclude:

$$\mathbf{h} \approx \mathrm{N}(\mu_h, \sigma_h^2) \tag{5.28}$$

where

$$\mu_h = \frac{X_r}{X_i} \tag{5.29}$$

$$\sigma_h^2 = \frac{\sigma_2}{A^2 \sin^2(\phi_0) N} \tag{5.30}$$

It ought to be noted that when the samples of r and i of random variables $\mathbf{r}$ and $\mathbf{i}$, respectively, are ready, whether we use the $\tan^{-1}(.)$ or $\cot^{-1}(.)$ procedure the end result is the same. The difference

between these two procedures is a matter of modeling, not of result. Using these two procedures we were able to approximate the distribution of $\mathbf{h}$ in both partitions of $\mathbf{B}$ and $\overline{\mathbf{B}}$. The reader may notice the duality of the two regions and the duality of the means and variances. For the moment we assume $\phi_0 \in \mathbf{B}$. Since $\boldsymbol{\varphi} = \tan^{-1}(\mathbf{h})$, and $f_{\mathbf{H}}(h)$ is as (5.27), $f_{\boldsymbol{\Phi}}(\phi)$ is found as follows.

$$f_{\boldsymbol{\Phi}}(\phi) = \frac{1+\tan^2(\phi)}{\sqrt{2\pi}\sigma_h} \exp\left(-\frac{(\tan(\phi)-\mu_h)^2}{2\sigma_h^2}\right) \tag{5.31}$$

Now we use the following variance approximation, which is also known as delta method: if $\mathbf{y} = g(\mathbf{x})$, then $\sigma_y^2 \cong (g'(\mu_x))^2 \sigma_x^2$ [105]. Employing this property, the variance of the phase is approximated as follows.

$$\sigma_\phi^2 = \frac{\sigma^2}{A^2 N} \tag{5.32}$$

Note that this variance is obtained provided that $\phi_0 \in \mathbf{B}$. When $\phi_0 \in \overline{\mathbf{B}}$, adopting the $\cot^{-1}(.)$ procedure results in the same variance approximation. Since we assumed that ϕ_0 has a uniform distribution in $\left[-\frac{\pi}{2}, \frac{\pi}{2}\right]$, $\mathbf{B}$ and $\overline{\mathbf{B}}$ has the same probability of 0.5; therefore using total probability theorem we conclude that $\sigma_\phi^2 = \frac{\sigma^2}{A^2 N}$ when ϕ_0 is arbitrary. Note that the above approximate variance for phase exactly equals the CRLB for phase estimation [99]. And note that to obtain (5.32) we discarded any noise contribution of nonlinear terms.

5.1.2 Variance Estimation for Frequency

In this section we derive an approximate analytical expression for variance of frequency, when the phasors are estimated using DFT and frequency using the difference between two consecutive phases. We assume the frequency is nominal. Therefore the exact frequency to be estimated is f_0. Suppose at time t_k and t_{k-1} the measured phases of the signal are ϕ_k and ϕ_{k-1}. We define the following random variables of phase difference and frequency.

$$\boldsymbol{\psi} = \boldsymbol{\varphi}_k - \boldsymbol{\varphi}_{k-1} \tag{5.33}$$

$$\mathbf{f} = \frac{\boldsymbol{\psi}}{2\pi\Delta t} = \frac{f_s}{2\pi}\boldsymbol{\psi} \tag{5.34}$$

We aim to find σ_f^2. Since we need the subscripts for other notations, we introduce any variable corresponding to t_{k-1} and t_k respectively without and with a prime; therefore (5.33) is written as

$$\boldsymbol{\psi} = \boldsymbol{\varphi}' - \boldsymbol{\varphi} \tag{5.35}$$

We take tan(.) of the two sides of (5.35):

$$\tan(\boldsymbol{\psi}) = \tan(\boldsymbol{\varphi}' - \boldsymbol{\varphi}) = \frac{\tan(\boldsymbol{\varphi}') - \tan(\boldsymbol{\varphi})}{1+\tan(\boldsymbol{\varphi}')\tan(\boldsymbol{\varphi})}$$

$$= \frac{\frac{\mathbf{i}'}{\mathbf{r}'} - \frac{\mathbf{i}}{\mathbf{r}}}{1+\frac{\mathbf{i}'}{\mathbf{r}'}\frac{\mathbf{i}}{\mathbf{r}}} = \frac{\mathbf{r}\mathbf{i}' - \mathbf{i}\mathbf{r}'}{\mathbf{r}\mathbf{r}' + \mathbf{i}\mathbf{i}'} \tag{5.36}$$

Similarly to section II, the following relations are obtained.

$$\begin{aligned} \mathbf{r} &= X_r + \xi_r, \quad \mathbf{r}' = X_r' + \xi_r' \\ \mathbf{i} &= X_i + \xi_i, \quad \mathbf{i}' = X_i' + \xi_i' \end{aligned} \tag{5.37}$$

Inserting (5.37) into (5.36), expanding expressions, neglecting the order two of error contributions (e.g. $\xi_r\xi_i'$), employing the approximation of $\frac{1}{1+\varepsilon} \cong 1-\varepsilon$ to get rid of the denominator, and performing some mathematical manipulations, we derive the following formula

$$\tan(\psi) \cong \frac{a}{b} + \frac{A^2}{b^2}\left(X_i\xi_r - X_r\xi_i - X_i'\xi_r' + X_r'\xi_i'\right) \tag{5.38}$$

Defining

$$\begin{aligned} \mathbf{q} &= \tan(\psi) \\ \mathbf{w} &= X_i\xi_r - X_r\xi_i - X_i'\xi_r' + X_r'\xi_i' \end{aligned} \tag{5.39}$$

We write (5.38) as

$$\mathbf{q} \cong \frac{a}{b} + \frac{A^2}{b^2}\mathbf{w} \tag{5.40}$$

To find the variance of frequency σ_f^2, we first find σ_w^2, then σ_q^2, then σ_ψ^2, and finally σ_f^2. The random variable $\mathbf{w}$ is a linear combination of four random variables of ξ_r, ξ_i, ξ_r', and ξ_i'; each of which has zero mean and variance of $\frac{\sigma^2}{N}$. We write $\mathbf{w}$ in the following vector form

$$\mathbf{w} = \mathbf{B}\mathbf{y} \tag{5.41}$$

Where

$$\begin{aligned} \mathbf{B} &= \left[X_i \quad -X_r \quad -X_i' \quad X_r'\right] \\ \mathbf{y} &= \left[\xi_r \quad \xi_i \quad \xi_r' \quad \xi_i'\right]^T \end{aligned} \tag{5.42}$$

The general normal pdf for random vector variable $\mathbf{y}$ is as follows

$$f_{\mathbf{Y}}(\mathbf{y}) = \frac{1}{(2\pi)^2\left|\mathbf{C}_y\right|^{1/2}}\exp\left(-\frac{1}{2}\mathbf{y}^T\mathbf{C}_y^{-1}\mathbf{y}\right) \tag{5.43}$$

where $\mathbf{C}_y$ is the covariance matrix associated with random vector variable $\mathbf{y}$ and defined as follows.

$$\mathbf{C}_y = \begin{bmatrix} E\left[\xi_r^2\right] & E\left[\xi_r\xi_i\right] & E\left[\xi_r\xi_r'\right] & E\left[\xi_r\xi_i'\right] \\ E\left[\xi_i\xi_r\right] & E\left[\xi_i^2\right] & E\left[\xi_i\xi_r'\right] & E\left[\xi_i\xi_i'\right] \\ E\left[\xi_r'\xi_r\right] & E\left[\xi_r'\xi_i\right] & E\left[\xi_r'^2\right] & E\left[\xi_r'\xi_i'\right] \\ E\left[\xi_i'\xi_r\right] & E\left[\xi_i'\xi_i\right] & E\left[\xi_i'\xi_r'\right] & E\left[\xi_i'^2\right] \end{bmatrix} \tag{5.44}$$

Then $\mathbf{w}$ is normally distributed with zero mean and variance σ_w^2:

$$\sigma_w^2 = \mathbf{B}\mathbf{C}\,\mathbf{B}^T \tag{5.45}$$

After calculating the covariance matrix $\mathbf{C}_y$, we calculate σ_w^2 using (5.45). After some manipulations the following relation is obtained.

$$\sigma_w^2 = \frac{2\sigma^2}{N}\left(A^2 + K + L + M + N\right) \tag{5.46}$$

where

$$K = -X_iX_i'\frac{(N-2)}{N}\cos\left(\frac{2\pi}{N}\right) \tag{5.47a}$$

$$L = X_iX_r'\frac{(N-2)}{N}\sin\left(\frac{2\pi}{N}\right) \tag{5.47b}$$

$$M = -X_r X_i' \sin\left(\frac{2\pi}{N}\right) \quad (5.47c)$$

$$N = -X_r X_r' \cos\left(\frac{2\pi}{N}\right) \quad (5.47d)$$

Simplifying (46) yields:

$$\sigma_w^2 = \frac{4\sigma^2 A^2}{N^2} \sin^2(\phi_0) \quad (5.48)$$

Finally we can write

$$\mathbf{f} \approx \mathrm{N}\left(\mu_f, \sigma_f^2\right) \quad (5.49)$$

where

$$\mu_f = f_0 \quad (5.50)$$

$$\sigma_f^2 = \frac{\sigma^2 f_0^2}{A^2 \pi^2} \sin^2(\phi_0) \quad (5.51)$$

5.1.3 Variance Estimation for Rate of Change of Frequency

In this section we derive an approximate analytic expression for variance of RCF, when the phasors are derived using DFT, frequency using the difference between two consecutive phases, and RCF using the difference between two consecutive frequencies. We assume the frequency is nominal. Therefore the exact RCF to be estimated is zero. At time t_{k+1}, t_k and t_{k-1} the measured phases of the signal be ϕ_{k+1}, ϕ_k and ϕ_{k-1}. Therefore we can write:

$$\boldsymbol{\psi}_k = \boldsymbol{\varphi}_k - \boldsymbol{\varphi}_{k-1} \quad (5.52)$$

$$\mathbf{f} = \frac{\boldsymbol{\psi}}{2\pi(2\Delta t)} = \frac{f_s}{4\pi} \boldsymbol{\psi} \quad (5.53)$$

$$\frac{d\mathbf{f}}{dt} = \frac{\mathbf{f}_{k+1} - \mathbf{f}_k}{\Delta t} = \frac{\boldsymbol{\psi}_{k+1} - \boldsymbol{\psi}_k}{2\pi \Delta t^2} = \frac{f_s^2}{2\pi}\left(\boldsymbol{\varphi}_{k+1} - 2\boldsymbol{\varphi}_k + \boldsymbol{\varphi}_{k-1}\right) \quad (5.54)$$

Since we need subscripts for other notations, we maintain the following notation during this part of report: $\mathbf{x}' = \mathbf{x}_{k+1}$, $\mathbf{x}' = \mathbf{x}_k$, $\mathbf{x} = \mathbf{x}_{k-1}$ where $\mathbf{x}$ may be any random variable. Therefore we can write:

$$\frac{d\mathbf{f}}{dt} = \frac{f_s}{2\pi} G \quad (5.55)$$

$$\mathbf{G} = \boldsymbol{\psi}' - \boldsymbol{\psi}' = \boldsymbol{\varphi}' - 2\boldsymbol{\varphi}' + \boldsymbol{\varphi} \quad (5.56)$$

We aim to find $\sigma^2_{\frac{df}{dt}}$. For this end we first find the variance of $\mathbf{q} = \tan(G)$, then we find the variance of G, and finally we find the variance of $\frac{d\mathbf{f}}{dt}$. Taking $\tan(.)$ from both sides of (5.56), using some manipulation and noting that $\boldsymbol{\varphi}' = \frac{\mathbf{i}'}{\mathbf{r}'}$, $\boldsymbol{\varphi}' = \frac{\mathbf{i}}{\mathbf{r}'}$, and $\boldsymbol{\varphi} = \frac{\mathbf{i}}{\mathbf{r}}$ we can write:

$$\mathbf{q} = \tan(\mathbf{G}) = \frac{\mathbf{r}\mathbf{r}'^2\mathbf{i}' - \mathbf{r}\mathbf{i}'^2\mathbf{i}' + \mathbf{i}\mathbf{r}'^2\mathbf{r}' - \mathbf{i}\mathbf{i}'^2\mathbf{r}' - 2\mathbf{r}\mathbf{r}'\mathbf{i}'\mathbf{r}' + 2\mathbf{i}\mathbf{r}'\mathbf{i}'\mathbf{i}'}{\mathbf{r}\mathbf{r}'^2\mathbf{r}' - \mathbf{r}\mathbf{i}'^2\mathbf{r}' - \mathbf{i}\mathbf{r}'^2\mathbf{i}' + \mathbf{i}\mathbf{i}'^2\mathbf{i}' + 2\mathbf{r}\mathbf{r}'\mathbf{i}'\mathbf{i}' + 2\mathbf{i}\mathbf{r}'\mathbf{i}'\mathbf{r}'} \quad (5.57)$$

Now we insert the following equivalents in above equation.

$$\begin{aligned}
&\mathbf{r} = X_r + \xi_r, \quad \mathbf{i} = X_i + \xi_i \\
&\mathbf{r}' = X_r' + \xi_r', \quad \mathbf{i}' = X_i' + \xi_i' \\
&\mathbf{r}'' = X_r'' + \xi_r'', \quad \mathbf{i}'' = X_i'' + \xi_i''
\end{aligned} \tag{5.58}$$

where the right side of (5.58), based on the subscription is either real or imaginary part of the 2^{N-1} corresponding DFT; for example $\xi_r = \frac{\sqrt{}}{N}\sum_{k=0}^{2^{N-1}} a_k \mathfrak{v}_{k-1}$, $\xi_r' = \frac{\sqrt{}}{N}\sum_{k=0}^{2^{N-1}} a_k \mathfrak{v}_k$, $\xi_r'' = \frac{\sqrt{}}{N}\sum_{k=0} a_k \mathfrak{v}_{k+1}$.

After some mathematical manipulations we obtain:

$$\mathbf{q} = \tan(\mathbf{G}) \cong \frac{A^6}{b^2}\left(\frac{ab}{A^6} + \mathbf{w}\right) \tag{5.59}$$

$$\mathbf{w} = -X_i\xi_r + X_r\xi_i + 2X_i'\xi_r' - 2X_r'\xi_i' - X_i''\xi_r'' + X_r''\xi_i'' \tag{5.60}$$

We aim to find σ_q^2; therefore we must first find σ_w^2. $\mathbf{w}$ is a linear combination of six random variables ξ_r, ξ_i, ξ_r', ξ_i', ξ_r'', and ξ_i'' each of which with zero mean and variance of $\frac{\sigma^2}{N}$. We write $\mathbf{w}$ in the following vector form

$$\mathbf{w} = \mathbf{B}\mathbf{y} \tag{5.61}$$

where

$$\begin{aligned}
&\mathbf{B} = \begin{bmatrix} -X_i & X_r & 2X_i' & -2X_r' & -X_i'' & X_r'' \end{bmatrix} \\
&\mathbf{y} = \begin{bmatrix} \xi_r & \xi_i & \xi_r' & \xi_i' & \xi_r'' & \xi_i'' \end{bmatrix}^T
\end{aligned} \tag{5.62}$$

The general Gaussian pdf for random vector variable $\mathbf{y}$ is as follows

$$f_{\mathbf{Y}}(\mathbf{y}) = \frac{1}{(2\pi)^2 |\mathbf{C}_y|^{1/2}} \exp\left(-\frac{1}{2}\mathbf{y}^T \mathbf{C}_y^{-1} \mathbf{y}\right) \tag{5.63}$$

Where $\mathbf{C}_y$ is the covariance matrix associated with vector random variable $\mathbf{y}$ and defined as follows.

$$\mathbf{C}_y = \begin{bmatrix}
E[\xi_r^2] & E[\xi_r\xi_i] & E[\xi_r\xi_r'] & E[\xi_r\xi_i'] & E[\xi_r\xi_r''] & E[\xi_r\xi_i''] \\
E[\xi_i\xi_r] & E[\xi_i^2] & E[\xi_i\xi_r'] & E[\xi_i\xi_i'] & E[\xi_i\xi_r''] & E[\xi_i\xi_i''] \\
E[\xi_r'\xi_r] & E[\xi_r'\xi_i] & E[\xi_r'^2] & E[\xi_r'\xi_i'] & E[\xi_r'\xi_r''] & E[\xi_r'\xi_i''] \\
E[\xi_i'\xi_r] & E[\xi_i'\xi_i] & E[\xi_i'\xi_r'] & E[\xi_i'^2] & E[\xi_i'\xi_r''] & E[\xi_i'\xi_i''] \\
E[\xi_r''\xi_r] & E[\xi_r''\xi_i] & E[\xi_r''\xi_r'] & E[\xi_r''\xi_i'] & E[\xi_r''^2] & E[\xi_r''\xi_i''] \\
E[\xi_i''\xi_r] & E[\xi_i''\xi_i] & E[\xi_i''\xi_r'] & E[\xi_i''\xi_i'] & E[\xi_i''\xi_r''] & E[\xi_i''^2]
\end{bmatrix} \tag{5.64}$$

And $\mathbf{w}$ is normally distributed with zero mean and variance σ_w^2:

$$\sigma_w^2 = \mathbf{B}\mathbf{C}_y\mathbf{B}^T \tag{5.65}$$

By performing some mathematical manipulations, we can finally find:

$$\sigma_w^2 = \frac{4A^2\sigma^2}{N^2}\left(\sin^2(\phi_0) + \sin^2(\phi_0 + \frac{2\pi}{N})\right) \tag{5.66}$$

Finally, we can write:

$$\sigma_{\frac{df}{dt}}^2 = \frac{f_s^2 f_0^2 \sigma^2}{A^2\pi^2}\left(\sin^2(\phi_0) + \sin^2\left(\phi_0 + \frac{2\pi}{N}\right)\right) \tag{5.67}$$

5.2 Analysis of Noise Effect in DFT Algorithm: Simulation Results

In this section we use simulation to verify the accuracy of the approximate analytic expressions of σ^2_f and $\sigma^2_{\frac{df}{dt}}$.

5.2.1 Variance of Frequency: Nominal Frequency Case

We assume that the frequency is nominal, and sampling frequency is integer N times the nominal frequency, i.e. $f_s = Nf_0$ (N=48). We use N+1 samples of a sinusoidal signal with nominal frequency of 60 Hz and rms value of 100. Different initial phases are selected. For each initial phase, the samples were polluted with normal noise, i.e. $N(0,1)$. Then using DFT of two consecutive windows, the frequency is estimated. This procedure is repeated 10000 times with different noise values of $N(0,1)$ for each initial phase and using this frequency estimation, we numerically calculate the variance of the frequency estimation. Figure 5.1(a) shows the comparison of approximate formula, i.e. (5.51), and the numerical variance of frequency estimation. As the figure shows the analytical of (5.51) is a good approximation for the actual variance. Figure 5.1(b) depicts the ratio of numerically calculated variance to the analytic one. As Figure 5.1(b) shows while the approximate formula is a good approximation of the actual variance for most initial phases (the ratio in the flat section is about 0.85), it is not good for initial phases at and around zero degrees, but still the prediction that minimum variance occurs at zero initial phase signal is verified in Figure 5.1(a).

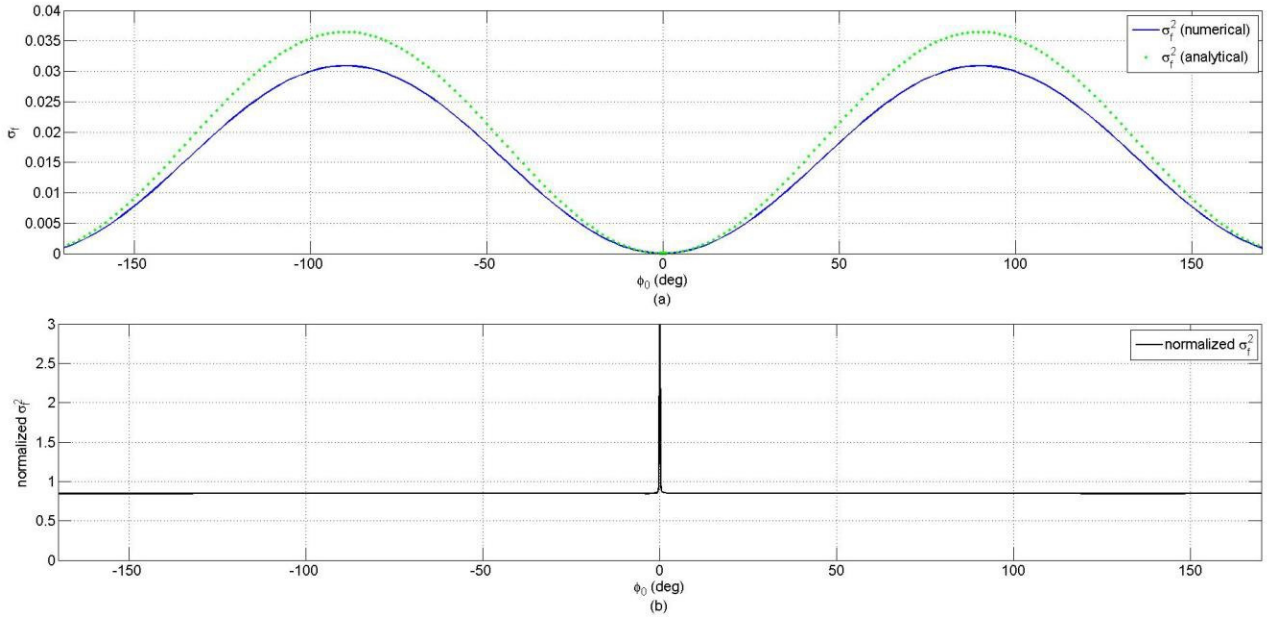

Figure 5.7 Variance estimation for nominal frequency (a) comparison of numerically calculated and approximate analytic variances (b) ratio of the numerical and theoretical variances

5.2.2 Variance of Frequency: Off-Nominal Frequency Case

In derivation of (5.51), one of the assumptions was that the signal has nominal frequency. Figure 5.2, shows the result of simulation when the frequency of the signal is 59 Hz. As it shows, (5.51) is still a

good estimation for the variance of frequency estimation when the frequency is off but around the nominal. The figure also shows that though the approximation is not good in vicinity of zero phase, the variance has much less values when the initial phase is around zero.

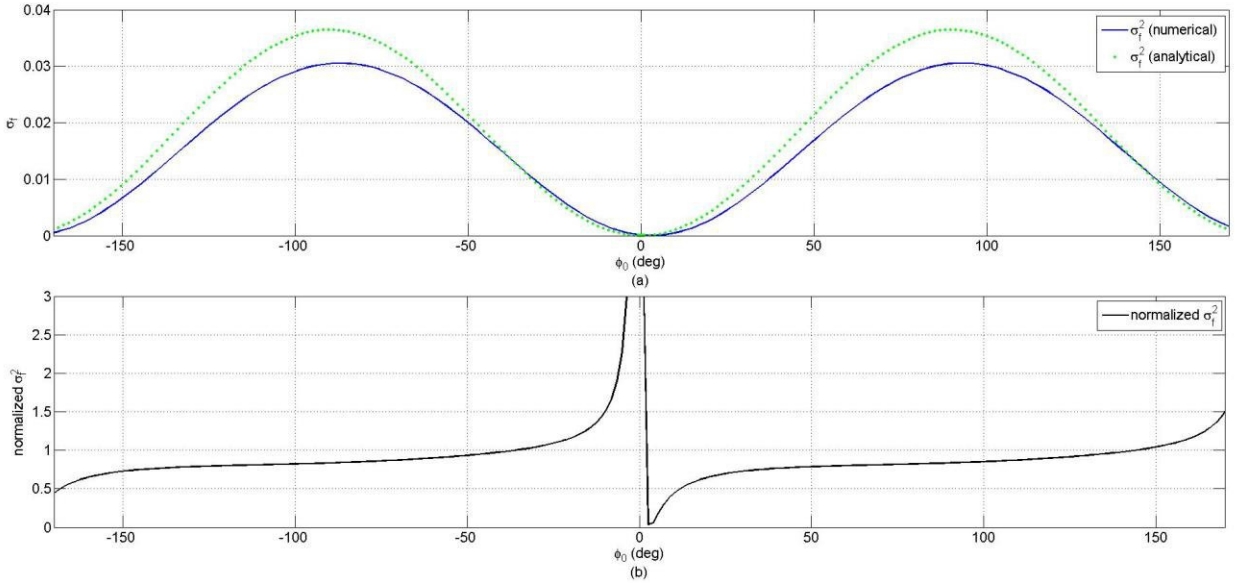

Figure 5.8 Variance estimation for off-nominal frequency of 59 Hz (a) comparison of numerically calculated and approximate analytic variances (b) ratio of the numerical and theoretical variances

5.2.3 Variance of RCF: Nominal Frequency Case

To verify the approximate analytic expression $\sigma^2_{\underline{df}}$ we need N+2 samples, to calculate three consecutive
dt
phases. We assume signal is sinusoidal with nominal frequency of 60 Hz and rms value of 100. Different initial phases are selected. For each initial phase, the samples were polluted with normal noise, i.e. $N(0,1)$. Then using DFT of two consecutive windows, the frequency is estimated. Since there are three consecutive windows, two values for frequency are achieved whose difference is used to estimate the RCF. This procedure is repeated 10000 times with different noise values of $N(0,1)$ for each initial phase and using this RCF estimation, we numerically calculate the variance of the RCF estimation.

Figure 5.3(a) shows the result of RCF variance. As this figure shows (5.67) is a good approximation for the actual variance of RCF estimation. Figure 5.3(b) depicts the ratio of these two ones. As Figure 5.3(b) shows the approximate formula is a good approximation for all initial phases, and Figure 5.3(a) shows that minimum variance occurs about $\phi_0 = \phi_c$.

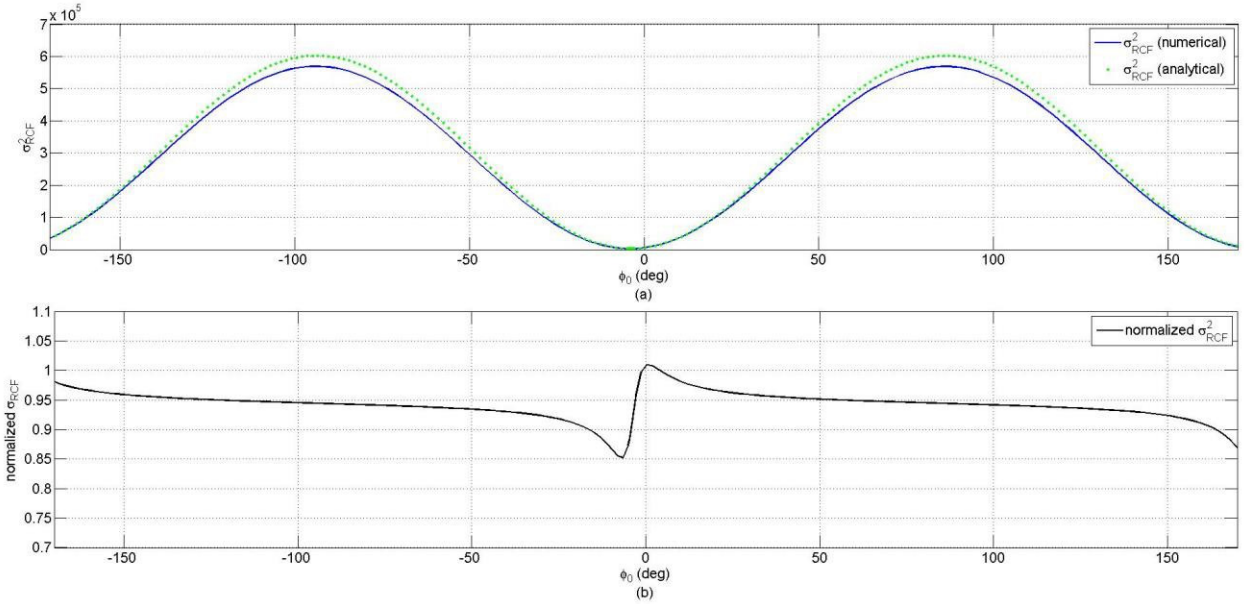

Figure 5.9 Variance of RCF at nominal frequency and RCF=0 (a) comparison of numerically calculated and approximate analytic variances (b) ratio of the numerical and theoretical variances

5.2.3 Variance of RCF: Off-Nominal Frequency and Non-zero RCF Case

In derivation of (5.67), one of the assumptions was that the signal has nominal frequency. As we show still this formula is a good estimate when the frequency deviates around the nominal frequency and even when the RCF is non-zero.

Figure 5.4 shows the result of simulation when the frequency of the signal is 59 Hz and the RCF -1 Hz/sec. As this figure shows, (5.67) is still a good analytical approximation for the variance of RCF estimation when the frequency is off, but around the nominal, and RCF is non-zero.

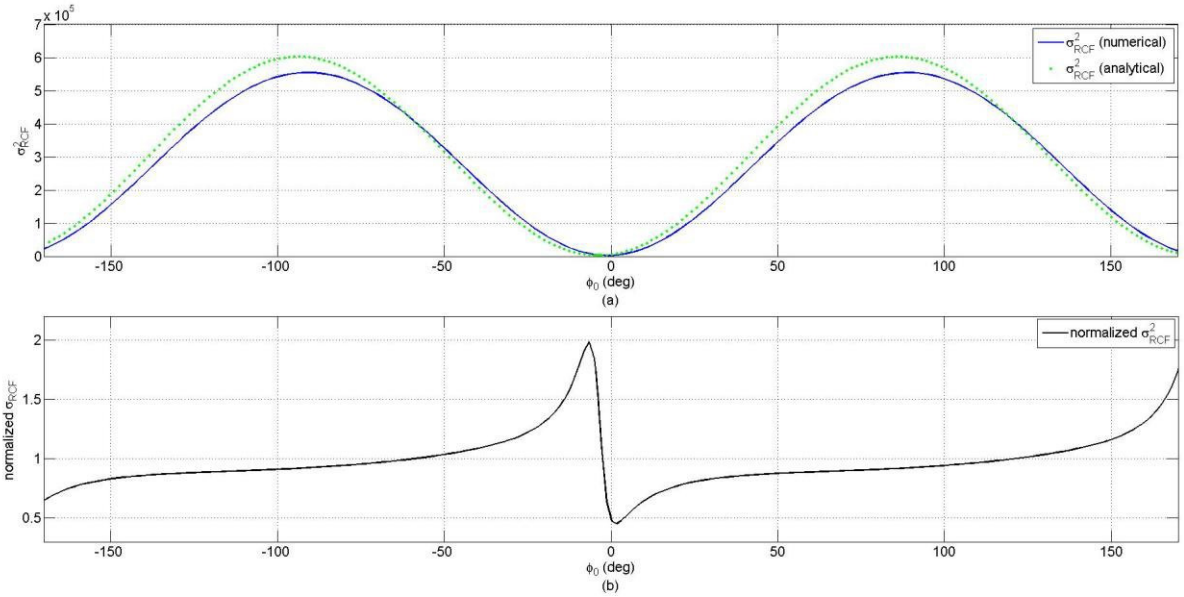

Figure 5.10 Variance of RCF at off-nominal frequency(59 Hz) and RCF=-1 (a) comparison of numerically calculated and approximate analytic variances (b) ratio of the numerical and theoretical variances.

References:

1. A. G. Phadke, "Synchronized phasor measurements in power systems," *IEEE Computer Applications in Power Systems*, 1993, 6(2): 10-15.
2. National Institute of Standards and Technology, US Dept. of Commerce, *NIST Framework and Roadmap for Smart Grid Interoperability Standards*. Release 1.0 (draft), 2009.
3. A. G. Phadke and J. S. Thorp, "History and applications of phasor measurements," *IEEE PES Power Systems Conference and Exposition*, Atlanta, USA, 2006.
4. D. Atanackovic, J. H. Clapauch, G. Dwernychuk, J. Gurney, and H. Lee, "First steps to wide area control," *IEEE Power Energy Magazine*, vol. 6, no.1, pp. 61–68, Jan./Feb. 2008.
5. J. Hauer, W. Mittelstadt, K. Martin, J. Burns, H. Lee, J. Pierre, and D. Trudnowski, "Use of the WECC WAMS in wide area probing tests for validation of system performance and modeling," *IEEE Trans. Power Syst.*, vol. 24, no. 1, pp. 250–257, Feb. 2009.
6. Eastern Interconnection Phasor Pro ect (EIPP), "Metrics for Determining the Impact of Phasor Measurements on Power System State Estimation", prepared by KEMA, March 2006.
7. J. Chen and A. Abur, "Placement of pmus to enable bad data detection in state estimation," *IEEE Transactions on Power Systems*, vol. 21, no. 4, pp. 1608–1615, Nov. 2006.
8. A. G. Phadke, J. S. Thorp, and K. J. Karimi, "State estimation with phasor measurements," *IEEE Transactions on Power Systems*, vol. 1,no. 1, pp. 233–238, Feb. 1986.
9. T. Baldwin, L. Mili, J. Boisen, M.B., and R. Adapa, "Power system observability with minimal phasor measurement placement," *IEEE Transactions on Power Systems*, vol. 8, no. 2, pp. 707–715, May 1993.
10. D.J. Brunei and L.S. Heath, "The PMU Placement Problem", SIAM Journal of Discrete Mathematics, vol. 19, no. 3, pp. 744 - 761, 2005.
11. L. Vanfretti, J. H. Chow, S. Sarawgi, and B. Fardanesh, "A Phasor-Data Based State Estimator Incorporating Phase Bias Correction," under review, *IEEE Transactions on Power Systems*, July 2009.
12. C. W. Hansen and A. S. Debs, "Power system state estimation using three-phase models ," *IEEE Trans. Power Syst.*, vol. 10, no. 2, pp. 818–824, May. 1995.
13. IEEE standard for synchrophasors for power systems [S]. IEEE C37.118 – 2005.
14. M. La Scala, M. De Benedictis, S. Bruno, A. Grobovoy, et al, "Development of applications in WAMS and WACS: an international cooperation experience," in *Proc. IEEE Power Eng. Soc. General Meeting*, Jun. 2006.
15. M. Begovic, D. Novosel, D. Karlsson, et al. "Wide-area protection and emergency control," *Proceedings of the IEEE Energy Infrastructure Defense Systems*, 2005, 93(5): 876-891.
16. A. G. Phadke, H. Voslkis, R. M. de Morales, et al, "The wide world of wide-area measurements," *IEEE Power Energy Mag.*, vol. 6, no. 5, pp. 52–65, Nov. 2008.
17. V. Madani, "Western interconnection experience with phasor measurements," *in 2006 IEEE Power Eng. Soc. Power Syst. Conf. Expo.* (*PSCE*'06), pp. 343–352.
18. Western Electricity Coordinating Council, *WECC Synchro-phasor project whitepaper*, July 17, 2009.
19. Western Electricity Coordinating Council, *Western Interconnection Synchrophasor Program* (*WISP*) *at a glance*, Jan. 2011.
20. C. W. Taylor, D. C. Erickson, K. E. Martin, R. E. Wilson, and V. Venkatasubramanian, "WACS—**W**ide-**A**rea Stability and Voltage **C**ontrol **S**ystem: R&D and On-Line Demonstration," *Proceedings of the IEEE* special issue on Energy Infrastructure Defense Systems, vol. 93, no. 5, pp. 892–906, May 2005.
21. P. Overholt, "The North American SynchroPhasor Initiative (NASPI) and DOE's Smart Grid Investment Grants," *EEI Transmission, Distribution and Metering Conference*, April 13, 2010.
22. North American Electric Reliability Corporation, *Real-time application of synchrophasors for improving reliability*, Oct. 18, 2010.

23. W. Fu, S. Zhao, J. D. McCalley, V. Vittal, N. Abi-Samra, "Risk Assessment for Special Protection Systems," *IEEE Transactions on Power Systems*, vol. 17, no. 1, pp 63-72, February 2002.
24. IEEE Industry Applications Society, IEEE Standard 493-1997 (IEEE Gold Book): *IEEE Recommended Practice for the Design of Reliable Industrial and Commercial Power Systems*, 1998.
25. W. Li, *Risk Assessment of Power Systems*: *Models*, *Methods*, *and Applications*, New York: IEEE Press and Wiley & Sons, 2005.
26. Y. Wang, W. Li and J. Lu, "Reliability Analysis of Wide Area Measurement System", *IEEE Transactions on Power Delivery*, 2010, 25(3): 1483-1491.
27. Y. Wang, W. Li and J. Lu, "Evaluating Multiple Reliability Indices of PMU networks in Wide Area Measuremen System", *Electric Power Systems Research*, vol. 79, no. 10, 2009, pp1353-1359.
28. Y. Wang, W. Li and J. Lu, et al, "Reliability Analysis of Phasor Measurement Unit using Hierarchical Markov Modeling", *Electric Power Components and Systems*, vol. 35, no. 5, 2009, pp517-532.
29. J. S. Thorp, A. G. Phadke, and K. J. Karimi, "Real Time Voltage-Phasor Measurement For Static State Estimation," *IEEE Trans. Power Apparatus and Systems*, vol.PAS-104, no.11, pp.3098-3106, Nov. 1985
30. B. Fardanesh, "Use of Phasor Measurement in a Commercial (or Industrial) State Estimator," EPRI, Palo Alto, California, Final Report 1011002, July 2004.
31. P. M. Anderson, B. LeReverend, "Industry Experience with Special Protection Schemes," *IEEE Trans. Power Systems*, vol. 11, no. 3, pp. 1166-1179, August 1996.
32. J. F. Hauer, C. J. Demeure, L. L. Scharf, "Initial results in Prony analysis of power system response signals," *IEEE Trans. Power Systems*, vol.5, no.1, pp.80-89, Feb 1990
33. J. J. Sanchez-Gasca, J. H. Chow, "Performance comparison of three identification methods for the analysis of electromechanical oscillations," *IEEE Trans. Power Systems*, vol.14, no.3, pp.995-1002, Aug 1999.
34. M. L. Crow, and A. Singh, "The matrix pencil for power system modal extraction," *IEEE Trans. Power Systems,* vol.20, no.1, pp. 501-502, Feb. 2005.
35. J. W. Pierre, D. J. Trudnowski, and M. K. Donnelly, "Initial results in electromechanical mode identification from ambient data," *IEEE Trans. Power Systems,* vol.12, no.3, pp.1245-1251, Aug 1997.
36. D. J. Trudnowski, J. W. Pierre, N. Zhou, J. F. Hauer, M. Parashar, "Performance of Three Mode-Meter Block-Processing Algorithms for Automated Dynamic Stability Assessment," *IEEE Trans. Power Systems*, vol.23, no.2, pp.680-690, May 2008.
37. D. J. Vowles, M. J. Gibbard, D. K. Geddey, D. Bones, "Benchmark testing methodology for continuous modal-estimation Algorithms," *IEEE PES General Meeting*, pp.1-8, 26-30 July 2009.
38. M. M. Begovic, and A. G. Phadke, "Voltage stability assessment through measurement of a reduced state vector," *IEEE Transactions on Power Systems*, vol.5, no.1, pp.198-203, Feb 1990.
39. L. Warland and A. T. Holen, "Estimation of distance to voltage collapse: Testing and algorithm based on local measurements," in *Proceedings of the 14th Power System Computation Conference (PSCC)*, Sevilla, Spain, Jun.2002.
40. M. Parniani, J. H. Chow, L. Vanfretti, B. Bhargava, and A. Salazar, "Voltage Stability Analysis of a Multiple-Infeed Load Center Using Phasor Measurement Data," *IEEE PES Power Systems Conference and Exposition 2006*, pp.1299-1305, Oct. 29, Nov. 2006.
41. P. Zhang, H. Xue and R. Yang, "Shifting window average method for accurate frequency measurement in power systems," *IEEE Trans. Power Delivery,* accepted for publication.
42. H. Xue and P. Zhang, "Subspace-Least Mean Square method for accurate harmonic and interharmonic measurement in power systems," *IEEE Trans. Power Delivery*, accepted for publication.
43. A. Abdollahi and P. Zhang, "Noise effect on phasor and frequency measurement," *to submit to IEEE Trans. Power Systems.*

44. S. Corsi and G. N. Taranto, "A real-time voltage instability identification algorithm based on local phasor measurements," *IEEE Trans. Power Systems*, vol. 23, no. 3, pp. 1271-1279, Aug. 2008.
45. M. Glavic and T. Van Cutsem, "Wide-area detection of voltage instability from synchronized phasor measurements. Part I: Principle," *IEEE Trans. Power Systems*, vol. 24, no. 3, Aug. 2009.
46. J. F. Hauer, D. J. Trudnowski, DeSteese, "A Perspective on WAMS Analysis Tools for Tracking of Oscillatory Dynamics," *IEEE Power Engineering Society General Meeting 2007,* pp.1-10, 24-28 June 2007.
47. J. F. Hauer, W. A. Mittelstadt, K. E. Martin, J. W. Burns, H. Lee, J.W. Pierre, D.J. Trudnowski, "Use of the WECC WAMS in Wide-Area Probing Tests for Validation of System Performance and Modeling," *IEEE Trans. Power Systems*, vol.24, no.1, pp.250-257, Feb. 2009.
48. R. Yu, P. Zhang, W. Xiao and P. Choudhury, "Communication systems for grid integration of renewable energy resources," *IEEE Network*, vol. 25, no. 5, pp. 22-29, Sept./Oct. 2011.
49. Y. Wang, W. Li, P. Zhang and B. Wang, "Reliability analysis of Phasor Measurement Unit considering data uncertainty," *IEEE Trans. Power Delivery*, accepted for publication.
50. M. Begovic, D. Novosel, D. Karlsson, et al. "Wide-Area Protection and Emergency Control," IEEE Energy Infrastructure Defense Systems, Vol. 93, No. 5, May 2005, pp. 876-891
51. Zhu Guolong, Aeng Qing i, Ye tong, et al. "Integrated Protection Strategy in IP over WDM Networks," Optical Network Technology, Vol. 27, No. 1, 2003, pp. 13-16
52. K. A. Fahid, P. Gopalakrishnan, S. Cherian. "PhasorNet: A High Performance Network Communications Architecture for Synchrophasor Data Transfer in Wide Area Monitoring, Protection and Control Applications," Proceedings of the Bulk Power System Dynamics and Control - VII, Revitalizing Operational Reliability, 2007 iREP Symposium, August 2007, pp. 1-4
53. C.H. Hauser, D.E.Bakken, A. Bose, "A Failure to Communication: Next-Generation Communication Requirements, Technologies, and Architecture for the Electric Power Grid," IEEE Power and Energy Magazine, Vol. 3, No. 2, March-April 2005, pp. 47- 55
54. S. Ramamurty, B. Mukher ee, "Survivable WDM Mesh Networks, Part I Protection," Proceedings of the Eighteenth Annual Joint Conference of the IEEE Computer and Communications Societies(Infocom '99), Vol. 2, New York, 21-25 March 1999, pp. 744–751.
55. S. Ramamurthy, B. Mukher ee. "Survivable WDM Mesh Networks, Part II-Restoration," Proceeding of the IEEE International Conference on Communication (ICC '99), Vol. 3, 6-10 June 1999, pp. 2023 - 2030
56. Qin Zheng; G. Mohan. "Protection Approaches for Dynamic Traffic in IP/MPLS-over-WDM Network," IEEE Communications Magazine, Vol. 41, No. 5, May 2003, pp. S24-S29
57. R. Billinton and R. N. Allan, Reliability Evaluation of Engineering Systems, Second Edition, Plenum Press, New York, 1992
58. B.G. Jozsa, D. Orincsay. A. Kern, "Surviving Multiple Network Failures Using Shared Backup Path Protection," Proceedings of the Eighth IEEE International Symposium on Computers and Communication (ISCC 2003), Vol. 2, 30 June - 3 July 2003, Kiris-Kemer, Turkey, pp. 1333- 1340
59. Y.G. Chen. "A Cut-Based Method for Terminal-Pair Reliability," IEEE Transactions on Reliability, Vol. 45, No. 5, 1996, pp. 413-416
60. Hung-Yau Lin, Sy-Yen Kuo, Fu-Min Yeh. "Minimal Cutset Enumeration and Network Reliability Evaluation by Recursive Merge and BDD," Proceedings of the Eighth IEEE International Symposium on Computers and Communication (ISCC 2003), Vol. 2, 30 June - 3 July 2003, Kiris-Kemer, Turkey, pp. 1341 – 1346
61. C. Singh, R. Billinton, "A new method to determine the failure frequency of a complex system," IEEE Transactions on Reliability, Vol. R-23, 1974, pp. 231-234
62. S. V Buldyrev, R. Parshani, G. Paul, H. E. Stanley and S. Havilin, "Catastrophic cascade of failures in interdependent networks," Nature, vol. 464, April 2010pp. 1025-1-28.
63. Rosato, V. et al. Modelling interdependent infrastructures using interacting dynamical models. Int. J. Crit. Infrastruct. 4, 2008, pp.63–79.

64. Peerenboom, J., Fischer, R. & Whitfield, R. Recovering from disruptions of interdependent critical infrastructures, in Proc. CRIS/DRM/IIIT/NSF Workshop Mitigat. Vulnerab. Crit. Infrastruct. Catastr. Failures (2001)
65. Rinaldi, S., Peerenboom, J. & Kelly, T. Identifying, understanding, and analyzing critical infrastructure interdependencies. IEEE Contr. Syst. Mag. Vol. 21, 2001, pp.11–25.
66. Laprie, J. C., Kanoun, K. & Kaniche, M. Modeling interdependencies between the electricity and information infrastructures. SAFECOMP-20074680, 2007, pp. 54–67.
67. Kurant, M. & Thiran, P. Layered complex networks. Phys. Rev. Lett. 96, 138701, 2006.
68. Panzieri, S. & Setola, R. Failures propagation in critical interdependent infrastructures. Int. J. Model. Ident. Contr. Vol. 3, 2008, pp. 69–78.
69. C. Rakpenthai, S. Premrudeepreechacharn, S. Uatrong it, and N. R. Watson, "An optimal PMU placement method against measurement loss and branch outage", IEEE Trans. Power Del., vol. 22, no. 1, pp. 101-107, Jan. 2007.
70. A. Antonopoulos, J.J. o'Reilly, P. Lane, et al. "A Frame work for the Availability Assessment of SDH Transport Networks," Proceedings of the 2nd IEEE Symposium on Computers and Communications, Alexandria, Egypt, July 1-3, 1997.
71. Hung-Yau Lin, Sy-Yen Kuo, Fu-Min Yeh. "Minimal Cutset Enumeration and Network Reliability Evaluation by Recursive Merge and BDD," Proceedings of the Eighth IEEE International Symposium on Computers and Communication (ISCC 2003), Vol. 2, 30 June - 3 July 2003, Kiris-Kemer, Turkey, pp. 1341 – 1346.
72. C. T. Nguyen and K. Srinivasan, "A New Technique for Rapid Tracking of Frequency Deviations Based on Level Crossings," IEEE Transactions on Power Apparatus and Systems, vol. PAS-103, no. 8, pp. 2230-2236, 1984.
73. M. M. Begovic, P. M. Djuric, S. Dunlap and A. G. Phadke, "Frequency tracking in power networks in the presence of harmonics," IEEE Trans. Power Del., vol. 8, no.2, pp. 480-486, 1993.
74. M. Sachdev and M. Giray, "A Least Error Squares Technique For Determining Power System Frequency," IEEE Transactions on Power Apparatus and Systems, vol. PAS-104, pp. 437-444, 1985.
75. R. Chudamani, K. Vasudevan and C. S. Ramalingam, "Real-Time Estimation of Power System Frequency Using Nonlinear Least Squares," IEEE Trans. Power Del., vol. 24, no.3, pp. 1021-1028, 2009.
76. A. Girgis and T. Daniel Hwang, "Optimal Estimation Of Voltage Phasors And Frequency Deviation Using Linear And Non-Linear Kalman Filtering: Theory And Limitations," IEEE Transactions on Power Apparatus and Systems, vol. PAS-103, no. 10, pp. 2943-2951, 1984.
77. P. K. Dash, A. K. Pradhan, G. Panda, "Frequency estimation of distorted power system signals using extended complex Kalman filter," IEEE Trans. Power Del., vol. 14, no. 3, pp. 761 - 766, 1999.
78. A. Routray, A. K. Pradhan and K. P. Rao, "A novel Kalman filter for frequency estimation of distorted signals in power systems," IEEE Transactions on Instrumentation and Measurement, vol. 51, no.3, pp. 469-479, 2002.
79. C. Huang, C. Lee, K. Shih and Y. Wang, "Frequency Estimation of Distorted Power System Signals Using a Robust Algorithm," IEEE Trans. Power Del., vol. 23, no.1, pp. 41-51, 2008.
80. M. Akke, "Frequency estimation by demodulation of two complex signals," IEEE Trans. Power Del., vol. 12, no.1, pp. 157-163, 1997.
81. M. Manana Canteli, A. Ortiz Fernandez, L. Ignacio Eguiluz and C. Renedo Estebanez, "Three-Phase Adaptive Frequency Measurement Based on Clarke's Transformation," IEEE Trans. Power Del., vol. 21, no.3, pp. 1101-1105, 2006.
82. T. S. Sidhu, "Accurate measurement of power system frequency using a digital signal processing technique," IEEE Transactions on Instrumentation and Measurement, vol. 48, no.1, pp. 75-81, 1999.
83. J. Szafran and W. Rebizant, "Power system frequency estimation," IEE Proceedings - Generation, Transmission and Distribution, vol. 145, no. 5, pp. 578-582, 1998.

84. A. Phadke, J. Thorp and M. Adamiak, "A New Measurement Technique for Tracking Voltage Phasors, Local System Frequency, and Rate of Change of Frequency," IEEE Transactions on Power Apparatus and Systems, vol. PAS-102, no. 5, pp. 1025-1038, 1983.
85. M. Wang and Y. Sun, "A Practical, Precise Method for Frequency Tracking and Phasor Estimation," IEEE Trans. Power Del., vol. 19, no. 4, pp. 1547-1552, 2004.
86. Jun-Zhe Yang and Chih-Wen Liu, "A precise calculation of power system frequency and phasor," IEEE Trans. Power Del., vol. 15, no. 2, pp. 494-499, 2000.
87. Y. Zhang, P. Markham, T. Xia, L. Chen, Y. Ye, Z. Wu, Z. Yuan, L. Wang, J. Bank, J. Burgett, R. W. Conners and Y. Liu, "Wide-Area Frequency Monitoring Network (FNET) Architecture and Applications," IEEE Transactions on Smart Grid, vol. 1, no.2, pp. 159-167, 2010.
88. Z. Leonowicz, T. Lobos and J. Rezmer, "Advanced spectrum estimation methods for signal analysis in power electronics," IEEE Trans. Ind. Electron., vol. 50, no. 3, pp. 514-519, 2003.
89. V. V. Terzija, M. B. Djuric and B. D. Kovacevic, "Voltage phasor and local system frequency estimation using Newton type algorithm," IEEE Trans. Power Del., vol. 9, no. 3, pp. 1368-1374, 1994.
90. V. V. Terzija, V. Stanojevic, M. Popov and L. van der Sluis, "Digital Metering of Power Components According to IEEE Standard 1459-2000 Using the Newton-Type Algorithm," IEEE Transactions on Instrumentation and Measurement, vol. 56, no. 6, pp. 2717-2724, 2007.
91. H. Karimi, M. Karimi-Ghartemani and M. R. Iravani, "Estimation of Frequency and its Rate of Change for Applications in Power Systems," IEEE Trans. Power Del., vol. 19, no. 2, pp. 472-480, 2004.
92. P. K. Dash, D. P. Swain, A. C. Liew, S. Rahman, "An adaptive neural network approach for the estimation of power system frequency," IEEE Transactions on Power Systems, vol. 11, no. 4, pp. 1730-1735, 1996.
93. I. Kamwa, A. K. Pradhan and G. Joos, "Adaptive Phasor and Frequency-Tracking Schemes for Wide-Area Protection and Control," IEEE Trans. Power Del., vol. 26, no. 2, pp. 744-753, 2011.
94. J. Ren and M. Kezunovic, "Real-Time Power System Frequency and Phasors Estimation Using Recursive Wavelet Transform," IEEE Trans. Power Del., vol. 26, no. 3, pp. 1392-1402, 2011.
95. M. Mojiri, M. Karimi-Ghartemani and A. Bakhshai, "Estimation of Power System Frequency Using an Adaptive Notch Filter," IEEE Transactions on Instrumentation and Measurement, vol. 56, no. 6, pp. 2470-2477, 2007.
96. A. Bracale, G. Carpinelli, Z. Leonowicz, T. Lobos and J. Rezmer, "Measurement of IEC Groups and Subgroups Using Advanced Spectrum Estimation Methods," IEEE Transactions on Instrumentation and Measurement, vol. 57, no. 4, pp. 672-681, 2008
97. I. Y. Gu and M. H. J. Bollen, "Estimating Interharmonics by Using Sliding-Window ESPRIT," IEEE Trans. Power Del., vol. 23, no. 1, pp. 13-23, 2008.
98. H. Xue and P. Zhang, "Subspace Least Mean Square method for accurate harmonic and interharmonic measurement in power systems," IEEE Trans. Power Del., Accepted for publication.
99. Kay S. M., Fundamentals of Statistical Signal Processing, Volume I: Estimation Theory, Prentice Hall; 1993
100. Rife D., Boorstyn R. "Single tone parameter estimation from discrete-time observations," IEEE Trans Information Theory, vol. 20 no. 5, pp. 591-598, Sep. 1974
101. Barry G. Quinn, "Estimating frequency by interpolation using Fourier coefficients" IEEE Trans Signal Processing, vol. 42 no. 5, pp. 1264-1268, May 1994
102. Kay S. "A fast and accurate single frequency estimator," IEEE Trans Acoustics, Speech and Signal Processing, vol. 37 no. 12, pp. 1987-1990, Dec. 1989
103. Tretter S. "Estimating the frequency of a noisy sinusoid by linear regression," IEEE Trans Information Theory, vol. 31 no. 6, pp. 832-835, Nov. 1985
104. A. G. Phadke, J. S. Thorp, Synchronized Phasor Measurement and Their Applications, New York: Springer Science+Business Media LLC, 2008

105. Papoulis A., Probability, Random Variables and Stochastic Processes, 3rd Ed., Mcgraw-Hill College, 1991.

Project Title: Plasmonic Nanostructures for Solar Energy Harvesting
Industrial Partner: SciTech Associates, LLC
PI: Brian G. Willis

Project Objectives:
Our objectives were to investigate plasmonic nanostructures for solar energy harvesting to extract power from radiation-induced local surface plasmon resonances in nanostructures. Our research program has focused on the nanofabrication of antenna and rectification elements for extracting DC power from plasmonic devices. These two elements – the antenna and the rectifier – form a rectenna and are the key components of the solar conversion device. Much of the previous work in the literature has been directed at the antenna component, but our unique contribution is to address the rectification element. There are no semiconductors or band gap limitations and power extraction is based solely on the interaction of light with metallic nanostructures. The plasmonic devices are compatible with the requirements of future technologies including high efficiency, roll-to-roll processing, low cost substrates, and the use of non-toxic, recyclable, and earth abundant materials.

Background:
Solar energy is widely expected to play a significant role for energy generation in the future, but making this a reality requires a significant improvement of efficiency and reduction of costs. Recently, the Department of Energy has stated a goal of $1/watt (installed) and has noted that reaching the goal will require new innovations beyond current technologies. Existing technologies are expected to continuously improve but are reaching limits. "Dramatically" new ideas are needed to make solar energy cost competitive with fossil fuels. Some concepts that should be considered for new technologies include high efficiency devices, roll-to-roll processing, flexible substrates, and the use of non-toxic, recyclable, and earth abundant materials. The current research project addresses these needs with a novel type of solar energy harvesting device concept.

Project Tasks:
The team consists of Dr. Willis and graduate research assistants at UConn, and scientists at SciTech Associates. SciTech is a small business with objectives to develop plasmonic nanostructures for solar energy devices and related technologies. The company has intellectual property and a long history with electromagnetic energy conversion devices. Paul Cutler, CEO of SciTech, is a former professor of Physics at Pennsylvania State University, State College PA. His group has performed fundamental proof-of-concept experiments for plasmonic solar energy devices. Dr. Willis and his group bring complimentary expertise in nanofabrication to make the proposed devices. A key requirement of our plasmonic nanostructures is to have asymmetric tunnel junctions with critical dimensions on the order of 1 nm. These dimensions both maximize the local field enhancement and allow charge to flow through the circuit. Dr. Willis has developed a unique and enabling capability based on atomic layer deposition (ALD) to fabricate the required nanojunctions. As a team, our objectives are to develop the science and technology of plasmonic solar energy conversion devices, including the fabrication of working prototypes.

Experiment:

Nanofabrication of rectenna devices was carried out at the Penn State Nanofabrication facility. Two separate designs were investigated in two rounds of nanofabrication. The first, shown in Figure 1, was an array of 10,000 antenna structures arranged in parallel. The antenna structures consist of multiple sets of paired metallic lines, each roughly 200 nm in width that run parallel to each other, with triangular tip structures on one structure projecting towards the other. The tip height is approximately 100 nm, and the spacing between the end of the tip and the adjacent line is 50 – 60 nm as fabricated. The goal of the tip geometry is to create an asymmetric tunnel junction at the narrow point between the tip and the adjacent line. The physics of tunneling is not described here, but is discussed at great length in our publications. The essential concept is that geometric asymmetry creates a diode like response in the tunneling current. The tips are made of Pd to promote selective area growth of Cu. Cu grows selectively on metals that do not have an oxide layer and catalzye hydrogen dissociation. To date, both Pd and Pt have been used successfully as seed layers to promote selective area ALD growth.

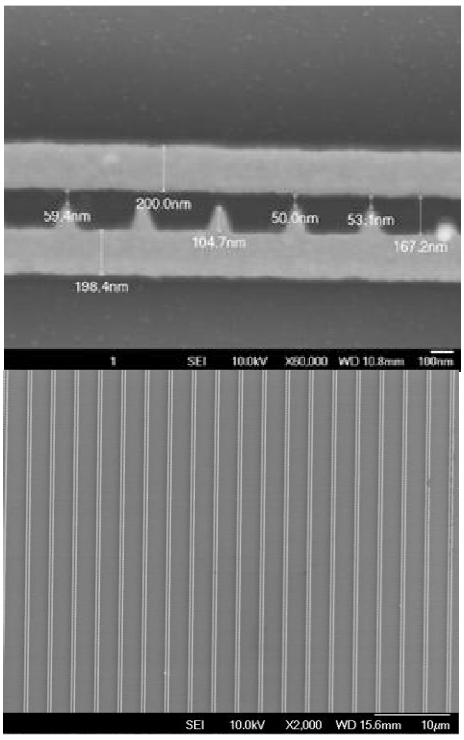

Figure 1. SEM image of first round of devices with 100 nm tip height. Top shows zoom of one electrode pair from bottom.

During the first round of experiments it was found that the device design, with multiple lines to create a large array of devices, led to practical difficulties due to electrical shorting between electrodes. Shorting occurred due to small particles that landed on the array between metal lines. Since our laboratory is not a cleanroom, it was not possible to control the particulates. Even a small number of particulates affect the electrical response of the array. A second design consisting of single rows of antenna with only 1000 tips was developed to overcome the shorting problem. Figure 2 shows a schematic of the second design. There are 10 separate pairs of electrodes, each with separate wire bonding pads. The use of separated pairs of electrodes in a single row greatly reduces the likelihood that particles will short all of the devices. A secondary electron microscopy image of the "as-fabricated" devices is shown in Figure 3. These antenna structures also have gap spacing near 50 nm, but the height of the tip is 200 nm to increase the aspect ratio, intended for greater asymmetry. The uniformity of the gap distance is improved over the first design, but ranges from 52 to 64 nm.

A custom reactor and sample holder were created to enable in-situ electrical measurements taken during ALD growth without disturbing the sample or having to remove it from the reactor. The devices are implemented on 5mm x 5 mm die from a silicon wafer. (Silicon wafers are not necessary, but are convenient for handling in the nanofabrication facility. We envision that future work will use quartz wafers.) The dies are fixed to a ceramic chip carrier and wire bonded to electrical connections for in-situ electrical measurements during ALD growth. The reactor is a 1.125" glass tube heated by an external furnace and fed by stainless steel piping with reactants and inert gases. The ALD growth temperature is near 200°C at reduced pressure near 1 Torr. Reactants include the Cu metal precursor and hydrogen gas. Helium is used as inert and purge gases to promote good temperature uniformity. The Cu metal precursor is 2,2,6,6- tetramethyl-3,5-heptanedionato Cu(II), also referred to as $Cu(thd)_2$. This precursor is known for its selective growth characteristics. It grows on metal seed layers, but not on insulating oxide regions.

We use the selective growth to modify the antenna tip structures without shorting the electrodes. Selective growth is enabling for this rectenna concept. The reactor was designed to have both low and high vacuum capability for growth and electrical measurements, respectively. We have previously discovered that high vacuum (10^{-6} Torr) is needed for field emission experiments to avoid damaging the devices. We have discovered that field emission can be used to monitor tip-gap spacing at large separation, before tunneling is reached. Direct tunneling from tips to counter electrodes in vacuum requires spacing near 2-3 nm, so that tunneling is only observed when the gap is very small. Field emission can be observed at much larger spacing so that the process can be monitored over a larger range of tip-gap separation.

Results:

ALD selective area growth of Cu was used to modify the tip-gap spacing of the antenna structures. The objective is to maintain the geometry of the tip while converging junctions to tunneling. Tunneling through vacuum requires that the tips be grown until the spacing is in the range of 2-3 nm. Deposition occurs on both the tips and counter electrodes so that for a 50 nm gap, approximately 24 nm must be deposited. The blanket growth rate for our Cu ALD chemistry is approximately 0.04 nm/cycle, so that in the best case, 600 cycles may be required to converge tips to tunneling. In practice, more deposition cycles are required to reach tunneling. This can partially be explained by a slowing of the growth that occurs as the tip-gap spacing narrows to nm dimensions. However, we believe other factors are also at play, including a slowing of growth as Pd seed layer effects attenuate. From our prior work, we know that Pd mixes with Cu during

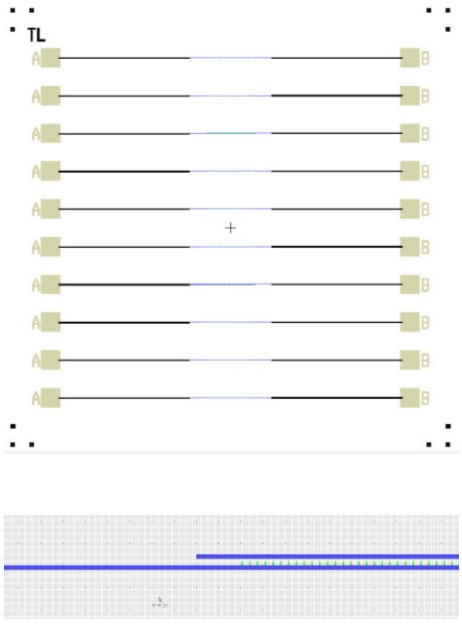

Figure 2. Schematic of second round devices. There are 10 sets of separate arrays with 1000 tips each.

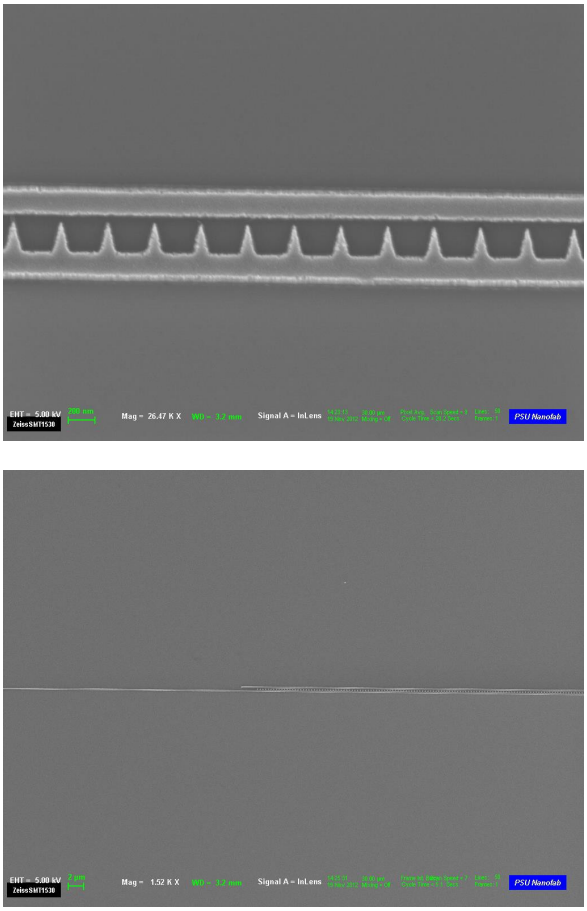

Figure 3. SEM images of second-round nanofabricated antenna arrays. Top image is a zoom of bottom image, which is an isolated single line of paired electrodes.

deposition and we anticipate that Pd promotes surface reactions. In particular, Pd likely plays a critical role in hydrogen chemisorption.

Examples of successful selective area growth on the antenna are shown in Figures 4 and 5 for the first and second round of devices, respectively. In Figure 4, growth is evident from the reduction of the tip-gap spacing and the increase in roughness. Figure 4, bottom shows a high resolution image of several tips after 700 ALD cycles at a sample temperature of 235°C. A rough grain structure of the films is evident. The tip-gap spacing varies between devices and is about 10 nm for the smallest. Note that very small gap spacing cannot be imaged by SEM. EDAX analysis and SEM imaging confirm that growth occurs selectively on Pd seeded regions and not on oxide covered area between electrodes. Devices shown in Figure 5 were grown at lower temperatures and have a smoother coating that is more conformal to the high aspect ratio of the tips. However, the tip-gap spacing is still quite large in the image. One of the conclusions from this work is that further study is required to better understand the evolution of nanostructure during ALD growth. It is expected that antenna nanostructure is strongly related to substrate effects from the Pd seed layer. Better understanding may aid in producing smooth, uniform tunnel junctions with high aspect ratio.

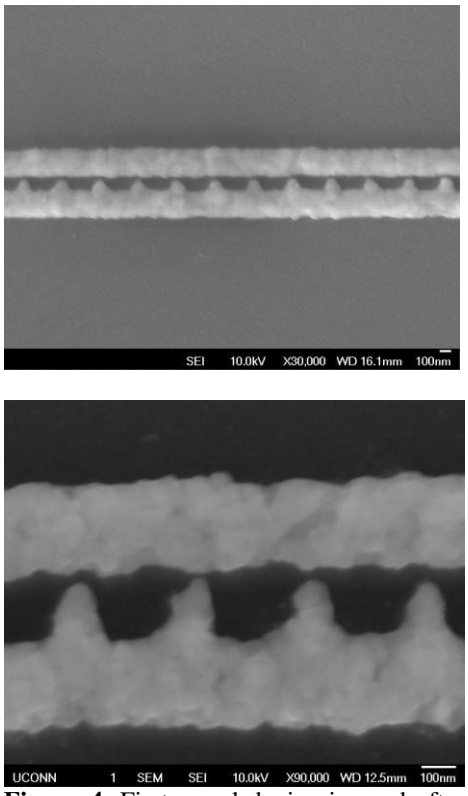

Figure 4. First-round device imaged after ALD deposition. The reduction of tip-gap spacing and granularity of the deposited Cu are evident.

Convergence to tunneling has been monitored by in-situ electrical measurements. It was expected that current-voltage (IV) curves would show a trend of increasing current with increasing number of ALD cycles. It was also expected that the tip geometry would create asymmetry of the electrical response with diode like character. Figure 6 shows experimental data taken in our reactor using electrical measurements. The procedure was to interrupt the process at several stages of growth and measure IV curves using a source meter unit connected to the samples through the chip carrier and wire bonds to the rectenna arrays. The data show IV curves after 50, 100, 200, 500, and 800 ALD cycles from one experiment. The trend is as expected, the current at a given voltage increases as the tip-gap narrows during growth. The curves also show the expected asymmetry with diode-like characteristics (ignore the data near -3 V, which is an artifact of the voltage sweep). At positive voltage, the upward curvature is less exponential than expected and may indicate that leakage currents also contribute to the total current. However, these data show proof-of-concept for the tunneling of the antenna electrical properties by selective area ALD.

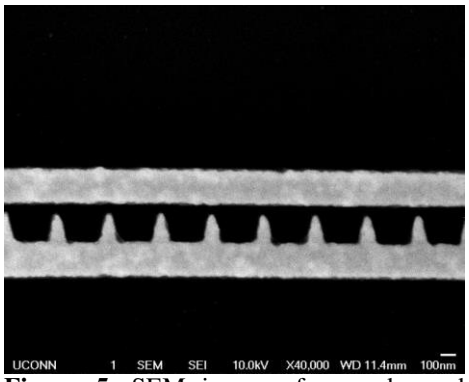

Figure 5. SEM image of second-round device after Cu ALD showing smoother growth at lower temperatures.

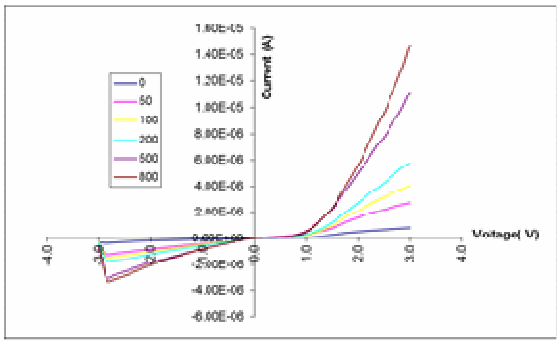

Figure 6. In-situ electrical data recorded during ALD experiments. The IV curves are plotted for increasing number of ALD cycles from 0 to 800.

measured experimentally.

Summary:

In summary, we have designed and nanofabricated nanoscale antenna devices to test selective area ALD growth for fabrication of nanoscale rectenna. Results show that antenna can be made into asymmetric tunnel diodes for rectification. Further study of the ALD processes is recommended to provide greater control for smoother electrodes. Solar conversion efficiency will depend on geometric asymmetry, which needs to be optimized. Preliminary electrical data show proof-of-concept for the asymmetric tunneling diodes. Static current-voltage data match expectations based on tunneling theory. New device array designs less susceptible to extraneous factors such as shorting by particulates are required to make further progress. One such design was successfully fabricated in this work. Lastly, it is recommended that antenna design be considered in future work to maximize the interaction between radiation and electrically active nanostructures.

Figure 7 shows another set of experimental data taken in-situ after 800 growth cycles. These data have strong asymmetry and clear exponential turn-on character. They match data expected for tunneling devices and show that the devices are working. From these data, it was possible to measure the responsivity, a key device characteristic related to power output. These data are shown in Figure 7(b). Mayer et al. have shown that critical device properties such as rectified voltage and quantum efficiency are proportional to responsivity (Mayer et al., J. Vac. Sci. Technol. B, v. 29 p. 041802, 2011). Further analysis requires assumption of the optically induced oscillation voltage, which has not been

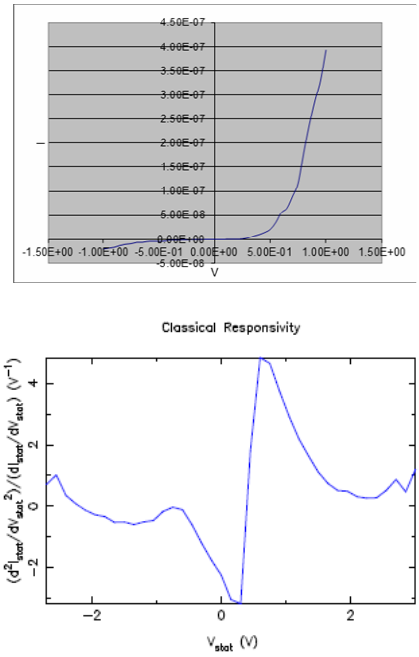

Figure 7. Current-voltage (top) and responsivity (bottom) curves from a sample after 800 cycles of growth. Top shows diode character.

Patents: No new patents were filed from this short work.

Publications / Presentations:

1. Portions of this work were presented at the Cambridge Nanotech User Meeting in Atlanta, GA, November 2011, the SPIE meeting, August 2013, San Diego, and the Hudson Chapter AVS meeting October, 2013.
2. A publication is in print, "Nanoscale Devices For Rectification Of High Frequency Radiation From The Infrared Through The Visible: A New Approach," by Nicholas M. Miskovsky, Paul H. Cutler, A. Mayer, Brock L. Weiss, Brian Willis, Thomas E. Sullivan and Peter B. Lerner, Journal of Nanotechnology v. 2012 ID 512379.
3. This work is also planned to be included as a chapter in a forthcoming book on alternative solar energy.
4. There is also a conference proceeding from the SPIE meeting, "The role of geometry in nanoscale rectennas for rectification and energy conversion," Nicholas M. Miskovsky; Paul H. Cutler; Alexandre Mayer; Brian G. Willis; Darin T. Zimmerman; Gary J. Weisel; James M. Chen; Thomas E. Sullivan; Peter B. Lerner, Volume 8824, Next Generation (Nano) Photonic and Cell Technologies for Solar Energy Conversion IV, Eds. Oleg V. Sulima; Gavin Conibeer San Diego, California, August, 2013.
5. Lastly, an additional manuscript is currently in preparation.